Predicting glacier accumulation area distributions

Katherine E. Arrell

Predicting Glacier Accumulation Area Distributions

Katherine E. Arrell

Thesis submitted for the degree of Doctor of Philosophy

Department of Geography
Durham University

June 2005

DECLARATION

This thesis is submitted in accordance with the requirements of the Durham University for the Degree of Doctor of Philosophy.

This thesis is the result of the authors own work. References to other authors contained herein are acknowledged at the appropriate point in the text.

ABSTRACT

A mass balance model based on energy balance at the terrain surface was developed and used to predict glacier accumulation areas in the Jotunheimen, Norway. Spatially distributed melt modelling used local climate and energy balance surfaces to drive predictions, derived from regional climate and topographic data. Predictions had a temporal resolution of 1 month and a spatial resolution of 100 m, which were able to simulate observed glacier accumulation area distributions.

Data were stored and manipulated within a GIS and spatial trends and patterns within the data were explored. These trends guided the design of a suite of geomorphologically and climatologically significant variables which were used to simulate the observed spatial organisation of climatic variables, specifically temperature, precipitation and wind speed and direction.

DEM quality was found as a critical factor in minimising error propagation. A new method of removing spatially and spectrally organised DEM error is presented using a fast Fourier transformation. This was successfully employed to remove error within the DEM minimising error propagation into model predictions.

With no parameter fitting the modeled spatial distribution of snowcover showed good agreement with observed distributions. Topographic maps and a Landsat ETM+ image are used to validate the predictions and identify areas of over or under prediction. Topographically constrained glaciers are most effectively simulated, where aspect, gradient and altitude impose dominant controls on accumulation. Reflections on the causes of over or under prediction are presented and future research directions to address these are outlined.

Sensitivity of snow accumulation to climatic and radiative variables was assessed. Results showed the mass balance of accumulation areas is most sensitive to air temperature and cloud cover parameterisations. The model was applied to reconstruct snow accumulation at the last glacial maximum and under IPCC warming scenarios to assess the sensitivity of melt to changing environmental conditions, which showed pronounced sensitivity to summer temperatures

Low data requirements: regional climate and elevation data identify the model as a powerful tool for predicting the onset, duration and rate of melt for any geographical area.

Acknowledgements

This PhD research project was funded by a postgraduate studentship from the Department of Geography, University of Durham.

I gratefully acknowledge the unstinting help, advice and encouragement of my departmental supervisors Dr. Ian S. Evans and Dr. Daniel N. M. Donoghue.

I would also like to thank both the Norwegian Mapping Institute: Statens Kartwerk for supplying the digital elevation data; and the Norwegian Meteorological Office for providing the climate datasets. Data that were essential components in the completion of this thesis.

I would like to take this opportunity to thank a number of different people for their help, encouragement and support throughout the completion of this thesis: to my family for accepting that I was going to be a perpetual student; to my fellow PhD students, in no particular order: Alona Armstrong, Vicky Holliday, James Smith, Matt Wright, Simon Nelis, Duncan Wishart, Sarah King, Kay McManus, Erin McClymont, Elizabeth Mackie, Huda, John Clayton, Andy Clarke; Dave Roberts, Gordon MacLeod and Dave Bridgland for making Durham so much fun. All of the support staff in the Department of Geography, especially Sharon, Lisa, Derek, Stella and Niamh for their kindness. Hatfield College for being the best college, and for all the fantastic MCR events and formals.

I also owe a special debt of thanks to the School of Geography, University of Leeds for helping to balance my career with the completion of my thesis!

I wish to express my thanks to Steve Wise and Antony Long for a most stimulating and enlightening discussion during the examination of this thesis

Finally a special thanks to Matt for being so much fun and being so supportive during the completion of this thesis.

Katherine E. Arrell
Durham, June 2005.

TABLE OF CONTENTS

LIST OF FIGURES

LIST OF TABLES

CHAPTER ONE
INTRODUCTION

1.1. Introduction and Research Rationale

Earth surface systems have known sensitivities to changing climate. However, the characteristics and behaviour of these sensitivities are not fully understood (Wilcock and Iverson, 2003). The cyrosphere in particular has been shown to respond to recent warming but responses are poorly understood, where isolation of cause and effect is problematic. This research provides a mechanism of improving our understanding of these sensitivities by developing a model to predict snow accumulation and melt as a function of climate and energy balance. By improving our understanding of the controls on snow accumulation better estimates and interpretation of responses to changes in these controls can follow.

1.2. Controls on Glacier Distributions

The controls on glacier accumulation can be conceptualised into topographic, climatic and energy balance variables. This research attempts to predict accumulation as a function of all three of these controls, in contrast to many other published approaches that largely focus on one or two, and can consequently only account for a proportion of observed variation (McKay and Gray, 1981). A spatially distributed model is presented where high spatial variability in modelled climatic inputs, results in high variability in resultant glacier accumulation distributions.

Temperature and precipitation form the major climatic controls on snow accumulation, where air temperatures less than ~ 1°C and positive precipitation receipts are required for snow to accumulate. Temperature and precipitation profiles above the surface also impose controls on accumulation, where atmospheric stability and altitudinal lapse rates determine their vertical

distribution and consequently a vertical control on snow accumulation. Climatic variables also impose controls on local energy balance variables. Atmospheric temperature and temperature gradients directly above the surface control longwave emittance and turbulent heat exchanges respectively; where the latter provides a more important control on determining the energy available to melt. Cloud cover is also important in determining the local energy balance, where it provides a dominant control on the magnitude and character of radiation reaching the ground.

Energy balance variables largely determine the amount of melt that can occur, driven by shortwave (direct and diffuse components), longwave and turbulent heat exchanges. Energy is largely conceptualised as a local balance where positive values indicate fluxes towards the surface. Controls on the net balance at a location, include atmospheric, topographic and temporal conditions. Where atmospheric transmittance and emisstivity, determined by atmospheric composition, temperature and cloud cover impose controls on the amount of radiation reaching the ground, termed global radiation and the longwave emittance of the atmosphere. High concentrations of particulates including aerosols, dust and heavy cloud cover conditions increase the scattering, reflectance and absorption of solar radiation, decreasing the amount of radiation incident at the top of the atmosphere reaching the ground. Topography, specifically geographic position and surface slope determine the amount of radiation reaching and transferred to the surface. Where relative position to the sun, determines the intensity and duration of solar exposure and surface slope determines the efficiency with which this radiation is transferred to the surface, where on steeper slopes less radiation is transferred. Topographic shading and exposure also impose local controls on the net radiation receipt. Temporal variations in radiation receipt controlled by time of year and day, control the amount of radiation reaching the surface at any one point, driven by changing solar position.

Topography places dominant controls on the magnitude and distribution of climatic and energy balance variables, and consequently is a major element of this thesis. Strong local gradients in climate (Barry, 1992) and energy balance (Dubayah *et al.*, 1990; Hock, 1999) exist in mountainous areas, driven by topographic variations, and result in a strong topographic component in observed glacier distributions.

Snow accumulation is also controlled by local changes in mass through redistribution, specifically avalanching and snow entrainment and deposition by wind. The relative contribution that these controls place is largely a function of topography (slope and convexity) and climate (wind speeds and precipitation receipts) (McClung and Schaerer, 1993).

Methods of predicting snow accumulation use information on these variables or their controls to predict snow accumulation and models differ in complexity and the approach they take to simulating accumulation patterns. Snow accumulation rather than glacier distributions form the focus of many models, and the research presented here, negating the need to study controls other than accumulation and melt alone control glacier extent, specifically flow.

1.3. Outline of model presented

A primary limitation of the models presented within the literature is obtaining a balance between data requirements and resolution of predictions. Highly simplified models, with little spatial variability in climatic inputs often fail to simulate observed spatial variability in snow accumulation. In contrast models that simulate local variability are often complex in nature, driven by local climate data (measured on the glacier) and cannot be applied to other study areas. This research addresses this limitation by developing a predictive model that is driven by readily available regional climate and topographic data to initially predict local scale climate and energy balance datasets and secondly to predict snow accumulation.

The inherent spatial element of this thesis uses a geographical information system (GIS) to store, manipulate and interpret datasets, with energy balance modelling completed within a number of Java programmes. The model is composed of topographic, climatic and energy balance components, which is reflected in the structure of this thesis.

This research presents a valuable snow melt modeling and addresses the following research aims.

1.4. Research Aims

The overall aim of this research is to predict small glacier accumulation areas using accessible data, providing a repeatable and flexible model that can be applied to other geographical areas in the future. Small glaciers, less than 5 km in length were the focus of this research as prediction of larger glaciers accumulation areas would require extensive modeling of local feedbacks and glacier self-regulation. Spatially distributed climatic, topographic and energy balance variables are identified as critical to predict the observed spatial variability in glacier distributions. To address this overall research aim three specific research objectives were identified.

Research Objective 1

To create a local climate dataset of temperature and precipitation, wind and cloud cover using regional climate and topographic data.

Research Objective 2

To create a suite of topographic variables from digital elevation data to improve earth surface process modelling.

Research Objective 3

To predict spatially distributed glacier accumulation areas using regional climate and topographic data.

1.4 Thesis structure

Chapter Two provides a review of the available literature relevant to the development of a snow accumulation model and predicting glacier distributions in mountainous areas.

Chapter Three Introduces the area of the Jotunheimen in southern Norway the chosen area of study for this thesis research. This chapter describes the geological and geomorphological history of the Jotunheimen, and outlines the contemporary climate in the region. This chapter forms a necessary context for the interpretation of model output data produced during this PhD study.

Chapter Four describes the methods by which a digital elevation model (DEM) of the study area was examined and interrogated using terrain analysis techniques in a Geographical Information System to derive a suite of geomorphological and climatologically significant variables to improve local climate predictions that were used in later modelling.

Chapter Five describes the climate data that have been collated from field stations in and around the study area, identifying seasonal and spatial trends in the data to better inform climate modelling techniques employed in predictive climate modelling in *Chapter Six*.

Chapter Six presents the methods by which the climate data collated for the study area have been used in conjunction with the terrain variables from *Chapter Four* to derive local lapse rates for temperature and precipitation, cloud cover data, wind speed and direction in Jotunheimen.

Chapter Seven presents a mass balance model with spatially distributed energy balance, heating and melt components to predict temporally and spatially distributed monthly snow accumulation in Jotunheimen using the predicted climatic datasets

Chapter Eight presents the resultant outputs of the model developed and discusses these results in the context of similar studies, evaluating the success and sensitivities of the model in comparison to the present day distributions of glaciers in Jotunheimen.

Chapter Nine presents the conclusions of this thesis, evaluates the success of the research techniques employed and makes recommendations for future work.

CHAPTER TWO

METHODS OF PREDICTING GLACIER DISTRIBUTIONS

2.1. Introduction

A glacier is an ice mass that persists in its topographic location throughout successive summer and winter seasons. Glaciers are characterised by an area that accumulates snow or ice (the accumulation area) and an area that loses snow or ice (the ablation area). Snow or ice can accumulate through gains by precipitation, wind drifting, avalanching, riming and hoar frost. Snow can ablate through losses by melting, evaporation, sublimation, wind drifting, avalanching and calving (if the terminus of the glacier enters a water body). Glaciers are not stationary, and have a transfer of snow or ice (mass) from the accumulation area to the ablation area. The characteristics of this movement or flow are determined by the glacier's bed conditions. Glaciers can be characterised according to their size, topographic context, basal conditions, temperature and changes in mass.

Glacier initiation, longevity and development is dependent upon a suite of climatic and topographic parameters that function over different spatial and temporal scales (Section 1. 2). Efforts to predict and understand glacier distributions largely attempt to quantify one or more of these parameters, but often only at small temporal and spatial scales (Hannah *et al.*, 2000). This chapter briefly summarises the contemporary approaches to predicting glacier distributions. Five types of prediction model are identified and presented with examples and are critically evaluated with respect to the aim of this research.

2.2. Classification of glacier prediction models

Glacier distribution prediction methods vary in complexity, data requirements, temporal and spatial scales and the parameters they model. These models can be categorised in different ways, Valentine *et al.* (2001) differentiates between statistical, conceptual, lumped, semi-distributed and

physically based models. This classification is conceptual and provides no indication of the parameters included or the scale of the predictions. The present research outlines a new classification of glacier prediction models, differentiating by modelled parameters, data requirements and scale, creating a more informative categorisation (Table 2.1). Progresssion from type 1 to type 5 moves from largely statistical point based methods to distributed complex process models. The character and limitations of these models are described in the subsequent sections.

Other approaches that do not directly fit into the above classification include quantifying glacier volume changes using a times series, of either topographic maps (Andreassen, 1999; Ostrem and Haakensen, 1999) or remotely sensed data such as terrestrial and airborne photography (Conway *et al.*, 1999; Mittaz *et al.*, 2002; Tapeiner *et al.*, 2001), airborne and orbital visible / infra-red sensors (Bitner *et al.*, 2002; De Wildt *et al.*, 2002) and airborne or orbital active imaging radar (Demuth and Pietroniro, 1999). Estimates derived using topographic maps are highly sensitive to the contour accuracy and are dependent upon a comparable time series of maps. Remotely sensed data is increasingly used in glaciological applications as it provides a cheaper, informative and repeatable survey of potentially remote and inaccessible areas. The remotely sensed data can be used both to delineate glacier extent and to monitor changes in glacier volume. Sensor data is used to create digital elevation models (DEMs) to represent the glacier surface: successive DEMs of the same area will show changes in the height of this surface, implying changes in glacier volume. Demuth and Pietroniro (1999) argued that airborne or orbital active imaging radar is preferential to alternative sensor data as it not restricted by cloud cover, shadow or time of day. This opinion is in contrast to Gao and Lui (2001) who conducted a comparative study of sensor suitability for glaciological studies, reporting that each had advantages and disadvantages and no one sensor type was optimal. Cogley *et al.* (2001) agreed with the findings of Demuth and Pietroniro (1999) that active imaging radar provides the most robust imagery, but they suggested that its cost and large file sizes limit its usability. They proposed that browse active imaging radar images provide a compromise; these reduce the resolution and information contact of the original image.

A review of remotely sensed investigations in the cyrosphere is provided by (Gao and Liu, 2001). Although this is a rapidly evolving area limitations still exist surrounding, data extraction, resolution, reliability and cost. Further advances in the calibration of remotely sensed data will hopefully provide a rapid glacier monitoring program to help improve our understanding of atmospheric, climatic and surface process interactions that could be fed into model development and parameterisation.

Level	Name	Parameters	Data requirements / calibration	Scale of predictions	Examples
1	Temperature altitude model	Altitude, temperature, precipitation	Altitude, local temperature and precipitation and altitude of ELA to calibrate.	Large spatial scale trends, doesn't model local variations although is locally calibrated. Long temporal scales, not short fluctuations.	Lie *et al*., 2003; Dahl and Nesje 1992
2	Temperature index model	Altitude, temperature	Altitude, temperature. Calibration of degree-day factor for each application requiring equilibrium line altitude (ELA).	Local spatial scale as calibrated in site. Long temporal scales, not short fluctuations.	Braithwaite and Olesen, 1989; Hannah *et al*., 2002; Hock, 1999
3	Local mass model (net and spatially distributed balance estimates)	Glacier mass changes, glacier runout	Mass balance changes (stake and snow density pits), runout, radiative and climatic measurements.	Local spatial scale as calibrated in site. Net balance approach poor at estimating variations within glacier. Temporal scale dependent upon frequency of measurements.	Wendler and Ishikawa, 1974
4	Local energy model	Radiative and thermal	Include, direct beam, diffuse and reflected radiation, turbulent heat exchanges, emitted radiation, advective exchanges and heat fluxes.	Only local as calibrated in site. Temporal scale dependent upon frequency of measurements – can be very fine scale.	Anderton *et al*., 2002;Boike *et al*,. 2003. Brock *et al*., 2000; Coughlan and Running, 1997; Foutaine *et al*., 2002; Greuell and Smeets, 2001; Tangborn, 1999, Williams, 1974
5	Global localised energy model	Terrain, radiative and climatic variables	Altitude, on site measurements of climatic and radiative .variables. Locally calibrated and can be parameterised.	Only local as calibrated in site. Temporal scale dependent upon frequency of measurements – can be very fine scale.	Blosch *et al*., 1991; Hannah *et al*., 2002;Hock, 1999, Fierz *et al*., 1997; Williams, 1974; Mittaz *et al*., 2002;
6	Global energy model	Terrain, radiative and climatic variables	Altitude and regional climate data, no site data collection or calibration / parameterisation.	Variable scale - can model local and regional trends. Intermediate temporal scale. Globally applicable.	Tapeiner *et al*., 2001

Table 2.1 Glacier prediction model classification scheme

2.2.1. **Type 1 prediction model: Temperature-altitude models**

Temperature, precipitation, ablation and altitude are highly correlated (Barry, 1980; Oke, 1987; Etzelmuller *et al.*, 2001; Gray and Male, 1981). As temperature and precipitation are much easier to record and predict than ablation, they are used to infer the equilibrium line altitude (ELA). This is the altitude at which losses of snow through ablation are equal to gains through accumulation for the balance year. It marks the altitude of instantaneous glaciation, and is calculated using local altitudinal gradients in precipitation and temperature and a relationship between winter precipitation and ablation-season temperature at the ELA (Lie *et al.*, 2003). The rate of change of temperature and precipitation with altitude at a location is given by the local lapse rates. Lapse rates are highly spatially and temporally heterogeneous varying as a function of topography and atmospheric conditions. Temperature altitude models often assume spatially uniform variations in temperature and precipitation with altitude resulting in a coarse temporal and spatial scale representation of predicted snow cover (Lie *et al.*, 2003).

Simple ELA models only account for snow accumulation by precipitation: as outlined in Section 2.1 this is not a valid assumption, as this is not the only process determining snow accumulation. Dahl and Nesje (1992) incorporated alternative methods of accumulation by differentiating between temperature – precipitation equilibrium-line altitude (TP-ELA) and temperature-precipitation-wind equilibrium-line altitude (TPW-ELA), these were found to give more accurate representations of snow distribution patterns.

Although ELA estimates only provide a coarse representation of predicted snow cover they have relatively low data requirements and can provide good correlations between observed and predicted distributions. Lie *et al.* (2003) had correlation coefficients of 0.8 – 0.84 between predicted and observed glacier distributions in southern Norway. However they stressed that estimates are very sensitive to uncertainties in lapse rates. This is in enforced by Plummer and Phillips (2003), who argued that the relationships derived between winter precipitation and ablation-season temperature when calculating ELAs are not transferable as they fail to account for the varying influence of topography on snow accumulation.

Correlations between altitude and temperature can be supplemented using information on the correlation between melt and temperature, where the amount of melt can be correlated with the duration of air temperatures above 0°C. These types of model are called a temperature index

models and they are based upon the relationship between positive air temperatures and net radiation.

2.2.2. Type 2 Prediction model: Temperature index models

Temperature index models or degree day models are based upon the correlation between air temperature and melt (See Hock, 2003 for a recent comprehensive review of their applications). Most positive air temperatures are correlated with recorded melt, (Braithwaite and Oleson, 1989, recorded a correlation of 0.96), derived either from direct on glacier measurements of flow or ablation or from melt predicted from an energy balance model (Hock, 2003). This correlation allows the calculation of a degree day factor (DDF) (Equation 2.1) usually expressed as mm d^{-1} K^{-1}.

$$\sum_{i=1}^{n} M = DDF \sum_{i=1}^{n} T^{+} \Delta t \qquad \text{Equation 2.1}$$

Where M is the amount of melt (mm), n is the number of time intervals, of duration Δt and T^{+} is the sum of positive air temperatures (°C) during this period.

The correlation between melt and temperature is predominantly driven by longwave radiation and sensible heat exchanges, which together provide up to 75% of energy required to drive melt (Hock, 2003). DDFs are variable through time and space representing the differing role of sensible heat exchanges and DDFs must be recalculated required for predictions for any new application area. DDF's also vary as a function of altitude, solar radiation and albedo (Hock, 2003). Despite this spatial and temporal variability they have been widely adopted for over 100 years, recording high prediction accuracies, low computation costs and low data requirements, lumping together energy balance and topographic controls on energy balance in the DDF. They do however require melt data to develop the factor of proportionality.

Derived temperature ablation relationships that are applied to altitudinal lapse rates and are not transferable only represent local relationships. Accuracy of predictions are limited by both the derived correlation and the temperature lapse rate used to predict melt from the temperature index model.

Temperature index models are restricted by their temporal (Lang, 1986) and spatial (Hock, 1999) resolution and fail to predict high frequency variations in snow accumulation and

ablation. Unlike the observed strong diurnal variations in ablation (Hock, 1999), a constant degree-day factor in temperature index models overestimates melt at night and underestimates melt during the day. Hannah *et al.* (2002) found that despite high correlation between ablation and their degree-day factors, their model could not replicate inter annual variability in snowcover and only simulated large temporal and spatial scale variations.

Hock (1999) adapted the standard degree-day model to incorporate potential radiation, in an attempt to increase the temporal and spatial resolution of estimates, this did improve predictions but still failed to simulate the spatial heterogeneity in observed snow cover. Like type 1 models, temperature index models are widely used because of a lack of other available data. They are only useful over long time scales as they fail to simulate high frequency trends unless extensive calibration is performed.

2.2.3. **Type 3 Prediction model: Local mass balance**

Mass balance models use field measurements of mass changes to simulate net or spatially distributed variations in accumulation and abaltion. Ablation stakes are used to record variations in snow depth at a series of discrete locations on the glacier surface. Changes in the snow depth measurements are converted to volume using the snow density, which is measured in a series of snow pits in the glacier. These point measurements are converted to surface estimates by creating isolines, and interpolating to a surface representing volume or mass change. Predictions are made in snow water equivalent, (SWE) which represents snow by the depth of water it would produce if melted, this measure eliminates density variations. Stakes are assumed to be representative of the elevation interval or terrain environment they are located in. It is therefore critical to the accuracy of the interpolation that this assumption is true (Williams, 1974). A time series of glacier mass changes, like the data for Storglaciaren, Sweden which has the longest mass balance record, with continuous measurements since 1945, provide an essential dataset to improve our understanding of the controls on glacier distributions by understanding the processes controlling local mass variations.

Estimates of changes in glacier mass balance can either predict spatially averaged annual mass balance, which provides an estimate of net balance for the whole glacier or spatially distributed mass balance changes. The latter requires the inclusion of a continuity equation that provides an estimate of the glacier flow field: this distributed approach produces a more informative dataset. The continuity equation can often be an area of uncertainty: Gudmunsson and Bauder (1999) suggested an alternative by modelling the kinetic surface conditions, where surface velocity

(derived from remotely sensed data), altitude and mass balance measurements are used to predict distributed mass change. The results showed that the model was highly sensitive to the assumptions used in velocity extraction, but provides a useful methodology for deriving spatially distributed mass changes.

However, mass balance measurements and studies are costly in both time and money (Hagen *et al.*, 1999; Andreassen, 1999), they are also subject to potentially large and unknown errors including uncertainty associated with density conversion models, systematic probing errors, stake ice melt processes and ablation gradient calculation (Østrem and Haakensen, 1999). Extensive research has been completed in an attempt to improve the estimates of these errors (Jansson, 1999; Hock and Jensen, 1999). Jansson (1999) concluded that mass balance estimates on Storglaciaren were not sensitive to measurement errors, but were sensitive to sampling locations. Comparative studies between mass balance measurements and the comparison of repeated mapping of glaciers have been inconclusive because of the inherent errors in both techniques (Andreassen, 1999). However Østrem and Haakensen (1999) argued that the maximum error could be quantified in comparison of repeated mapping, which is better than the unknown maximum error in mass balance studies. Despite the clear limitations of the intensive field data collection and error uncertainty, mass balance studies still provide valuable information on glacier mass changes. Hagen *et al.* (1999) and Theakstone *et al.* (1999) provided examples of coupled models, combining traditional mass balance measurements with global positioning system (GPS) and remotely sensed data to improve and refine mass change estimates.

2.2.4. **Type 4 Prediction model: Local energy models**

Model types 1–3 are all limited by data collection and scaling problems. Type 4 models quantify surface energy exchanges to simulate melt and accumulation over a surface.

The surplus or deficit of energy over time is known as the energy balance (Benn and Evans, 1998). A surplus of energy will lead to snow or ice ablation, where energy is initially used to raise the snow or ice surface to 0°C, and then to melt [at 0°C], evaporate or sublimate mass [at any temperature] from its surface. A deficit of energy will lead to a cooling of the surface and possible accumulation of ice by condensation or freezing of water (Benn and Evans, 1998).

Energy balance models commonly take the form:

Energy flux available for melt = Q_m

$$Q_m = Q_{sn} + Q_{ln} + Q_{rt} + Q_{en} + Q_h + Q_e + Q_g + Q_p \quad \text{(Equation 2.2)}$$

Where,
Q_{sn} = Net short-wave radiation
Q_{ln} = Net long-wave radiation
Q_{rt} = Net reflected radiation from surrounding terrain
Q_{en} = Net emitted radiation from surrounding terrain
Q_h = Sensible heat flux from the air
Q_e = Latent heat flux from snow-air interface
Q_g = Heat flux from the snow-ground interface
Q_p = Heat flux from precipitation

Q_{sn} is the most significant parameter and accounts for most of the energy available for melt (Gray and Male, 1981; Streten and Wendler, 1968), in most conditions, however, in cloudy and maritime environments turbulent exchanges can significantly contribute to melt (Streten and Wendler, 1968).

Energy models can be fed either by field measurements (Brock *et al.*, 2000a,b) or by predicted surface energy components (Anderton *et al.*, 2000).

Williams (1974) estimated ablation per pixel by predicting the heat and water exchange of the snow with it surroundings. His model used predicted clear sky, diffuse and longwave radiation components, sensible and latent heat transfers between the snow and atmosphere, surface energy flux and heat conduction to and from the substrate. Predictions were made on a daily basis driven by recorded climate data and albedo. Results showed reasonable results for the study area, although the model was driven by locally recorded climate data, it adopted an innovative approach to precipitation prediction, suggesting that standard lapse rate models should be replaced by multiple regressions incorporating slope, altitude and local relief. The topographic controls on snow accumulation raised by Williams (1974) have subsequently been the focus of much research exploring the spatial variability of snowmelt processes. Luce *et al.* (1998) argued that despite extensive research on the role of topography in radiative and snowfall input, predictions of snow accumulation still fail to account for spatial variability in snowcover. These authors suggested that the point measures of snowmelt are inaccurate and predictions should consider global measures such as snowdrift. At their study site the effects of snowdrift were more important than topographic effects on radiation.

Cline *et al.* (1998) claimed that there were no widely suitable models for mapping snow cover in rugged terrain, and that accurate estimates were only possible by intensive field sampling that captures its high spatial heterogeneity. They proposed that remote sensing might provide the technique to do this. Surface energy balance and reflectance properties have been increasingly retrieved using remotely sensed data (Cline *et al.*, 1998; De Wildt *et al.*, 2002; Dubayah, 1992; Duguay and LeDrew, 1992; Gratton *et al.*, 1993; Koike and Guodong, 2002; Wang *et al.*, 2000). This method provides a repeatable and accessible means of collecting the radiative components of surface energy balance and has been found to show good correlations with field measurements (Wang *et al.*, 2000). A time series of remotely sensed energy balance data can provide a higher spatial and temporal resolution dataset than is possible using the predictive models outlined above. However, this information is not explicitly available within the remotely sensed data. A radiative transfer algorithm has to be derived to convert spectral reflectance values to more useful energy balance measures: the details of this are still an active area of ongoing research. Dubayah (1992) stressed the importance of including additional topographically induced radiation effects on radiative transfer algorithms.

Intensive field surveys and point energy balance models fail to simulate the temporal and spatial heterogeneity of snowcover. Hock (1999) stressed the need to create a spatially distributed global model to account for the spatial and temporal variability in snow cover.

2.2.5. **Type 5 Prediction model: Global localised energy models**

Global localised models predict local energy balance at a location using local and global data, but are limited by their locally driven input data. Global data refer to variables or parameters that are dependent upon or calculated using their surroundings. Global variables that are significant when considering glacier distributions include topographic shading, exposure and relative altitude (Hannah *et al.*, 2000; Pomeroy *et al.*, 1998; Young *et al.*, 1997).

Hock (1999) developed a hybrid model that predicted hourly snow ablation as a function of potential clear sky radiation, topographic shading and observed global radiation. Ablation is predicted using a melt parameter that requires local calibration. Predicted distributions were highly correlated with the observed, but high data requirements (hourly climate data, and global radiation) limit its applications to accessible and monitored glaciers. The hourly temperature data is interpolated over the glacier surface using a constant temperature lapse rate, restricting the spatial heterogeneity of the temperature and consequently melt surface. Hock (1999) reports that one of the climate stations used in this interpolation process was discarded due its proximity

to a valley wall and consequently showed a local climate signal. This is similar to the approach of Richard and Gratton (2001) who created 'synthetic stations', but contrasts with the approach outlined by Arrell and Evans (2003) who argued that these local signals should be included in temperature predictions as they represent commonly occurring conditions. Aizen *et al.* (1997), Fierz *et al.* (1997) and Richard and Gratton (2001) also stressed the importance of accurate and terrain dependent climate predictions in glacier distribution models. Aizen *et al.* (1997) completed a study in the Central Tien Shan and argued that accurate climate and snowcover predictions needed to consider not only terrain parameters but also the scale of the study area and the annual variability in the climate processes.

Global localised models can effectively model snow cover distributions by considering process spatial and temporal heterogeneity, but these models are locally parameterised and driven by locally recorded climate data. This restricts their application to accessible study areas: global models attempt to remove these restrictions.

2.2.6. **Type 6 Prediction model: Global energy model**

Global models predict local energy balance at a location using local and global data, and are not driven by point data; requiring only commonly available regional data.

Tapeiner *et al.* (2001) stressed the importance of modelling the spatial variability in climate and accumulation processes when predicting glacier distributions. Using only readily available data and a series of derived topographic variables they compared a linear regression and artificial neural network (ANN) approach to predict a known distribution of snowcover. Results showed that the ANN approach provided better results with a correlation of 0.81, highlighting the dominant influence spatial variability in terrain and climatic variables has on snowcover. Although the model is globally applicable and has low data requirements the 'black box' effect of ANN modelling leaves many unanswered questions about surface, terrain and atmospheric interactions.

2.3. **Conclusions**

The range in predictive models not only highlights a chronology of knowledge and scientific advancement but also the complexity of glacial systems. No one model or type of model can be identified as optimal as this is largely dependent upon the data available, scale, the climatic characteristics of the study area and the desired spatial and temporal resolution of model output.

With respect to the aims of this research it is considered that type 5 models provide the most suitable framework to develop the predictive model within. Few type 5 models have been found within the literature, as most melt models require either local calibration or locally streamed datasets. It is suggested that iterative calibration of the models (outlined in section 2.2.5) will eventually provide them with global parameters and applicability. Efforts should be made to derive local climate datasets from regional data using the methods outlined by Aizen *et al.* (1997), Arrell and Evans (2003), Fierz *et al.* (1997) and Richard and Gratton (2001) to aid in facilitating the global application of these models.

Evaluation and examination of the predictive models described in this chapter stresses the dominant control that local factors have on the rate and character of spatially distributed snow and ice melt. The Jotunheimen, Norway with active glaciation at high altitudes is a typical example of an area with strong localised controls on snow accumulation within varied terrain. A brief description and summary of these local controls and topographic character of the Jotunheimen is presented in the following chapter and was used to determine the structure and parameters used within the predictive snow accumulation model.

CHAPTER THREE

JOTUNHEIMEN 'THE HOME OF THE GIANTS'

3.1 Introduction

This chapter presents a brief geological and geographical introduction to the region of Jotunheimen, Norway. First, the broad scale geological evolution of the region since the Pre-Cambrian is presented. This is then followed by a description of the geomorphology of the region, specifically discussing present glacial conditions. Finally the contemporary environment of Jotunheimen is considered with particular reference to the present day climate acting upon the region.

3.2 Location

The region, and in particular the glaciers, of Jotunheimen, situated in the centre of southern Norway between 7°30' – 9°E and 61°10' – 61°45'N are the focus of this research. Jotunheimen is the highest mountain block in Scandinavia and northern Europe. It is composed of three major massif complexes, Horungerne, Skvettebothogda and Bygdin. Their peaks reach between 2,000 – 2,400 m above sea-level (asl) extending 500 – 1,000 m above the regions' mountain plains, or plateaus. The Jotunheimen is part of the Fjeld region of Southern Norway. It is bordered by Jostedalbreen and Boverdal to the west, Gudbrandsdal to the east, Ottadal to the north and Valdes to the South. Jotunheimen lies within the counties Oppland and Sogn og Fjordane. Since 1980, 1145 km^2 of the Jotunheimen area has been regulated as a National Park. The national park and the glaciers therein are easily accessible and amongst the best investigated in Norway. e.g. Storbreen (Østrem *et al.*, 1988).

3.3 The Geological evolution of the Jotunheimen Region

The Caledonian mountain range, of which Jotunheimen is part, lies northeast southwest along the Scandinavain Peninsula. It is situated in the most part along the boundary of Norway and Sweden. The Jotunheimen was formed during the Caledonian period, and is composed almost entirely of basic igneous strata, namely 'Jotun-norit' a composite of mangerit, norite, gabbro and olivine diabase. Ahlmann (1922) suggested that the preservation of the Jotunheimen area is not only a result of the natural resistance of Jotun-norit and its distance from the base of erosion, but also because it was centrally positioned during the Caledonian orogeny forming a kernal in the building of the mountain chain and the core of the Baltic Shield.

To understand the present landscape of the Jotunheimen it is essential to consider the geological evolution of the region with particular reference to two of the major structural events that have impacted on the region, namely: the formation of the Baltic Shield; and the Caledonian orogeny. Following on from these events has been the major geomorphological remodelling of the landscape during the Tertiary and Quaternary periods to create the landscape in the region that we see today.

3.3.1 *Pre Cambrian*

The oldest surfaces in the Jotunheimen date to the Pre Cambrian during the time of the formation of the Baltic Shield. The oldest area of the Baltic Shield is believed to have formed part of the original structural core of the European continent with a crust some 250-300 km thick. It is composed mostly of Archaen and Proterozoic gneisses and which have undergone numerous deformations through tectonic activity. In what is now Norway some of the younger (dating from as recently as 800 Ma) gabbros, granites and gneisses prevailed.

3.3.2 *Caledonian Orogeny*

The Caledonian mountain range in Scandinavia was created as a result of compression and uplift of the Caledonian geosyncline which formed during the continental collision of the ancestral North America and Europe during the period from the Early Palaeozoic to the end of the Silurian. The geosycline was largely composed of eroded materials from the Baltic Shield from the Pre-Cambrian. The Caledonian Orogeny lasted for c. 250 million years and was a complex period of successive uplift and deformation. Uplift was accompanied by extrusions and intrusions of igneous

material, folding was accompanied by over thrusts and shearing. These extreme pressures lead to metamorphosim resulting in gneiss formation, largely found in Western Norway. The multifaceted patterns of uplift, deformation, shearing and thrusting resulted in a complex mountain range that is thought to have reached altitudes of more than 5,000 m asl. It is believed that this impressive range of intricate ridges and extensive troughs has since been subject to extensive fluvial, frost and wind weathering processes, removing all but the oldest strata.

3.3.3 *Tertiary Pre-Glacial Landscape*

The Tertiary period was characterized by intensive denudation throughout Scandinavia during warm moist climatic conditions, more intense periods followed uplift during the Alpine Orogeny. It is believed that at least fifteen of these uplift and erosion cycles occurred, creating a series of erosion surfaces divided by more intensely eroded scars. The Jotunheimen area emerged as a high altitude land mass and deeply incised fjord river valleys were created on the coast. Despite these two prominent land surface elements, records of the erosion cycles have been preserved in the landscape as palaeosurfaces, (Gjessing, 1967). By the end of the Tertiary denudation, had lowered and altered the surface, and the palaeosurfaces were heavily incised by valleys and gorges.

3.3.4 *Quaternary Glaciations*

The boundary that denotes the end of the Tertiary and the beginning of the Early Pleistocene (*circa* 2.4 Ma BP) saw a large fall in global temperatures and the onset of a succession of major glaciations within the Northern hemisphere. These glacial-interglacial (warming and cooling) periods were induced by the uplift of the Tibetan plateau and further amplified by orbital forcing. The timing of this onset is still a contested issue, some evidence suggests that localized glaciations may have started as early as 4 million years ago (during the Pliocene), but widespread onset of intermittent glaciations had occurred by the Early Pleistocene. At the maximum cooling of a glacial period, a single ice sheet covered most of Fennoscandia, and during less intensive cooling periods more localized glaciations occurred. The high altitude, northerly latitude, relative maritime postion and incised form of the Jotunheimen area also lead to locally increased receipts of precipitation.

The transition from localized glaciations to more extensive regional ice sheets was recognised by John (1984) as ordered stages that marked key demarcations in the successive advancement of the glaciation (Figure 3.1). However it should be remembered that this is really a continuum that is not

only controlled and propagated by external forcing but also by its own climatic and energy balance feedbacks. The successive glaciations during the Pleistocene will have advanced and retreated along this spectrum. In northwest Europe it is well established that there have been three major glaciations termed the Elsterian, Saalian and the Weichselian, and also referred to as marine oxygen isotope stages (MOIS) 12, 6 and 2. There may, however, have been significantly more glacial periods prior to the Elsterian but terrestrial evidence to support this is limited (Lowe and Walker, 1997). The timing and extent of these events is poorly constrained (Houmark-Nielsen and Kær, 2003). Although the North Atlantic climate system played a significant role in the determining the timing and extent of these events, local parameters in Scandinavia need also to be taken into consideration. Houmark-Nielsen and Kær (2003) stressed the importance of the distribution of fjords and lakes and Helmke *et al.* (2003) described the significant impact of the fjords and Norwegian Channel had on the ice sheet dynamics and equilibrium. Helmke *et al.* (2003) proposed that investigations at individual sites off the Norwegian coast bring into question current assumptions about the influence of the Greenland and European ice sheets on the local glacial conditions, which will affect the timing and frequency of interglacial and glacial conditions.

Jotunheimen has almost certainly been ice covered and modified by successive Quaternary glaciations. The location and altitude of Jotunheimen, suggests that it may have been at the centre of Norwegian Ice accumulation during past glaciations and was entirely covered at least once (Ahlmann, 1922). However, evidence for this is somewhat limited because morphological evidence in the region suggests that the majority of the glacial landforms of Jotunheimen were a product of the last (Devensian) glaciation. The evidence supporting this claim is outlined by Ahlmann (1922), who argued that the sharp alpine forms such as Store Skagatolstind would not be present had they been acted on by successive glaciations. He also argued that the extent of the Devensian ice sheet covering Jotunheimen might not have been that great, and that ice thickness was largely controlled by topography with the deepest ice occurring in outflow valley glaciers.

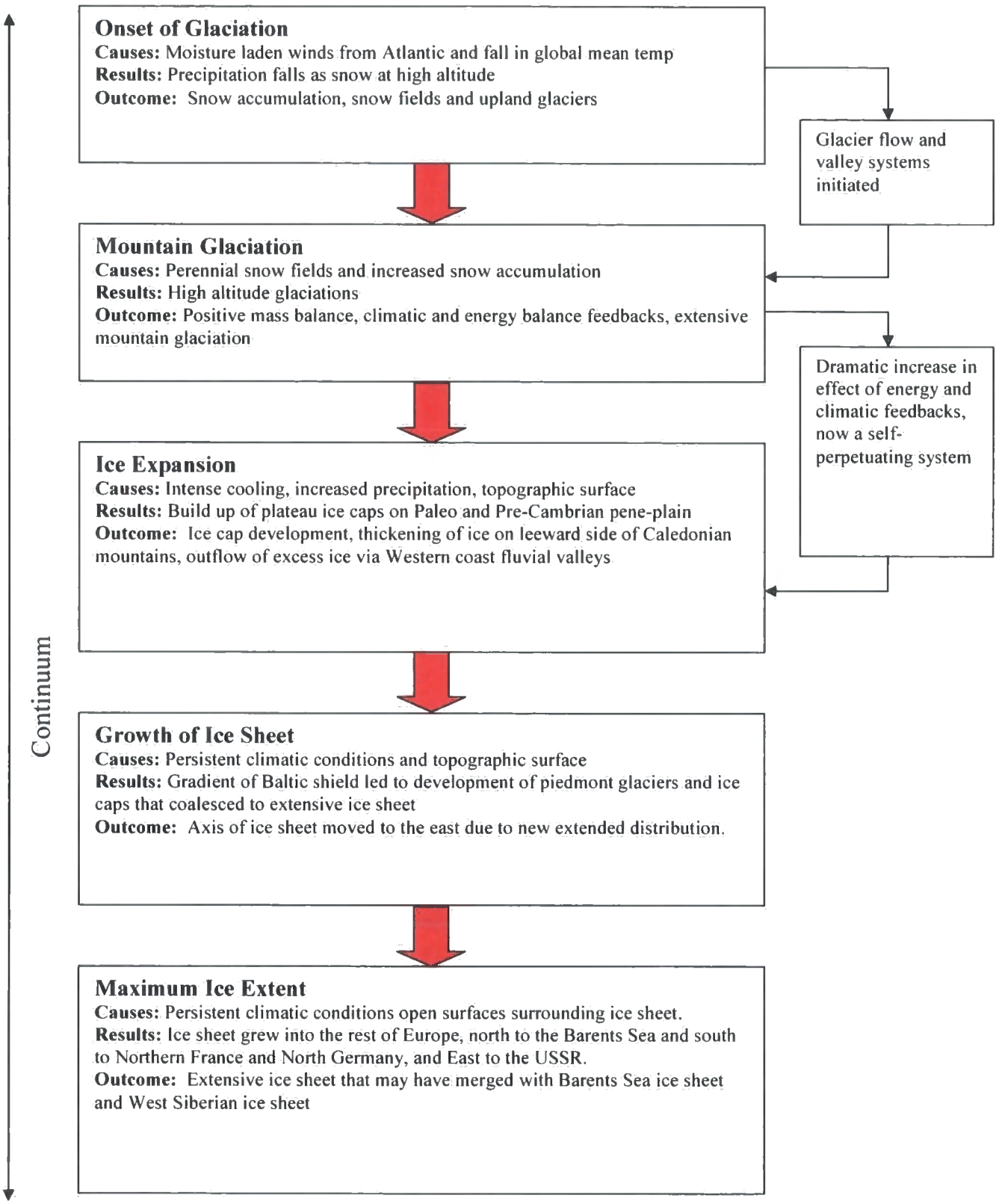

Figure 3.1: Adapted from John (1984; p. 46)

3.4 Geomorphology

The Jotunheimen area is composed of large open palaeovalleys (Tertiary) with younger (Pleistocene) valleys advancing towards its centre. The palaeovalleys are remnants of a previous terrain and erosion surface created and shaped before the last glacial maximum (LGM). Using Davis' (1899) model this should be a mature and well smoothed terrain, with broad, flat valleys. The younger tertiary valleys are much less smooth and are characteristic of deeply incised glacial troughs, heavily modified during the Devensian glacial maximum. Jotunheimen is characterized by majestic mountain massifs and glaciers. The country's highest mountain peak - Galdhøpiggen (2,469 m asl) - is situated within the study area. The area has many lakes, of which Gjende is the largest.

The valleys dissect the Jotunheim into three regions of massifs extending from the NE to SW.

1. Horungerne - Kvittingskolen. Containing the Horungerne, Smorstabb, Galdhoerne, Glittertind and Kvittingskolen massifs.
2. Containing the Skvettebothogda, Raubergene, Koldedal, Uranaastinderne, Raudalstinderne, Memurmassive and Naugarssen massifs
3. Bygdin massif proper and Gjendin.

These massifs are old huge bodies with vaulted contours and young, sharp alpine forms at and near the present day glaciers and snowfields. The vaulted land surfaces are the oldest part of the Jotunheimen and form the initial topography at the centre of the massifs which contrasts starkly with the younger alpine landforms. The peak of Galdhøpiggen is a vaulted part of the central massif. Multiple similar peaks suggest that there was a flat peneplain palaeosurface at 2,000 – 2,300 m, but Ahlmann (1922) suggested that it simply represents a long denudation period that has lowered the original terrain surface to a uniform level.

Successive Early Pleistocene glaciations have shaped the landscape and the resultant forms were dependent upon the local depth of ice, conditions (warm or cold) at the ice-rock interface and the underlying topography. During less intensive glacial periods existing fluvial valleys were often reworked by the glaciers that flowed from more upland areas, eroding deep glacial troughs and flowing down through the evolving smaller lowland valleys and the coastal fjords on the West.

Each successive Quaternary glaciation modified the landsurface, but it is believed that the terrain surface and its constituent landforms observed today were shaped by glaciers during Marine Oxygen Isotope Stage six (MOIS 6) (~150 ka BP) and that subsequent glaciations may have only slightly modified the erosional landforms (Helmke *et al.*, 2003).

During the last glacial maximum, the offshore Norwegian Channel contained a large ice stream moving north, this was active during several of the glacial advances during the Pleistocene but reached its maximum extent during the last glacial maximum (LGM). Raunholm *et al.* (2003) used digital terrain models and sedimentological investigations to investigate the interactions between the inland ice and the ice stream during deglaciation. The orientation and sedimentology of erosional and depositional landforms was used to reconstruct the channel deglaciation, suggesting that the inland ice sheet developed altering its dynamics giving it a new equilibrium, with localized areas of early deglaciation or glacial advance.

3.5 **Present Day Glacier Distributions**

The glaciers of Norway are more extensive than those of any other European country other than Iceland. They are concentrated into two major groups: those in the north of Norway between latitudes of 66° and 69°N (792 glaciers in an area of 1954 km^2); and those in the south between 60° and 62°N (950 glaciers in an area of 1900 km^2; Denton, 1970) many of which lie within the Jotunheimen region (Figure 3.2). Under the present climate, firn lines are around 1600 m in the northwest of Norway rising to 2200 m in the southeast of the country. Glaciers also tend to be more concentrated to the west of Norway. Higher latitudes in the north can account for the distinct gradient in firn line altitudes. However, Von Buch (1922) suggested that increased cloudiness at the western (Atlantic) coast might be the driving mechanism for a longitudinal (W to E) gradient in firn line altitudes that also occurs. Forbes (1922) proposed that the difference was purely a response to the maritime influences on temperature, whereas Ahlman (1922) argued that temperature gradients were only responsible for a relatively small component of the longitudinal gradient in the firn line altitudes, and that the major component of the trend is a result of the spatial distribution of precipitation receipt.

Most glaciers in the Jotunheimen region are cirque or valley glaciers (Østrem *et al.*, 1988). The distributions of glaciers in Jotunheimen are dependent upon the range of factors outlined in section 1.2. However, a range of different factors have been found to dominate their distributions in relation to their locality, which in part, is evident through different glacier orientations. The more maritime climate in the west of the area facilitates the growth of large plateau glaciers and ice fields where snow accumulation and milder climates lower the firn line.

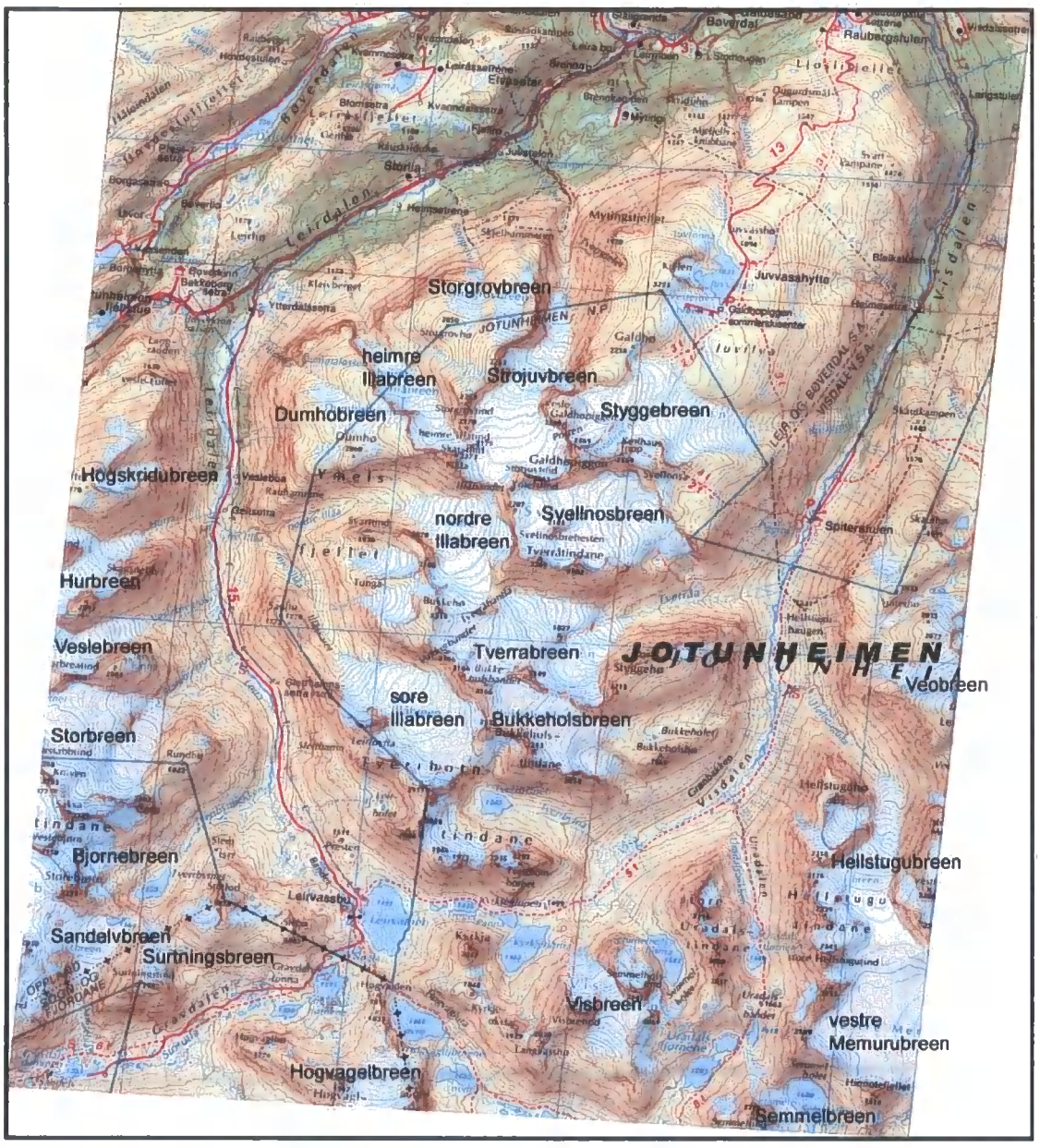

Figure 3.1: Geocorrected topographic map of the study area highlighting the distribution of glaciers (in white). Source: the 1:100000 Statens Kartverk topographic map of Jotunheimen, updated in 1997. Although the map was updated in 1997 it is unclear if the glacier boundaries were updated at this time.

The more varied and steeper terrain of central Jotunheimen leads to complex glacier fields and large cirque glaciers developing within sheltered cavities, where wind blown snow and lower insolation allows the growth and merging of glaciers. The drier and warmer (in summer) conditions in the east of the region lead to smaller cirque glaciers and ice fields. Since 1750 most of the glaciers in the Jotunheimen area have been retreating (Østrem *et al.*, 1988).

3.6 **Recent changes in glacier extents**

Multi-proxy evidence suggests that recent retreat and thinning of Norwegian glaciers is a result of warming and reduced precipitation. Berstad *et al.* (2003) reconstructed sea surface temperatures in a sediment core taken from offshore on the Southern Norwegian continental margin. This reconstruction was compared with contemporary measurements taken from the Ocean Weather Ship. The research concluded that the last 70 years have been the warmest in the region for the past 600 years. These data that suggested a warming trend for Norway have been borne out by the retreat of many of the glaciers in Jotunheimen. For example Storbreen in the Leirdalen Valley in the central part of Jotunheimen has the longest series of mass balance change measurements in Norway, spanning over 52 years (Kjøllmoen, 2001). Over this time the glacier has shown a net mass balance change of -0.20 m water equivalent, and during the period between 1900 and 1988 the snout of the same glacier retreated over 1 kilometre (Kjøllmoen, 2001). Similar figures of mass balance change and retreat have been noted for other glaciers in Jotunheimen, including Hellstugubreen and Gråsubreen (Kjøllmoen, 2001).

3.7 **Current climate**

Norway's climate is not only influenced by its position in the northern hemisphere and the tracking of pressure systems and winds, but also by the influence of the North Atlantic Ocean, the Baltic Sea and its own land mass. Except for the west coast of Norway, its climate is part of the Boreal Forest climatic zone in the Koppens system, with a mean temperature of the coldest month is 0 °C with snowcover every year. Some areas of Northern Norway exhibit a polar climate where the average temperature of the warmest month does not rise above 10 °C.

Norway's position north of 50°N latitude provides it with a negative annual radiation balance, with less energy is received than is emitted. The annual deficit is 40 000 cal cm $^{-2}$ at 55° N and 67 000 cal cm $^{-2}$ at 70° N. These values would be far greater if short winter days where not compensated for by long light summer nights. The energy deficit is compensated for by energy derived partly from latent heat released by condensation and partly by horizontal advection from more southerly latitudes.

The location of Norway on the eastern side of the North Atlantic means that the climate is affected by the abnormally warm Atlantic Ocean (i.e. the Gulf Stream). Temperatures can be more than 9 °C warmer than other landmasses at the equivalent latitudes. Prevailing winds carry this warmth inland leading to a maritime climate in the west, giving rise to milder winters, cooler summers and more abundant precipitation. The lessened influence of the Atlantic in the east of the country results in a more continental climate with greater extremes of temperature and less precipitation, giving rise to fewer rainy days, lower relative humidity and less cloud and wind force compared to the west. Latitude as you travel north has only a nominal effect on Norway's climate as the northward drift of the warm Atlantic waters largely negates it.

3.7.1 **Pressure systems and winds**

The weather of Norway is largely controlled by the passage of depressions and cyclones along its coast. The Scandinavian Peninsula is dominated by westerly and southwesterly winds during all seasons as the net result of the interaction between the high altitude, mid latitude westerly jet stream, and polar fronts that develop between cold air masses from the polar regions descending from the north and tropical, more mild air masses rising from the south. The strong westerly current corresponds to the polar front at the surface and the cyclones formed at the front move with the jet stream leading to the predominantly westerly and southwesterly winds. The net result of the passage of these depressions is a tendency for high-pressure systems to form in the centre of the country during winter and low-pressure systems forming in summer. These climatic characteristics produce systems of winds around the mass of southern Norway that circle in anti-clockwise directions during the winter and clockwise directions in the summer. Winter is characterised by large temperature anomalies due to the ocean atmosphere interaction above the Gulf Stream and heavy precipitation especially in the west. Under these conditions summer is cool and strong vertical convective currents bring frequent rain showers.

These conditions do not always dominate and the westerly system can be broken down when deep troughs and ridges are formed in the pressure system of the upper atmosphere, blocking the westerly current. High-pressure ridges bring warm air north and troughs transport cold air southwards. Seasonal weather is highly dependent upon the location of the ridges. In winter winds can be easterly or north easterly bringing with them continental polar or artic air. This produces very low temperatures, but lighter snowfall than under westerly conditions and very little snow on the leeward west coast. In summer ridge locations have clear, dry, hot weather, east of the ridge, north westerly polar air brings frequent showers but precipitation falls west of ridge where southerly winds bring cyclonic activity.

3.7.2 **Precipitation**

Precipitation patterns in Southern Norway are controlled by complex interactions of multiple controls. These include atmospheric circulation, distance to open sea, altitude and exposure or protection due to altitude. Because of the prevailing westerly to southwesterly winds the western areas of Norway receive the most precipitation, with the majority falling during the winter months when cyclonic activity is strong. Proximity to the coast is a secondary factor because moisture saturated air masses and cyclones move onshore from the sea and lead to a strong linear decrease in precipitation inland from the coast. Locations in the west of Jotunheimen can have annual precipitation levels as high as 3000 mm. In contrast, easterly locations may only receive 400 – 500 mm per year.

This strong linear relationship is helped by the orographically induced precipitation, further diminishing the moisture reaching the east by deflecting it to the north and so acting as a topographic divide between the predominantly maritime conditions in the west and continental conditions experienced in the east. Precipitation largely falls as snow during the winter months, between November and April, in southeast Norway and from the end of September till the end of May in northern Norway. During these periods precipitation decreases rapidly. Locally topoographically induced precipitation increases snowfall on windward slopes, and as winter temperatures decrease in line with latitude and altitude, higher snowfalls are recorded in areas of higher altitude and latitude. Precipitation exceeds evaporation by 200 – 300 mm a year. In western and northern Norway, where maritimity is pronounced, winter precipitation is dominant (January, October and November) and spring is the driest season.

3.7.3 **Temperature**

Norway's position on the west coast of the Eurasian continent and the surrounding North Atlantic Ocean and Baltic Sea lead to its temperature having strong maritime characteristics. These maritime influences lead to a very small amplitude between the mean of the coldest and warmest months. In the winter the lowest temperatures are found in the area farthest from the sea, and the warmest temperatures are found nearest to the sea, where the ocean and the warm air that blows over it have warmed the land and air. In summer the lowest temperatures are found in the coastal strip. Higher latitudes have slightly lower temperatures and there is a strong correlation with latitude and the amplitude of the mean of the coldest and warmest months.

In winter, Artic weather is dominated by frequent temperature-inversions, which occur when warmer temperatures are overlaid with a colder air layer.

3.7.4 **Sunshine**

Norway's high latitude limits the solar altitude during the winter months, leading to short daylight hours and long nights. Frequent cloud cover and topographic shading also further reduce sunshine. This is most frequent and dense on the west coast during autumn and winter Insolation levels reaching the ground are further decreased by coastal and radiation fog. Fog is most extensive during spring and summer where all of coastal Norway is liable to fog, but it is largely confined to the eastern valleys of southern Norway during autumn and winter. Radiation (or land) fog originates over cold surfaces and is restricted to the eastern part of southern Norway during autumn and winter. Cloud and fog create significant feedbacks within the climate system, reducing the direct beam component of radiation, and increasing the importance of reflected and diffuse radiation and so decreasing the solar heating of the land surface. Cloud and fog layers can act as barrier trapping convective heat near the surface, warming the surface (by trapping the heat in) and they also increase the adsorption and attenuation of radiation in the atmosphere.

3.8 **Conclusion**

The topography of the Jotunheimen has been shaped by successive Quaternary glaciations resulting in a heavily eroded and shaped glacial landscape. Extinct cirques formed when cooler environmental conditions prevailed lie near occupied cirques and larger valley glaciers. Climatic conditions in the Jotunheimen are driven by micro, meso and macro scale processes and create strong localised gradients in temperature and precipitation exhibiting distinct seasonal cycles. Historical evidence suggests that the glacier accumulation in the study area is particularly sensitive to small changes in temperature and precipitation (Ahlmann, 1922). This makes the Jotunheimen a particularly interesting area to study. Topography plays an important role in controlling the magnitude of these climatic gradients and is also a dominant control on local energy balance. Topographic data detailing the pronounced local geomorphology, and methods of characterising topographic controls on climatic variables is addressed in the next chapter.

CHAPTER FOUR

TERRAIN ANALYSIS

"Many of the physical processes operating in the landscape are locally dependent on landscape geometry"

Drymond *et al.* 1992, p 53

4.1. Introduction

Terrain analysis is the investigation, quantification and characterisation of topographic information. Extraction of quantitative form measures and derivatives of elevation have long been recognised as having a geomorphological significance (Evans 1972). This chapter aims to introduce a new suite of topographic parameters that build upon existing quantitative surface measures to improve our understanding of the interactions between the earth surface processes and terrain. These are presented following an introduction to the methods of characterising digital elevation data.

Any analysis of terrain data needs to account for and incorporate any known or suspected error. A new method of identifying and removing spatially and spectrally organised error within a DEM is presented. An improved viewshed algorithm is also developed to ensure computational efficiency.

4.2. Geomorphology and Digital Elevation Data

Geomorphology is the investigation, understanding and characterisation of landforms and landscapes, their formative processes and the environment and system within which they currently lie. Changing and evolving paradigms have led to different approaches to geomorphological exploration and investigation. Their direction and form have largely been dictated by available data sources. Geomorphology has been characterised by a clear division between form and process studies.

Despite the need often to separate form and process studies, the value of geomorphology can only be optimised when form and process are considered simultaneously and their inter-relations realised and appreciated. However the historical lack of a routine quantitative approach to surface characterisation and a mechanism for the interpretation and manipulation of quantitative data sets restricted any successful coupling.

The development of the microcomputer and the start of the digital era supplied the mechanisms and data to allow this coupling. This was achieved not only by providing an efficient and rapid way of storing and analysing existing data sets, but also by supplying many digital data sets. These were acquired by either the digitising of existing data or through new and automated collection mechanics such as remote sensing. This has allowed more varied analyses to be completed.

The spatial distribution of phenomena had always been a dominant feature of any geographical analysis, and continued to be so through the development of an area of geography called Geographical Information Systems (GIS). Before the onset of digital data and GIS, geomorphologists had not been able to model spatial patterns effectively. With the use of GIS this was a relatively simply procedure. Consequently, more emphasis was placed on the analysis of the internal spatial distribution of form-process relations and less on empirical process studies. These developments allowed the study of form (that had been identified as lagging behind that of process (Pike, 1995)) to receive renewed attention. GIS provided a mechanism for the characterisation and quantification of form and land surfaces, by facilitating large dataset manipulation and analysis or areas in the same geographical area.

Methods of quantifying topographic form are identified as important when considering glacial systems (Benn and Evans, 1998; Unwin, 1973; Evans, 1977). Allen (1998) in his study of alpine glaciers in Montana, linked negative mass balance trends to topographic modification of climatic variables. He reported that topographic parameters are significant at both the regional and local scale when predicting the local ELAs of snowfields, ice fields, cirque glaciers and niche glaciers. This supported the work completed in Greenland by Warren (1991) who proposed that topographic forcings are critical in understanding glacier systems.

4.2.1. Sources of Digital Elevation Data

Three main methods of capturing digital elevation data exist, manual surveying (commonly using a geographical positioning system, GPS), digitising graphical representations of elevation

data (commonly contour lines and spot heights) and remotely sensed data capture (either airbourne sensors or satellites). Digital elevation data can be characterised by their spatial resolution, spatial and absolute accuracies; the data capture techniques used, the required processing techniques and cost. Each capture method has associated advantages and disadvantages and the selection of data capture technique should be based on data resolution and accuracy considerations.

4.2.2. **Terrain models and Data storage**

Digital elevation data can be stored in three main ways, a raster tessellated grid, a triangular irregular network (TIN) or as a contour model. The method chosen is largely dependent on the data available and the intended purpose and use of the data. However the storage mechanisms can be collectively termed Digital Elevation Models (DEMs); Burrough and McDonnell (1998; 300) defined a DEM as:

> " a quantitative model of a part of the earth's surface in digital form"

A DEM provides a method for subdividing a landscape into surface elements or spatial units in an attempt to represent the local topography, which in reality is a continuous surface and would require an infinite number of points to be accurately represented. DEMs represent the surface topography by simply storing a sample of surface elevation points. No single storage mechanism or DEM is optimal, but each has its own advantages and disadvantages. Most geomorphological studies are effectively modelled and completed using a gridded altitude matrix (Evans, 1972). This research uses a raster based elevation dataset: this not only facilitates spatial modelling through its common spatial aggregation units, essential within this research project, but also provides considerable computational savings (processing speed and file size 23.5 MB for a gridded DEM of study area, compared to 246 MB for a TIN of the equivalent area). A gridded DEM also provides conceptual advantages over alternative surface representations and regular sampling intervals and spatial aggregation units, facilitate any volume and area calculations.

DEMs have allowed the dimensionality of data analysis to be increased replacing one-dimensional morphometric statistics with two and three-dimensional studies. Previously geomorphological studies had been limited to small space and time scales: the improved data sets and data storage mechanisms remove these restrictions and limitations. They allow a

wealth of space and time scales to be used and investigations into the important concept of the coupling of processes at different time and space scales to be completed. Scale is an important concept throughout this study and will be discussed in many of the subsequent chapters.

4.2.3. **Scale**

DEM scale can be viewed as analogous to map scale in cartography (Hutchinson and Gallant, 2000). DEMs can be categorised on many different levels either by the source of the elevation data (Section 4.2.1), the structure of the surface or the method employed to store the data (section 4.2.2). However scale must be viewed as one of the most critical parameters when using any surface representation (if not the most important besides elevation error). The importance of scale in geomorphology was discussed by Schumm and Lichty (1965), where it was identified that landforms and processes are scale dependent. It was argued that different landforms and processes are dominant at different scales and that it is not possible to assume that a form or process present at one scale will be present at a different one (Table 4.1). Schumm and Lichty (1965) discussed scale in both its spatial and temporal dimensions.

Scale	**Example applications**
Micro 5 – 50 m	- spatially distributed hydrological modelling - soil moisture - channel change - specific geomorphometry applications
Fine meso 50 – 200 m	- applications with DEMs - aspect related micro-climatic variations, radiation balance, evaporation and vegetation modelling - broader scale distributed parameter modelling - specific geomorphometry applications
Meso 200 m – 5 Km	- topographically dependent representation of surface temperature and precipitation linking to biological activity - general geomorphometry applications - agricultural modelling - wind modelling
Macro 50 – 500 Km	- broad atmospheric modelling - GCM (General circulation modelling used for climate change predictions) - projects that require high levels of generalisation where accuracy is not critical

Table 4.1: Spatial scale and geomorphic processes

The introduction of DEMs has facilitated scale-based investigations as simply altering the DEM resolution changes its scale. Wood (1986), MacMillan *et al.* (2000), Arrell *et al.*, (2001) and Fisher *et al.*, (2004) all investigated the scale dependence of landform classification. These

authors found that the same position in a landscape could be considered part of different landforms simultaneously depending on the scale and context in which it is viewed. MacMillan *et al.* (2000) suggeseted that a local ridge identified at a small scale was classified as crest or divide at a larger scale and a mid-slope position at a larger scale still. Similar scale dependence was found by Wood (1986) where investigation was not only focused on changing landform classifications but also on the persistence of landforms with scale. In Arrell *et al.* (2001) a landform was identified as persistent if it was found at all classification scales: this persistence or dominance of a landform was generally found to be associated with extreme elevation values, for example peaks or pits (a pit is a local minimum surrounded by higher altitude values) or strongly delineated landforms such as ridges. Wood (1986) examined how elevation derivatives varied with scale and suggested that this scale based progression of characteristics is more useful than a single morphometric measure. He suggests that parameterisation of geomorphic surfaces should include reference to the scale based characteristics of the unit.

The scale dependence of landform classification identifies the importance of choosing a suitable scale of source data and DEM resolution. The scale of the DEM and its interpretations should be matched to the natural scales of terrain and its constituent landforms of interest to the application: the DEM resolution should approximate less than half the average dimensions of one complete cycle of topographic variation in the landform of interest. This principle was mathematically defined by Tobler (1969:181) in his description of the sampling theorem, which states that:

> " if a function has no spectral components of frequency higher than w, then the value of the function is completely determined by a knowledge of its values at points placed $1/(2w)$ apart, if the smallest significant wavelength is s then the spacing everywhere must be $(1/2)s$ or less."

A trial and error process is often necessary to define the optimal spatial resolution, which is deemed to match the dominant local wavelength e.g. crest to crest.

Visual examination in the present study of the dominant local wavelengths in Jotunheimen, identifies 2, 000 m as the first order or primary variation (large glacial valleys), and 700 m (smaller cirque valleys) as the second most dominant wavelength. Although these measures are highly subjective this type of approach is required to identify the spacing of landforms that are of critical importance to this glacial geomorphological application. These measures do not of

course account for the range in spatial extents and resolutions of each of the landform components that contribute to glacier initiation, but simply aim to verify that cirques, convexities and ridges will be apparent in the surface representation. Mark (1975a) conceptualised this multi-resolution characteristics of terrain surfaces; texture and grain, where texture is the finest roughness present in the surface (where roughness can be interpreted as landform elements) and the grain is the coarsest repeated landform or surface roughness element present in the surface. These two components of the surface should be viewed as a continuum, and applied to Jotunheimen, the grain could be conceived as a large mountain ridge such as the Galdhoppigen (> 2km) and the texture as gullies and small channels.

In this research application a 100 m DEM was used, supplied by the Norwegian Mapping Agency Statens Kartverk. This was in Digital Terrain Elevation Data format (DTED) and with a UTM Zone 33 N projection. This was selected as the most suitable product based on spatial resolution, recorded accuracy and cost. However, the interpolation procedures performed by the Statens Kartverk left both spectrally and spatially dominant artefacts in the dataset that are clearly not reflected in their vertical accuracy estimate (addressed in Section 4.5). This spatial resolution is coarser than the 25 m DEM used by Bloschl *et al.* (1991) in their snowmelt simulations, but in agreement with Evans and Cox (1995) who suggest a 200 m horizontal dimension of the smallest cirques in the Lake District. Although finer spatial resolution DEMs provide a more detailed surface representation it is not clear that predictions or simulations would be more accurate, as any predictions are only as good as the coarsest or highest error within the input datasets unless successful downscaling is performed. In both the present and Bloschl *et al.'s* (1991) studies the highest uncertainties and errors are associated with climatic data. It is suggested here that although combining multiple datasets of different resolutions can be fortuitous in increasing the surface process variability modelled it can also introduce and propagate errors in the coarser scale input data that cannot be resampled with sufficient accuracy to match the finer resolution of other datasets. This is a common problem in many modelling applications where consistency in the complexity of modelled parameters is not maintained, leading to unquantifiable error propagation. This is particularly evident in this application where broad spatial and temporal scales are used throughout. This research project has attempted to create a compromise between accuracy and resolution, and proposes a 100 m DEM as an adequate and sufficiently detailed surface representation. This selection of surface resolutions was also determined by a lack of a finer spatial resolution terrain model.

Digital elevation data in its raw form has limited use, but analysis between and within datasets can produce much more useful data. The types of spatial analysis performed within this research are outlined in the following sections.

4.3. GIS and Spatial Analysis

It is possible to characterise a location based on varying inclusion of its surrounds. Locations can be characterised by their individual attributes, the attributes of the locations within a specified distance or direction from them, the attributes of locations within the same zone or by the attributes of the whole dataset. These different spatial aggregation units are most commonly associated with the raster data model and were first proposed by Tomlin (1980) in her categorisation of cartographic modelling capabilities. From here on these will be referred to as local, focal, zonal and global spatial analysis aggregations.

It is also possible to identify different methods of characterising, describing and quantifying these different spatial aggregations. GIS facilitates these different analytical processes and spatial operations, allowing the manipulation of geographically coherent areas; this functionality can be viewed as spatial analysis.

Analysis within a GIS is not restricted to a single data model or within data of the same spatial or temporal resolution. Standard spatial analysis techniques can be modified and extended by the user within the GIS, creating a flexible, dynamic and robust spatial analysis toolbox. Typical raster-based GIS facilitate the manipulation of DEMs, and have provided valuable environments for the analysis of surface form in contrast to early manual approaches qualitative (Hammond, 1964) and quantitative (Fenneman, 1946).

4.4. Geomorphology and Geomorphometry

DEMs provide quantitative elevation datasets but these elevation data in their raw form have limited use. It is the characterisation and extraction of useful measures from these raw data that form more informative data. Morphometry deals with the extraction of surface measurements and the mathematical characterisation of surfaces. Evans (1972) identified morphometry as a suitable mechanism to achieve a quantitative characterisation of land surfaces. Richards (1990) recommended that a scientific geomorphology required and demanded such quantification. Evans (1972) called this application of morphometry to land surfaces geomorphometry.

The geomorphometric measures extracted from a surface are dependent on the type of surface and the specific objectives of the study. As this study is interested in the controls that local topography place on meteorological processes it is sensible to select geomorphologically and meteorologically significant measures. The first and second derivatives of elevation (slope: gradient and aspect, and curvature: especially plan and profile curvature) are the most commonly used (Evans, 1972). Slope affects the use of gravity for geomorphological work and curvature controls the acceleration and convergence of water and flows (Table 4.2). It has been suggested that higher derivatives do not provide useful information (Evans, 1979; Skidmore, 1989; Wood, 1986).

Although it is possible to apply the principles of morphometry directly to land surfaces, a degree of modification is required to produce sensible results, as the language used to depict continuous terrain is not systematically equated with measurable attributes of form (Pike, 1995). This requires the definition of sensible areal units over which the measurements are calculated in an attempt to subdivide the surface intelligently. Evans (1990) suggested that it is necessary to analyse the earth's surface in more manageable components than those provided by the DEM. Clearly there is a large range of possible surface components and Evans (1972) suggested that these possibilities could be seen to fall into two categories, which he called specific and general geomorphometry.

4.4.1. **Specific Geomorphometry**

Specific geomorphometry examines and characterises individual landforms and provides the most detailed form of geomorphometry (although still dependent upon scale). Jarvis and Clifford (1990; 63) defined this approach as the:

> "measurement and analysis of specific surface features defined by one or more processes and separated from adjacent parts of the land surface according to clear criteria of delimitation"

Landforms are defined detached from their surroundings to isolate the landform signature from the 'noise' of the surrounding land. This concept of landform signatures was discussed by Evans (1972), Pike (1988) and Arrell *et al* .(2001), and it is based on the principle of a certain element or object being composed of a collection of parts, which when viewed together allow its unique identification. This principle is utilised in remote sensing when performing

Surface Measure	Elevation Derivative	Description	Geomorphological Significance
Elevation / altitude	0	Height of location above sea level.	Provides a measure of the relative position in the landscape if the range of values present is considered. May provide information on the resistance to erosion of the location. Creates an instant impression of the topography of an area i.e. upland-lowland, rough-smooth
Slope -Gradient	1	Slope magnitude (gradient) is the maximum rate of change of altitude	Slope is defined by the plane tangent to the surface and is composed of two vector components, gradient and aspect. Gradient controls the affect of gravity. Evans (1972) suggests that by examining the two slope components separately confusion produced by hybrid results can be avoided.
Slope -Aspect	1	Slope orientation (aspect or azimuth), which is the compass direction of the maximum rate of change of slope.	Aspect affects the incidence of radiation and wind.
Convexity -Profile	2	Rate of change of slope gradient	Controls the acceleration and deceleration of near surface water flows.
Convexity -Plan	2	Rate of change of slope aspect, i.e. rate of change along contour lines	Controls the convergence and divergence of near surface water flows.

Table 4.2 Surface measures suggested by Evans (1980)

classifications of spectral images. Here the surface topography characteristics are viewed together to allow the identification of landforms.

4.4.2. General Geomorphometry

The more general approach to geomorphometry characterises a landscape unit as a whole and attempts to identify the overall signature of the area rather than specific features. General geomorphometry defines the landscape as a continuous rough surface. Such measures aim to facilitate the identification of the relationships between form and process that act on a landscape.

Wood (1986) suggested that the distinction between specific and general geomorphometry made by Evans (1972) is polarised and that it could be more appropriately viewed as a continuum (Figure 4.1).

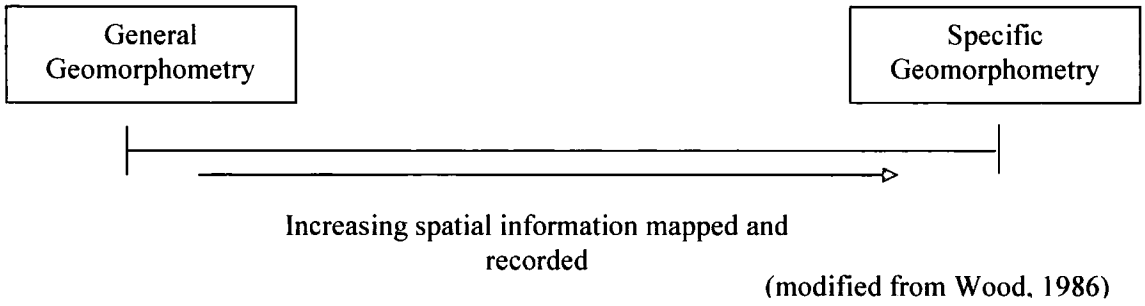

Figure 4.1: Geomorphometry spectrum

Evans (1987) discussed the examples of studies that fit onto this continuum and identified slopes and drainage basins as having elements of both specific and general geomorphometry.

4.4.3. Surface measure derivation

Although geomorphometry was developed in an attempt to avoid the limitations of previous approaches by adopting a repeatable and mathematical form of description, the problem of a lack of universal consistency persists. Evans (1980) commented that although there had been much work on the quantitative analysis of landforms, there had been little attempt to standardise geomorphometric methods and little agreement on the derivatives used. The simplest approach to extracting surface derivatives is first order finite difference methods that calculate the derivatives by computing the differences between the neighbourhood units or windows (these

terms describe the area that is considered when deriving the derivatives) and then move the window of interest through the surface model (Table 4.3).

It should not be assumed that the more data points used to extract the derivative measures, the more accurate the values. Assessing which of these models provides the best or the most accurate set of solutions is a difficult task because performance is dependent on a number of factors including surface roughness and data precision (Schmidt *et al.*, 2003). For example, many extraction and surface characterisation methods work well in variable and steep topography where signal to noise ratios are high, but they may break down in areas of shallow topography because of low signal-noise ratios. Skidmore (1989), Hodgson (1995) and Schmidt *et al.* (2003) completed an assessment of the different approaches above and found the second and third order difference models to be the most accurate.

However the accuracy of Skidmore's (1989) assessment has been brought into question, as the 'true' values were themselves estimates. Hodgson (1995) suggested that methods that examined data in four surrounding orthogonal raster cells (Rooks case) performed better than in those that examined data in eight (Queens case), this result was attributed to the higher autocorrelation between the data in the four cells. Jones (1997) proceeded to suggest that although four cells are more accurate for smooth surfaces (which are typically characterised by high autocorrelation) eight cells provide a more accurate option in more complex or 'rough' surfaces, which will have a lower autocorrelation.

The two most commonly used algorithms and two of the most accurate are the second order finite difference methods used by Evans (1980) and Zevenbergen and Thorne (1987). The former fits a five-term polynomial to the attributes of a 3*3 window (see Equation 4.1).

$$Z = Ax^2 + By^2 + Cxy + Dx + Ey + F \qquad \text{(Equation 4.1)}$$

Despite the superiority of this model to others in terms of accuracy, it was criticised because least squares are used to determine the equation coefficients. Consequently it is unconstrained by not forcing the surface through the central cell. It was argued by Zevenbergen *et al.* (1987) that as the central cell is often the cell of most importance when calculating surface derivatives, the accuracy of the surface model had to be questioned. Skidmore (1989) defended this model by suggesting that the unconstrained nature of the local quadratic, only calculating six constants from the nine recorded cells, acts as an advantage by using the three spare cells to smooth the surface damping noise and error. Schmidt *et al.*, (2003) also found this model to be less sensitive to errors in the elevation data producing more stable estimates.

Type of Model	Algorithm creator and year	Description
First order finite difference	Travis (1975)	Selects maximum downward gradient from those computed by comparing the elevation of every grid cell in the DEM with those of its eight nearest neighbours Local errors in terrain elevation contribute heavily
Second order finite difference	Ritter (1987)	Computes gradient and aspect from only the nearest four elevation points (rooks case)
	Flemming and Hoffer (1979)	Four grid points used and gradients taken at 45^0 to the principle axis of the DEM – 'ruler length'
	Evans (1980)	Six-term polynomial (Equation 4.1, pg 38) to the interior grid point of a moving three by three window
	Zevenbergen and Thorne (1987)	Nine-term partial quartic (Equation 4.2, pg 40) Deduce coefficients of a partial quartic trend surface, which passes exactly through the nine elevation points of the 3*3 DEM kernel.
Third order finite difference	Horn (1981) Sharpnack and Akin (1969)	Uses all eight surrounding cells and assigns different weightings. Weights are proportional to the reciprocal of the distance and use all eight grid points.
	Wood (1986)	Constrained quadratic surface. Quadratic regression surface that is constrained to go through the central elevation point of the local 3*3 window.

Table 4.3 Existing derivative algorithms, creator and description

Zevenbergen and Thorne (1987) developed a nine-term partial quartic (Equation 4.2) that is constrained through the centre cell and also passes through the centre of the window cells, providing an improved alternative to Equation 4.1. The nine coefficients A – I can be

determined by Lagrange polynomials. The equation has a degree of flexibility as it alters to fit the surface with the inappropriate coefficients equalling zero.

$$Z = Ax^2y^2 + Bx^2y + Cxy^2 + Dx^2 + Ey^2 + Fxy + Gx + Hy + I \quad \text{(Equation 4.2)}$$

Wood (1986) argued the suggestions of Evans (1979) and Skidmore (1989), that there is no good geomorphic reason for resorting to polynomials of order greater than two. This suggests that Equation 4.2, despite being more general, does not provide the better option. However the constrained nature of the surface has clear advantages if it is the central cell that is of greatest importance. Schmidt *et al.* (2003) also warned against the use of this model as they found it to be less reliable in flatter areas where it was found to be sensitive to error in the elevation data. As the study area is characterised by high altitude steep terrain, smoothing from the local quadratic algorithm (Equation 4.1) was viewed to be problematic, where local maxima are of primary importance in predicting glacier accumulation. Although it can be argued that smoothing a terrain surface smoothes the error present within the DEM, it does so at the expense of maintaining any original values. In this research DEM error was analysed and removed separately, and consequently smoothing the terrain at this stage was not necessary. However, in this study flat areas are not of primary importance and accurate measures that are not dominated by error are most critical. Therefore surface morphometric measures (given as the nine coefficients A – I) were extracted using Equation 4.2.

4.4.4. **Elevation Derivatives**

Morphometry and consequently geomorphometry simply refer to the process of characterising and representing surfaces mathematically. There are no rigid guidelines as to what should be measured and which statistics should be used. A main reason for characterising a land surface is to learn and understand more about the processes that are occurring or have occurred on it and to understand the effects on a process and the cumulative effect of past processes. It is therefore necessary to select geomorphologically significant measures.

The measures suggested by Evans (1980) (Table 4.2) do not form an exhaustive list and Speight (1974), Wood (1986), Depraetere (1987) and Pike (1987, 1988) use a larger collection of measures. However it is suggested by Evans (1979), Wood (1986) and Skidmore (1989) that elevation derivatives higher than two have no geomorphic meaning and by their extraction there is a risk of placing to much emphasis on the empirical rather than the geomorphological aims.

Moore *et al.* (1991) suggest that the added complexity and statistics that these extra variables bring questions their overall usefulness.

These derivative measures are used in a wide range of research areas, varying from hydrological, geological, engineering and biological applications, and more recently in landform classification (Arrell *et al.*, 2001). Although these measures of surface form provide valuable information about how earth surface processes interact with the terrain surface as individual measures, they are likely to account for only some characteristics of a process, and it could be argued that a more comprehensive interpretation of a process or set of processes is possible through composite terrain measures.

4.5. Composite and contextual terrain Parameters

Although Wood (1986) and Skidmore (1989) dispute the use of elevation derivatives greater than two (Section 4.4.4), compound or contextual parameters are often used in geomorphological studies. Scheidegger (1970) attempted to expand upon the surface derivatives measures as a tool for characterising landscapes and landforms, suggesting that a study of derivative interplay is important, examining the system as a whole and identifying order within it.

Composite topographic measures extract meaningful characteristics of the terrain surface, commonly by combining elevation derivatives or measures that describe the spatial organisation of the surface, its characteristics and components.

Types and combinations of these parameters are numerous and the application area largely determines their composition. Hydrological applications commonly incorporate upslope characteristics, both area and gradient. Soil modelling applications use information on the upslope area and the vertical distribution of soil characteristics. Archaeological applications examine exposure using the spatial distributions of finds and sites in relation to altitude and visibility.

Two types of measures are identified here that characterise geomorphological position and geomorphological context. Geomorphological position refers to location within a landform rather than within any two-dimensional coordinate system. Geomorphological context extends this by quantifying how geomorphological position fits in to the landscape, where position would provide slope profile position and context would quantify its position within the mountain range or valley.

A quantified representation of landscape position and context can be extracted from within a DEM, but to do so requires a consideration of what landforms are present in the landscape, which are critical in understanding the earth surface processes of interest and what parameters are required to capture and quantify these terrain and process interactions.

Terrain is important in controlling glacier accumulation areas (Hock, 2003), because it controls local climate and snow redistribution. Identifying measures that characterise local and surrounding terrain as important to understand and quantify. To characterise these types of terrain process interactions it is often necessary to consider more than a simple focal area of 9 or 12 pixels to understand the process or parameter, where a surrounding zone may provide more useful information. The problem arises in identifying what this zone is and how to define or delineate it.

A series of parameters are now discussed that are thought to be useful variables in improving are ability to predict characteristics of earth surface and atmospheric processes; specifically temperature lapse rates, precipitation lapse rates, near surface wind flow and snow redistribution.

4.5.1. **Relative Height**

Local measures of altitude can often provide spurious results if assumed to be characteristic of the surrounding area or the driver for locally recorded climatic parameters. This is largely a function of differing scales of process and measurement. Two different techniques for capturing more representative elevation values are reported; relative measures of local height and characterisation of the scale dependence of altitude within a zonal area.

Relative altitude characterisation employs different measures of central tendency and distribution characteristics (maximum and minimum) to provide the most representative altitude value and characterises the variability in altitude within a zone. The scale dependency characterisation quantifies the variability in altitude as the size of a zonal area varies, quantifying the spatial variability in altitude values relative to a central cell. This is particularly useful in quantifying the degree to which local maxima or minima extend beyond the local area.

These are examples of geomorphological position measures and are important to alleviate some of the limitations of a fixed grid size.

4.5.2. Slope position

Slope position is an important variable in understanding many geomorphological processes, including discharge and velocity in fluvial geomorphology, landslides and sediment transfer in hillslope processes and avalanches in glaciology.

Climatology is also influenced by slope, which initiates temperature inversions, turbulent heat transfer exchanges, modification of wind strength and direction, and cloud development (Barry, 1992; Oke, 1987). In these contexts slope position refers to the relative location as bounded by ridge and valley / plain locations along the slope profile.

Glacial valleys are scale specific (Evans, 2003; Evans and McClean, 1995), and are delineated by the valley head and its bounding ridges, which mark the top of the steep valley sides. This distinctive form is largely apparent on topographic maps, although more complex and coalesced forms do exist. Delineating valleys on topographic maps requires evaluation of contextual and local topographic variations, with an inherent consideration of scale: although this will be explicit within the map and the contour intervals, it is very difficult to automate the extraction of this type of information from a DEM. The primary reason for this difficultly is the difference in scales of the landform and the resolution of a DEM. Although it is possible to classify a DEM into its constituent elements or landforms, these to date have largely only considered cell-by-cell (local) classification, where context if at all used is secondary. Consequently classifications only identify landforms smaller than the pixel resolution and that are internally consistent preventing mixed pixel classifications. Common classifications include types of slope, peaks, pits, ridges and passes (Skidmore, 1999; Wood, 1986; Arrell *et al.*, 2001). Valleys are significantly larger than commonly used pixel resolutions, and would not be identified in a DEM unless topographic context was considered.

A methodology for extracting slope position and delineating valleys is proposed on the following page, although its implementation was not possible within the scope of this research. Algorithms that extract ridge or channel networks commonly break down as a result of two primary problems, DEM resolution and surface complexity. Both algorithms for ridges and channels are dependent upon a persistent trend in the land surface, surface convexity and surface slope respectively. However, in reality surfaces are highly complex and local scale roughness can often intervene, distorting these theoretically persistent trends. Where this roughness intervention occurs, unless the algorithm has spatial thresholds for local variation, the classification of channels or ridges networks breaks down. A disjointed network results, that is highly restrictive if any landform or process modeling follows. This lack of flexibility in the

algorithms prevents them from extracting the topographic structure information stored within the elevation surface, although representativeness of this information is entirely dependent upon its spatial resolution of the classified data.

Surface resolution is the second major limitation to the effectiveness of network extraction algorithms. Although digital elevation data is becoming increasingly finer scale and the general research consensus is that the finer the resolution the better (Lane, 2003) this statement is entirely dependent upon the surface analysis technique used. At this point it is important to evaluate ridges and valleys separately. Both ridges and valleys are scale specific (Skidmore, 1999; Wood, 1986; Arrell *et al.*, 2001; Evans, 2003) and cannot be effectively considered at all surface resolutions. However although the most appropriate spatial resolution could be selected (Arrell *et al.*, 2001), it is essential to consider scale specificity when extracting any landform from an elevation surface. Commonly any attempt to extract channel or ridge networks from an elevation surface will misclassify small-scale surface elements as larger scale landforms, over predicting channels and ridges with dense disjointed networks. Although the topographic characteristics between these micro and macro scale features are the same, the landform component they represent differs, primarily as a function of scale. There is therefore a need to incorporate scale into any meaningful land surface characterisation.

An approach that incorporates scale and flexibility in extracting valley and channel networks is proposed here. It initially identifies potential valley floors and channel thalwegs using slope gradient. Areas of low gradient are flagged as potential valley floors and areas that concentrate local flow are flagged as potential channel thalwegs. This currently can be implemented within a GIS, however it has been identified above that more robust techniques are required to verify and integrate these initial observations. These initial landform classifications will adopt a fuzzy classification, representing more and less marginal classifications. Fuzzy logic has successfully been applied in landform classifications quantifying landform continuums and is believed to provide a more robust interpretation and categorisation of landforms and landscapes (Irvine *et al.*, 1997; Lagacherie *et al.*,1997). By extracting cross sectional profiles orthogonal to valley and channel centres and examining the variation in elevation values along these profiles it is possible to identify channel, valley and ridge locations. A ridge is not identified as the first convexity encountered, but the first persistent convexity that occurs at an appropriate scale for the study area and the DEM resolution. Equally, channel thalwegs can be flagged as the most significant (persistent) concavity, and valley floors identified as areas bounded by significant changes in gradient and aspect. Significance would be tested by the persistence of local variations by removing the prior limitations of local scale roughness.

This procedure would require an estimation of the dominant spacing of valleys within an area either through local knowledge or map integration or the use of semi-variograms. This would ensure that the scale specificity of landforms would be incorporated into the classification, but would not dominate the extraction procedure, as the most significant changes in gradient or convexity would determine the landform delineation but would simply be used to ensure that this was at an appropriate scale.

Although a theoretical methodology has been proposed, its implementation was not possible within the constraints of this research project. It was therefore necessary to adopt a simpler quantification of valley and slope boundaries that although it gives a less accurate classification provides significant computational and timesavings.

Commonly glacial valley systems exploit and enlarge fluvial valley networks, where valleys are orientated downslope. A common GIS functionality is the extraction of drainage networks, although the algorithms used to extract flow paths are subject to uncertainties and calculation artefacts associated with these are largely constrained to fine scale flow patterns where the DEM is too coarse to accurately represent the network. Higher order streams and channels are more accurately represented, but they too may be subject to DEM resolution artefacts. Flow paths are extracted by initially identifying the steepest downslope direction for each pixel, indicating the direction that water would flow out of the cell. This either identifies four orthogonal or eight (Rook or Queen's cases) possible outflow directions. Here the Queen's case is used as this is found to provide more accurate results. A flow network is extracted by adding a 'seed' or water droplet to each cell in the DEM, and tracking its path through the surface, the total number of water droplets passing through each cell is recorded and represents the intensity of flow through each pixel. Jenson and Dominque (1988) provide details of the flow extraction method. A user-defined threshold is implemented to specify the flow intensity at which concentrated overland flow constitutes a channel. This threshold is dependent upon the drainage and hydrology characteristics. Tarboton *et al.* (1991) proposed a methodology for determining an appropriate threshold value for stream network delineation.

Implementing a high flow threshold identifies only the largest channels within the DEM (Figure 4.2 shows DEM used in subsequent classifications), the select of this threshold value is subjective and optimal values are hard to establish. The appropriateness of the threshold can be performed by a visual verification of the extracted network overlaid on the DEM. Using this method a threshold of 100 was used extracting both main and smaller tributary channels (Figure 4.3). Although the pixels identified as channels should create a network, the sensitivity of the algorithm to local slope and the fixed pixel resolution result in breaks and gaps in the network.

This is most apparent in the valley floors, which are flat with gentle gradients (Figure 4.4). As the identification of these lowland areas was critical to the prediction of the meteorological variables it was necessary to force their inclusion in the extracted network. The characteristic feature of the glaciated valley floors is their low gradients; these were successfully delineated by selecting all areas with a slope less than or equal to 3°, at an altitude less than 1500 m (Figure 4.5). Although this might appear a rather clumsy delineation method the results showed surprisingly strong agreement with a manual classification. The success of this procedure is largely related to the characteristic form of glaciated terrain, where rapid changes in gradient mark the edge of channel floors, with predominantly steep eroded slopes. These valley floor areas were combined with the extracted channel network, creating a raster layer representing valley and channel floors (Figure 4.6a,b). This layer formed the basis of many of the topographic measures discussed hereafter. This result compared favourably to morphometric landform classifications of Wood (1986) and Arrell (2000). Wood (1986) used the landform classifications proposed by Skidmore (1999), peak, pit, ridge, pass, channel and planar units (Figure 4.7). Although these units appear to have clear geomorphological meaning, a lack of contextual verification or aggregation and the local nature of the classification limits the representativeness of the landform units.

Of these landform units channel and planar both describe valleys: by combining the fuzzy memberships to each of these units it is possible to create a composite landform class. However this fails to identify broad and gently undulating valley floors and was rejected (Figure 4.7).

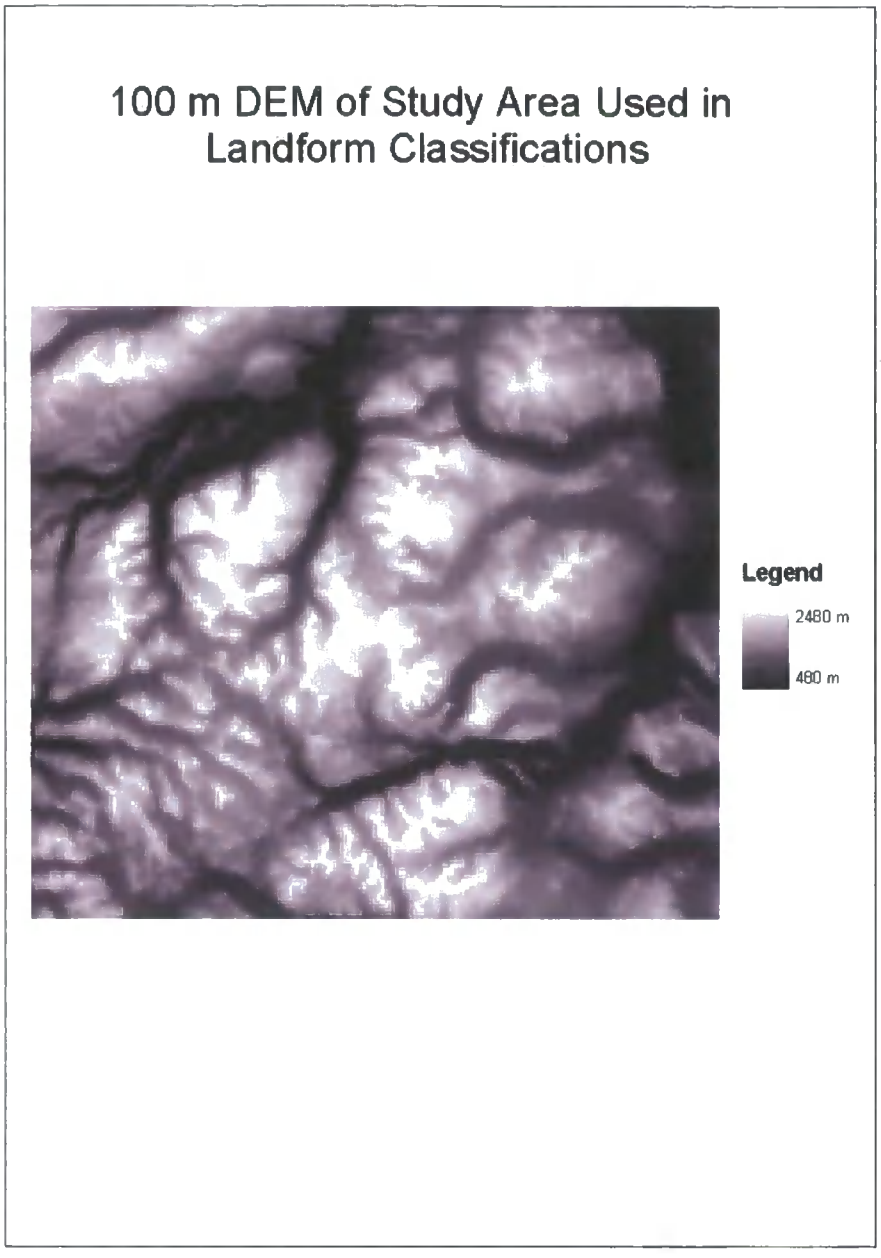

Figure 4.2: Study area DEM used within landform classifications

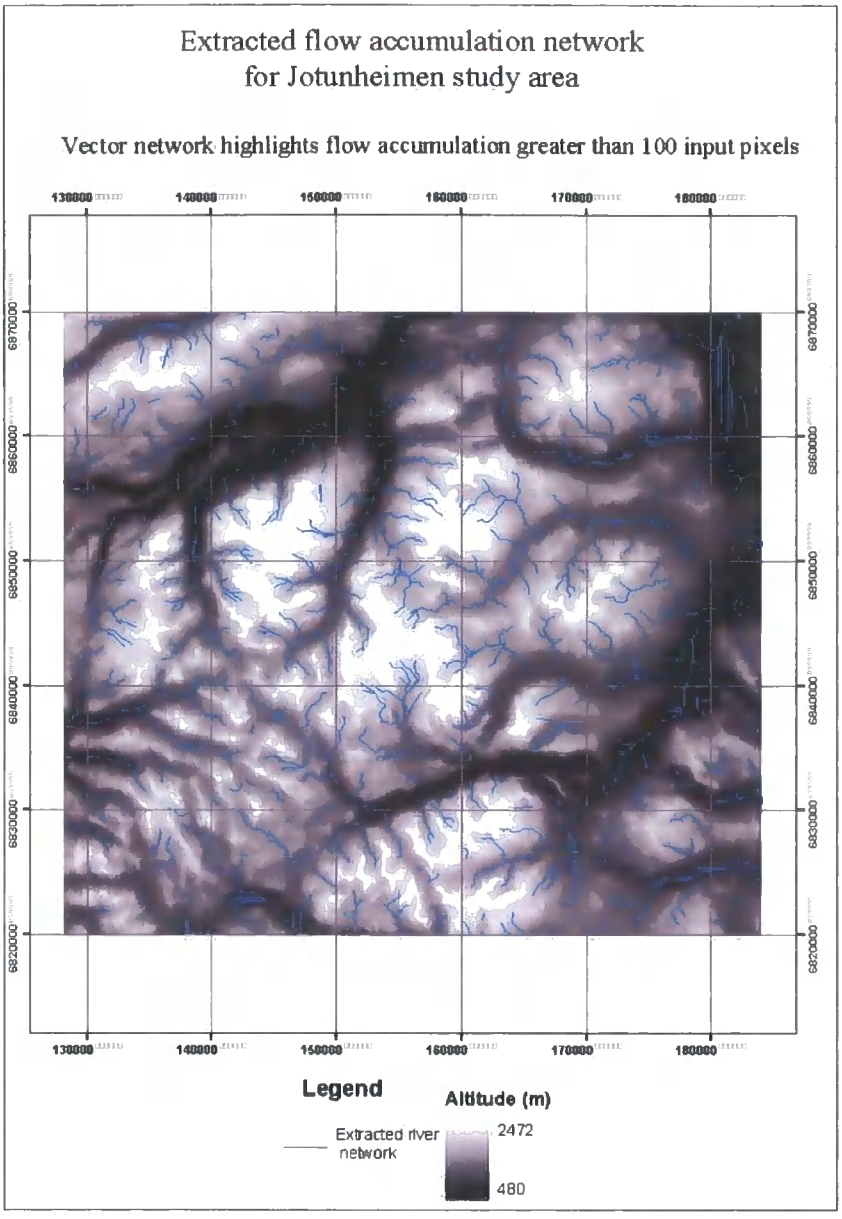

Figure 4. 3 Flow accumulation surface, highlighting flow concentrations greater than 100. This indicates that at least 100 pixels flow are predicted to flow into each of the highlighted pixels.

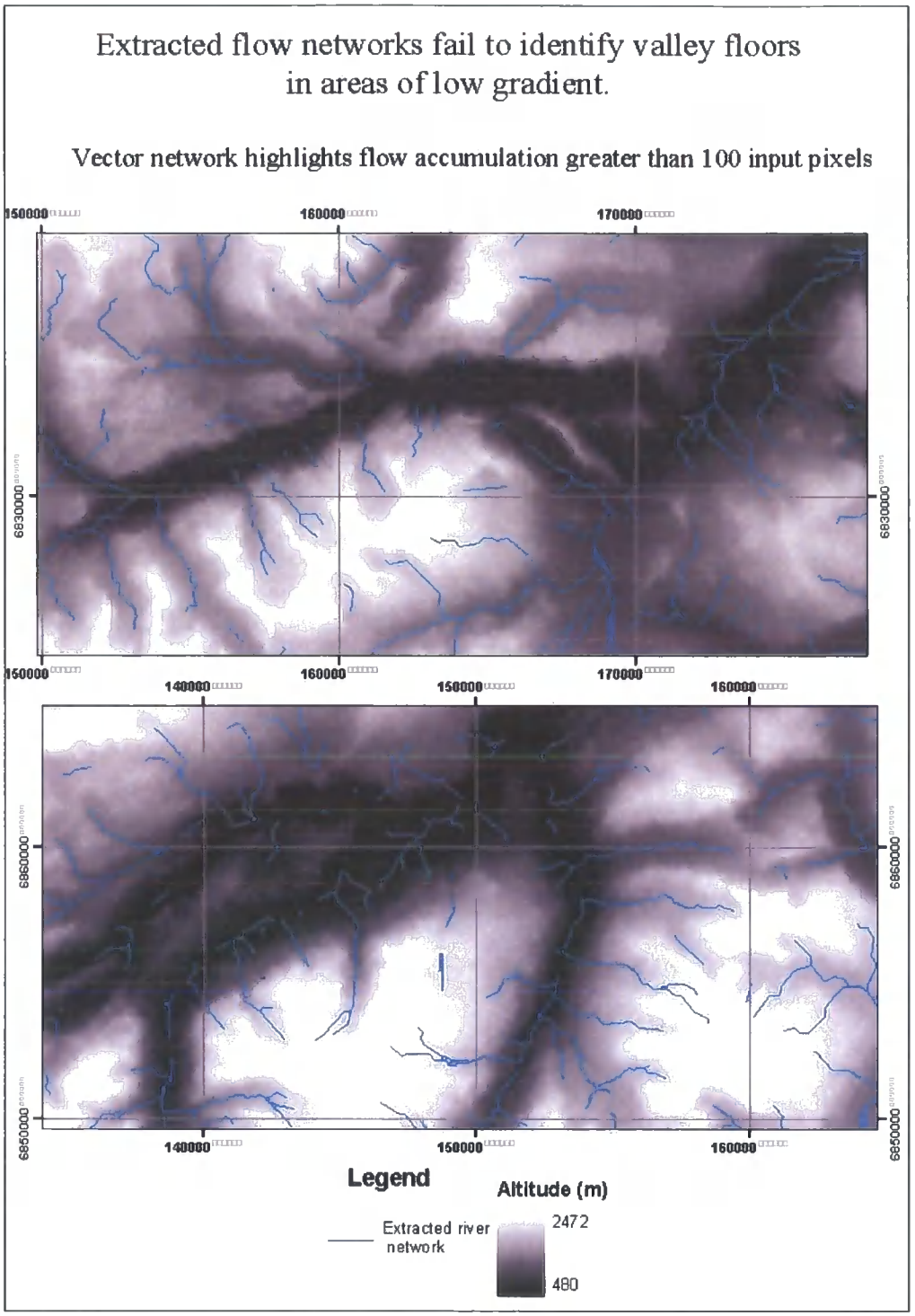

Figure 4.4 Poor connectivity in flow networks in areas of shallow gradient – valley floors are not simulated

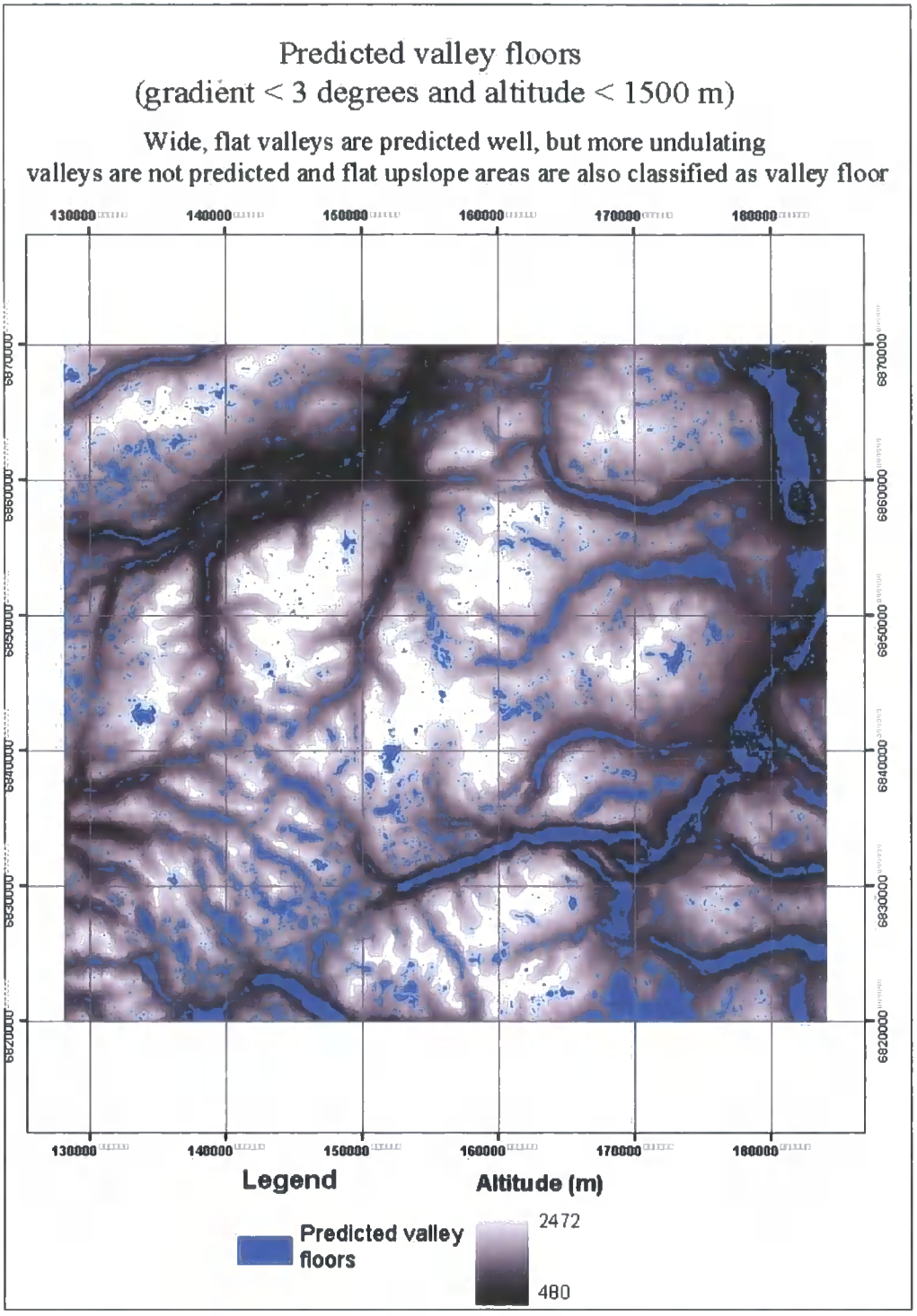

Figure 4.5 Predicted valley floors, areas of low gradient and low altitude

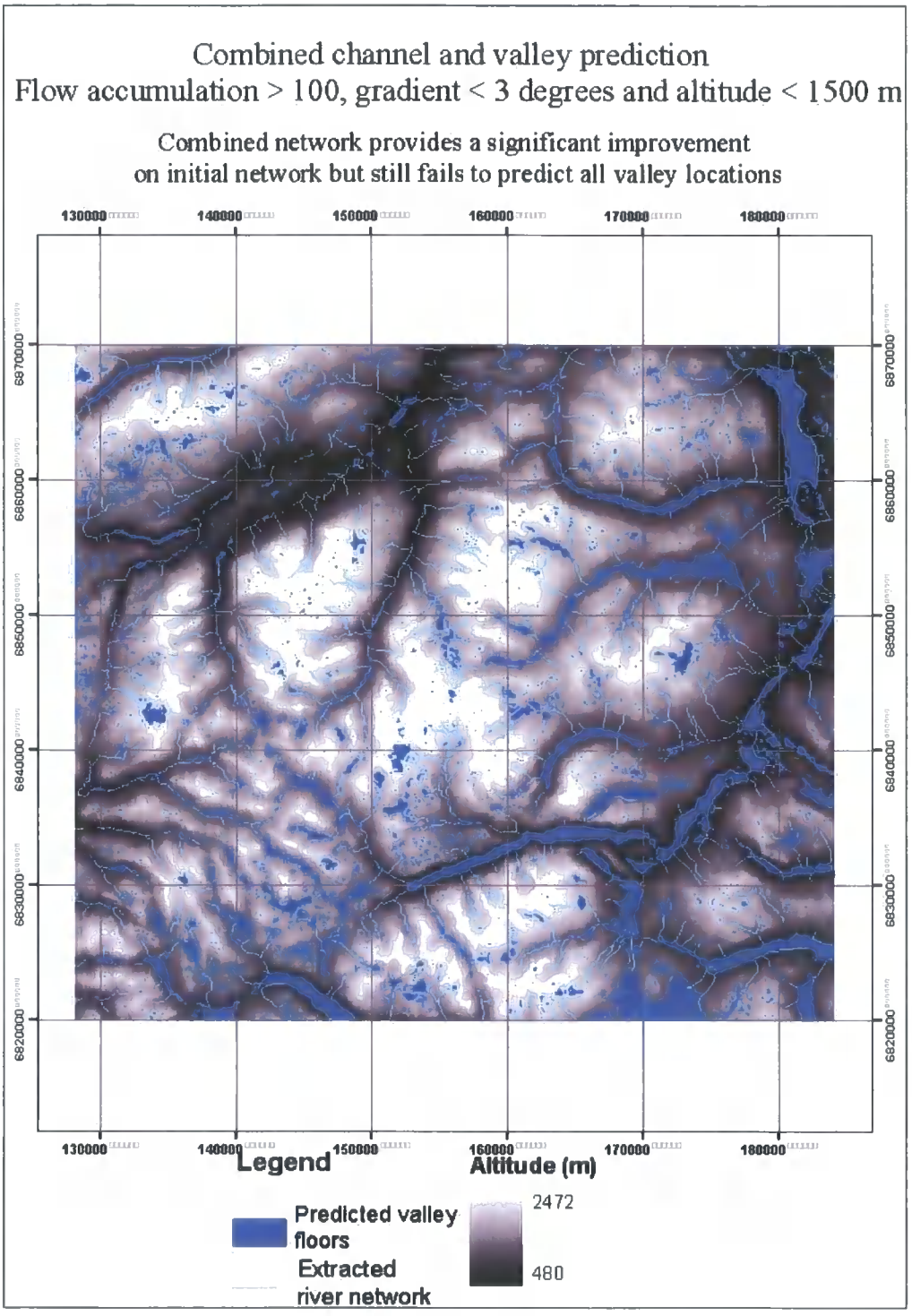

Figure 4.6 a Combined flow network, primary and secondary channels identifying fluvial and glacial structures.

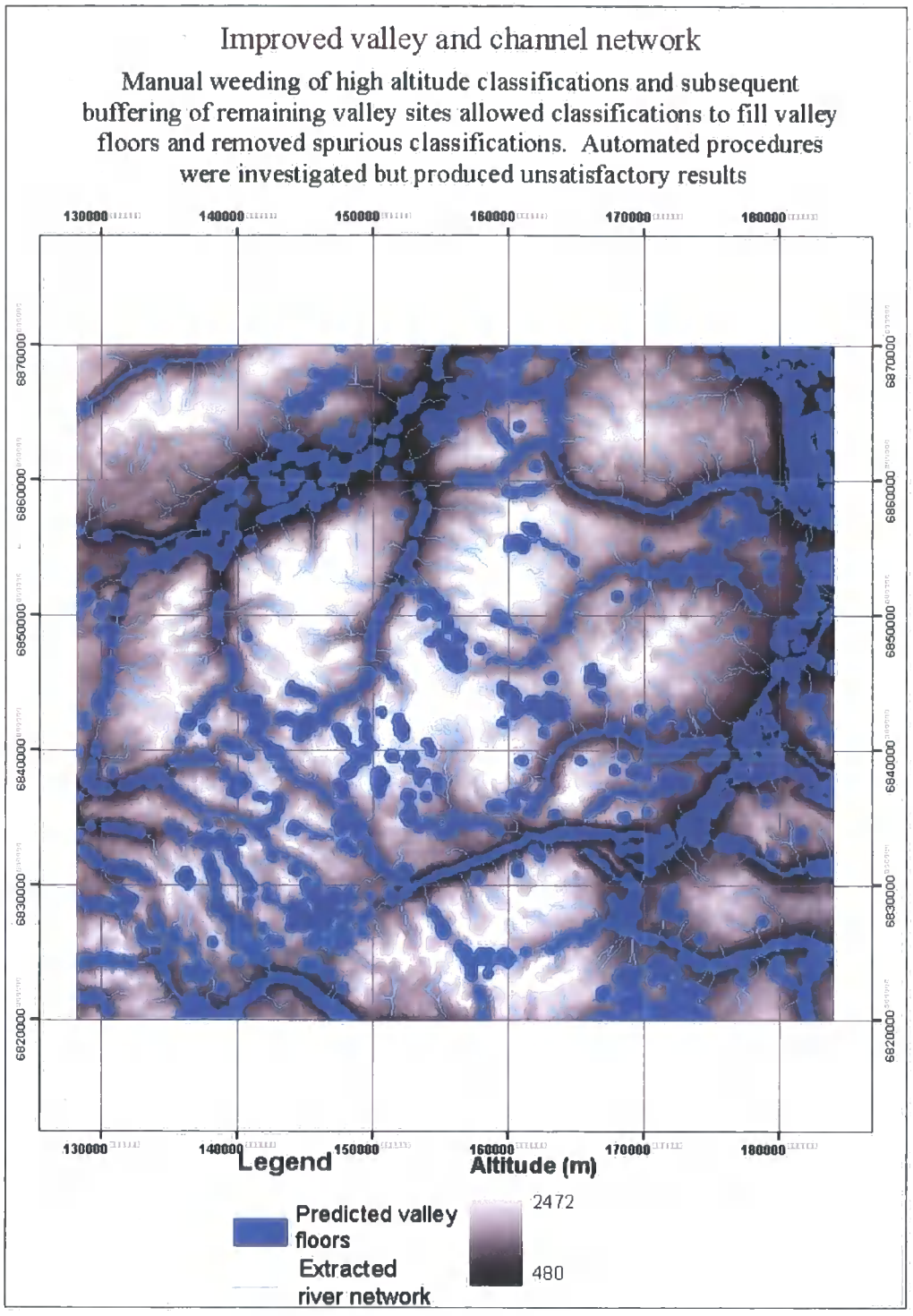

Figure 4.6 b Improved combined flow network, small spurious valleys removed and primary valleys expanded to fill observed valley floors.

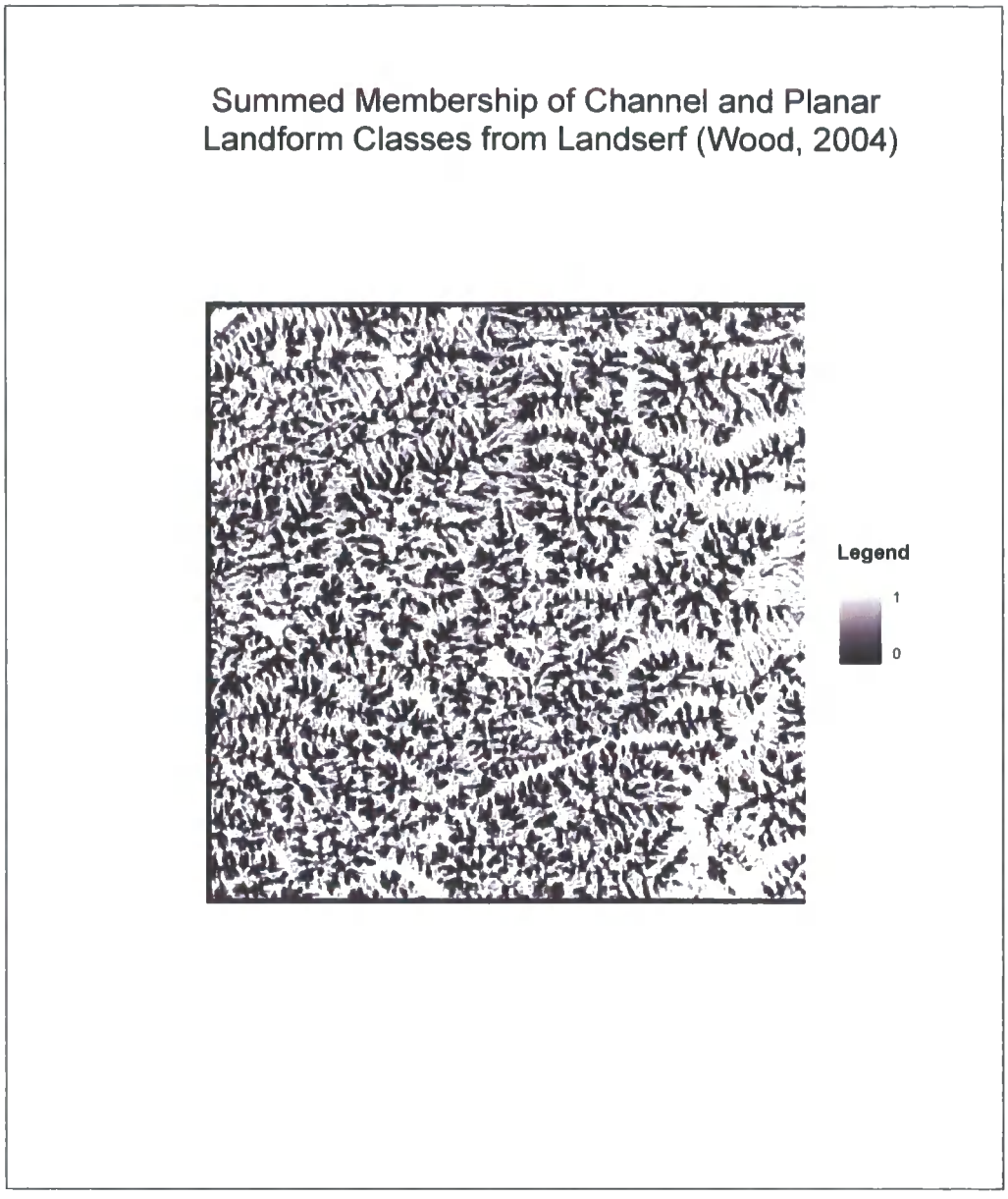

Figure 4.7: Study area DEM and composite landform class extracted using Landserf (Wood, 2004).

Channel and valley terms have been used interchangeably, as the primary difference between the two is scale; their climatic implications are the same although their area and degree of influence will differ. It is possible to tentatively apply a classification identifying secondary valleys as channels and primary valleys as glacial valleys.

Like valleys slopes play an important role in earth surface processes and can be assumed to start at the edge of a valley floor and extend up to the ridge boundary (if present), some indication of position on this slope may be of importance in predicting meterological parameters. By calculating the distance of each cell away from the nearest valley or channel centre it is possible to quantify this position and the degree to which valley or slope dominate. The ESRI ArcInfo

GRID command *linedistance* was used to calculate the distance to the nearest channel or valley within a 15 km radius, where larger values indicate a greater distance to a channel and smaller values indicate a greater proximity to a channel (Figure 4.8).

This is an example of a geomorphological position measure and a global spatial analysis technique as each pixel in the output accumulation raster is dependent upon all of the pixels in the input DEM.

4.5.3. **Valley context**

This relative slope position only provides a measure of local slope position, and does not take any account of the slope within the landscape for example, whether the slope lies within a small tributary or whether it marks a major divide between two valley systems. It is therefore necessary to associate this measure with a geomorphological context measure to identify its location within larger scale features, whether they are valleys or mountain ranges.

The extracted network can be used to quantify this position, as it not only holds information about local channel characteristics but also contains topological information about arcs and their intersections and origins allowing the extraction of more contextual measures. Valley context was represented by the distance from the start of each valley (the distance from the start of the upstream line).

Although this operation is easily applied to the channel network extracted using the ArcInfo algorithm, where flow direction governs the orientation and structure of the flow network, it is not easily implemented using the composite valley network created in Section 4.5.2. Here flow direction is not consistent and gradients are shallow and fluctuate: it is therefore necessary to consider each of these networks separately. Conceptually this is acceptable as smaller valleys (named secondary valleys), leading down to the main valley floor (named primary valleys) are likely to be controlled mainly by this distance to valley, rather than distance down valley. This distance from secondary to primary valleys can be extracted using the ESRI ArcInfo Grid *flowlength* command: this uses the arc coverage file and the flow direction raster generated earlier to identify the upslope direction and calculate the distance from the bottom of the valley. Distance upslope from the end of the channel and distance downslope from the top of the valley were recorded and used to calculate relative distance up the local slope

$$\text{Relative distance} = \text{distance upslope} / (\text{distance upslope} + \text{distance downslope})$$

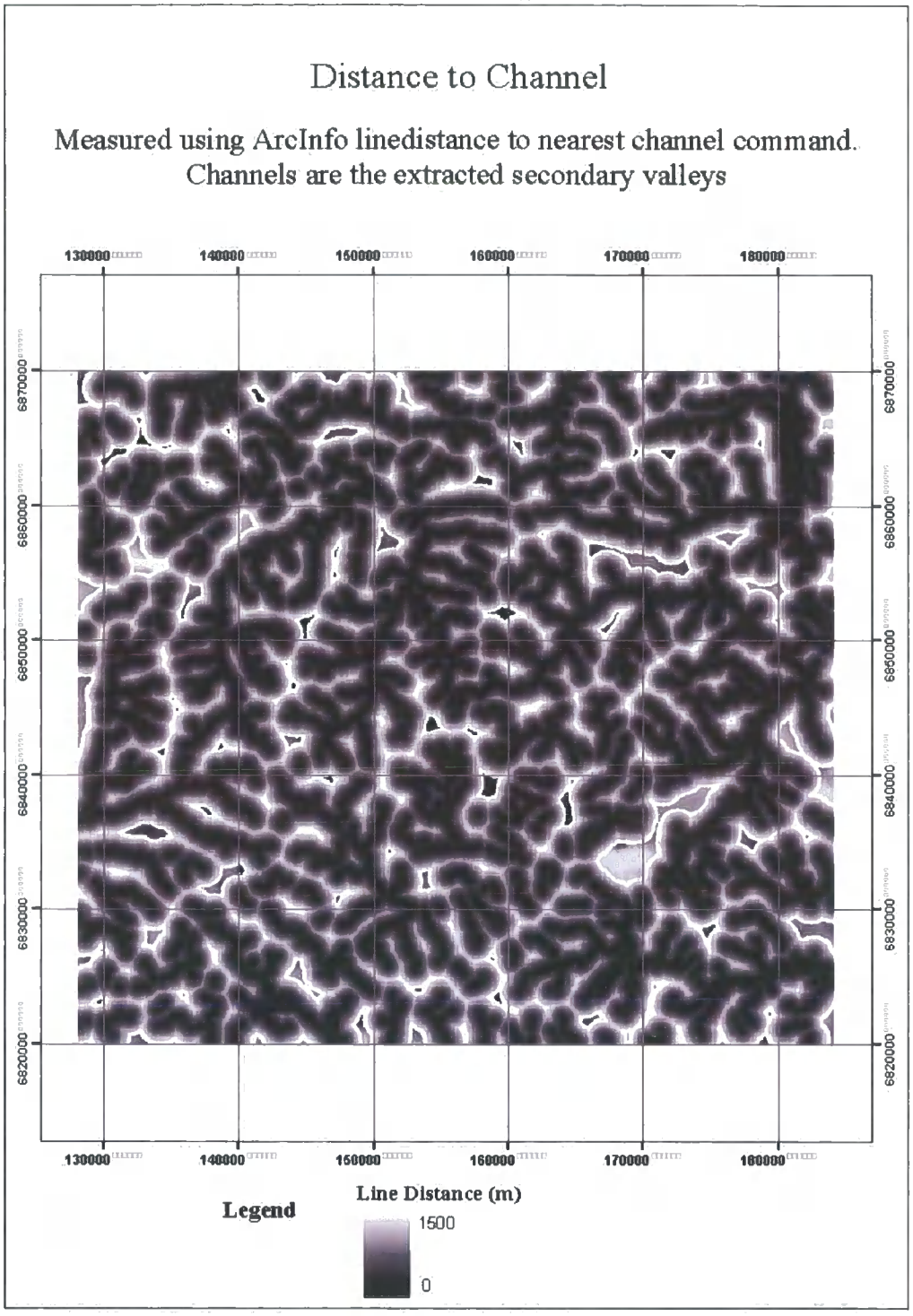

Figure 4.8 Line distance: Highlighting distance from nearest secondary channel

Distance down primary valleys was more difficult to extract, as valley floors are more than one pixel wide and do not share the surface characteristics of secondary valleys. Initial attempts used a polygon representation of the valley classification, seeded at the upslope end and used in a cost surface analysis to represent down valley distance. However polygons were disjointed,

after merging and buffer valley polygons an improved representation was created, but distance measures represented per polygon downslope distance and did not show a meaningful measure. Consequently only secondary valley context measures were used in subsequent analysis (Figures 4.9a, 4.9b).

This is an example of a geomorphological context measure and is a zonal analysis operation as it only requires evaluation of cells along the same arc to calculate the output value.

4.5.4. **Valley orientation**

Although distance down slope and down valley is important when considering topographic modifications to climatic variables, its effect is often enhanced or reduced by the orientation of a location with the local (whether primary or secondary) valley. The orientation of each cell to the nearest valley was extracted using the Esri's ArcInfo Grid *linedirection* command. This calculates the average direction of lines in a neighbourhood from 0 – 360°: the difference between this and the pixel aspect provides information on the valley orientation. Again this measure was only found to produce meaningful results for secondary valleys where surface aspect of valley floors and weak vector representations did not create robust results (Figure 4.10).

4.5.5. **Maritimity**

Although local scale topographic modifications give feedbacks to local climatic parameters, large regional scale influences are also integral to understanding climate. One such influence is maritimity or the distance from the open ocean. Initially this was calculated as the distance from the Norwegian coastline (Figure 4.11a) highlights distance measure), however this provided a misleading measurement as it recorded the distance from sea, that is distance from the complex fjord system not open ocean. To avoid this misrepresentation it was necessary to initiate distance measure from off the coastline (Figure 4.11b). This provided a more useful measure of maritimity, representing the degree of continentality.

An alternative approach would have been to simplify the coastline using a smoothing line simplification algorithm (rather than point removal algorithm) to remove some of the more complex fjord systems. This approach would still have lead to a complex coastline that would not represent the influence of the open ocean.

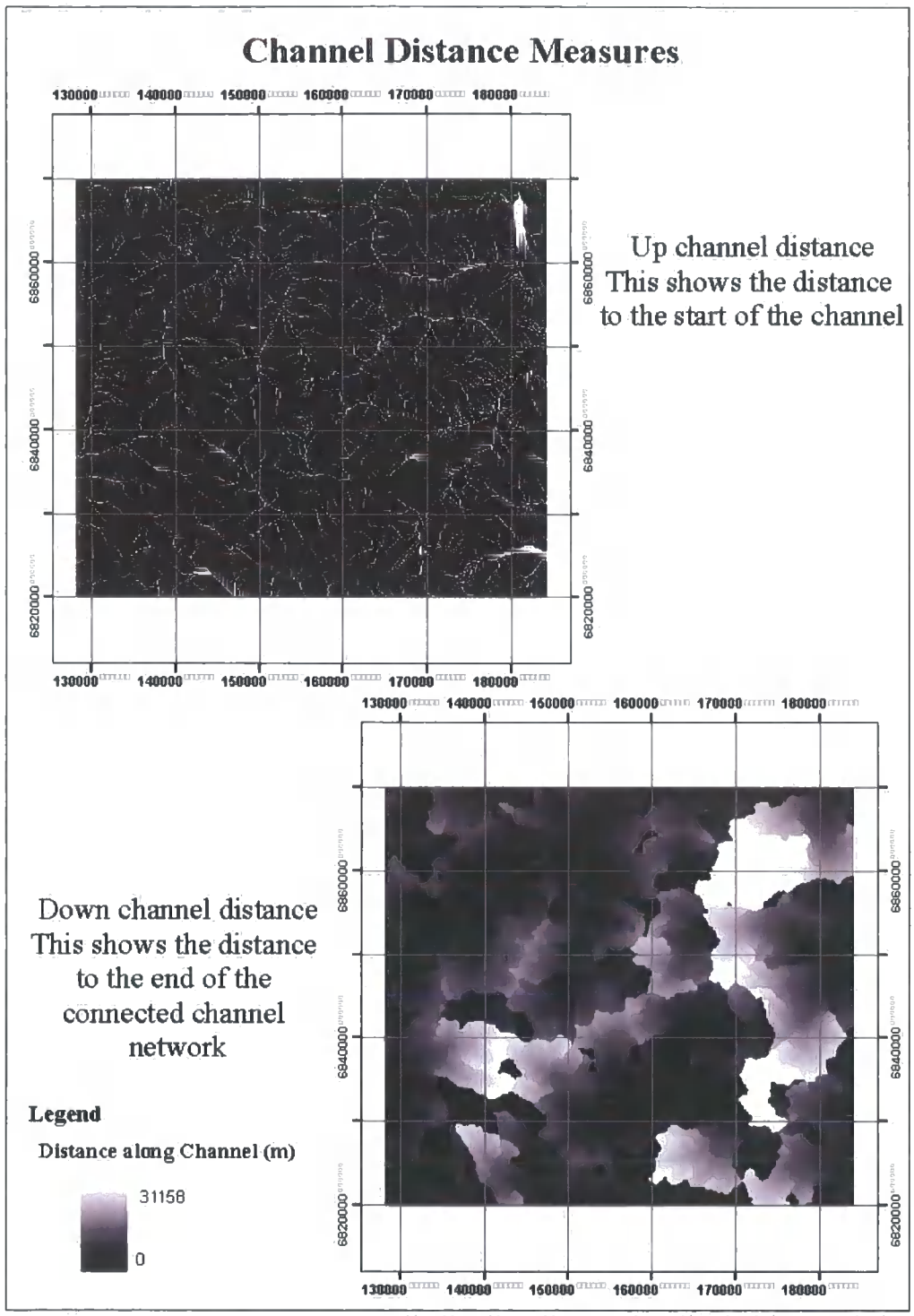

Figure 4.9 a Flow length measures, highlighting up and down channel lengths calculated from the secondary channel network.

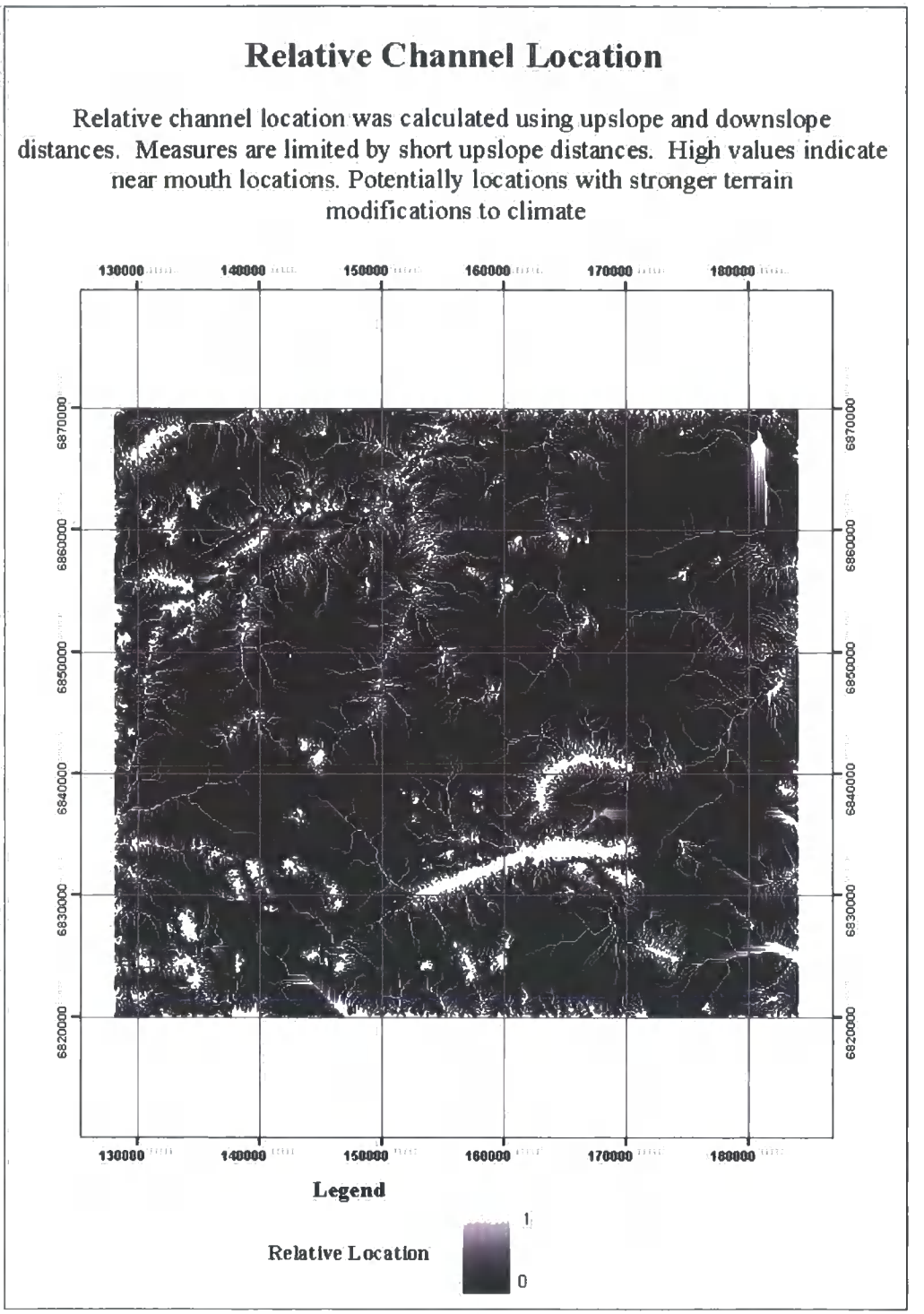

Figure 4.9 b Relative channel location calculated from channel length measures, highlighting position within the extracted secondary channel network

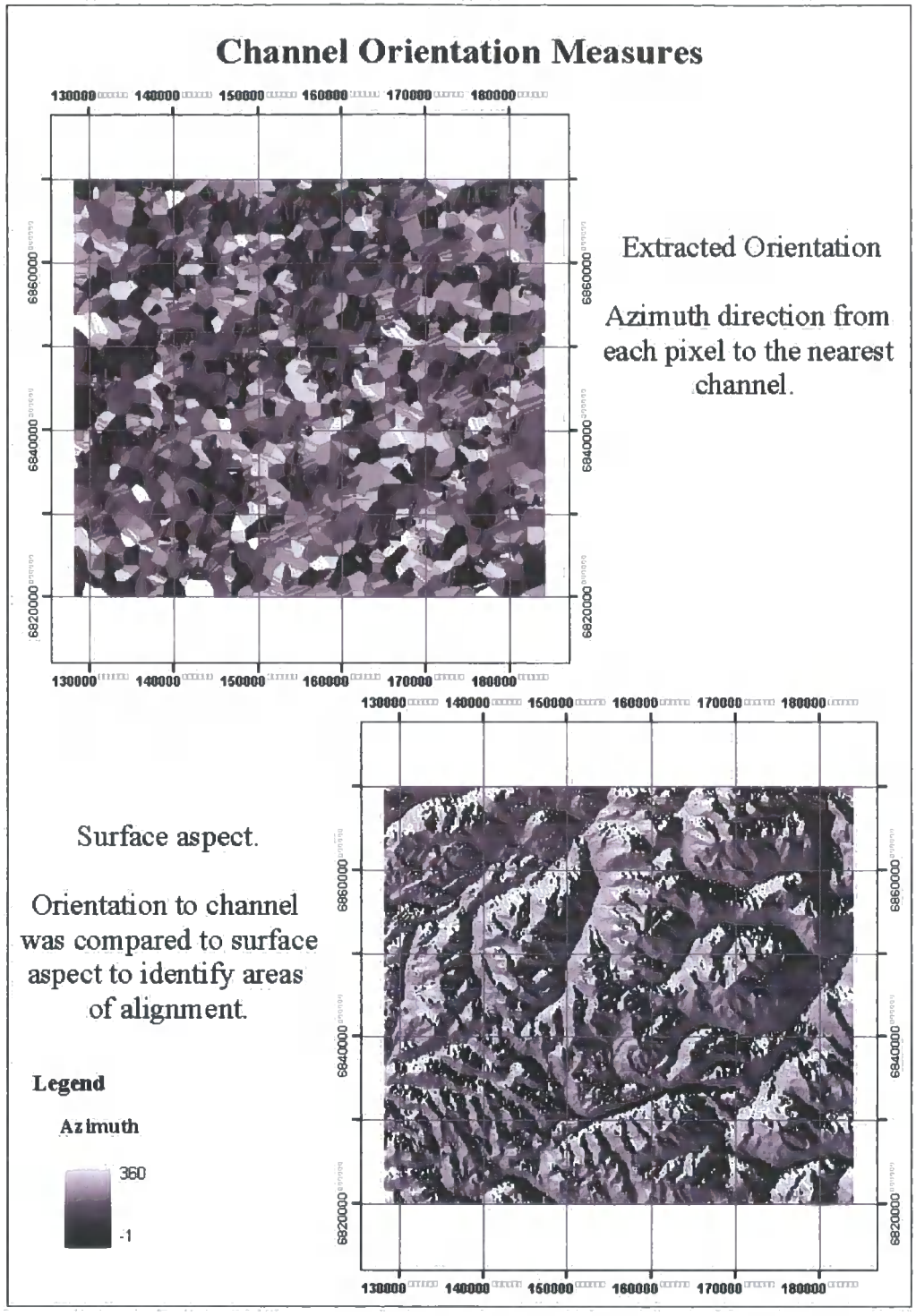

Figure 4. 10 Channel orientation measures, calculated from extracted secondary channel network and surface aspect.

Figure 4.11a Maritimity measure derived from coastline, yellow to purple denoting increasing distance

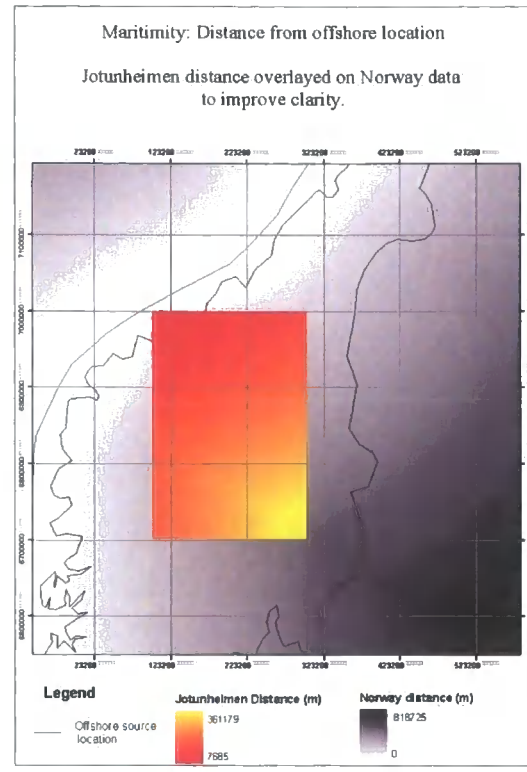

Figure 4. 11b Maritimity measure derived from an offshore location.

Exposure to coastal wind and pressure systems is only one measure of exposure that can be extracted from DEMs.

4.5.6. **Exposure**

Topographic exposure is another geomorphologically significant parameter, and can be conceptualised and measured at many different spatial scales. This multi-scale existence can be conceptualised as mirroring the multi-scale character of earth surface processes, where exposure at any spatial scale can be quantified using an appropriate topographic search radius.

Exposure describes the degree to which an area is subject to external processes and forcings. An exposed location is geomorphologically conceptualised here as subject to more frequent and faster winds and more extreme temperatures, where little or no shelter is provided by the surrounding topography. Simple conceptualisations measure exposure as the local differences in height – largely based on the relative height measures outlined in section 4.5.1. Although

this does provide a measure of how a location is positioned relative to its surroundings more representative or useful measures are available.

Two types of exposure measure are detailed here, largely drawing on measure outlined in sections 4.5.1 – 4.5.4, type 1 quantifying the degree to which a location is exposed to air as a result of high surface roughness and type 2 the degree to which a location is orientated in the direction of channelised or constricted flow. Type 2 measures included slope postion, valley context and valley orientation. Two primary variants on type 1 exposure were used here: where subpixel altitudes are known it is possible to compare that height with the encompassing pixel height, quantifying how locally rough or exposed a location may be (for example climate station alitude). A coarser scale measure of relative exposure quantifies how a pixel altitude compares to its surrounding neighbourhood, taking an arithmetic mean.

4.6. **Surface Roughness**

Measures of altitude variability can be thought of as measures of exposure and are also one of the most commonly used measures of surface roughness.

Although surface roughness is commonly employed to explain chaotic states or variability in earth surface processes, its quantification and scale varies considerably, largely according to the scale at which the process is operating. When deriving a surface roughness index, it is important to consider what characteristics of the terrain surface results in the process behaviour. The index proposed here uses variations in altitude and aspect (Equation 4.2). Standard deviations were used to quantify this variability, where large standard deviations indicate high variability suggesting a rougher surface. The two variables were multiplied to produce a composite measure to characterise surface roughness. Large changes in surface aspect commonly result in breaks in slope which are often instrumental in altering earth surface processes.

$$\text{Surface Roughness } S_R = \sigma(Z) * \sigma(\sin\Theta) \qquad \text{Equation (4.3)}$$

A composite altitude and aspect measure attempts to provide a quantification of surface variability specifically addressing geomorphologically significant variables over any spatial area (Figure 4.12).

Exposure is, in part, related to shade. Although shade is easily calculated within many GIS large uncertainties surround these calculations. Shade is also an important variable when

considering surface energy balance, where strong local gradients can exist between areas exposed to the sun for different lengths if time.

Figure 4.12 Surface roughness calculated at increasing spatial resolutions. Identifying areas of rapid and slow change in surface aspect and altitude.

The accuracy of terrain derivatives is dependent upon, and sensitive to, the quality of the DEM. Large uncertainties and inaccuracies propagate through the derivative calculations where spatially and frequency distributed error is present in the original data.

4.7. Error and Uncertainty

Error and uncertainty are present in all sampled data, the magnitude and types of error and uncertainty vary between datasets and data collection methods. As elevation data is commonly sampled at points and interpolated to a surface, many of the surface elevation values within the DEM will be estimated. It is therefore important to assess the accuracy of these estimates and look for any interpolation artefacts.

Terminology surrounding error and uncertainty is sometimes vague, DEM error refers to the difference between the observed value and the recorded value.

Error is commonly measured or recorded as the Root Mean Square Error (RMSE) which provides an estimate of the squared mean deviation above or below the recorded value. Normally this value is not spatially distributed, but assumed constant throughout the surface. Although this measure is useful, error is often spatially organised, especially in terrain surfaces (Guth, 1999; Li, 1994; Wood and Fisher, 1993; Monckton, 1994). This is to be expected if it is considered that a landscape (in terms of its landform components) is spatially organised and, as Wood and Fisher (1993) suggest, that elevation accuracy is not independent of local topography. This therefore leads to a hypothesis that error within a DEM will have a degree of spatial autocorrelation.

Research has focused on accounting for and visualising error associated with the vertical resolution of the DEM, by adding noise to the data, performing Monte Carlo error surface iterations, and through educating users of the certainty with which they can use the altitude surface. It is possible to differentiate between systematic, spatially and spectrally organised error. The former is significantly simpler to remove as it is tends to be uniformly distributed across the surface. However spatially and spectrally organised error present in a DEM needs to be removed with respect to this spatial and spectral organisation, avoiding global smoothing.

Although RMSE's are commonly reported, users of elevation data must acknowledge and manage these errors if the data are to be optimally used. However, Gao (1997) argued that only

limited research had been carried out to date to assess the impact of source data and processing errors in elevation surfaces.

Although error is inherent in elevation surfaces due to measurement precision and data sampling, unnecessary error is often created as a result of the use of an inappropriate interpolation algorithm or interpolating at a too fine resolution. This can incorporate distinctive and problematic artefacts into the data surface that become difficult to remove because they are both spatially and spectrally organised. Similar artefacts can be introduced during interferometry or as artefacts of overlapping satellite swath data.

4.7.1. Study Area DEM Error

The DEM, purchased from Statens Kartverk, was studied to look for spatially and spectrally organised error by examining a histogram of surface elevation values and by viewing the higher order elevation derivatives, gradient and profile curvature. These higher order surfaces are very sensitive to small errors in height (Wise, 1998), with errors propagating rapidly. These techniques identified significant interpolation artefacts in the data that if not removed would propagate significant errors throughout the prediction model (Heuvlink *et al.*, 1989).

Two interrelated error components are present in the elevation surface, contour altitude spikes due to the over sampling of contour altitudes in the interpolation process and two diagonal trends persisting in the data resulting from the interpolation kernel structure.

Interpolation from contour lines to a surface often results in many pixels of contour altitude values in the output surface. This is a function of the estimation algorithm that predicts an unknown value using the surrounding sampled values. If the surrounding sampled values (these are normally selected using a search radius or the nearest required number of points) all represent one contour line then the predicted value will also have the contour altitude. This is apparent in output surfaces where the original contour lines are often bordered by bands of the same value, with rapid changes in altitude values as other contours are approached creating a terraced appearance to the elevation surface and a spiky elevation histogram.

Further spikes are apparent in slope and aspect surfaces if altitude is recorded only to meter precision, as arctangent calculations only allow a finite number of possible slopes.

Elevation Histrogram

Common *interpolation* artefacts are the over sampling of contour interval elevations in the interpolated surface.

These appear as spikes on a histogram, where contour interval elevations are significantly more frequent than values = contour altitude ± 1m

These regular spikes propagate significant errors in elevation derivates and give an artificial stepped representation of the surface.

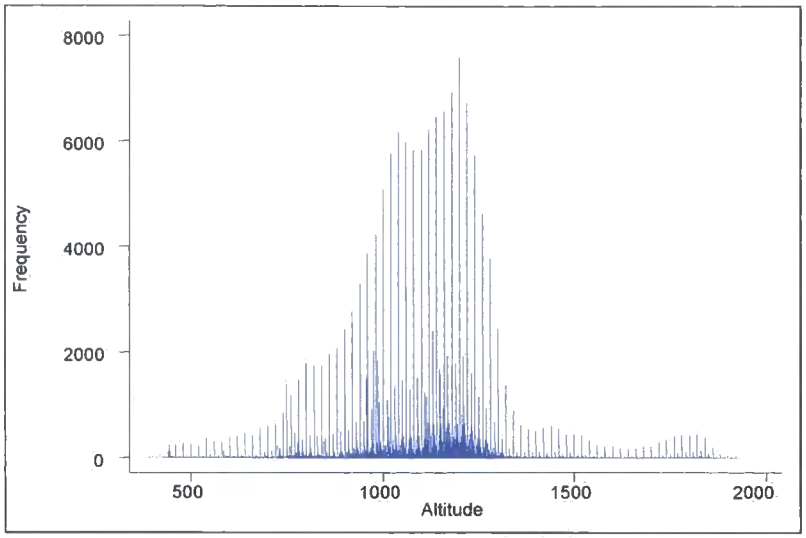

Slope Gradient Surface

Interpolation artifacts are propagated and can be visualized spatially and are most easily seen in derivative plots.

This image is the surface gradient, here most of the pixels have low gradients (dark pixels), few have intermediate gradients and areas of high gradients are spatially organised following the original contour lines, as over sampling along the line has created rapid changes in altitude either side of the contour.

Note also the diagonal trends.

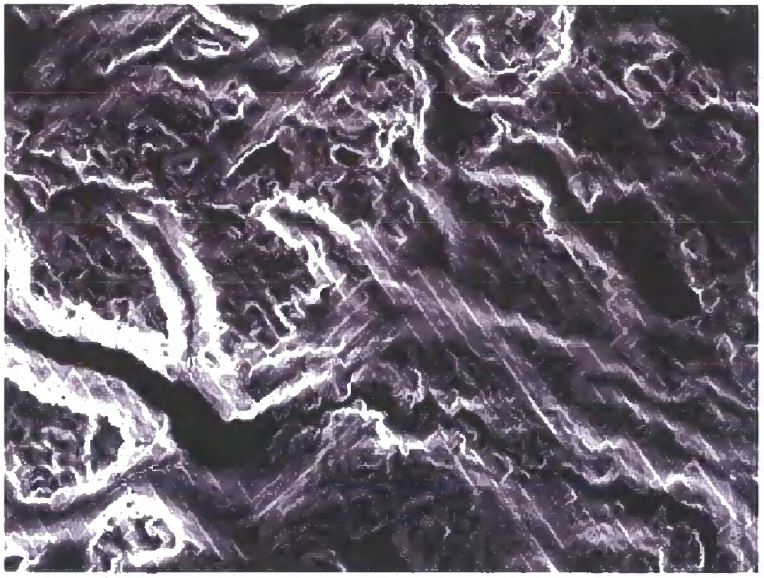

Figure 4.13: Types of error present within the DEM

Wise (2004) identifies a similar diagonal trend created when using the INTERCON command in IDRISI GIS (Clarke Labs.) This procedure interpolates from contour lines, by constructing several profiles, one horizontal along the rows, one vertical profile along the columns and two diagonal profiles (upper left to lower right, upper right to lower left). The presence of these diagonal lines in the elevation derivatives suggests that the algorithm weights the influence of these diagonal profiles too heavily, resulting in persistent trends in elevation values in these directions. IDRISI GIS (Clarke Labs.) suggest smoothing the resultant DEM at least once with a mean filter. Clearly an intelligent or accurate algorithm would not require these post

processing steps, which will significantly smooth the surface, removing extreme values (low maxima and minima) from the surface.

Statens Kartverk applied a nearest neighbour algorithm to interpolate their DEM: it is proposed here that similar kernel shape was applied during the interpolation process resulting in similar diagonal artefacts; fortunately however no mean filters appear to have been applied.

4.7.2. **Error removal**

Most of the error detection and removal procedures outlined here describe processes that are commonly applied to remotely sensed raster images (Mather, 1999), however these are equally applicable to DEMs, which store information in the same format as image files, but where the digital number (DN) represents altitude instead of spectral or reflectance information.

4.7.2.2. **Spatial Filtering**

Spatial filters are commonly applied to raster images and use a local sample of values in an arithmetic operation. Local values are sampled using a kernel. Different size kernels can be used: a larger kernel samples more data and produces a smoother result. A kernel is a rectangular or square window centered on the pixel under consideration (shaded in red in Figure 4.14). A commonly used 3*3 window uses the eight surrounding cells (shaded in blue in Figure 4.14) in conjunction with the center cell to calculate its new value.

The surrounding eight cells can be weighted in different ways to produce different arithmetic operations (Figure 4.15): common applications include smoothing and edge enhancement filters.

Low pass filters are commonly applied to noisy or artefacted data. These remove any high frequency components (locally rough data) by averaging throughout the kernel and have a similar effect to mean, median or mode filters. However, it is argued by many (Wood, 1986) that high frequency components (equivalent to Marks' (1975), grain elements) exist in a landscape and cannot be differentiated from noise within existing filter algorithms: this discourages their use in this context. In removing the high frequency components within the surface, these smoothing filters provide an overall smoothing and remove local maxima and minima. In this particular research application local roughness, maxima and minima were suspected to be of significant importance in creating strong localised gradients in microclimatic

variables. Although they were applied to assess their ability to remove the error within the DEM, they were later rejected.

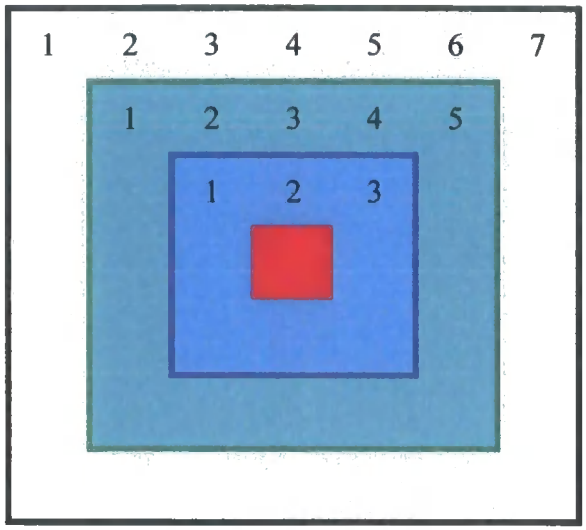

Figure 4.14 Kernel structure with varying size

Low pass filters with a 3*3, 5*5 and 9*9 kernel window were applied to the DEM: although all these filters smoothed the data and muted the diagonal trends and spikes they failed to remove a significant proportion of the artefacts after two consecutive applications. The 5*5 kernel removed the largest proportion of the error, but the localised smoothing failed to remove all contour spikes (Figure 4.16 shows original DEM, 4.17 shows smoothed DEM). Smoothing filters were rejected as a mechanism for reducing the error within the DEM.

Although simple spatial filtering techniques do not provide effective removal procedures, here the United States Geological Survey (USGS) apply a complex procedure of consecutive filters to remove horizontal banding artefacts within their photogrammetrically derived DEM (USGS, 2004). However, the procedure in removing the majority of the artefacts also applies a global smoothing, and it is therfore not considered to be applicable in removing diagonal components.

Although a number of complex filtering techniques exist none were found, during the present study, to be capable of redistributing the error within the DEM effectively, therefore a more intelligent redistribution method was required.

High Pass Spatial Filter
Preserves the high frequency components of an image.

-1	-1	-1
-1	+8	-1
-1	-1	-1

Low Pass
Preserves the low frequency components of an image.

0.111	0.111	0.111
0.111	0.111	0.111
0.111	0.111	0.111

Directional (45°)
Enhances or removes directional components in the image

-1.4142	-0.7071	0
-0.7071	0	0.7071
0	0.7071	1.4142

Figure 4.15 Spatial filters

4.7.3. Kernel Density Estimation

Kernel density estimate (KDE) plots are an extension of histograms, removing their two main limitations: only plotting data within set bin widths and only plotting data between a maximum and minimum value. Plot data appears continuous, but still as the frequency of points within a bandwidth.

Statistical density estimation involves approximating a hypothesized probability density function from observed data, in this case pixel elevation values. Kernel density estimation is a

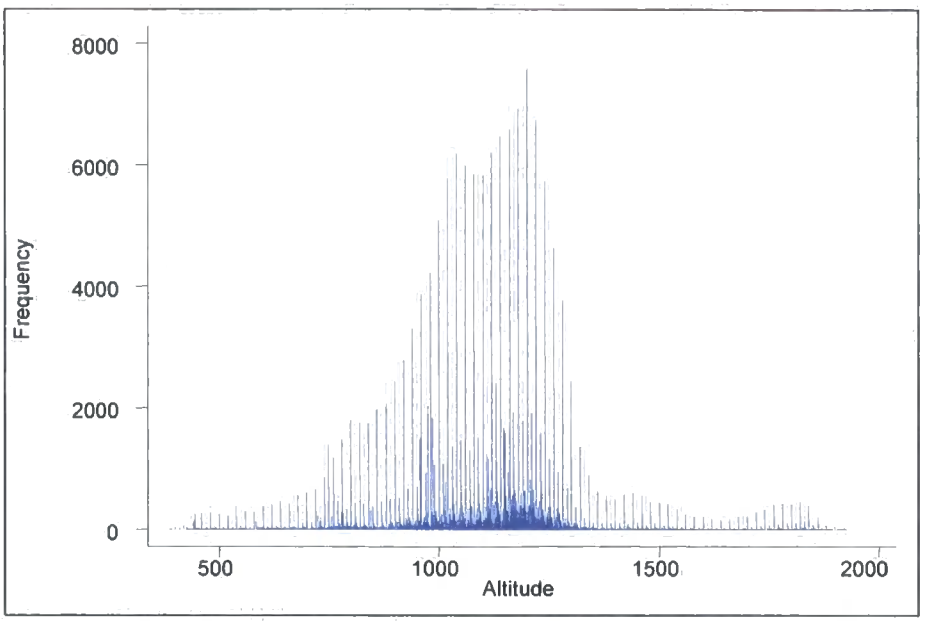

Figure 4:16 Altitudes within original DEM with contour spikes

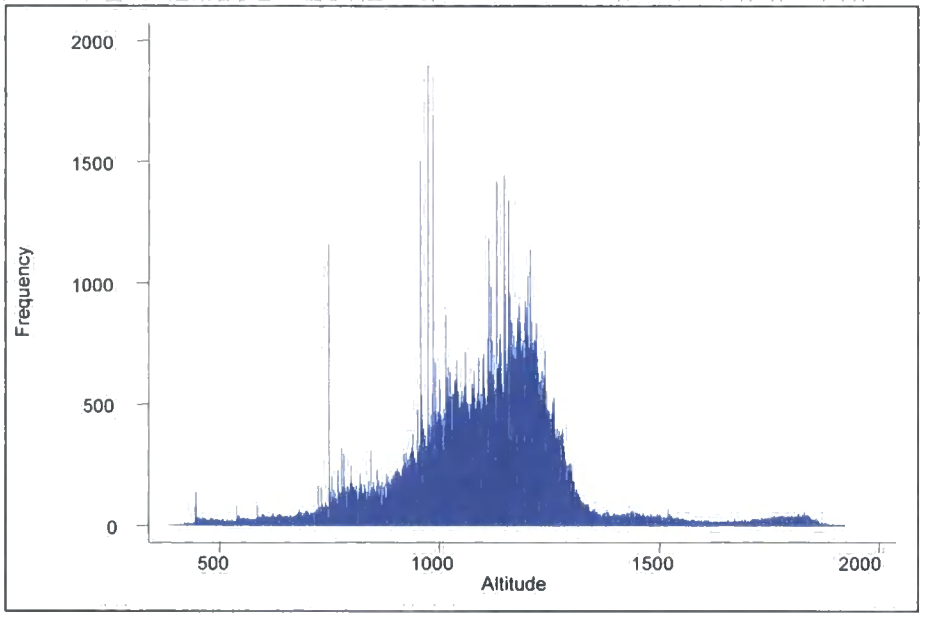

Figure 4.17: Altitudes within smoothed DEM with 5 * 5 low pass filter

nonparametric technique for density estimation in which a known density function (defined by the kernel) is averaged across the observed data points to create a smooth approximation, by redistributing values within the kernel width. This technique was identified as a potentially useful procedure for identifying and removing the error present within the DEM, as it performs analysis within the frequency domain, a domain we know the error to be prominently distributed within. KDE redistributes the high frequency altitudes representing the contour

intervals to values ± 10 m, the kernel width. A Gaussian distribution was used within the kernel to redistribute the values.

The *mdensity* command in STATA was used to produce kernel density estimates for the elevation values within the DEM. A kernel width of 5 m was used as this was felt to be adequate to redistribute spikes but smaller enough to avoid over smoothing the data.

mdensity produces a graphical output, the kernel density estimation plot. Results showed a much smoothed distribution where values had been redistributed to deprived altitude bands surrounding spikes (Figure 4.18). Although this approach showed good results KDE does not operate in the spatial domain, only in the frequency domain, and consequently any adjustments to the altitude values could no longer be related to an x,y location, so this approach had to be rejected.

It did, however, identify analysis in the frequency domain as a method for distinguishing and redistributing artefacts or error and data values. Another technique that examines and performs analysis on data within the frequency domain is fourier series analysis.

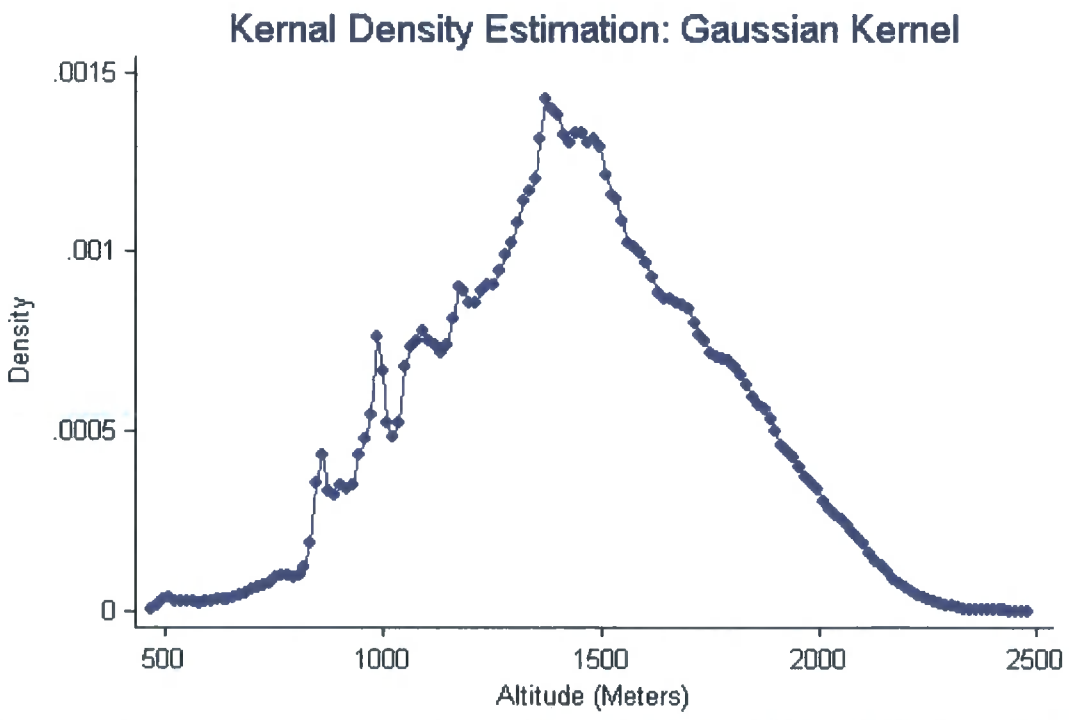

Figure 4.18: Kernel Density Estimation Plot: Gaussain Kernel, 10 m width, 150 points estimated

4.7.3. Spectral Analysis and Fourier Transformations

Rayner (1971) stated that any variable or phenomenon that can be ordered according to increasing or decreasing wavelengths can be viewed and treated as a spectrum. Viewing the variation in elevation values in the DEM it is possible to conceptualise them as variations along a spectrum, where the x axis represents space. Spectral analysis is the mathematical characterisation of these variations. If viewed in the frequency domain, cyclic changes in elevation values would be apparent due to the spatial autocorrelation of the surface and its spiky frequency distributions (Figure 4.13).

Spectral analysis is more commonly applied to variables that exhibit cyclic or harmonic characteristics similar to a sine curve (Figure 4.19).

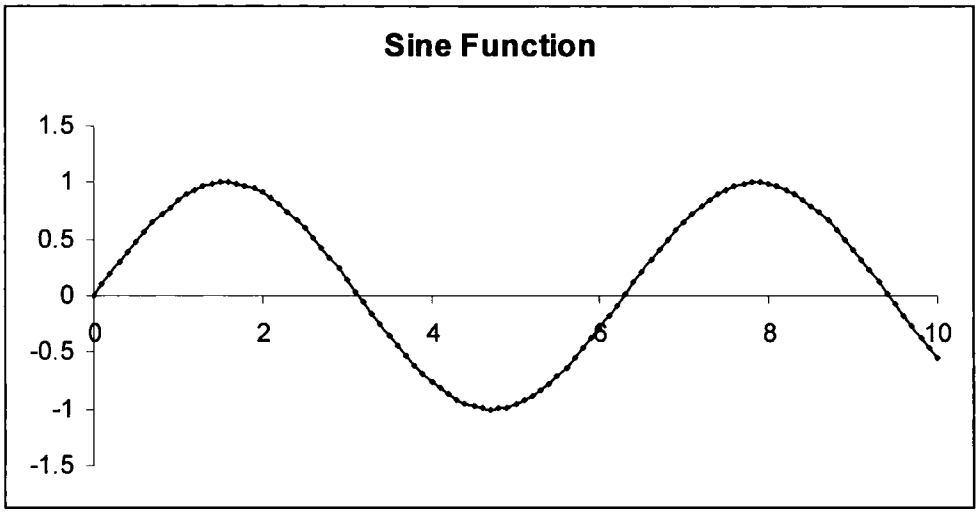

Figure 4.19: Sine function in Radians

Despite the error's small magnitude relative to the expected altitude, Champeney (1973) stated that "if a quantity varies periodically with time it can be analysed into its harmonic components" (Champeney, 1973:1). However, by substituting time with space we can analyse the harmonic or Fourier series components of the repetitive variation in elevation values in the frequency domain by using a Fourier transformation. Specifically considering the DEM interpolation artefacts it is possible to say that

> if $f(t)$ represents the quantity that varies through space,
> and if τ is the repetition period (distance between stripes)
> then $2\ \Pi / \tau$ is the fundamental frequency
>
> (adapted from Champeney, 1973)

Rayner (1971, 2) described a spectrum as the scale breakdown of a phenomenon in space or time. In the present application the harmonic characteristics of elevation were evaluated with respect to space. The calculation of a spectrum involves the fitting by least squares of sinusoidal curves and quantifying their amplitude and phase angles to a set of data that may be in one, two or n dimensions. Applying a Fourier transform is simply the process of fitting these curves, and the inverse Fourier transform describes the process of returning to the original data from the Fourier coefficients.

Although the data are continuous and non periodic the error within the data is periodic. Continuous or non periodic data create a unbroken spectrum of values, in this case the elevations in area, for example 0, 1, 2, 3, 4, 5 m. A discrete spectrum however has a finite number of frequencies that the data can represent, in this case the contour intervals, for example 0, 5, 10, 15 m. The type of spectrum the data represent determines the type of transformation that can be applied.

The Fast Fourier Transform routine available within ENVI was applied to a sample of the DEM: the operation can be identified as having three stages (Figure 4.20). The initial stage of the process, the forward transform, converts the data into its sine and cosine components, moving from the spatial domain into the frequency domain.

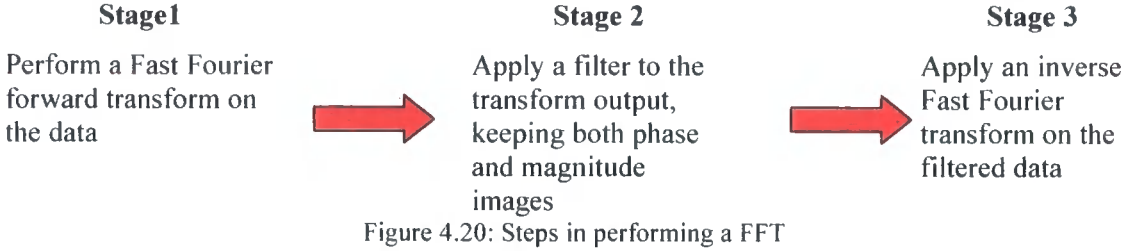

Figure 4.20: Steps in performing a FFT

The frequency or magnitude output represents the frequency of every point in the input image, representing both the horizontal and vertical spatial frequency components (Figure 4.21). The average elevation (the zero frequency component) is shown in the centre of the image, pixels at an increasing distance from this central pixel represent increasing spatial frequency components. A phase output is also created but often provides little information about the structure of the spatial domain image. The frequency or magnitude image is most commonly displayed as this contains most of the information about the geometric structure of the spatial domain image, where brightness represents the magnitude of the frequency component.

Interpretation of the frequency or magnitude output is very important as it provides valuable information about the structure of the error. However these outputs are complex and it is first

necessary to understand how regular inputs are displayed in the frequency domain. Artificial datasets were created using to test the model under known conditions. Although the application of Fourier transforms to remove error within a DEM is new, the application of Fourier transforms to remove systematic errors within remotely sensed data is not. Despite their common application, literature surrounding interpretation of the frequency outputs is limited, therefore it was necessary to apply the FFT to artificial datasets.

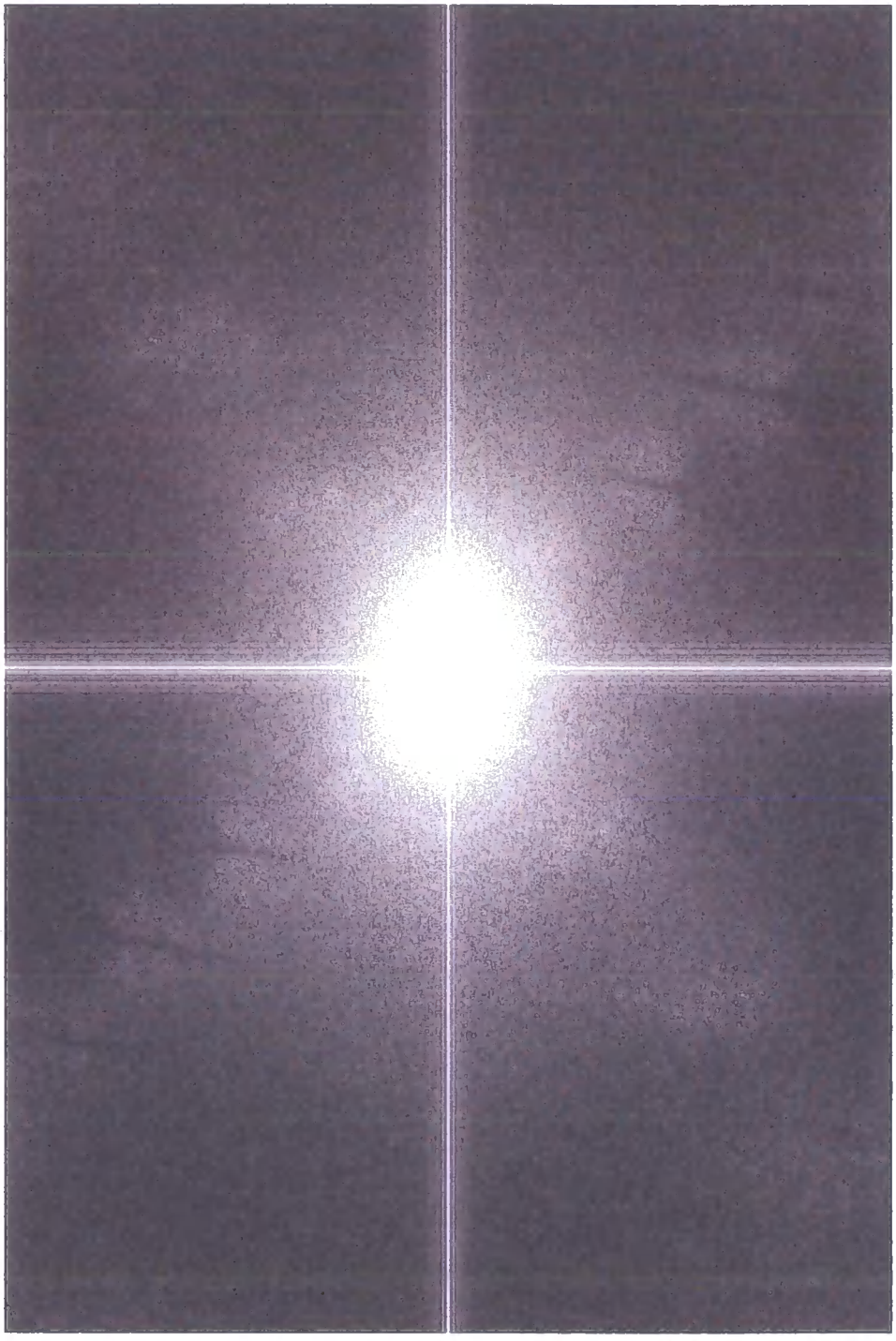

Figure 4.21: Fast Fourier Transform magnitude output for the Jotunheim

Frequency output plots revealed how differently spatially organised frequency components in the input surface were represented in the frequency output (Figure 4.21), these could also be examined in a histogram of the frequency domain which identified the frequency of the error components (Figure 4.22). These results allowed a more informed interpretation of the frequency output from the sample DEM. A FFT was also applied to an Ordnance Survey 50 m DEM of Loughrigg Fell, Lake District (Figure 4.23). Although containing error, Ordnance Survey DEMs do not have a spatially or frequency dominant error component, largely as improved interpolation algorithms and significant amounts of post processing have been applied. It was therefore possible to use this as an indicator of how a continuous elevation surface should be represented in the frequency domain.

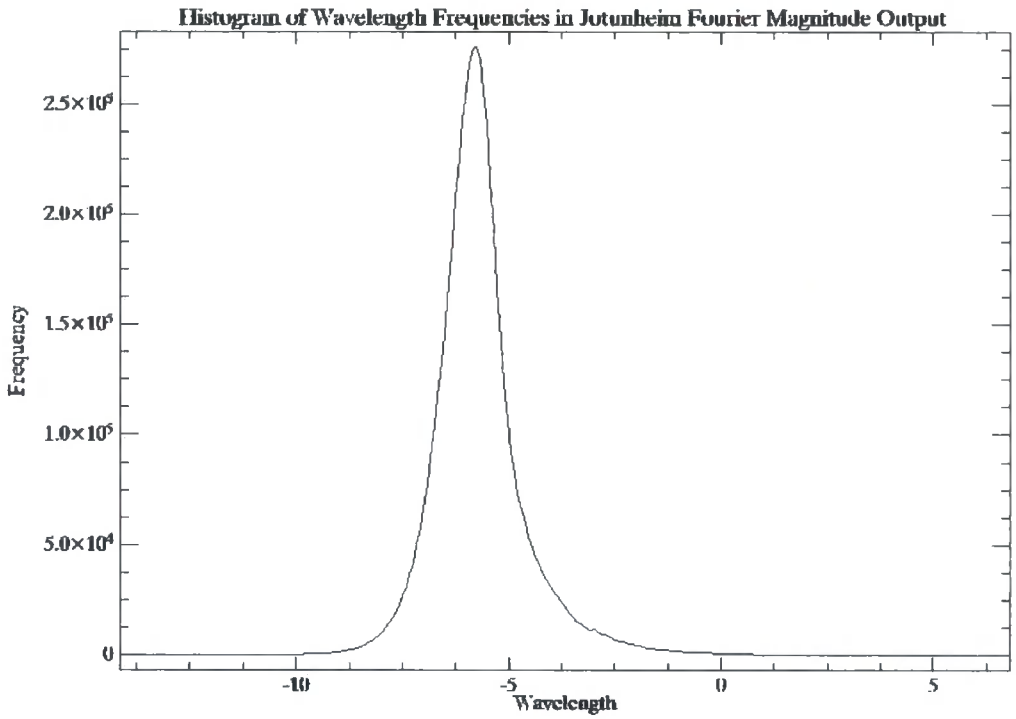

Figure 4.22 Frequency histogram of FFT output

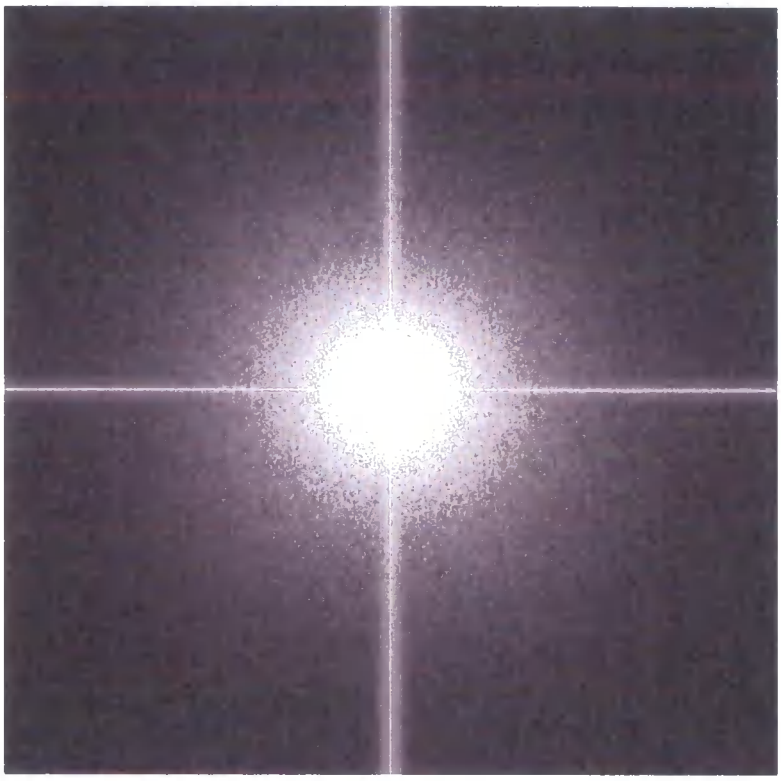

Figure 4.23: Fast Fourier Transform magnitude Output for Loughrigg Fell, Lake District

Results from the artificial surfaces confirm that strong crosshairs will be present in any Fourier magnitude surface if there is a variation in values at the start and end of rows and columns (Figure 4.24). This high frequency variation in the spatial domain is very apparent in the magnitude output, here representing an artefact of the Fourier algorithm applied to finite data rather than an interpolation artefact or information about landform organisation. Although there is evidence of multiple horizontal and vertical lines surrounding these cross hairs they are likely to represent the high frequency variations between adjacent pixels. Attempts to differentiate between artefact and data in this area proved highly subjective and potentially damaging to the terrain surface and is not suggested.

However other components of the frequency output can be identified confidently as spectrally and spatially organised error within the DEM. These are the diagonally organised components highlighted in Figure 4.21; although they can be identified, their boundaries are soft making their delineation difficult and highly subjective. The extent and organisation of these error patches appears vague, suggesting that the error may vary as a function of the topography. Examination of a smaller subset (Figure 4.25) produced a much more clearly delineated diagonal component.

Most non-systematic error in terrain surfaces is topographically organised (Wood, 1986): this organisation is apparent in the dominance of diagonal striping in the derivative surfaces where areas of moderate terrain exhibit a more highly scarred surface.

By passing the two error components through the inverse FFT (using a pass rather than a cut filter) it is possible to visualise these two error components (Figure 4.26).

Topographically organised error is largely a function of surface roughness: areas which are relatively flat have a small range of possible altitude values, and consequently any over sampling near the contour line is not readily apparent in the output surface. Areas of rough or steep terrain will have narrow or frequently spaced contours and again any over sampling will not lead to locally apparent banding in values as narrowly spaced contours will implicitly increase the local altitude variability. Areas of moderate terrain tend to be the more affected by interpolation errors, where moderate spacing of contour lines leads to clearly delineated banding in the output surface.

Columns

Fourier output has horizontal banding, indicating frequency variation along a row.

Spacing equivalent to columns

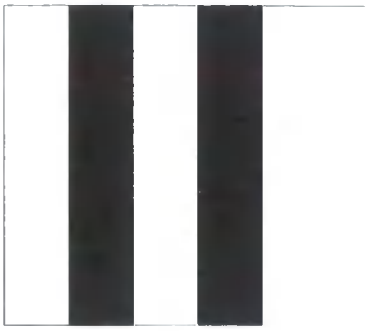

Rows

Fourier output has vertical banding, indicating frequency variation down a column.

Spacing equivalent to rows

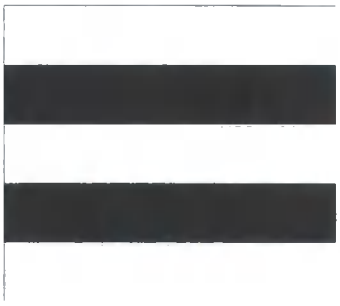

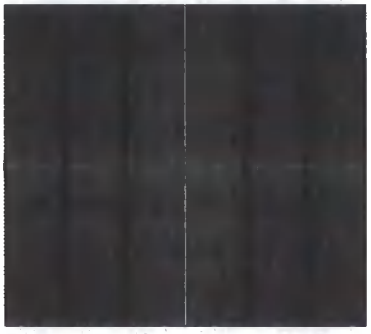

Edge

Fourier output has dominant cross hairs throughout especially though the centre indicating high frequency variation.

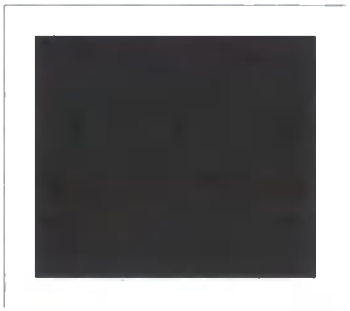

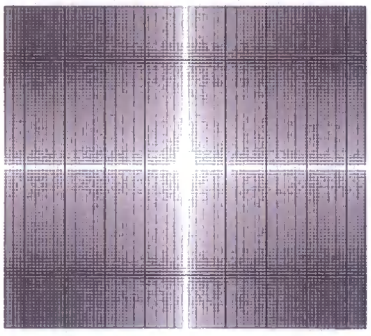

Diagonal

Fourier output has dominant cross hairs throughout, diagonally and horizontally orientated. Less steeply angled in the same direction as input.

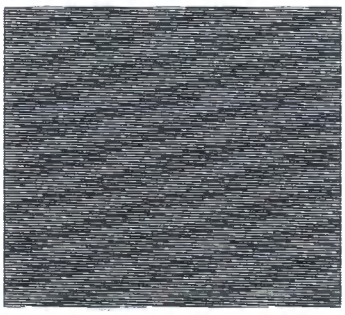

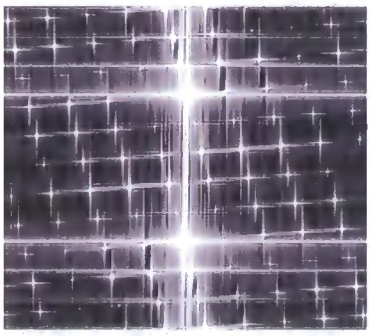

Increasing

Fourier output has dominant cross hairs especially a horizontal band indicating high frequency variation along a row (difference between start and end)

Figure 4.24 Artificial surface FFT output.

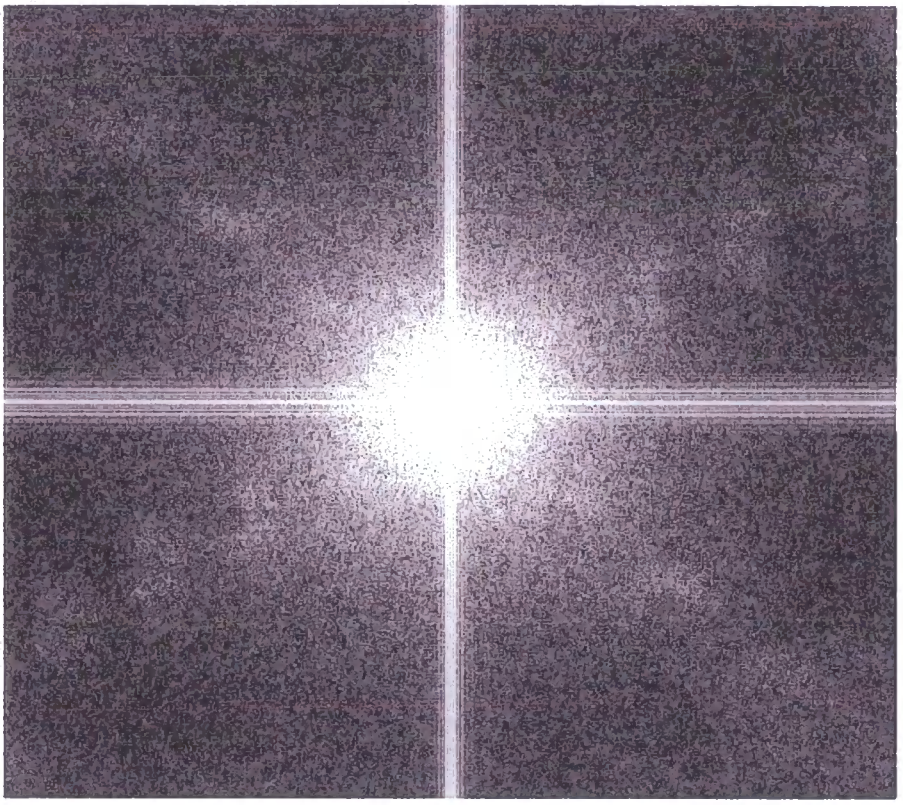

Figure 4.25: Fast Fourier Transform magnitude Output for the Horung Massif.

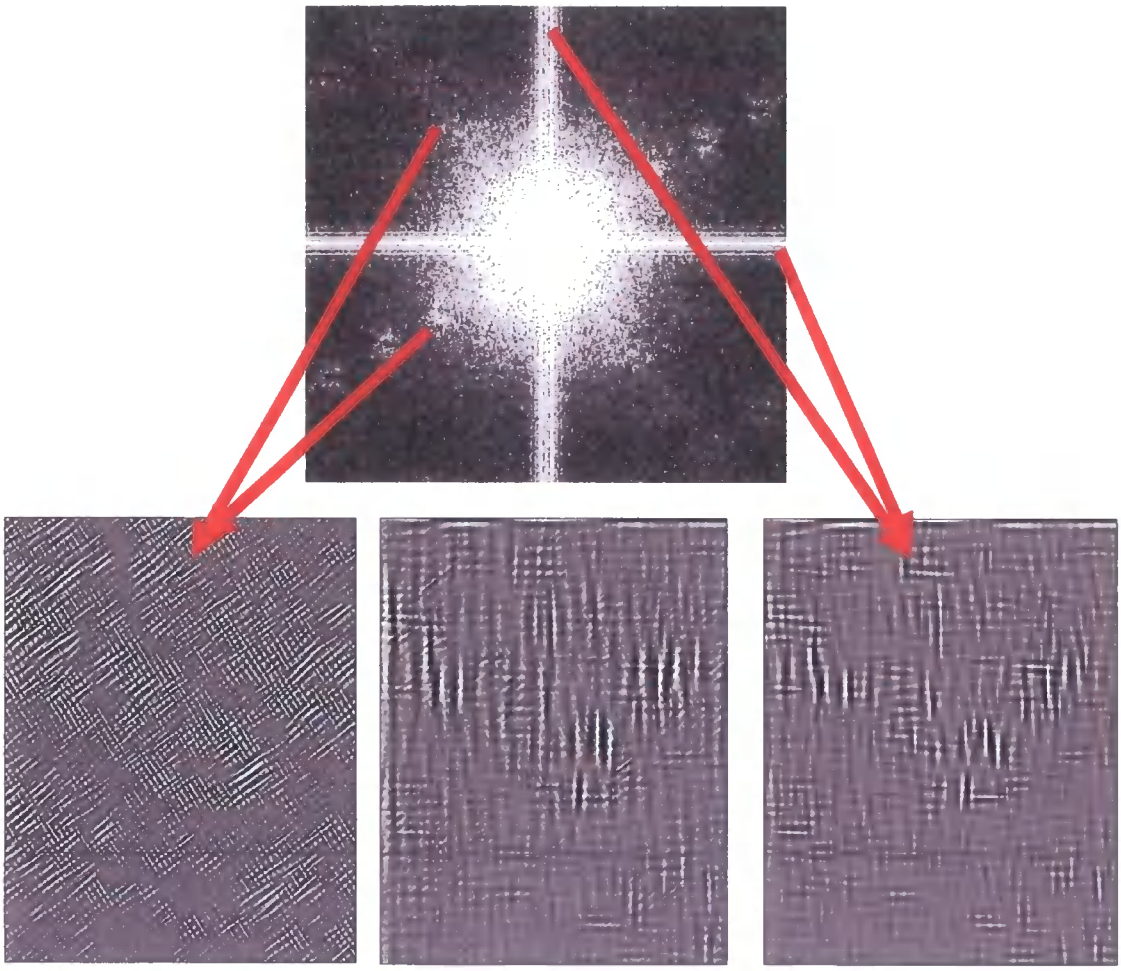

Diagonal components | Combined noise components | Orthogonal components

Figure 4.26: Error components passed through inverse FFT

Subsets of the study area were used as the input to the Fourier transform to facilitate the delineation of the error in an attempt to avoid removing frequency components of the elevation surface rather than just the error (Figure 4.27). The success of this approach was largely dependent upon the homogeneity of the land surface within the subset.

To remove the components identified as error it is necessary to overlay polygon structures on to the image and use these as the filters, acting as a Boolean overlay cutting them out of the magnitude image. The inverse transform can then be applied to estimate the missing values using the spatial and spectral frequency trends within the modified input image.

Examination of the 'input minus output' DEM, showing what was removed by the FFT highlights the effectiveness of the procedure as the raster largely consists of diagonal stripes (Figure 4.26). A histogram of this image also highlights the effectiveness of the procedure as it is dominated by the original contour spikes.

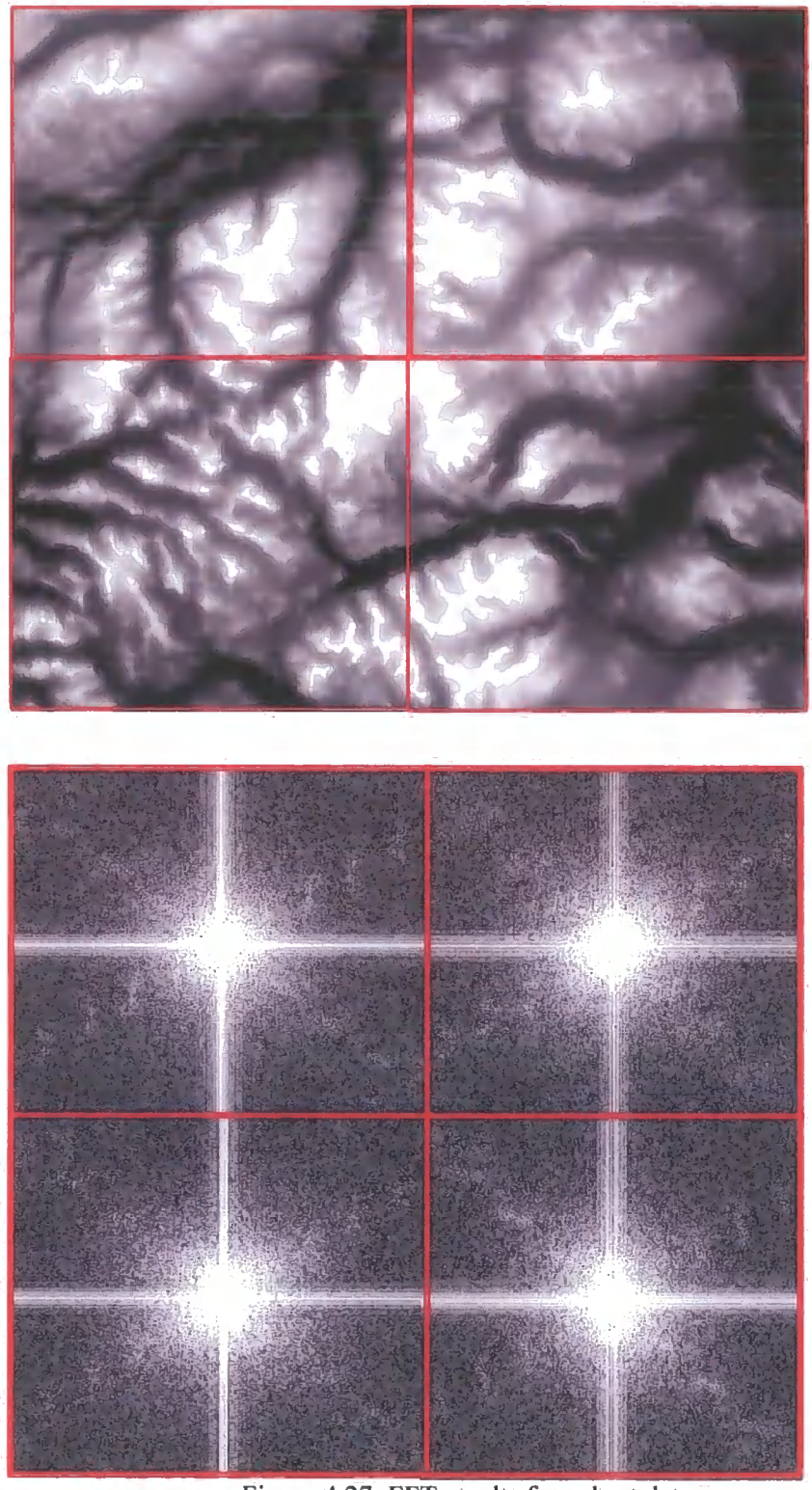

Figure 4.27: FFT results for subset data

By identifying an effective removal procedure it is possible to revisit the initial hypothesis that the error was spatially autocorrelated and linked to terrain roughness – predominantly areas of moderate relief. Two statistical measures of autocorrelation, Moran's I and Gearys's C, were used to compare the organisation of the elevation surfaces before and after error removal.

Comparison of the spatial autocorrelation present in the initial and FFT output indicate a reduction in the spatial autocorrelation, supporting the hypothesis that the error was spatially autocorrelated (Tables 4.4 and 4.5).

Geary c	Moran I	Interpretation
$0 < c < 1$	$I > 0$	Similar, regionalized, smooth, clustered
$c=1$	$I = 0$	Independent, uncorrelated, random
$c>1$	$I < 0$	Dissimilar, contrasting, checkerboard

Table 4.4: Interpretation of Spatial autocorrelation statistics

	With Error	After Error Removal
Moran's I	0.9955	0.9959
Geary's c	0.0045	0.0040
	More smooth and clustered	Less smooth and clustered

Table 4.5: Spatial autocorrelation data before and after analysis

Examination of the changes in the distribution of gradients in the initial and FFT output DEM, showed that pixels with steeper gradients had been changed, suggesting that these were the most affected by DEM error in the original surface (Figure 4.20).

Comparison of the frequency distributions of the original and FFT output DEM show some changes, most notable is the lowering of the highest altitudes. The histogram of the output DEM showed removal of most spikes and showed a much more representative distribution. (Figure 4.21). Although every attempt was made to reduce the smoothing effect of the error removal procedure, some smoothing did occur. Removing high frequency components from the FFT magnitude output will in some cases remove high frequency landform components, where the soft boundary between noise and data is unclear. Although this procedure has in places smoothed accurate input data it is clear from the components removed (Figure 4.22) that this is not where most of the changes have occurred and that it is predominantly the spatially and spectrally organised error that has been removed from the dataset.

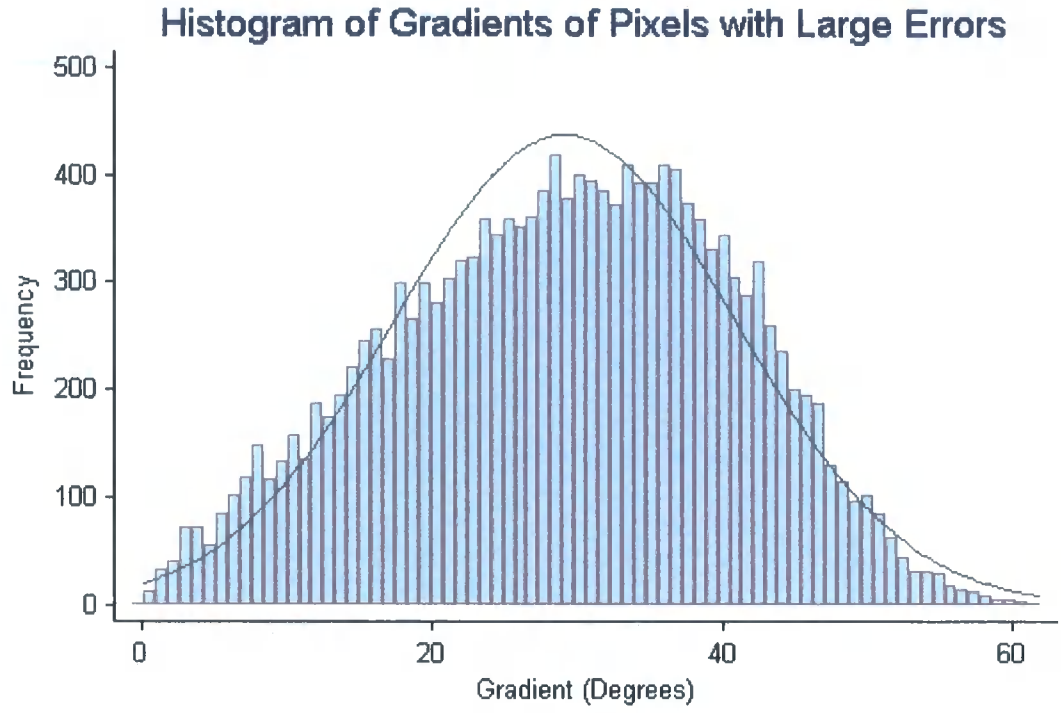

Figure 4.28 Gradients of pixels with large errors

FFT was applied to 25 subsets of the study area and was also applied to Southern Norway in one application. It is clear that simply applying the FFT to such a large geographical region will potentially lead to over smoothing: the FFT magnitude output (Figure 4.21) shows a harmonic signal, where multiple high frequency components are present at increasing frequencies. This is potentially representing the different degrees of surface roughness or different weightings within the interpolation kernel. The difference between the Jotunheimen and the study area identifies the smaller geographical area applications as more accurate for error removal, but the application to Southern Norway allows initial discussions of its surface characterisation and geomorphometric characteristics to be made.

The Fast Fourier transform identified the spatial and spectral characteristics of the error present within the DEM. This technique avoids smoothing the whole dataset and simply alters the data identified as error. However, care is required as the landscape does contain high frequency components and filter definition is identified as a subjective procedure.

a)

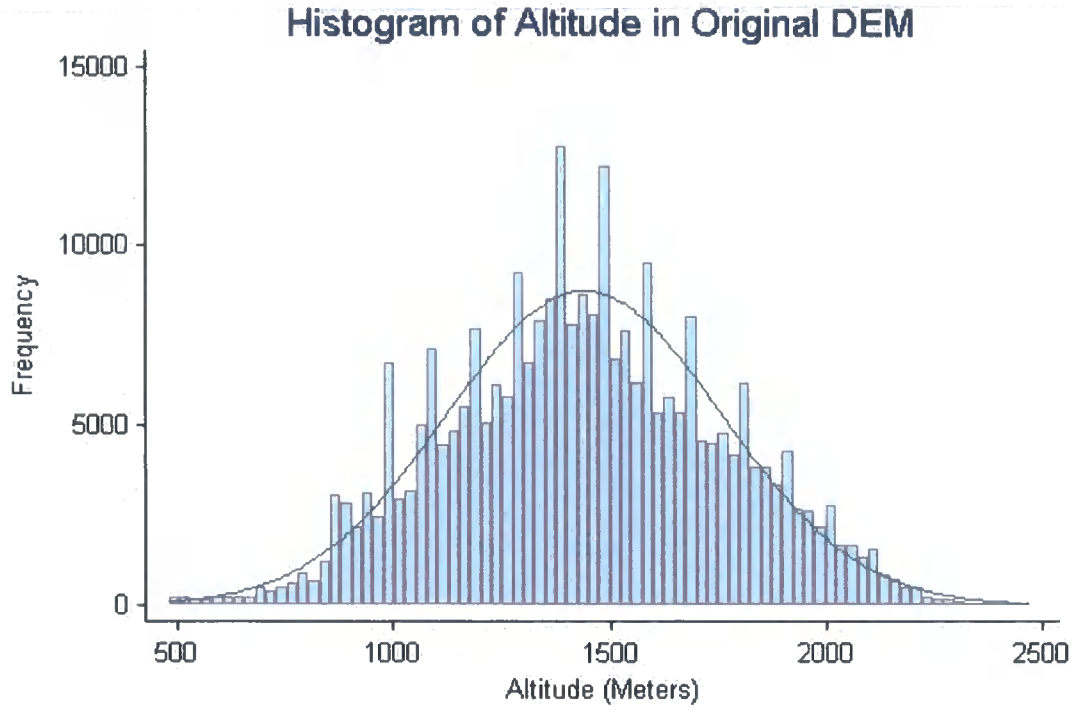

b)

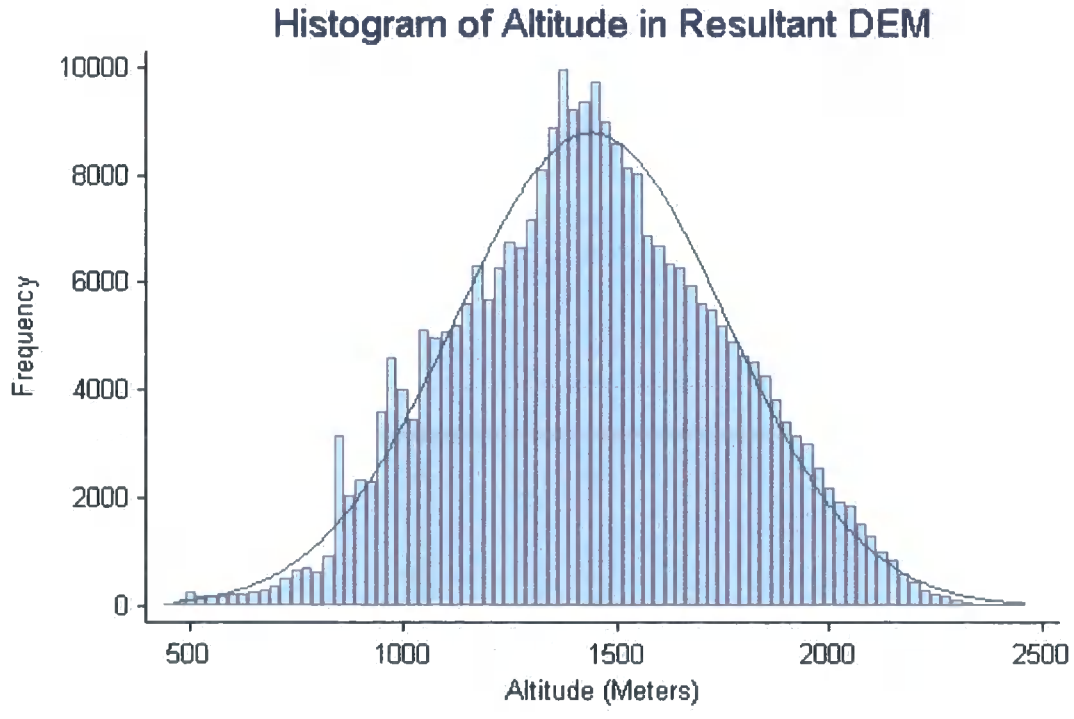

Figure 4.29 Histogram plots of after and before FFT a) before b) after

Examination of the spike plot (Figure 4.30) identifies 3 modal peaks: commonly peaks in an elevation distribution indicate paleo-erosion surfaces, where earth surface processes eroded the

terrain surface as a function of climate, geology and sea level. As climate and sea level change through time, so to do the level of erosion surface and the earth surface processes acting on them. These are comparable to those described in Chapter Three.

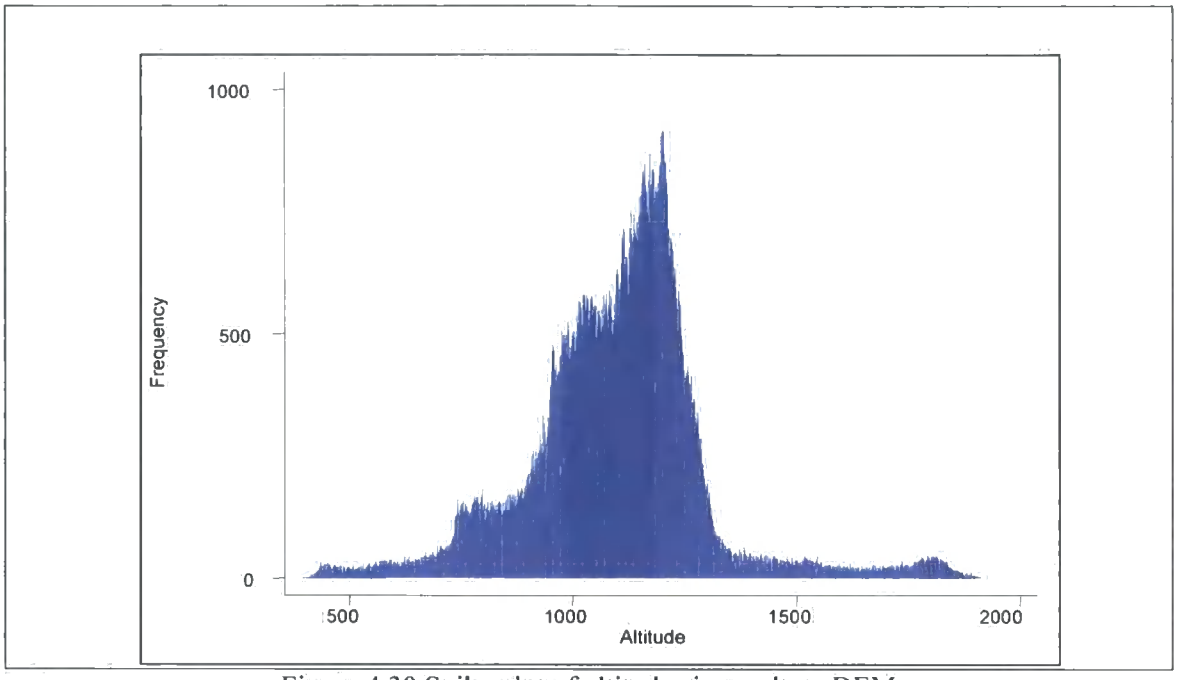

Figure 4.30 Spike plot of altitudes in resultant DEM

Removal of the error present within the DEM was essential to minimise propagation into resultant glacier accumulation distributions. Digital elevation data processing can be a computationally intensive component of a radiative model, specifically shading calculations that require multiple line of sight calculations. The following section outlines a method developed during this research to improve the efficiency of this process.

4.8. Viewshed and visibility calculations

Viewshed analysis looks at the intervisibility of two or more points in a surface, commonly on a elevation surface. The same calculations can also be applied when considering solar viewsheds which examine the intervisibility of a location on the land surface and the sun, where the sun's position is given by its solar altitude and azimuth.

Areas where the line of sight between the sun and surface are intercepted for a given solar position will be in shade. As a significant component of this research was the calculation and interpretation of the temporal and spatial distributions of direct beam solar radiation it was not feasible to calculate each of the viewshed maps within a GIS, as the computational and time

costs would have been too great. It was therefore necessary to integrate a viewshed algorithm into the radiation component of the model.

4.8.1. **Algorithms**

Many different viewshed algorithms exist, these differ both in how they determine if two locations are mutually visible (Sorensen and Lanter, 1993; Wang *et al.*, 1996), how they extract geomorphometric measures from the DEM (for example slope and aspect) (Skidmore, 1989) and the data structures they are designed for (Lee, 1991; Floriani *et al.*, 1994). Commonly used methods can be seen in Figure 4.31, using the gradient or angle between the source and the intermediate cells to evaluate if the line of sight (LoS) has been intercepted.

When A = Source

B = Sun

D = Pixel in azimuth direction

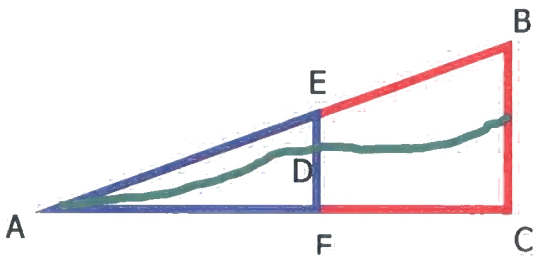

A is illuminated if:

1. FE>FD

OR 2. Gradient AB>AD

OR 3. CÂB>EÂD

Figure 4.31: Commonly used methods of calculating the mutual visibility of A and B

Viewshed algorithm research has largely been divided between improving efficiency (Wang, 1996; Dozier and Frew, 1990; Rana and Morley, 2002; and Huss and Pumar, 1997), developing and interpreting visibility algorithms and their resultant viewsheds (Sorensen and Lanter, 1993, Fisher, 1991) and quantifying and representing their associated uncertainty (Felleman and Griffin, 1990; Fisher, 1995). However the efficiency of viewshed algorithms as a function of surface complexity and spatial organization has received little attention. Computational efficiency was important, as it is a requirement of developing a multi-component model; therefore viewshed algorithm efficiency was investigated.

This research suggests that viewshed algorithm efficiency, like elevation surface error, is landscape dependent, and therefore varies with terrain type; specifically terrain roughness. This study further develops the research reported by Huss and Pumar (1997) who investigated the role of surface roughness in viewshed accuracy and found that the viewsheds of rougher surfaces were more reliable, less sensitive to error and smaller than those for smoother surfaces.

As viewshed calculations are sensitive to variables other than those mentioned above (Fisher, 1991) this research only examined the role of surface roughness on one viewshed algorithm. The algorithm used compares the altitude of each successive element in the DEM to that of the source, to assess if it lies above or below the line of sight (LoS) between the source and destination (Figure 4.32). In this case the latter is in sun, defined by its solar altitude and azimuth.

4.8.2. **Algorithm efficiency**

A topographically sensitive algorithm was created that accounted for surface roughness specifically slope reversals and breaks to minimize the number of pixels that are evaluated before a pixel is found to be in shade. This topographic dependence was identified using a tracking in vs. tracking out version of the viewshed algorithm (Figure 4.32).

Tracking out was anticipated to improve efficiency in a 'rough' terrain or where A is significantly lower than the surrounding pixels: alternatively if the terrain is relatively smooth or if A is significantly higher than its surroundings tracking in was anticipated to improve efficiency.

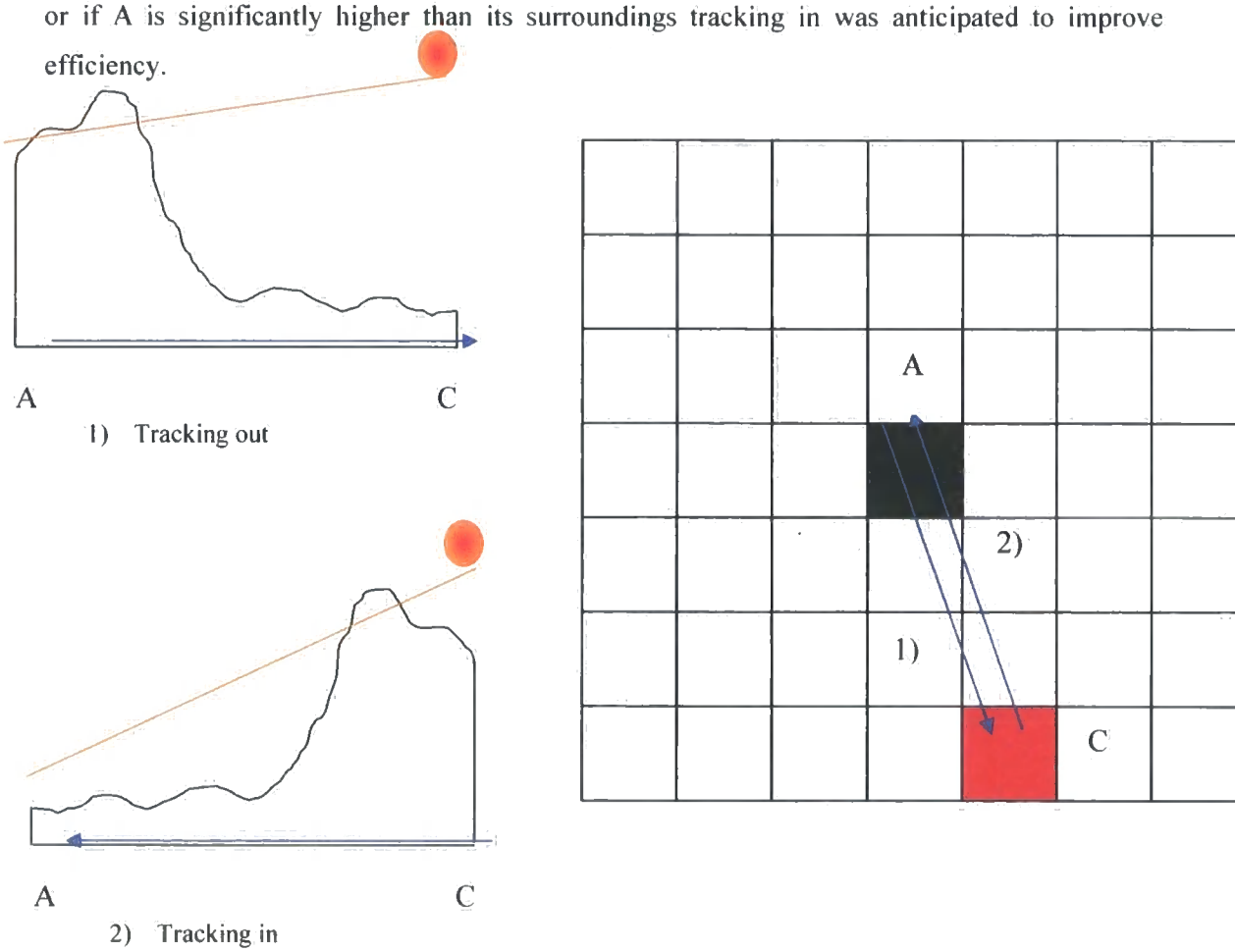

Figure 4.32: Schematic of the tracking in and tracking out search mechanisms in the viewshed algorithm

Dozier and Frew (1990) identified the successive examination of every pixel in the azimuth direction as an inefficient algorithm and suggested that extracting, sorting and evaluating the pixels in the azimuth direction in descending order was more efficient. This method has a topographical component as it assumes that higher areas are most likely to cause shade, but it does not consider how A compares to its surroundings and where the extracted higher areas are located. Therefore, although this method does provide computational savings it still fails to create a topographically optimal viewshed solution. In an attempt to create such a method Rana and Morley (2002) extended the work of Lee (1994) and suggested that a morphometric characterisation of the land surface into its constituent landform components can provide information on the potential visibility dominance of a pixel. This approach does improve viewshed algorithm efficiency by using a subset of the DEM pixels, identified by the landform classifications to reduce the number of observer target pair comparisons. However its usefulness is restricted by the uncertainties in performing landform classification (Wood 1996; Arrell, 2001) and the generalizations in the resulting viewsheds created as a result of minimizing the number of pixels considered.

Viewshed efficiency was quantified using a count variable, the recorded the number of pixels within the DEM that the algorithm had to evaluate before location A was found to be in or out of shade. Smaller counts (higher efficiency) indicate local shading and higher counts (greater inefficiency) indicate longer shadows where shade is cast from further away. The algorithm was run for the three summer and winter months and calculated at eleven time intervals each day. This methodology was applied to a sample DEM (Figure 4.33). The terrain in this region is varied with a rougher more complex topography in the North West, an extensive valley system in the North East and a gently undulating terrain in the South. The methodology was repeated on a smoothed version of the DEM, the smoothing was performed by running a 9*9 mean filter through the raster, maintaining the 100 m pixel resolution.

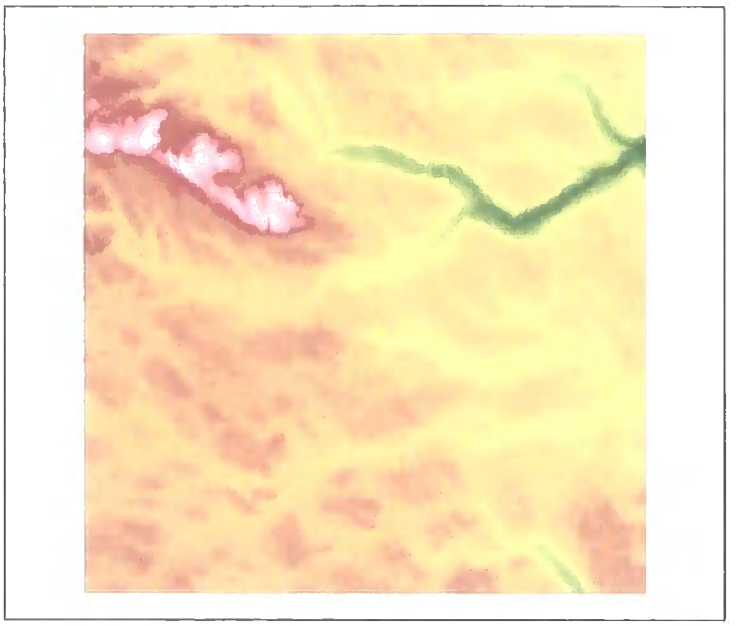

Area: 25000Km^2

Figure 4.33: DEM of Southern Norway

It was possible to interpret the results at a number of different levels. Initial interpretations could be made about the spatial organisation of count values with respect to the spatial distributions of altitudes and aspects within the DEM. The role of temporal variations in solar altitude and azimuth was examined through a comparison of summer and winter viewsheds and the role of surface roughness was suggested through an examination of a smoothed and unsmoothed DEM.

A summary of the counts can be seen in Table 4.6, these counts are the total number of pixels examined during each 90 day period. Figures 4.34 and 4.35 show the spatial distribution of counts, darker colours indicate higher counts.

Count Statistic	UnSmoothed DEM		Smoothed DEM	
	Summer	Winter	Summer	Winter
Minimum	0	0	0	0
Mean	328	974	443	1142
Maximum	6135	11865	6765	11280

Table 4.6: Summary of count statistics

a)

b)

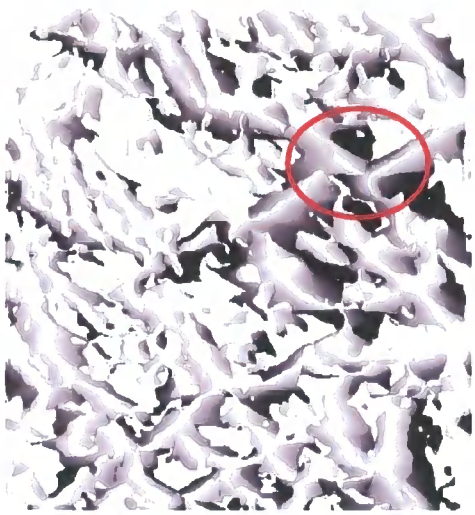

Figure 4.34: Summer count values, a) DEM b) Smoothed DEM

a)

b)

Figure 4.35: Winter count values, a) DEM b) Smoothed DEM

4.9. Topographic Interpretation

The spatial distribution of counts allows a topographic interpretation of the variation of shade within the DEM. The higher and more complex area in the northwest has much lower counts, indicating that local shading is predominant (Figure 4.36a). This is in contrast to the valley in the East and the smoother surface in the South (Figure 4.35b and 4.36b). These have much higher counts indicating longer shadows where shade is cast some distance away from the pixel; this pattern has been identified as separate from higher values simply indicating more shade. The longitudinal axes of valleys have lighter pixels (lower counts) indicating local shading from valley walls and higher counts on the steeper valley sides (Figure 4.35b). This trend is present throughout the DEM, where counts increase as distance upslope increases.

The moderate terrain in the south has a complex shade pattern, where the valley pattern is supplemented by a strong aspect-dependent shade distribution. Slopes that are aligned with the strong east west valley network have higher counts than southerly slopes. Moderate terrain is largely dominated by these two trends and as the standard deviation of altitudes within this region is significantly lower than in the northwest there is little potential for locally cast shade.

Landscape position or context is also an important determinant of shade. Although the higher area in the northwest of the study area is characterized by self-shading, an area of moderate terrain just to its northeast lies predominantly in its shadow (Figure 4.36b).

4.9.1. Seasonal Interpretation

Trends in efficiency are not only spatially dependent but there is a strong temporal variation in viewshed efficiency. Solar altitude and azimuth range vary through the day and year and it is therefore important to consider the implications that this will have on algorithm efficiency.

Higher counts were expected for winter when solar altitudes are lower leading to longer shadows and consequently more shade. Although this was true for the unsmoothed DEM this trend is not found for maximum values on the smoothed DEM, where it is likely that ridge and peak smoothing has reduced maximum shadow length and consequently pixels subject to shade. The spatial distribution of shade also changes between summer and winter months, largely as a function of azimuth range.

4.9.2. Surface Generalisation Interpretation

By artificially smoothing the elevation surface it was possible to make suggestions about the role of surface roughness in viewshed algorithm efficiency. Maximum count values are found for the smoothed surface indicating that shade is not cast from pixels near the source. This supports the research hypothesis that rougher surfaces casts more local shadows, advising a tracking out version of the algorithm. Smoother surfaces are likely to be subject to shade from afar and therefore support the adoption of a tracking in algorithm. Results show that varying the algorithm according to surface roughness improves efficiency.

4.9.3. Algorithm Selection

Interpretation of the count rasters identified viewshed efficiency as landscape dependent and found that calculating viewsheds on smoother surfaces is more computational intensive than on

rougher surfaces using existing algorithms. Improved efficiency is possible by selecting the correct algorithm for the terrain under consideration and algorithm selection should be based on global and focal measures of surface roughness. Selection of the most appropriate algorithm improved efficiency by approximately an order of magnitude.

Although it may be possible to identify a topographically optimal viewshed algorithm for a land surface based on surface roughness and the number of slope reversals and breaks it would be more efficient still to imagine an algorithm that alternated between a tracking in and out algorithm based on local evaluation. If a pixel is significantly greater than its surrounding kernel, shade is more likely to be cast from further away suggesting tracking in: alternatively if a pixel is significantly lower than its kernel mean then tracking out is likely to be more efficient. It is suggested that a combination of focal and global measures is required to select the optimal viewshed algorithm, however as the study area is locally rough the tracking out algorithm was always selected as the most efficient and was used to calculate solar shade.

4.10. **Conclusions**

The description of surface geometry contained in a DTM offers the opportunity to objectively evaluate surface processes (Hutchninson and Gallant, 2000; Dymond *et al.*, 1992, 1995; Wilson and Gallant, 1997; Moore *et al.*, 1991, 1993). The usefulness of these descriptive measures is dependent upon the type of application and the measures used. Earth surface processes that are strongly correlated with terrain characteristics such as glaciology, fluvial geomorphology and climatology can be characterised using terrain parameters. Optimal parameters capture an element of how earth surface processes interact with the terrain surface by quantifying topographic position, context and exposure. The chapter outlined the difficulty in extracting topographic valley structures from digital elevation data and proposed a methodology for future study.

The variables predicted within this chapter are used to inform climatic predictions in Chapter 6, where temperature, precipitation and wind are strongly dependent upon topographic form (Barry, 1980). Accurate climatic predictions are an essential component of accurate energy balance and melt modelling and therefore necessitate a detailed analysis of topographic form.

This chapter has highlighted the need to account for error within elevation data, with the error present within the DEM most effectively removed using a FFT technique to minimise the error propagated through the model into melt predictions. The techniques and methods outlined in

this chapter provide a valuable toolbox to optimise the usefulness of geomorphometric measures and emphases the need to effectively manage error within digital elevation data.

A methodology for using terrain information to improve viewshed algorithms was presented which highlights the need for equivalent investigations for other terrain dependent applications. This application was used to guide shading algorithm design in Chapter Seven.

CHAPTER FIVE
CLIMATE DATA

5.1. Introduction

This chapter presents the climate data obtained from the Norwegian Meteorological Institute for climate stations in and around the Jotunheimen. The chapter initially outlines sources of climatic data, discussing their temporal and spatial resolutions and justifies the utilization of monthly 30 year normal data to derive local lapse rates and drive energy balance and melt predictions. Temperature, precipitation, cloud and wind are discussed, identifying spatial and temporal trends within the data that are used to aid climatic predictions in Chapter 6.

Climatic data were an essential component of this predictive model as earth surface systems especially those within the cyrosphere are at least in part driven and regulated by climate (Richard and Gratton, 2001).

5.2. Data Resolution

The climatic controls on glacier melt and initiation can be largely attributed to precipitation, temperature, wind and cloud cover. The main focus of the research was the prediction of glacier accumulation areas, strong localised gradients exist in mountains (Barry, 1980) necessitating the creation of a local scale climatic dataset. As a flexible and repeatable prediction model was an aim of this research the spatial and temporal resolution of the initial climate data was restricted to those that are freely available for any geographical area without the need for field data collection, specifically regional climatic data from local weather stations.

Although interpolation between altitude spot heights or contours can create a representative surface, where altitude varies continuously and exhibits a high degree of spatial autocorrelation, the strong localised gradients and sparse climate station locations prevented such an estimation process being used here. These strong localised gradients both, in time and space are largely

initiated by topographic variations and controlled by the complex interactions of a number of climatic parameters.

5.2.1. **Spatial resolution**

The discrete point measurements from climate stations cannot drive a spatially distributed melt model and required the creation of continuous climatic surfaces. Because the interaction between topography and climate is critical to the effective modelling of glacier initiation and melt, a spatial resolution common to both would facilitate the quantification of these types of interactions. The suitability of a 100 m spatial resolution dataset was evaluated by examining the sub pixel climatic variability and the contribution that this may have on glacier accumulation and the accuracy with which climatic estimates could be made. A 100 m resolution was found to provide a compromise between estimation accuracy and process resolution. Clearly the suitability of the different climatic parameters varies and cloud cover was identified as having the largest uncertainties at such a spatial resolution.

5.2.2. **Temporal resolution**

Glacier mass balance has a distinct annual cycle. This is largely driven by the annual cycles in climatic and radiative parameters. Temporal resolution of the climatic component of the predictive model therefore needed to be a maximum temporal resolution of 1 month, so that the monthly variation in accumulation and melt could be modelled. Temporal resolutions finer than one month may be advantageous for some climatic parameters where extremes or the persistence of values maybe the most critical. However the reliability and representativeness of input data at a daily or sub daily temporal resolution restricts the number of potential sources and raises questions about the most useful dataset.

5.3. **Data Sources**

A number of different climatic datasets are available, differing in their spatial and temporal resolution, the data retrieval mechanism and whether it represents a recorded or modelled value. The recent increase in the number of datasets available is largely a result of the current research focus on climate and environmental change and increased numbers of satellite and imaging sensors. An increasingly large number of climate datasets are created within numerical weather and climate prediction models.

5.3.1. **Modeled data**

The spatial resolution of contemporary GCM predictions is still too coarse to represent local and regional weather and climate, where topographic forcing from individual mountain ranges cannot be resolved within the model (Pielke *et al.*, 1996). Features significantly smaller than GCM resolutions (generally greater than 1km) can provide considerable surface forcing on weather and climate (Atkinson, 1981; Pielke, 1984; Pielke and Segal, 1986; Avissar and Verstraete, 1990; Cotton and Peilke, 1992; Doran *et al.*, 1992; Segal and Arritt, 1992). Peilke *et al.* (1996) proposed a mesoscale model as a method of downscaling GCM predictions.

A recent venture to combine recorded and predicted data is Re-analysis data, this is the output of a joint project between the US National Center for Environmental Prediction (NCEP) and the US National Center for Atmospheric Research (NCAR). This is an analysis and forecasting system, which produces atmospheric retrospective datasets from 1948 using a suite of different environmental and earth observation datasets. Historical rawinsonde, surface marine and land synoptic data and satellite and aircraft sensor data are used to interpret, predict and validate time series of climatic data. A suite of climatic parameters are predicted, largely at a diurnal temporal scale, however the spatial resolution of the predictions is still too coarse to use directly within the model.

The European Centre for Medium Range Weather Forecasts (ECMWF) devised a project (ERA-15) to create a consistent and invariant data assimilation system, building upon the experiences of the NCEP project. The project created a 15 year dataset of assimilated data running from 1979 to 1993. One of the primary objectives of the project was to create a reliable climatic dataset that was consistent in its design and formation because previous attempts had been characterised by evolving methodologies and technologies. The 'Set I' products from the deterministic ECMWF atmospheric model are the most appropriate for use within small-scale process models and form gridded datasets with an approximate 40 km spatial resolution. They consist of monthly mean datasets created using a ten-day integration for the re-analysis. Eight-day "reforecasts" were also produced every five days and for the period 1985-1990, 50-day forecasts from the reanalysis were performed every day. An improved terrain surface using mean, standard deviation, orientation, anisotropy and slope of the sub-grid orography was used within the model. Although this more detailed measure of surface form did improve the ability of the model to resolve finer scale processes it still represents a coarse and smoothed surface. In conjunction with the reanalysis retrospective datasets 50 years of observational data including 6 hour forecast were produced interpolated to the observation location.

The ERA-15 project shows considerable improvements on the NCEP project using a greater number of observations, recording a larger number of global fields with an improved vertical resolution and provided and overall improvement on output quality (website ref).

The NASA Data Assimilation Office 10 year re-analysis (also known as the GEOS re-analysis) is another example of a major reanalysis project. Multiple reanalysis datasets allows valuable estimates of their reliability and an appreciation of variability between them.

ISCCP the World Climate Research Program collect and analyse satellite radiance measurements to monitor the global distribution of temperature, precipitation and cloud cover. This used a collection of national meteorological satellites starting on the 1st July 1982 to create a spatially distributed dataset from 1984 onwards. Although this dataset does contain all of the meteorological parameters required to drive the glacier prediction model like the NCEP/NCAR dataset a spatial resolution of 280 km only provides a very coarse surface representation that would not resolve local scale processes. The slightly finer spatial resolution of the IPCC global surface climatological database at a 0.5° grid, would still require significant downscaling to represent local scale climatic gradients.

5.3.2. **Remotely Sensed Data**

Although remotely sensed datasets have a long history of use in capturing surface reflectance characteristics they are increasingly being used to capture meteorological parameters including temperature, precipitation and cloud cover. This method of data capture provides many advantages over point based measurements, data are spatially distributed and represented as a continuous surface. Although the data are not restricted by terrain and accessibility, they are restricted by their spatial and temporal resolution. The spatial resolution is dependent upon the sensor used and its calibration and the temporal resolution is either dependent upon the return cycle of the satellite if it is polar orbiting or data streaming if a satellite is geostationary.

Calibration and transfer functions are required to convert the digital reflectance and surface properties recorded by the sensor to estimates of the meteorological parameters.

Precipitation is the most commonly recorded variable with passive microwave sensors (e.g. TRMM) providing the most robust estimates. Since the 1950s increasing use has been made of radar to observe the density and distribution of precipitation. Where different reflectance values indicate varying intensities of rainfall, differentiation is also possible between rainfall intensity

and height, synoptic weather conditions may provide information on possible duration and form.

Cloud cover and type can be derived from a number of different sensors (e.g. AVHRR and MODIS), as the interaction of clouds, aerosols and radiation was flagged as an area uncertainty by the IPCC (2001) the applications within earth observation sensors have recently increased. Stereo matching of images allows the estimation of cloud height, and cloud properties can be derived from information from thermal bands. Applications within the crysosphere are significantly more complex than other geographical areas, as the surface reflectance characteristics and brightness temperatures of snow, ice and clouds are very similar (Lubin and Morrow, 1998). Cawkwell and Bamber (2002) outlined a methodology where stereo-matched nadir and forward view Along Track Scanner Radiometer-2 (ATSE-2) are used to extract elevation differences at its 1 km ground resolution, and then it is possible to consequently derive either the presence or absence of cloud, and cloud height. This technique created a significantly finer spatial resolution than modelled alternatives and confirmed that coarser resolutions did mask high spatial variability in the extent and characteristics of cloud cover. It is also considered that the introduction of RADARSAT 2 will significantly help to address this problem (Dr D.N.M. Donoghue *pers. comm.*). Radiosonde soundings of temperature and relative humidity have also been utilised to good effect in the identification areas of cloud cover, delineating areas of atmospheric change.

The accuracy of these meteorological measurements is largely dependent upon factors that affect the quality of the remotely sensed data, cloud cover, atmospheric transmisstivity and radiometric and geometric distortion. However, further uncertainties and errors are introduced during the conversion from reflectance to meteorological information.

Although remotely sensed data capture does provide clear advantages in producing continuous data coverages, variable temporal resolution between satellites, high costs and data sensitivity to cloud cover still restricts the usefulness of this data capture mechanism for long term datasets. Small temporal and spatial applications may be less sensitive to these disadvantages, where capture slots may either be requested on demand or easily repeated. Equally large temporal and spatial applications may also be less sensitive to localised poor data quality, moderate scale applications are likely to be the least suited to such a dataset, where reliable temporal and spatial coverage cannot be guaranteed.

5.3.3. **30 year normal regional climate data**

Climate is constantly changing and evolving, consequently the length of the data period over which climatic means and normals are calculated greatly effects the value recorded. In 1935 the International Meteorological Organisation proposed the adoption of 30 year 'normals' as the optimum resolution (Sumner, 1988). This time period was felt to provide a balance between removing the high variability and noise present in shorter time periods whilst still capturing significant changes and longer-term oscillations in climate. This value was also felt to reflect a sensible time period that would not obscure or highlight known temporal cyles in the climate system, for example the 11 year sun spot periods (Tveito *et al.*, 2000). It was also argued by Tveito *et al.* (2000) that there are significant changes in climate at the decadal scale that should be represented. There is a case for this argument when analysing the variation in air temperature during the last 30 year normal period 1960 – 1990, for nine sample climate stations within and around the study area of this research, where mean daily temperatures exhibit an oscillating pattern through the normal period (Figure 5.1).

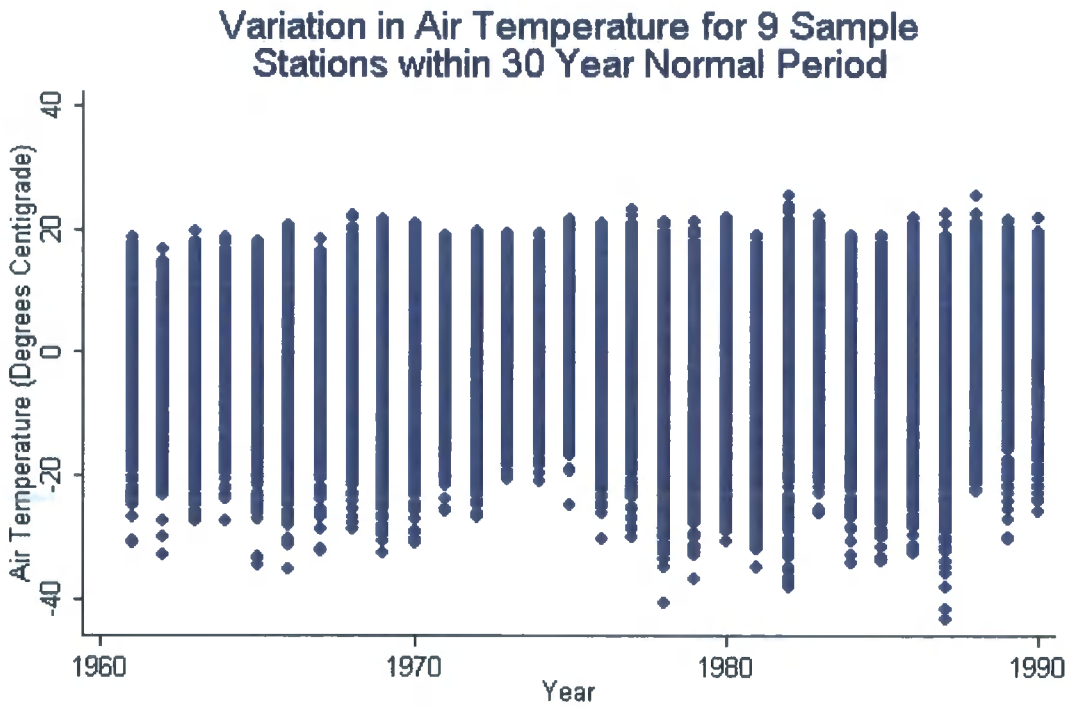

Figure 5.1: Variations in air temperature within the 30 year normal time period

Initial interpretations of this variability propose cyclical trends in minimum and maximum monthly temperatures, but as the present research project is primarily interested in predicting glacier distributions as a function of terrain and climate, it is considered that short-term climate fluctuations would not alter the ability of the model, but would potentially introduce

unnecessary complexity. Thirty year normals were identified as the optimal climatic dataset and were used to drive the energy and mass balance model.

Thirty year normals (1961-1990) of climate for stations in and around the study areas were extracted by the Norwegian Mapping Agency using a map-function linked to their database. Some stations are very close to one another, usually as a result of station closure during the 30 year normal period, and the consequent introduction of a new station established in close proximity.

The spatial distribution of climate stations is altitude limited with few high altitude stations. This introduces a sample bias where limited representation of high altitude conditions creates unrepresentative variable distributions. Where higher, colder, wetter and windier sites are not captured in frequency statistics. This problem is noted in many climatic applications and is an essential consideration in data interpretation and prediction (Susong *et al.*, 1999).

5.4. **Precipitation**

Precipitation describes any form of water reaching the earth's surface including, rain, sleet, hail, snow and rime. Precipitation is highly variable in time and space and occurs when moisture is precipitated or super cooled in the atmosphere. In mountainous areas it is often necessary to conceptualise precipitation and orographic precipitation, as the location, intensity and duration of precipitation events is largely controlled by the position, orientation and dimensions of topographic barriers with respect to synoptic weather conditions. As the orographic component of precipitation produces localised variability in precipitation receipt the representativeness of point climate station data needs to be considered with respect to topographic context. High variability over shorter temporal periods, where datasets are commonly skewed identifies monthly normals as the most informative and appropriate dataset. As statistical measures, such as means, cannot sensibly be calculated over daily skewed datasets (Sumner, 1988). If shorter time periods are required Sumner (1988) suggested the number of rain days, wet days and dry days are more useful measures.

5.4.1. **Spatial distribution**

A total of 119 climate stations in and around the study area have 30 year monthly normals for precipitation. Recording stations are largely positioned within valleys at lower altitudes, the mean station altitude is 780 m with heights having a standard deviation of 290 m. The maximum altitude station is 2062 m and the minimum is 27 m. Stations are well distributed

throughout the Southern Norway, with approximately 15 in or directly surrounding the study area (Figure 5.2).

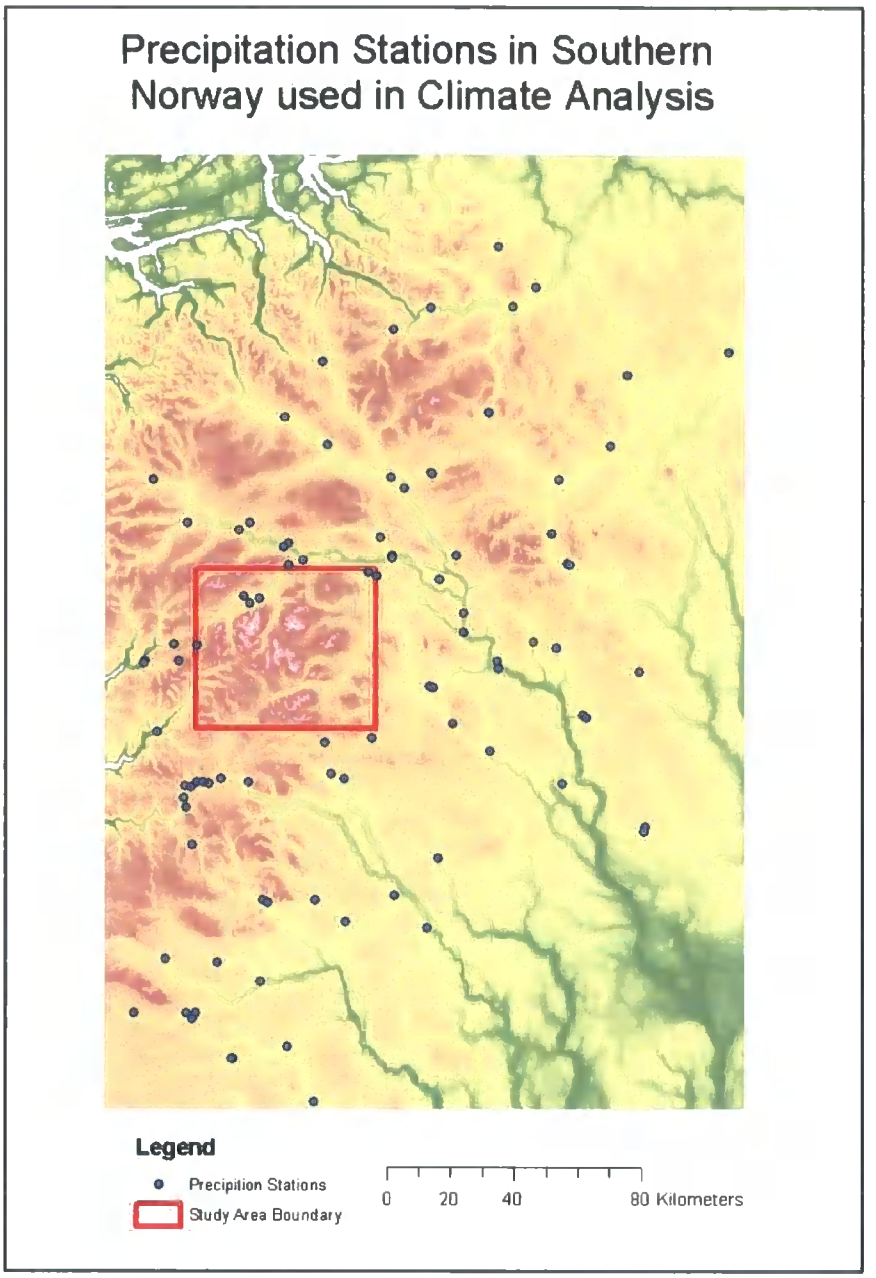

Figure 5.2: Location of precipitation weather stations

Although the distribution of station altitudes is positively skewed with very few above 1000 m (Figure 5.3), the stations do exhibit a dispersed distribution in geographical space.

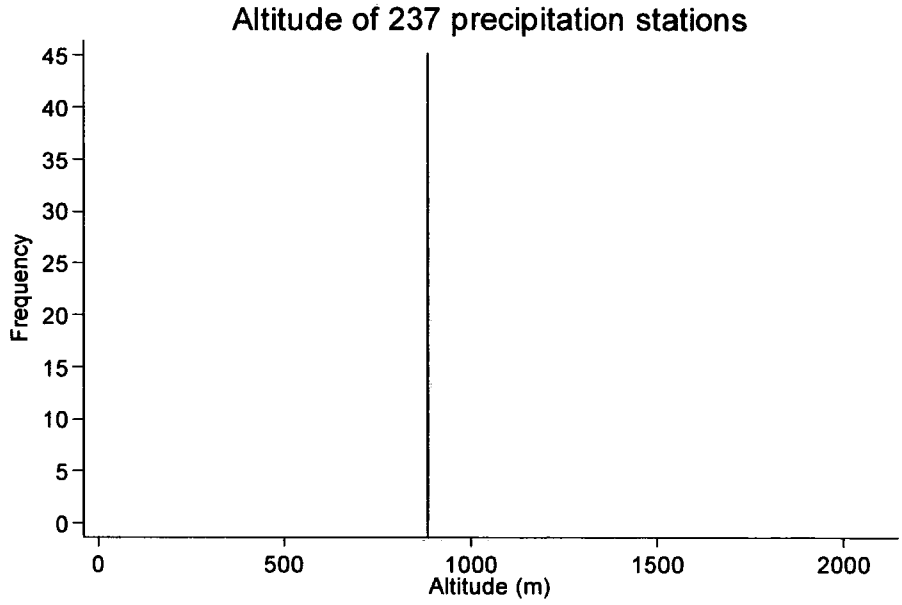

Figure 5.3: Altitudinal Range of Precipitation Weather Stations

5.4.2. **Annual trend**

Precipitation interannual variability is strongly linked to seasonal atmospheric circulation, changes in air stability and air mass characteristics and insolation changes (Sumner, 1988; Barry, 1980). Annual variability within the sampled stations exhibit a clear annual cycle in receipt where maximums occur between July and January and minimums occur in April (Figure 5.4). It is possible to identify a series of different climatic signals or trends within the sampled stations. These have been identified as Type 1, Type 2 and Type 3 precipitation variations, with a sub group 2b associated with Type 2 stations. By identifying slightly different annual trends it is possible to understand the controls on precipitation within the region.

All stations share a common trend through the end of winter and the start of spring from January to April. This is a period of an overall decrease in precipitation receipt, with a small increase evident in March. Precipitation receipt increases from April until around October.

Type 1 precipitation stations have the greatest range in values and receive the highest annual precipitation receipt and show a relatively rapid increase in precipitation from April, maxima occurs between July and November and this period is characterised by moderate variability. This can either be attributed to the high variability and localised nature of precipitation events or a progression temporal variation within the 30 year normal period. Type 1 stations are largely the most westerly stations. One station exhibits a significantly higher winter

precipitation receipt; this station is the highest station (2062 m) and suggesting a non-linear increase in precipitation with altitude. Temperatures largely remain above zero between April and October (Figure 5.7) suggesting that October, November, December, January, February and March are critical months for snow accumulation, although snow may fall earlier and later at higher stations.

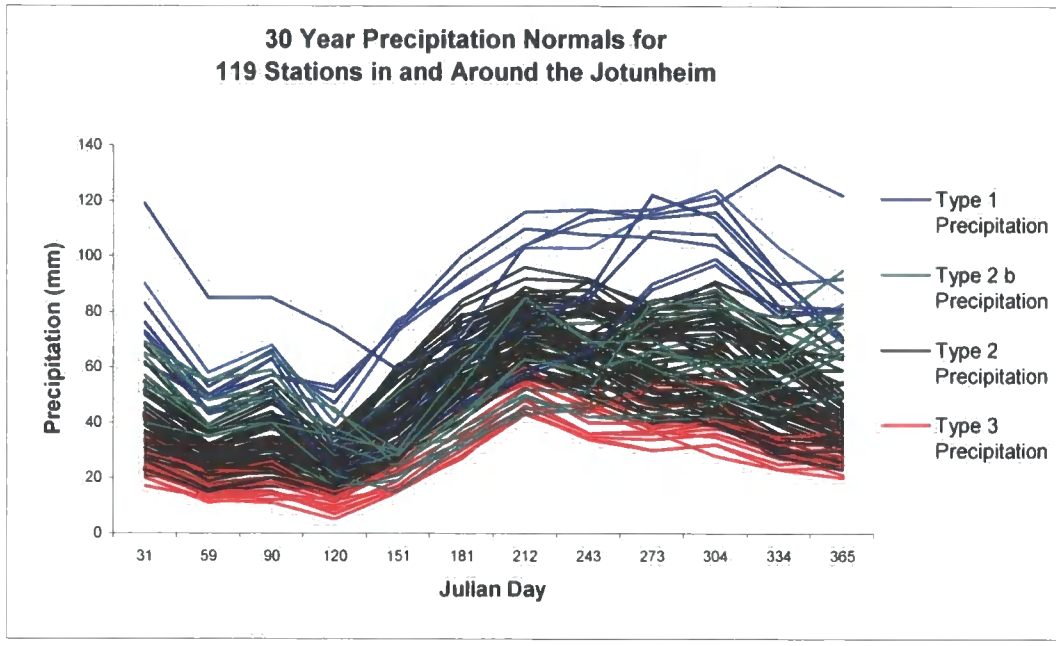

Figure 5.4: Annual trend in observed precipitation receipts

Type 2 and 3 stations show an overall similar pattern, and differ from type 1 stations both due to their slightly drier conditions and reduced variability. Type 2 stations do exhibit a large range in monthly values but each station has a lower variability than type 1 stations. Type 2 stations have a higher annual receipt than type 3 stations. It is possible to attribute the large range in monthly values exhibited by type 2 stations to the larger geographical area the stations occupy. Although the absolute monthly receipt varies between stations the annual cycle in values remains constant, it is therefore possible to propose that these stations are subject to similar climatic forcings. Type 2b precipitation stations exhibit a similar pattern to type 2 stations except they achieve their maximum precipitation receipt in December.

Type 3 precipitation stations have the lowest annual precipitation receipt and have the lowest range in values. Minimum precipitation receipt is in April and the majority of stations have their maximum in July, these stations are largely at lower altitudes with a preference for easterly locations.

5.4.3. Error estimate

Accurate measurements of precipitation receipt at climate stations are known to have large uncertainties, due to their restricted altitudinal range, the localised nature of mountain precipitation events and unreliable instrumentation. The effectiveness of instrumentation is largely associated with obstructions, wind effects and horizontal interception, with a smaller observer error. Precipitation measurements have been found to be highly sensitive to wind direction and magnitude (Black, 1954; Larson and Peck, 1974; Neff, 1977; Helvey and Partic, 1983; Sharon, 1980; Sevruk, 1982, 1986; Folland, 1988; Sharon *et al.*, 1988). Quantitative approaches to instrument design (Folland, 1988) and adjustment parameters (Sharon, 1980) have alleviated some of the problems associated with measurement accuracy, but do not tackle the less manageable problem of the representativeness of local precipitation, both as a function of altitude and topographic context and exposure.

The sensitivity of the different forms of precipitation to gauge and instrument accuracy varies. Barry (1980) attempted to quantify some of these errors associated with the differential rain catch of different gauges (Table 5.1), although he stressed that these correction factors will not remain constant for different gauges and proposed that the largest uncertainties are still associated with local and micro scale controls on precipitation receipt. Precipitation as snow has significantly higher errors than rain, largely associated with dominant role that wind entrainment of snow can have on localised collection and the ability of the gauges to remain exposed and accessible during an snowfall event.

Error	Rain	Snow
Wind field deformation above gauge	2 – 10 %	10 – 15 %
Losses from wetting of internal walls of the collector and measuring container	2 – 10 %	2 – 10 %
Losses through evaporation	0- 4 %	0- 4 %
Splash in splash out	1 – 2 %	1 – 2 %
Overall potential error	**5 – 15 %**	**20 – 50 %**

Table 5.1: Sensitivity of rain gauges adapted from Barry (1980)

5.5. Temperature

Air temperature predominantly varies as a function of altitude and has a dominant control on snow accumulation, determining the character of precipitation and the snow surface

temperature. Potential temperature is sometimes used to record spatial variations in air temperature at different altitudes. The temperature of air parcel behaving adiabatically is related to pressure. In order to compare parcels at different pressures (levels of the atmosphere) it is helpful to change them to have one standard pressure. Potential temperature θ represents the temperature of an air parcel brought adiabatically to 1000mb pressure, thus

$$\theta = T(1000/p) \exp (R/c_p) \qquad \text{(Equation 5.1)}$$

where p = pressure (mb)

T = temperature (°K)

R = gas constant for dry air

c_p = specific heat of dry air at constant pressure

$R/c_p = 0.288$.

Potential temperature is often used instead of the observed temperature to standardise conditions to compare parcels at different levels in the atmosphere. It represents the temperature an air parcel would have if it were at 100 kPa. It is then possible to see how the temperatures would vary at the DALR and therefore may assumptions about their relative stability. Potential temperatures are commonly used where there is variation in atmospheric stability through a vertical profile in the atmosphere. Although potential temperatures do offer conceptual advantages mean monthly air temperatures were supplied by the Norwegian Meteorological Institute and are used in this research.

5.5.1. **Spatial distribution**

A total of 37 climate stations in and around the study area have 30 year monthly normals for temperature, this is considerably less than the number of precipitation stations, largely due to the duration of climate recording and the increased regional importance of precipitation. The topographic constraints on station position apply here as they did for the precipitation stations, with the majority of stations in sheltered valley positions (Figure 5.5). The mean station altitude is 761 m with heights having a standard deviation of 343 m, the mean is slightly lower than the precipitation stations, and a temperature stations exhibit a slightly larger standard deviation. The highest and lowest stations are the same as those recorded precipitation at 2062 m and 27 m respectively; this creates the same range of altitudes as the precipitation stations but with explaining the higher standard deviation as the number of stations is less. Although the population of stations is smaller they are still well distributed throughout the study area, with 10

in or directly surrounding the study area (Figure 5.6). Although the distribution of station altitudes is positively skewed with very few above 1000 m, the stations do exhibit a dispersed distribution in geographical space.

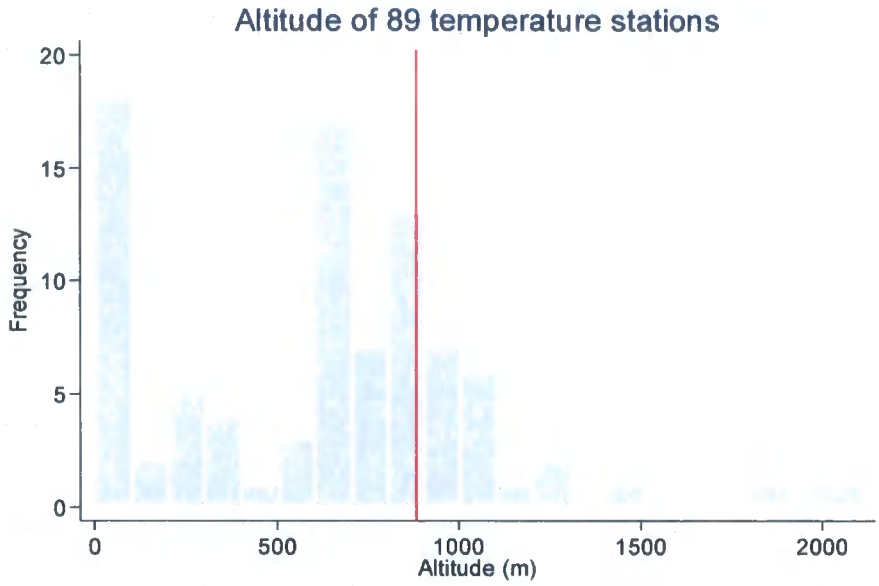

Figure 5.5: Altitudinal distribution of temperature climate stations

5.5.2. **Annual trend**

Temperature interannual variability is strongly related to changes in solar irradiation, where maximum temperatures occur during the month of maximum solar radiation receipt. All stations exhibit a similar annual cycle, where differentiation is possible by station temperature range and maximum minimum values (Figure 5.7).

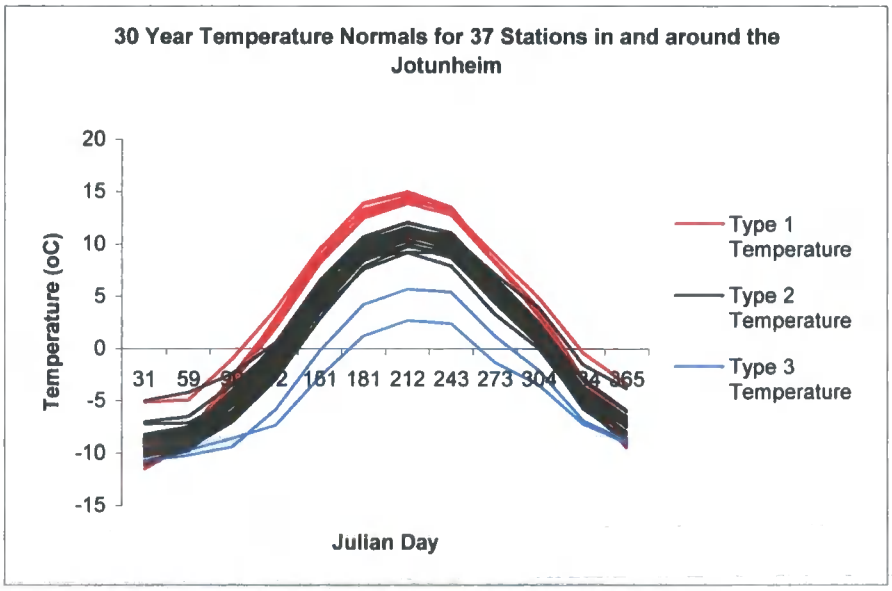

Figure 5.7: Annual variation in temperature

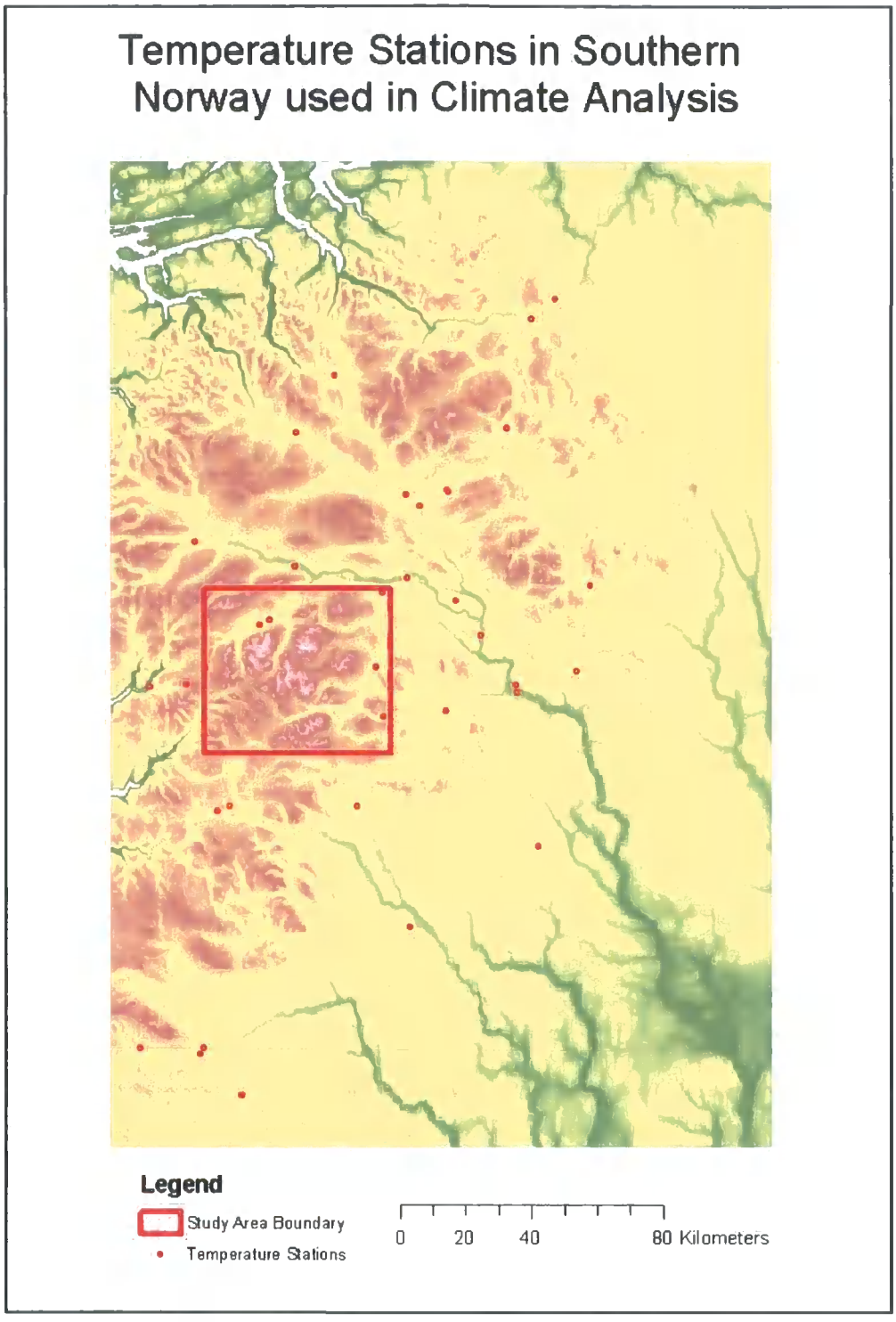

Figure 5.6: Spatial distribution of temperature climate stations

The maximum annual station value is 15 °C in July at station 13550, altitude 241 m, and the lowest –11.5 °C in January at the same station. A measure of continentality is reflected in the annual range of mean temperature, this can be seen to vary with geographical position of the stations, where lower values are found nearer the coast where the maritime influence on atmospheric and energy exchanges is greatest. Variations in temperature trends cannot solely be attributed to continentality, where topographic position also controls the range of temperatures present at a site.

Temperature variations through the year can be segmented into thermal season, which are demarked as a function of monthly mean temperature and synoptic weather conditions. In this region thermal spring starts in March where temperatures start to rise from below 0° C to above 5 °C. Temperatures above 5 °C mark the start of the thermal growing season, between April and May. Summer is characterised by mean daily temperatures above 10 °C and around May / June with maxima occurring in July. Autumn marks the lowering of temperatures below 10 °C starting in September, and winter is characterised by mean temperatures below 0 °C and lasts from December to February. The timing and duration of these thermal periods varies as a function of latitude and continentality, with the coastal maritime regions responding earlier.

Although all stations exhibit a similar annual cycle three distinct groups are evident within the station population (Figure 5.7). Differentiation between groups is primarily based upon temperature maximums in July, where type 1 stations exhibit the highest summer temperatures, and type 3 the coolest summer temperatures. All stations have similar winter minimum temperatures (December range: 6.1 °C, January range: 6.5 °C) and differences only start to emerge in spring and summer, where the range of monthly temperatures exceeds 12 °C.

Type 1 stations as a group experience the most extreme climate, with the coldest winters and warmest summers. Station 13550 at 241 masl has the coldest winter and hottest summer, station 55160 at 27 masl, the lowest altitude station, has the mildest temperature conditions. June temperatures do not fall below 12.5 °C and have a range of only 1.4 °C, in contrast to a January range of 6.4 °C. The increased variability in the winter months is potentially attributable to less persistent atmospheric conditions and localised exposure. It is clear that altitude and continentality alone cannot account for station temperature characteristics born out in Figure 5.8 which locates type 1 stations in sheltered positions within extensive valley.

Temperature variations at Type 2 stations are the most common (78 % of all stations exhibit this annual pattern), maximum temperature in July is 12.1 °C with a range of 2.9 °C. January is the coldest month with temperatures falling to –11.2 °C. This group of stations does not have the

highest or lowest altitudes and are distributed throughout the terrain largely within smaller valley systems.

Type 3 stations experience the coldest conditions with summer maximums not exceeding 5.7 °C, these two stations are the highest within the sample at 1413 masl and 2062 masl. The higher station experiences the cooler temperatures. Although the temperatures are cooler the range in temperatures is smaller than at other stations with a delayed rise in temperatures in early spring, suggesting that winter cooling starts in October / November but does not end until April, with temperatures not rising above 0° C until June for station 55230. Temperatures at 55230 only stay above 0 °C for 3 months, in contrast to lower Type 1 stations which experience 9 months of above 0° C temperatures. Both stations in Type 3 are located close to the study area and potentially provide the most representative data for high altitude climate.

5.5.3. **Daily Time Series**

Even though a monthly temporal resolution has been adopted as the primary period within the model developed during this study, processes critical to glacier initiation act over a range of temporal scales. Diurnal variations, in temperature, control and drive a number of meteorological processes including; changing the direction of energy exchanges above the ground; controlling the strength and direction of mountain and valley winds; and determining vertical structure of atmospheric stability. Daily time series for 9 stations higher than 400 masl in and around the study area, for the last normal period (1961-1990), have provided a characterization of the magnitude and structure of diurnal temperature variations within this alpine terrain environment. The variations captured within a diurnal timescale show high variability, chaotic process where the signal to noise ratio is low. Examining a period of diurnal change does not provide a clearer signal and where noise dominates any graphical representation.

5.5.4. **Error estimate**

The Norwegian Meteorological Institute state that unless there is a technical error the instrument error will be less than the error of the human data recorder. They state that the combined reader and instrument error is in the region of ± 0.1 °C.

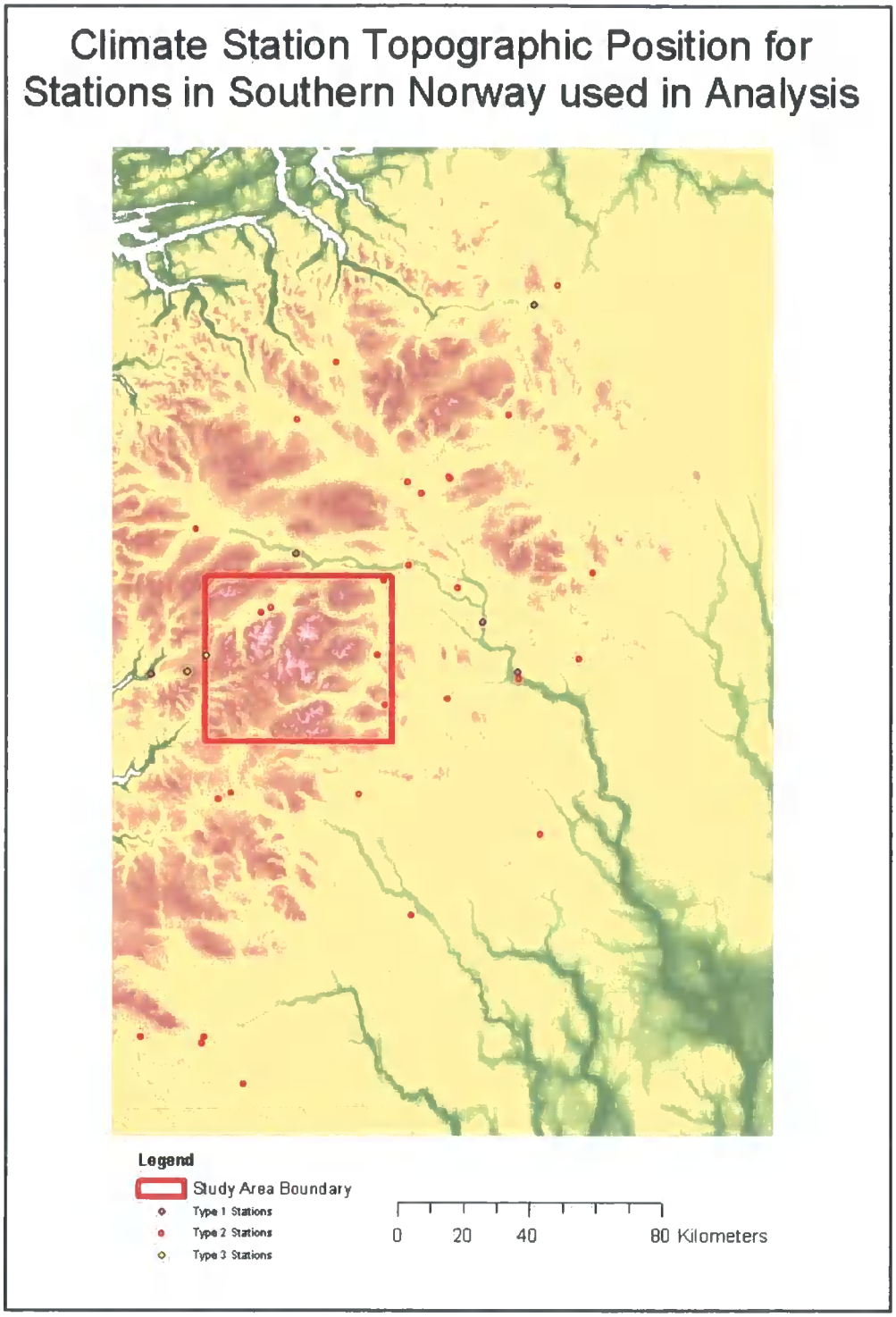

Figure 5.8: Locations of temperature climate stations by type

Perhaps more important uncertainties associated with temperature measurements are those surrounding the representativeness of a daily or monthly mean temperature when maximum or minimum temperatures may be more informative or critical to the process under investigation.

5.6. Cloud

Clouds exert a major influence on the exchanges of short and longwave radiation at the earths surface and form an essential part of an energy balance model (Oke, 1987). Clouds can be characterised by the extent of their sky coverage, base height and composition. The latter is defined by the 1987 World Meteorological cloud classification scheme. Cloud types within the classification vary in their height, density and structure. Although cloud height and type do determine the specific reflectance and absorption characteristics of a cloud, these are still highly variable and are largely determined by airmass type and vertical atmospheric stability profiles. As these two parameters lie outside of the scope of the present study only cloud coverage was used to calculate surface energy balance.

Five stations within and around the study provide monthly cloud data for the period 1981-2000. The data consists of the number of days with sky clear, calculated as not more than a total of 4 oktas of clouds on the three main daytime observations (0600, 1200, 1800 hours), the number of days with fair weather, when there are not more than 9 oktas on the three main daytime observations (0600, 1200, 1800 hours), and not more than 4 on any one of the three observations. The number of days with overcast conditions, which have a total of 20 oktas or more and the mean okta coverage for the three observations times 0600, 1200, 1800 hours.

5.6.1. Spatial distribution

The five recording stations within the study area all occupy valley locations, and are positioned at 621 masl, 626 masl, 712 masl, 890 masl, 1414 masl, with a mean altitude of 852 masl. Ten further stations lie in relatively close proximity to the study area (Figure 5.9) and have been included in the datasets displayed below to provide a more robust representation of monthly cloud variation.

Cloud cover and characteristics are in part controlled by topography, with strong diurnal cycles occurring within valley systems. Although monthly mean values provide a coarser scale dataset smoothing some of the finer scale variability they still represent a local signal that cannot be viewed as representative for the surrounding area.

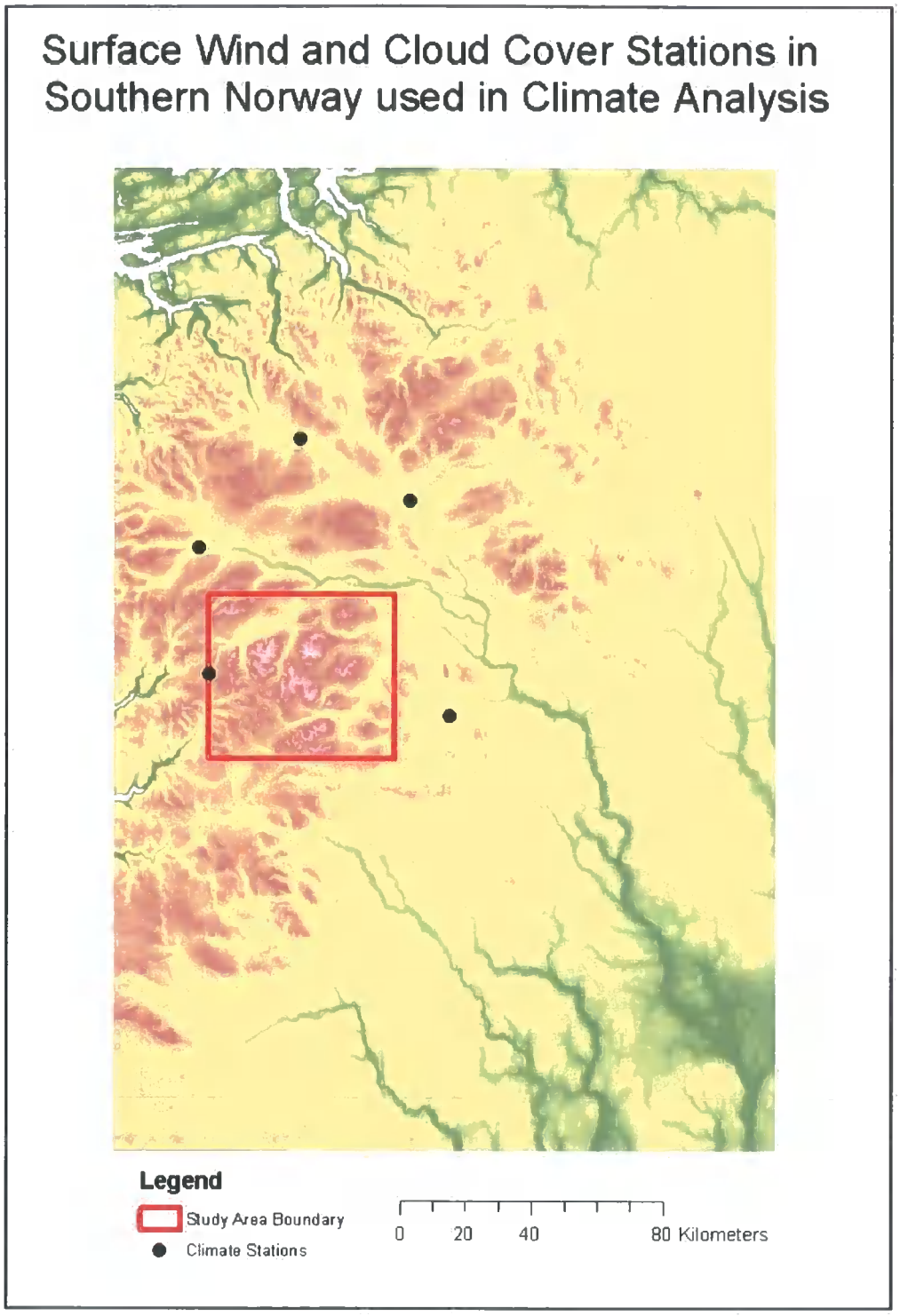

Figure 5.9: Locations of cloud and wind climate stations

5.6.2. **Annual trend**

Air mass characteristics and solar insolation have already been identified as important variables in cloud formation and persistence. As these both annual exhibit annual or seasonal trends these have propagated into the annual cloud trends. The number of clear sky days, where they are not more than 4 oktas at the three time intervals exhibit a distinct seasonal variation with a summer minima and winter maxima. The maximum number of monthly clear sky days occurs in December, where 8 days remain clear. June, July, August and October all have Monthly variability that is greatest in winter.

Within the cloud data it is possible to differentiate two distinct trends among the recording stations. These have been classified as type 1 and type 2 stations (Figure 5.10); Type 1 stations exhibit clearer conditions, with a larger number of clear or fine days, fewer overcast days and lower monthly mean cloud cover.

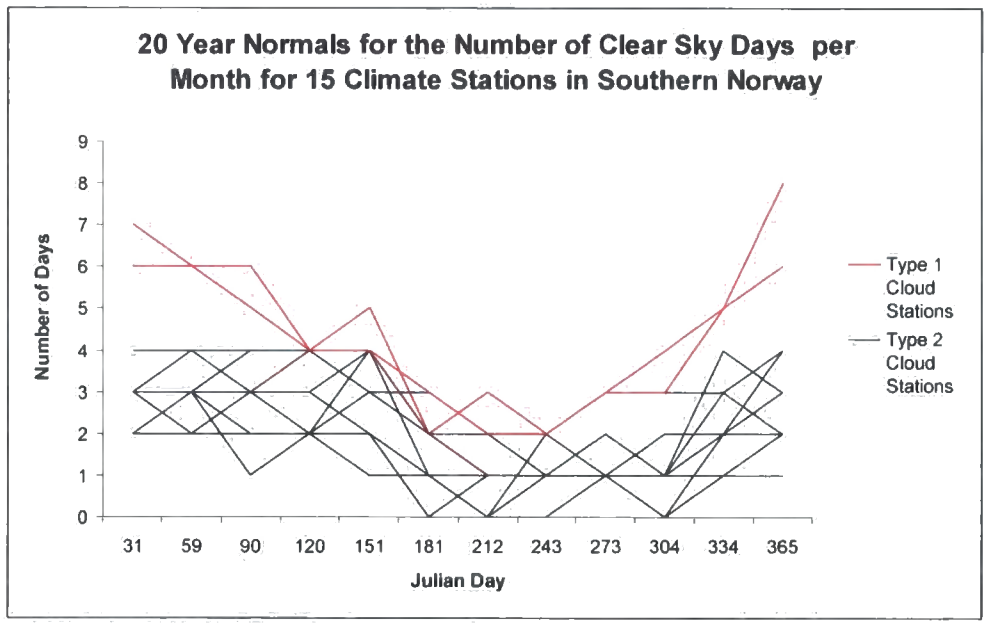

Figure 5.10: Annual trend in the number of clear sky days

Fair weather days, where no more than 9 oktas cloud cover exist at the three time intervals, show a less pronounced annual cycle (Figure 5.11). August, September and October have the smallest number of fair weather days and November through to May / June experience the largest number of fair weather days. The maximum range in values again occurs in December with a total of 9 days, in contrast to August with only 3 days difference.

The less distinct trend is the number of fair weather days indicates that this level of cloud cover may be indicative of change.

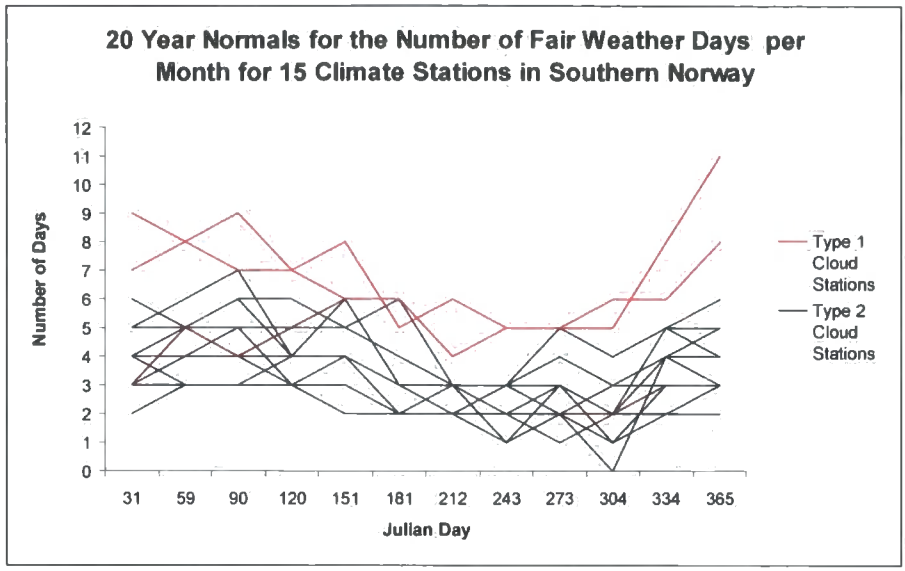

Figure 5.11: Annual trend in the number of fair weather days

Annual variability in cloud cover exhibits a smoother annual variation than the number of clear sky days, with a maximum between July and October (Figure 5.12). Minimum cloud cover occurs in December and increases through winter and spring to reach a maximum in late summer early autumn. Winter months experience a slightly higher range in values (2.2 oktas in December compared to 1.2 oktas in July and August). Type 2 stations have annual average cloud cover of 6.0 oktas in contrast to Type 1 stations that have an average of 4.6 oktas. Type 2 stations have a higher range in values with a standard deviation of 0.41 in contrast to 0.30 for Type 1 stations.

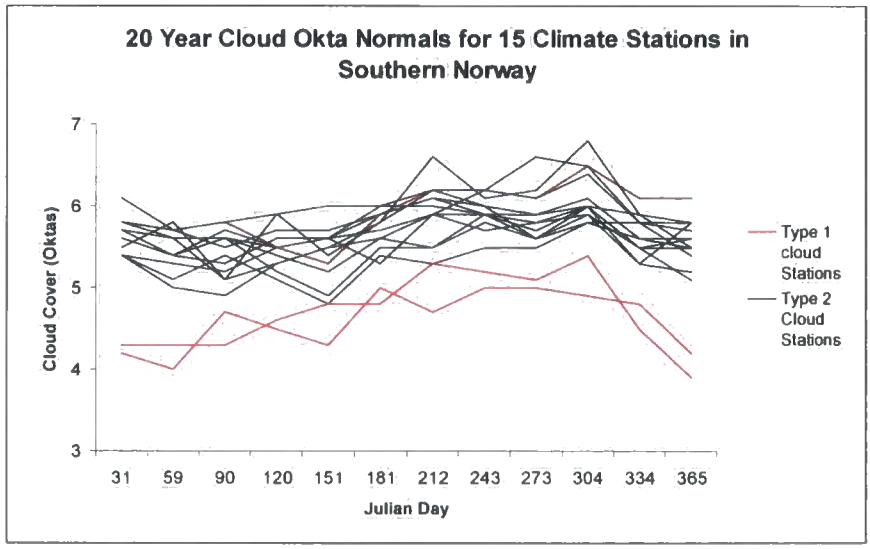

Figure 5.12: Annual trend in average monthly okta cover

The number of overcast days shows very little seasonal variability especially in type 2 stations (Figure 5.13). The maximum numbers of overcast days occur in July and October where 20 days out of the month are overcast for type 1 stations and in October and December for type 2 stations when 10 days are overcast. Type 2 have a minimum number of overcast days in July when only 4 days are overcast, in contrast to type 2 stations where the minimum occurs in May when only 8 days are overcast.

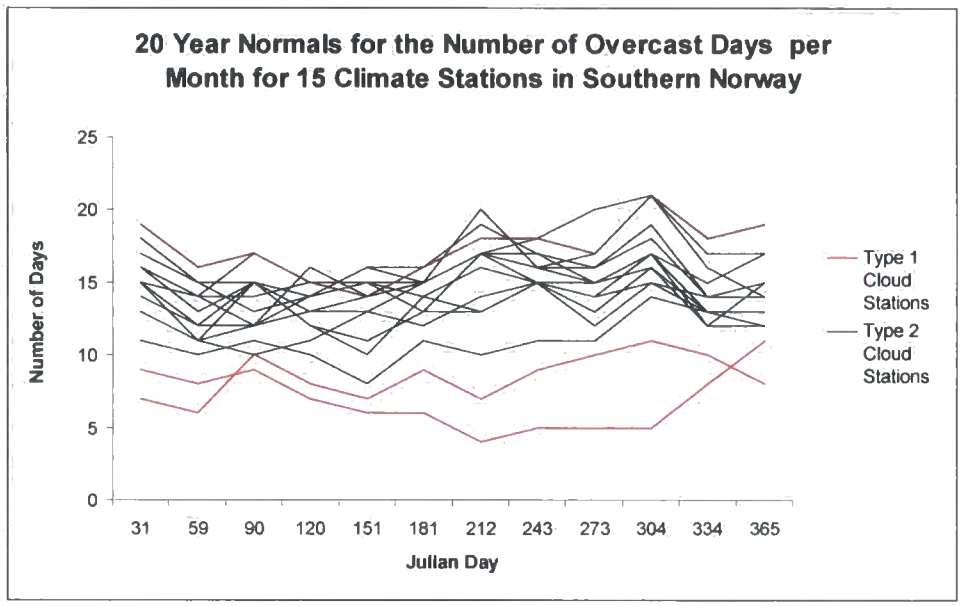

Figure 5.13: Annual trend in the number of overcast days

5.6.3. **Daily Air Temperature and Cloud Cover**

Cloud cover in part controls air temperature, a relationship that involves feedbacks, where although an increase in cloud cover will lead to a reduction in the amount of direct beam radiation incident upon the surface and therefore reducing its heating effect, warming will occur due to retention of long-wave radiation underneath the cloud base. Increased cloud cover acts to reduce the daily temperature range, lowering daily maxima and increasing evening mimima (Barry and Chorley, 1982). Temperature fluctuations will adjust atmospheric stability and consequently the height and characteristics of cloud cover.

This complex relationship is born out through the utilisation of a daily 30 year normal cloud cover and air temperature dataset for 9 climate stations in Southern Norway, from in and around the study area. The size of this dataset, and the range of data attributes limit the effectiveness of any graphical representations of the dataset as a whole. Examination of the correlations

between air temperature and cloud cover per station (Table 5.2 and Figures 5.14 – 5.22) provides some information about the potential relationships between the variables, although any statistical deductions are not significant.

Station	Correlation Coefficient
All	0.1041
700	0.2093
13670	0.0516
18960	-0.0578
23160	0.0918
25590	0.0668
25840	0.1392
29770	0.1801
50300	0.1778
61770	0.2991

Table 5.2: Correlation, by station for mean monthly air temperature and cloud cover

Station numbers 700, 25590, 50300, 23160 all exhibit a similar trend where warmer and cooler temperatures tend to have less cloud cover with most stations with complete cloud cover have temperatures between –10 °C and –15 °C, where clear sky conditions have temperatures ranging between –20 °C and 20 °C. This data, that represents one year seasonal variations, may be the primary driver for this trend, where clear sky conditions increase the proportion of solar insolation reaching the ground, thus allowing temperatures to reflect solar heating, where the annual trends in insolation create annual variations in surface temperature. A similar explanation is possible for the range in temperatures in overcast conditions.

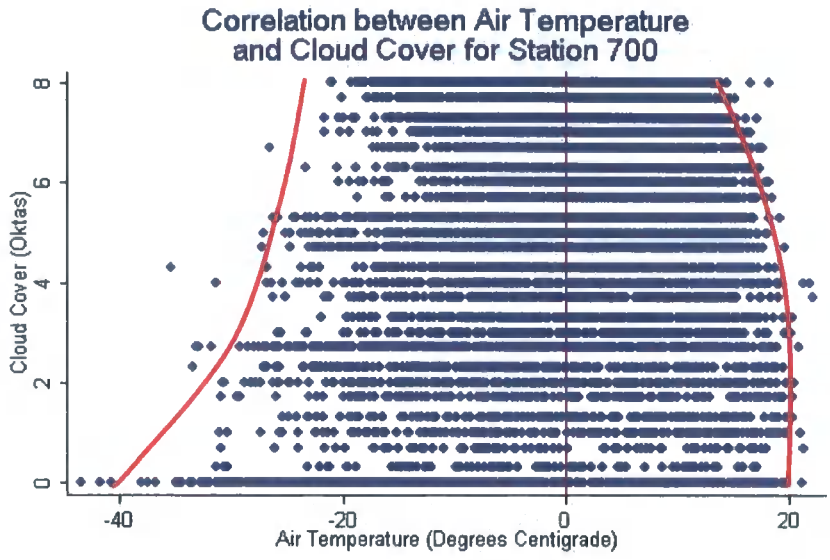

Figure 5.14: Correlation between air temperature and cloud cover for station 700

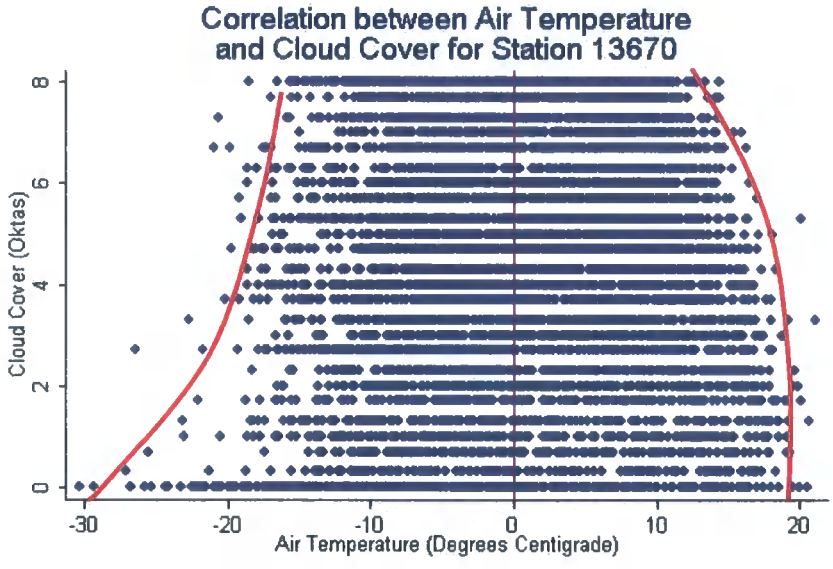

Figure 5.15: Correlation between air temperature and cloud cover for station 13670

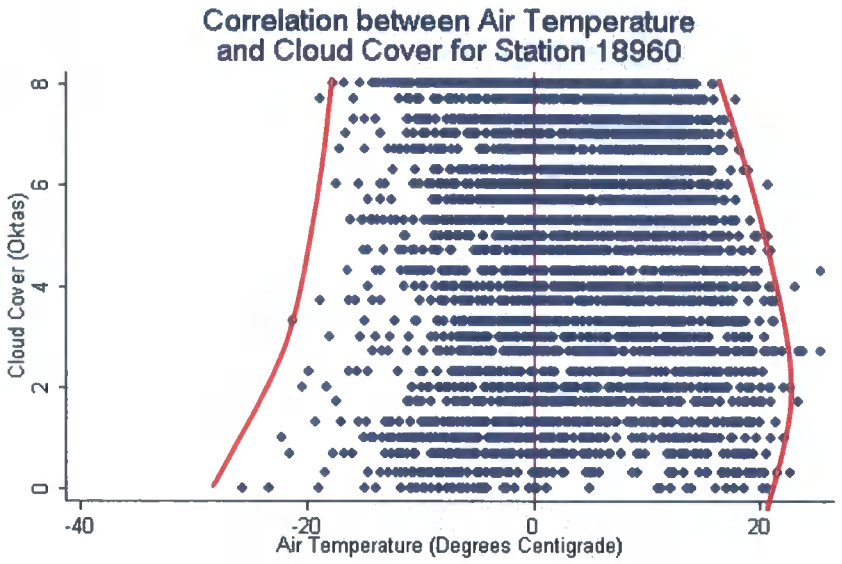

Figure 5.16: Correlation between air temperature and cloud cover for station 18960

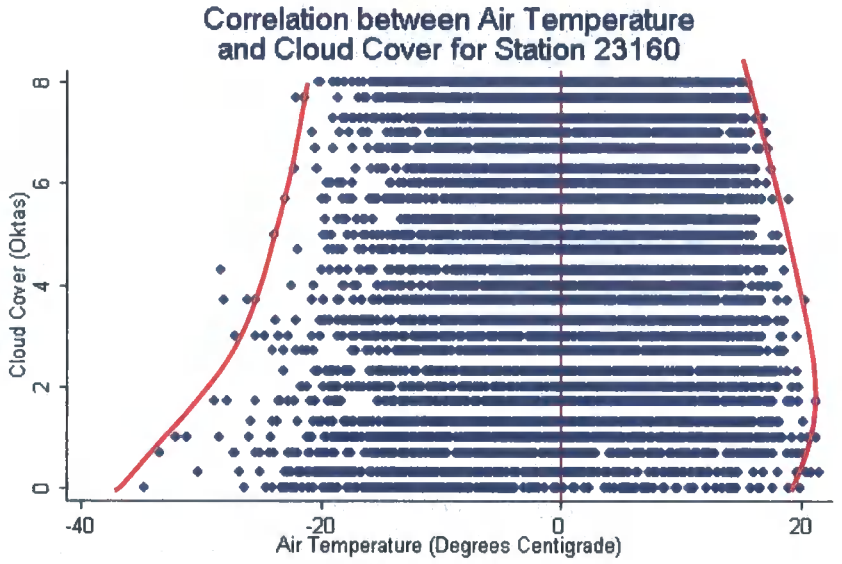

Figure 5.17: Correlation between air temperature and cloud cover for station 23160

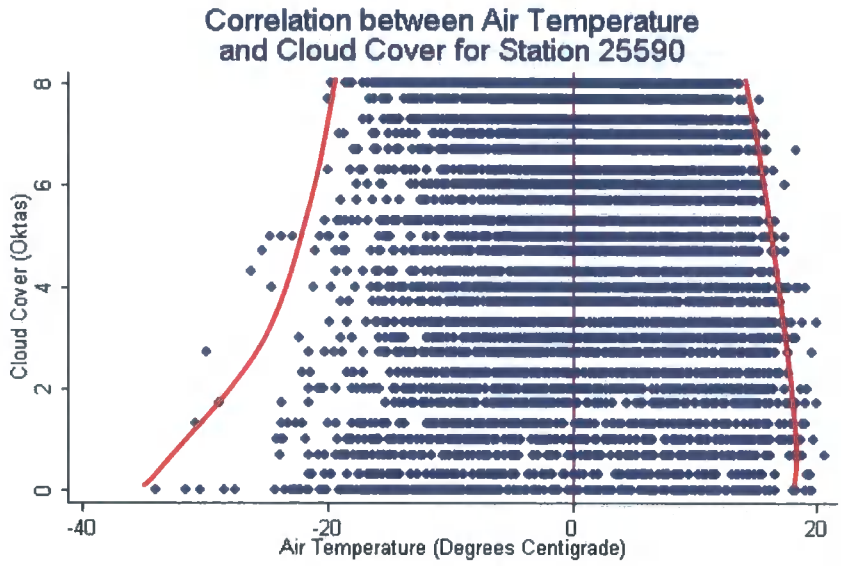

Figure 5.18: Correlation between air temperature and cloud cover for station 25590

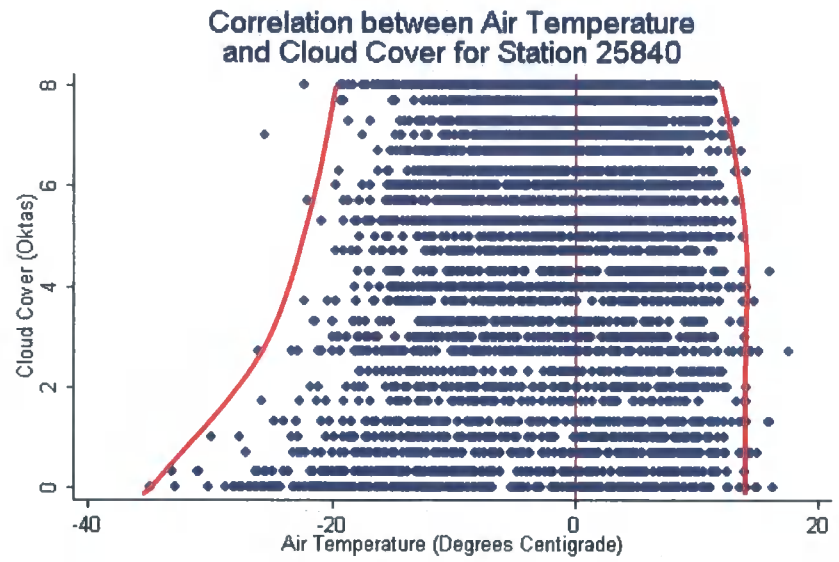

Figure 5.19: Correlation between air temperature and cloud cover for station 25840

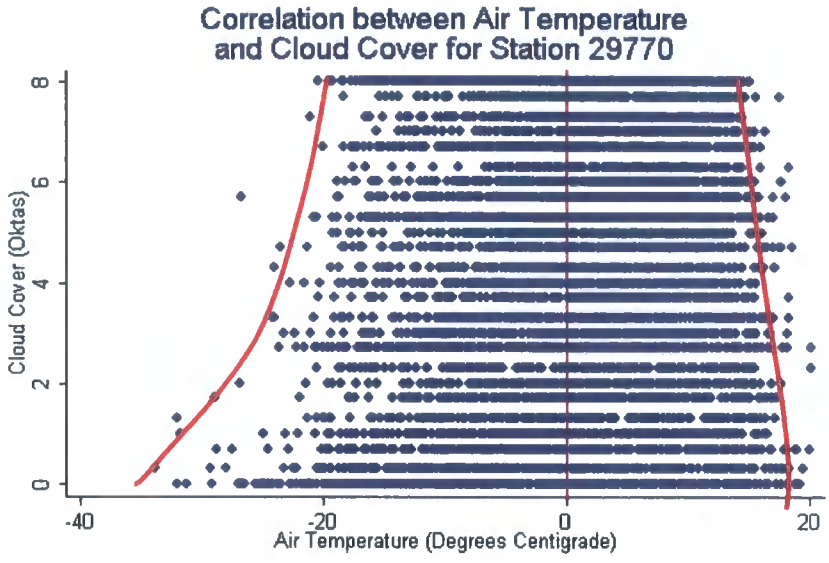

Figure 5.20: Correlation between air temperature and cloud cover for station 29770

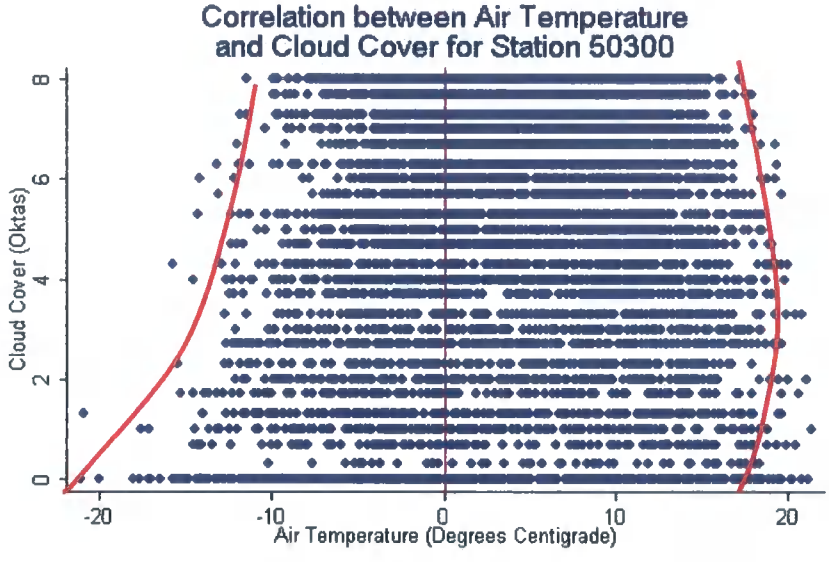

Figure 5.21: Correlation between air temperature and cloud cover for station 50300

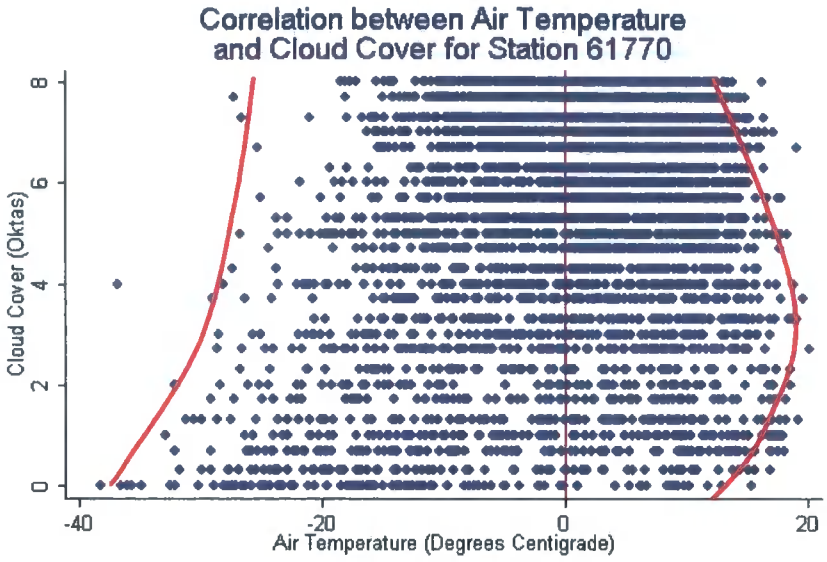

Figure 5.22: Correlation between air temperature and cloud cover for station 61770

5.6.4. **Error estimate**

Cloud cover data is possibly the most difficult to assign a quantified error estimate to as its measurement is entirely subjective, it is also unlikely that the reader error will be equally distributed throughout each okta segment, where differentiation between 0 and 1 and 7 and 8 oktas cover significantly easier to distinguish than 4 to 5 oktas cover. A reader error of +- 0.5 oktas is proposed. Although questions exist about the objectivity of cloud cover measurements more important concerns arise about the representativeness of these measurements. Repeat measurements during the day provide more robust estimates to allow a regional pattern to emerge.

5.7. **Wind**

Wind acts over a large range of spatial scales; those that are characteristic of the earth's circulation, such as the trade winds; and those that are induced by local mountains and surface terrain such as valleys winds or very local phenomena where obstacles induce small eddies and flow separation.

Two scales of wind data have been selected to use within the model in the present study; surface wind vectors measured by ground level climate stations; and, free air wind vectors recorded using radiosondes. These two datasets provide very different information; free air vectors supply information about regional wind directions and speeds indicative of synoptic weather conditions. Surface wind vectors in part represent the terrain modification to flow; faster flows are indicative of smoothed exposed or channelised areas where little drag is imposed by the

surface; and slower wind speeds occur where high frictional drag, from the terrain surface, retards the flow near to the ground.

Altitude, season and atmospheric stability also impose important controls on surface wind vectors.

5.7.1. **Surface wind**

Wind speed is recorded using an anemometer; unlike older models new designs are not sensitive to wind direction removing the increased lags associated with the falling limb of wind speeds. Wind vectors used in this study are 20 year normals for the period 1981 - 1990, these were calculated by selecting four observations per day. The values are split into the eight wind-sectors (each a 45° segment of the whole 360° of possible wind directions) and speed in incremental groups of 2.5 ms^{-1}. The data were divided into four seasons, each of three months starting with December to February. Data coverage between the stations varied significantly and none of the stations recorded throughout the night (Table 5.3).

Station	Daily Coverage
13670	75 %
15720	70 %
16740	75%
55290	67%
61770	72%

Table 5.3: Daily coverage of wind data at climate stations

Wind not only plays a critical role in the entrainment of snow but surface wind speeds also determine the magnitude of turbulent heat exchanges at the Earths surface.

5.7.1.1. Spatial distribution

The same stations recording cloud cover record surface wind (Figure 5.9). Wind vectors are likely to highlight dominant valley winds rather than regional wind directions, where valley locations limit the use of these data, where regional trends would allow the prediction of local terrain modifications.

5.7.1.2. Annual trend

Wind direction, expressed as the cardinal direction from which the wind blows is recorded, like slope aspect on a circular scale, at an interval measurement scale. Consequently statistical measures of central tendency need to be used with caution and replaced with more appropriate measures.

Wind direction does not show a strong annual trend (Table 5.4), all stations have a dominant wind direction aligned with valley aspect, where flow is predominantly up and down valley according to the time of day. Variability around modal directions may either be indicative of variable or gusty wind condition, or represent diurnal thermally driven circulations.

Station	Spring	Summer	Autumn	Winter
13670	S and still	S and still	S and still	S and still
15720	East and West	East	East	East
16740	West and East	West and East	East	East and West
55290	West, South and still	West and still	West, South and still	West, South and still
61770	West and East	West	East	East and West

Table 5.4: Seasonal trend in modal wind direction

Wind speeds show a very weak annual trend (Table 5.5), with slowest winds largely occurring in Spring. As the data is only recorded to a precision of 2.5 ms^{-1}, a continuous scale would provide more information on the distribution of wind speeds. Seasonal trends in surface wind speeds recorded in valley stations largely reflect the degree of surface modification to seasonal free air winds and consequently exhibit only a weak annual trend.

Station	Spring	Summer	Autumn	Winter
13670	0 – 2.5	0.1 – 2.5	0 – 2.5	0 – 2.5
15720	2.6 – 5	2.6 – 5	2.6 – 5	2.6 – 5
16740	2.6 – 5	2.6 – 5	2.6 – 5	0.1 – 5
55290	0.1 – 2.5	0.1 – 2.5, 2.6 - 5	2.6 – 5	Mixed
61770	2.6 – 5	2.6 – 5	5 – 7.5	2.6 - 5

Table 5.5: Seasonal trend in mean wind speed ms^{-1}

Autumn and winter exhibit stronger wind speeds than summer and spring, these seasons are characterised by high pressure systems and turbulent conditions if the westerlies are broken by the development of high pressure ridges (Section 3.8).

Information on regional wind data is provided from free air wind speeds that represent flow direction without modification by underlying terrain.

5.7.2. **Free air wind**

Free air vectors, recording regional wind characteristics above the boundary layer were taken at altitudes of 300 m, 600 m, 900 m, 1200 m, 1800 m, and 2700 m above sea level using a radiosonde at four stations for the period 1987 – 1994. Wind speed is provided on an interval scale with 2 ms^{-1} class widths. Wind direction is also recorded on an interval scale with 30 ° class widths, values are provided as annual and seasonal means.

5.7.2.1. Spatial distribution

Three of the four provided stations are located around the study area, allowing an impression of regional wind flow through the Jotunheimen. Bodo is further North providing information on the distribution of winds throughout Norway. As data is describing regional trends sparse station is not considered to be a major limitation during the present study.

5.7.2.2. Annual trend

Each station has 30 records for each season and altitude and one annual mean dataset. The data provides information that will be used to determine the regional wind direction and air speed throughout the year within the Jotunheim. Detailed statistical analysis of the variability within and between the stations is not considered necessary for this research project.

All stations exhibit and increase in the variability of wind direction with increased altitude of measurement, borne out through the increase in the standard deviation of direction with altitude (Table 5.6).

Station	300 m ms^{-1}	2700 m ms^{-1}	Modal Class
Gardermoen	3.71	6.56	210,210,210,240,240,270
Ørland	6.21	7.19	270,270,270,270,270,270
BodØ	5.41	6.68	120,240,240,240,240,240
Sola	5.57	6.91	180,180,180,330,210,270

Table 5.6 Variations in wind speeds and direction by station

Despite the increased variability in wind direction the modal class largely remains constant. Vertical profiles of wind speed provide information on the atmospheric structure and layer boundaries (Figure 5.23).

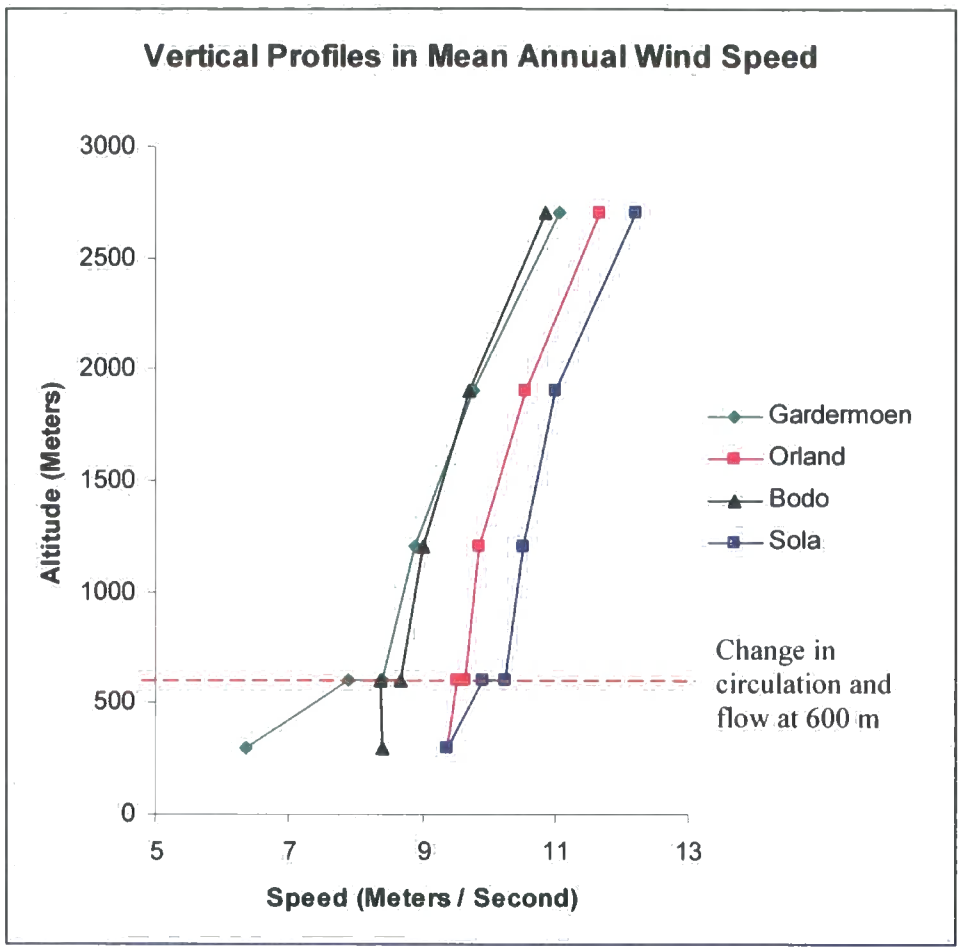

Figure 5.23: Variation in wind speed with altitude by station

Wind direction provides the more informative dataset that can be used to drive the regional wind component of the model.

5.8. Conclusions

Monthly 30 year normal data were identified as the most appropriate dataset for this research forming an available and robust indicator of monthly climate. Systematic examination of the frequency and spatial variability within monthly mean 30 year normal data of precipitation, temperature, cloud cover and wind speeds exhibited marked spatial and temporal variability. Topographic position was found to play a dominant role, governing temperature and precipitation variations where local and contextual controls were found to play a dominant role. These distinct trends are used in Chapter 6 to predict spatially distributed climate surfaces, but

the limitations are acknowledged and over using correlations present within the data is identified as a potential problem.

Limited altitudinal range of climate stations restricts the representivenss of observed records where high altitude conditions are not represented.

Wind and cloud data provided the weakest climate datasets, where seasonal and spatial patterns were weak, limiting their use in climate modelling (Chapter Six).

CHAPTER SIX
CLIMATIC MODELLING

6.1 Introduction

Climate, specifically temperature, precipitation, wind and cloud cover are known to be important parameters controlling the rate and distribution of snow accumulation (Martin *et al.*, 1997; Kayastha *et al.*, 1999). This chapter outlines the methodology employed to create a series of spatially distributed climatic datasets used to drive melt in Chapter Seven. The methodology uses the topographic variables created in Chapter Four and the observed seasonal and spatial trends described in Chapter Five to create a suite of local climate datasets for air temperature, precipitation, cloud cover and wind speeds and direction.

A flexible and repeatable approach to climatic predictions was employed to facilitate application to other geographical areas. Local factors including pressure systems, the maritime influence, and temperature inversions were accounted for in predictions, which attempted to reconstruct climate in glacier accumulation areas.

The chapter initially identifies available approaches to predicting spatially distributed climate variables and then discusses the predictive approaches employed for each of temperature, precipitation, cloud cover and wind speed and direction. A range of temporal scales are predicted within the climate model and justifications are provided for each.

6.2 Modelling Techniques

It was necessary to reject several different methods of creating local scale climate surfaces as they were inappropriate for this study. Standard lapse rate models have already been identified as too

generalised for this research as they cannot replicate topographically induced temperature and precipitation patterns (Section 2.2.1). Downscaling from a global climate model (GCM) was also rejected as the uncertainties and error associated with this procedure are greater than those created by interpolating between climate stations (Section 5.3.1). A quantitative approach to predictions using relationships within the meteorological datasets was also rejected as it failed to account for the modification of lapse rates by the terrain (Chapter 5).

This research predicted local scale climate by extracting quantitative relationships within and between meteorological and topographical data. The approach quantified terrain forcings and the terrain modification of the adiabatic process by characterizing geomorphological context. Accurate local scale climate predictions can only be made if the processes controlling the climate variables are parameterised. Therefore, although the model was designed to be flexible and repeatable it was necessary to incorporate local factors to make accurate climate predictions. In Norway these were the strong maritime influence in the west evident especially when considering precipitation; the frequent occurrence of temperature inversions in winter, which result in cold valley floor temperatures, and the dominant role that the seasonally variable pressure systems have on the climate.

Data regression and general linearised modeling were identified as successful techniques for quantifying and predicting the complex relationships between terrain and climatic parameters.

6.2.1. **Regression**

Regression analysis predicts a dependent variable from one or more independent variables. Linear regressions take the form of :

$$y = a + bx \qquad \text{(Equation 5.1)}$$

Where y is the dependent variable, x in the independent variable, b is a coefficient and a is a constant. Results can either be plotted as observed vs. predicted or represented as a regression line fitted to the data. The quality of a regression model is normally evaluated by describing the amount of variation within the dataset that is accounted for by a linear model. The sum of the square of the residuals provides a measure of how much of the data is not explained by the linear model. This value, normalised by the standard deviation is called the coefficient of determination, R^2. An

adjusted R^2 accounts for the number of fitted constants as well as the size of dataset, as larger samples will in general provide stronger regressions. An F-test can be used to test the significance of the coefficient of determination, giving an F-distribution result (Equation 5.2).

$$F = \frac{\left[r^2 / \kappa\right]}{\left[(1-r^2)/(n-\kappa-1)\right]} \qquad \text{(Equation 5.2)}$$

with $(n-\kappa-1)$ degrees of freedom,

where κ is the number of terms in the equation.

A number of other parameters can also be used to assess the ability of the regression to account for variability within the dataset. These and other descriptive statistics are provided in the subsequent regression result tables, and are described in Figure 5.1.

6.2.1.1. **Multiple Regression**

Multiple regressions predict the dependent variable from more than one independent variable. Here the regression takes the form:

$$y = a + b_1x_1 + b_2x_2 + b_3x_3 + \ldots \qquad \text{(Equation 5.3)}$$

Where again, y is the dependent variable, a is the constant, b_1, b_2 and b_3 are the independent variables and x_1, x_2 and x_3 are the coefficients. Statistical interpretation of the regression remains the same, however visualisation should be restricted to plots of observed vs. predicted.

Regression analysis is a powerful and useful tool to quantify relationships between data, however it is important to critically evaluate model predictions, both their statistical significance and physical meaning. Fitting more constants requires larger sample sizes.

6.2.2. **Generalised Linear Models**

Nonlinear relationships can be modeled effectively using generalised linear models (GLM): these are a form of regression but use a link function such as a log link to avoid the problem of having to

transform a dataset, then back transform when predicting the dependent variable. This technique is particularly effective when dealing with nonlinear relationships. A GLM can be set up to ensure physically meaningful predictions, i.e. precipitation can always be positive. Link functions available within GLM include reciprocal, power or log functions.

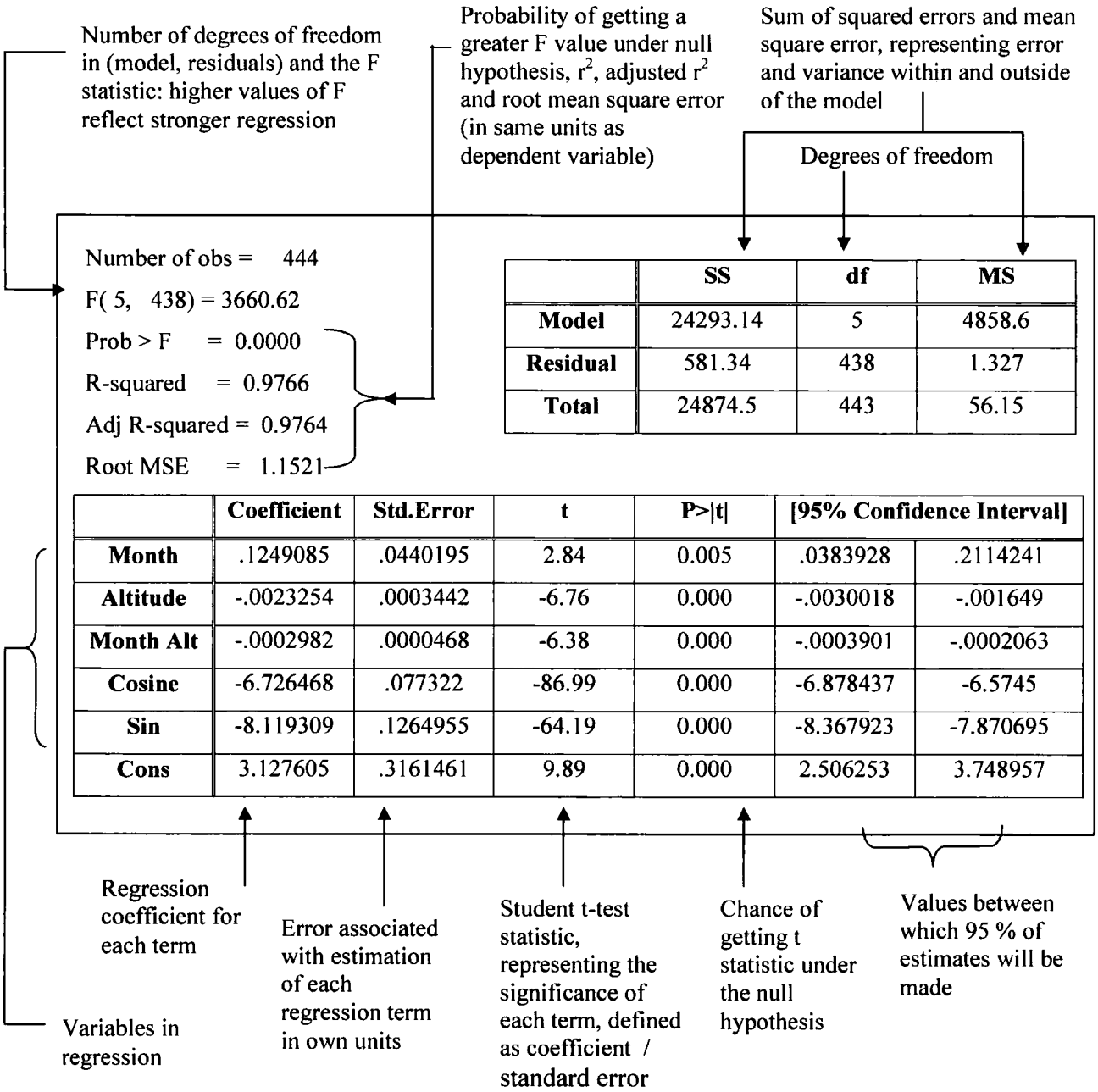

	SS	df	MS
Model	24293.14	5	4858.6
Residual	581.34	438	1.327
Total	24874.5	443	56.15

	Coefficient	Std.Error	t	P>|t|	[95% Confidence Interval]	
Month	.1249085	.0440195	2.84	0.005	.0383928	.2114241
Altitude	-.0023254	.0003442	-6.76	0.000	-.0030018	-.001649
Month Alt	-.0002982	.0000468	-6.38	0.000	-.0003901	-.0002063
Cosine	-6.726468	.077322	-86.99	0.000	-6.878437	-6.5745
Sin	-8.119309	.1264955	-64.19	0.000	-8.367923	-7.870695
Cons	3.127605	.3161461	9.89	0.000	2.506253	3.748957

Figure 5.1: Interpretation of regression statistics used within this chapter.

6.2.3. **Predictive Parameters**

Initial investigations identified the need for a suite of predictive parameters that could account for the variation in climate both through the year and through the terrain. These can be split into cosine and sine functions that parameterise annual cycles, topographic measures that account for local or regional surface modifications to climate, and interaction terms that attempt to quantify the inter-relationships between these two groups.

6.2.3.1. **Cosine and sine functions**

Most climatic variables show strong seasonal variations that are apparent on a monthly temporal scale. These trends were apparent in the temperature, precipitation, cloud and wind datasets discussed in chapter 5, where precipitation and temperature exhibited annual maxima (October and July) and minima (April and January) respectively (sections 5.4.2 and 5.5.2).

Sine and cosine functions provide a mathematical method of simulating this annual cyclic behaviour. Where month is the month number with December as month 1:

$$\text{Cosine function} = \text{Cosine}\,(2\,\Pi\,(\text{month} - 0.5)/12) \qquad \text{(Equation 5.4)}$$

$$\text{Sine function} = \text{Sin}\,(2\,\Pi\,(\text{month} - 0.5)/12) \qquad \text{(Equation 5.5)}$$

6.2.3.2. **Topographic parameters**

Topography plays a dominant role in controlling local climatic gradients over complex terrain (Geiger, 1965; Raupach and Finnigan, 1997; Barry, 1992). Incorporating parameterized measures of topographic form allows more accurate estimates of surface climate to be made (Ryan, 1977; Lapen and Martz, 1983, 1996; Barry, 1980).

It is possible to conceptualise topographic controls at three spatial scales; sub continental where the overall dimensions and orientation of continental shields and coastal margins govern climate modifications; regional scale where relief and terrain shape impose the greatest modifications and local scale where slope angle and aspect are critical in predicting the modification. Barry (1980) suggested that these scales are more informative when combined with information on the thickness

of the boundary layer (< 1000 m or 10 – 100 Km), the characteristics of the climatic processes and larger scale synoptic processes. Maritimity and measures of relief are examples of regional scale measures, the remaining variables outlined in Section 4.5.5 largely characterise slope or valley form and position and are examples of local measures. Coarser scale predictions (500 m or greater) like those of Running and Thornton (1999), Thornton *et al.* (1997) and Cline *et al.* (1998) can alleviate the need for these local complex topographic measures, where correlations between temperature and precipitation and altitude were used to create daily climate predictions. Similarly short temporal resolution predictions such as those outlined by Furman (1978) can be driven by the previous day's temperature and he found that locational parameters were not significant. Others employ derived altitude lapse rates in attempt to reduce the complexity of the climatic modelling, however in the case of Winstral and Marks (2002a, 2002b) modelling snow accumulation, this creates potential weaknesses within in the model, where wind speed is modelled in much greater detail, compromising the validity of outputs.

Although altitude is argued to be the most dominant control on mesoscale climate in mountainous areas (Sutherland, 1984) other topographic measures including slope and aspect impose important controls (Evans, 1977; Wendler and Ishikawa, 1974). Hess *et al.* (1975) moved away from analysis of individual variables and quantified topographic controls by identifying topoclimates, topographic units, defined by their altitude, convexity and slope and linked these through regression analysis to their characteristic climates. The methodology outlined here builds upon this approach, linking terrain attributes to climatic parameters but adopts a spatially distributed output instead of spatially aggregated surfaces. The approach adopted here addresses some of the criticisms made by Barry (1980) of Hess's broad spatial scale study that did not account for spatial variability in climatic lapse rates.

Although the inclusion of topographic form and contextual measures can alleviate some of the local signals recorded by climate stations, in some examples local trends can obscure regional patterns entirely. Richard and Gratton (2001) reported such a case and consequently created synthetic stations in an attempt to remove the local effects that obscured station records.

A detailed description of all of the topographic parameters used within this research can found in section 4.5.

6.2.3.3. **Interaction terms**

Topographic variables quantify the modification to or processes controlling local climate. Processes controlling climate vary through the year, and lead to distinctive differences in meteorological patterns, as reported by Tveito *et al.* (2000) who found lapse rates to vary through the year, with lowest gradients in winter and highest in spring and autumn; and Jonsson (1937) who stressed that there is a seasonality to synoptic forcings. As climatic processes exhibit annual trends, so too does the effectiveness of these parameters. In an attempt to quantify these dynamic relationships, interaction terms were used to relate parameters and months.

The most successful of these terms was sine of the month * altitude, subsequently termed *monthalt*. This term provided good results as it assists in characterising the monthly variability in altitudinal relationships as reported by Tveito (2000). Interaction terms were also employed by Hayhoe and Lapen (1999) who used the product of monthly wind speed and altitude to aid temperature predictions in the Rocky Mountains.

6.2.4. **Annual and Seasonal consistency**

In conjunction with the use of the *monthalt* interaction term, further seasonality trends were introduced in an attempt to capture the strong seasonal and synoptic patterns observed in the climatic data from the Jotunheimen.

Two different conceptual approaches were used for predicting monthly lapse rates: an annual lapse rate model and a seasonal lapse rate model. The former identifies months as arbitrary divisions that have no meteorological significance as the 1st January is not climatically different from the 31st December and should therefore not be treated as such. This approach predicts using data from all months and does not identify boundaries between months. Predicting monthly estimates of meteorological parameters using the same independent variables and coefficients throughout the year restricts seasonality in the predictions. The seasonal lapse rate model accepts that months are arbitrary boundaries but recognises that there is seasonality to the processes that control air temperature. This seasonality was used as the basis for the second type of predictive model which predicts using only months within the same season. Seasonal lapse rates reflect the strong variation in meteorological controls throughout the year, where seasonal boundaries are defined using the

variability within the dataset. The sensitivity of the model and the accuracy of the results using these two different datasets will be assessed to determine the most appropriate technique.

Monthly normal data do not provide any information on variability within a month, however all the meteorological variables examined in this research are known to exhibit monthly variation. Two techniques were used to estimate this variability: extension of sine and cosine terms for daily temperature.

Within-month trends were quantified by extending the sine and cosine parameters to include sub-month estimates of the meteorological variables: where the month term, originally an integer 1, 2, 3... December 1st, January 1st February 1st respectively, was supplemented with month fractions relating to day number using the following lookup table.

Day	Month Days	Fraction
1	28	0.04
7	28	0.25
15	28	0.54
19	28	0.68
25	28	0.89
1	30	0.03
7	30	0.23
15	30	0.50
19	30	0.63
25	30	0.83
1	31	0.03
7	31	0.23
15	31	0.48
19	31	0.61
25	31	0.81

Table 5.1: Daily month fraction to use in sine and cosine function

This methodology assumes that meteorological variables vary smoothly through the month, the application of this method therefore necessitates the satisfaction of this characteristic.

For meteorological variables that do not exhibit a smooth within-month variation, for example, precipitation, an alternative methodology is required to provide estimates of variability within a month. Characterizing the potential variability within a month using a measure of standard deviation or variance and using the monthly mean estimated value from the prediction model it is possible to predict values with a frequency distribution defined by its shape determined by the mean and standard deviation terms. Gaussian and gamma distributions are the functions most commonly used for normal and skewed datasets respectively. Using inverse distribution functions it is possible to predict the value of the meteorological variable at any quantile location.

6.3 Temperature Predictions

Spatially distributed temperature surfaces are critical when predicting snowmelt (Richard and Gratton, 2001; Tveito, 2003) and melt is argued to be more sensitive to temperature than to precipitation.

The importance of spatial scale in temperature controls has already been discussed (section 5.4.1), but important temporal variations in the controls on temperature also exist. These were discussed by Catchpole (1972), who states that variations occur over a continuum of temporal scales identifying annual, seasonal and diurnal scale processes.

Monthly temperatures are largely dependent upon seasonal synoptic conditions, where measures of terrain form and altitude distinguish between dominance in stable or unstable atmospheric conditions. Geiger (1965) proposes surface slope is the most influential control on day temperatures where imbalances in slope irradiation set up temperature and pressure gradients that control the local air temperature, and identifies altitude as the primary control on air temperatures during the night where surface cooled air falls creating altitude temperature gradients. Barry (1992), however, argued that although aspect and altitude can successfully be used to predict mean seasonal weather they are less effective at predicting temperatures at finer temporal resolutions.

6.3.1. Controls on temperature

Topography in part controls local and regional variations in temperature (Barry, 1992). These controls are largely accepted as altitude, aspect, maritimity and geomorphological context, each will be discussed briefly with respect to their role in controlling temperature.

6.3.1.1. **Altitude**

Temperature varies with altitude as a function of the environmental lapse rate (ELR), this approximates 6 °C km^{-1} in the free atmosphere (Barry, 1992), and varies locally predominantly as a function of the atmospheric water content and as a result of radiative and turbulent heat exchanges over a slope. The dry adiabatic lapse rate (DALR) provides a theoretical maximum rate of temperature change at 9.8 °C km^{-1}, although this can be increased as a result of surface heating. If the air becomes saturated and water droplets condense, they release latent heat reducing the rate of cooling to the local saturated adiabatic lapse rate (SALR), which varies with the local temperature (between 5 °C km^{-1} above 20 °C, and roughly the same as the DALR at –40 °C; Barry, 1992).

Strong correlations between altitude and temperature are largely driven by the exchanges of energy between incident solar radiation and the Earth's surface, where absorption of terrestrial infra-red radiation and turbulent heat exchanges transfer heat energy to the ground (Barry, 1992). Part of this absorbed energy is then emitted and heats the air above the ground, the ability of the atmosphere to transfer this heat determines the environmental lapse rate, as lower altitudes are closer to the Earth's surface more heat energy is transferred and the air is warmer, although changes in atmospheric composition at high altitudes also affect the ability to transfer heat.

Convection is the primary process by which heat energy is transferred in the lower atmosphere (Oke, 1987). A major control on the type and extent of convection is the vertical temperature structure as expressed by the concept of stability. A discrete parcel of air moving up through the atmosphere adiabatically does not give or receive any heat to the surrounding air. As it rises the parcel of air expands, as its relative pressure compared to the surrounding atmosphere increases. As it expands the air parcel cools as heat energy is used up. When an equilibrium altitude is reached the air parcel will cease to rise, and release any remaining heat by mixing with air at that level. The variation in the degree of mixing with altitude is a primary reason for the variation in lapse rates with altitude, where small amounts of mixing near to the ground lead to large temperature gradients, and large amounts of mixing at higher levels lead to small temperature gradients.

Over a short time scale, vertical turbulent transfers drive the diurnal surface temperature variations, as outlined in table 5.2.

Time	Radiation Budget	Temperature Variation
Night	Negative: Long wave emission	Surface cooler than air
After Sun Rise	Positive: Surface insolation	Surface warming but mixing prevented by inversion layer above
Mid morning	Increasingly positive	Convective mixing degrades inversion layer.
Midday	Increasing positive	Surface warmer than air.
Afternoon	Positive	Convectively unstable maximum temperature. Mixing equalises temperature and wind speeds, but often capped by inversion higher up in atmosphere. Higher mixing can occur when thermals develop above local surface temperature maxima.
Sunset	Negative	Surface cooling re-establishes radiation inversion

Table 5.2: Diurnal controls on temperature

This describes an idealised situation that is modified by local weather, where increases in surface wind or cloud cover lead to reductions in the daily range of temperature.

Complex relationships between altitude, aspect and synoptic conditions often limit the applicability of constant relationships. McCutchan and Fox (1986) criticise the work of Geiger (1965) and Barry (1973) for failing to present clear and generalised relationships between meteorological variables and altitude and aspect. McCutchan and Fox (1986) investigated the complex relationships between altitude, aspect, temperature and wind speed and direction on an isolated peak, reporting the dominant altitudinal control on temperature and the more variant control of aspect, changing with time of day, season and synoptic weather conditions.

6.3.1.2. **Aspect and Slope**

Many authors argue that aspect and slope cannot be considered separately in relation to temperature (Evans, 1977; Barry, 1992) as they interact together to determine local surface energy balance. Slope gradient determines the angle of incidence of solar rays on surface slope, determining the amount of radiation transferred to the surface. Correlations between temperature and aspect can lead to significant temperature differences between solar and non-solar facing slopes. For example up to and over 7 °C of difference was measured between south and north facing slopes at Hohenpeissenberg, Bavaria (Grunow, 1952). Differential radiation receipts (as a function of the duration of exposure to direct beam radiation) induce an imbalance in heat exchanges between the ground and the atmosphere on different slopes. These differential radiative and turbulent heat exchanges are often highly influential in controlling temperature gradients above a mountain and inducing local circulations (Geiger, 1965; Yoshino, 1975). This composite effect was employed by Gill (1982) who used a simple altitude lapse rate to predict temperature at high altitude and only applied aspect variations at slopes steeper than 20° following the research of Fuh (1962).

Local surface azimuth in part determines when and for how long a location is heated by direct beam radiation, and was consequently expected to be a significant variable in a multiple regression analysis. However, when included it was generally found to be insignificant, this was initially thought to be attributable to the scale of aspect correlations, whereby the aspect included in the regression was an incorrect representation of the aspect of the climate station. Initial regressions used the aspect raster with 100 m grid spacing. However, this is only a representation of the aspect within 1000 m^2 pixel area. The actual azimuth of the climate station is unknown and can only be represented by the azimuth given by the DEM. Any attempt to resample the DEM to a resolution less than the original data would incorporate error into the analysis. The role of aspect within the climate data is also likely to reduced as climate stations are unlikely to be positioned on steep slopes.

An alternative to using local aspect (100 m) is incorporating a measure of mountain range aspect, where the local azimuth with respect to the larger scale landform features is likely to provide the main control rather than a local azimuth within the mountain range (although this is clearly scale and process dependent and a generalized version of this statement should not be adopted). The DEM was resampled to resolutions of 200 m through to 2000 m in an attempt to capture 'landform or massif' scale measures. However, slope and aspect still appeared insignificant in the regression

analysis. This was a surprising result as aspect is closely linked to incident radiation and temperature, however prediction validation and regression statistics were driven by aspect values extracted from the DEM at station sites and consequently are unlikely to provide accurate estimates of their actual surface characteristics, where within pixel variation may be great.

6.3.1.3. **Maritimity**

Larger scale topographic and contextual measures also impose controls on temperature. Maritimity plays two key roles in modifying climate; it provides proximity and exposure to prevailing winds and air masses moving on land, and alters the overall moisture and heat balance due to the differing thermal capacities of the land and water. High maritimity leads to very small amplitude between the mean of coldest and warmest months. The Scandinavian mountain range provides a very effective barrier to the effects of maritimity and eastern Norway has a marked continentally to its climate.

Brooks (1918) investigated the role of continentality in controlling temperature and predicted temperature using altitude, radiation receipt and degree of continentality (defined by percentage land within the surrounding 10° circular area). Although the relationship between temperature and distance from coast has been exploited within the literature and successfully used as a predictive variable in Norway for both temperature (Zheng and Basher, 1996; Tveito *et al.*, 2000; Tveito, 2003) and snow accumulation (Chorlton and Lister, 1968); it failed to provide statistically significant predictions in these regressions.

6.3.1.4. **Context**

Difficulties in predicting climatic parameters from climate station records are largely associated with the dominant role that contextual and local parameters have on modifying local climate. Consequently lapse rates exhibit high spatial variability (Lautensach and Bogel, 1956; Barry, 1980; Richard and Gratton, 2001; Strasser *et al.*, 2004) both within and between climatic zones and seasons. Air mass type and synoptic forcings provide strong controls on lapse rates (Jonsson, 1995; Tveito, 2003) and accurate predictive models must incorporate contextual measures. Atmospheric circulation and air mass characteristics have been used as predictive parameters (Tveito, 2003; Chen, 1999; Lindersson, 2001; Corault and Monestiez, 1999; Huth, 2001) but the large variability

in temperatures within air masses or circulation systems is high, limiting the success of such an approach and rendering it inapplicable in this study.

Tabony (1985) proposes that the scale of shelter provided by the surrounding terrain imposes different controls on temperature throughout the year, where larger scale shelter is more important in winter months and local shelter is most important in autumn when the influence of soil moisture is important. Within the seasonal lapse rate model (section 5.4), such a relationship can be parameterised.

Despite a long history of applying regressions to temperature and altitude (Douguédroit and de Saintignon, 1970; de Saintigon, 1976; Pielke and Mehring, 1977) most attempts to simulate temperatures fail to predict areas of frequent temperature inversions (Tveito and Forland, 1999; Tveito, 2003), which although consistently located in valley floors, are hard to characterise using this position using common terrain attributes (Section 4.5.2). Temperature inversions are areas where temperature gradients are reversed over limited vertical distances. As cold air is heavier than warm air, once an inversion forms the air within the inversion layer is very stable. Mixing that would normally occur by the rising of warm air is inhibited. Inversions may occur due to nocturnal radiative cooling, large-scale subsidence or advection of a warm over a colder surface. Barry (1992) noted the lack of statistical research on predicting their occurrence and proposes the use of polynomials in lapse rates to characterise valley floors. Research has attempted to predict the elevation of the thermal belt with respect to the valley floor. Obrebska-Starkel (1970) studied valleys in Europe and summarised the mean upper limit of inversion layer in hilly terrain (<500 m), and found the centre of thermal belts to be 100-400 m above valley floor. Aulitsky (1967) studied inversion depths in high mountains finding a strong seasonal variation from 350 m in summer to 700 m in winter, a result of deeper cold air in winter providing more stable inversion conditions. However, the altitude of the top of the inversion layer is highly variable and thought to be largely determined by slope profiles rather than altitude alone (Kock, 1961). This was also raised as a predictive approach by Barry (1992) who proposed the use of lapse rates for different slope profiles. In the present research, measures of relative height and valley context measures attempt to quantify this valley position.

Radiation inversions are the most likely type of inversion within the Jotunheim, and are most common during clear nights with low winds in winter. Clear skies are necessary for the surface

radiation to escape and overlying clouds or fog absorb thermal radiation and radiate this back to the surface.

6.3.2. **Predictive approaches: Temperature**

Predictive methods employed within the literature adopt either a multiple regression approach or a spatial interpolation algorithm that accounts for the spatial organisation of the climate stations in an attempt to simulate topographic structure.

Simpler approaches can be used successfully, if local high-resolution datasets are available. For example Hock *et al.* (2002) employed a constant annual lapse rate of 0.55 K per 100 m in an application of their glacier snowmelt model. This was based on average conditions recorded in a previous field season to interpolate the hourly temperature data recorded at a local automatic weather station. However, they did not discuss the accuracy of these estimates and as the model is largely parameterised it is difficult to ascertain the uncertainties introduced using this lapse rate.

Regression approaches are far more common, as variables other than the local topography combine to control temperature. Barry (1992) proposed that multiple regression provides the most informative and intelligent interpolation. Lennon and Turner (1995) adopted four different approaches, simple interpolation, thin plate splines, multiple linear regression, and mixed spline regression.

Kriging provides an alternative solution; it uses information on the spatial organization and trends present within an input dataset to predict the spatial variability within the predicted surface. Tveito (2002) used residual kriging, with synoptic weather conditions, latitude and longitude and a suite of topographic parameters including slope, curvature and several contextual parameters including the mean and lowest altitude in the surrounding 20 km and sea coverage within the surrounding 50 km; to predict monthly temperature in Southern Norway and in unpublished data has found this approach to create significant results for daily estimates, but in both cases failed to accurately predict high altitude and winter minima temperatures (Ole Tveito, *pers .comm.*). He found that terrain parameters provided significant contributions to the accuracy of predictions and synoptic weather added little.

Residual kriging overcomes the assumptions of stationarity by extracting the deterministic component from the data. For example, the altitudinal component of temperature variations, leaving what is termed the 'reference level' data and performing the kriging interpolation on this reference level dataset. Climatic surfaces are created by combining the kriged interpolations and the deterministic components, creating a composite surface. Hudson and Wackernagel (1994) also adopted a kriging method and identified altitude to be the most significant predictor of temperature, showing seasonal variability, where July temperatures showed the weakest altitudinal trends due to the stronger correlations with latitude in summer. Susong *et al.* (1999) used detrended kriging to create temperature and precipitation surfaces at 75 m resolution for a mountainous area near Park City, Utah. A detrended data set was used, as kriging requires statistically stationary variable fields, a characteristic not initially present in the data, which was highly spatially variable resulting from the strong orographic control. However the resultant climatic surfaces failed to predict the spatial variability of the climatic processes where topography played a dominant role in modifying local lapse rates. It is felt that this approach would not simulate the high spatial variability in meteorological variables and an approach using measures of the terrain and its influence on topographic parameters would provide a more accurate and representative output.

Kriging is only one example of a geostatistical technique: Lapen and Hayhoe (1998) and Hayhoe and Lapen (1999) compared the ability of a range of techniques including ordinary kriging, cokriging, modified residual kriging, kriging with an external drift, classification trees and artificial neural networks to predict temperature and precipitation and compared their performance with that of simple interpolation operations including inverse distance weighted interpolation. They found that geostatistical techniques performed consistently better but were much more time consuming and computationally intensive. They should be used if accurate estimates are required: simpler interpolations also created reasonable estimates but failed to account for all of the spatial heterogeneity within the dataset. Overall they concluded that kriging with an external drift factor provided the most reliable results.

The high spatial and temporal variability in lapse rates often limits the success of applying locally derived lapse rates at different temporal scales or in different areas (Tveito and Forland, 1999; Tveito *et al.*, 2000; Tvieto, 2003). Ficker (1926) proposed that true lapse rates cannot be determined in mountainous areas as temperature inversions, föhn and katabatic winds create a very noisy local pattern. Richard and Gratton (2001) suggested use of regional climate stations for more representative temperature estimates, especially when temporal resolutions greater than weeks are

required. Barry (1980) stressed the need to distinguish between the effects of local topography on diurnal variations in temperature, and large scale topographic effects that modify the atmospheric structure.

Multiple regressions were used to predict monthly temperatures: the results presented in the forthcoming sections report the ability of the different regression models to predict temperature. Although examination of the statistical significance of the regressions provides information on the ability of the independent variables to account for the variation within the dataset, examination of the distribution of values within the spatial and frequency domains is also essential to assess the representativeness of the spread of the predicted values.

6.3.3. **Annual lapse rates**

Annual lapse rates were predicted using each month's data in one regression, with altitude, an interaction term and topographic measures as the independent variables, the results are presented below. Note: Figure 5.1 can be used to aid interpretation.

6.3.3.1. **Cosine and sine functions**

Sine and cosine terms used to simulate the cyclical temperature variation through the year accounted for the variation in mean monthly temperatures with an adjusted R^2 value of 0.97 using all 37 temperature station records. 444 observations were used in total, as each monthly record for each station was included (37 * 12).

The regression is statistically significant at the 95% confidence level and each of the independent variables provides a statistically significant contribution in accounting for the variability within the dataset (Table 5.4). The root mean square error is 1.2 °C and altitudinal lapse rate is 0.004 °C per m.

Number of obs = 444
F(3, 440) = 5415.34
Prob > F = 0.0000
R-squared = 0.9736
Adj R-squared = 0.9735
Root MSE = 1.221

	SS	df	MS
Model	24218.5623	3	8072.85412
Residual	655.924668	440	1.49073788
Total	248474	443	56.15

	Coefficient	Std.Error	T	P>|t|	[95% Conf. Interval]	
Altitude	-.004264	.0001711	-24.92	0.000	-.0046002	-.0039278
Cosine	-6.7265	.0819453	-82.08	0.000	-6.887521	-6.565415
Sine	-7.724999	.0819453	-94.27	0.000	-6.887521	-7.8597
Constant	3.93951	.1425014	27.65	0.000	3.659442	4.219578

Table 5.4: Regression statistics: Mathematical Modelling

The regression coefficients provide the following model where temperature T is given by:

$$T = -0.0043 \text{ Altitude} - 6.7265 \text{ (Cosine function)} - 7.725 \text{ (Sine function)} + 3.939$$

and implemented in a spatial model as:

T = (-0.0043 * [Jotunheim]) - (6.7265 * (Cos(2 * PI * ((1-0.5) / 12)))- (7.725 * (Sin(2 * PI * ((1-0.5) / 12)))) + 3.939)

Building the monthly temperature surfaces and comparing predicted and observed station statistics provides the following monthly temperature statistics (Table 5.4, Figures 5.2 to 5.4).

Month	Minimum	Maximum	Mean	Range
January	-15.187	-4.558	-9.652	10.629
February	-16.909	-6.28	-11.374	10.629
March	-15.893	-5.264	-10.358	10.629
April	-12.411	-1.782	-6.876	10.629
May	-7.397	3.233	-1.861	10.629
June	-2.193	8.437	3.342	10.629
July	1.806	12.436	7.341	10.629
August	3.528	14.158	9.063	10.629
September	2.512	13.142	8.047	10.629
October	-0.97	9.66	4.565	10.629
November	-5.985	4.645	-0.449	10.629
December	-11.189	-0.559	-5.653	10.629

Table 5.4: Predicted study area monthly temperature data for mathematical modelling

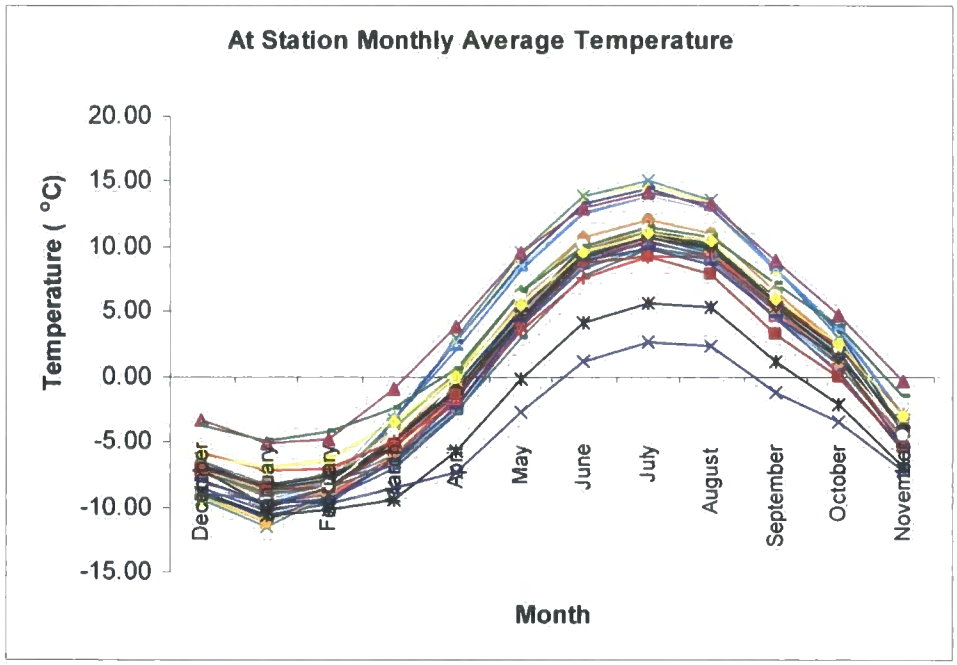

Figure 5.2 Observed at station monthly climate data

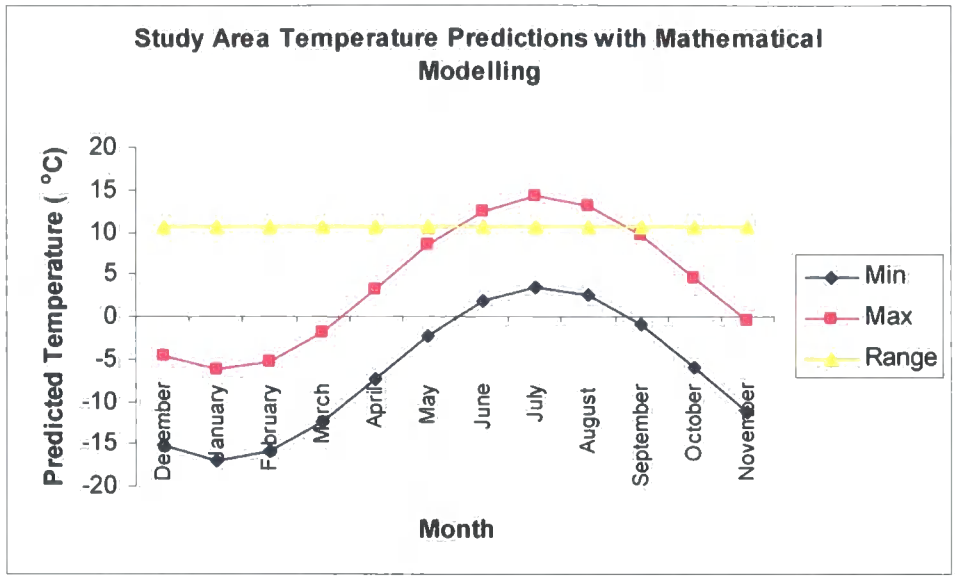

Figure 5.2: Predicted Study area monthly temperature statistics

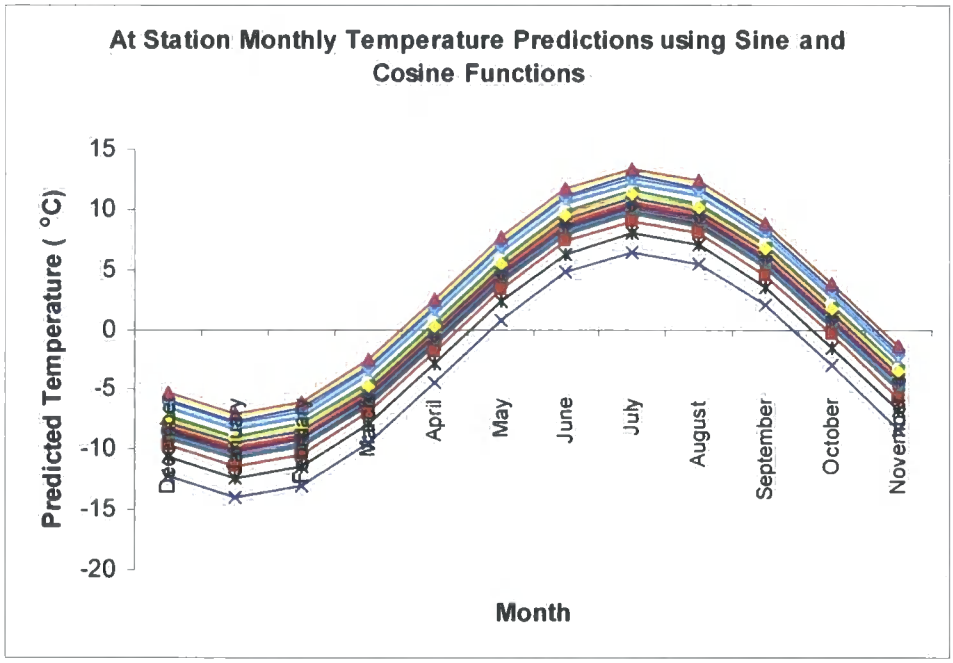

Figure 5.3: Predicted Study area monthly temperature statistics

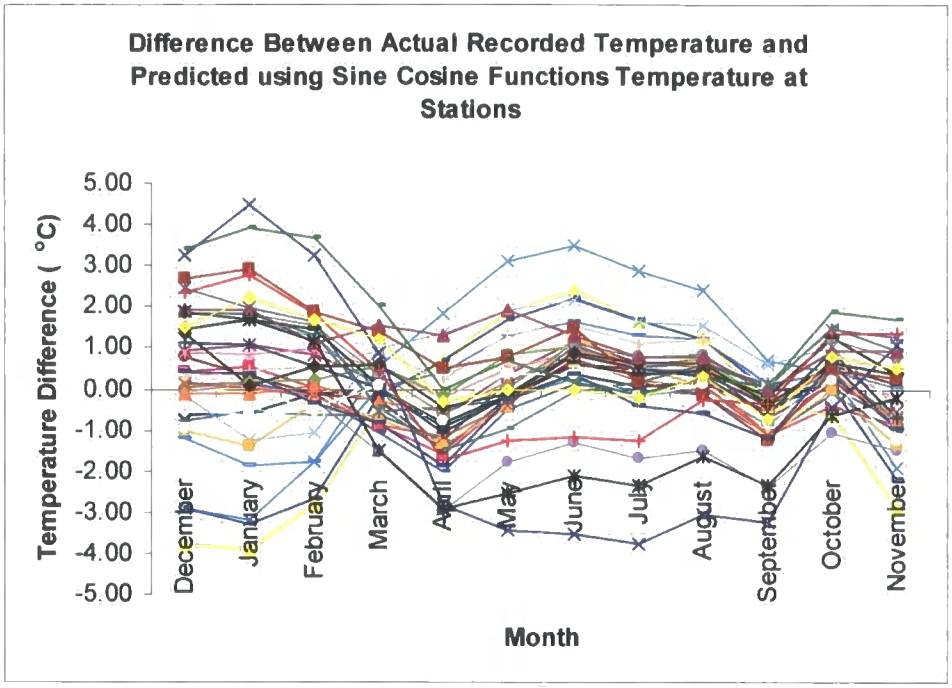

Figure 5.4: Actual – Predicted monthly average temperature

Mean monthly temperature is predicted to within 4 °C by the model (Figure 5.4). Summer estimates are the most robust and only a very weak seasonal trend is evident in the data. This suggests that there is only a small structured component to the remaining variation within the data.

Mean and maximum temperatures are predicted well, but monthly minima are predicted less accurately. Although there had been initial concerns about predicting winter temperature inversions the model performs worse when predicting summer minima temperatures, where the model under predicts summer minima and over predicts winter minima. Examination of the residual plot highlights a distinct seasonal trend is evident in the residual data suggesting that variability within the data is not accounted for.

Monthly temperature range appears to be the most poorly predicted variable failing to match the observed trend. The constant range illustrates the inability of the model to predict between month variability and therefore suggests the need to further characterise topographic and climate interactions. Where recorded range exhibits summer maxima, when convectional heating, unstable air masses and variable cloud cover lead to greater variability in lapse rates. Smaller observed ranges in winter occur as stable air masses and inversions dominate.

Although the model predicts mean monthly temperature accurately (Figure 5.2) it fails to predict variability within the data. Therefore it was necessary to include additional variables in an attempt to account for this variation.

6.3.4. **Mathematical modeling with interaction variable**

The most effective interaction term for this dataset was the month-altitude variable. This allowed topographic and monthly variation to be superimposed onto the cosine model presented in section 6.3.3.1. This coupled model accounted for more of the variation within the data, consequently providing improved predictions accounting for the variation in mean monthly temperatures with an adjusted R^2 value of 0.98 using all 37 temperature station records. 444 observations were used in total, as each monthly record for each station was included (37 * 12).

The regression is statistically significant at the 95% confidence level and each of the independent variables provides a statistically significant contribution to accounting for the variability within the dataset. The root mean square error is 1.16 °C and altitudinal lapse rate is 0.003 °C per m.

Number of obs = 444
F(4, 439) = 4501.46
Prob > F = 0.0000
R-squared = 0.9762
Adj R-squared = 0.9760
Root MSE = 1.1613

	SS	Df	MS
Model	24282.4566	4	6070.61416
Residual	592.030372	439	1.34858855
Total	24874.487	443	56.15

	Coefficient	Std.Error	t	P>|t|	[95% Confidence Interval]	
Altitude	-.0030227	.0002429	-12.44	0.000	-.0035001	-.0025453
MonthAlt	-.000191	.0000277	-6.88	0.000	-.0002455	-.0001364
Cosine	-6.726468	.0779405	-86.30	0.000	-6.879651	-6.573285
Sin	-8.286523	.1128265	-73.44	0.000	-8.50827	-8.064775
Cons	3.93951	.1355371	29.07	0.000	3.673128	4.205892

Table 5.4: Regression statistics for mathematical modeling with interaction term

The regression coefficients provide the following model where temperature T is given by:

$$T = -0.0030\text{Altitude} - 0.00019\text{MonthAlt} - 6.7265(\text{Cosine function}) - 8.286(\text{Sine function}) + 3.939$$

(Equation 5.7)

and implemented in a spatial model as

```
T = (-0.0030 * [studyArea]) - (0.00019 * ([studyArea] * n))
        -(6.7265 * (Cos(2 * PI * ((1 - 0.5) / 12))))
            - (8.286 * (Sin(2 * PI * ((1 - 0.5) / 12)))) + 3.939)
```

(Equation 5.8)

Building the monthly temperature surfaces and comparing predicted and observed station statistics provides the following monthly temperature statistics (Table 5.5, Figures 5.5 to 5.7).

Month	Minimum	Maximum	Mean	Range
January	-12.589	-4.703	-8.482	7.886
February	-14.562	-6.676	-10.456	7.886
March	-13.691	-5.806	-9.585	7.885
April	-10.209	-2.324	-6.103	7.885
May	-5.049	2.836	-0.943	7.885
June	0.406	8.292	4.512	7.886
July	4.695	12.581	8.802	7.886
August	6.669	14.554	10.775	7.885
September	5.798	13.684	9.904	7.886
October	2.316	10.202	6.422	7.886
November	-2.844	5.042	1.262	7.886
December	-8.299	-0.414	-4.193	7.885

Table 5.5: Predicted study area monthly temperature statistics

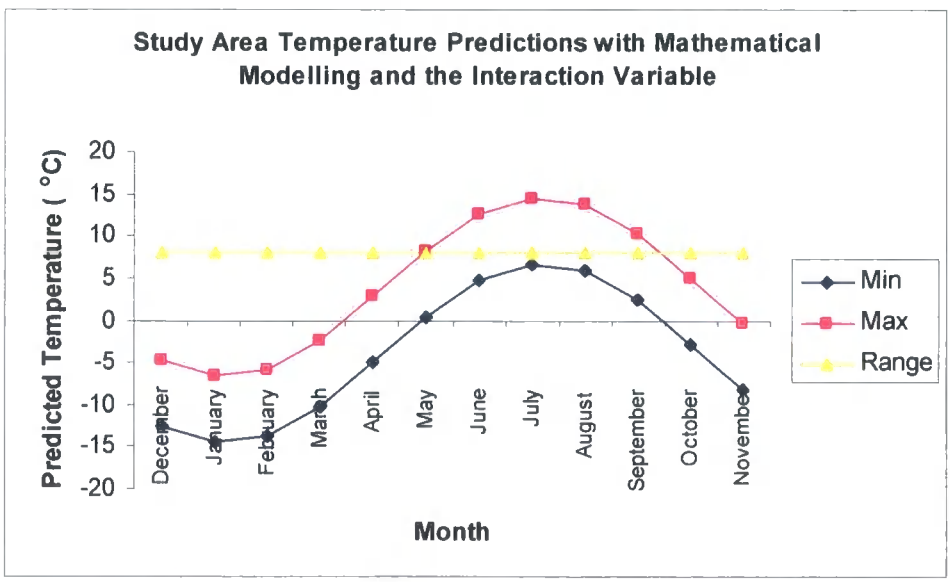

Figure 5.5: Predicted study area monthly temperature statistics

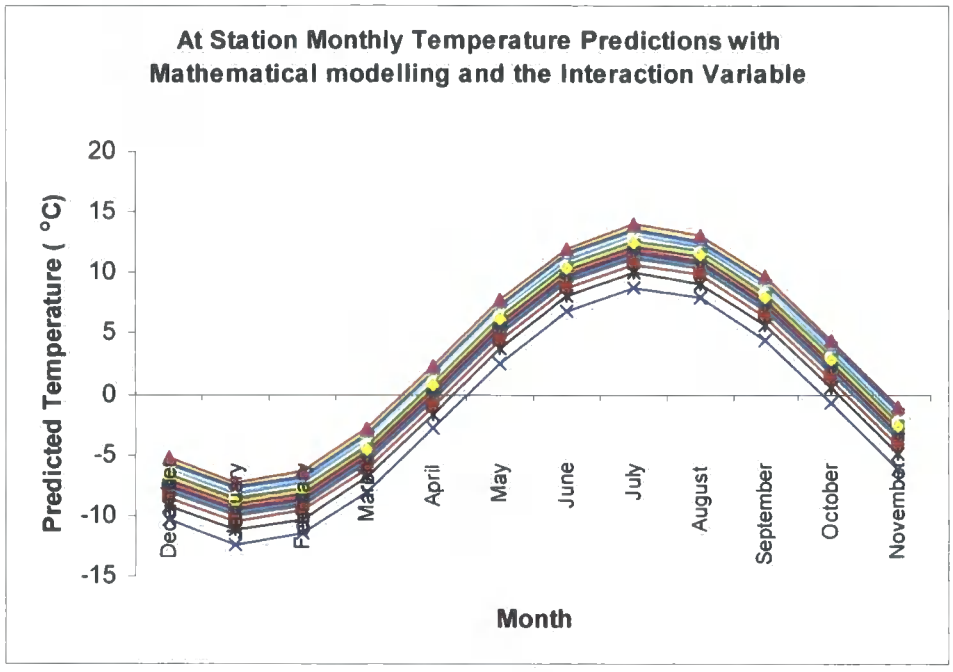

Figure 5.6: Predicted study area monthly temperature statistics

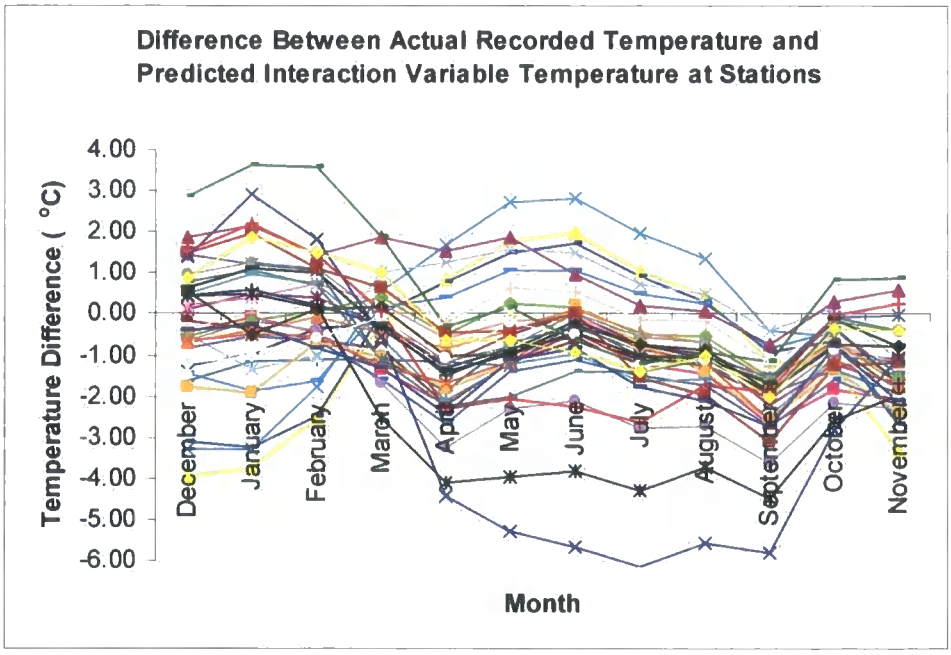

Figure 6.7: Predicted study area monthly temperature statistics

Despite a reduction of the RMSE, an increase in the adjusted R^2 and a reduced trend in observed – predicted monthly average temperatures the model still performed poorly for some stations. In an attempt to understand the local factors that were failing to be accounted for within the model it was necessary to examine the topographic conditions at each station. Again a seasonal trend is evident in the residual data suggesting that variability within the data is not accounted for. Examination of the contextual controls acting at the stations identified strong topographic influences, including exposure to free air and valley winds, sheltering and maritime influences in or near fjord inlets (Table 6.6 and Figures 6.8 and 6.9).

Station No.	Altitude (Meters)		Gradient (°)	Aspect (°)	Plan Curvature (1/100 U)	Profile Curvature (1/100 U)	Description
Warm stations 55160	**27**	**180**	35	276	**-0.1**	**-0.2**	Located towards the head of a valley at the base of concave slope at the valley intersection in a sheltered position. The actual altitude is much lower than the DEM pixel. This station is very sheltered and has less exposure to valley winds and other cooling topographic factors.
63710	625	580	2.3	**180**	0	-0.08	This station is located on a rectilinear sheltered slope at the junction of two valleys. The valley is part of the fjord system, which increases the maritime effect on the temperature range resulting in a milder climate.
Cold stations 55230	2062	1827	22	320	**0.2**	**0.4**	This station is located on a local maximum, it is highly convex and is a peak. This increases its exposure and reduces the temperature making it unusually cold for its height.
55290	1403	1426	11	212	0.03	0.06	This station is located on a slope that is part of a larger valley system. The station is not part of a fjord network and therefore is not under a strong maritime influence. It is exposed to cooling valley winds that lower the temperature below the expected value for its height.

Table 6.6: Problem climate stations

Although these topographic conditions are unusual within the station data supplied by the Norwegian Meteorological Institute they are not unusual within the study area. It was therefore necessary to attempt to quantify these local factors in an attempt to improve climate predictions.

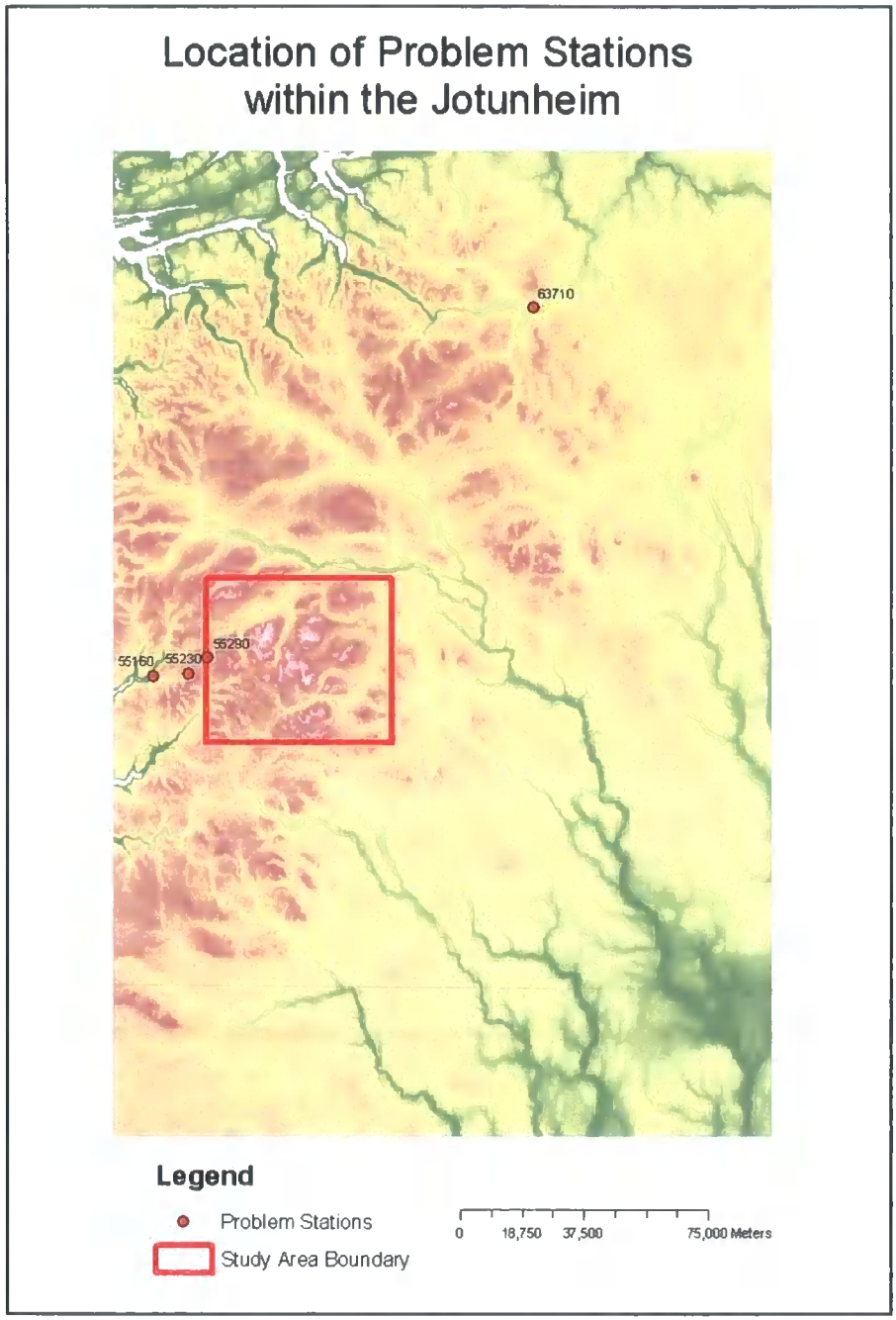

Figure 6.8: Location of problem climate stations

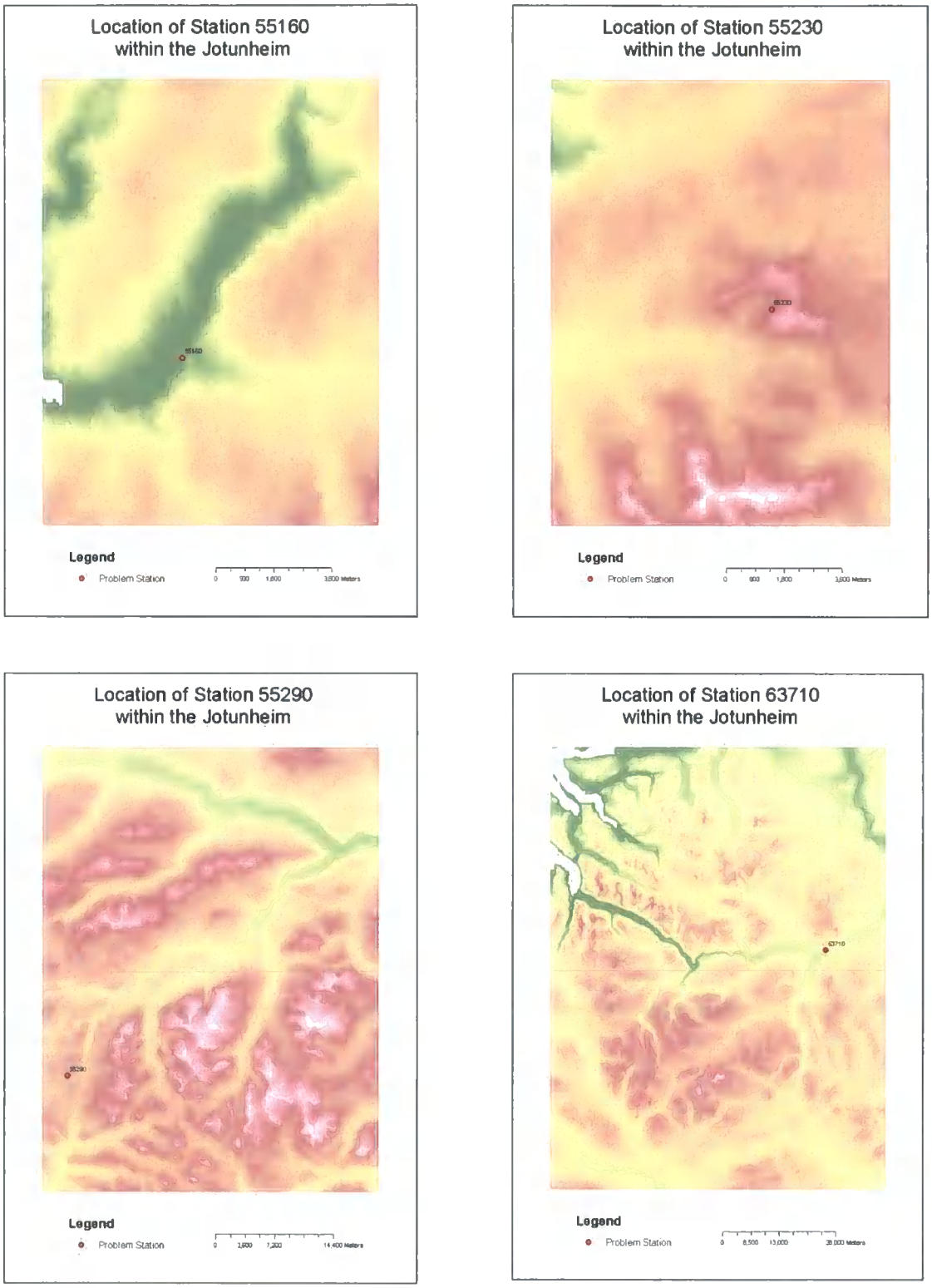

Figure 6.9: Local conditions at problem climate stations

6.3.5. **Mathematically modeling with topographic variables**

Although strong correlations between temperature and altitude are published (Barry, 1992; Hock, 1999; Geiger, 1965), analysis and modeling of the present climatic data showed that altitude alone could not adequately predict the variability within the data, specifically monthly minima and range.

In an attempt to optimise the prediction process correlations between the suite of topographic variables discussed in section 4.5 and monthly mean data were explored and a series of regressions performed to investigate their ability to improve the climatic predictions. Topographic variables were calculated at a number of different scales and over different kernel sizes to find the most representative scale for the terrain. The temperature dataset was explored and topographic exposure was found to be the dominant variable controlling terrain modification of adiabatic process.

Two types of exposure were identified, exposure due to surface roughness (Type 1) and exposure to channelised air flow (Type 2). The exposure measures were calculated in Arc/INFO for every pixel in the DEM.

A high or low surface roughness identifies sheltered or exposed sites that are warmer or cooler than they would be if altitude was the only control. This roughness can either be at a focal (surrounding pixels) scale where the pixel is identified as higher or lower than the surrounding area, or at local scale where the altitude of the climate station (used in predictions) is higher or lower than the pixel it is located within.

Type 2 exposure quantifies how exposed a pixel is to channelised air flow. Valley winds can have a strong cooling effect that is larger further down the valley and nearer the valley center. This exposure measure also identifies valley floors that are frequently subject to temperature inversions where air temperatures are colder than they would be if altitude was the only control.

Variable	Description	Significance	Interpretation
Exposure Type 1: exposed to air as a result of high surface roughness	Station altitude higher than pixel altitude	Not significant	Representing features at too fine a scale
	Pixel altitude higher than surroundings, using measures of standard deviation, mean, range, difference between local and focal mean, maximum, minimum and the ranges of temperatures within a 5, 10 and 20 km radius of the cell	20 km radius reported the best results. Standard deviation, minimum, maximum, range and mean measures were all statistically significant in predicting monthly temperature	Correlations exist for some variables, but they only account for a small amount of the variability within the dataset. Again scale is important: 20 km represents larger scale variations but results are still restricted by limited range of station context.
Exposure Type 2: orientated in direction of channelised / constricted flow	Direction of channel in relation to pixel, down valley flow length, distance from channel center	Not significant	Conflicts between scale of DEM and local variations are compounded by inaccuracies in channel extraction
Aspect	Pixel and surrounding buffer, 5 km, 10 km and 20 km	Not significant	Station pixel aspect is not a useful measure of aspect, larger scale measures also failed to account for any variation in temperature variations
Curvature	Pixel and surrounding buffer, 5 km, 10 km and 20 km.	Significant for annual mean but not for monthly predictions	Curvature does not play a significant role in accounting for temperature variations each month and had to be rejected from the annual lapse rate model.
Maritimity	Distance from coast	Significant annually but not on monthly temporal intervals	Distance from coast does not play a significant role in accounting for temperature variations each month and had to be rejected from the annual lapse rate model.

Table 6.7 Predictive variables used within climate regressions

Performance of variables was mixed (Table 6.7), the most effective term, improving temperature predictions was *diffmax*, which was calculated as the difference in pixel altitude from the surrounding 20 km focal maxima. This was successful in predicting extreme values (maximum and minimum temperatures) where topographic parameterisation of position enabled the model to account for these values more effectively. Mean gradient was also used in the predictions, which combined with *diffmax* can identify flat areas with altitudes lower than local maximums (valley floors) and steep areas with altitudes similar to local maximums (peaks).

The regression is statistically significant at the 95% confidence level and each of the independent variables provide a statistically significant contribution to accounting for the variability within the dataset. The root mean square error is 1.14 °C and altitudinal lapse rate is 0.003°C per m.

Number of obs = 444
F(6, 437) = 3056.16
Prob > F = 0.0000
R-squared = 0.9771
Adj R-squared = 0.9768
Root MSE = 1.1416 °C

	SS	df	MS
Model	24304	6	4050
Residual	569	437	1.3
Total	24874.5	443	56.15

	Coef.	Std.Err.	t	P>|t|	[95% Conf.	Interval]
Altitude	-0.0033057	.0003454	-6.86	0.000	-.0030476	-.0016899
Cosine	-6.726468	.0772543	-87.07	0.000	-6.878305	-6.574632
Sin	-8.119309	.1263849	-64.24	0.000	-8.367707	-7.870911
Monthalt	-0.000191	.0000467	-6.38	0.000	-.0003901	-.0002064
Diffmax	-0.0003464	0.0001743	-1.99	0.047	-0.0006889	-3.90* 10-6
meangrad	0.0282689	.0001856	1.33	0.000	-.000118	.0006114
Cons	3.058706	.3200933	9.56	0.000	2.429593	3.68782

Table 6.8: Topographic modeling regression statistics

The regression coefficients provide the following model where temperature T is given by:

T = (-0.0033057 * Altitude) – 6.726468 * (Cosine function) – 8.119309 * (Sine function)
*(-0.000191 * monthalt) -(0.0003464 * diffmax)- (0.0282689 * meangrad) + 3.058706

6.4 Seasonal Lapse Rates

The processes that control the variation of monthly mean temperature are not constant through the year and attempts to predict this variability with an annual lapse rate cannot account for the observed variability between summer and winter lapse rates. Seasonal lapse rates were used with topographical predictors to investigate their ability to improve climatic predictions.

Predicting temperature using just altitude highlighted a strong seasonality with large seasonal disparities between summer and winter months (Figure 6.10). This trend represents variability in controls upon temperature, process complexity and interaction, shown in the annual variation in RMSE and adjusted R^2 for altitude lapse rates (Figure 6.10). Summer temperatures were accurately predicted using altitude alone, as dry and saturated adiabatic lapse rates are then primary controls on temperature variations. Winter month temperatures (January, February, November and December) are controlled by a more complex suite of factors, including atmospheric stability relationships and the frequent occurrence of temperature inversions, and so were significantly more difficult to predict.

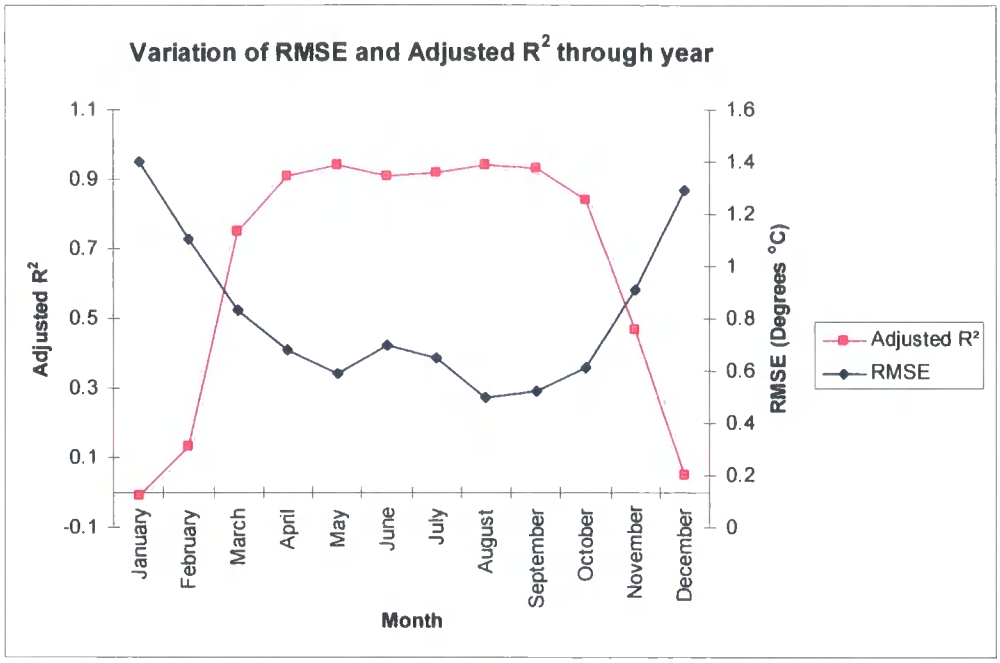

Figure 6.10: Variation of RMSE and adjusted R^2 through year for altitude driven predictions

Similar trends in monthly regression coefficients were found by Tveito *et al.*, (2000) who also found that different variables have variable importance in different months, specifically the annual trends in the significance of average and station altitude, differentiating between stations higher or lower than the surrounding terrain and consequently temperature inversions that frequently occur in valley floors.

Winter and spring months were found to require topographic variables; specifically those identifying valley floors were found to improve predictions, as these located the sites of frequent inversions. As the attributes of climate station pixels can be unrepresentative of local surface form it was necessary to employ more focal measures by examining the surrounding 8 pixels, (examining 300 * 300 m areas), identifying valley and larger landform signals. A 2 km kernel window provided the most useful results for predicting local temperature, where measures of mean altitude and gradient provided the best topographic indicators of temperature.

The inclusion of topographic variables significantly improved the monthly predictions. The most robust predictions were made using the variables displayed in table 6.9 and corresponding lapse

rates are presented in table 6.10. All parameters listed provided statistically significant contributions.

Month	Variables	Adjusted R^2	RMSE °C
January	Profile300, meanGrad, distance,	0.46	1.05
February	Profile300, meanJot, meanGrad	0.49	0.87
March	Plan300, meanJot, meanGrad	0.89	0.55
April	Altitude	0.91	0.68
May	Altitude	0.94	0.59
June	Altitude	0.91	0.70
July	Altitude	0.92	0.65
August	Altitude	0.94	0.50
September	Altitude	0.93	0.52
October	Altitude	0.84	0.61
November	Altitude, profile300, meanGrad	0.64	0.75
December	Profile300, meanJot, meanGrad, distance	0.49	0.95

Table 6.9: Seasonal lapse rate regression statistics

Month	Regression Equations
January	19.69 (Profile300) + 0.638(mean Gradient)- 0.00001(distance) – 8.328
February	19.257 (profile300) + 0.047(meanGrad) – 0.002(meanJot) – 7.64
March	-16.21(plan300) + 0.054 (meangrad) – 0.005 (meanJot) – 1.824
April	-0.006 (altitude) + 5.99
May	-0.007 (altitude) + 10.42
June	-0.007 (altitude) + 14.72
July	-0.006 (altitude) + 15.91
August	-0.006 (altitude) + 14.57
September	-0.005 (altitude) + 9.83
October	-0.004 (altitude) + 4.86
November	-0.003 (altitude) + 16.63 (profile300) + 0.032(meanGrad) - 2.85
December	17.08(profile300) – 0.001(meanjot) + 0.69(meanGrad) – $8.92*10^{-6}$ - 5.89

Table 6.10: Seasonal lapse rates

Comparison of RMSE and R^2 after the inclusion of topographic and exposure parameters show that there was a reduction in the seasonal disparity: accuracy of winter predictions increased where sites liable to temperature inversions are predicted (Figure 6.11).

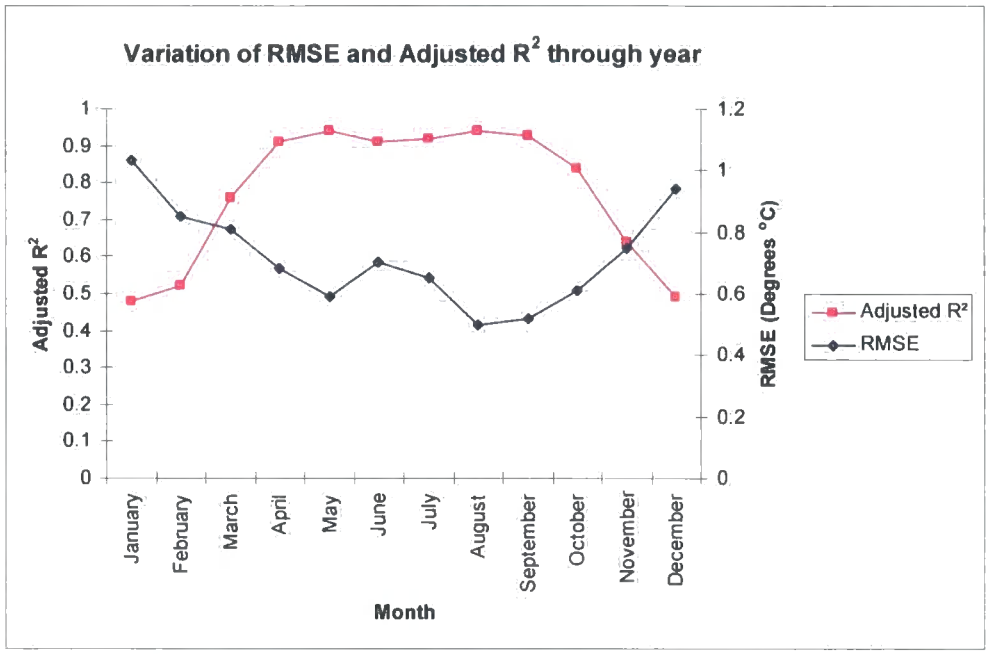

Figure 6.11: Variation in RMSE and adjusted R^2 after inclusion of seasonal lapse rates

Examination of the predicted monthly range and maxima indicate improved estimates, with more variability within the dataset accounted for. Simulation of this variability is important within this research, as maxima and minima temperatures impose controls on melt.

6.5 Monthly Temperature Surfaces

The most accurate (based on R^2, 0.98) and sensible results were achieved using the geomorphic lapse rates, but the seasonal model also created robust results for both winter and summer temperatures.

Initial predictions used sine and cosine functions in a multiple regression with altitude, these gave an adjusted R^2 of 0.97 with an RMSE of 1.2 °C. However the model predicted a constant monthly range, failing to account for the variability in the dataset. An interaction term was created to account for some of this variability. The most useful term was sine of month * altitude. The coupled model (sine and cosine and interaction term) accounted for more variation within the dataset (adjusted R^2 = 0.98); but despite a reduction in RMSE (to 1.15 °C) the model still performed consistently poorly for some stations.

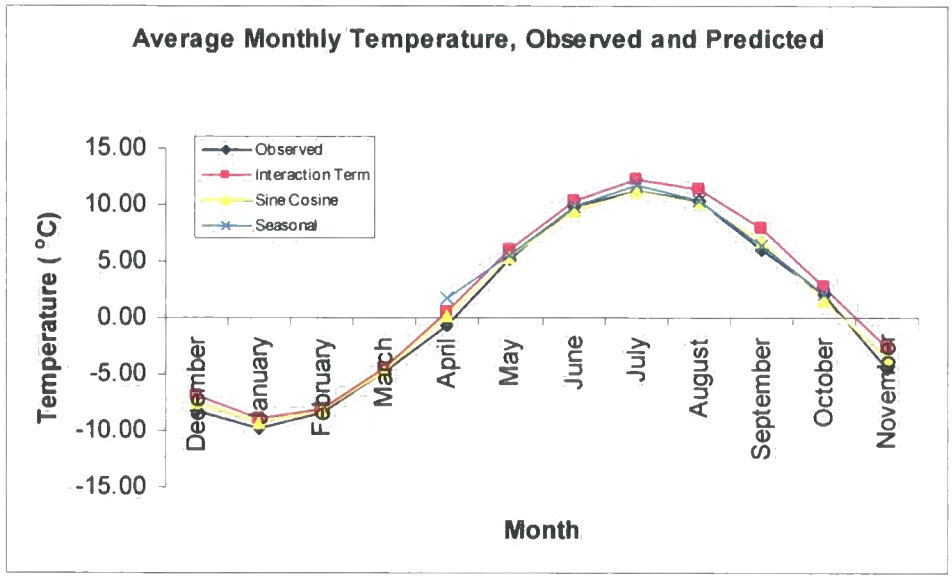

Figure 6.11: Average monthly temperature, observed and predicted.

The inclusion of geomorphic measures, specifically type 1 and 2 exposure variables improved station predictions although their usefulness was varied. Relative altitude (*diffmax)* was the most successful and created the best predictions (adjusted R^2 = 0.98, RMSE = 1.15°C), the other measures were useful for predicting other climatic variables especially wind. Distance from channel centre identified areas that were subject to cooling by temperature inversions and valley winds. Although the model accounted for more of the variability within the data it still under predicted monthly range with the coldest and warmest station temperatures not being predicted.

The seasonal lapse rate model addressed this problem, where profile curvature, average altitude, gradient and distance to valley centre were significant when predicting temperature in all of the winter and spring months. Altitude alone was used to predict temperature in summer and autumn.

The seasonal lapse rate model accounted for the monthly range and terrain modification of the adiabatic process better than the annual lapse rate model.

Both the geomorphic and seasonal lapse rate models provided robust predictions accounting for most of the variation in temperature present in the dataset. Both were used in the glacier prediction model, where their relative performances were assessed.

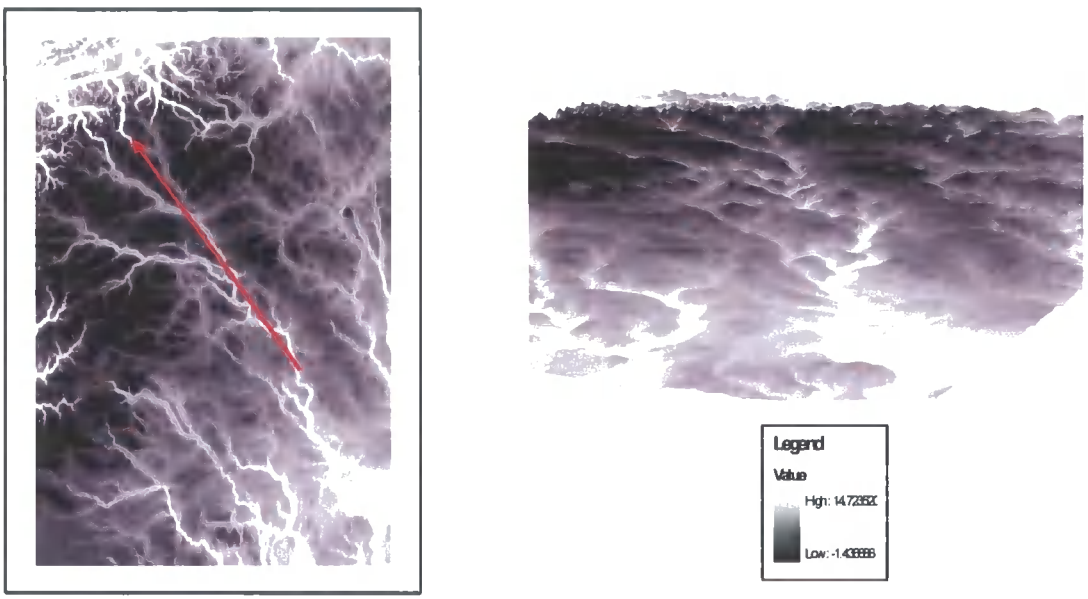

Figure 6.12: June temperature surface for Southern Norway, 3D view looks up valley towards Fjord system as indicated by the arrow.

6.5.1 **Diurnal temperature**

Diurnal temperature variations drive sensible heat exchanges, governing the timing of the direction reversal and are consequently required to accurately predict glacier melt.

Barry and Chorley (1982) suggested that the delay in the occurrence of maximum air temperature is until approximately 2 pm: air temperatures lag behind the diurnal variation of solar insolation and minimum temperatures do not occur until after sunrise as heat energy emitted from the ground continues to warm air temperatures. Controls on diurnal temperature changes include local advection, the downward flux of solar radiation and albedo variations. Barry (1992) proposes that

altitude does not impose controls on diurnal temperature variations where summit and mountain slope sites exhibit the same amplitude of diurnal temperature range.

Catchpole (1969) differentiated between cyclical and irregular components of diurnal temperature variations, cyclical changes driven by solar heating and irregular changes driven by advective heating and cooling from air mass movement. He proposed that the use of daily range measures account for both of these components in one, with a measure of the amplitude of daily variations representing cyclical change. Geiger (1965) termed the difference between the warmest and coolest hourly average the periodic daily fluctuation and the difference between the average daily maximum and minimum, the aperiodic fluctuation. Similar themes where also discussed by Steinhauser (1937) who identified periodic and aperiodic controls on diurnal temperature variation, periodic controls determined the daily range over long temporal resolutions but aperiodic controls were highly significant in controlling average daily conditions and extreme values. Steinhauser concluded that these aperiodic controls were more significant in predicting and determining diurnal temperature fluctuations where local factors provide the greatest control. This was corroborated by Dobremez (1976) and Mitsudera and Numata (1967) who also stressed the importance of local factors.

As scale plays a dominant role in governing the processes and controls on temperature in mountainous areas, attempts to develop a complex predictive model comparable to the monthly predictions for diurnal variations were not possible. Analysis of the cyclical variation of air temperature on a diurnal scale (the periodic fluctuations discussed by Geiger, 1965; Catchpole, 1969; and Steinhauser, 1937) was used to predict the magnitude and timing of variations.

The first term from a Fourier series was used to extract the characteristic diurnal trend in temperature for the year 2000 at all stations: months exhibited distinct trends largely driven by air mass stability and surface energy balance variations, similar to those identified in section 5.3.2. Monthly series are presented in table 6.11, although winter months exhibit a less significant diurnal oscillation, noise within the data and the strong local trends associated with station characteristics (Section 4.4.1) obscure the trends and it is argued that diurnal oscillations do occur and should be included to drive turbulent heat exchanges.

Month	Cosine Coefficient	Sine Coefficient	Constant	Adjusted R^2	RMSE
January	-0.638	-0.984	-6.968	0.01	7.78
February	-1.149	-1.404	-3.872	0.1	3.84
March	-1.178	-1.381	1.169	0.21	2.46
April	-2.149	-2.264	8.846	0.25	3.79
May	-2.102	-1.859	11.451	0.21	3.86
June	-2.050	-1.959	14.715	0.29	3.14
July	-1.655	-1.521	12.821	0.34	2.19
August	-1.027	-1.009	8.65	0.15	2.41
September	-0.712	-0.610	6.497	0.05	2.90
October	-0.505	-0.384	0.075	0.02	3.12
November	0.003	0.219	-3.61	0.00	6.27
December	-1.178	-1.381	1.169	0.01	3.18

Table 6.11: Diurnal Cycles

The diurnal data exhibit large seasonal variations, suggesting that in September, October December and January temperature does not vary systematically through the day. This could be due to the reduction in solar heating of the Earth's surface in the months with reduced daylight hours and lower solar altitude. Equally it is also essential to consider the degree to which local conditions at station sites govern temperature. As diurnal temperature variations are well documented, each months daily temperature variation was predicted using Fourier series which showed good agreement between published and predicted maxima and minima, where the former is lagged by two to three hours after solar noon (Figure 6.14).

Variations in the adjusted R^2 and RMSE through the year highlight a pattern similar to that shown in section 6.4 where winter month predictions show the greatest uncertainty associated with the reduced solar heating and dominant pressure systems (Figure 6.13).

Mean monthly values, extended using the Fourier series outlined in section 6.3.3 to day temperatures were used as the base constant in the diurnal Fourier series, using the sine and cosine functions below. To increase computational efficiency sub-monthly temperature predictions were performed within the sensible heat Java program 'on the fly', and not created as individual surfaces.

Sine function = sine(2*π(hour-0.5))/24

Cosine function = cosine(2*π(hour-0.5))/24

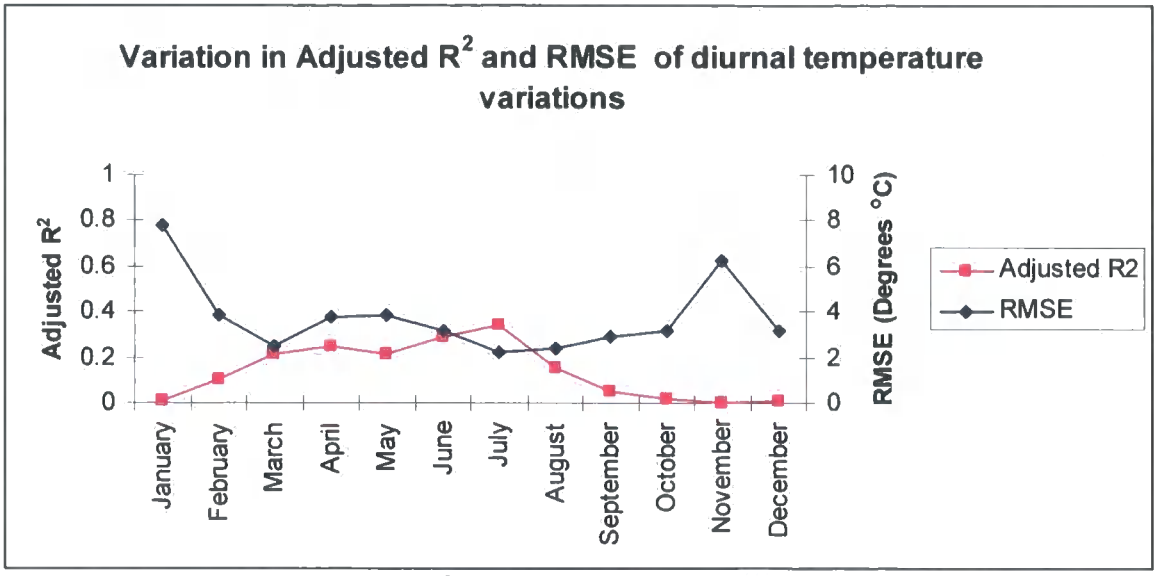

Figure 6.13: Variations in the adjusted R^2 and RMSE for monthly predictions of diurnal temperature variations

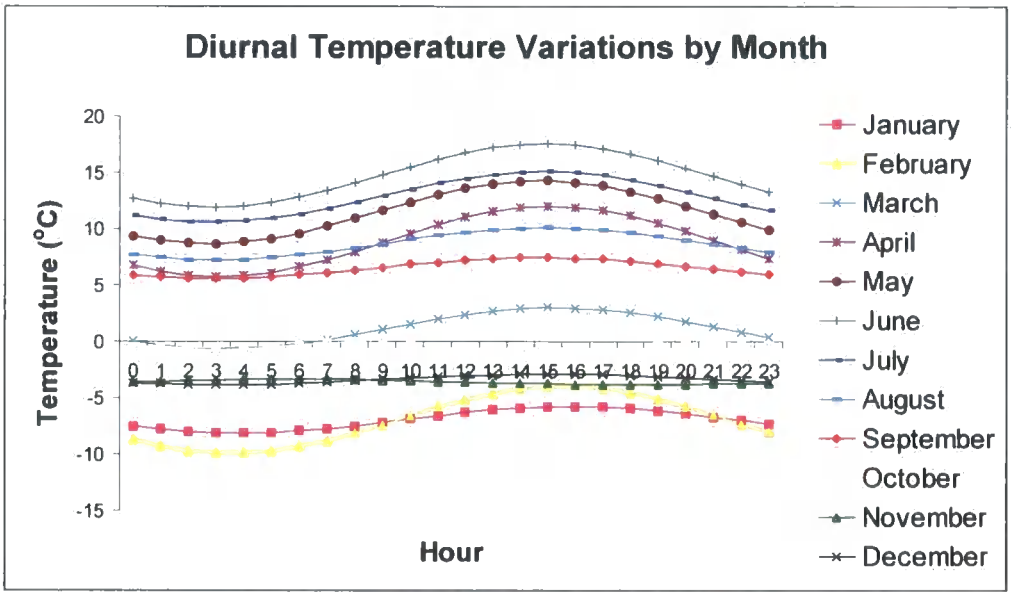

Figure 6.14: Predicted diurnal temperature variations by month

6.6 Precipitation Predictions

Monthly mean precipitation is controlled by a complex interaction of influences including distance from open sea, altitude, topographic orientation and exposure. Predicting monthly mean precipitation provides an average receipt for the month, removing the need to predict individual events that are highly variable through time and space (Sumner, 1988; Huff and Neil, 1957; Jackson, 1969). Intense precipitation events are often highly localized and may not ever be captured within a station radius. This temporal complexity is largely driven by highly variable atmospheric stability and moisture conditions. Although the complexity of precipitation processes is minimised using monthly predictions, simulating spatial variability was essential within the model. This variability is largely driven by complex local and regional topographic factors and synoptic wind direction (Hay, 1948).

6.6.1. Controls on Precipitation

The controls on this high spatial variability were viewed largely as topographic and contextual. Determining both the available water content (altitude, distance to open sea and orientation to synoptic wind and air masses) and the probable interaction between air parcels and terrain features (exposure, relative height, curvature), the latter collection of terms largely relate to the orographic component of precipitation receipt.

6.6.1.1. Altitude

Higher altitudes tend to yield an increased intensity and duration of precipitation events (Atkinson and Smithson, 1976) as air rises and reaches the condensation level. In reality precipitation systems are complex where topographic form and maritime influences are strong and dominate spatial distribution patterns. Exploration of the data revealed the overall altitudinal trend to have an adjusted R^2 less than 0.01. Although altitude does impose a degree of control a composite approach using other parameters is essential in complex terrain (Barry, 1992; Sumner, 1988).

6.6.1.2. Maritimity

Proximity to open ocean and moist air masses brought on land by prevailing westerlies and frontal systems increases the available moisture content in coastal areas. Strong precipitation gradients

exist between west and east Norway, with the largest receipts of rainfall and greatest numbers of wet days by the coast (Lauscher, 1976). The precipitation gradient between east and west Norway is nonlinear, with a large reduction in the available moisture content occurring after the Jotunheimen.

6.6.1.3. **Orographic precipitation**

The large reduction in available moisture content found east of the Jotunheimen results from the increased precipitation receipt or orographic rainfall within the mountains. Spatially distributed precipitation predictions in mountainous areas need to account for the orographic component of local precipitation (Hevesi *et al.*, 1992a; 1992b). The orographic component is the additional precipitation produced by the various mechanisms encountered near mountains (Bonacina, 1945), where prevailing winds are forced up slope and the rising air column cools and becomes saturated. The orographic component also includes modification to processes by lee-wave formation, enhanced cyclonic convergence and convective currents of air surrounding mountain peaks. The intensity of precipitation events is dependent upon the amount of available moisture, the height and longitudinal extent of the barrier, and lower troposphere circulation. Where prevailing winds are down-slope, local precipitation receipt is reduced, termed the rain shadow effect (Roe, 2002).

Simple models of orographic precipitation (P) take the form:

$$P = c_o + c_1 (H) + \varepsilon \text{ (mm)} \qquad \text{(Equation 6.9)}$$

Where P is in mm, c_o is the rainfall at sea level, c_1 is the rate of increase in precipitation with altitude, H is the station height in m and ε is an error term. (Brunsdon *et al.*, 2001).

Orographic influences on precipitation occur largely on a regional scale, with small peaks in a larger mountain range not exhibiting an orographic component to their precipitation. However relationships are rarely quantified in the field and it has often been necessary to parameterize relationships. For example, Gill (1982) assumed twice as much precipitation on windward rather than leeward slopes, where the gradient is greater than 20° and there is no higher land within the surrounding 1 km in the windward direction.

6.6.2. Approaches to prediction

In topographically smooth areas Sumner's (1988) approach, using a simple interpolation from local precipitation means, could be used to create precipitation surfaces, but these would not be suitable for areas of complex topography, like the Jotunheim, where strong local gradients exist. The few investigations into altitudinal precipitation gradients have shown to vary between 75 and over 300 mm per 100 metres in Norway (Johnsson, 1937) or exhibit no altitudinal gradient, varying as function of topography, specifically distance from highest surrounding peak (Blumer and Lang, 1995).

Gregory (1968) recognised the need to account for these strong local gradients and complex interaction of factors. He used multiple regression to predict annual precipitation in Sierra Leone, a mountainous maritime environment, using distance inland, longitude, latitude and an altitude factor defined as $\frac{altitude}{distance}$ where distance is distance inland. He found distance inland and altitude accounted for more than 60 % of the variation within the dataset. However the R^2 value still remained below 0.75 and plotted residuals highlighted the weakness of the model simulating orographic precipitation. Improved results were received when a directional relative factor was included increasing R^2 to 0.9.

Spreen (1947) in his study based in Western Colorado found that regressions including maximum relief within 8 km, exposure (defined as the fractional circumference of a circular area with a diameter of 32 km not containing a barrier higher than the station) and orientation of the station to the direction of maximum exposure increased the R^2 value from 0.55 for elevation alone to 0.94. Later approaches included the work of Chaun and Lockwood (1974), where focal measures of mean altitude were used, and Hill *et al.* (1981) where directional focal mean altitudes were used to account for synoptic and terrain conditions. Weston and Roy (1994) also discussed the use of directional components to improve precipitation estimates. Rhea and Grant (1974) performed a similar study predicting snow depth from the number of upwind barriers to flow and a directionally adjusted measure of slope for 200 km upwind, with an R^2 of 0.8. The work of Spackman (1993) and Basist *et al.* (1994) are further examples of the successful application of multiple regression: the former used over 30 parameters describing contextual and topographic measures.

Brunsdon *et al.* (2001) stressed the need to employ spatially variant models and proposed the use of geographically weighted regression as a method of incorporating spatially variant regression coefficients to improve the ability of the model to accurately predict local precipitation receipt.

Kriging has been less frequently used due to the non-stationarity of spatially distributed precipitation (Garen *et al.*, 1994) (as discussed in section 6.2). Kriging is possible if the data are detrended for the altitudinal effect, as implemented by Chua and Bras (1982), or as proposed by Dingman *et al.* (1988) who accounted for the nonstationarity using a precipitation delivery factor.

Other approaches include spline interpolation exploiting the complex dependencies between aspect and altitude and precipitation (Hutchinson, 1995) and trend surface analysis creating isohyets representing lines of equal precipitation (Unwin, 1969).

Multiple regression has been the most commonly and most successfully used prediction technique and was selected as the initial technique for prediction within this research.

6.6.3. **Monthly precipitation prediction**

Monthly precipitation surfaces were used in conjunction with monthly temperature predictions to determine monthly snowfall, where air temperature estimates determined precipitation state. R^2 values for altitudinal lapse rates were lower than those for temperature (maximum 0.064) reflecting the more complex relationship between precipitation and elevation.

Three different approaches to predicting precipitation were adopted. Precipitation is significantly more difficult to predict than temperature, summer is characterised by localised convection events and winter precipitation is predominantly fed by arriving pressure systems. The processes and pressure systems that control the type, location and duration of precipitation events change between months and so it was not possible to predict precipitation using the same lapse rate for the whole year.

Although temperature lapse rates were determined seasonally it was felt that the strong dependence of precipitation on pressure systems necessitated monthly predictions.

6.6.3.1. **Dual Lapse rate model**

The strong maritime influence in the West of Norway weakens the altitudinal increase in precipitation ($R^2 < 0.01$), restricting the success of any local predictions using altitude (Figure 6.15). This strong maritime influence is borne out in Figure 6.18, showing the strong non - linear relationship. Exploiting this relationship and dividing the climate stations by easting (120000) reveals two distinct altitudinal relationships, a dual lapse rate model was developed to account for these two trends (Figures 6.16, 6.17). Distance from coast could also have been used here, however the usefulness of this value is highly dependent upon the off coast starting point and the trajectory of the incoming westerly systems; easting was selected as this was less subjective and repeatable and in other geographical areas.

Precipitation receipts for westerly stations, where the orographic precipitation component is weak are largely determined by distance from coast (most successfully characterised as easting), which accounts for most of the variation within the dataset (Table 6.13). The easting coefficient was found to decrease through spring to summer and then increase through autumn to winter. This matches changes in pressure systems as westerly winds become less and then more influential in providing precipitation. Summer months are fed by convective rain events, which are not as dependent on distance from coast, accounting for the reduction in the coefficient.

Month	Regression	Adjusted R^2	RMSE
December	-0.0037x + 505.3	0.9776	6.142
January	-0.0032x + 438.0	0.89	12.12
February	-0.0023x + 308.1	0.95	5.75
March	-0.0027x + 357.6	0.91	9.18
April	-0.0013x + 167.5	0.91	4.46
May	-0.0011x + 152.3	0.73	6.76
June	-0.0010x + 155.3	0.74	6.08
July	0.0008x + 147.1	0.89	2.96
August	-0.0012x + 199.1	0.67	8.71
September	-0.0032x + 443.8	0.9	11.13
October	-0.0034x + 485.6	0.86	14.66
November	-0.0032x + 438.1	0.88	12.87

Table 6.13: Regression coefficients for westerly stations

Prediction of monthly precipitation receipts in eastern Norway, required the inclusion of topographic parameters to account for the variability within the dataset. Although a range of the topographic parameters created in chapter 5, altitude and easting were found to provide the most robust regression using a seasonal lapse rate model to account for the strong seasonality in prevailing weather systems (Table 6.14).

Winter months when westerlies dominate were most effectively predicted using altitude and easting. Altitude had a much greater control on precipitation receipt with an altitudinal lapse rate of between 0.029 and 0.039 mm per m: easting had a weaker control and precipitation was found to decrease between 0.00009 and 0.00025 mm with every m inland. April is renowned in Norway as transition month between different dominating climate systems, and was most effectively predicted using altitude alone, with a lapse rate of 0.027 mm per meter. Summer months between May and August exhibit an increase of precipitation with easting: during summer very different pressure systems dominate and convectional rainfall is common and increases orographic effects. The dominant role that topography (valleys for convectional rainfall and upland areas for orographic rainfall) has on increased precipitation receipt is borne out in the easting coefficient, where more mountainous easterly areas yield higher rainfall. Precipitation receipt during autumn months, before the arrival of westerly pressure systems, is largely governed by topographic effects and altitude alone was found to provide the most robust estimates, with greatest altitudinal lapse rates of 0.051 mm per m.

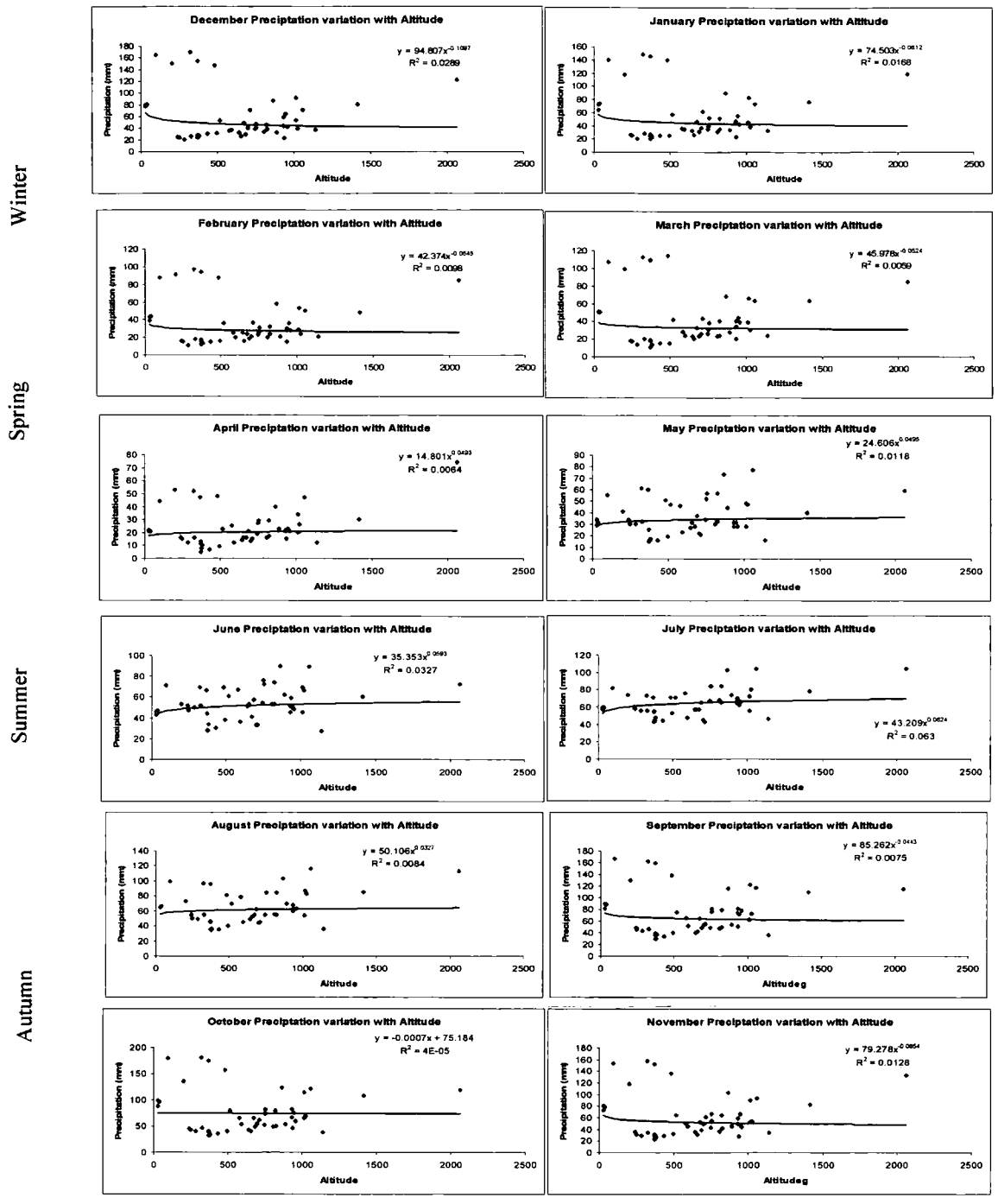

Figure 6.15: Seasonal trends in altitudinal variation in precipitation for all climate stations

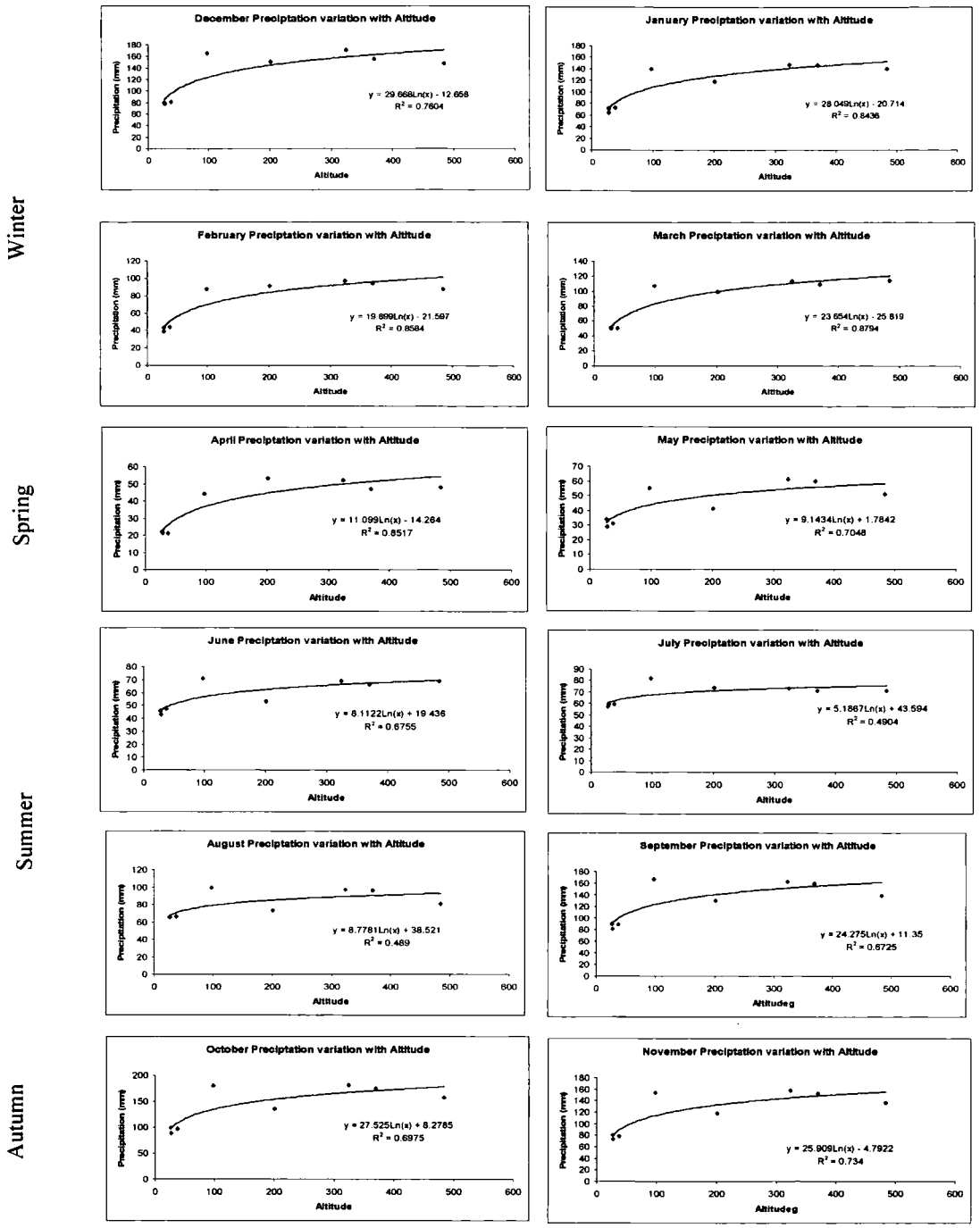

Figure 6.16: Seasonal trends in altitudinal variation in precipitation for easterly climate stations

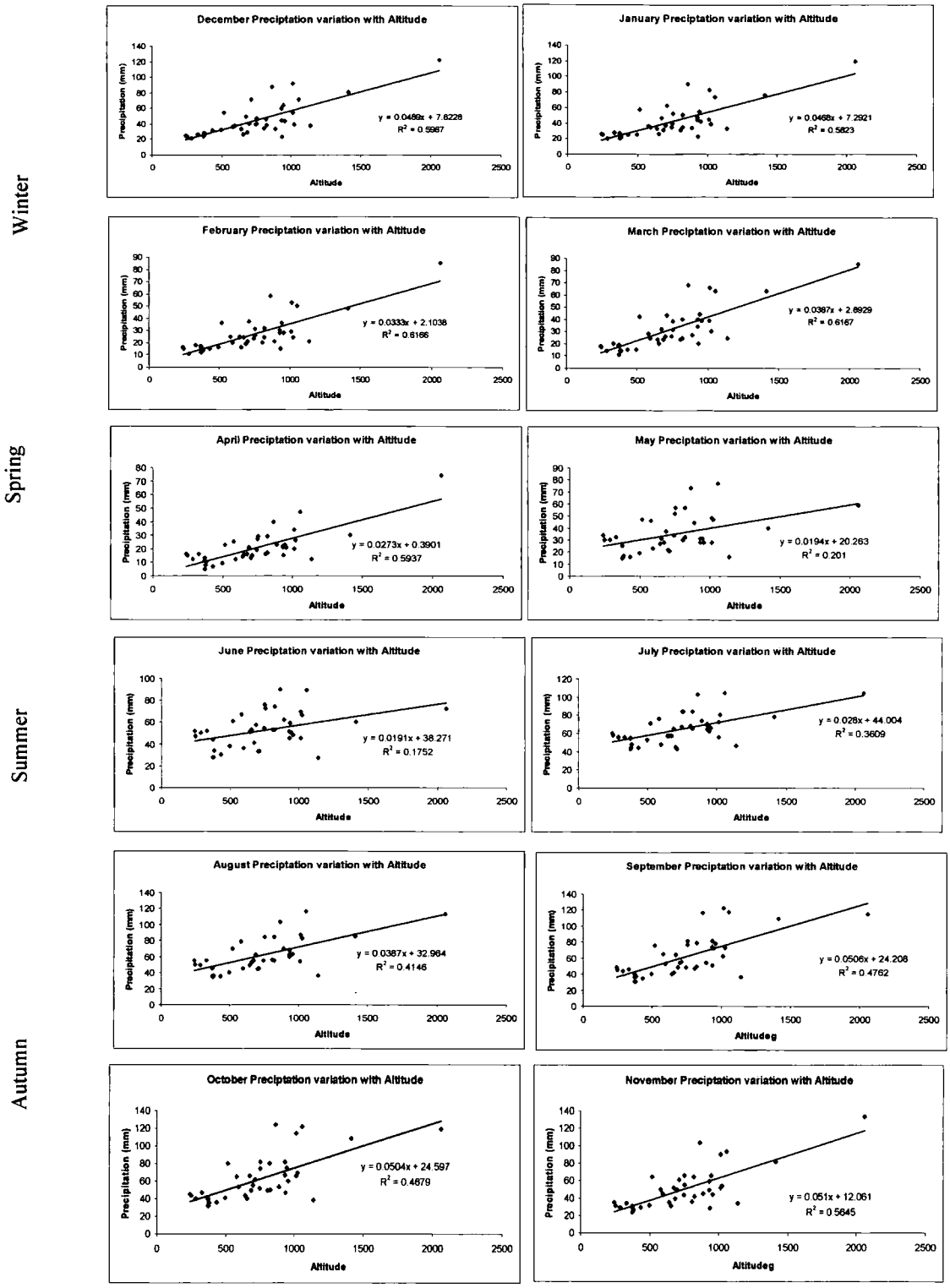

Figure 6.17: Seasonal trends in altitudinal variation in precipitation for westerly climate stations

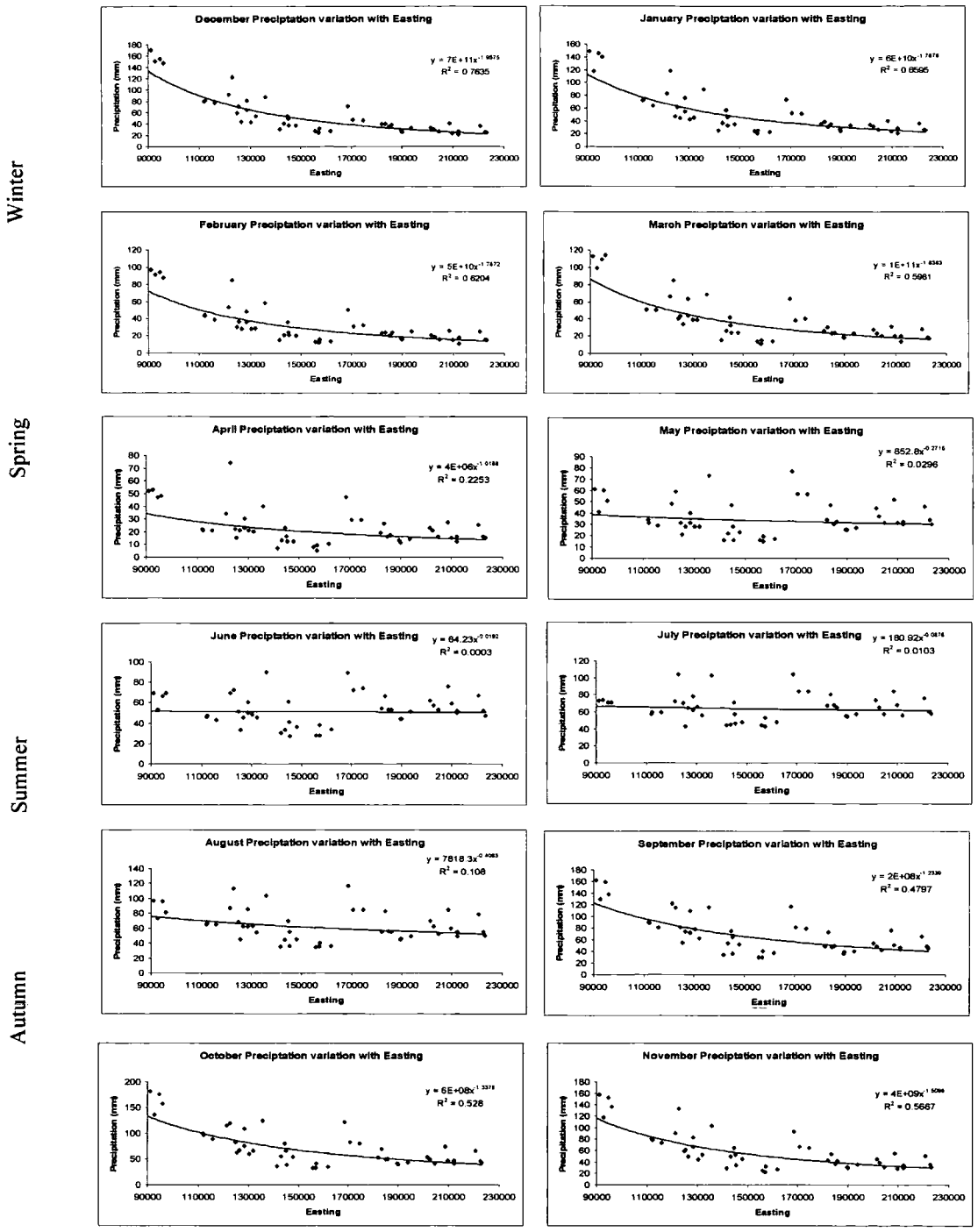

Figure 6.18: Seasonal trends in variation of precipitation with easting for all climate stations

When the precipitation surfaces from the easterly and westerly lapse rate models were combined an unrealistic surface was created. The dual lapse rate model was rejected as the resultant precipitation surface exhibited a large jump in precipitation at the boundary between the different lapse rates.

6.6.3.2. **Generalised linear model (GLM)**

Examination of all of the precipitation climate stations reveals that there is strong easting effect. (Figure 6.18) Even though there is a topographic barrier through southern Norway, linear divides and steps are not realistic and a less disjointed model than described in section 6.6.3.1 is needed to replicate the nonlinear decrease in precipitation. A regression on a transformed data scale might allow this, however a GLM does the transformation and back transformation using a link function removing the need for the additional steps required in a normal regression. A GLM can also be designed to ensure physically meaningful predictions e.g. precipitation should be non-negative. A GLM with a reciprocal link function was used to predict precipitation using a single lapse rate. The reciprocal link function was chosen as it accounted for the non-linear decrease in precipitation with easting.

Month	Regression		Adjusted R^2	RMSE
December	0.037z - 0.00025x + 57.8	Winter precipiation	0.68	12.46
January	0.039z - 0.00017x + 41.7	decreases with	0.61	13.32
February	0.029z - 0.00009x + 19.5	distance from coast:	0.62	9.07
March	0.033z - 0.00012x + 27.3	Westerlies	0.64	10.36
April	0.027z + 0.39	Transition period	0.58	7.99
May	0.027z + 0.00017x - 13.5	summer precipitation	0.26	12.98
June	0.031z + 0.00024x - 11.2	increases with easting:	0.33	12.97
July	0.037z + 0.00019x + 5.4	local valley convection	0.44	12.16
August	0.047z + 0.00018x - 2.7		0.44	15.64
September	0.051z + 24.2	Autumn precipitation	0.46	18.77
October	0.050z + 24.6	varies only as a	0.45	19.03
November	0.051z + 12.1	function of altitude	0.55	15.84

Table 6.14: Monthly trends in precipitation predictions

Month	Goodness of fit
December	0.961
January	0.932
February	0.933
March	0.928
April	0.784
May	0.294
June	0.300
July	0.484
August	0.483
September	0.836
October	0.860
November	0.892

Table 6.15: GLM monthly goodness of fit statistics

GLM predicted precipitation well and matched (Table 6.15) the non-linear decrease in precipitation from the westerly to easterly stations (Figure 6.19).

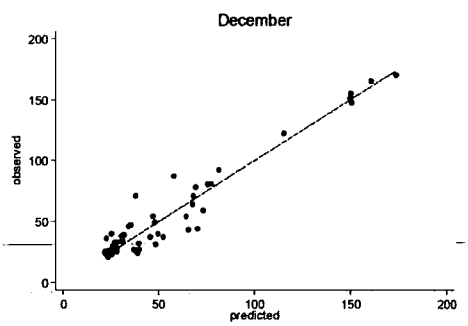

Figure 6.19: Generalised linear model precipitation predictions for December

However the model predicted negative precipitation as a result of the reciprocal function being used and GLMs were rejected as a prediction tool for precipitation as no other link function could predict the non-linear decrease.

6.6.3.3. **Power function**

A power function was developed with altitude, log of easting and the sine and cosine functions (see 6.2.3.1) to try and account for the non-linear decrease in precipitation with easting as an alternative to the GLM. Where the log of monthly precipitation is given by:

$$\text{LogP} = a(\text{altitude}) + b(\log X) + c(\text{Sine function}) + d(\text{Cosine function})$$

(Equation 6.10)

Predicted monthly precipitation estimates for the study area simulate the heterogeneity of receipts expected within a variable topography, but overestimate monthly maxima and range compared to station statistics. The power function model performed strongest in winter (R^2 0.7 – 0.8) where estimates had an average error of < 5mm although individual station predictions are largely less than 20 mm (Figure 6.16, 6.17). The seasonal pattern in these winter errors was limited suggesting that this may be solely attributable to local variations or noise, where predictions were not consistently under or over estimating. However, predictions for summer receipts were significantly less successful, R^2 values falling to 0.3. This strong seasonal variation in accuracy suggests that processes or parameters outside of those modeled impact upon summer monthly receipts (Figure 6.21), where estimates are consistently under-estimating summer precipitation. Although consistent over- or under-estimates are an indication of an area for improvement within the present study, summer precipitation will not contribute to the accumulation of snow during a mass balance year. Rain on snow events are not simulated within the melt component of the model and so will not contribute to ablation. Consequently the under prediction of summer precipitation does not restrict the performance of the model for the present study.

This model was used in the glacier prediction model as it provided the most accurate monthly precipitation estimates, where all parameters were significant in each monthly regression (Figure 6.16).

Examination of individual surfaces exhibits the seasonality in the role of pressure systems discussed in section 5.5.1, where winter receipt is largely driven by proximity to windward (Figure 6.23) and summer receipts are driven by local convective events and the fixing of high pressure systems to the East (Figure 6.24).

Month (Log)	Adjusted R^2	RMSE
December	0.85	0.226
January	0.79	0.266
February	0.78	0.282
March	0.77	0.299
April	0.65	0.627
May	0.33	0.341
June	0.34	0.245
July	0.36	0.183
August	0.44	0.244
September	0.68	0.268
October	0.69	0.272
November	0.72	0.281

Table 6.16: Precipitation Power prediction statistics

Month	Minimum	Maximum	Range	Standard Deviation
December	25.8	192.6	166.8	29.0
January	24.2	192.5	168.3	27.2
February	15.6	145.9	130.3	19.5
March	0.7	37.4	36.7	6.8
April	3.1	54.6	51.5	10.5
May	45.8	143.8	98.0	13.6
June	39.5	169.4	129.9	19.1
July	40.7	232.3	191.5	29.0
August	41.1	211.9	170.8	27.3
September	33.0	217.9	184.8	28.7
October	25.8	192.6	166.8	29.0
November	24.2	192.5	168.3	27.2

Table 6.17: Power function monthly study area predictions for the climate stations

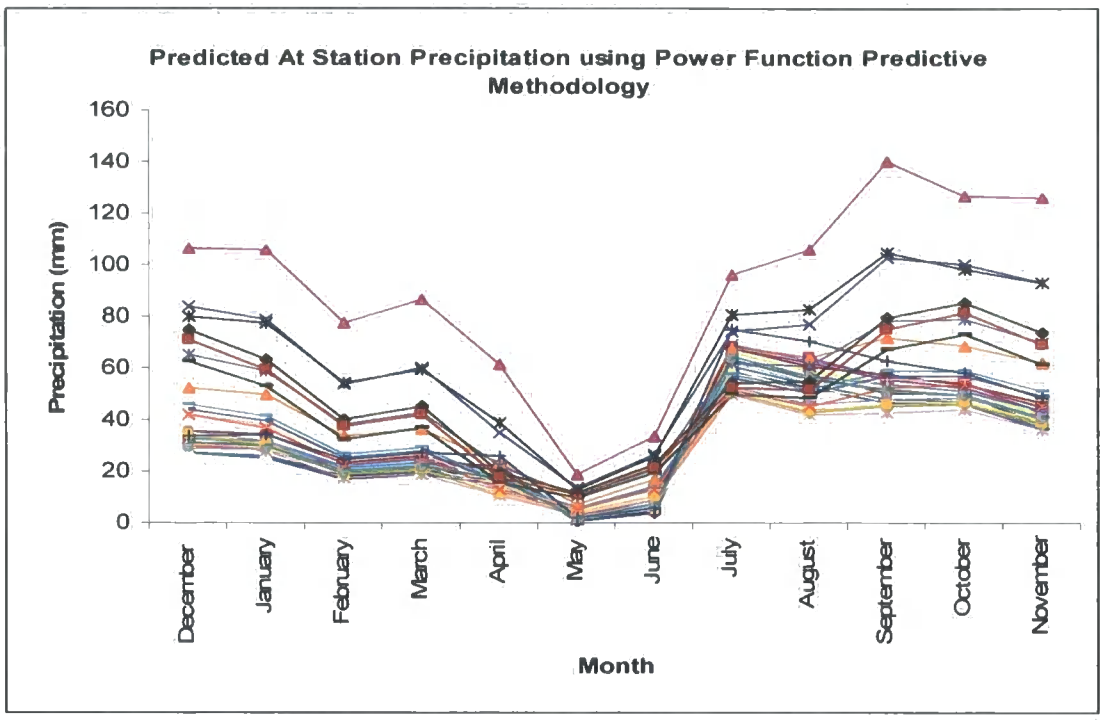

Figure 6.20: Predicted at station monthly precipitation

Month	Minimum	Maximum	Range
December	21	122	101
January	20	119	99
February	11	85	74
March	11	85	74
April	5	74	69
May	15	59	44
June	27	76	49
July	43	104	61
August	34	113	79
September	30	122	92
October	32	119	87
November	23	133	110

Table 6.18: Recorded Climate Station Precipitation

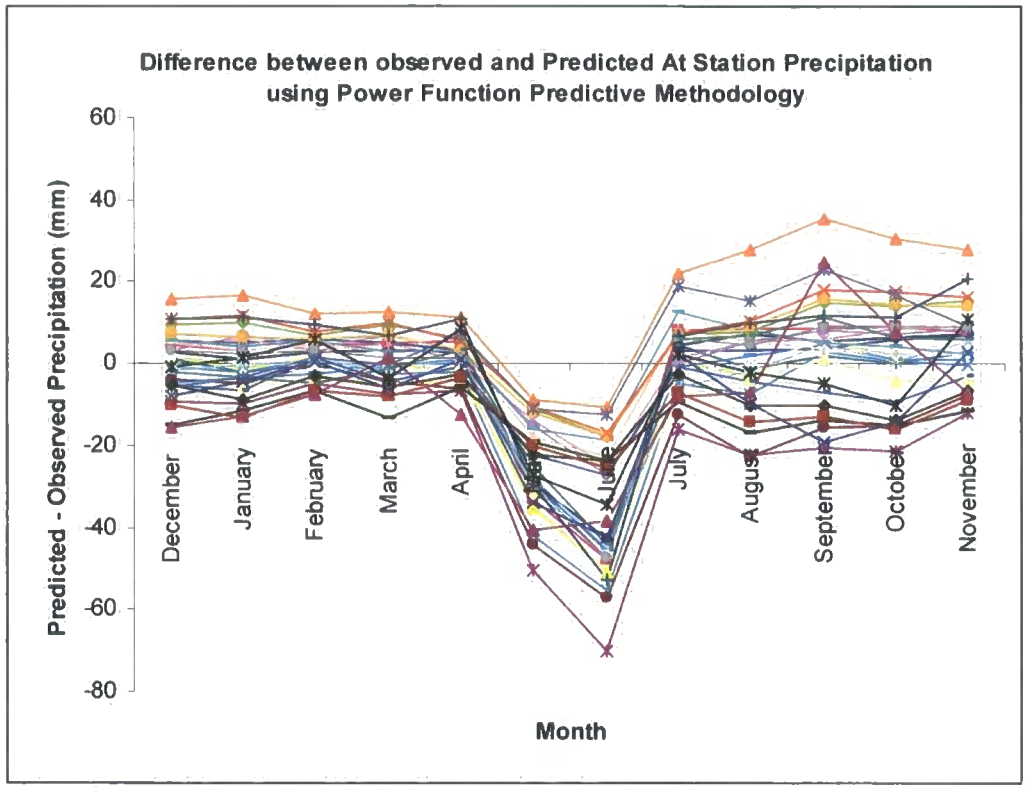

Figure 6.21: Predicted – Observed at station monthly precipitation

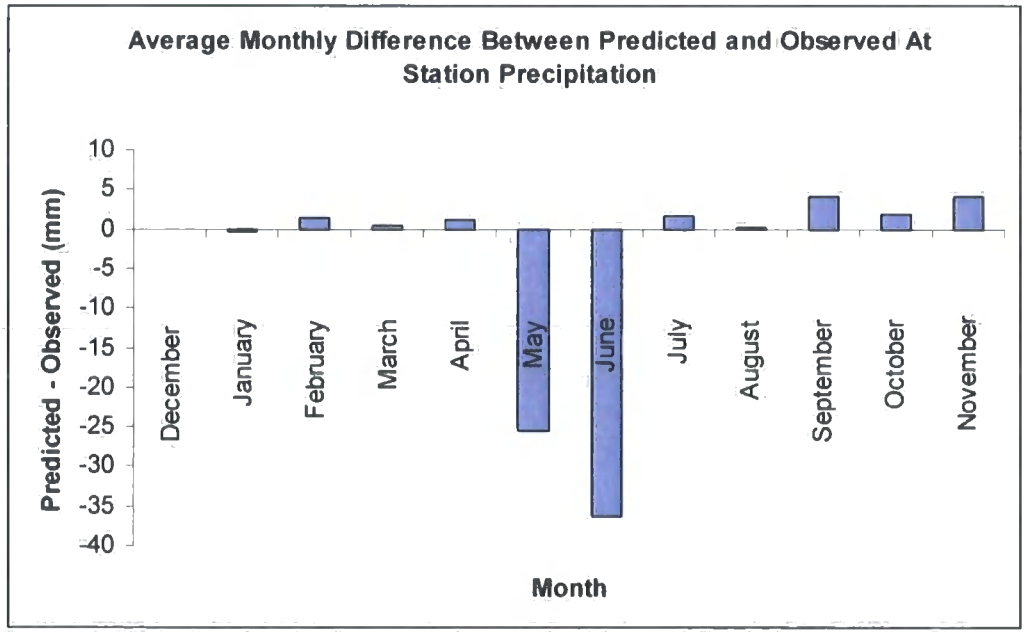

Figure 6.22: Average Predicted – Observed at station monthly precipitation

Figure 6.23: Power function February predicted temperature surface

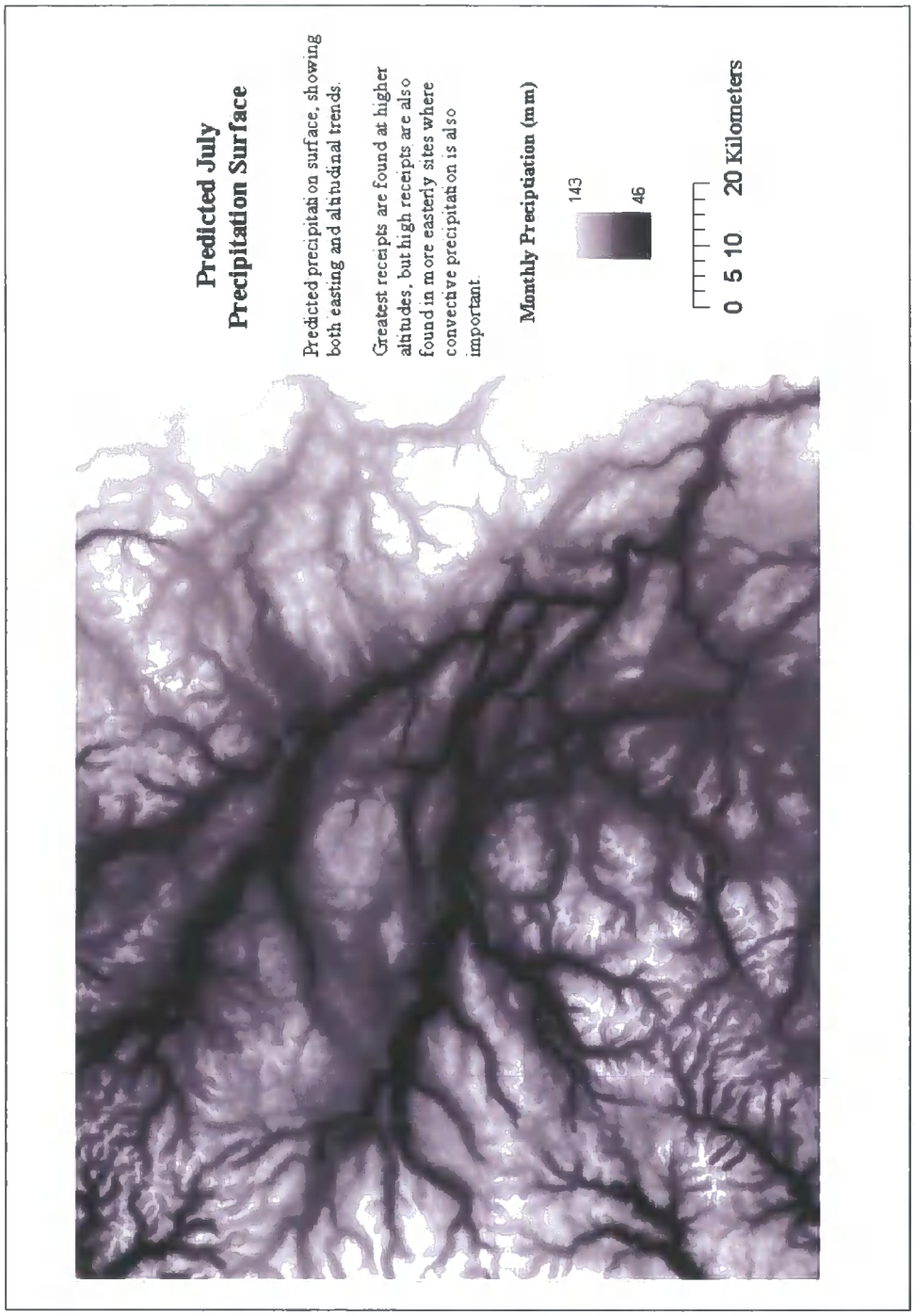

Figure 6.24: Power function July predicted temperature surface

6.6.4. Monthly precipitation surfaces

A number of predictive approaches were investigated to identify the most accurate method of predicting monthly precipitation receipts. The dual lapse rate was rejected as although it accounted for the strong gradient in precipitation it produced an unrealistic trend in receipts. The GLM provided improved predictions and successfully modelled the altitudinal and easting components to data, however the GLM returned extreme values that fell outside realistic ranges. Predictions from the power function model outlined in Section 5.5.3 provided the most accurate predictions and although summer receipts were consistently over estimated, winter estimates, most critical for this study, were strong.

6.7 Cloud cover

Cloud cover not only exerts dominant controls on local energy balance estimates (Oke, 1987; Cawkwell and Bamber, 2002) but also affects local temperature variations (reducing solar heating and night time long wave cooling (Oke, 1987)) and precipitation receipts (Peppler, 1931). Strasser *et al.* (2004) in their detailed study of glacier meteorology during an ablation season found clouds to reduce incoming radiation by approximately 30 %. Cloud cover impact on radiative and climatic systems identified by Strasser *et al.* (2004) is dependant upon cloud type (Barry, 1992), cloud base height, time of day, cloud coverage and air mass characteristics. The complexity and feedbacks associated with these systems and their high temporal and spatial variability (Schweiger, 2004) restricts the resolution with which they can be modelled.

6.7.1. Controls on Cloud cover

Despite the complexity of the processes leading to these highly variable temporal and spatial trends it is possible to make some general comments and discuss major controls. Cloud cover is, in general more frequent and thicker over mountains where increased orographic or mechanical uplift and convective activity from slope heating result in greater amounts of cloud with increased water content. This is further increased by the local and frictional drag imposed on surface flows by the increased relief of the terrain (Barry, 1992). Topography can further increase local cloud cover where clouds form in eddies in the lee of sharp isolated peaks (Whiteman, 2000).

Air temperature, humidity and condensation level all impose strong controls on the occurrence, depth and altitude of cloud cover (Tompkins, 2003). Complexity is introduced as multiple feedbacks exist between these climate system components, where processes at a number of different scales interact to create a suite of local conditions, and cloud type is largely determined by air mass characteristics which in turn are driven by regional climate (Barry, 1992).

6.7.2. **Approaches to predicting cloud cover**

Holistic approaches to predicting local cloud cover are not common and are largely restricted to large spatial and temporal scale GCMs. Exploratory techniques examining long term climate datasets including temperature and atmospheric humidity for a variety of cloud cover conditions identified noncausal relationships between temperature and humidity but failed to simulate these within GCM models (Groisman *et al.* 2000). Groisman *et al.* (2000) investigated the performance of GCM predictions for different types of cloud systems: frontal, convective and low level cloud. They found that all three showed areas for improvement and that variance between observed and predicted estimates was greater than the variance between the different system predictions, suggesting that large uncertainities within these complex predictive models severely restrict their use in local scale studies.

Attempts to characterize individual cloud cover attributes are more commonly employed, where two or three parameter correlations may provide locally significant predictions. Barry (1992) correlates cumulus cloud cover base height, Z_b (m) with air temperature (T_A) and dew point temperature, (T_D) using:

$$Z_b = 120\,(T_A - T_D) \qquad \text{(Equation 6.13)}$$

where T_D varies as a function of altitude, lapse rates and atmospheric pressure. Equivalent techniques correlate diurnal temperature changes with daily cloud cover fraction (Prof. Chris Burn *pers. Comm.*, 2003). Lane *et al.* (2002) parameterize cloud size and spacing using known statistical distributions, where cloud size was modeled exponentially with the number of clouds.

Cloudiness can also be conceptualised as the transmissivity of the atmosphere, Thornton *et al.* (1997) and Susong *et al.* (1999) use the algorithm supplied by Bristow and Campbell (1984) to

predict a daily average cloudiness correction to atmospheric transmissivity from diurnal temperature range, as:

$$P_t = 1.0 - \exp(-bD_{tr}^{c}) \qquad \text{(Equation 6.14)}$$

where P_t is the proportion of clear-sky transmissivity, D_{tr} is the diurnal temperature range and b and c are empirical parameters. Thornton *et al.* (1997) discuss the application of this algorithm in complex topography where they found diurnal ranges in temperature tend to decrease with altitude, leading to a decrease in transmittivity with altitude in contrast to the theoretically reported increase in transmittivity with altitude, as optical air mass decreases. The solution proposed by Thornton *et al.* (1997) is simply to remove the altitudinal lapse rates when predicting diurnal temperature range, clearly this is not an acceptable solution for the spatial resolution of this research, where it is felt that the maritime climate of Norway may in fact lead to an increase in cloud cover with altitude during certain parts of the day. Stochastic radiative transfer models such as those reported by Lane-Veron and Somerville (2004) and Lane *et al.* (2002) identify cloud optical parameters including cloud water content and cloud droplet effective radius as determinants in the effectiveness of transmittance.

Comparative studies have examined the correspondence between remotely sensed cloud cover estimates and ground based recordings. Ground based instruments examined largely consist of fish eye lens sensors retrieving cloud cover fraction within the visible range. Comparisons showed good consistency in cloud fraction cover (Schweiger, 2004), although when combined with a radiative transfer model ground based measurements were found to underestimate incident global solar radiation by 25 – 32 % in contrast to equivalent estimates from remotely sensed sensors which only recorded a 3 – 7 % underestimate (Martins *et al.* 2003). This suggests that the additional information captured by the remote sensor quantifying cloud optical thickness is of key importance when considering local energy balance estimates. The sensitivity of local energy balance to cloud cover fraction was further explored by Cawkwell and Bamber (2002) who recorded differences up to 40 Wm^{-2} in the local energy balance and 1 K change in temperature.

6.7.3. **Monthly Predictions**

Predictive approaches explored within this research were largely driven by availability of data, limiting the use of parameterisations of atmospheric pressure and dew point temperatures, which

were not available within this research. Although cloud type and height impose controls on the transmissivity of the cloud the complexity of the processes governing these parameters identifies this level of prediction outside of the scope of this research, where cloud cover fraction was the only characteristic predicted as this has the most dominant influence on absorption and reflectance of radiation (Cawkwell and Bamber, 2002).

Initial investigations into the correlations between diurnal temperature fluctuations and daily cloud cover were made using a four year hourly dataset, however the signal to noise ratio prevented any statistically significant conclusions being made and was rejected as a useful climatic indicator for this research. Equivalent investigations were made between monthly average oktas, temperature and altitude each returning an insignificant correlation, clearly showing the restrictiveness of parameterising complex systems in a simplistic manner.

Cloud cover predictions were required primarily to modify potential radiation estimates, where cloud fraction determined the proportion of incident direct beam radiation reaching the ground surface. Information supplied within the 30 year normals described in Section 5.6 was used to drive this adjustment although station data was limited and only one climate station (55920) was located within the study area or an equivalent location. To avoid identifying maritime or lowland trends and to avoid complex spatial interpolations with no statistically significance spatially uniform cloud predictions were made. Although this may seem an initially crude estimation, the spatial resolution and extent of the study area still falls within any GCM prediction and attempts to simulate distributed estimates would propagate large uncertainties through the model.

The monthly distribution of clear sky, fair weather and overcast days was used with monthly average okta data to reconstruct daily cloud cover. To reconstruct the average distribution of cloud cover conditions within a month using this method, it was necessary to make a number of assumptions. Using guidance from the Norwegian Meteorological Institute allocations of a representative daily Okta coverage for clear, fair and overcast conditions were made (Table 6.21).

Cloud Conditions	Oktas
Clear sky days	1.5
Fair weather days	3
Overcast days	6.5

Table 6.21: Estimated okta cloud fraction for sky conditions

Cloud cover fraction predictions were made at the same temporal resolution as incident radiation predictions (Chapter Seven), where conditions were assumed constant for 6 days. An assumption of monthly average okta cloud cover for the whole month was not possible, as clear sky and overcast conditions impose strong alterations to local energy balance and had to be included in an attempt to avoid large monthly over or under estimates.

Reconstruction of monthly estimates was integrated into the radiation modelling by allocating five daily okta cloud fractions for each month, using information on the number of days each sky condition existed for from the 30 year normal data (Table 6.22). These fractions could then be converted to cloud cover oktas using Table 6.21.

Month	Overcast Days	Clear Sky Days	Fair Weather Days	Days Remaining	Average Oktas
January	16	4	5	6	5.7
February	14	4	5	5	5.4
March	17	4	5	5	5.7
April	15	4	5	6	5.5
May	15	3	5	8	5.6
June	13	3	6	8	5.3
July	17	2	3	9	5.9
August	18	1	2	10	6.2
September	20	1	1	8	6.6
October	21	1	2	7	6.5
November	17	4	5	4	5.8
December	17	3	4	7	5.8

Table 6.22: Parametersiation of cloud data incorporated within the model

Monthly distributions (Table 6.22 and Figure 6.25) identify a late summer and autumn maximum in overcast conditions accompanied with a reduction in clear sky and fair weather days when convective and westerly systems dominate

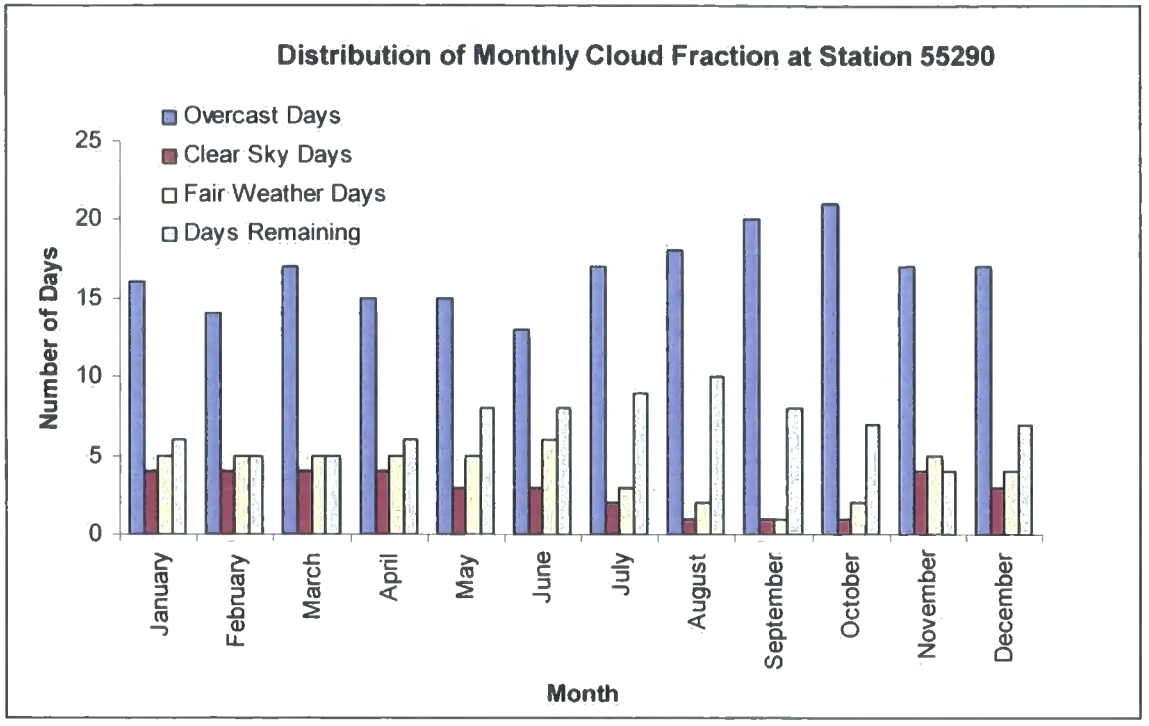

Figure 6.25: Cloud fraction histogram

6.8 Wind

Wind flow in a valley can be viewed as a composite of thermodynamically driven and terrain driven flows. Thermodynamic flows have a strong diurnal component and are highly sensitive to sky conditions: terrain forced flows exhibit more consistent characteristics for a given area but are sensitive to air mass properties (Barry, 1992, Oke, 1987). Geiger (1965) conceptualizes flows as active and passive effects of mountains on wind: active topographic effects where differences in temperature and pressure induce local circulations, and passive effects where existing flows are deflected and modified by topographic forms. Resultant wind vectors represent the composite conditions of all flows operating over a range of temporal and spatial scales and modifications to the background flow. The high spatial and temporal variability of modifications to background flow render a simple interpolation between mountain climate stations unmeaningful. Further uncertainty surrounds the degree to which climate station wind vector normals represent local or regional trends, where station exposure and context can lead to a 10 – 25 % adjustment to local speeds (Wieringa, 1986). Although some authors simplify wind flow modeling by using an elevation driven lapse rate where wind speeds decreased by 0.0092 $ms^{-1}m^{-1}$ such as the study reported by Cline *et al.* (1998) (where wind flow was only a small component of a larger model).

The complex topography and drift systems present within the Jotunheimen rendered this technique unsuitable.

Wind fields in the boundary layer are largely controlled by the frictional drag exerted by the surface. The force exerted on a surface air moving over it is called the surface shearing stress (τ) and is expressed as a pressure: pressure is also exerted on the air by the surface as frictional drag. Air acts like a fluid and the friction exerted at the base does not act through the bulk of the atmosphere. This results in a marked velocity profile characterized by a rapid decrease in horizontal wind speed as the surface is approached. In the absence of strong thermal effects the depth of this retardation is dependent on the surface roughness.

Motivations for this component of the research identified surface wind speeds within the lower part of the atmospheric boundary layer (ABL) as the primary requirement for the wind surface dataset. Efforts were consequently focused on deriving accurate estimates of the surface speed rather than the profile.

Accurate wind flow estimates were required for two elements of this research, initially to drive the turbulent heat energy exchanges (Chapter Eight), where surface flow velocities control the magnitude of the exchanges between the surface and the base of the boundary layer directly above it and to highlight areas of potential drift.

6.8.1. **Controls on wind flow**

Two interacting but separately driven components to wind flow in mountain areas have been identified. The controls governing the characteristics of these flows are considered separately.

6.8.1.1. **Thermal**

Thermodynamically forced flows, induced as a result of differential insolation receipt and local buoyancy effects on slopes; exhibit high spatial and temporal variability and accurate estimates of the individual components require a high resolution climatic dataset, not available here. The smallest of these flows are slope winds, larger scale winds occur flowing along valley axis termed along valley winds, at an equivalent scale but perpendicular to these are across valley winds. The largest of the mountain circulations occupy the entire valley termed drainage and mountain-plain

winds. In a similar classification Ohata (1989a) used spatial scale to differentiate and classify wind systems occurring on snow and ice masses (SIM) in summer into three types, general wind at scales over 100 km, local scale within valley or mountain range, or SIM scale for example katabatic winds. All are driven by horizontal temperature differences and are prominent at different times of the day. Although these flows are significant for deriving small temporal and spatial energy balances they are not to be investigated or modeled here as they operate at a finer temporal scale than required within the model.

Strasser *et al.* (2004) found similar results to Oerlemans and Klok (2002) and Oerlemans and Grisogono (2002) when they analaysed a high temporal and spatial resolution dataset using a set of 6 climate stations positioned on and around a glacier during the ablation period of 2001 to investigate the spatial and temporal variability of meteorological variables across an alpine glacier. They found glacier winds largely dominated the wind regime and had mean speeds of 2.8 ms^{-1}.

Consequently, topographically forced flows will be the primary focus of this study, where winds are largely assumed to flow from modal wind directions, deflected by terrain, with no diurnal component.

6.8.1.2. **Topographic**

Topography provides the dominant control on wind speed and direction in mountainous environments, where altitude, local slope, aspect, curvature and larger topographic features modify the speed and direction of flow by altering both the frictional drag and by wind direction by deflection. Although direct correlations with altitude are complex, global circulation patterns do lead to an overall increase in wind speeds with altitude (Raiter, 1963), with hill crests tending to be windier than valleys. Exact relationships between altitude, slope, aspect, wind direction and speed and free air characteristics are still not fully understood (Barry, 1992). This section will attempt to disaggregate some of the more dominant influences in an attempt to paramaterise terrain modifications to flow.

Scale is an essential concept when considering the role of topography in governing flow. Whiteman (2000) introduced the term effective topography to identify the extent of the surrounding terrain that modifies flow characteristics, where, in rough terrain the effective topography may extend further

than local valleys, or roughness elements, with flows over mountains responding to larger scale features of the topography and not to the smaller scale roughness elements (Whiteman, 2000).

Whiteman (2000) reports that wind speeds generally increase with height through the mid-troposphere, where speeds in the lowest 10% of the boundary layer (up to 100 m) generally increase logarithmically driven by the rapid decrease of frictional drag from the Earth's surface with increased distance above it. Frictional drag imparted by the earth's surface varies with surface landcover and structure. Published roughness indices primarily quantify vegetation and urban landcover types and do not provide meaningful measures for complex terrain surfaces. For smooth uncomplex terrain, parameterisation with existing indices is possible as used by Weiringa (1986) who proposed a method of adjusting recorded wind speeds to account for local conditions by quantitfying local exposure and roughness interactions within and above the ABL. Similar studies predicted meso scale winds (U_m) using a logarithmic altitudinal lapse rate and surface roughness measures (Z_o) with station measured wind speed (Us), observed at height (Zs), where (U_m) was given by:

$$U_m = U_s \ln (60/Z_0)\{\ln(Z_s/Z_0)\}^{-1} \qquad \text{(Equation 6.15)}$$

As existing roughness classifications do not provide estimates of roughness coefficients for complex or rough terrain in mountainous environments such as the Jotunheim, it was consequently necessary to derive more applicable measures relating to fetch and exposure from the DEM and use these in conjunction with more quantitative measures of terrain surface roughness (section 4.6). Complex modeling of surface velocity profiles over snow and terrain focuses on micro scale surface roughness elements, eddies and turbulent perturbations in the vertical velocity profile, especially on flow within the first 10 cm above the surface (Smeets *et al.*, 1999; Brock,, 1997). Larger scale roughness features, affecting the first 10 meters above the surface have not, to the authors knowledge, received quantitative classifications relevant to frictional drag and flow retardation for areas of complex terrain.

Although local roughness controls the frictional drag on near surface flows, it is also possible to associate areas of faster and slower flows with larger landform scale features, where high wind speeds are found in gaps, passes, forges, exposed areas, summits and elevated plains or plateaus,and slower speeds are found in sheltered and protected sites, upwind of mountain barriers or areas of high surface roughness (Whiteman, 2000). Subsequent discussion focuses on modelling terrain

modifications to flow at the landform scale, although parameterisation occurs at 100 m DEM resolution.

Flow around mountains areas can be conceptualised in a stratified or nonstratified atmposphere. Under nonstratified conditions induced pressure fields result in greatest near surface flows at summits and lowest in valleys. Under stratified flow conditions, the atmosphere is more stable and reacts to the vertical displacement of an air parcel with a responsive buoyancy force (Whiteman, 2000). This is largely evident in wave like responses to flow over a mountain, resulting in asymmetric flow conditions on the lee and windward aspects. Mountainous areas in the Jotunheim will largely extend above the ABL (depth of around 1000 m) and are consequently subject to stratified flow conditions, with smaller hills lying within the ABL are characterised by nonstratified flow conditions.

Characteristing how flow in nonstratified conditions is deflected and modified by terrain requires quantification of deflection and flow retardation by terrain obstacles. Terrain obstacles can generate turbulent eddies and wakes. A wake is an area extending downwind of an obstacle characterised by slower wind speeds and increased gustiness. Winds are slowed downslope approximately to distances 15 times the obstacle height (Verge and Williams, 1981). Eddies form within and around the wake, as a result of wind shear or convection. The response of flows to obstacles can be in part be characterised by their form and orientation.

Whiteman (2000) states that three factors determine the behavior of an approaching flow in response to a mountain barrier, the stability and speed of the approaching air and the terrain form. The behaviour proposed by Whiteman (2000) is summarised in Table 6.23.

	Fast flow	Slow Flow
High stability	Over	Round
Low stability	Over	Over
High terrain	Over	Round
Low terrain	Over	Over

Table 6.23: Idealised stability and flow over terrain

It is also important to consider the shape of the terrain, including length, elongation and contextual measures such as the presence of valleys and basins that impose controls on wind speed. Sites low in a valley (a contextual location similar to most of the stations used in this analysis) are often protected from prevailing winds, although strong upper winds can lead to gusty conditions in a valley.

6.8.2. **Approaches to predicting wind flows**

Simulation of flow largely follows two broad approaches, parameterisation of retardation and deflection and momentum and energy conserving equations of motion. The latter set of approaches are not directly discussed here, as it lies outside of the scope of this research. Parameterisation approaches are more commonly employed within studies comparable to this research as they provide computationally efficient solutions that capture the spatial variability in process with sufficient accuracy.

Ryan (1977) developed a sheltering factor to quantify the retarding effect of the terrain, defined as:

$$F_u = E` \arctan (0.17Y_u)/100 \qquad \text{(Equation 6.16)}$$

Where Y_u is the slope in percent to the horizon upwind, E` is a parameter representing air mass characteristics, specifically the degree of mixing. Under stratified conditions the sheltering effect of topography is greater and E` is defined as:

$$E` = 2 - 0.0016E \qquad \text{(Equation 6.17)}$$

Where E is the altitude, and E` varies from 0 at 1220 m to above 1 at 610 m. These values can be modified to reflect local terrain scale.

The wind speed after the terrain modification V_{sd} is then defined as:

$$V_{sd} = V_b - (F_u V_b) \qquad \text{(Equation 6.18)}$$

Where V_b is the wind speed before the terrain modification.

Wind direction is modified by diverting factor F_d defined as,

$$F_d = -0.225Y_d \sin[2(A_d-\Theta_b)] \qquad \text{(Equation 6.19)}$$

Where Θ_b is the wind direction, A_d is the slope aspect and Y_d is the slope in percent downwind. Flow is diverted clockwise, if slope aspect is counterclockwise less than 90° from the wind direction, and diverted counterclockwise if slope aspect is clockwise less than 90° from the wind direction. No diversion occurs if flow is parallel or perpendicular to the slope. The calculated diversion angle can then be added to Θ_b providing the resultant wind vector (Ryan, 1977).

Ryan (1977) also provides algorithms for predicting slope and valley wind components on an hourly time scale to create a composite flow prediction, finding an additive approach provided good results. Although these topographic flows do alter the magnitude of flow during the day they are highly dependent upon cloud cover and temperature estimates, and consequently the magnitude of the error introduced into the model by parameterizing these flows outweighs the resultant benefits of their inclusion.

Purves *et al.* (1998, 1999) successfully employed the diverting factor devised by Ryan (1977) and combined it with a shelter index to create ordinal surfaces of wind velocity vectors, entrainment potential and snow accumulation through drift using a rule-based model. Initiated with a constant wind speed, slope and aspect rasters of the Cairngorm Mountains and the Nevis Range were used to calculate topographic exposure to winds from different directions. The shelter index used a remap table to differentiate between leeward and windward slopes, based on divergence from the mean aspect of leeward slopes. Simulated wind vectors of deflection and an ordinal index of speed reduction showed good agreement with typical flows as reported by local experts.

Winstral and Marks (2002a, 2002b) also employ parameterized measures of shelter to derive spatially distributed wind fields used to drive a snow redistribution model. Winstral and Marks (2002a, 2002b) also addressed the role of flow separation in contributing to localised wind vectors and snow depths, an area not tackled by Purves *et al.* (1998, 1999). Winstral and Marks (2002a, 2002b) developed their model from data at two topographically opposing climate stations, a ridge based exposed site and a sheltered site. The wind flow data at these two stations were viewed as the extreme values along a speed spectrum, with intermediate topographic exposure locations scaled along this continuum. Exposure was calculated for all possible wind directions at 5° intervals.

Directionally specific exposure was quantified as the maximum upwind slope parameter (Sx) in a specified azimuth. Sx is calculated by examining all cells along the azimuth direction, and retrieving the cell forming the greatest slope with the cell of interest. The retrieved cell is termed the shelter-defining cell and Sx is defined as:

$$Sx_{A,d\max}(x_i, y_i) = \max\left[\tan^{-1}\left(\frac{elev(x_v, y_v) - elev(x_i, y_i)}{\left((x_v - x_i)^2 + (y_v - y_i)^2\right)^{0.5}}\right)\right] \quad \text{(Equation 6.20)}$$

where A is the azimuth direction, *dmax* determines the lateral extent of the search, (x,y_i) are the coordinates of the cell of interest and (x_v,y_v) are the set of all cell coordinates located along the azimuth search vector. Negative values of Sx record local exposure where the cell of interest is higher than the examined cells. A more robust measure recorded average Sx within 30° azimuth sectors. Derived values of Sx were highly sensitive to *dmax*, and although the authors discuss appropriate distances for specific processes, for example drift modeling, no mention is made of terrain roughness or scale. Clearly these parameters will play a large role in determining values of Sx and it is suggested by the author here, that these should also factor in the selection of *dmax*. This issue is explored in section 6.8.3.1.2.

Winstral and Marks (2002a,b) also developed a measure of upwind slope breaks, S_b, identifying areas of flow separation. S_b is derived using two instances of Sx, describing local and outlying measures of slope, separated by *sepdist*, a user defined distance (equivalent to *dmax*, 60 m in the application reported): the difference between these two measures defines S_b. Large values of S_b indicate a large break in slope, which may result in flow separation and eddy development. These characterize areas of low flow, where the reduction in speed may lead to the deposition of snow. Winstral and Marks (2002a, b) used evidence of past drift to derive measures for *sepdist* and a threshold measure for S_b. Calibration of values of S_x and S_b to match conditions at the two station sites (less than and greater than 5° respectively in this example) before deriving distributed values for the study area for all wind directions. Application of these parameters to a semi-arid site in southwestern Idaho, showed strong correlations between predicted and observed drift and scour sites, implying representative simulations of local wind flows.

Lapen and Martz (1993) also extracted topographic measures from a DEM as surrogates for wind vectors, namely fetch and directional relief, to characterise the degree of wind sheltering at a location. These are comparable to Y_u and directional *Sx* in Ryan's (1977) and Winstral and Marks's (2000a,b) studies. Fetch at a location x,y was defined as the distance in a specified direction to the obstacle defined as

$$Z_{test} \geq z_{core} + NI \qquad \text{(Equation 6.21)}$$

where, z_{core} is the altitude at (x,y), z_{test} is the altitude at the cell being examined as a potential obstacle, *I* is the altitude height increment in meters and N is the distance from (x,y) to the Z_{test}. *I* represents the extent of the shelter created by an obstacle, which Verge and Williams (1981) report to be 15 times the obstacle height. Lapen and Martz (1993) found outputs to be highly sensitive to the value of *I* and recommend a value of 0.025, although the most appropriate value is entirely dependent upon the scale of the analysis (process and terrain).

Directional relief represents the relative altitude of (x,y) compared with the average altitude in the direction of fetch. Lapen and Martz (1993) found both parameters to be useful and indicative of areas where snow was entrained or deposited. They found a negative correlation between fetch and snow depth, where areas close to an obstacle had deeper snow cover than those far away from an obstacle.

Other approaches to predicting surface winds use geostrophic winds (Ekström, 2002) and synoptic forcings (Jonsson, 1995) as the primary drivers.

6.8.3. **Predicting wind flow**

Two different approaches were used to estimate wind vectors, a parameterisation approach utilising free air and surface wind records and the application of 3dvom2.6.5, a three dimensional model based upon linearised equations of motion (Vosper, 2002).

The usefulness of both wind surfaces to predict spatially distributed flow vectors will be assessed within the model.

6.8.3.1. **Parameterisation of terrain modification**

In line with the findings of McKendry (1983) the great spatial and temporal variability shown in the Jotunheimen wind regime illustrates the difficulty in using data from any one site to characterize the wind regime of an area. This modelling approach needed to cover a variety of processes acting over a range of spatial scales and consequently it was necessary to select geomorphologically appropriate variables which did not always provide the most statistically significant prediction of meteorological station data. This is common in many fields of predictive geomorphology but is especially justified here as only a small number of stations were available to include into the analysis and the representativeness of these measurements is not clear.

The methodology outlined here attempted to couple free air and surface wind circulations by parametertising the terrain modification to flow. This was performed in three steps, initially characterizing annual trends and controls on flow including local roughness and exposure to obstacles. This approach is in keeping with other work by Ryan (1977), Haltiner *et al.* (1980), and Winstral and Marks (2002a,b) who used a cumulative approach to predictions.

6.8.3.2. **Direction: Terrain Deflection**

Analysis of the directional component of the station recorded wind data showed a strong correspondence with valley orientation, where all flows aligned along valleys, representing the deflection of regional winds by surface flow (Table 5.4).

Season	Incident Wind Direction								
	337 - 21	22 - 66	67- 111	112- 156	157 - 201	202 - 246	247 - 291	292 - 336	Still
13670									
Winter	6.92	1.87	2.06	2.02	**8.90**	6.79	8.55	7.05	**55.85**
Summer	11.63	6.36	11.52	7.10	**17.16**	7.90	4.38	7.25	**26.70**
Autumn	7.67	2.58	4.84	3.94	**13.53**	8.41	7.31	6.06	**45.66**
Spring	7.59	4.53	6.16	4.18	**17.28**	9.26	7.74	7.05	**36.21**
15720									
Winter	11.64	5.29	9.79	0.61	4.01	7.25	**42.62**	18.71	0.08
Summer	8.03	6.04	9.95	1.02	9.54	11.78	**42.06**	11.34	0.23
Autumn	11.26	7.23	14.20	1.37	5.80	7.32	**38.04**	14.64	0.13
Spring	9.00	5.35	13.20	0.81	9.48	11.55	**37.78**	12.80	0.02
16740									
Winter	8.66	14.68	**42.05**	6.76	1.33	1.37	10.56	11.34	3.25
Summer	9.06	5.27	**22.12**	12.52	3.19	1.81	20.38	21.09	4.57
Autumn	7.16	12.69	**38.50**	11.83	1.58	1.26	11.92	11.59	3.46
Spring	9.29	6.97	**27.45**	15.04	4.75	2.70	16.65	14.76	2.39
55290									
Winter	4.95	3.93	5.21	9.09	14.85	4.99	**30.05**	6.19	**20.74**
Summer	4.80	5.70	4.30	10.90	15.30	6.10	**32.70**	5.60	**14.80**
Autumn	3.34	2.79	3.07	13.83	21.06	7.33	**30.86**	5.45	**12.27**
Spring	4.83	4.91	5.27	13.53	20.49	4.59	**21.62**	4.95	**19.81**
61770									
Winter	1.20	**24.19**	**35.80**	9.44	0.25	0.02	**22.16**	6.87	0.08
Summer	1.76	**10.89**	**14.47**	11.56	2.05	0.04	**47.32**	10.54	1.38
Autumn	1.22	**21.28**	**30.90**	10.31	1.24	0.00	**25.76**	8.89	0.40
Spring	1.92	**15.52**	**23.84**	12.89	1.63	0.02	**32.42**	11.56	0.20

Table 6.25: Seasonal percentage of wind receipts at climate stations from eight directional sectors

	Directional Deflection			Absolute Deflection	
	Minimum	**Maximum**	**Mean**	**Minimum**	**Mean**
East	-19.5	18.621	0.04	0	0.78
South East	-17.64	18.05	-0.075	0	0.75
North	-18.98	18.69	-0.06	0	0.79
North East	-16.85	17.08	0.09	0	0.77
South	-19.14	17.89	-0.06	0	0.81

Table 6.26: Deflection statistics for different wind directions

The behaviour of wind from an incident wind direction on a slope of known gradient and azimuth was modelled using the previously discussed diverting factor, F_d, derived by Ryan (1977) and employed by Purves *et al.* (1992), where the diversion in degrees is given by:

$$F_d = - 0.225G_p\sin[2(A_d-W_d)] \qquad \text{(Equation 6.22)}$$

determined as a function of wind direction W_d, aspect A_d and gradient G_p (%) of terrain downwind of an obstacle. Five versions of the algorithm were created, one for each of the dominant wind directions found within the free air records, South, South-East, East, North and North-East. For each iteration all cells were initialised with each of the modal directions as the downwind slope direction (Table 6.26).

Resultant directional surfaces were visualized, and showed good correspondence with terrain features (Figures 6.27 – 6.31) and all subsequent analysis was performed on each of the five iterations.

6.8.3.3. **Speed**

Each of the three steps used to predict surface flow velocities are described in turn, initially this involved quantifying the local surface modification at the five climate stations, secondly identifying areas of potential flow separation and finally quantifying the role of local surface features including roughness and altitude.

I. Surface Modification

Recorded free air wind speed records were used to predict the vertical velocity profile of flow within the bottom 2,700 m of the atmosphere. This was used to estimate speeds at the base of the free air layer, 1 m above the surface. Estimated speeds were compared to observed records and the difference was recorded as the degree of modification to flow (T_m) imposed by terrain for each of the climate stations. The strong seasonal component to the other datasets used within this research is also apparent within free air speeds, with pronounced seasonality in the strength and characteristics of prevailing winds.

The estimates for each of the five climate stations were compared with the observed seasonal mean speed at the climate station: the difference between the two speeds was termed the terrain modification factor, (T_m). Although in part it may contain errors within the predictions, it provides a quantitative measure of the difference in speeds associated with the local and focal terrain structures that arguably would not be present if the terrain were uniform.

Figure 6.27:

Surface Wind Deflection under Southerly Conditions

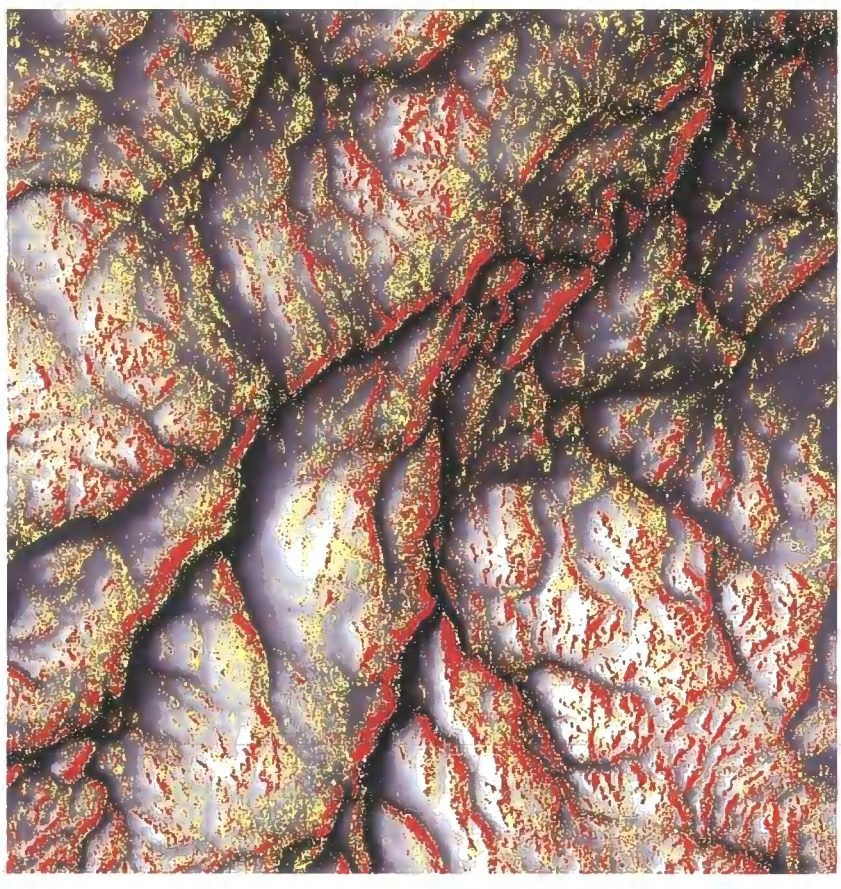

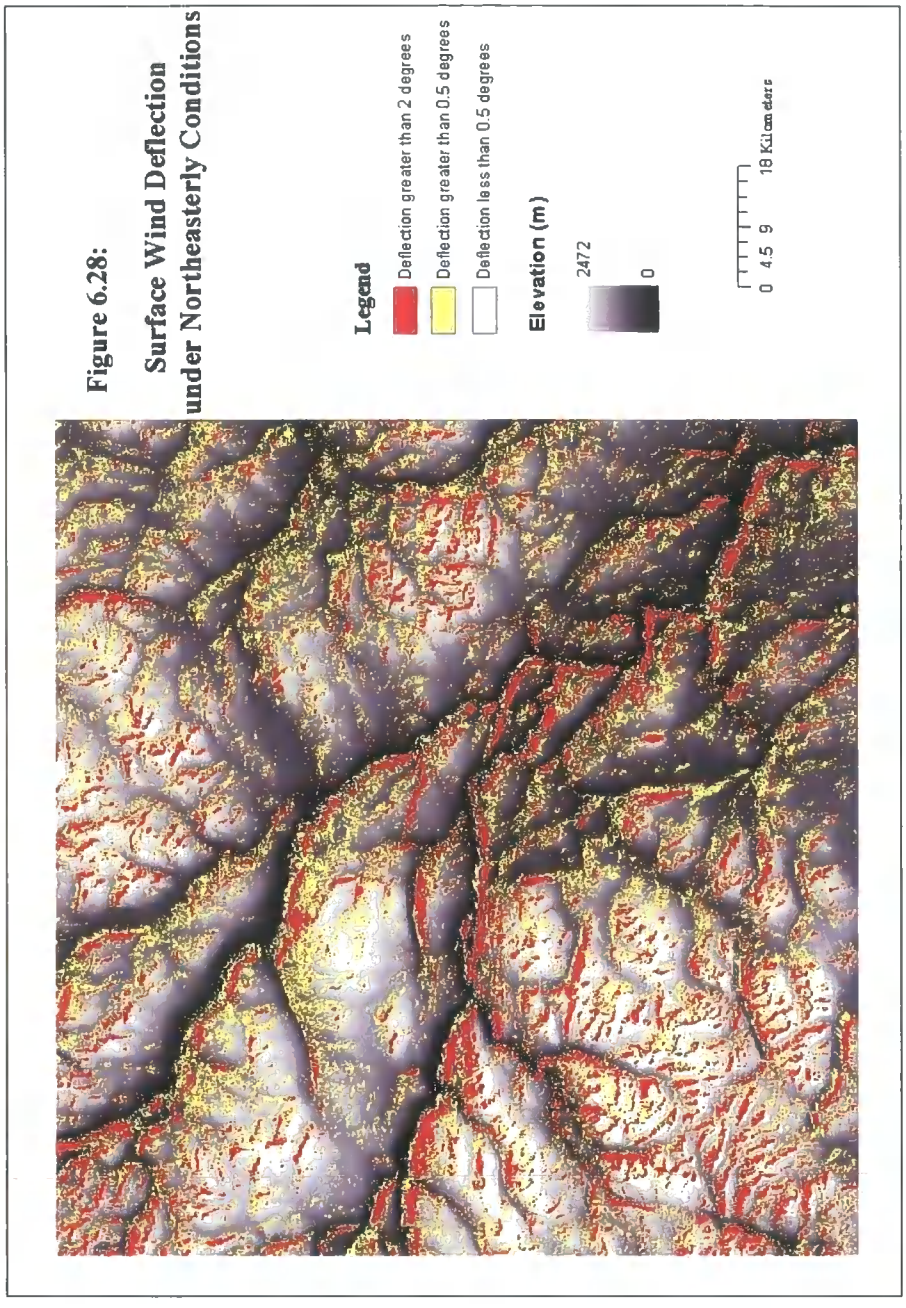
Figure 6.28:
Surface Wind Deflection under Northeasterly Conditions
Legend
Deflection greater than 2 degrees
Deflection greater than 0.5 degrees
Deflection less than 0.5 degrees
Elevation (m)
2472
0
0 4.5 9 18 Kilometers

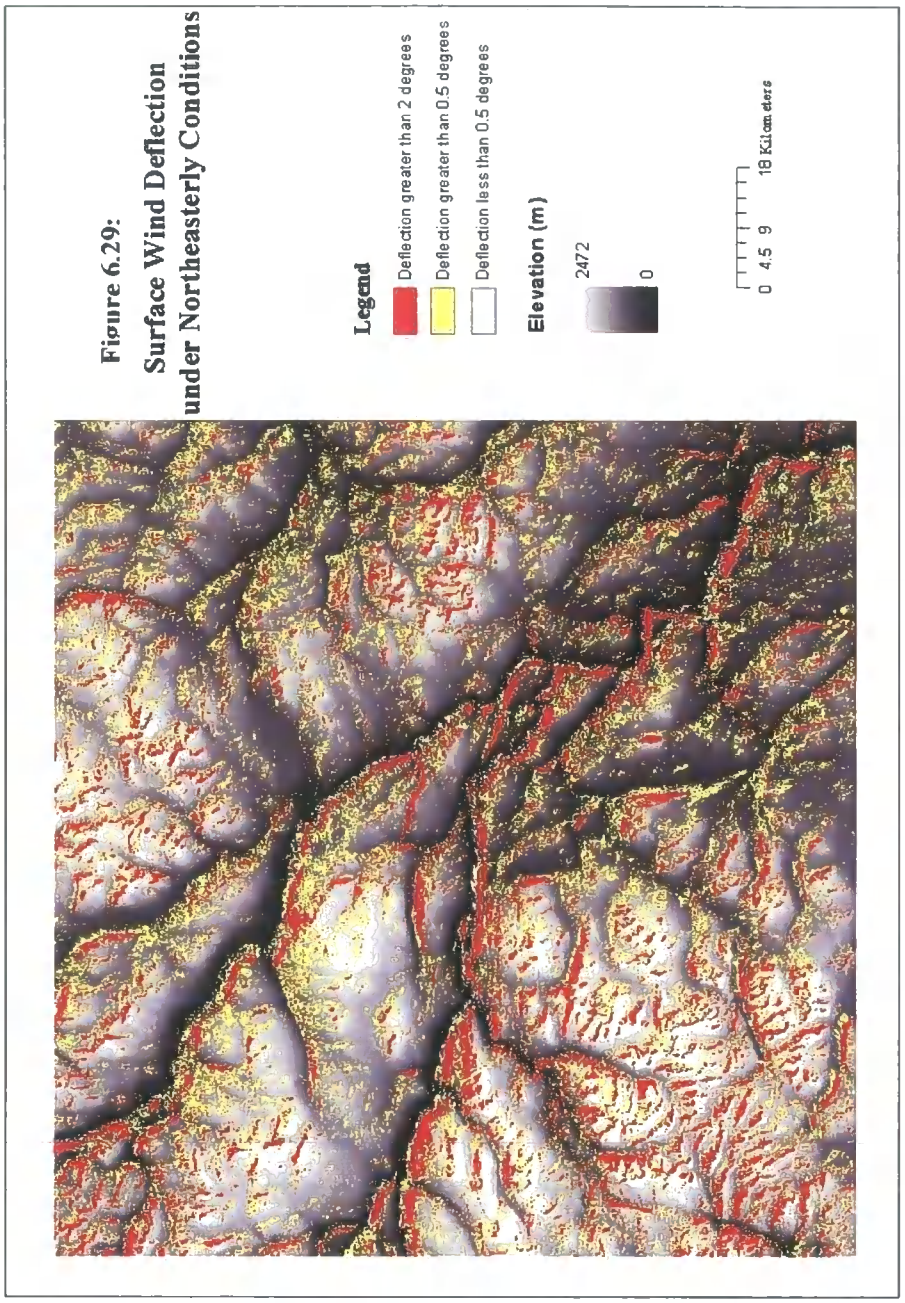
Figure 6.29:
Surface Wind Deflection
under Northeasterly Conditions
Legend
Deflection greater than 2 degrees
Deflection greater than 0.5 degrees
Deflection less than 0.5 degrees
Elevation (m)
2472
0
0 4.5 9 18 Kilometers

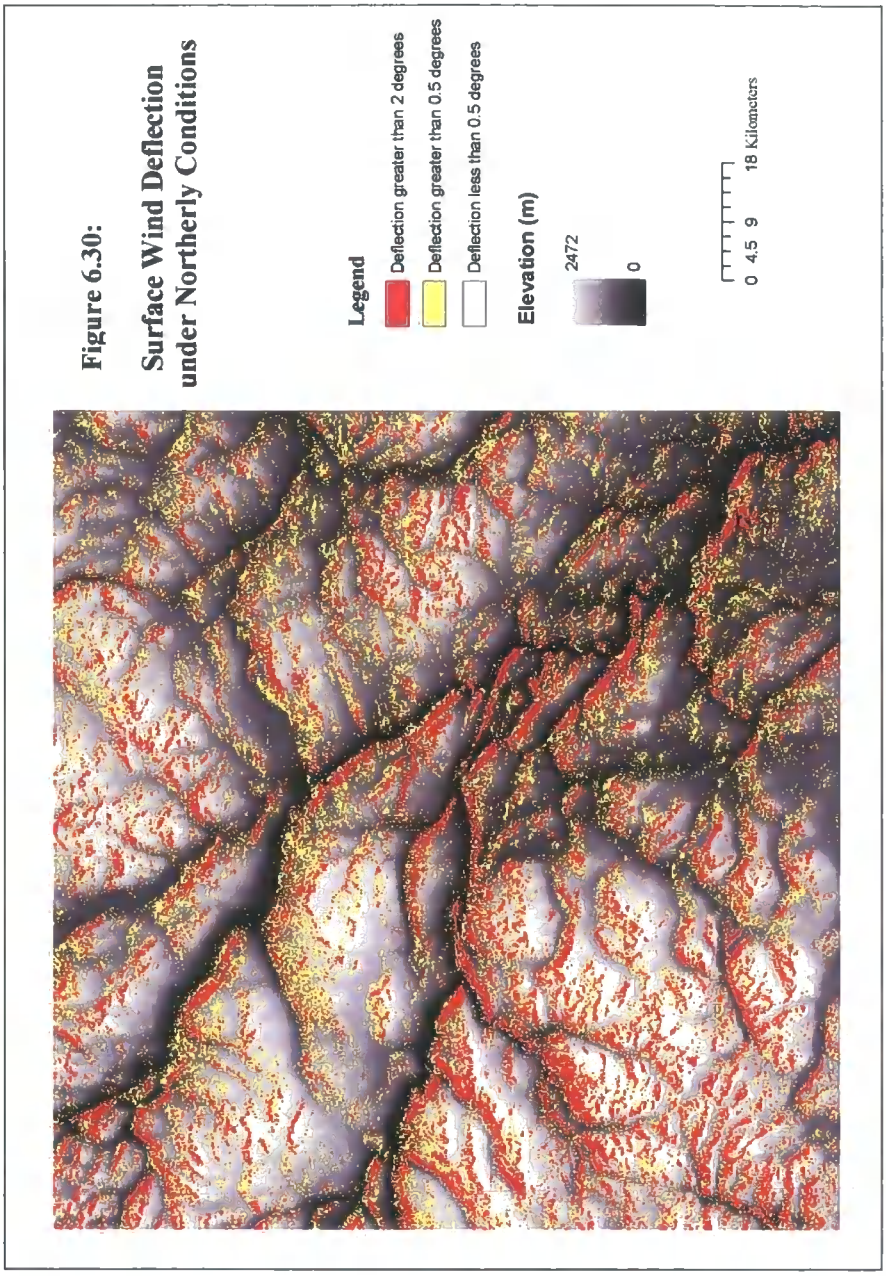

Figure 6.30:

Surface Wind Deflection under Northerly Conditions

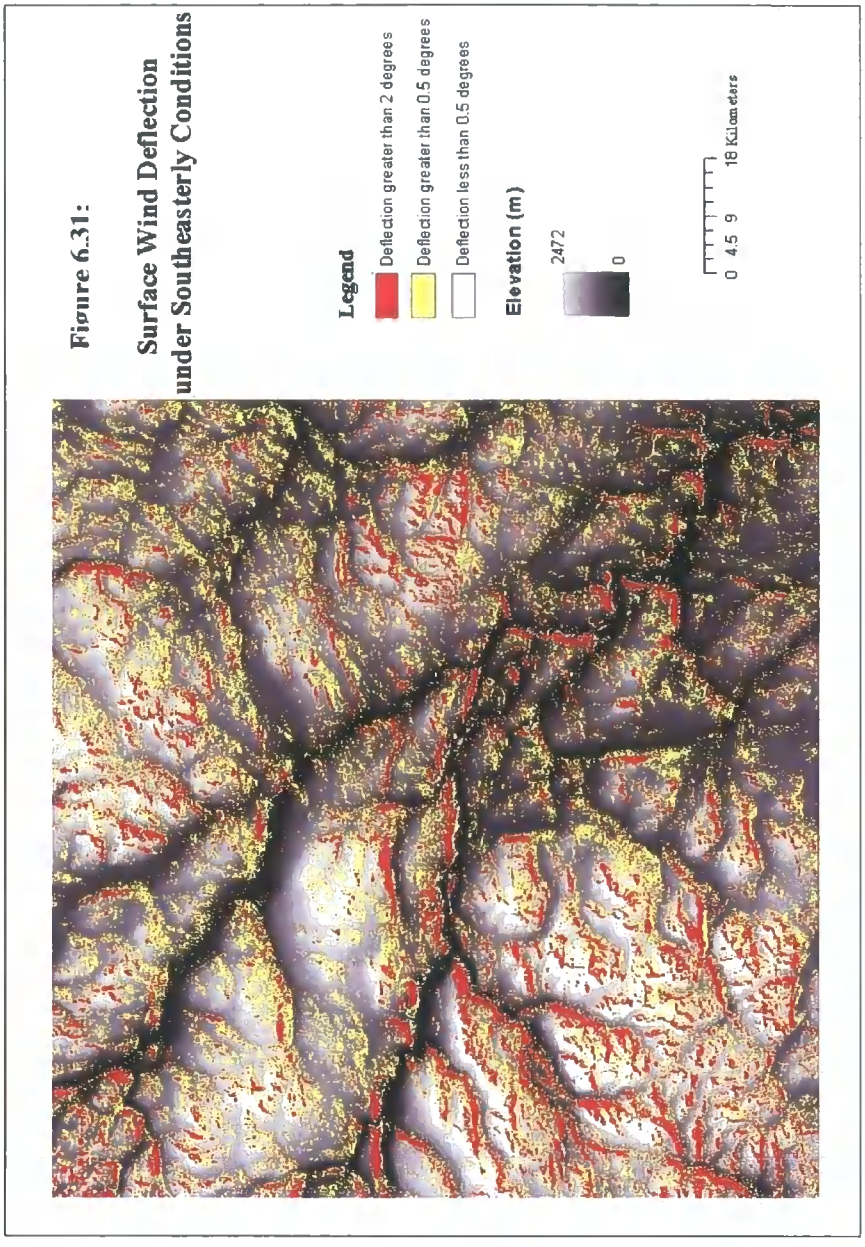
Figure 6.31:
Surface Wind Deflection under Southeasterly Conditions
Legend
Deflection greater than 2 degrees
Deflection greater than 0.5 degrees
Deflection less than 0.5 degrees
Elevation (m)
2472
0
0 4.5 9 18 Kilometers

Seasonality was predicted using sine and cosine components as discussed earlier in section 6.2.3.1 (Table 6.27) and used in a regression analysis with the altitude at which the free air measurement was taken to predict seasonally variant velocity profiles. This procedure is summarised in Figure 6.32.

Cosine Function	Sine Function	Season
0.707106781	0.707106781	1: Winter
-0.707106781	0.707106781	2: Spring
-0.707106781	-0.707106781	3: Summer
0.707106781	-0.707106781	4: Autumn

Table 6.27: seasonality predictions

Ninety six observations were used in the regression analysis, four stations for four seasons at five altitudes. The regression is statistically significant at the 95% confidence level and each of the independent variables provide a statistically significant contribution to accounting for the variability within the dataset. The root mean square error is 1.15 m s^{-1} and altitudinal lapse rate is 0.001 m s^{-1} per meter.

The regression coefficients provide the following model where speed V is given by:

V = 0.001(Height Above ground) + 2.055(Sine function) – 2.397(Cosine function) + 9.943

and implemented in a spatial model as

V = (0.001 * 1) +(2.055 * (sine(2 * PI * ((2 - 0.5) / 4))))
- (-2.397 * (cos(2 * PI * ((2 - 0.5) / 4)))) + 9.943)

Examination of the values of T_m show positive values for all stations, indicating slower flows than predicted (Table 6.29). Predictions were made on a seasonal temporal scale which was the most suitable resolution for the data which was provided in seasonal format. This temporal resolution was further justified as seasonal variations are also present in the distribution of free air flows,

suggesting that processes within the boundary layer and surface interactions impose controls on surface flow.

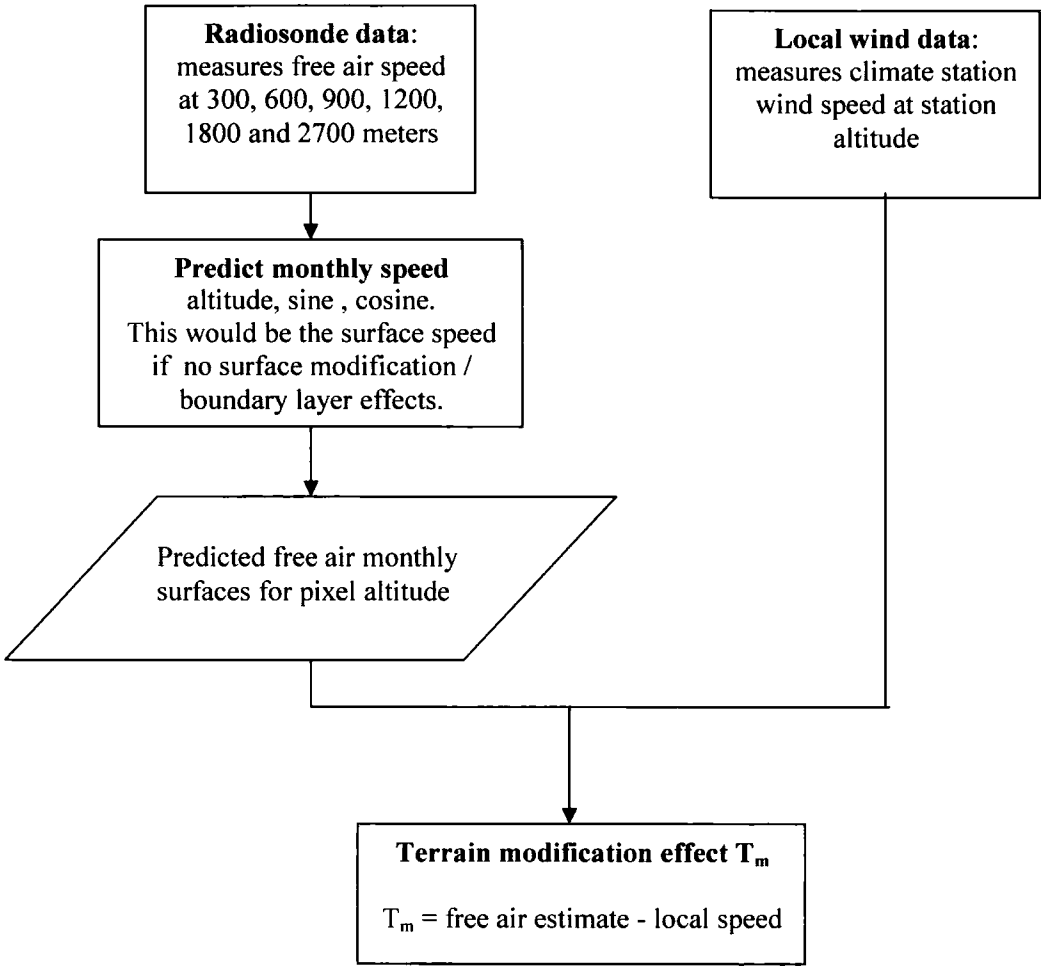

Figure 6.32: Initial stage of flow predictions

Examination of the spatial variation in the degree of modification provides a limited insight into the geomorphological characteristics of these sites, as the limited number of stations prevents statistically meaningful interpretations. Yet it is possible to suggest that local topographic conditions are related to the extent of the modification, as summarized by Table 6.30.

Number of obs = 96
F(3, 92) = 77.21
Prob > F = 0.0000
R-squared = 0.7157
Adj R-squared = 0.7064
Root MSE = 1.5882

	SS	df	MS
Model	584.242	3	194.747
Residual	232.059	92	2.522
Total	816.3	95	8.593

	Coef.	Std.Err.	t	P>|t|	[95% Conf.Interval]	
Altitude	0.0013088	0.0002022	6.47	0.000	0.0009027	0.0017104
Sin	2.055029	0.2292369	8.96	0.000	1.599745	2.510313
Cosine	-2.397387	0.2292369	-10.46	0.000	-2.852671	-1.942102
Cons	9.942974	0.3002875	33.11	0.000	9.346577	10.53937

Table 6.28: Regression statistics for wind profile predictions

Station	Ranked Modification	Terrain Description
13670	1	Sheltered
15720	3	Valley
16740	5	Valley
55290	2	Sheltered
61770	4	Valley

Table 6.30: Local modifications and terrain

T_m exhibits seasonal fluctuations indicating variations in degree of modification imposed by the surface on the vertical velocity profile (Table 6.29 and Figure 6.35). Autumn and winter exhibit the greatest values of T_m when westerly patterns are dominating. This suggests that although the flow characteristics of the different pressure systems are represented in the free air records different near surface processes also contribute to surface flow vectors. This may be in part a function of the local thermal regime where spring and summer, when convectional cells develop, are characterized by lower values of T_m where flows are faster, and more stagnant convective conditions in winter and autumn result in lower surface flows where topographic sheltering can more effectively retard flows.

Station	Winter			Spring		
	Speed (m/s)	Predicted (m/s)	T_m (m/s)	Speed (m/s)	Predicted (m/s)	T_m (m/s)
13670	0	13.1	13.1	0.0	6.8	6.8
15720	3.8	13.1	9.3	3.8	6.8	3.0
16740	3.8	13.1	9.3	3.8	6.8	3.0
55290	1.3	13.1	11.8	1.3	6.8	5.5
61770	3.8	13.1	9.3	3.8	6.8	3.0
	Summer			Autumn		
	Speed (m/s)	Predicted (m/s)	T_m (m/s)	Speed (m/s)	Predicted (m/s)	T_m (m/s)
13670	0	9.7	9.7	0.0	10.2	10.2
15720	6.3	9.7	3.4	3.8	10.2	6.4
16740	6.3	9.7	3.4	1.3	10.2	8.9
55290	3.8	9.7	5.9	6.3	10.2	3.9
61770	6.3	9.7	3.4	3.8	10.2	6.4

Table 6.29: Predicted wind speed and terrain modification effects by station and season

Attempts to characterize these contextual controls followed two main strands, modelling flow separation and characterizing roughness. Contextual measures such as valley and ridge structures were not explored.

II. Flow separation

Obstacles on a terrain surface can modify the direction and speed of surface flows. The parameterization of flow vectors moving around or over obstacles is possible at a number of different complexity levels, ranging from complex 3-dimensional flow models to simpler measures, using focal rather than landform scale modifications. The approach adopted here was selected to provide the most appropriate modification to flow for the terrain characteristics. Large glaciated valleys, smaller tributary valleys and steep slopes dominate. Flow on and within these landforms with directional modification is dependent upon upwind structures, specifically breaks in slope. In addition to landform scale modifications, where flow is simulated diverging around the structure as an integrated whole, simulations are also possible using focal or local terrain information. The latter provides significant computational and time savings and can predict upwind breaks equally as

effectively. Landform scale predictions are more suited to larger scale climatic modelling rather than small valley scale processes.

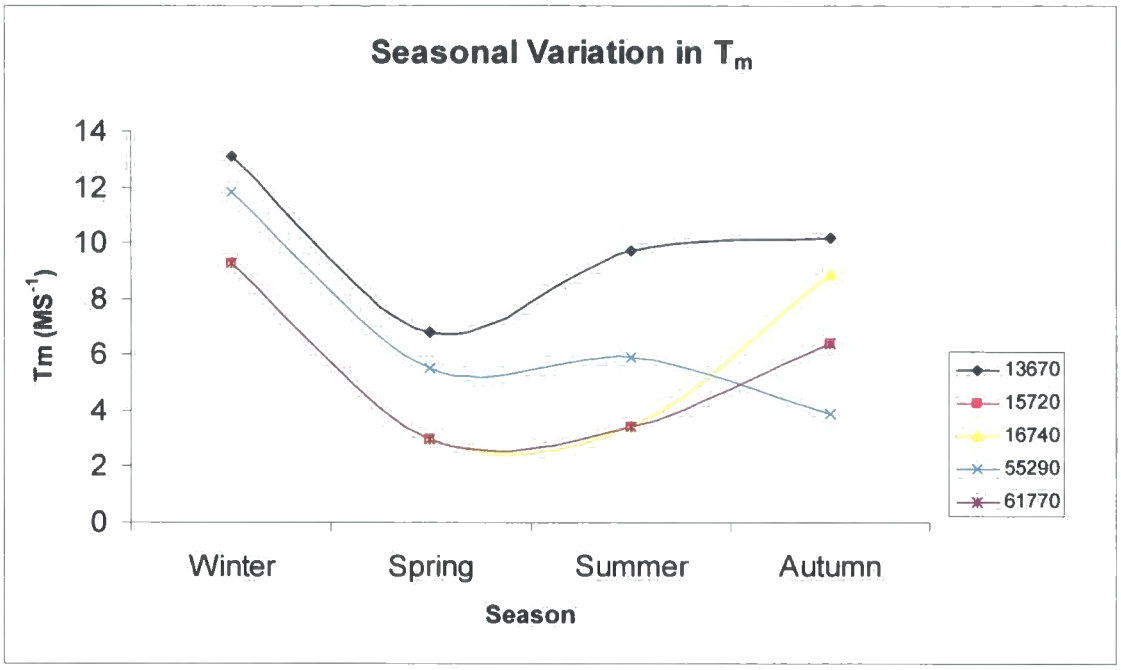

Figure: 6.33: Seasonal varations in T_m

Ryan's (1977) sheltering effect, F_u, characterizing the shelter-defining cell, the cell with greatest upward slope, was used to model upwind breaks of slope and flow separation, but was applied at a number of spatial scales to ensure meaningful and appropriate results. This was to ensure that the most critical or influential break was selected rather than just the nearest. This evaluation is a component critical to any analysis on a DEM, where local noise or roughness is differentiated from landform or land surface trends or variability,

$$F_u = E' \arctan (0.17G_p)/100 \qquad \text{(Equation 6.25)}$$

where, G_p is percentage slope to the upwind horizon (maximum of 100%), under mixing conditions (a non stratified atmosphere, section 6.8.2). E' varies as a function of elevation. Ryan (1977) fixed E' for the maximum elevation in the data (1220 m). This was adjusted to account for the greater range in altitudes found within the Jotunheim and was changed from:

$$E' = 2 - 0.0016\ E \qquad \text{(Equation 6.26)}$$

to,

$$E' = 2 - 0.0008\,E \qquad \text{(Equation 6.27)}$$

Using the calculations outlined by Ryan (1977) where E' was set to vary from 0 at the maximum altitude (2500 m) and 1 at the minimum altitude (0 m).

Two applications of the shelter-defining algorithm were used to identify local and outlying obstacles, to establish which provided the most useful measure. Clearly the distance to and size of the obstacle will alter its impact on flow. Search distances employed vary between authors however focusing on the absolute value of this distance alone can be misleading as consideration of the terrain roughnes and DEM resolution is also necessary. In contrast a 1,000 m search distance was used by Winstral and Marks (200a,b). In this research the nearest upslope gradient and the maximum within 500, 1,000, 5,000 and 10,000 m upwind were investigated. The variability in the upwind slopes through each of these buffer sizes provided information on the variability of terrain for each of the stations in the analysis (Figures 6.34-6.36 and Table 6.31).

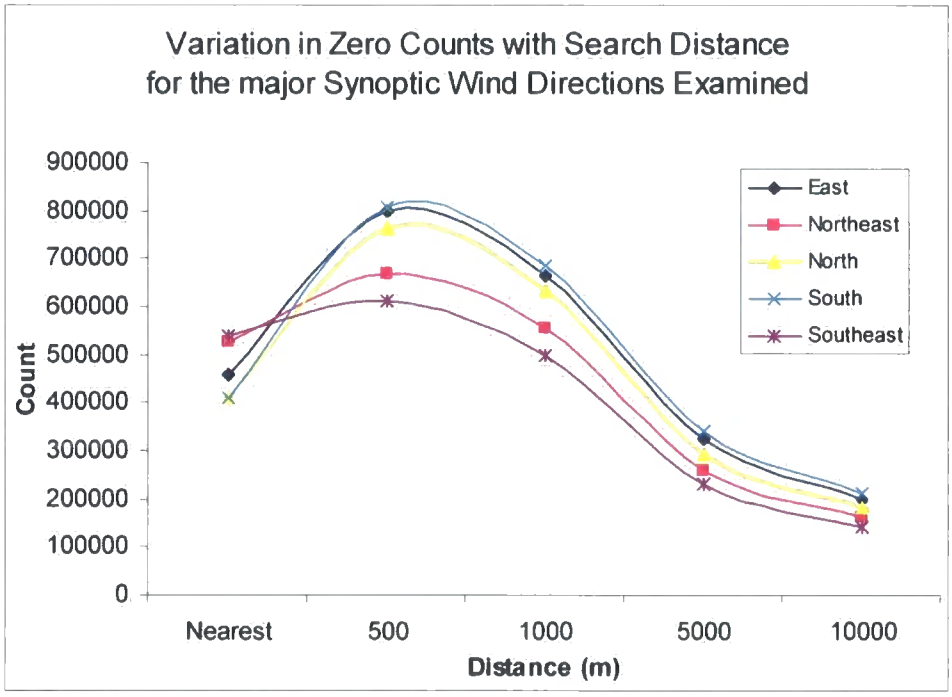

Figure 6.34 Variation in zero counts with search distance

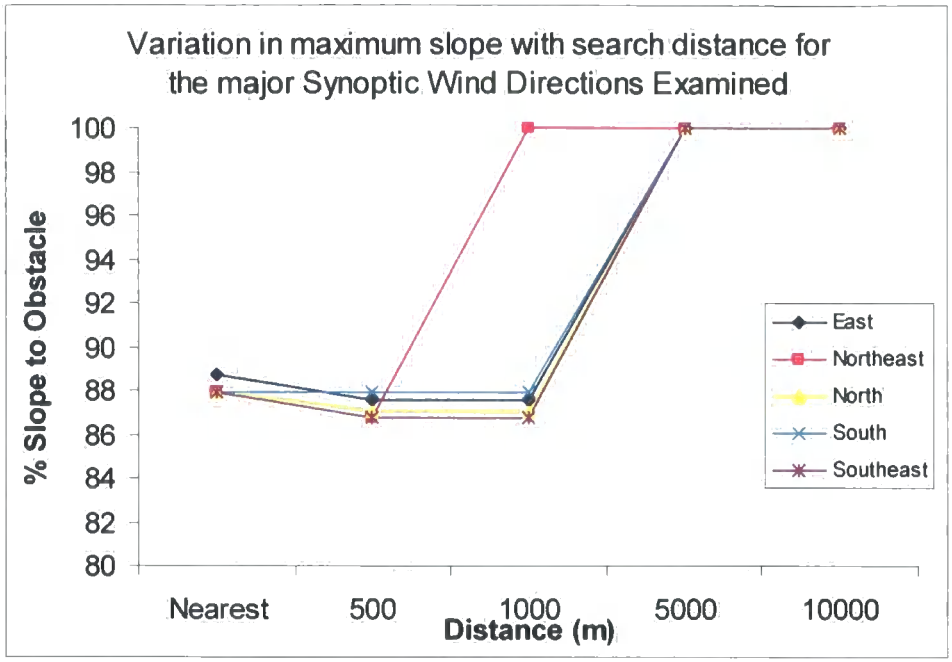

Figure 6.35 Variation in maximum slope with search distance

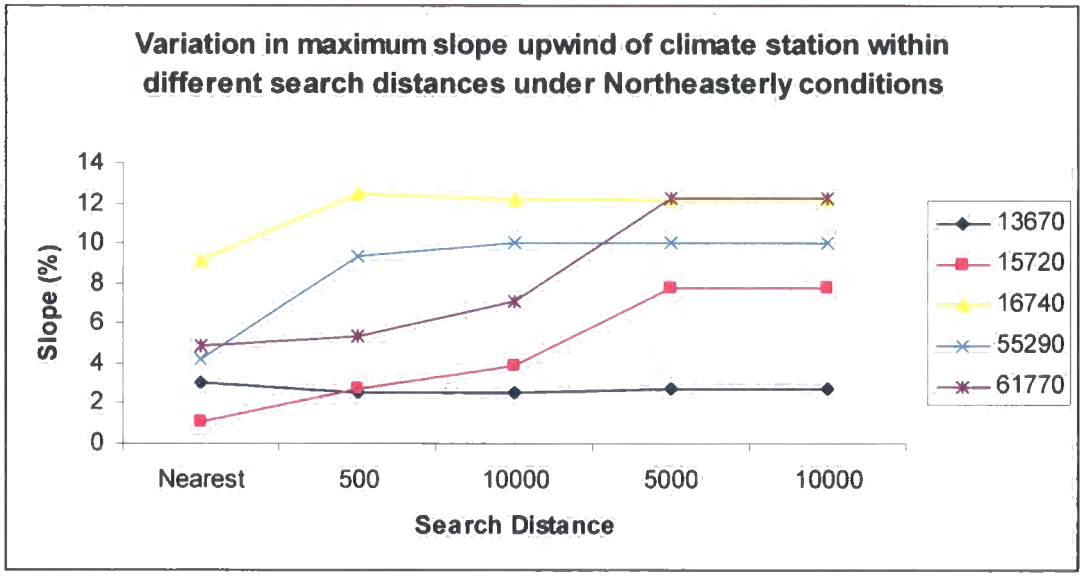

Figure 6.36 Variation in maximum upwind slope at climate stations

Stations 15720 and 61770 exhibit achieve greater upwind gradients with increasing buffer distances, the other stations exhibit a consistent upwind gradient, this uniformity could result under two conditions, either on a regularly structured landform with spatially organised structures or on a

slope, with breaks in slope marked by smaller structures located on the slope (Figure 6.36). Stations 15720 and 16740 are located within valleys, indicating upwind is upslope which has an increasingly steep gradient.

Wind Direction	Distance (m)	Min	Max	Mean	Stdev	Zeros
East	Nearest	0	88.71	8.82	10.30	459161
	500	0	87.58	6.20	9.57	797093
	1000	0	87.58	6.92	9.76	665005
	5000	0	100	8.28	9.59	322524
	10000	0	100	8.66	10.15	199299
South	Nearest	0	87.91	9.44	10.42	410037
	500	0	87.91	6.51	9.93	808177
	1000	0	87.91	7.33	10.16	684492
	5000	0	100	8.86	9.99	339505
	10000	0	100	9.24	10.44	211930
Southeast	Nearest	0	87.91	7.36	9.17	540841
	500	0	86.84	6.81	9.17	612433
	1000	0	86.84	7.65	9.39	499121
	5000	0	100	9.02	9.27	231941
	10000	0	100	9.32	9.65	143310
North	Nearest	0	87.91	9.44	10.42	409861
	500	0	87.03	6.61	9.74	761909
	1000	0	87.03	7.43	9.94	634301
	5000	0	100	8.94	9.71	293541
	10000	0	100	9.29	10.19	181965
Northeast	Nearest	0	87.91	7.50	9.24	528811
	500	0	86.84	6.51	9.02	668585
	1000	0	100	7.29	9.25	556583
	5000	0	100	8.82	9.24	258483
	10000	0	100	9.21	10.00	161201

Table 6.31: Distribution of slopes to obstacles for study area

On balance, the greatest slope within 5,000 m, was found to provide the best results when modified estimates were compared to observed measurements and when the nature and scale of the breaks were investigated within the surfaces in conjunction with consideration of landforms and structures within the valleys. Although the largest upwind break in slope within this search radius may ignore smaller less significant breaks closer to the source pixel, these local features are largely very small and are expected to have only a minor impact on flow as show in Table 6.32 and Figure 6.37.

Wind Direction	Distance (m)	Min	Max	Mean	Stdev
East	Nearest	0	0.27	0.02	0.02
	500	0	0.27	0.01	0.02
	1000	0	0.26	0.01	0.02
	5000	0	0.37	0.02	0.02
	10000	0	0.34	0.02	0.02
South	Nearest	0	0.26	0.02	0.02
	500	0	0.25	0.01	0.02
	1000	0	0.25	0.01	0.02
	5000	0	0.34	0.02	0.02
	10000	0	0.34	0.02	0.02
Southeast	Nearest	0	0.27	0.01	0.02
	500	0	0.26	0.01	0.02
	1000	0	0.26	0.01	0.02
	5000	0	0.28	0.02	0.02
	10000	0	0.32	0.02	0.02
North	Nearest	0	0.26	0.02	0.02
	500	0	0.26	0.01	0.02
	1000	0	0.26	0.02	0.02
	5000	0	0.29	0.02	0.02
	10000	0	0.29	0.02	0.02
Northeast	Nearest	0	0.27	0.01	0.02
	500	0	0.26	0.01	0.02
	1000	0	0.26	0.01	0.02
	5000	0	0.32	0.01	0.02
	10000	0	0.34	0.01	0.02

Table 6.32: F_u distributions for seasons and distances for the study area

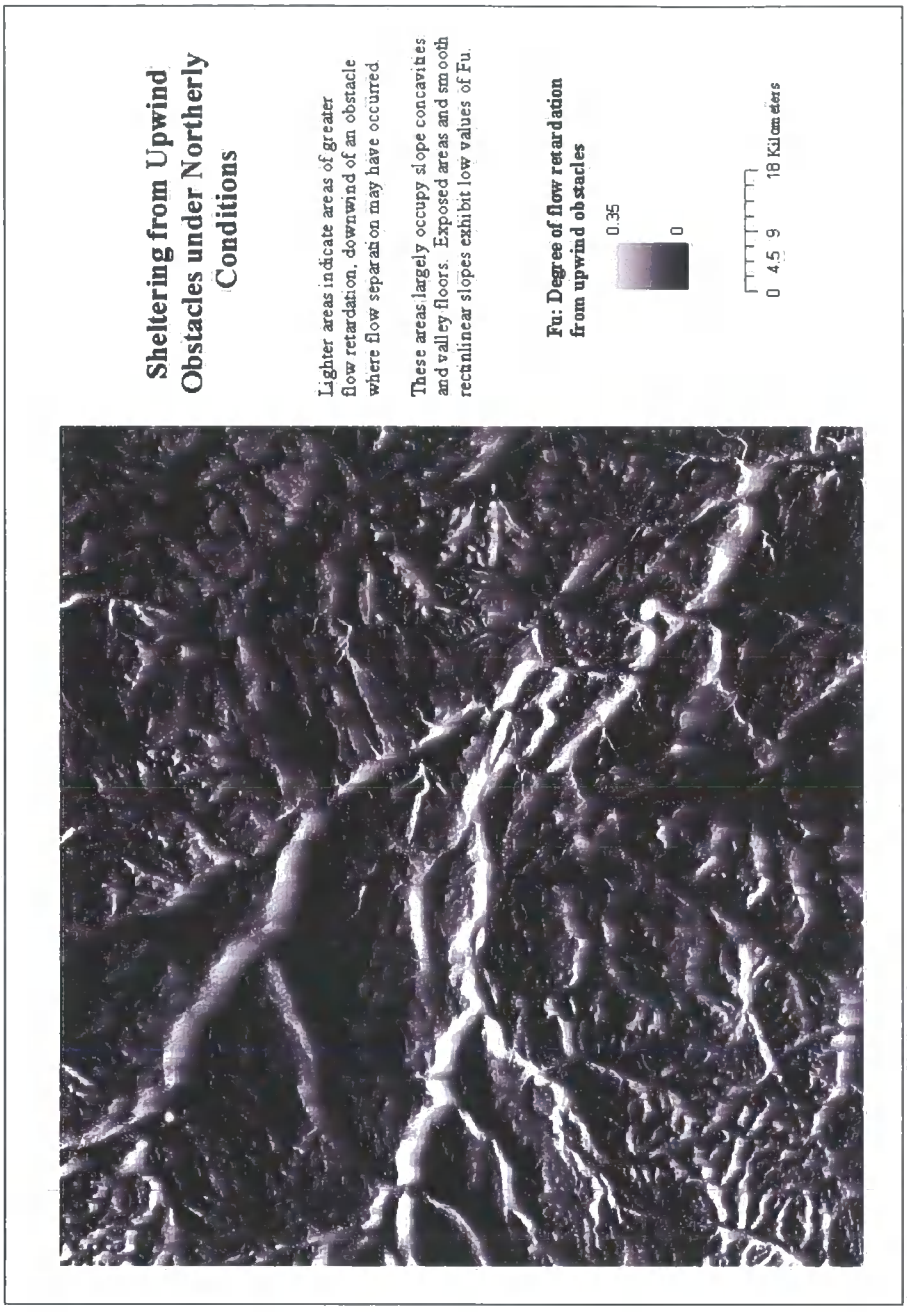

Figure 6.37: Sheltering from upwind obstacles under northerly conditions

A number of stages were needed to calculate the effect of upwind obstacles these are outlined in Figure 6.38.

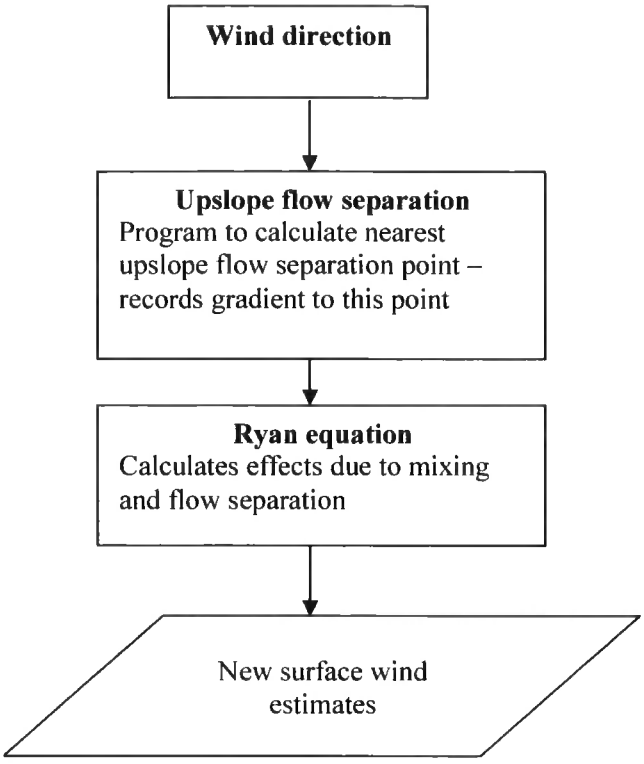

Figure 6.38: Accounting for the effect of upwind obstacles

A Java program was written to extract the upwind obstacles. Called *UpSlope.java*, it contained two different methods; getMaxGradient and getNearGradient.

New surface wind velocities were calculated, modifying initial wind velocities (V_b), which were uniformly set throughout the DEM: data to create more informed estimates was not available. This was felt to provide the most accurate initial surface as predicting spatial variability in complex terrain using data from five stations would not produce statistically significant results. This is in line with other approaches where initial or boundary conditions are set at the start of a model run.

$$V_u = V_b - (F_u V_b) \qquad \text{(Equation 6.28)}$$

Resultant surfaces showed meaningful spatial distributions, but they imply that it is possible to improve predictions using roughness measures extending the work reported by Ryan (1977) and Purves *et al.*, (1998) which only looked upslope for flow separation and did not account for the

large modification that terrain imparts on wind speeds. Surface roughness was examined as a method of improving these predictions.

III. Roughness

Surface roughness plays a critical role in controlling flow characteristics near the surface. Although upwind obstacles define separation points and the downwind wake area, they cannot characterise or quantify spatially distributed structures or regions. Surface roughness measures provide a method of quantifying spatial organisation, variability and smoothness by measuring the topographic variation within an area. Rougher areas impose a greater frictional drag and consequently retard surface flows to a greater degree than smoother surfaces which impose less drag.

Roughness measures exist in a number of different forms characterizing different terrain components. The surface roughness measure developed here used breaks of slope and altitudinal change to quantify topographic variability. Roughness, R is defined as:

$$R = Z_{sd} * A_{sd} \qquad \text{(Equation 6.29)}$$

Where Z_{sd} is the standard deviation of altitude and A_{sd} is the standard deviation of the sine of aspect in degrees. Breaks of slope and altitudinal variation were used as these were felt to most effectively characterize terrain roughness for flow applications. The area over which the calculations are made determines the scale of the measurement and should be based on the scale of landform, landscape or process under investigation. Examining the rate of change of roughness at different scales provides information on the structure of the landscape, topographic form and context (Figure 6.12).

Examining the rate of change of roughness within the study area, specifically looking at areas centered on the climate stations, provides information on how flows may operate at these sites and aids the interpretation of recorded flows. Surface roughness was calculated for kernels of width 3, 5, 9 and 12 pixels, 300, 500, 900 and 1200 m respectively (Figure 6.39).

Stations 1, 2 and 3 are located within a topographically rougher area at coarse resolutions whereas stations 4 and 5 are fairly isometric with respect to the surface roughness measures presented here. As roughness is scale dependent the rate of change (R_r) of roughness provides a more useful

measure, calculated here as the difference between the coarsest and finest measure of roughness over the distance of 900 m.

Rate of change of roughness (R_r) was defined as:

$$R_r = (R_{12} - R_3) / 900 \qquad \text{(Equation 6.30)}$$

Where, R_{12} is the surface roughness within a 12 pixel width kernel and R_3 is the surface roughness within a 3 pixel width kernel.

	Minimum	Maximum	Mean	Standard Deviation
Rough 33	0	201	12.7	11.6
55	0	213	21.8	17.9
99	0	278	37.5	27.5
12	0	306	47.7	32.8
Scaled Rate	0.265	-0.04	0.039	0.027
Rough 3L	0	0.401	0.025	0.023
5L	0	0.426	0.044	0.036
9L	0	0.555	0.075	0.055
2L	0	0.612	0.095	0.066
SR 3	0	0.589	0.039	0.037
5	0	0.707	0.068	0.057
9	0	0.965	0.117	0.088
2	0	1.079	0.149	0.106
Roughp 3A	0	0.879	0.408	0.114
5A	0	0.917	0.477	0.113
9A	0	0.991	0.554	0.111
2A	0	1.019	0.592	0.110

Table 6.34 Roughness statistics

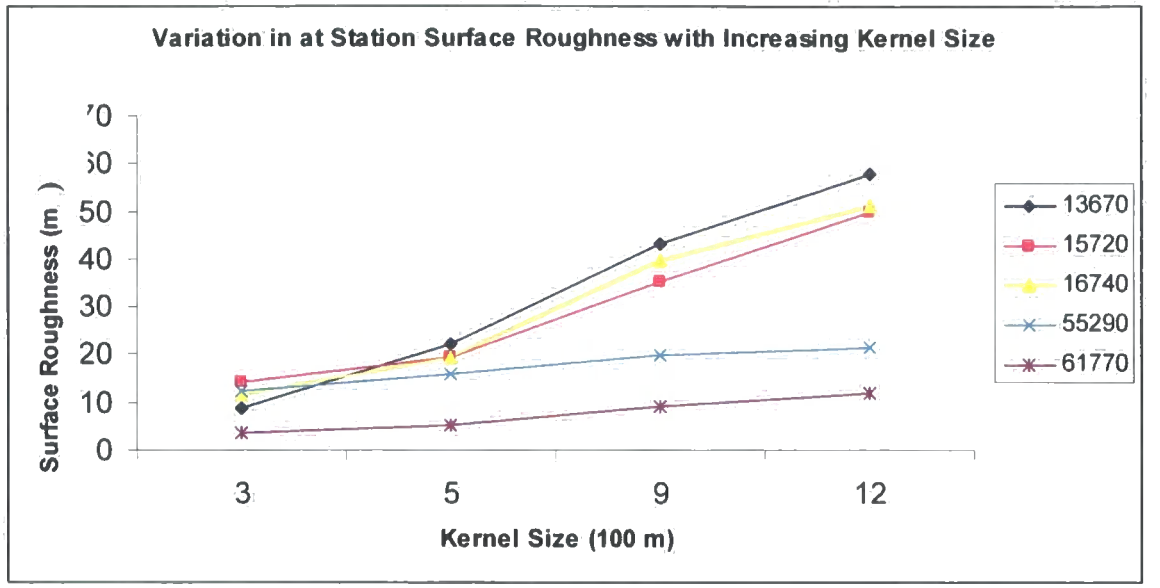

Figure 6.39: Rate of change of roughness with kernel size for climate stations

Both the rate of change of roughness and the finest scale roughness are important when considering flow. Local roughness provides information about terrain conditions immediately surrounding a location, which will impose a local modification to the flow. Although influential, local modifications need to be considered along side larger scale processes, considering the terrain within the focal area to establish whether this will also impose an amplified or alternative terrain modification effect. However, this is a local measurement and only records a small scale phenomenon located within a larger environment. Considering the rate of change of roughness at a location, three scenarios are possible:

I. An area is locally rougher than at a larger scale – a negative rate of change in roughness

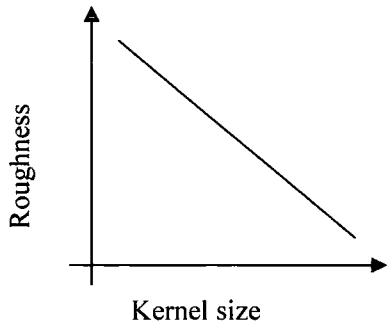

Under these conditions micro scale (100 – 300 m) wind speed decreases more than meso scale flows (300 – 900 m), flow is locally retarded but this is only a local modification to a potentially faster flow.

II. An area is smoother at the local scale and rougher at the coarser scale – a positive rate of change of roughness.

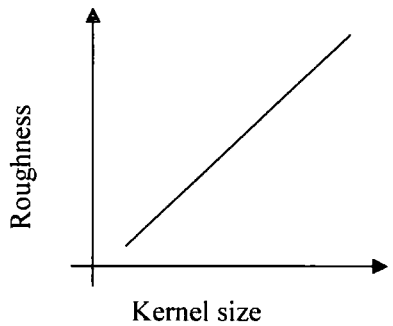

Wind speed at the meso scale decreases more than local speeds, locally flow is retarded but this effect is mirrored with a larger scale modification to slower wind.

III. An area has no variation in roughness with changing scale – no rate of change in roughness.

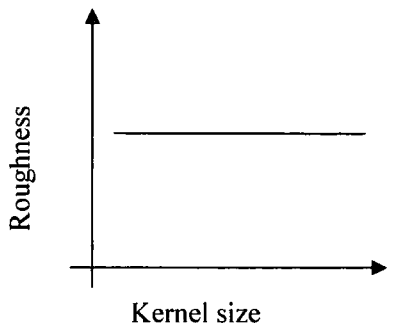

Wind speed at the meso scale and micro scale decreases equally, locally flow is retarded but this is part of a larger scale modification to slower wind.

Using these scenarios it is possible to develop a rule-based model to characterise how the rate of change of surface roughness will modify flow.

By scaling the measure of roughness and the rate of change of roughness, it is possible to use these parameters to modify the velocity estimates created earlier. Roughness and the rate of change of roughness were calculated for an extended study area covering most of the Jotunheimen and valleys to the east (this provides a more representative range of values), and the minimum and maximum values for these derived measures were used to calculate the scaling algorithms, scaling is achieved by:

$$\text{Scaled value} = (\text{Observed} - \text{minimum}) / (\text{maximum} - \text{minimum}) \qquad \text{(Equation 6.31)}$$

Giving scaled rough values R_s as:

$$R_s = (\text{value} - 0) / (500 - 0), \text{ values ranging from } 0 - 0.619 \text{ for study area}$$

And scaled rate of scaled rate of change R_{rs} as:

$$R_{rs} = (\text{value} - -0.5) / (0.5 - - 0.5), \text{ values ranging form } 0.46 - 0.84 \text{ for study area.}$$

These were integrated as

If rate >= 1

$$\text{RoughS}_r = R_s * (1 + R_{rs})$$

If rate < 1

$$\text{RoughS}_r = R_s - (R_s * (1 + R_{rs}))$$

To use the amended roughness parameter to calculate the resultant windspeed, V_{ur}, gives:

$$V_{ur} = V_u - (V_u * (\text{RoughS}_r^{\wedge 0.25}) \qquad \text{(Equation 6.32)}$$

where an exponent of 0.25 gives the nonlinear change associated with near surface flows (Barry, 1980).

d Results indicated that the relationship between surface roughness and wind velocity was non linear. Thus it was modelled here using an exponential function: this type of relationship is present in many other physical systems including some of the climatic parameters modeled within this research.

Although a vertical velocity profile was predicted using free-air data, altitude quantified height above the surface not height above sea level. Altitudinal relationships were briefly discussed in section 6.8.3.1.2 and it was felt that within an alpine environment when exposure to free air varies considerably between valley ridge locations an altitudinal relationship would improve velocity predictions. This was incorporated as an altitudinal flow factor, Z_f, scaled using the maximum and minimum altitudes within the extended study area, given by:

$$Z_f = (\text{value} - 0)/(2472 - 0) \qquad \text{(Equation 6.33)}$$

Where the resultant predicted velocity, V_p is given by:

$$V_p = V_{ur} - (V_{ue} * Z_f) \qquad \text{(Equation 6.34)}$$

Spatially distributed values of V_p show geomorphologically meaningful results, with higher wind speeds around mountain peaks and in the center of the larger valleys and lower wind speeds over the rougher more undulating terrain and along the valley sides (Figure 6.45).

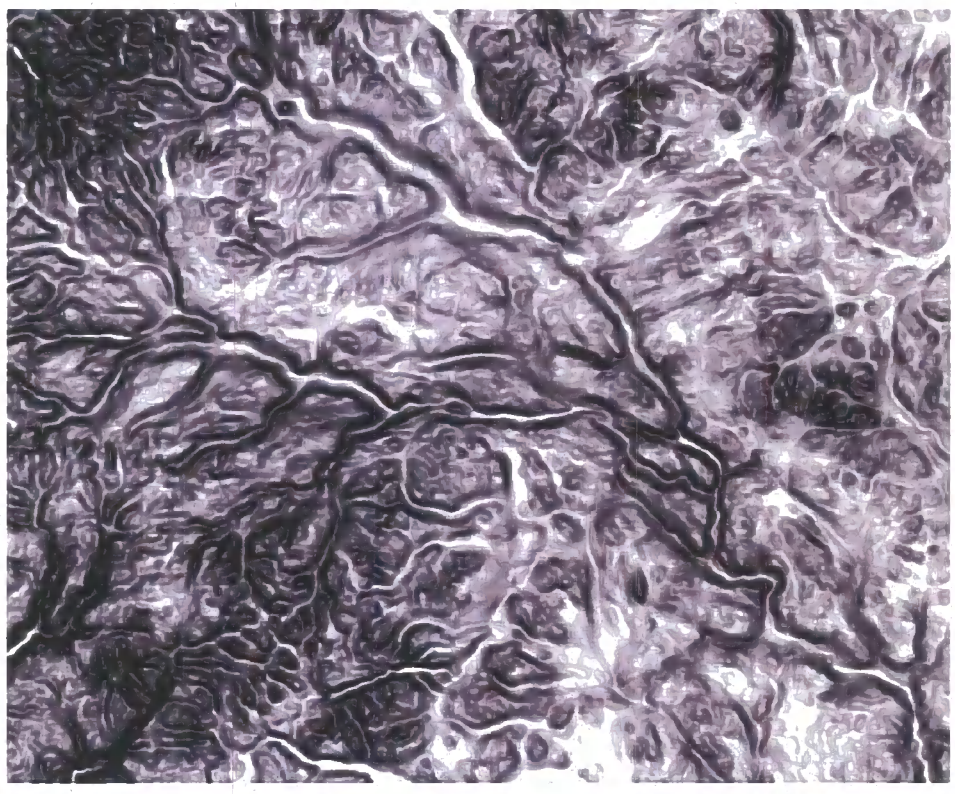

Figure 6.41:

Vur: Roughness and Obstacle Resultant Winter Wind Field under Easterly Conditions

Composite wind velocity field, representing retardation of flow by upwind obstacles and surface roughness. Roughness measures accounted for local and focal trends. Highest flows are found in exposed sites away from upwind obstacles. The strong terrain component in this prediction process is evident in the resultant image.

Figure 6.42:

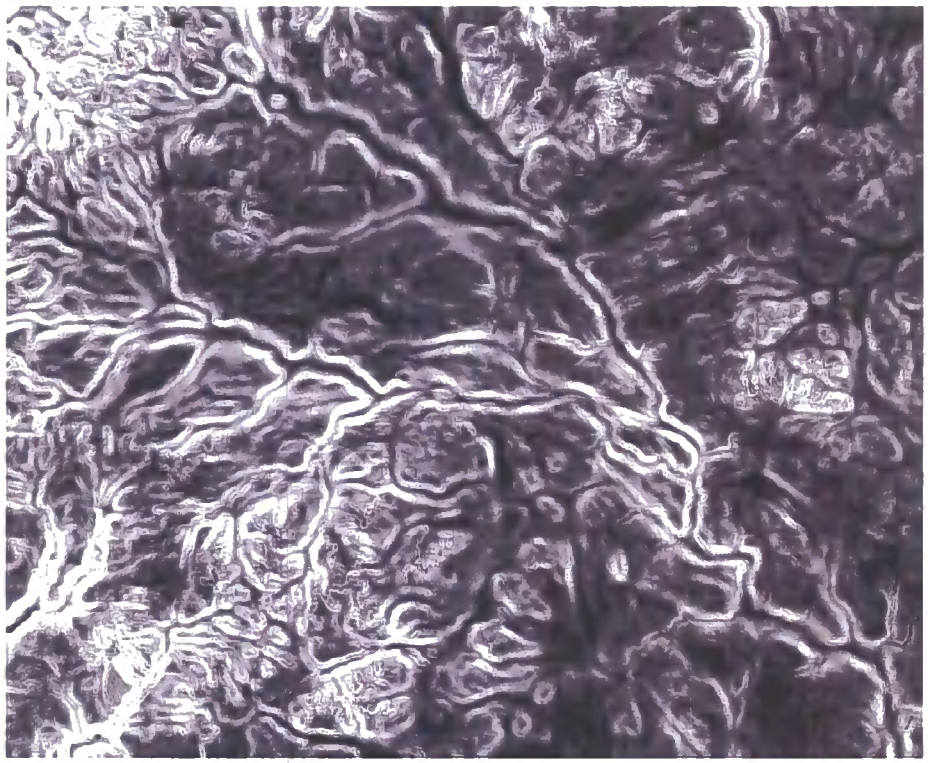

Rrs: Scaled Rate of Change of Surface Roughness

Scaled rate of change of surface roughness. Areas of high change indicate transitions from smoother to rougher areas, these occupy footslope locations and areas adjacent to ridges and troughs.

These areas are important to identify in climatic predictions as it provides a measure of the representativeness of local measures, for example how representative local station values may be. Areas with a high rate of change of surface roughness may suggest heterogeneous conditions and less representative local records.

Areas with low rate of change of surface roughness suggest homogenous conditions where local measures are likely to be indicative of larger scale trends.

Surface Roughness

1
0

0 5 10 20 Kilometers

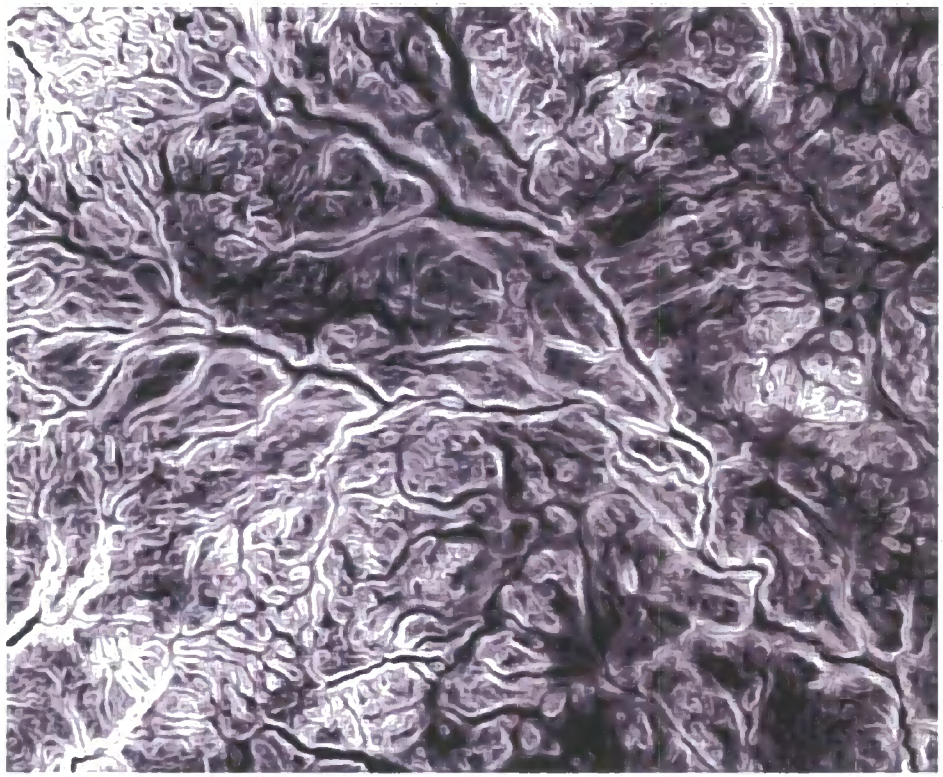

Figure 6.43:

RoughSr: Resultant Roughness Parameter: 9 * 9 Kernel

Resultant roughness parameter surface accounting both for local variability within a 9 * 9 kernel and the rate of change of roughness within the surrounding area.

Highest flow retardation occurs at steep breaks in slope and in complex relief areas, these are apparent on foothills and in the upland areas in the southwest of the study area. These areas of complex terrain inhibit laminar flow unlike areas with lower parameter values which are both locally and focally smooth.

Surface Roughness

1
0

0 5 10 20 Kilometers

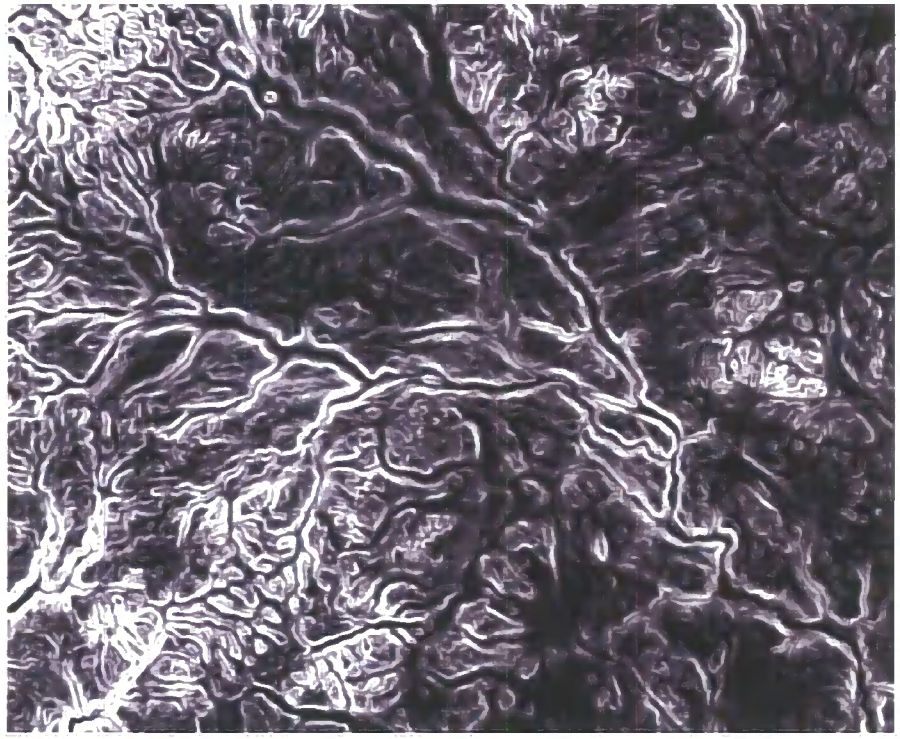

Figure 6.44:

Scaled local Roughness within a 9 * 9 kernel

Scaled surface roughness for a 9 * 9 kernel. Areas of highest roughness are found at sharp breaks in surface gradient, here shown around contour lines.

Areas of high surface roughness are associated with slow flows. Areas of low surface roughness are found along valley floors and on rectinlinear slopes, where faster flows are commonly found.

Surface Roughness

1

0

0 5 10 20 Kilometers

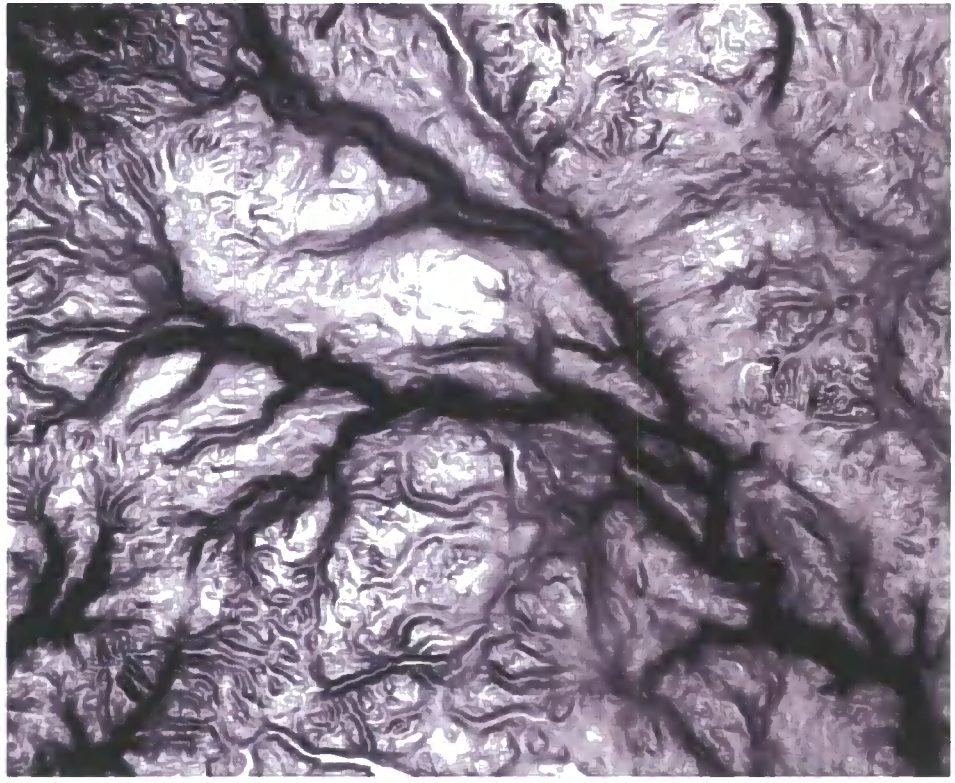

Figure 6.45:

Vp: Resultant Winter Wind Field under Easterly Conditions

Resultant wind velocity field, a composite of upwind obstacles, local and focal roughness and altitude. The terrain component in this prediction process is evident in the resultant image where highest velocities occur around peaks, but fast flows are also found along large valley apex.

The steps used to create the roughness modification are given in Figure 6.46 and Figure 6.48 summarises all of the steps in the wind flow prediction model.

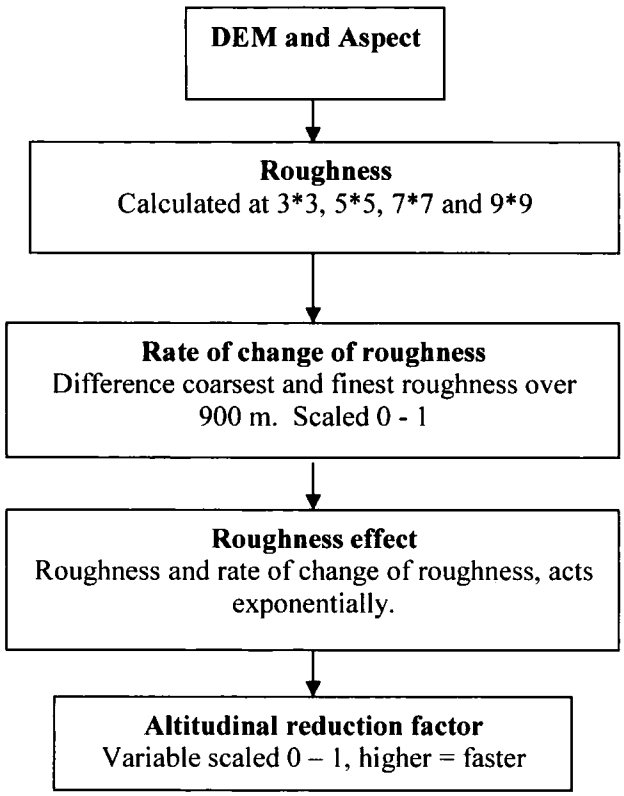

Figure 6.46: Steps used to create the roughness modification

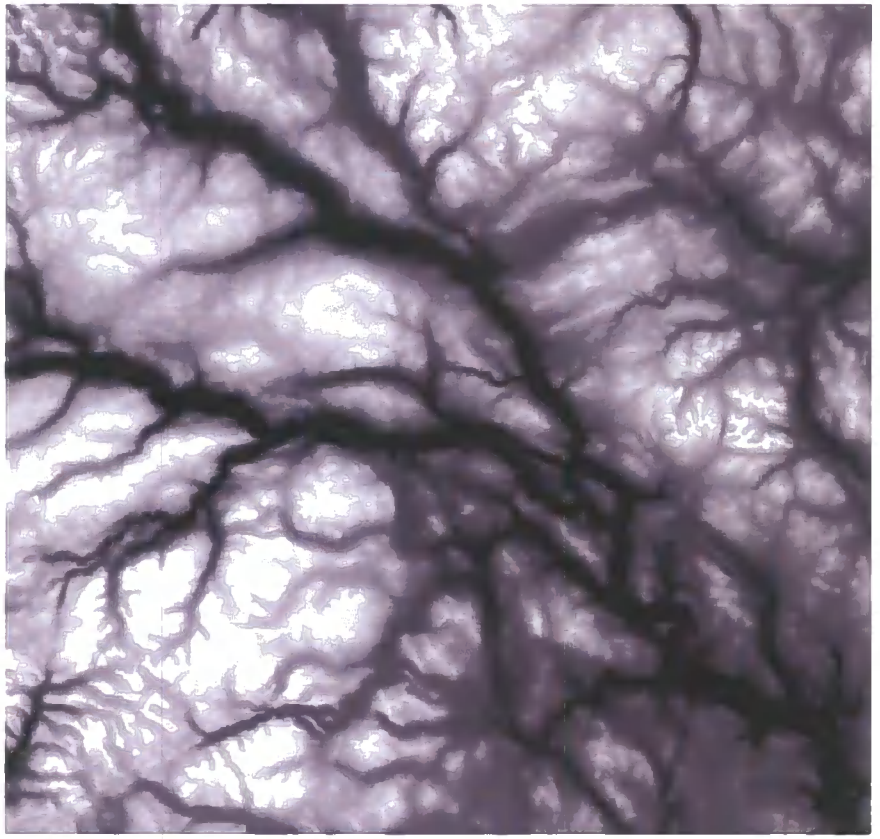

Figure 6.47:

Scaled Altitude Layer

Scaled Altitude Layer differentiating between different terrain conditions, lower sites received reduced flows.

Legend

High : 1.0

Low : 0.0

0 4.5 9 18 Kilometers

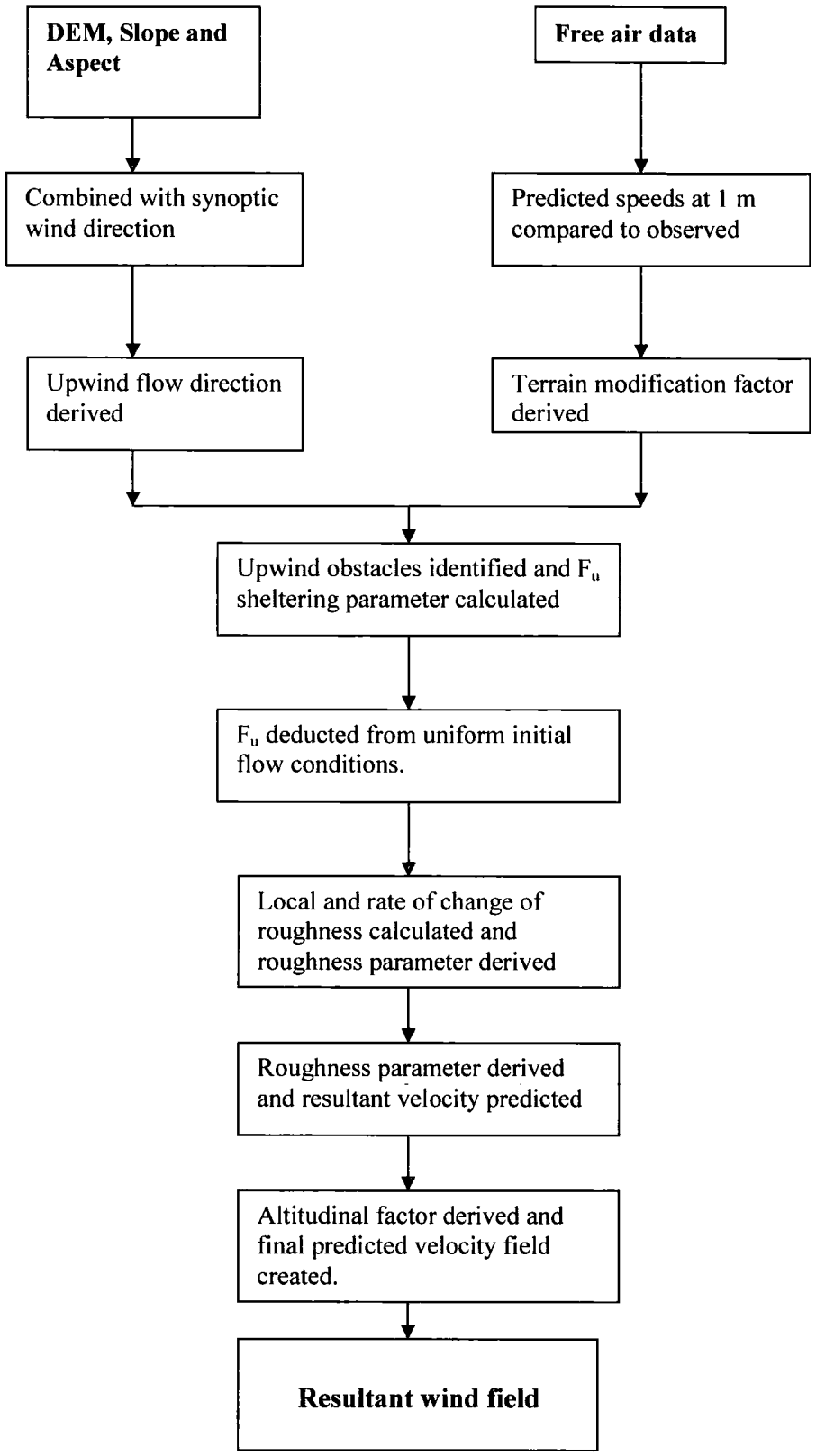

Figure 6.48: Summary of the wind flow prediction model

Wind speeds were assumed constant throughout a season, varying only as a function of wind direction. Initial investigations were made to predict local variability in wind speeds from local topographic form with promising results for further study. Analysis of the shape of frequency histogram of station wind speeds revealed correlations with local terrain (Table 6.35).

Station	Skewness	Kurtosis	Standard Deviation
1	2.37	5.5	14.73
2	3.4	11.98	18.97
3	2.59	6.48	16.04
4	1.48	1.45	12.55
5	3.64	13.43	22.22

Table 6.35 Wind speed distribution characteristics

Stations 2 and 5 have consistently peaked histograms and are located close to valley centers reporting faster flow. This implies that conditions are consistent and valley winds dominate. Station 4 has predominantly slow flow and is located in a more exposed site with less consistent wind speeds, where more unpredictable flow modification takes place. This initial analysis suggests that it may be possible to predict the standard deviation of wind speeds at a location using distance from valley apex and local roughness.

Other predictive wind flow models or analytical solutions exist. These include *MS3DJH/3R* developed by Walmsley *et al.* (1982) and utilized by Essery (2000) and Essery *et al.* (1999), and also the work undertaken by Jackson and Hunt (1975) on the changes in wind speed and shear stress around hills of different sizes and shapes. However, the model developed by Vosper (2002, 2003) is considered more suited to the terrain in the Jotunheimen and could be manipulated and used more effectively with in-house developers. Although both models become unstable in areas of steep terrain the model developed by Walmsley *et al.* (1982) is specifically designed for low hills, but the model developed by Vosper (2002, 2003) was tested on the Isle of Arran, a formerly glaciated mountainous area.

		Free Air	V_u			V_{ur}			V_p		
			Min	Max	Mean	Min	Max	Mean	Min	Max	Mean
Winter	NE	13.10	8.97	13.10	12.88	0.10	13.10	5.75	0	7.23	2.74
	E	13.10	8.69	13.10	12.90	0.10	13.10	5.76	0	7.27	2.74
	S	13.10	8.68	13.10	12.88	0.10	13.10	5.75	0	7.31	2.74
	SE	13.10	9.39	13.10	12.88	0.10	13.10	5.75	0	7.27	2.74
	N	13.10	9.28	13.10	12.87	0.11	13.10	5.75	0	7.29	2.74
Spring	NE	6.80	4.65	6.80	6.69	0.05	6.80	2.99	0	3.75	1.42
	E	6.80	4.51	6.80	6.69	0.05	6.80	2.99	0	3.77	1.42
	S	6.80	4.51	6.80	6.69	0.05	6.80	2.99	0	3.80	1.42
	SE	6.80	4.87	6.80	6.69	0.05	6.80	2.99	0	3.77	1.42
	N	6.80	4.82	6.80	6.68	0.06	6.80	2.98	0	3.78	1.42
Summer	NE	9.70	6.64	9.70	9.54	0.07	9.70	4.26	0	5.36	2.03
	E	9.70	6.44	9.70	9.56	0.07	9.70	4.27	0	5.39	2.03
	S	9.70	6.44	9.70	9.55	0.07	9.70	4.26	0	5.42	2.03
	SE	9.70	6.96	9.70	9.55	0.07	9.70	4.27	0	5.59	2.03
	N	9.70	6.88	9.70	9.54	0.08	9.70	4.26	0	5.40	2.03
Autumn	NE	10.19	6.98	10.19	10.02	0.07	10.19	4.48	0	5.63	2.13
	E	10.19	6.76	10.19	10.03	0.07	10.19	4.48	0	5.66	2.13
	S	10.19	6.76	10.19	10.02	0.07	10.19	4.48	0	5.66	2.13
	SE	10.19	7.31	10.19	10.02	0.07	10.19	4.48	0	5.65	2.13
	N	10.19	7.22	10.19	10.02	0.09	10.19	4.47	0	5.67	2.13

Table 6.36 Seasonal variation in wind speed variables

6.6.8.4. **Three dimensional modeling**

The model *3dvom2.6.5* developed by Vosper (2002, 2003), predicts wind vectors through terrain using three-dimensional linearised equations of motion. Using the boundary conditions of the free air direction the model assumes a steady upstream geostrophically balanced wind and potential temperature field varying as a function of altitude. Further inclusion of a parameterisation of the Coriolis force, acceleration due to gravity, conservation of momentum and thermodyamic equations (not relating to those mentioned earlier) modifies the flow vector in three dimensions. Further modifications and perturbations to flow by turbulence and eddies are included using eddy viscosity

and the shear stress Reynolds divergence term which modifies background shear stresses and determines mixing lengths as a function of Richardson number. Output wind vectors are estimated using finite difference approximations and are initially driven by Reynolds shear stresses and turbulent heat fluctuations driving change in potential temperature fields and flow velocity. Further details of the model can be found in Vosper (2003). During the present study the model was run with five of the dominant free air directions, north, northeast, east, southeast and south on a grid of 128 rows and 128 columns with a 500 m resolution. A mean resampling algorithm was used to create the coarser scale resolution. Resampling was necessary in part to reduce the computational intensity of the operation and also to reduce the surface complexity, improving the performance of the model, whilst still retaining a sufficiently detailed wind field.

Further modifications to the DEM were required to minimise edge effects within the model. At the east and west edges the height of the topography at the outer 8 columns of the grid was set to 0. On the north and south edges 14 rows were set to have a zero height. Topography was smoothed linearly down to zero over 20 grid points (10 km from the edge of the data) to prevent sudden jumps at the edge of the DEM. A small amount of smoothing was applied after that to minimise grid-scale noise that can lead to numerical instability.

6.6.9. **Monthly wind surfaces**

Both the topographically derived flow modification wind vectors and the three dimensionally modelled wind vectors were used in the mass balance model, where modal wind conditions were used for each season.

Parameter	Temporal Resolution
Temperature	
Mathematical Modeling	Monthly
Mathematical Modeling with interaction term	Monthly
Mathematical modeling with topographic variables	Monthly
Seasonal lapse rates	Monthly
Diurnal Temperature	
Mathematical Modelling	Hourly
applied to temperature datasets	
Precipitation	
Power Function	Monthly
Cloud	
Monthly mean	Monthly
Proportional Predictions	5 days
Surface Wind	
Terrain predictions	Seasonal
3Dimensional modeling	5 days

Table 6.37: Climatic datasets used within the mass balance model

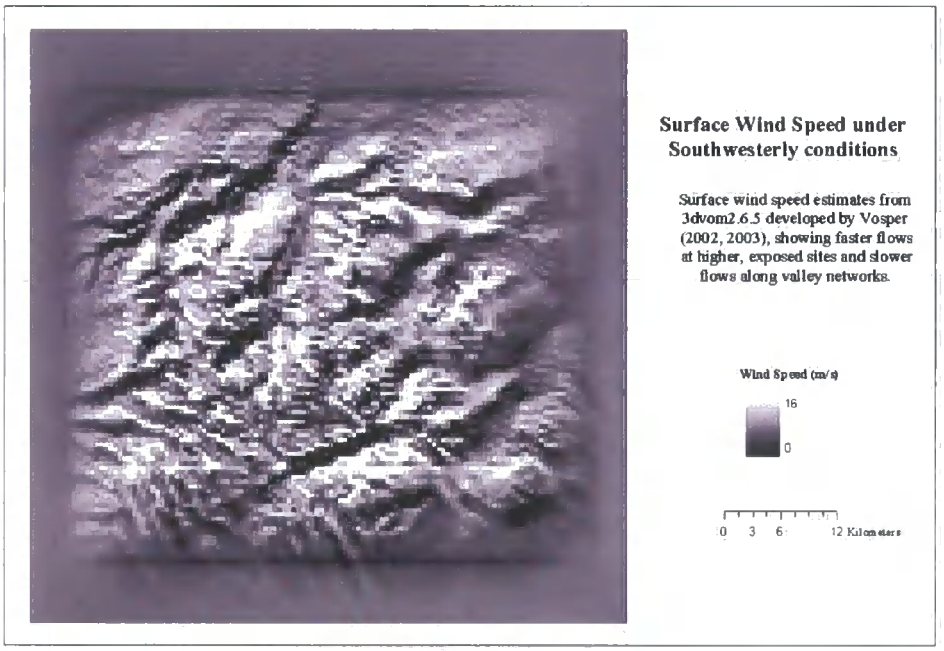

Figure 6.49: Surface wind speed under southwesterly conditions

6.7 Conclusions

In Norway, summer months are characterised by convection where precipitation is very difficult to predict and temperature is more easily predicted. In contrast winter months are dominated by tracking pressure systems facilitating better prediction of precipitation events and leading to less predictable temperature lapse rates. Temperature and precipitation in such complex meteorological systems cannot be predicted using standard lapse rates.

CHAPTER SEVEN

MASS BALANCE MODELLING

7.1. **Introduction**

This chapter outlines the mass balance model, providing a justification and explanation of each of its components. The model structure is initially described and is compared to existing alternatives. A detailed description of the modelled energy components follows with a discussion of published parameterisations. An outline of the implemented energy and mass balance models discusses spatial and temporal resolutions, modelled feedbacks and initial conditions.

Local energy balance drives melt (Ohmura *et al.*,. 1992; Male and Granger, 1981). Energy balance models and temperature index models allow the quantification of melt (ablation) but do not account for accumulation and consequently cannot be termed mass balance models. This chapter presents a mass balance model that uses spatially distributed temperature and precipitation receipt predictions with an energy balance model to predict spatially distributed melt.

"Mass balance studies are concerned with changes in the mass of a glacier and the distribution of these changes in space and time " (Paterson, 1981,43). Changes in mass predicted within this research will not account for changes driven by convergence or divergence of ice flow or due to processes at the glacier bed.

7.2. **Model Structure**

Radiation modelling was performed using a series of Java programmes, that read-in files from and write-out files to a GIS (Table 7.1). Computational efficiency and simplicity are achieved by balancing complexity and prediction accuracy. Existing approaches to predicting glacier distributions are largely limited by two main factors (for examples see Table 7.2), firstly over dependence on locally derived data leading to restricted applicability and, secondly, large

parameterisations from sparse climatic data leading to poor representation of spatially and temporal variations where altitude and temperature are commonly used to derive melt.

Model Component	Java Program	Methods include:
Net radiation balance	NetRadiation.java	getDirectBeam getDiffuse getLongwave getSensibleHeat getNetRad
Surface temperature	GetSurfaceTemp.java	
Albedo	GetAlbedo.java	
Melting	MeltingMonth.java	heatNew meltNew heatOld meltOld

Table 7.1: Java programs: available to download from author's website

Hock (2003) stresses the need for spatially distributed melt models that account for more than just altitudinal variations in accumulation. Where strong topographic gradients drive accumulation (Dubayah and Katwijk, 1992). The research presented here presents a temporally and spatially distributed melt model that is driven by radiative and climatic forcings. Climatic data derived from topographic variables account for strong local gradients using multi-scale elevation data. Accumulation and melt are predicted on a monthly time scale and data are stored and interpreted within a GIS.

The radiation or energy balance describes the balance between the radiation incident on a surface and that reflected or emitted from it. Radiation is a form of energy created due to the rapid oscillations of electromagnetic fields and is transferred by photons, which have particle and wavelike characteristics. Radiation can be characterised by its wavelength; short-wave or solar radiation has wavelengths of 0.15 – 3.0 μm and long-wave radiation has wavelengths of 3.0 – 100 μm. Radiation can be further classified according to whether it is direct beam radiation, diffuse or scattered radiation, or emitted radiation. These different types of radiation need to be considered separately and contribute differently to the local radiation balance.

The energy flux from the atmosphere towards the glacier surface (Q_o) consists of the following components:

$$Q_o = S\downarrow (1-\alpha) + L\downarrow - L\uparrow + Q_H + Q_L + Q_R \qquad \text{(Equation 7.1)}$$

Where $S\downarrow$ is the incoming short wave flux, α is the albedo, $L\downarrow$ is the incoming long wave flux, $L\uparrow$ is the outgoing longwave flux, Q_H is the sensible heat flux, Q_L is the latent heat flux and Q_R is the heat flux supplied by rain (Greuell and Genthon, 2004) schematically represented in Figure 7.1. The radiation balance is an important factor when considering glacier mass balance (the relationship between accumulation and ablation on a glacier), as it is a major control on the amount of energy available at a location for glacier ablation (melting).

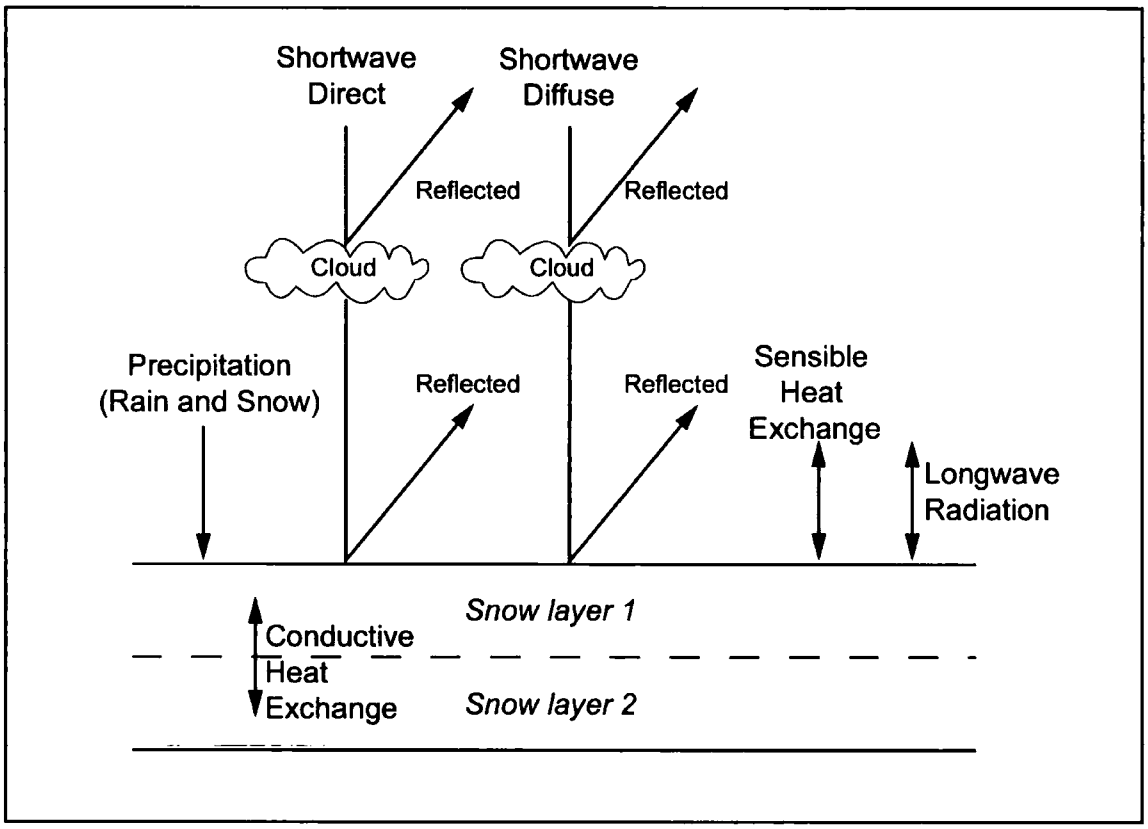

Figure 7.1: Conceptual diagram of energy balance snowmelt model.

The relative contributions that each of these components have to melt differs, latent heat exchanges and rain on snow events are known to only provide a minor contributions to melt and are not modelled within this study. where large Bowen ratios (Q_H / Q_L) dominate.

The amount of the radiation incident on a surface differs from the amount transferred to the surface. Radiation incident on a surface can either be absorbed or reflected, the proportion absorbed is dependent upon a number of factors primarily the surface albedo and the angle of

incidence. However, other controls exist that govern the magnitude of each of the fluxes in Equation 3.1 reaching the surface, including atmospheric transmissivity, aspect and screening.

Before a more detailed description of the model follows a brief evaluation of recent alternative models is presented to justify the character and structure of the model employed here.

7.3. **Alternative Models**

Heggem *et al.* (2001) stressed that radiation models are intrinsically localised in form and cannot easily be transferred between regions that may experience strong localised correlations and controls on receipt. Empirical models, including the research reported here, are largely concerned with spatial patterns and not absolute values (Heggem *et al.*, 2001), therefore although wrong parameterisations can lead to gross over or underestimates spatial distributions and coherence are of primary importance here. This can also be viewed as the role of the different scale controls on local energy balance which operate at a global (solar constant and solar position), meso (atmospheric attenuation and air mass ratio), topographic (local incidence angles and shade) and micro (plants and microclimatology) scale (McKenney *et al.*, 1999) and they therefore require a degree of localised parameterisation.

Utilising the regression and time series analysis of the seasonal and spatial patterns of melt and meteorological variables it is possible to quantify their inter-relationships and predict system responses, specifically annual mean mass balance (M_n). Where M_n is given by:

$$M_n = c_0 + c_1T_w + c_2P_w \qquad \text{(Equation 7.2)}$$

Where $c_0 - c_2$ are the coefficients determined using the regression analysis and T_w and P_w are the annual mean precipitation (a range of months commonly between October and May) and temperature (ablation season months only). See Hodgkins (2001) for example studies.

Model	Locally Driven	Models mountain scale variability	Temporal Resolution	Short wave Radiation	Longwave Radiation	Sensible Heat Exchanges	Notes
Swift, 1976	Yes	Yes	Daily	Potential radiation	No	No	
Dozier, 1980		Yes	Variable	Net radiation	Yes	No	Driven by wavelength specific attenuation
Nunez, 1980	Yes	No	Daily	Derived from cloud data	No	No	Assumes meso scale processes to be independent of the physical properties of the receiving surface.
Hock, 1999	Yes	Yes	Hourly	Potential radiation	No	No	
Marks *et al.* 1999	Yes	Yes	Hours	Requires net solar radiation	No	Yes	High climate data requirements, predicts melt
Brock and Arnold, 2000	Yes	Yes	Daily / hourly	Direct and diffuse	Yes	No	
Tian *et al.*, 2001	Yes	Yes	Daily	Direct and diffuse	No	No	Model driven by local global radiation measurements
Fierz *et al.*, 2003	Yes	Yes	Daily	Direct and diffuse	No	No	

Table 7.2: Examples of alternative energy balance models

Application of degree day models (Section 2.2.2) are known to produce robust results at low data costs. Laumann and Reeh (1993) record DDF of 4.5, 3.5 and 4.0 for snow in Alfotbreen, Hellstugubreen and Nigardsbreen (Norway) respectively, and 6.0, 5.5 and 5.5 for ice on the same glaciers extracted for the time period 1961 - 1990.

Despite their clear advantages, temperature index models oversimplify melt relationships, driven by temperature alone and therefore fail to simulate small temporal and spatial patterns. They are highly dependent upon the quality of the distributed temperature data. DDF's are particularly sensitive to conditions when mean daily temperatures are just above 0°C, authors alter temperature index models to account for these conditions (Greuell and Genthon, 2004). Hock (2003) stressed the need to develop spatially distributed melt models driven by low input data requirements and proposed the extension of a degree day model with energy balance parameters. A number of these types of model have been implemented, using clear sky global radiation (Cazorzi and Fontana, 1996), scaled topographic receipt and albedo (Dunn and Colohan, 1999), potential direct beam radiation (Hock, 1999) and an accumulated temperature index (Daly *et al.*, 2000). Each of the these models have accounted for an improved resolution of the smaller scale temporal and spatial patterns of melt.

Although many energy balance models are developed, calibrated and driven by climatic and radiative data collected by automatic weather stations (AWS) or field season records (Hock, 1999; Hock, 2004; Molg and Hardy, 2004) their application is limited. As these locally calibrated models, where in some cases one or two stations provide climatic or radiative data, can contain model errors are hidden within tuned coefficients and often fail to model complex local variations or trends where patterns are over simplified and highly restrictive in their scope (Williams *et al.*, 1972; Fierz *et al.*, 2003)

This research attempts to build upon the strengths of degree day models and create a composite approach by supplementing the temperature melt relationship with distributed radiation balancing estimates improving the ability of the model to account for heterogeneity in melt driven by topographic shading, slope and aspect.

A number of authors have achieved this by adding a radiation term to the product of positive temperatures and a melt factor. Where the model results are calibrated to match known distributions. Examples include Kane and Gieck (1997) who found melt to be proportional to

short wave radiation balance and Kustas *et al.* (1994) who found melt to be proportional to net radiation.

These approaches add a radiation term to the temperature dependent melt are reported to be less effective than the approach adopted by Hock (1999) which scales the DDF rather than using the product of DDF and temperature. Where melt (M) (mm h^{-1}) is given by:

$$M = \begin{cases} (fm+al)T, & T > 0 \\ 0, & T \leq 0 \end{cases} \qquad \text{(Equation7.3)}$$

and *fm* is a melt factor (mm h^{-1} K^{-1}), *a* is radiation coefficient (mm m^2 h^{-1} K^{-1}), I is potential direct solar radiation at the surface (W m^{-2}), and T is air temperature (°C).

Calibration of the melt and radiation factor to local conditions using measured ablation and runoff results in varying the values of *fm* and *a*, which for Hock (1999) on Storglaciären, Norway was between 0.9 and 2.7 for *fm* and between 0.3 and 0.9 * 10^{-3} for *a*. Varying values of *fm* was found to yield a near homogenous increase in melt in contrast to *a*, which due to the strong topographic control on incident radiation results in increased spatial variability in melt. Verbunt *et al.*, (2003), Flowers and Clarke (2000), Schneeberger *et al.* (2001) and Schler *et al.* (2002) also successfully adopted this technique. Although these parameters were optimised for Storglaciären they were not found to be simulate melt as accurately at alternative sites, where differences in local energy balance, lapse rates, albedo and locally significant meteorological parameters and processes imposed a dominant control on local melt rates. This dominance of local conditions on melt reduces the effectiveness of this type of calibrated factor model which reduces the ability of the model to be effectively applied in multiple study areas.

Hock (1999) and Hock *et al.* (2002) implement this blended model by incorporating potential direct solar radiation. Verbunt *et al.* (2003) extend Hock's model including seasonally variant melt factors (MF) to account for seasonality in melt not simulated using temperature trends alone. The model produced good results but was heavily tuned to local conditions and was driven by AWS data.

Although improved degree day models address many of the limitations of the classic degree day model they still fail to account for observed spatial patterns and are highly constrained to a geographical area. This research outlines a climatic and radiative forcing model that is not

geographically restricted creating a robust and flexible mass balance model. Correlations between synoptic weather conditions and melt rates (Hock, 2004) strengthen the case for a climatic and radiative forcing model as developed within this research that are able to account for the terrain driven spatial variability and the temporal variability driven by synoptic conditions which are simulated in Chapter Six.

7.4. **Surface energy balance**

Each of the components identified in Equation 7.1 and Figure 7.1 provide a different contribution to melt, and are dependent upon different environmental conditions. Methods and algorithms for predicting each of these components follows.

The local energy balance model described and implemented in this research predicts incident radiation using variables outlined in Table 7.3, organised by group.

Group	Factor
Radiative	Solar Constant
Astronomical / temporal	Solar Altitude Solar Azimuth Solar Declination
Topographic / geographic	Solar Altitude Topographic shading Altitude Slope (Azimuth and gradient) Surface albedo
Atmospheric / geometric	Path length Air pressure Ozone Water vapour Cloud Cover

Table 7.3: Variables used to predict incident radiation, adapted from Dozier (1980)

Terrain and landcover heterogeneity can result in high spatially variability in surface energy balance (Elder *et al.*, 1991; Fierz *et al.*, 2003). Sridhar *et al.* (2003) examined the role of spatial scale of input datasets in determining the accuracy with which accurate local energy balance estimates could be made under different land surface heterogeneity conditions. Sensitivities were most pronounced for latent and sensible heat predictions and found the most appropriate scale for predictions to be dependent upon the heterogeneity of landcover. Landcover within the

study area in radiative terms can be viewed as snow and non-snow. Although local heterogeneities exist, initial model conditions of no snow cover, and spatially organised accumulation patterns minimise the errors associated with data resolution and sensible heat predictions.

Atmospheric and topographic interactions result in spatially heterogeneous distributions of incident radiation. Although these interactions are complex it is possible to accurately quantify and parameterise their individual components using a suite of solar variables defining both solar position and daylight hours.

7.4.1 **Solar Variables**

Incident radiation is a function of solar position, determining (with local topography) the efficiency of transfer of solar radiation and the duration of exposure it is therefore critical to any local energy balance calculations. Solar position is defined by it spherical coordinates, declination (δs), altitude (α) and azimuth (a_s) recording its passage through the year, its passage through the day is quantified using the hour angle (h_s). Defining how far east or west the sun is from the local meridian, where at solar noon when the sun is directly overhead the hour angle is 0, and varies by 15° for each hour prior to, or after noon, with positive values denoting positions before noon and negative values indicating positions after noon. This removes the need to convert to local time, remaining in solar coordinates.

Conversion to local time, requires a four minute time alteration for each degree of longitude difference between the actual and reference longitude, so converting between solar (T_s) and local (T_l) time:

$$T_l = T_s + ((L - L_r) * 4) \qquad \text{(Equation 7.4)}$$

Where L is latitude in degrees and L_r is the reference latitude.

Solar declination defines the angle between the direction to the sun and the plane of the earth's equator. Following the work of Duffie and Beckham (1991) and Kumar *et al.* (1997) this is given by:

$$\delta s = 23.45 * \sin(360° * (284 + N) / 365) \qquad \text{(Equation 7.5)}$$

Where N represents day number, January 1st = day 1.

Solar declination varies between - 23.45° when the sun lies to the south of the equator and 23.45° when the sun lies to the north (Figure 7.2).

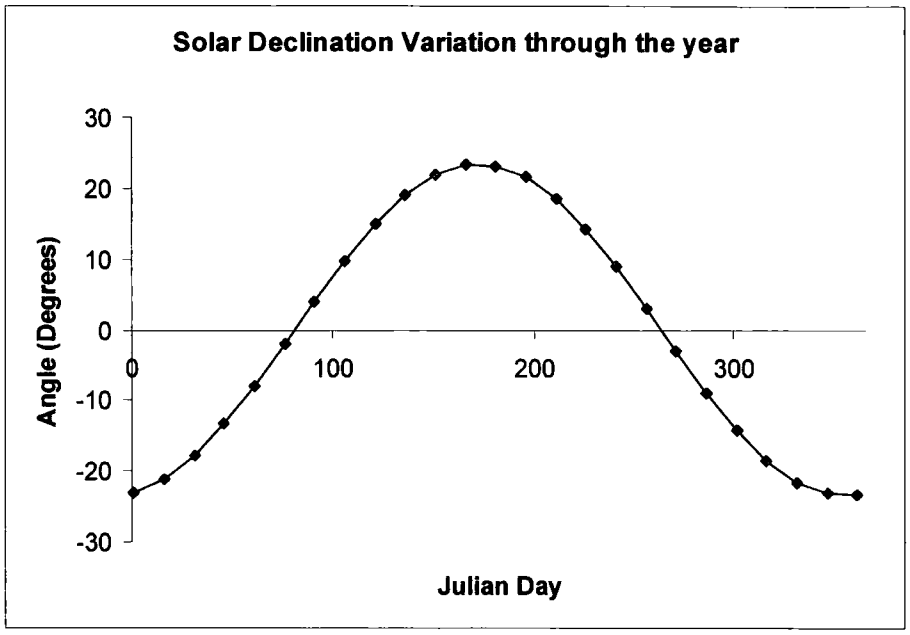

Figure 7.2: Variation in solar declination through a year as predicted by energy balance model

Solar altitude defines the angular height of the sun above the ground and is given by:

$$\text{Sin } \alpha = \sin L * \sin \delta + \cos L * \cos \delta * \cos h_s \qquad \text{(Equation 7.6)}$$

Where L denotes latitude in degrees, δ denotes solar declination and h_s denotes the hour angle. Variation through the day and year are shown in Figure 7.3 where lower solar altitudes are found in winter.

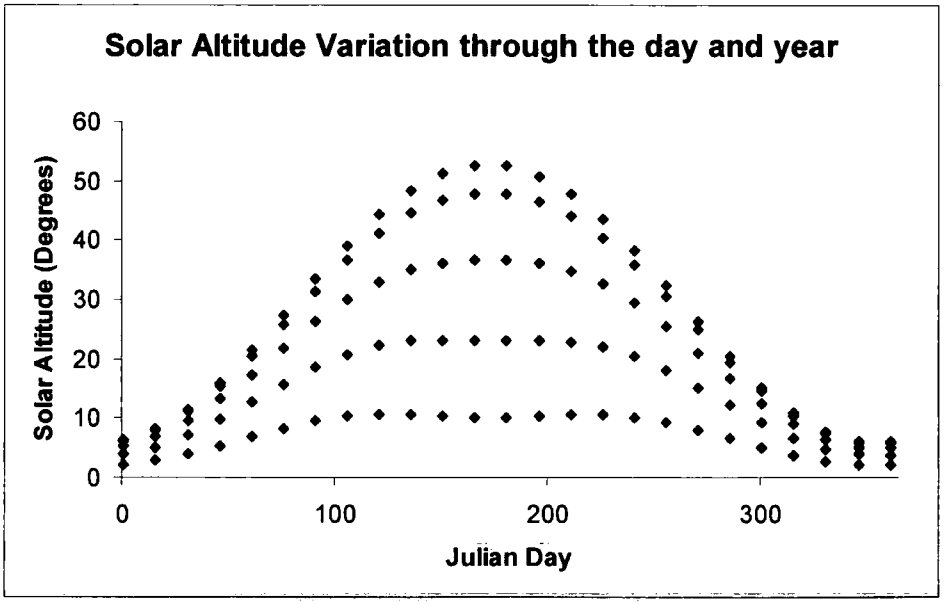

Figure 7.3: Variation in solar altitude through a year as predicted by radiation model

Solar altitude can be related to the hour angle, where the hour angle at sunrise (h_{sr}) and sunset (h_{ss}) has a solar altitude of 0°, although Flemming (1995) proposed that solar altitude is -0.8333° at sunrise and sunset if atmospheric refraction is accounted for) and can be quantified as:

$$\text{Sin } \alpha = 0 = \sin L * \sin \delta_s + \cos L * \cos \delta_s * \cos h_{sr}(\alpha = 0) \qquad \text{(Equation 7.7)}$$

Which gives:

$$h_{sr} = \cos^{-1} (-\tan L \tan \delta_s) \qquad \text{(Equation 7.8)}$$

$$h_{ss} = - h_{sr} \qquad \text{(Equation 7.9)}$$

Solar azimuth defines the horizontal direction of the sun relative to North and is given by:

$$\text{Sin } a_s = \cos \delta * \sin h_s / \cos \alpha \qquad \text{(Equation 7.10)}$$

And varies through the day and year as shown in Figures 7.4 and 7.5.

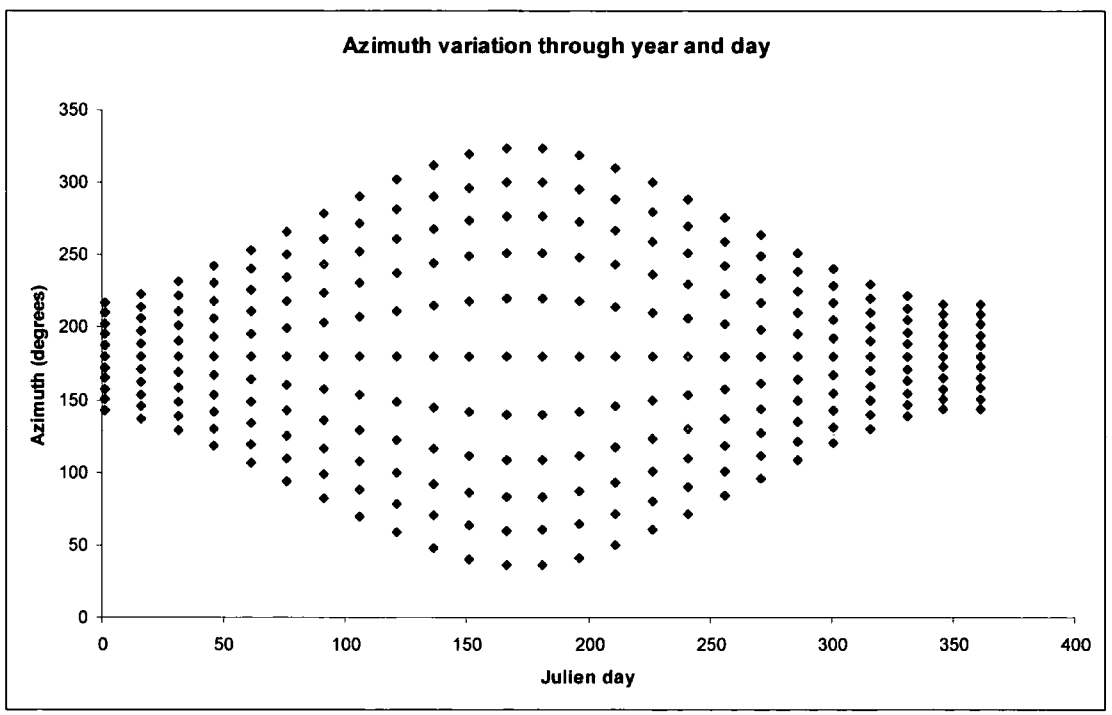

Figure 7.4: Variation in solar azimuth through a year as predicted by radiation model

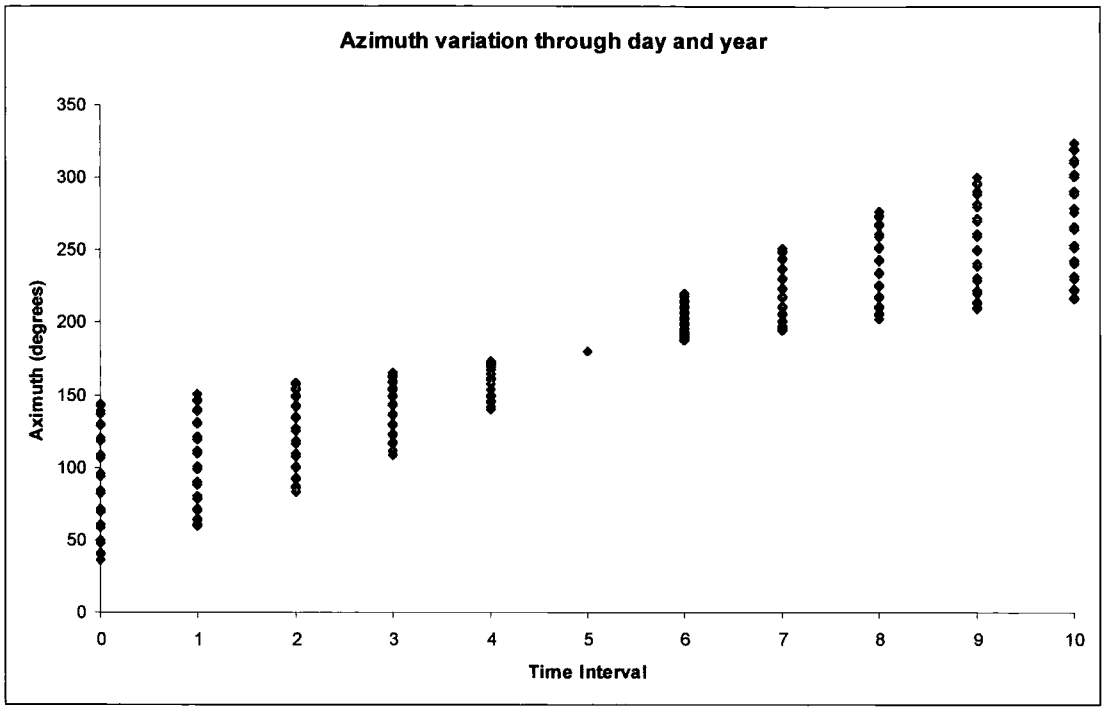

Figure 7.5: Variation in solar azimuth through a day and year as predicted by radiation model

Shortwave radiation receipt at the surface occurs during daylight hours, between sunrise and sunset. As a results of varying solar position the number of daylight hours varies through the year as shown in Figure 7.6.

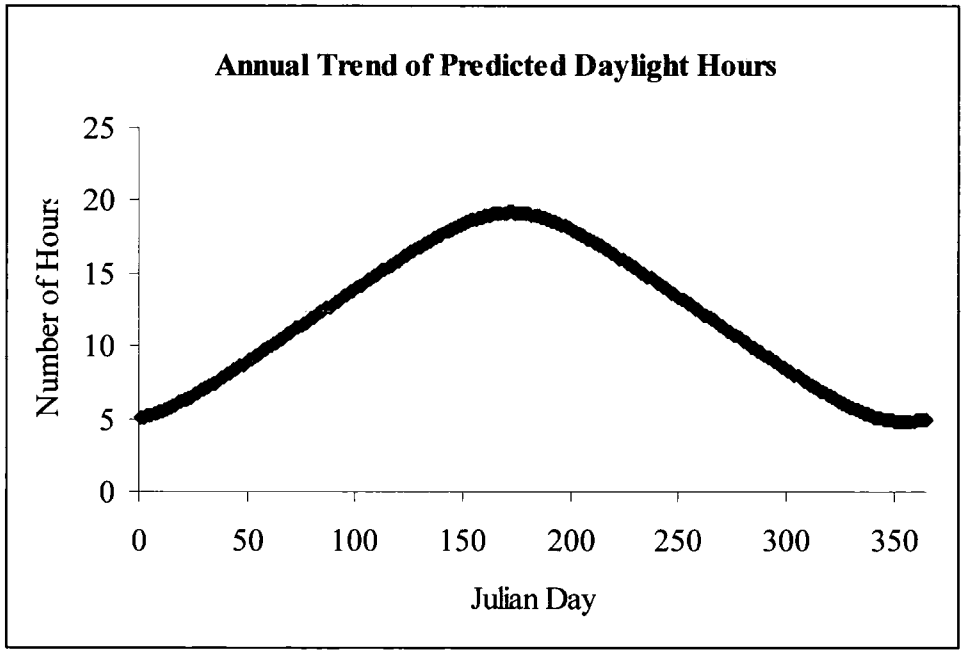

Figure 7.6: Annual variation in daylight hours through the year.

7.4.2 **Albedo**

The shortwave radiation absorbed by a surface is commonly expressed as $(1 - \alpha)\ S\downarrow$, where α is the mean reflectance or albedo. Variations in surface albedo exert a strong influence on snow surface energy balance and melt, especially following a fresh snowfall event (Sauberer and Dirmhirn, 1951; Paterson, 1981 and Brock *et al.*, 2000b). Heggem *et al.*, (2001) suggested that failing to include surface albedo leads to an overestimation of accumulation and an incorrect spatial distribution. Snow surface albedo varies over short spatial scales and diurnal temporal scales, as a function of angular and spectral distributions of incoming radiation, solar altitude (Carroll and Fitch, 1981), cloud cover (Carroll and Fitch, 1981; Melloh *et al.*, 2002), snow age (Barry, 1992), snow grain size (Nolin and Stroeve, 1997; Melloh *et al.*, 2002), snow subsurface variations and any material or debris surface cover (Gerland *et al.*. 1999; Knap *et al.*, 1999; Melloh *et al.* 2002) (Table 7.2).

Parameter	Effect on Albedo
Solar Altitude	Albedo increases with decreasing solar altitude
Cloud Cover	Albedo increases with increasing cloud cover
Snow Age	Albedo decreases with increasing snow age
Snow grain size	Albedo decreases with increasing grainsize
Surface debris cover	Albedo decreases with increase debris cover

Table 7.2: Controls on snow surface albedo

Quantification of high temporal and spatial variations in surface albedo has been undertaken using satellite remotely sensed data (Culter and Munro, 1996; Nolin and Stroeve, 1997; Robinson, 1997; Knap *et al.*, 1999; Kloh *et al.*, 2003; Brock *et al.*, 2000), aerial photography (Corripio, 2002) or high resolution temporal sampling (Brock, 2004). Remote sensing does provide accurate albedo measurements, however, these are restricted by the fixed wavelength of the sensors and therefore cannot be viewed as representative of the whole spectrum.

Land Cover	Albedo (α)
Earth	0.31
Average Surface	0.4
Global Surface	0.14-0.16
Global Cloud	0.23
Cumulo-nimbus	0.9
Strato-cumulus	0.6
Cirrus	0.4-0.5
Fresh Snow	0.8-0.9
Melting Snow	0.4-0.6

Table 7.3: Land cover albedo estimates (Barry, 1992)

Where remotely sensed estimates are not available it is necessary to predict albedo variations, because many of the controls outlined in Table 7.2 are unlikely to be available it is necessary to use proxy variables to simulate these parameters (Greuell and Genthon, 2004). Brock *et al.*, (2000a) used regression analysis to predict albedo as a function of maximum daily temperature, differentiating between shallow (less than 0.5 cm SWE) and deep (greater than 0.5 cm SWE) snow cover where exponential and logarithmic functions are used respectively. Where the albedo for deep snow (α_{SD}) is given by:

$$\alpha_{SD} = c_1 - c_2 {}^{10}\log T_{ma} \qquad \text{(Equation 7.11)}$$

Where T_{ma} is the accumulated amount of daily maximum temperatures above 0°C, $c_1 = 0.71$, $c_2 = 0.11$. The daily maximum temperatures attempt to account for changes in the grain size and rheology of the snow, for small T_{ma}, α_{SD} is constrained by a maximum value of 0.85.

Brock (2004) attempting to improve on these estimations used data collected on high frequency variations in local albedo (measured at 10 minute intervals over an 11 day period on Haut Glacier d'Arolla, Switzerland) to develop a new method of calculating local albedo, where variability is driven by cloud cover and predicted using the difference between measured and potential incident radiation. Brock (2004) proposed that failure to account for increased albedo under cloudy conditions could lead to the overestimation of melt by between 1 – 3 mm snow water equivalent (SWE) day^{-1}. Earlier studies had also identified strong correlations between cloud cover and albedo, this positive correlation, is largely driven by the multiple reflection of diffuse radiation between the snow surface and the cloud base (Male and Grainger, 1981).

Although local energy studies within the cyrosphere attempt to differentiate between small temporal and spatial scale variations in albedo within a snowpack over diurnal time scales, studies focusing on larger temporal scales and more varied landcover types assume homogeneity within snow assigning an albedo of between 0.6 and 0.9 with sufficient accuracy (McKenney *et al.*, 1999). It is therefore a question of resolution and scale in assigning model parameters, aiming to maintain consistency in the complexity each component is modelled. Brock and Arnold (2000) propose albedo of values of 0.9 and 0.85 for fresh snow and old snow respectively for conditions when other variables are unknown, average albedos for landcovers are given by Barry (1992) (Table 7.3).

7.4.3 **Long wave radiation**

Absorption and emittance of longwave radiation occurs within a volume rather than at a surface and fluxes decay exponentially with increased distance from the surface (Barry, 1992). Snow and ice are almost full radiators in the longwave section of the radiation spectrum, but absolute values are low, because the surface temperature is low (Oke, 1978).

The net longwave radiation flux emitted from the sky and surrounding terrain provide only a small contribution to melt (Price, 1986; Röthlisberger and Lang, 1987; Hay and Fitzharris, 1988; Braithwaite and Olesen, 1990; Paterson, 1994; Arnold *et al,*. 1996; Brock and Arnold, 2000). Fierz *et al.,*. (2003) however, stressed the importance of longwave fluxes, especially emittance from surrounding rock surfaces, where they found estimates of local balance without longwave fluxes, poorly predicted net balance, often overestimating and propagating error to melt calculations. This contribution was contested by Greuell *et al.*, (1997) and Kayastha *et al.*, (1999) who found that for study areas in the Alps and the Himalayas inclusion of longwave radiation from surrounding slopes made only a marginal contribution to the net energy balance.

Parameterisations of the incoming longwave radiation flux are largely driven by clear sky emittance, temperature and vapour pressure, either 2 m above the surface or at several points in a column above the surface. For clear skies, the incoming longwave radiation flux ($L\downarrow$) is represented by,

$$L\downarrow_{cs} = \varepsilon_{cs}\sigma T_{2m}^4 \qquad \text{(Equation 7.12)}$$

Where ε_{cs} is the effective emissivity of the sky, σ is the Stefan – Boltzmann constant (= 5.67 * $10^{-8}Wm^{-2}K^{4}$) and T_{2m} is the 2 m above the surface temperature in Kelvin. Several parameterisations of ε_{cs} exist and the method proposed by Konzelmann *et al.* (1994) and Greuell and Genthon (2004) is outlined here where ε_{cs} is given by:

$$\varepsilon_{cs} = 0.23 + c_L\left(\frac{e_{2m}}{T_{2m}}\right)^{1/8} \qquad \text{(Equation 7.13)}$$

Where C_L is a tuning parameter and e_{2m} is the vapour pressure at 2 m.

An alternative similar approach is given by Arnold *et al.* (1996) where ε_{cs} is given by:

$$\varepsilon_{cs} = (1 + kn)\ \varepsilon_o \qquad \text{(Equation 7.14)}$$

where n is cloud cover (0 – 1.0) and k is a constant depending on cloud type. Where ε_o is the clear sky emisstivity given by

$$\varepsilon_o = (8.733 * 10^{-3}) * T_a * 0.778 \qquad \text{(Equation 7.15)}$$

where T_a is air temperature.

Brock and Arnold (2000) proposed a value for k of 0.26, which following values reported by Braithwaite and Olesen (1990) as the mean value for altostratus, altocumulus, stratocumulus, stratus and cumulus cloud types.

Predictions of L↓ and ε_{cs} are highly sensitive to temperature and vapour pressure profiles and cloud cover. Sugita and Brutsaert (1993) provided a number of prediction algorithms for clear sky receipts with quantified sensitivity to cloud cover. Inclusion of tuned parameters for cloud cover limit the application of these algorithms which are only able to predict local trends.

The outgoing longwave radiation flux (L↑) is driven by surface temperature and emissitivity (ε_s), the latter is close to 1.0 for snow and ice (Greuell and Genthon, 2004) simplifying L↑ from:

$$L\uparrow = \varepsilon_s \sigma T_s^4 + (1 - \varepsilon_s)\, L\downarrow \qquad \text{(Equation 7.16)}$$

To:

$$L\uparrow = \sigma\, T_s^4 \qquad \text{(Equation 7.17)}$$

A further simplification is the assumption of the surface to be 0°C (Brock and Arnold, 2000) where the surface radiates as a black body there is a constant outgoing flux of 316 Wm^{-2} (Oke, 1987).

7.4.4 **Direct beam radiation**

The solar radiation received at a site is not only a function of solar position and local topography but also is also controlled by a suite of atmospheric and solar parameters determining the amount of radiation entering the top of the atmosphere, the optical air mass (defining the path of the radiation through the atmosphere) and attenuation of the radiation by aerosols and water vapour.

Following from Kreith and Kreider (1978) the solar flux entering the atmosphere (I_o) in Wm^{-2} accounting for elliptical variations in the earth's path around the sun is given by:

$$I_o = S_o\,(1 + 0.0344 * \cos(360° * N / 365)) \qquad \text{(Equation 7.18)}$$

Where S_o is the solar constant, defining the irradiance of an area perpendicular to the sun's rays just outside the atmosphere. Estimates from NASA record S_o as 1353 $Wm^{-2} \pm 1.6\%$ (Kreith and Kreider, 2000), with a constant figure under much debate and subject to uncertainties a value of 1367 Wm^{-2} is used here following the findings of Duffie and Bechman (1991), Kreith and Kreider (2000) and Kumar *et al.* (1997).

Attenuation by atmospheric aerosols and water vapour reduces the mount of radiation reaching the surface, this is largely parametrised using Bouger's law, stating that the radiation passing through the atmosphere, the 'terrestrial radiation' (I_b) is given by (Kreith and Kreider, 1978):

$$I_b = I_o\, e^{-km} \qquad \text{(Equation 7.19)}$$

Where, k is the absorption coefficient and m is air mass ratio

The air mass ratio quantifies the mass of air encountered on the path of the radiation through the atmosphere to the earth's surface, representing the ratio between the path length mass and the mass when the sun is overhead. *m* varies as a function of the direction of the path and surface altitude. Variations in m driven by path direction are accounted for using the zenith angle (ψ) between the path and the point on the celestial sphere above the earth's surface.

Where for $\psi < 70^{\circ}$ Gates (1980) proposed the use of a secant approximation where,

$$m = 1 / \cos \psi \qquad \text{(Equation 7.20)}$$

and for $\psi > 70^{\circ}$, when the secant approximation underestimates solar energy as atmospheric refraction and the earth's curvature are not considered and an adjusted approximation is given by:

$$m = [1229 + (614 \sin \alpha)^2]^{0.5} - 614 \sin \alpha \qquad \text{(Equation 7.21)}$$

Variations in mass associated with surface altitude are quantified using variations in local atmospheric pressure, where altitude adjusted airmass (m_a) proposed by Williams *et al.*, (1972) is given by:

$$m_a = (\rho / \rho_o)\, m \qquad \text{(Equation 7.22)}$$

where ρ is the local pressure and ρ_o is the pressure at sea level.

Parameterisation of solar radiation attenuation can incorporate wavelength dependent variations (Monteith, 1990; Monteith and Unsworth, 1990), accounting for water vapour, O_3 and CO_2 absorption (Hottel, 1976), molecular Raleigh scattering or Mie scattering by aerosol scattering by particulates (Kumar *et al.*, 1997). Where absorption heats the surrounding atmosphere and scattering simply redirects the beam (Monteith and Unsworth, 1990).

Beer's law states atmospheric transmittance τ_b is given by:

$$\tau_b = s_p(0)^{(-\tau m)} \qquad \text{(Equation 7.23)}$$

Where $s_p(0)$ is direct beam irradiance below an aerosol free atmosphere, τ is the turbidity coefficient and m is the air mass. Where τ is a function of wavelength absorption and atmospheric concentrations. $S_p(0)$ varies as a function of air mass and zenith, these parameters

were quantified by Kreith and Kreider (1978) and atmospheric transmittance (τ_b) and can be modelled as:

$$\tau_b = 0.56 (e^{-0.65m} + e^{-0.095m}) \qquad \text{(Equation 7.24)}$$

Where the constants represent average wavelength attenuation for aerosol absorption and Raleigh scattering. Cartwright (1993) reported that this method estimates within 3% of recorded values for clear sky conditions, with atmospheric transmittance values ranging between 0 and 1. This parameterisation was also successfully used by Kumar *et al.* (1997) Wavelength dependent attenuation algorithms were outlined by Dozier (1980), but have not been discussed directly here because average wavelength approximations provide acceptable results.

Attenuation of solar radiation entering the atmosphere creates two distinct directional components to the solar radiation reaching the ground, direct beam and diffuse. The latter created by molecular scattering and absorption.

Shortwave radiation striking a surface normal to the sun's rays (I_s) can be shown as:

$$I_s = I_o \tau_b \qquad \text{(Equation 7.25)}$$

An alternative methodology was proposed by McKenney *et al.* (1999) who used published monthly average extraterrestrial and terrestrial radiation, and altitude to predict average irradiance (accounting for atmospheric attenuation) at 10° latitudinal bands, and fitted a polynomial with and R^2 of 0.99. Both of these methods produce estimates of the radiation normal to the surface but further adjustments are required to account for the amount of direct beam radiation transferred to an inclined surface. Kreith and Kreider (1978) define this as:

Direct Beam Radiation = radiation normal to the surface * cos (angle of incidence)
on a sloping surface

Where *i* is the angle of incidence and cos *i* is given by:

$$\text{Cos i} = (\sin \delta_s (\sin LR * \cos \Theta - \cos LR * \sin \Theta * \cos asp) + \cos \delta_s * \cos h * (\cos LR * \cos \Theta + \sin LR * \sin \Theta * \cos asp) + \cos \delta_s * \sin \Theta * \sin asp * \sin h)$$

(Equation 7.26)

Accounting for solar position and surface slope provide an estimate of potential shortwave radiation. However cloud cover has a marked influence on the proportion of short wave radiation incident at the surface. The characteristics of this relationship depend on the type and extent of cloud cover. A number of models of quantifying this relationship exist based on hours of sunshine (Angström, 1924), cloud cover type and amount (Haurwitz, 1948; Davies, 1975) or cloud layers (Suckling and Hay, 1977). Heggem *et al.* (2001) found that cloud cover had a less significant role on the spatial distribution of incident radiation than albedo where the effect was restricted to very steep terrain areas.

Kasten (1983) concluded that incident radiation predictions in mountainous areas were highly dependent on cloud cover, where higher than expected receipts were found under cloudy conditions where refraction on the sides of clouds increased local receipts. Izioman and Mayer (2001) further developed this relationship and found that the most robust estimates of incident radiation were found when monthly mean cloud cover fraction was used rather than more complex predictive approaches. This was also found by McKenny (1999) whilst investigating the relationship between total daily irradiance and cloud cover, finding that there was no correlation and that day length provided much more informed estimates. These findings do however, suggest that cloudiness is a significant component of radiation models.

Cloud cover has two primary effects on the net shortwave flux reaching the surface, initially scattering, reflecting and absorbing radiation (determining global radiation) and secondly determining the proportion of radiation received as direct and diffuse components.

Parameterisations of global radiation receipt are commonly incorporated into potential radiation estimates unless detailed cloud cover information is available (Male and Gray, 1981). Geiger (1965) records correlations between cloud cover okta and global radiation.

Brock and Arnold (2000) use a diffuse fraction to determine the proportion of recorded global radiation received as diffuse and direct components, where the diffuse fraction is given by:

$$D_f = 0.65 * n + 0.15 \qquad \text{(Equation 7.27)}$$

where n is the cloud cover fraction (with complete cloud cover having a value of 1.0). This proportion calculation needs to be calculated before adjustment for a sloping surface using I_s.

7.4.5 **Diffuse radiation**

Diffuse irradiance is reflected direct radiation or reflected radiation that is scattered by atmospheric particulates and / or clouds. This has two components, isotropic homogenous throughout the hemisphere and circumsolar originating from within 5° of the direct solar beam (McKenney *et al.*, 1999). Diffuse radiation is largely assumed to be isotropic because although there are slight variations with topography these are largely linked to gradient and are similar to direct beam radiation distributions (Dubayah and Rich, 1995; Dubayah *et al.*, 1989). Inclusion of diffuse radiation components are found to accentuate spatial distribution patterns of direct beam radiation (Williams *et al.*, 1972). Although diffuse radiation is assumed to be isotropic throughout the sky the proportion of sky, that an area on the ground is exposed to varies. This can be modelled using a sky view factor (Dozier, 1980; Dubayah and Rich 1995) which accounts for spatial differences in sky exposure to diffuse radiation. The sky view factor can be defined as the hemispherical fraction of unobstructed sky visible from a point. Liu and Jordan (1960) reported a negative correlation between direct and diffuse radiation where recorded under clear sky conditions, when direct beam radiation receipts are the greatest, only a small diffuse component is recorded with a maximum possible value not exceeding 200 Wm^{-2}. Highest recorded values of diffuse radiation are recorded when cloud cover is approximately 50 % (Monteith and Unsworth, 1990).

Gates (1980) parameterised diffuse radiation as (I_d)

$$I_d = I_o \tau_d \cos^2 \beta / 2 \sin \alpha \qquad \text{(Equation 7.28)}$$

Where τ_d is the radiation diffusion coefficient and can be related to τ_b using a parameterisation proposed by Liu and Jordan (1960) relating higher direct beam transmittances to lower diffuse transmittances.

$$\tau_d = 0.271 - 0.294 \tau_b \qquad \text{(Equation 7.29)}$$

Following on from the work of Brock and Arnold (2000) and using the diffuse fraction (Equation 7.27) this then allows the diffuse component of incoming shortwave radiation to be shown as:

$$I_d = D_f * I_s * \cos^2 (\theta/2) + \alpha_M * I_s * \sin^2(\theta/2) \qquad \text{(Equation 7.30)}$$

Where the first part of the parameterisation quantifies the diffuse proportion of radiation incident on a surface from the sky hemisphere assuming isotropic conditions, and the second component represents diffuse radiation from the surrounding terrain where α_M can be assumed to be the snow albedo because contributions from surrounding rock faces are small and hard to quantify. This approach is in contrast to that outlined by Fu and Rich (1999). In these authors solar analyst application, sky view factor and terrain view factors were used to determine each of these components.

7.4.6 **Turbulent energy exchanges**

The local sensible heat balance is and important mechanism of energy transfer identified in Equation 7.1 as a control on glacier initiation. Although usually playing a subtler role in the local energy balance, its influences is important and must be considered when predicting glacier distributions (Martin and Lejeune, 1998; Marsh *et al.*, 1997; McGregor and Gellatly, 1996; Prowse and Owens, 1982; Moore and Owens, 1984; Scherer *et al.*, 1998; Granger *et al.*, 2002 and Figure 7.7 a and b) especially during early spring melt when net shortwave radiation receipts are lower and air temperatures are above 0°C. Nordbogletsher (Figure 7.7a) and Quamanarssup sermia (Figure 7.7b), in the Greenland ice sheet show examples of the magnitude of these variations.

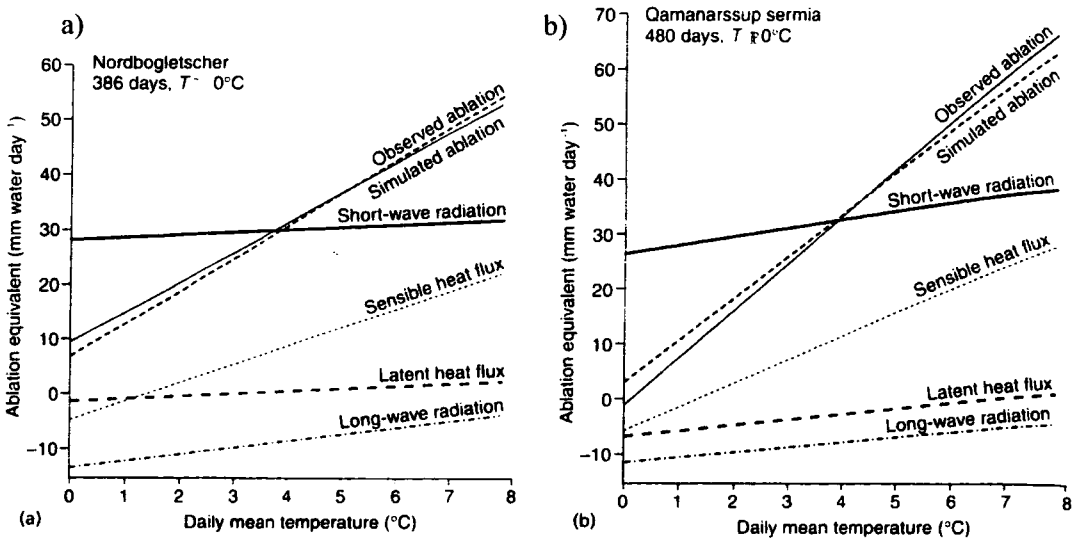

Figure 7.7: Relationship between temperature and the different components of local energy balance (Benn and Evans 1998, p74, after Braithwaite and Oleson, 1990)

Convection transports heat to and from the atmosphere in both its sensible and latent forms. The process of convection involves the vertical interchange of air masses and can only occur in

liquids and gases. Sensible heat transfer is an example of a turbulent transfer commonly performed by eddies which transport energy and mass from one location to another. Eddies may be set into turbulent motion by free or forced convection.

Free convection is due to the parcel of air being at a different density to the surrounding air. This situation commonly exists when the earth's surface is heated by solar radiation. If the state of the atmosphere is conducive to free convection the atmosphere is said to be unstable. The atmosphere near the earth's surface may be physically put into motion when it flows over obstacles. This is forced or mechanical convection and depends on the roughness of the surface and the speed of the horizontal flow. Frequently free and forced convection coexist and give rise to mixed convection.

If the addition or subtraction of energy to a body is sensed by a temperature rise or fall then it is referred to as sensible heat. The energy or heat required to change a substance to a different form at the same temperature is called latent heat, and is released when the substance returns to its initial state. Energy is taken up to move in the direction of a higher energy state.

It is possible to identify local or climatological factors (free convection) and static or topographical factors (forced convection) that control the sensible heat balance. Free convection is most dependent upon the presence of eddy fluxes, if stable air is present above the surface eddy fluxes and consequently sensible heat transfers are suppressed. Forced convection is largely controlled by local topography and wind speed.

Prevailing air mass conditions, altitude, time of year and terrain features influence the relative importance of turbulent heat transfers (Marsh *et al.*, 1997; Male and Grainger, 1981). Obled and Harder (1979) identified a number of controls on turbulent heat exchanges specific to alpine environments. Their work largely focused on thermal circulation patterns in mountains and their topographic impact on temperature and humidity patterns. Marsh *et al.* (1997) examined the role of sensible heat exchanges in driving melt over heterogeneous (patchy) snow cover. Greater temperature gradients between the glacier surface and the air and higher wind speeds drive greater exchanges. However Paterson (1981) reports that glacier winds inhibit ablation by convection, by cooling the air temperature and reducing local turbulence.

Spatially distributed estimates of sensible heat exchanges resulting from turbulences in the boundary layer directly above the snow surface have received little attention (Fierz *et al.*, 2003) and are infrequently included in distributed melt models (Table 7.2).

Methods of predicting and measuring sensible heat fluxes vary in scale and complexity, measurement of eddy covariance, recording turbulent mixing and can be used to quantify turbulent heat exchanges over a surface. Applications of this method are restricted by high cost of equipment, the high spatial and temporal resolution data requirements and instrument sensitivity. However, limited field records are often use to test and validate predicted exchanges (Arck and Scherer, 2002; Martin and Lejeune, 1998). Parameterisation of sensible and latent heat fluxes provides significant advantages and are frequently used in local energy balance studies.

The 'profile' method uses measurements of wind speed, potential temperature and specific humidity at a number of levels above the surface to resolve local flux estimates (see Greuell and Genthon, 2004 for estimation methodology). This estimation process is complex and requires multiple altitude level meteorological data, which are commonly not available. An alternative method that Denby and Greuell (2000) and Arck and Scherer (2002) hypothesised to provide better results are termed the 'bulk' method which integrates velocity, humidity and temperature from one altitudinal level to the surface. Where Q_H is shown as:

$$Q_H = \rho_a C_{pa} \frac{\kappa^2 u(\mathrm{T} - \mathrm{T}_S)}{\left(\ln\frac{z}{z_O} + \frac{\alpha_m z}{L_{ob}}\right)\left(\ln\frac{z}{z_T} + \frac{\alpha_h z}{L_{ob}}\right)} \qquad \text{(Equation 7.31)}$$

and Q_L is given by:

$$Q_L = \rho_a L_s \frac{\kappa^2 u(q - q_S)}{\left(\ln\frac{z}{z_O} + \frac{\alpha_m z}{L_{ob}}\right)\left(\ln\frac{z}{z_q} + \frac{\alpha_h z}{L_{ob}}\right)} \qquad \text{(Equation 7.32)}$$

C_{pa} is the specific heat capacity of air (1005 J $Kg^{-1}K^{-1}$), L_s is the latent heat of sublimation (2.84 * 10^6 JKg^{-1}), K is the Von Karman constant (0.4), z is the height (m) above the surface. T_s is the surface temperature, q_s is the specific humidity at the surface and q at a given height z. z_o, z_r and z_q are the roughness lengths for velocity (u), temperature (T) and water vapour. These are defined as the distances above the surface where the profiles of u, Θ and q reach their surface values. Much debate has surrounded the appropriate scale of roughness parameter and how well it correlated with mesoscale surface features. Roughness lengths over glacier surfaces are generally in the order of millimetres but can be significantly greater in areas of complex

topography (Brock, 1997; Brock and Arnold, 2000). For snow values of z_o varying between 0.01 mm to 10mm, the latter apply when large scale ablation features such as ablation hollows dominate and values for ice range between 0.1 mm and 10 mm. Over snow, T_s can adopt the zero degree assumption or can be given by subsurface temperature modelling. Specific humidity (q_s), is driven by T_s and is shown as:

$$q_s = 0.621 \frac{e_{sat}(T_s)}{p} \qquad \text{(Equation 7.33)}$$

Where p is the atmospheric surface pressure. Further parameterisation is required to calculation the Monin-Obukhov length (L_{ob}) using α_m and α_h empirical functions in stability for momentum and sensible heat respectively. Iterative calculations are required to calculate exchanges using this method and although it is possible to simplify these algorithms, error increases (Greuell and Orelemans, 1986) and costs are still high (Arck and Scherer, 2002)

An alternative method proposed by Young and Woo (1997) and Arck and Scherer (2002) specifically for determining sensible heat flux over snow offers significant computational savings using an alternative bulk method, where Q_H is shown as

$$Q_h = \rho c_{pa} C_h u(T_p - T_s) \qquad \text{(Equation 7.34)}$$

C_h is a dimensionless drag coefficient for heat and T_p is the potential temperature.

$$C_h = C_{cn} = \frac{K^2}{\left[\ln\left(\frac{Z-d}{z_0}\right)\right]^2} \qquad \text{(Equation 7.35)}$$

This assumes neutral conditions(C_{cn}), with air temperature varying at the DALR and logarithmic wind speed profiles. These conditions have been argued to be uncommon above melting ice, which are believed to be more accurately represented under a stable boundary layer, where cool air lies above the surface and reduces turbulent exchanges (Gill, 1982; Paterson, 1994; Hock and Holmgren 1996). Although other authors (Grainger and Lister, 1966; Munro and Davies, 1977; Halberstam and Schieldge, 1981; Brock and Arnold, 2000) have argued that insufficient field data is available to qualify this statement.

Accounting for stable conditions requires the inclusion of Richardson Numbers (R_i) that quantify atmospheric stability, and are given by:

$$R_i = \frac{g}{T} * \frac{\Delta \bar{T} / \Delta z}{[\Delta \bar{u} / \Delta z]^2} \qquad \text{(Equation 7.36)}$$

Over snow it is possible to assume that T and surface wind speed are 0.0. The numerator relates buoyancy to turbulent flow represented by the denominator; (free and forced convection respectively) (Oke, 1987). Where a negative R_i indicates unstable conditions when free forces dominate and a positive R_i indicate stable conditions when inversions dominate and little convection occurs. Where ΔT and $\Delta \bar{u}$ are the difference between surface and reference height values.

Price and Dunne (1976) use R_i to adjust the drag coefficients for atmospheric stability giving the stable drag coefficient (C_{cs}) as:

$$C_{cs} = C_{cn} / (1 + 10\ R_b) \text{ for } R_i > 0 \qquad \text{(Equation 7.37)}$$

And under unstable coefficients (C_{cu}) the coefficient is

$$C_{cu} = C_{cn} * (1 + 10\ R_b) \text{ for } R_i < 0 \qquad \text{(Equation 7.38)}$$

Where C_{cs} replaces C_{ch} in equation 7.35

Where the potential temperature T_p is

$$T_p = T\left(\frac{1000}{p}\right)^{R/C_p} \qquad \text{(Equation 7.39)}$$

Where p is atmospheric pressure (mbars) and R/C_p, Cp is the constant heat capacity of air, R is the specific gas constant the constant of proportionality can be taken as 0.285 (McIlveen, 1992)

7.5. **Energy Balance Model**

The structure of the energy balance model is shown in Figures 7.1 and 7.8. A computationally efficient and accessible modular structure facilitates modifications and user defined parameter

or component alterations. Driven by inputted monthly climatic data and a DEM the model calculates daily and diurnal temperature variations and predicts monthly net radiation, surface albedo and temperature.

7.5.1 **Model Prediction Resolution**

Local mass balance calculations are made at the DEM resolution, 100 m, which it is at the upper limit of the recommendations made by Heggem *et al.* (2001) in their study of energy balance models in periglacial studies, but it is felt during this study that a smaller resolution in the radiation component of the model could not be supported by the other model components and would increase sensitivity to DEM error that would be incorporated by resampling the elevation data. Isard (1983) investigated the role of temporal and spatial scale on irradiance calculations in alpine terrain and found that both were most pronounced in topographically rough areas where topographic shading played an important role. Dubayah *et al.* (1990) investigated the role of DEM resolution on incident radiation calculations. In their study radiation variance was found to decrease with increasing pixel resolution due to lower surface slopes and radiation spatial autocorrelation increased with increasing pixel resolution where larger organised landform features were dominant within the DEM. The 100 m spatial resolution utilised in this research project is supported by the findings of other studies that showed an optimal scale to resolve landforms and surface processes (McKenney *et al.*, 1999; Arrell, 2000), where local topographic parameters are only a component of the global and meso scale systems controlling melt.

Important energy balance exchanges operate on a diurnal and daily temporal resolution. Much discussion has been reported in the literature surrounding optimal time steps and prediction accuracy (Fierz *et al.*, 2003). Where Hock (1998) reported improved accuracy with increased temporal resolutions, and conversely the WMO (1986) and Plüss (1997) reported little or no improvement with increased temporal resolution. It is suggested in this study that these discrepancies are simply highlighting sensitivities to prediction algorithms, data quality and spatial resolution, terrain type and local factors, where it is proposed here that it is not possible to make generic statements about optimal time steps.

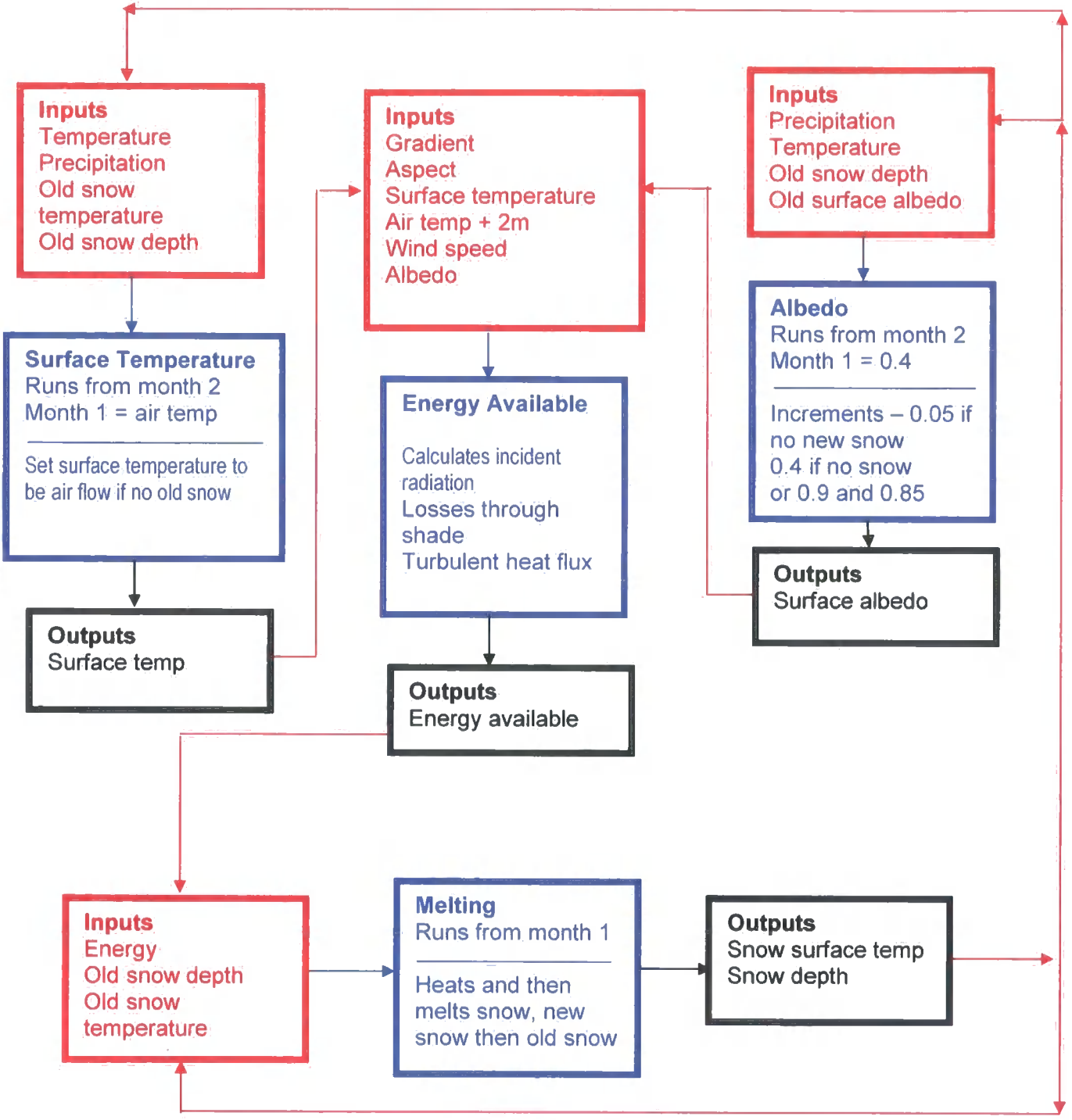

Figure 7.8: Energy balance model inputs and outputs

Monthly and diurnal time scales were used within the energy balance model, where process modelling was optimised using the most appropriate resolution. The temporal resolutions used within the full mass balance model are outlined in Table 7.6.

Variable	Resolution	Justification
Flux Normal to the Surface	5 Days	• Little Variation occurs within shorter time periods
Direct Beam Radiation	10 times a day	• 10 time intervals during daylight hours, constant for 5 day time period.
Diffuse Radiation		• Driven by solar position
		• Daily and seasonal trends modelled with little variation lost.
Sensible Heat	Hourly	• Driven by temperature and fluxes present day and night
		• Strong diurnal trend, driven by diurnal temperature data.
Longwave Radiation	Hourly	• Driven by temperature and fluxes present day and night
Net Radiation	Monthly	• Computational efficiency
		• Melt has a known sensitivity to climatic data and these are most robust using monthly mean values.
Albedo		• Potential error propagation from unrealistic albedo or surface temperature predictions from extreme climatic events limited the temporal resolution to monthly.
Surface Temperature		
Melt		• Consistency and data availability lead to melt and accumulation calculations at monthly time steps
Snow Accumulation		

Table 7.6: Temporal resolutions used within the model

7.5.2 **Initial conditions**

The energy and mass balance model is initiated at month 1, August, with no snow cover and a mean surface albedo of 0.4. The surface temperature is set as the mean monthly air temperature. At month 2, September, albedo and surface temperature are predicted using the output from August calculations. August was the first month to ensure that all accumulation was captured within the mass balance year predictions. Predictions where made every month through the mass balance year with the model year ending at the end of August the following year. Subsequent year calculations were not made as advection is not modelled within the mass balance predictions where annual variations would only show deepening snowpacks.

7.5.3 **Modelled direct beam radiation**

The solar constant was assumed as 1.367 Wm^{-2} (Kreith and Kreider, 1978) and variation through the year was modelling following Kreith and Kreider (1978) and given here in Equation 7.18. Following Gates (1980) air mass was given by Equation 7.21 using the secant approximation. Solar attenuation by aerosols was also modelled following Kreith and Kreider (1978) shown here in equation 7.24, where wavelength dependence was not believed to provide a large contribution to melt.

The normal to the surface was predicted using Equation 7.25 and the incident radiation on a sloping surface was derived using Equation 7.26. These approximations were successfully used by Kumar *et al.* (1999).

Normal to the surface estimates were made every five days with a constant flux assumed for that period. Sunrise and sunset times were also estimated for that time period, allowing calculation of the number of day light hours which was used to calculate the sub daily time steps. Each day was divided into 10 time intervals, during which radiation fluxes were assumed constant. This was believed to create a representative net daily radiation receipt and maintain computational efficiency. Direct beam radiation calculations were made and topographic shading was incorporated for each calculation using the methods outlined in Chapter Four. Predictions were in made in Joules per m^{-2} and were multiplied by 60 (to minutes) *60 (to hours) * time interval in hours to convert to time step totals, which were then summed for the day, 5 day period and month.

7.5.4 **Modelled Diffuse Radiation**

Diffuse radiation was modelled following the work of Brock and Arnold (2000), who recorded good results and lower computational costs and simulated accurate spatial receipt patterns. Diffuse radiation was given by Equation 7.30, where the diffuse fraction turned to 1 under clear sky conditions and under cloudy conditions was given by Equation 7.27. The diffuse fraction was used to allocate the proportion of incident short wave radiation (given here as the normal to the surface) that was received as diffuse radiation.

Predictions of diffuse radiation followed the same pattern as outlined for direct beam radiation in section 7.5.3. where both short wave components are only received during daylight hours.

7.5.5 **Modelled Longwave Radiation**

Longwave radiation was modelled as an incoming and outgoing flux, where positive values indicate fluxes towards the surface. The incoming radiation flux was predicted following Oke (1987), given here in Equation 7.12. Effective and clear emissivity were predicted following Brock and Arnold (2000) Equations 7.14 and 7.15 respectively. These parameterisations were found to give realistic results and good accurate approximations.

The outgoing longwave flux following Brock and Arnold (2000) was held as a constant at 316 Wm^{-2}. This assumption was not reported to limit predictions and is supported by Oke (1987).

Unlike shortwave fluxes (7.5.3 and 7.5.4) longwave radiation driven by temperatures and surface and atmospheric emissivity properties operate during the day and night and were calculated hourly for each of the five day periods. Mean monthly temperature read into the model was used to predict diurnal variations using sine and cosine functions (section 6.4). Predictions of incoming and outgoing fluxes were made in Joules m^{-2} and converted to minutes and hours and summed for the day, each 5 day period and month to create monthly net flux estimates.

7.5.6 **Modelled Cloud Cover**

Cloud cover data outlined in section 6.6.3 was used to drive cloud cover parameterisations in the energy balance model. Five different cloud simulations are modelled to allow their effect on

accumulation to be assessed and the most optimal model for snow accumulation to be identified. Cloud cover was used to both create predictions of global radiation, where losses through scattering, absorption and reflectance were accounted for and to proportion radiation into its diffuse and direction components as a function of cloud cover. A description of the cloud variables and parameterisations uses within the model are outlined in Table 7.7.

Parameterisation / Variable	Description
Average Monthly Okta	• Average monthly okta • Constant for the month • Global radiation = normal to surface * (1 – average okta)
Variable cloud Okta	• Variable cloud cover okta • 5 day estimates • Global radiation = normal to surface * (1 – variable okta)
Diffuse Fraction	• Following Brock and Arnold (2000) (Equation 7.27) divides global radiation into diffuse and direct components
Cloud Parameterisation 1	• Variable cloud cover okta • 5 day estimates • Global radiation = normal to surface * (1 – variable okta) (Following Geiger, 1965) • Following Brock and Arnold (2000) (Equation 7.27) divides global radiation into diffuse and direct components
Cloud Parameterisation 2	• Variable cloud cover okta • 5 day estimates • Global radiation = normal to surface * (1 – (variable okta – 0.1)) (Following Geiger, 1965) • Following Brock and Arnold (2000) (Equation 7.27) divides global radiation into diffuse and direct components

Table 7.7 Details of cloud parameterisation included within the model

7.5.7 **Modelled Turbulent Heat Exchanges**

Large uncertainties surround all estimates of sensible heat especially over snow cover (Arck and Scherer, 2002) and in complex terrain (Martin and Lejeune, 1998) where where topographically induced turbulence often leads to exchanges exceeding average values. Strategies to address this problem proposed the use of improved roughness measures that considered upwind variations. This was incorporated into the predictions of this study within the wind speed modelling component in a 'bulk' prediction method, selected for its reduced computational costs and lower data requirements.

Local estimates of the sensible heat flux, driven by diurnal temperature predictions and local wind speeds followed the Young and Woo (1997). Where the sensible heat flux was given by Equation 7.34, 7.35, 7.37 and 7.38, Richardson numbers were calculated using Equation 7.36 following Oke (1978) and the stable and unstable drag coefficients following Price and Dunne (1976) Equations 7.37 and 7.38. This methodology was chosen as it found to produce robust results in a review of prediction models by Arck and Scherer (2002) and allowed for the parameterisation of stable and unstable conditions above the glacier surface.

Predictions of sensible heat followed the same pattern as outlined for longwave radiation in section 7.5.5.

7.5.8 **Example Energy Balance Output**

The net radiation available to melt was summed at the end of each month, the energy balance components outlined in sections 7.5.3 – 7.5.6 were also summed and used to validate estimates and interpret glacier accumulation predictions.

Example output from the energy balance component of the model is shown in Figure 7.9 a - e. All energy balance components exhibit a marked spatial organisation, where differential receipts are topographically organised. Direct and diffuse components (Figure 7.9 a and b) show some evidence of propagated DEM error, but this is not found in resultant glacier predictions, and is noticeable due to the strong slope components to predicted direct and diffuse radiation.

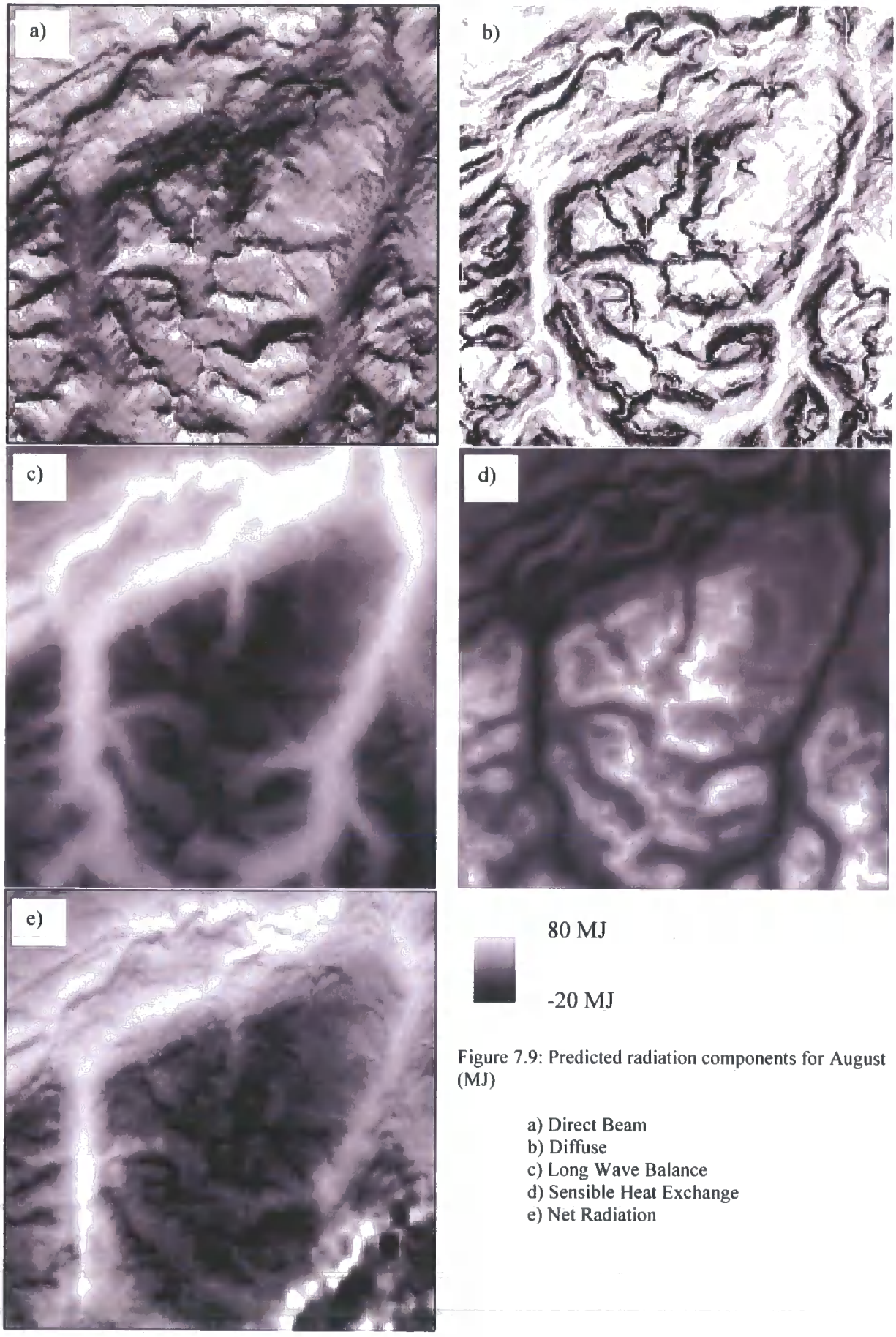

Figure 7.9: Predicted radiation components for August (MJ)

a) Direct Beam
b) Diffuse
c) Long Wave Balance
d) Sensible Heat Exchange
e) Net Radiation

Predictions also exhibited diurnal, daily and monthly trends congruent with expectations.

7.6. **Mass Balance Model**

Predicted monthly net balance, precipitation and temperature were used to predict monthly snow accumulation. Each of these components are known to have an important contribution to melt, supported by the research of Marks *et al.* (1999), who used distributed climate and net radiation to predict melt for known precipitation events and stressed the need for accurate climate forcing surfaces.

A two layer snow pack was used to represent new and old snow, where melt only occurred when there was a positive flux towards the surface and the snow temperature was at or above melting point (0°C) or could be warmed to this temperature. Melt occurred until all the energy or snow was extinguished, and if energy remained heating and melting could occur on the old snow.

The model structure presented here is supported by the work of Greuell and Genthon (2004) who state that spatially distributed temperature and precipitation fields must be used when predicting spatially distributed melt.

7.6.1 **Snow pack model**

Bulk subsurface models (Greuell and Genthon, 2004) differentiated between layers of snow, their albedo and melt rates. This research used a two layer snow pack model, representing fresh snow (layer 1, from month n) and the previous months snow (layer 2, from month n-1). Only two snow layers exist at any one time requiring merging of old snow layers, where snow remaining from the month before, month (n –2), is combined with the snow from month (n –1) by adding the two remaining depths. Each snow layer maintains its surface temperature.

A two layer snow pack model was believed to provide advantages over a single layer model, where surface temperature could be maintained for each, providing a representation of snow rheology which is known to be distinct between events (Male and Gray, 1981).

7.6.2 **Heating Algorithm**

Many ablation models use a zero degree assumption when calculating melt. This assumes the snow or ice surface to be at 0°C, melting point. Under these conditions if there is a positive

energy flux towards the surface all is available for melt, which is expressed (Greuell and Genthon, 2004) as:

$$\frac{dRoff}{dt} = \frac{Qo}{Lf} \qquad \text{(Equation 7.40)}$$

Where dR_{off} is the change in runoff, dt is the time interval, Q_o is the energy flux towards the surface and Lf is the latent heat of fusion ($0.334 * 10^6$ J kg^{-1}), with no melt occurring if the energy balance towards the surface is negative. Although this assumption is largely valid for many mid latitude glaciers, it does not hold for high altitude or high latitude glaciers when the snow surface frequently drops below zero or for early spring ablation. This was confirmed by Oerlemans *et al.* (1991, 1992), where a depth equivalent to 2 meters of ice was heated at the beginning of the ablation season and was only available to melt when this was warmed to 0°C. The method outlined by Oerlemans *et al.* (1991, 1992) was extended here to account for monthly precipitation events, where each months precipitation fell at the predicted atmospheric temperature (T_a), and when $T_a < 1$ °C energy from the net predicted balance warmed the layer to 0°C when melt could occur. At the end of the month the most recent snow layer was combined with the previous layer (section 7.6.1). Resultant merged layer snow surface temperature was calculated by averaging the values from month (n-1) and month (n-2).

The specific heat capacity of ice is 2009 J (Oke, 1987), which is the energy required to heat 1 kilogram of water by 1 °C. Snow weight was calculated by multiplying snowfall depth in meters by water density (1000kg/m^{-3}). The steps in the heating programme are outlined below:

Snow Heating Algorithm

1) Extract snow surface temperature
2) Calculate degrees of heating required to raise temperature to 0°C.
3) Extract snow depth and convert to meters
4) Calculate snow weight (kg) by multiplying by water density
5) Required energy = Snow weight * degrees of heating required * specific heat capacity.
6) Extract energy available to heat snow
7) Calculate available – required energy to establish surplus or deficit.
8) If surplus, energy left saved to use in melting algorithm, snow temperature set to 0°C. If deficit, snow is heated to temperature possible within available energy, snow temperature set and available energy set to 0.

7.6.3 **Melting Algorithm**

The latent heat of fusion is the energy required to convert 1 kilogram of snow to water, for ice this is ($0.334 * 10^6$ J kg^{-1}). Snow weight was calculated by multiplying snowfall depth in meters by water density (1000kg m^{-3}). The steps in the melting programme are outlined below:

Snow Melting Algorithm

1) Extract snow surface temperature
2) If snow temperature >= 0 °C and energy available > 0 J melting can occur.
3) Extract snow depth and convert to meters
4) Calculate snow weight (in kg) by multiplying depth (in m) by water density
5) Required energy = Snow weight * Latent heat of fusion.
6) Extract energy available to melt snow
7) Calculate available – required energy to establish surplus or deficit.
8) If surplus, energy left saved to use in heating layer 2 snow, snow left in layer 1 set to 0 m. If deficit, part of snow pack is melted by depth possible within available energy, energy available to heat layer 2 snow set as 0 and snow accumulation set as net depth from layer 1 + layer 2.

If energy remains after melting new snow, heating and melting of last months snow (snow layer 2) occurs. If energy remains after melting snow layer 2 the remaining energy is assumed to be absorbed by the ground and is not available for the following months heating or melting.

7.6.4 **Example Mass Balance Output**

Snow accumulation was calculated at the end of each month and used to model variations in mass balance through the year.

Example output from the mass balance component of the model is shown in Figure 7.10 a - e. All accumulation predictions showed active melt throughout the year imitated on southerly exposures where net balance receipts were higher. Results show a dominant topographic control on accumulation and the development of snow cover followed expected annual trends.

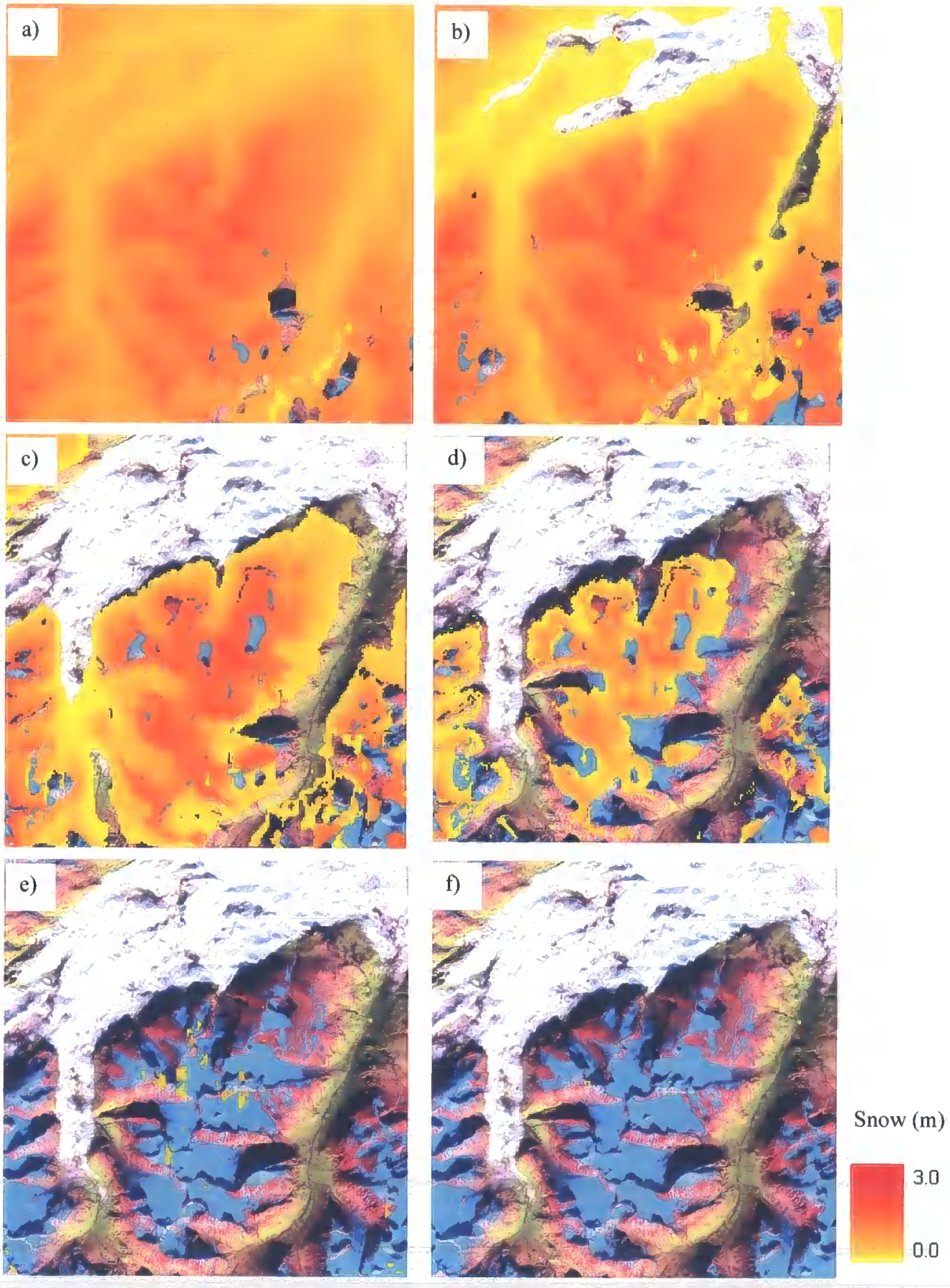

Figure 7.11 Example of snow accumulation output, figures a – f show months May to August

7.6.5 **Model Feedbacks**

Two main feedbacks are incorporated within the mass balance model, surface temperature and surface albedo.

Surface temperature is driven by air temperature and snow surface temperature. Initial model conditions set the surface temperature equal to the monthly mean air temperature. This assumption continues under no snow cover conditions. When monthly mean air temperature at a pixel falls below 1 °C and precipitation falls as snow, surface temperature is driven by snow surface temperature, which is determined by the net radiation balance (Section 7.6.2) and monthly precipitation. Under new snow conditions (when monthly mean air temperature at a pixel falls below 1 °C) snow surface temperature is equal to monthly mean temperature. This temperature will be adjusted if the net radiation balance is positive and heating occurs, as outlined in Section 7.6.2. If the net radiation balance is negative, no energy is available to heat the snow and its temperature remains unchanged. When the snow cover is ablated surface temperature returns to the monthly average air temperature. Surface temperature is an important variable as it drives sensible heat exchanges, where cooler snow surface temperatures (when snow cover remains into the ablation season when air temperatures are greater than 0 °C) than air temperatures initiate negative sensible heat fluxes to the atmosphere.

Surface albedo determines the proportion of incident radiation reflected by the surface and is dependent upon surface spectral characteristics. Snow albedo is included as a feedback within the model that is driven by precipitation, temperature and time since last snowfall. Variations in monthly albedo control the energy available to melt, where less energy is absorbed by the surface under new snow conditions.

Two different albedo variations are modelled to allow their effect on accumulation to be assessed and the most optimal model for snow accumulation to be identified. For both, initial model conditions assume no snow cover and surface albedo throughout the study area is set to 0.4 (average land surface albedo, Table 7.5). Under parameterisation 1, new snow is set to have an albedo of 0.8, which decreases by 0.05 for each month with no new snow cover. This assumes a linear decrease in the reflectivity of snow and is in line with published albedos for different age snow. Under parameterisation 2, following Brock and Arnold (2000). Initial snow albedo is set to 0.9, which decreases to 0.85 for any month with no new snow cover. The latter model reduces the proportion of radiation reaching the ground and reduces the rate of melt.

Snow surface albedo was calculated each month, using precipitation, air temperature and the previous months snow fall. Monthly variations in albedo, resulted in modifications to net radiation available to melt, specifically direct and diffuse components which are dependent on surface albedo. Higher albedos, reduce the proportion of radiation reaching the ground, which reduces the energy available to melt and increases the opportunity for new or maintained snow accumulation – resulting in maintained albedos (new or old snow). Lower albedos, increase the proportion of radiation reaching the ground, which increases the energy available to melt and decreases the opportunity for new or maintained snow accumulation – resulting in lower albedos (old snow or bare ground).

7.7. **Conclusions**

The mass balance model addresses limitations in existing approaches, by using spatially distributed climatic surfaces and monthly net balance to drive a spatially distributed melt model. Albedo and cloud are recognised as important controls on accumulation and have received specific attention within the model. Parameterisation of radiative fluxes was optimised for data availability, climatic and stability conditions on the surface and to ensure the model maintained consistent complexity within each model component.

Temporal and spatial resolutions of the model are optimised for process modelling, data resolution limitations and computational efficiency. Multiple model runs driven by different climatic and radiative parameters outlined in Table 7.8 were used to identify sensitivities of snow accumulation and the model to different model inputs.

Climatic Variables	Radiative Variables
Mathematical Modelling	No cloud cover
Mathematical Modelling with interaction term	Monthly average cloud cover
Seasonal Lapse rates	Variable cloud cover
Geomorphic Lapse rates	Diffuse fraction
IPCC warming extreme prediction	Cloud Parameterisation 1
LGM reconstructions	Cloud Parameterisation 2
	Without Diffuse Radiation
	Without Sensible Heat Exchanges
	Without Topographic Shade

Table 7.8: Climatic and radiative parameters used to investigate snow accumulation sensitivity

CHAPTER EIGHT

RESULTS AND DISCUSSION

8.1. Introduction

This chapter presents and discusses model glacier accumulation area predictions, examining their climatic and radiative sensitivities and their ability to simulate observed glacier distributions.

Discussion and sensitivity analysis of the model is structured around climatic and energy balance variables, identifying variations in winter accumulation maximum, onset of melt, rate of melt, energy balance characteristics and the spatial distribution of melt throughout the ablation period. A discussion of the sensitivity of melt to both climatic and energy balance model components follows, with later comments on topographic sensitivities found through the study.

Model predictions do not account for ice flow, and predictions only identify accumulation areas, defined by their positive annual mass balance. Validation data delineates glacier extent and accumulation areas are not individually identified. Accumulation area ratios (AAR) are commonly used to predict the ELA and down glacier extent of the accumulation area. A value of 0.7 suggested by Glen (1963) is the most commonly used (Paterson, 1981).

Analysis of resultant glacier accumulation area distributions evaluates the spatial extent of predictions, their topographic organisation and the rate and onset of melt. Interpretation is aided by draping the predictions on a Landsat ETM+ colour composite scene and examining temporal sequences of melt.

8.2. Study Area Glaciers

The glaciers within the study area are shown in Figure 8.1. This central Jotunheimen area was selected as it contains over 20 glaciers of differing sizes, aspects, topographic position and shape.

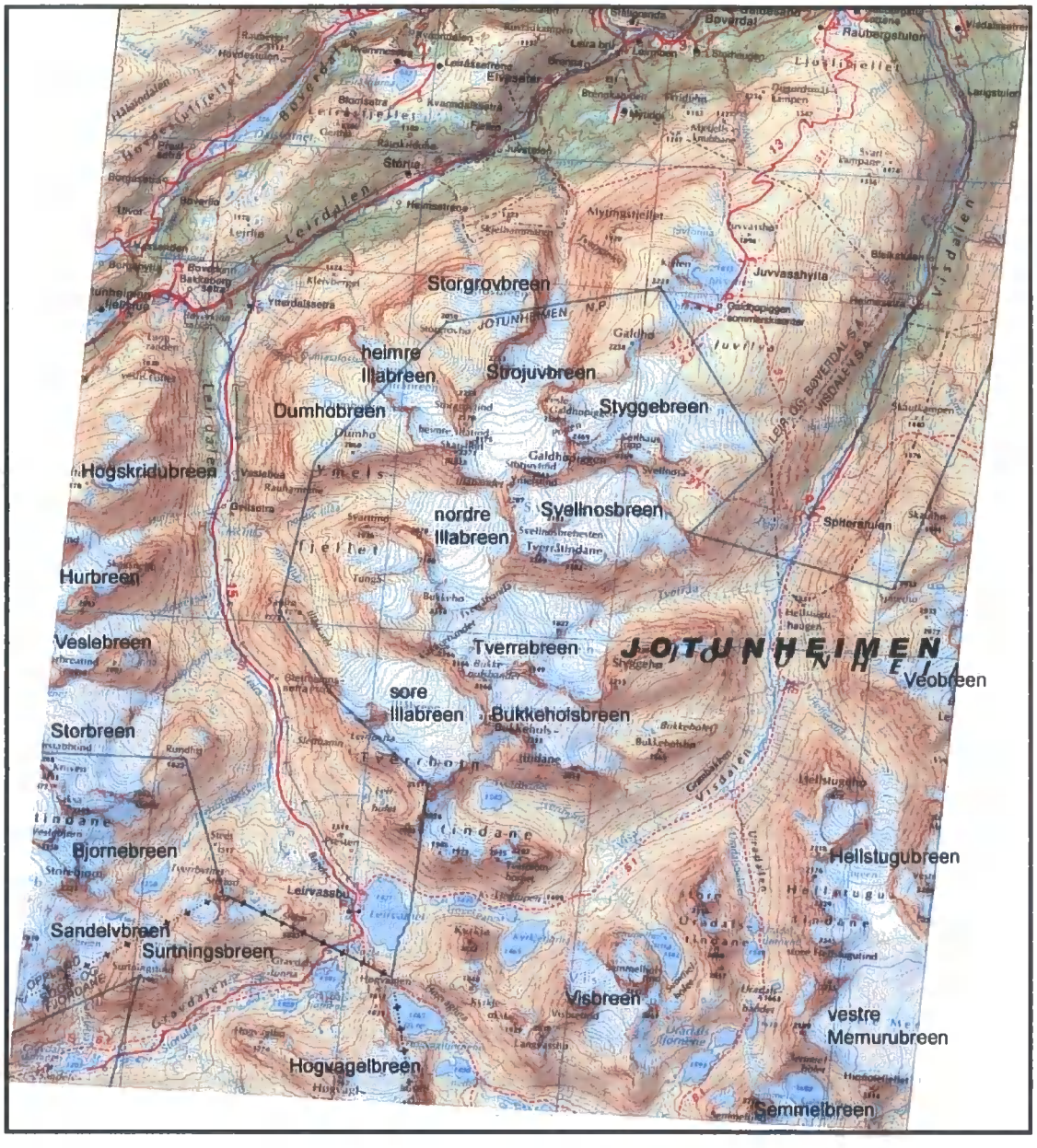

Figure 8.1: Geocorrected topographic map of the study area highlighting the distribution of glaciers (in white). Source: the 1:100000 Statens Kartverk topographic map of Jotunheimen, updated in 1997. Although the map was updated in 1997 it is unclear if the glacier extents were updated at this time. Little disagreement is shown between the map and the Landsat ETM+ scene used in the present study.

8.3. Model Summary

The glacier accumulation prediction model used within this discussion chapter has a temporal resolution of one month (see Table 8.2 for other resolutions used within predictions) and a spatial resolution of 100 m. Accumulation occurs where there is insufficient energy to melt snow precipitation, where energy balance is calculated using direct, diffuse and turbulent heat exchanges at the surface.

8.3.1. Initial conditions and mass balance seasons

Month 1 = August, no snow cover and albedo of 0.4.
At month 2, September, albedo and surface temperature are predicted using the output from August calculations.
Predictions are made every month for net radiation balance and melt.
Predictions continue until the end of the following August.

8.3.2. Prediction sensitivities

This chapter addresses the sensitivity of the glacier accumulation model to the factors laid out in Table 8.1.

Climatic Variables	Radiative Variables
Mathematical Modelling	No cloud cover
Mathematical Modelling with interaction term	Monthly average cloud cover
Seasonal Lapse rates	Variable cloud cover
Geomorphic Lapse rates	Diffuse fraction
IPCC warming extreme prediction	Cloud Parameterisation 1
LGM reconstructions	Cloud Parameterisation 2
	Without Diffuse Radiation
	Without Sensible Heat Exchanges
	Without Topographic Shade

Table 8.1 Variables that will be varied during the model testing

Variable	Resolution	Justification
Flux Normal to the Surface	5 Days	• Little variation occurs within shorter time periods
Direct Beam Radiation	10 times a day	• 10 time intervals during daylight hours, constant for 5 day time period
Diffuse Radiation		• Driven by solar position • Daily and seasonal trends modelled with little variation lost.
Sensible Heat	Hourly	• Driven by temperature and fluxes present (day and night) • Strong diurnal trend, driven by diurnal temperature data
Longwave Radiation	Hourly	• Driven by temperature and fluxes present (day and night)
Net Radiation	Monthly	• Computational efficiency • Melt has a known sensitivity to climatic data and these are most robust using monthly mean values • Potential error propagation from unrealistic albedo or surface temperature predictions from extreme climatic events limited the temporal resolution to monthly • Consistency and data availability lead to melt and accumulation calculations at monthly time steps
Albedo		
Surface Temperature		
Melt		
Snow Accumulation		

Table 8.2: Temporal resolutions of modelled processes.

8.4. Validation Data

A Landsat ETM+ scene (Path: 199, Row 17) captured on the 21st September 2001 provided the major validation data set. The topographic map seen in Figure 8.1 was registered to the Landsat image and both datasets were used to aid prediction interpretation and validation. Landsat

ETM+ images have frequently been used in investigations within the crysophere for identifying and characterising snow and ice surfaces through their spectral reflectance properties.

This multi-band sensor provides a high temporal and spatial resolution dataset that, with spectral resolutions greater than SPOT provides an affordable and well researched dataset.

The factors influencing the spectral reflectance characteristics of snow were discussed in section 7.4.2, and published information on the spectral reflectance properties of snow and ice surfaces was used to inform this research.

Dozier (1990) discussed the complex spatial and spectral signatures found in alpine terrain, specifically discussing spectral reflectances of shaded snow. Hill *et al.* (1988) used information on the varied spectral reflectance characteristics of glacier surfaces to infer process or environmental differences or similarities, suggesting that accumulation areas can be partitioned into wet snow, percolation and dry snow facies. Attempts to identify these areas on all of their study area glaciers failed, however, and such delineation was not possible during this research.

Classification of the 8 bands within Landsat data bands 2, 3, 4, 5 and 7 provided the most information. Band 1 was not used within the classifications as it was highly saturated. Hill *et al.* (1998) proposed the use of a band 5:4:2 colour composite to delineate snow and ice landcover. This was successfully employed within this research (Figure 8.2), delineating the study area glaciers and other smaller areas of potentially non-permanent snow cover.

The colour composite image provided a raster overlay but a vector polygon coverage was created using an ISODATA classification which identified two classes of snow and ice cover which were merged to one glacier class (Figure 8.3).

Study area glaciers delineated in 5:4:2 composite of Landsat ETM + scene captured on 21st September 2000.

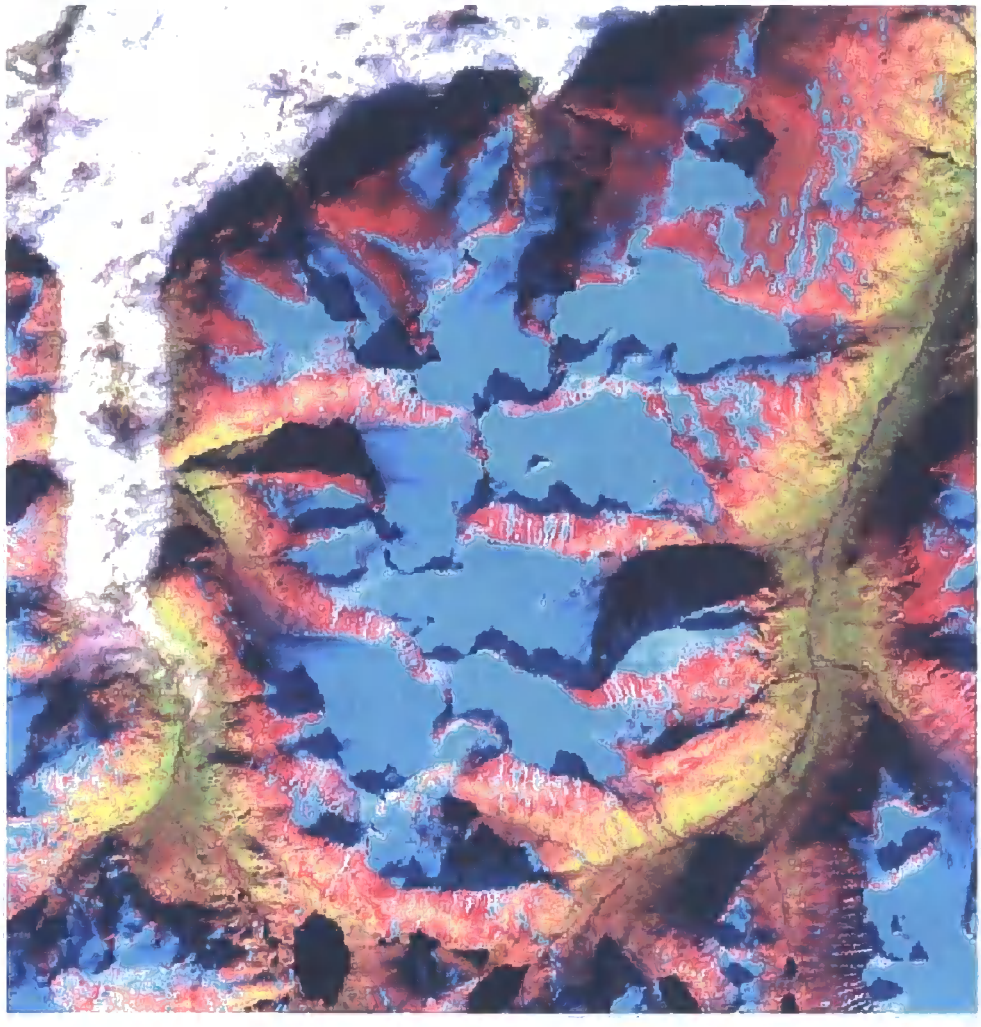

0 0.5 1 2 Kilometers

Snow and glacier ice are visible in cyan on the 5:4:2 composite of the Landsat ETM+ scene.

This clear delineation also identifies smaller snow covered areas that are likely to represent snow patches and avalanched snow.

Figure 8.2: Landsat ETM+ 5:4:2 Colour Composite of Study Area

Classification of Landsat ETM+ image, glacier and cloud are shown in blue class which is draped over colour composite

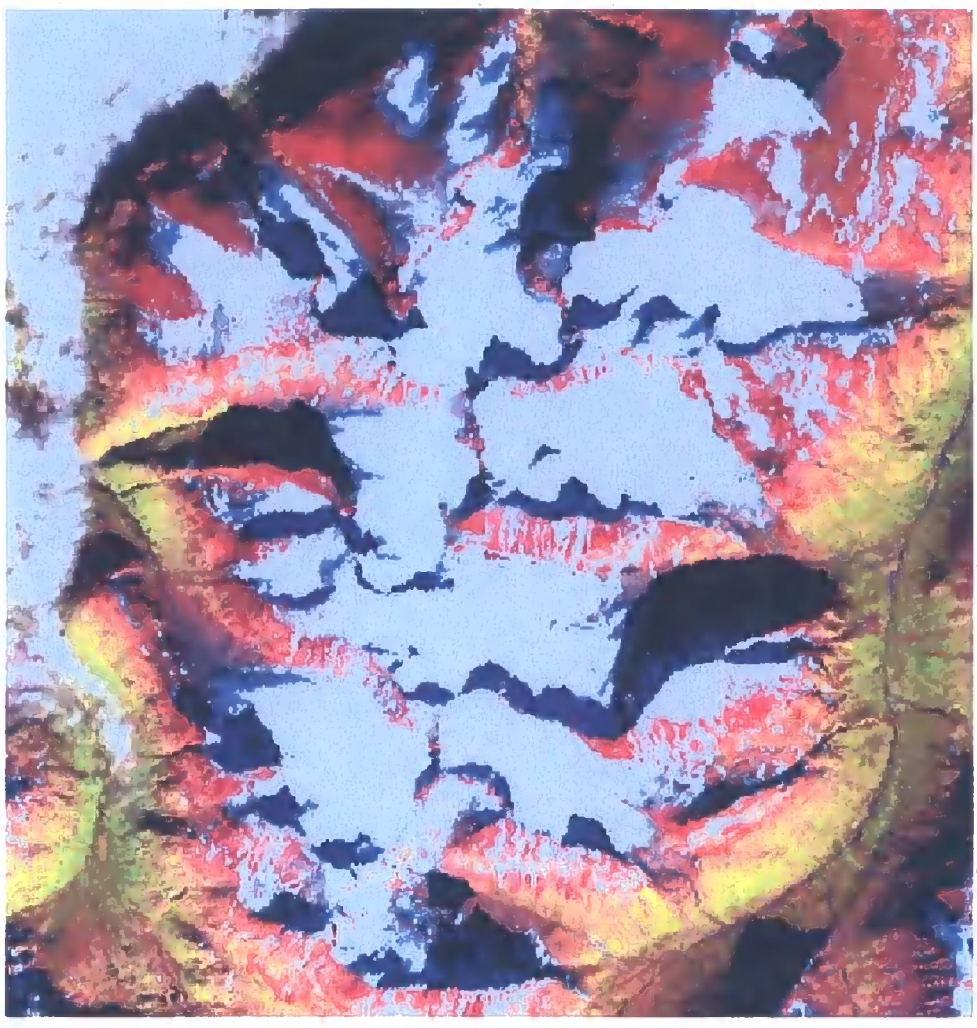

An unsupervised ISODATA classification of bands 2,3,4,5 and 7 was found to be the most successful technique for delineating glacier extent with 4 bands in the classified image.

0 0.5 1 2 Kilometers

Topographically shaded and illuminated snow were identified as two different classes, but were merged for this application. Initial attempts to delineate accumulation areas proved unsucessful and will be estimated using the contours on the topographic map.

Figure 8.3: Unsupervised ISODATA Classification of Study Area

Attempts to differentiate between glacier and cloud cover were not possible within the present study and consequent vector representations of the classified image are noisy. Without extensive generalisation and filtering, vectorised datasets provides a less useful tool than

expected. Glaciers are well represented and delineated but Boolean overlay was no longer feasible as an efficient validation tool where false positive overlay results of observed vs. predicted glacier would mask true patterns. The greatest value of the Landsat and classified image was gained from using them primarily as a visual validation tool and as a simple overlay validation dataset.

Validation of glacier accumulation area predictions were performed, primarily to assess the ability of the model to accurately predict the spatial distribution of snow accumulation. Examination of areas of match and mismatch were performed by the user to identify any topographic sensitivities in the model's predictive abilities. Quantitative measures of degree of match, derived from the remotely sensed image, would not provide useful statistics and a more meaningful measure of relative performance for different aspects, altitudes, surface concavities and glaciers was possible by visual examination. Quantitative measures of degree match, between the remotely sensed classification and predictions, would include all incorrectly classified pixels, and this would consequently provide an erroneous statistic with limited use. Assessment of the accuracy of predicted snow depth can currently not be quantified, but if a snow depth validation dataset were available, it would provide an optimal accuracy assessment tool and will be explored as a validation dataset for the future.

8.5. **Model predictions**

8.5.1. **Lapse Rate 2**

Initial model predictions exhibited pronounced sensitivity to high altitude summer temperatures, these had been over predicted within the mathematical and mathematical with interaction term modelled datasets and consequently limited the duration of winter accumulation. The predicted 0.0043 $^{o}C\ m^{-1}$ lapse rate from the mathematical modelling with interaction term was replaced with a commonly reported lapse rate of 0.006 $^{o}C\ m^{-1}$ (Barry, 1992) to investigate accumulation sensitivity. This lapse rate is now referred to as lapse rate 2.

Initial model runs with the precipitation surfaces created in section 6.2 were found to under predict high altitude snowfall, with all snow ablated by April under full energy balance conditions. Snowfall predictions simulated the spatial distribution of snowfall but underestimated high altitude receipt using the limited climate station data available. Although efforts were made to use regional climate data and statistically significant relationships, poor representation of high altitude climate failed to account for extreme conditions and could not

simulate high altitude receipts. Comparison of predicted and observed altitudinal gradients of precipitation using mass balance records for Norwegian glaciers confirmed the underprediction and were used to adjust the altitudinal component of the precipitation lapse rates. Using records from seven glaciers (Table 8.3) a value of 0.002 m m^{-1} was implemented but found to overpredict snowfall with annual sums exceeding 30 m. Although the lapse rate is observed in mass balance records within the accumulation area, where net accumulation is analogous to net precipitation, gradients can be over steepened as they incorporate ablation areas which record no accumulation. A reduced lapse rate of 0.001 m m^{-1} was applied and generated an annual net precipitation maximum at Galdhøpiggen (2469 m) of 3.4 m which is within expected values (Barry, 1992; Dr Ian Evans *pers. comm.*). This altitudinal gradient is used in all subsequent predictions.

Glacier	Maximum Altitude (m)	Height Difference (m)	Winter Balance Difference (m)	Derived Precipitation Gradient
Jostefonn	1600	640	0.8	0.001
Nigardsbreen	1800	1400	1.83	0.001
Austdalsbreen	1650	400	1.3	0.003
Hardangerjbreen	1800	700	1.21	0.002
Storbreen	2000	600	1.14	0.002
Hellstugubreen	2100	600	0.78	0.001
Engabreen	1400	1200	4.95	0.004

Table 8.3 Derived altitudinal gradients in precipitation from mass balance records.

Conditions: Temperature: Lapse rate 2
Precipitation: Adjusted Log Surface (Section 6.6.3.3)
Cloud Cover: 80% cloud cover
Albedo: 0.8 new snow, - 0.05 per month with no new snow

Maximum winter accumulation occurred in April (Figures 8.4a – 8.4f and 8.5) and records the highest accumulation of any simulation, where cooler temperatures lead to a greater and maintained snow precipitation fraction. Snow cover persists throughout the year with maximum melt occurring in July. Positive energy balance and temperatures occur in May and June respectively but the lag in maximum temperatures limited widespread melt until June and July.

Melt is initiated in valley floors and exposed gentle slopes where energy is efficiently transferred to the surface. Extensive melt occurs in June where most high altitude snow is ablated and only localised areas of snow remain (Figure 8.4 d). The spatial distribution of melt indicates that predicted snowfall at high altitudes is insufficient to support perennial snowcover and that surface slope plays a dominant role in determining the spatial distribution of net radiation. Although the model fails to predict extensive accumulation areas; topographically

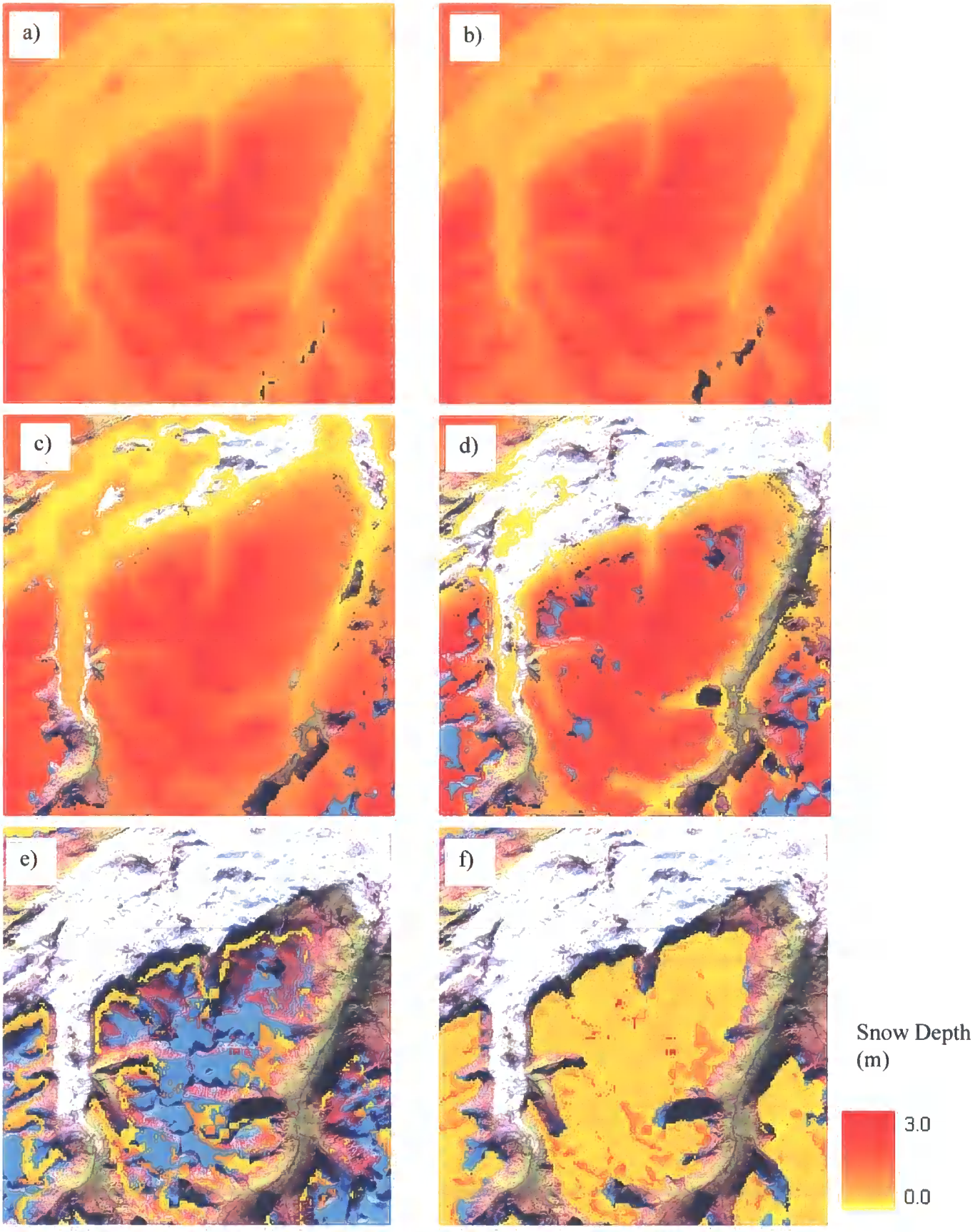

Figure 8.4: Lapse Rate 2 Time Sequence of Monthly Accumulation Area Predictions
a) March, b) April, c) May, d) June, e) July and f) August.

constrained glaciers are accurately predicted (Figure 8.6 b). Snow accumulation is largely predicted on steep slopes where incidence angles lead to less efficient transfers of radiation. The snow on these slopes is likely to be redistributed downslope, which is supported by observed snowpatch distributions.

Extensive accumulation occurs in August when cooler temperatures lead to widespread snowfall which is only partly ablated (Figure 8.4 f). Lapse rate 2 provides unrealistic snow accumulation area predictions but is effective in predicted topographically constrained accumulation areas.

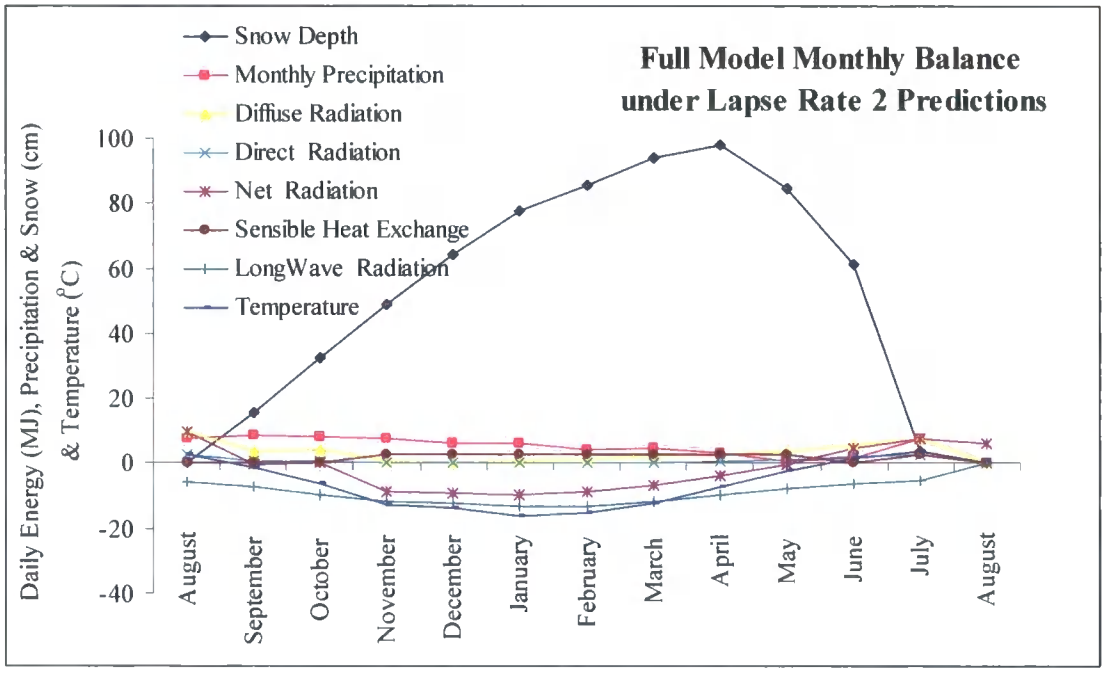

Figure 8.5: Full Model Monthly Balance for Lapse Rate 2 Model

8.5.2. **Seasonal Lapse Rates**

Lapse rate 2 model predictions failed to predict realistic summer and winter temperatures using the steepened temperature lapse rate (Figure 8.4 f). Seasonal lapse rates accounted for distinct trends in temperature gradients in both summer and winter months and were combined with the improved precipitation lapse rate under full energy balance conditions.

Conditions: Temperature: Seasonal Adjusted Lapse Rates
Precipitation: Adjusted Log Surface (Section 6.6.3.3)
Cloud Cover: 80% cloud cover
Albedo: 0.8 new snow, - 0.05 per month with no new snow
Energy Balance: Full

Maximum winter accumulation occurred in April when mean air temperature and monthly net balance were below zero (Figure 8.8). Accumulation occurs throughout the year with maximum melt in July. Topographically derived lapse rates drive melt in early spring, when melt is concentrated in valley locations. Lower altitude sites are ablated in May and June with some high altitude sites still accumulating snow. Extensive melt occurs in July when net balance and temperature are at their maximum (Figure 8.8). Topographically derived lapse rates constrain melt to lower altitudes with snow remaining in high altitude accumulation zones through July and August.

The spatial distribution of accumulation in July achieves a more representative prediction than seen in 8.4.1 where glacier accumulation areas are predicted. August ablation reduces the number of glaciers predicted but constrains predictions to glacier accumulation area locations.

The model predicts both topographically constrained and high altitude glaciers, but is more consistent in predicting high altitude glaciers [Box A in Figure 8.7 f], where lower temperatures and higher precipitation results in greater accumulation. Less robust predictions are made in topographically constrained areas [Box B in Figure 8.7 f] where topographic shade, local microclimate and redistribution of snow are important in controlling accumulation.

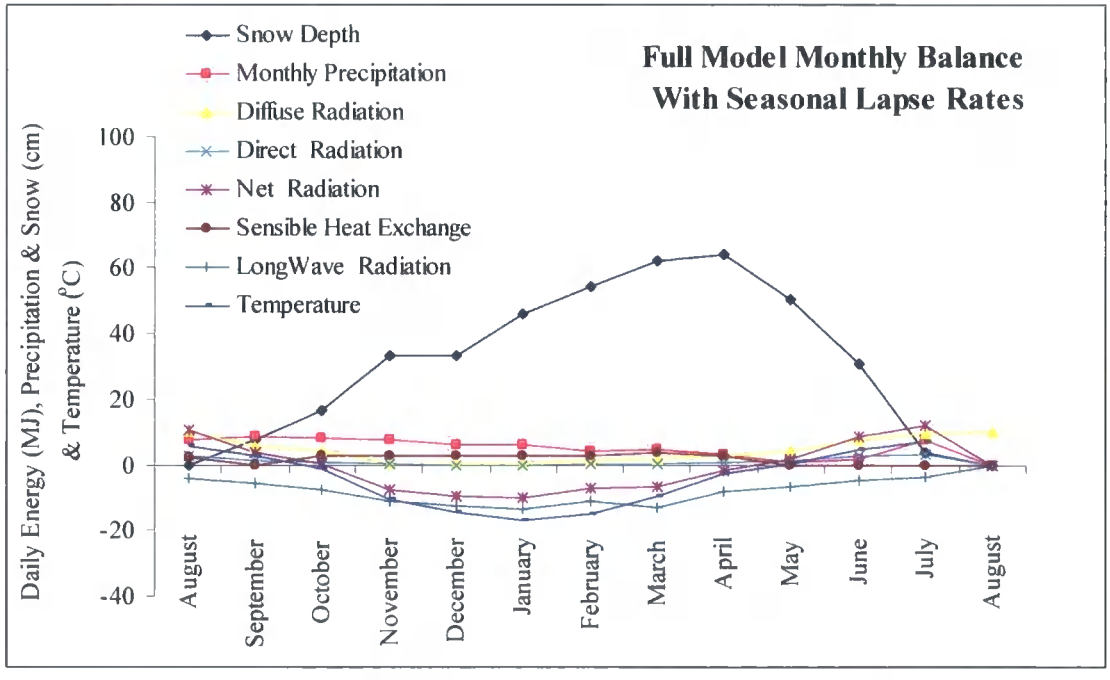

Figure 8.8: Full Model Monthly Balance for Seasonal Lapse Rate Model

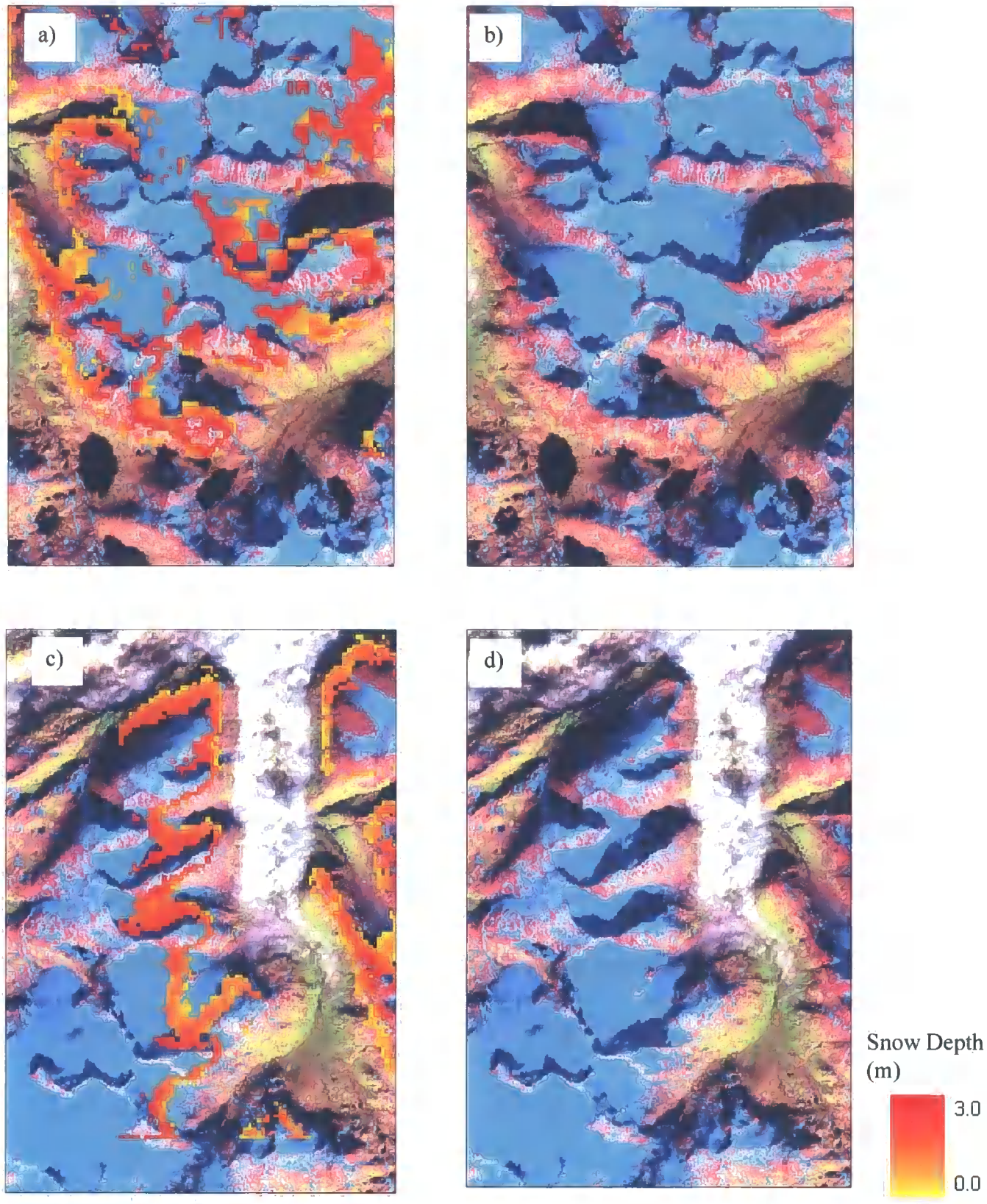

Figure 8.6: Lapse Rate 2 July Accumulation Scenes. a) Central massif area, b) Cirque Glaciers (right: unsupervised Landsat classification; left: ditto with snow accumulation areas).

8.5.3. Geomorphic Lapse Rates

Seasonal lapse rates improved snow accumulation predictions by accounting for topography in spatially distributed temperatures. Further characterisation of terrain-constrained melt using geomorphologically derived lapse rates was investigated.

Conditions: Temperature: Adjusted Geomorphic Lapse Rate
Precipitation: Adjusted Log Surface (Section 6.6.3.3)
Cloud Cover: 80% cloud cover
Albedo: 0.8 new snow, - 0.05 per month with no new snow
Energy Balance: Full

Maximum winter accumulation occurred in March as a result of a slightly warmer spring with maximum melt occurring between April and June (Figure 8.10). High autumn temperatures limit accumulation before October and gradual melt occurs through summer driven by slowly increasing temperatures and net radiation receipt. The annual variation in net balance exhibits a pronounced annual cycle that is driven by temperature and ablation trends (Figure 8.10).

The spatial distribution of predicted temperatures results in more topographically constrained melt, largely focused within the major valleys (Figure 8.9b). Summer maximum melt occurs within shallower slopes at higher altitudes (Figure 8.9c, Box A) with thinning of accumulated snow throughout.

July and August snow cover is constrained to accumulation areas but under predicts distributions as warmer summer temperatures drive greater ablation at all but the highest glaciers.

The model accurately predicts topographically distributed temperatures but is restricted by the climate dataset, it over predicts high altitude summer temperatures. Topographically constrained glacier accumulation areas are not evident in July and August simulations and are not effectively predicted by the model which identifies them as warmer convex locations.

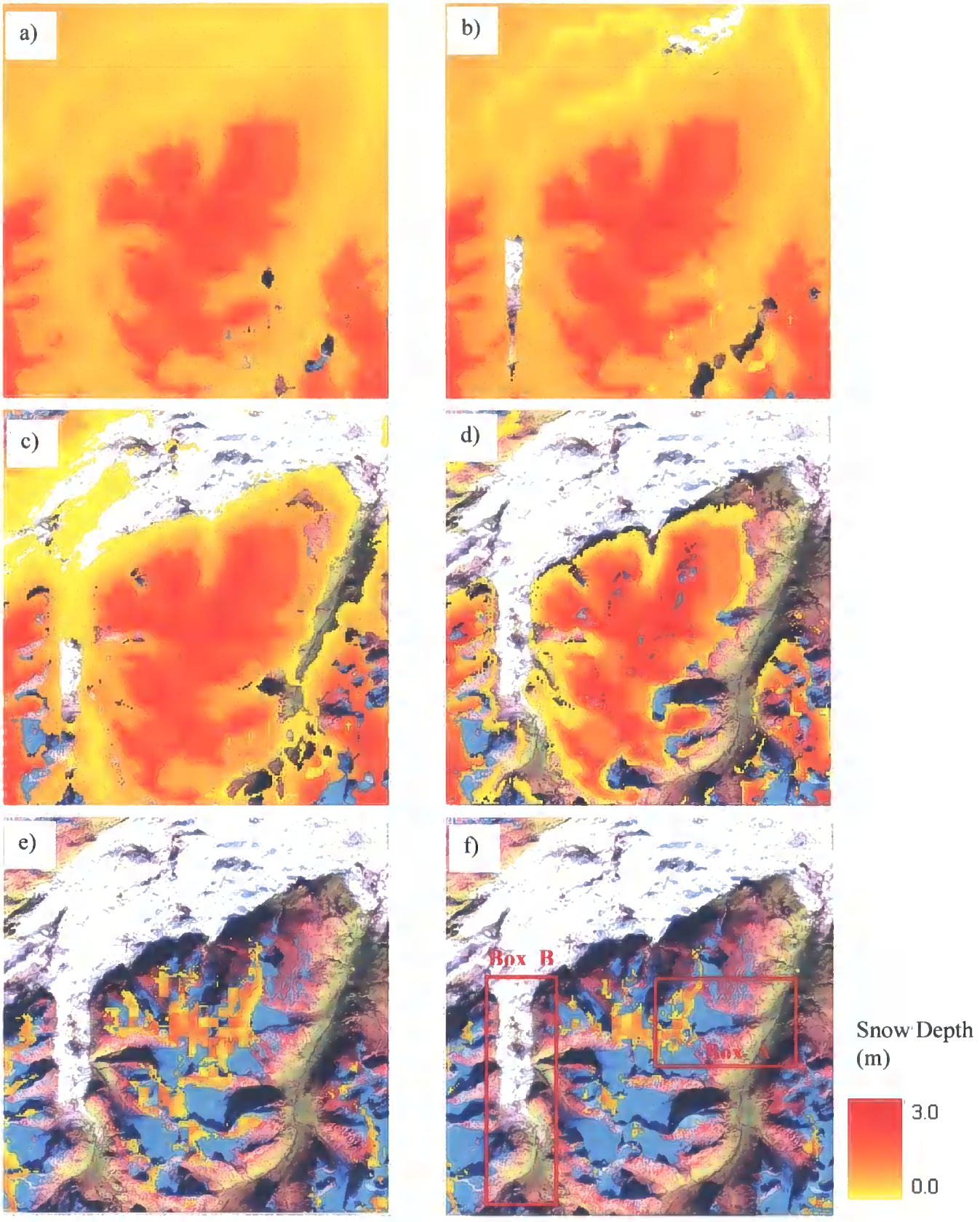

Figure 8.7: Seasonal Lapse Rate Time Sequence of Monthly Accumulation Area Predictions
a) March, b) April, c) May, d) June, e) July and f) August.

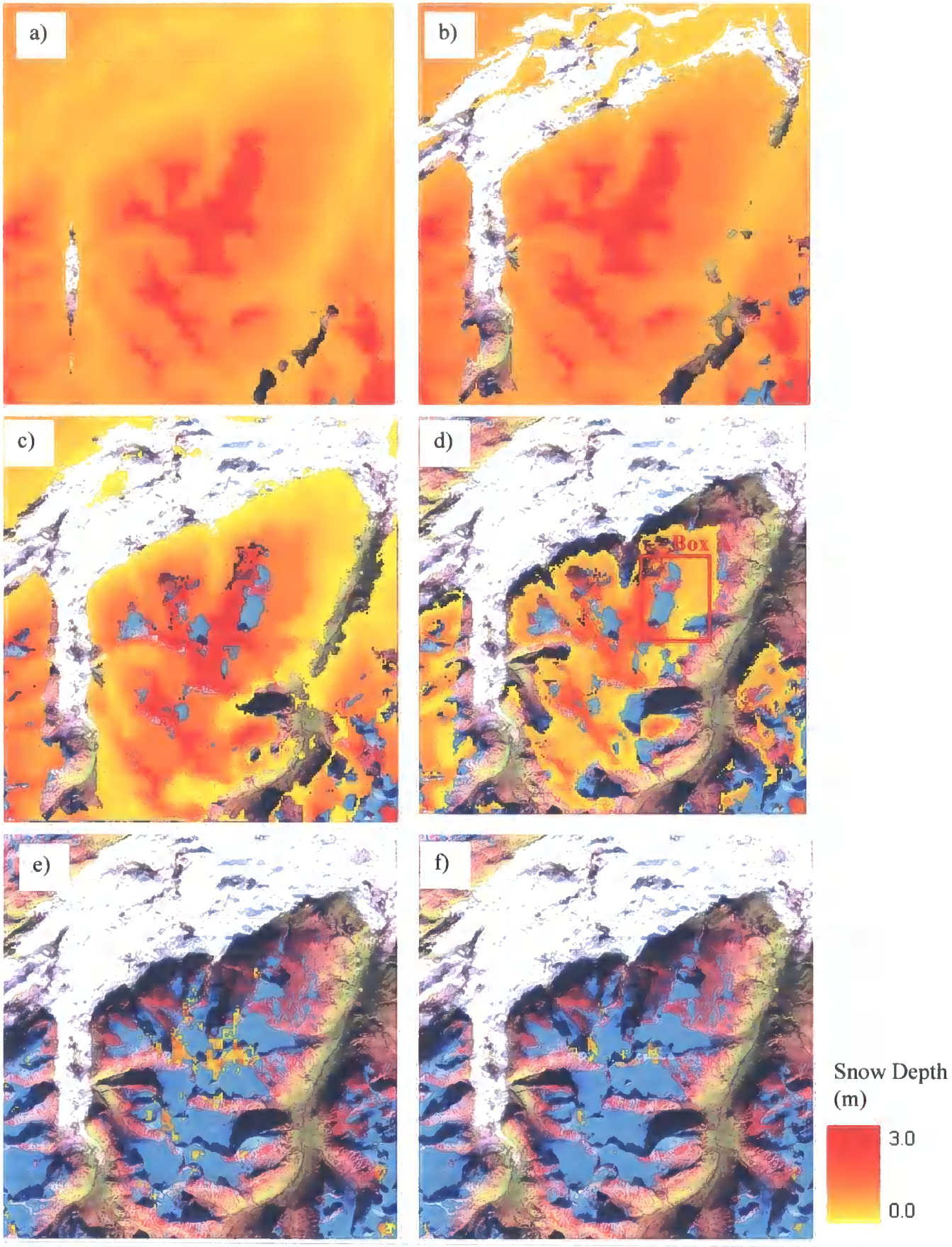

Figure 8.9: Geomorphic lapse rate time sequence of monthly accumulation area predictions

a) March, b) April, c) May, d) June, e) July and f) August.

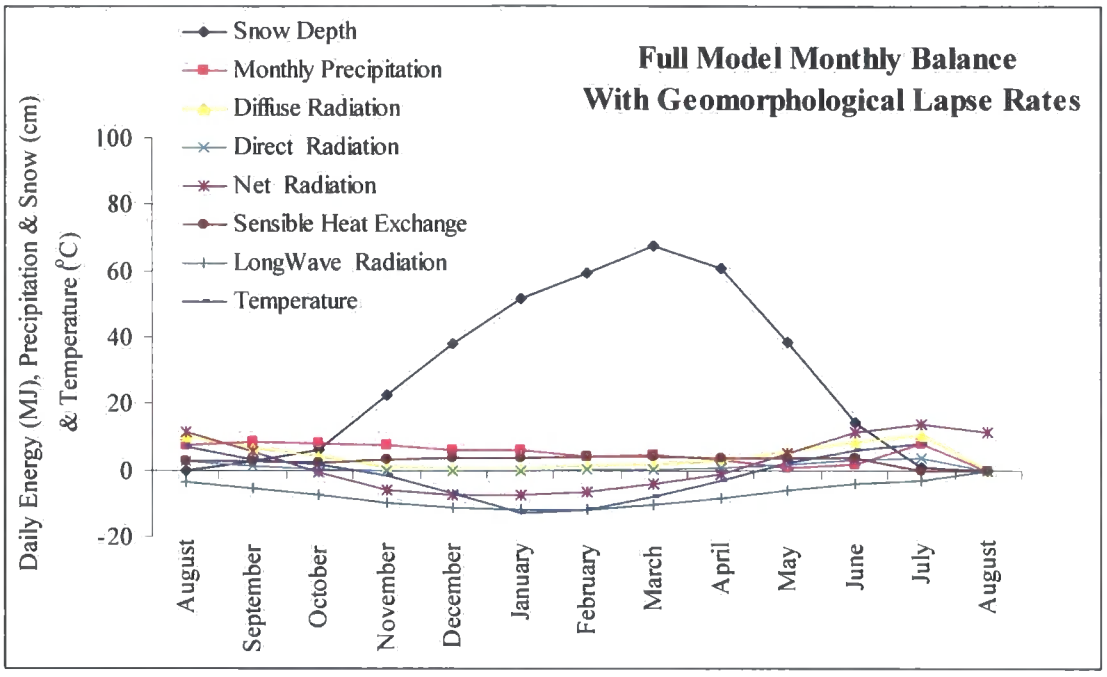

Figure 8.10: Full model monthly balance for geomorphic lapse rate model

8.5.4. IPCC

Sensitivity of glacier accumulation to climatic change is a research question of critical importance and has received recent attention (Brun *et al.*, 1997 and Hock *et al.*, 2002). A simplistic sensitivity approach using IPCC extreme future climate change predictions of 3.5 °C warming by 2100 (IPCC, 2001) was used to drive the glacier accumulation area model. No other climatic parameters were changed.

Conditions: Temperature: Seasonal Adjusted Lapse Rates + 3.5 °C
Precipitation: Adjusted Log Surface (Section 6.6.3.3)
Cloud Cover: 80% cloud cover
Albedo: 0.8 new snow, - 0.05 per month with no new snow
Energy Balance: Full

Maximum accumulation occurred in March, with accumulation largely restricted to the period October to July. Localised melt occurs in March and April on shallow and southerly facing slopes. Extensive melt occurs in May and June with only localised areas of snow remaining in July. Highest melt rates occur in June when low altitude valley floors and shallow slopes receive maximum net radiation receipt and increased melt from positive sensible heat fluxes towards the surface.

Air temperature has a dominant influence on the mass balance and annual net radiation balance, where positive temperatures from May drive positive energy balances peaking in July and warmer winter temperatures limit accumulation (Figure 8.12). The rate and distribution of melt are in agreement with a global mean sensitivity of – 0.37 m $^{\circ}C^{-1}$ $year^{-1}$ reported in Dyurgerov (2003), where sensitivities predicted within the model here are – 0.51 m $^{\circ}C^{-1}$ $year^{-1}$ for maximum snow depth prediction. However this value represents an average for the entire study area and as discussed by Dyurgerov (2003) and Braithwaite (2002) sensitivities will differ within and between catchments.

The spatial distribution of melt is consistent with the warmer trends found with the geomorphic lapse rates in Section 8.4.3, where low altitude shallow slopes are initially melted with all topographically constrained accumulation ablated by July. Limited highly localised snow remains through the year where topographic shade and aspect limit net radiation receipt (Figure 8.11 f).

Future warming imposes clear controls on snow accumulation with limited and localised pockets of snow remaining under this warming scenario. Although surface temperature and albedo feedbacks are incorporated within the model further feedbacks or climatic changes have not been modelled and must be completed in future research to assess the robustness of accumulation predictions. However, it is still clear that mean monthly temperature has a dominant influence on winter accumulation and summer melt.

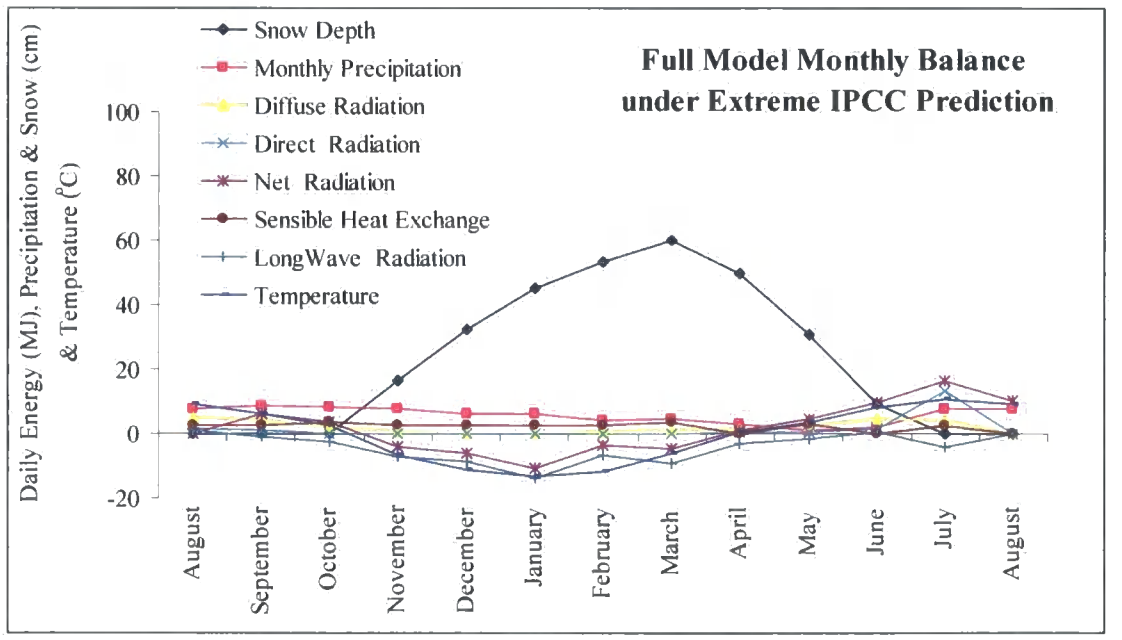

Figure 8.12: Full model monthly balance for IPCC warming scenario model

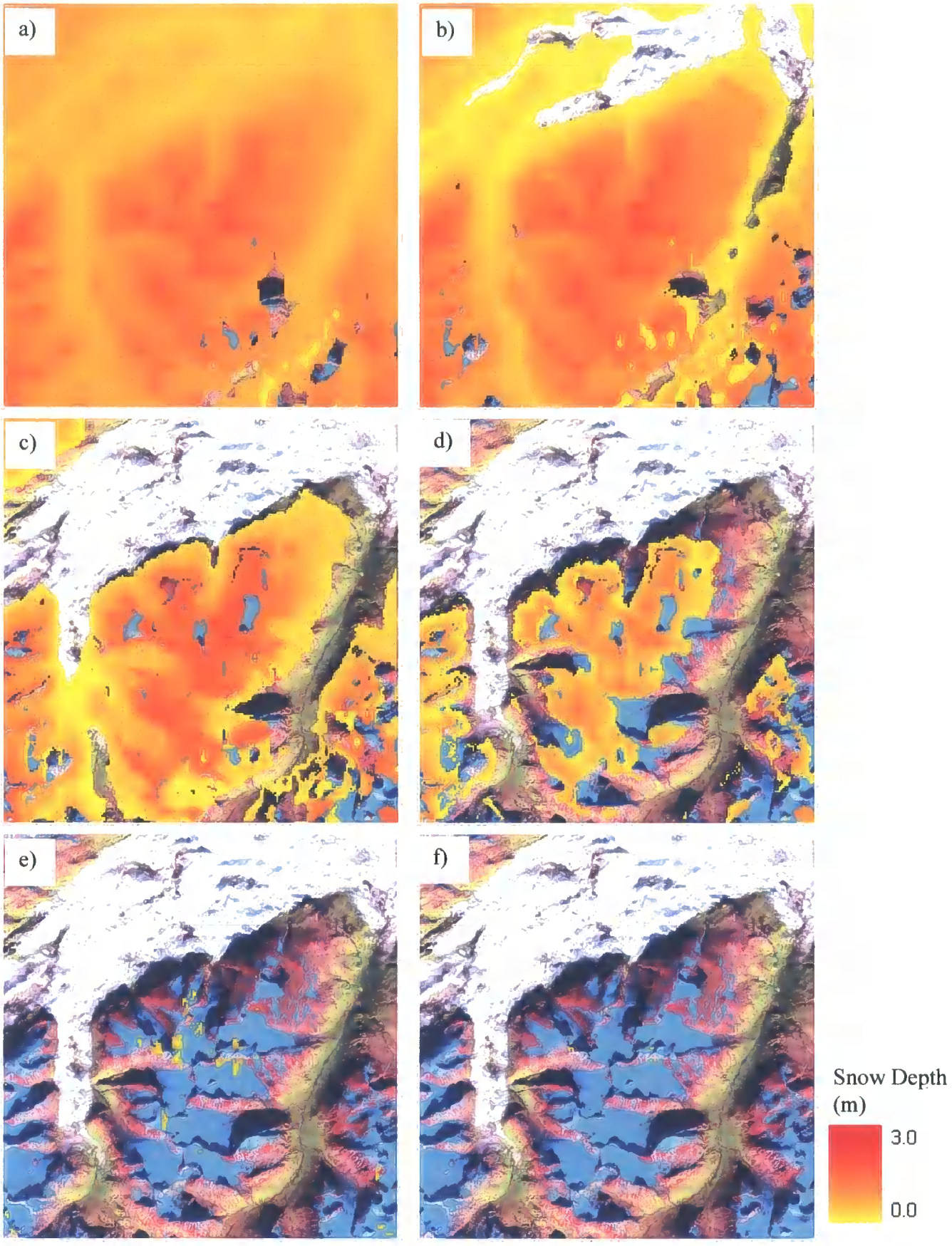

Figure 8.11: IPCC warming time sequence of monthly accumulation area predictions
a) March, b) April, c) May, d) June, e) July and f) August.

8.5.5. Last Glacial Maximum Reconstruction

Consideration of the sensitivity of the cryosphere to future climatic change can be complemented by reconstructions of past climatic change and known glacier extents. The Last Glacial Maximum (LGM) has received much attention and climatic reconstructions are widespread within the literature. Barron *et al.* (2003) found that oxygen isotope reconstructions under estimate temperature. In their LGM 60 km grid climate reconstructions they proposed a 15 °C monthly average temperature fall and 15 mm day^{-1} precipitation reduction from present day conditions for Norway at the LGM. These conditions were used to drive the accumulation area prediction model to investigate how Northern Hemispheric glacial climatic conditions, cooler and drier, influence snow accumulation.

Conditions: Temperature: Seasonal Adjusted Lapse Rates – 15°C
Precipitation: Adjusted Log Surface (Section 6.6.3.3) – 15 mm day^{-1}
Cloud Cover: 80% cloud cover
Albedo: 0.8 new snow, - 0.05 per month with no new snow
Energy Balance: Full

Reduced precipitation leads to less winter accumulation, but higher altitudes receive snow precipitation throughout the year. Maximum accumulation during the first mass balance year occurs in March at high altitude locations (Figure 8.14), but these deep snow areas (2.9 m) laterally expand in subsequent mass balance years where no ablation occurs (Figure 8.13f). A positive energy balance is found from April, but melt is constrained by lower temperatures that require more energy to bring snow to melting point.

Melt is initiated in March (Figure 8.14) and is distributed through lower altitude, shallower areas where warmer conditions and more efficient radiation transfer are found. Later melt occurs on south facing exposed sites, but melt is limited and topographically constrained. Predicted snow accumulation rises in July when precipitation increases and areas of earlier melt are replenished.

Perennial snowcover throughout the study area for the entire mass balance year significantly alters initial model conditions, where higher surface albedo and lower surface temperatures will lead to increased accumulation in future model years. Small predicted areas of no snow cover would, accumulate snow by advection throughout the year. This result is congruent with reported glacier extent at the LGM when the area was covered by the Fennoscandian ice sheet and with reconstructions of cooling in Southern Norway (Lie *et al.*, 2003b).

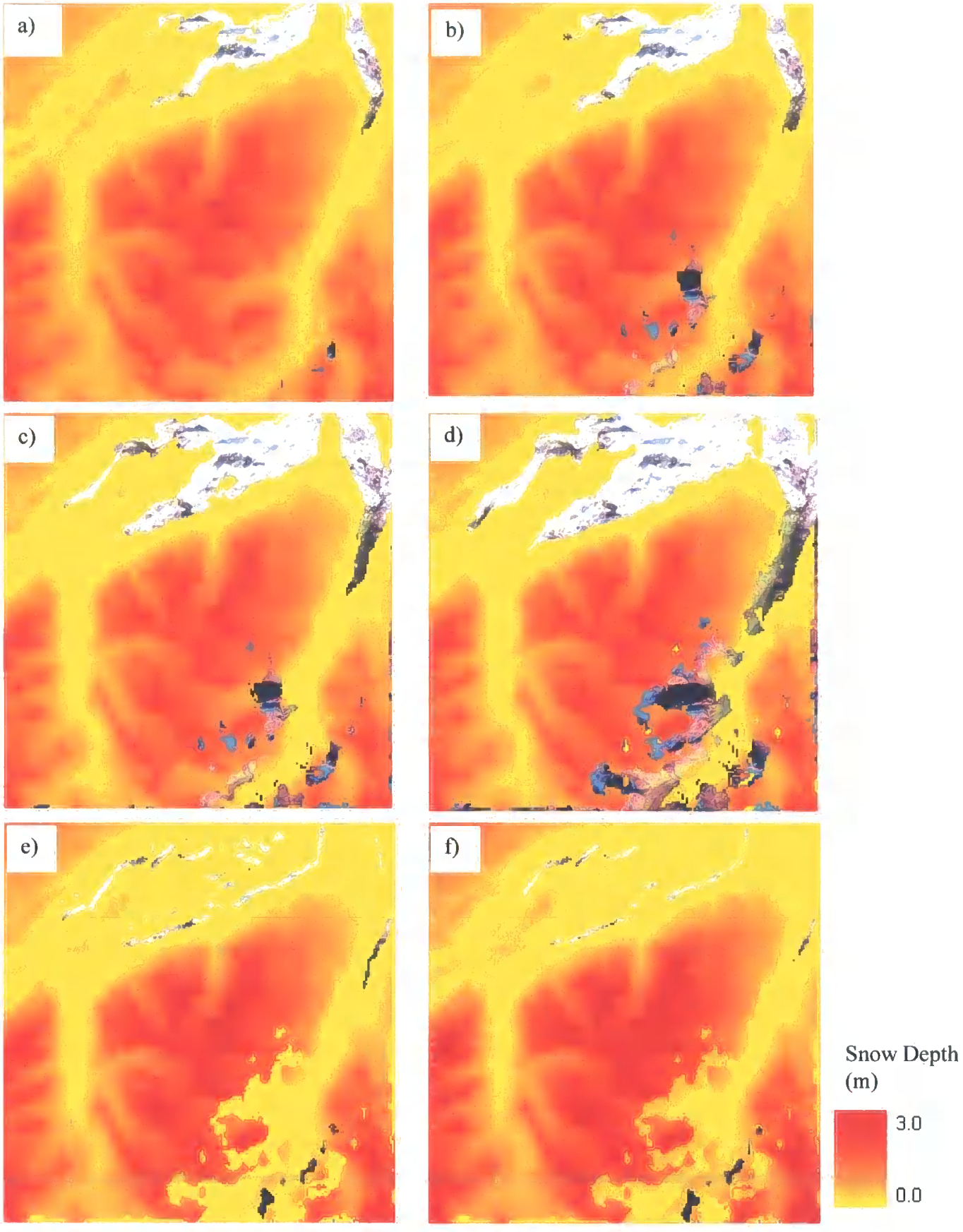

Figure 8.13: LGM reconstruction time sequence of monthly accumulation area predictions a) March, b) April, c) May, d) June, e) July and f) August.

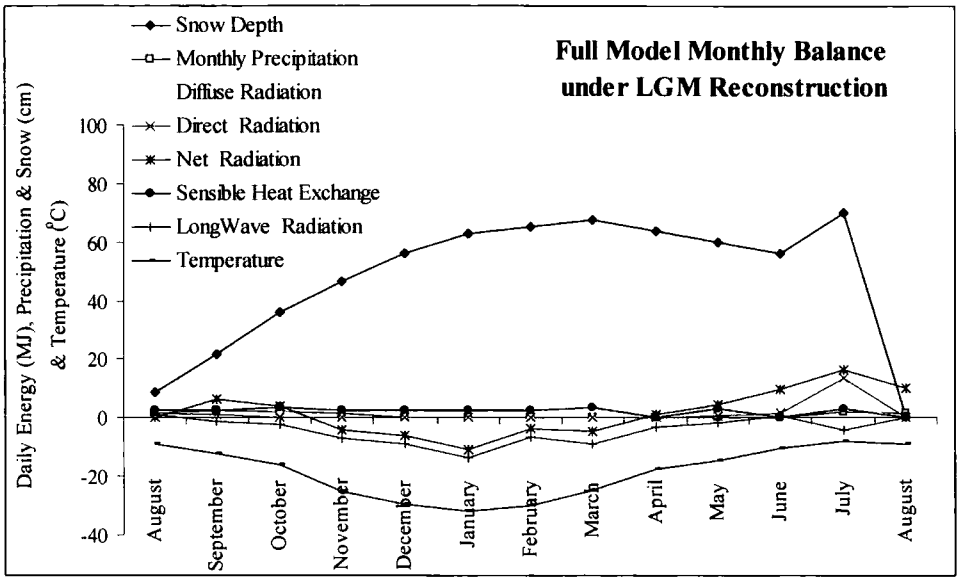

Figure 8.14: Full model monthly balance for LGM reconstruction model

8.5.6. Monthly Average Okta Cloud Cover

Temperature and precipitation have been found to provide dominant controls on the amount and timing of accumulation, but radiation also plays a critical role in determining the persistence and distribution of snowcover. Cloud cover determines both the proportion and characteristics of radiation reaching the ground and consequently exerts strong control on the timing and extent of melt. A further model run therefore uses observed mean monthly cloud cover, averaged throughout the area.

Conditions: Temperature: Seasonal Adjusted Lapse Rates
Precipitation: Adjusted Log Surface (Section 6.6.3.3)
Cloud Cover: Mean Monthly Okta
Albedo: 0.8 new snow, - 0.05 per month with no new snow
Energy Balance: Full

Winter accumulation occurred between October and March when it reached a maximum (Figure 8.16). Extensive melt occurred in April when the radiation balance was positive and the increased proportion of radiation reaching the surface resulted in greater melt where snow cover at lower altitudes and shallow slopes was heated and ablated. Deep snow cover remains in sheltered high altitude sites in April (Figure 8.15b) where steep slopes and cooler temperatures limited wide spread melt until May, all remaining snow is ablated by June. The strong diffuse component in this simulation drives the majority of melt with direct beam radiation providing only a small proportion of the net radiation under cloudy sky conditions. Maximum net balance

occurs in July and strongly positive balances persist during summer when average cloud cover is lower than winter.

Average Okta cloud cover increases net radiation and highlights the sensitivity of accumulation area predictions to radiative components. Sensitivity to this simulation is most pronounced as lower summer cloud cover accelerates melt rates.

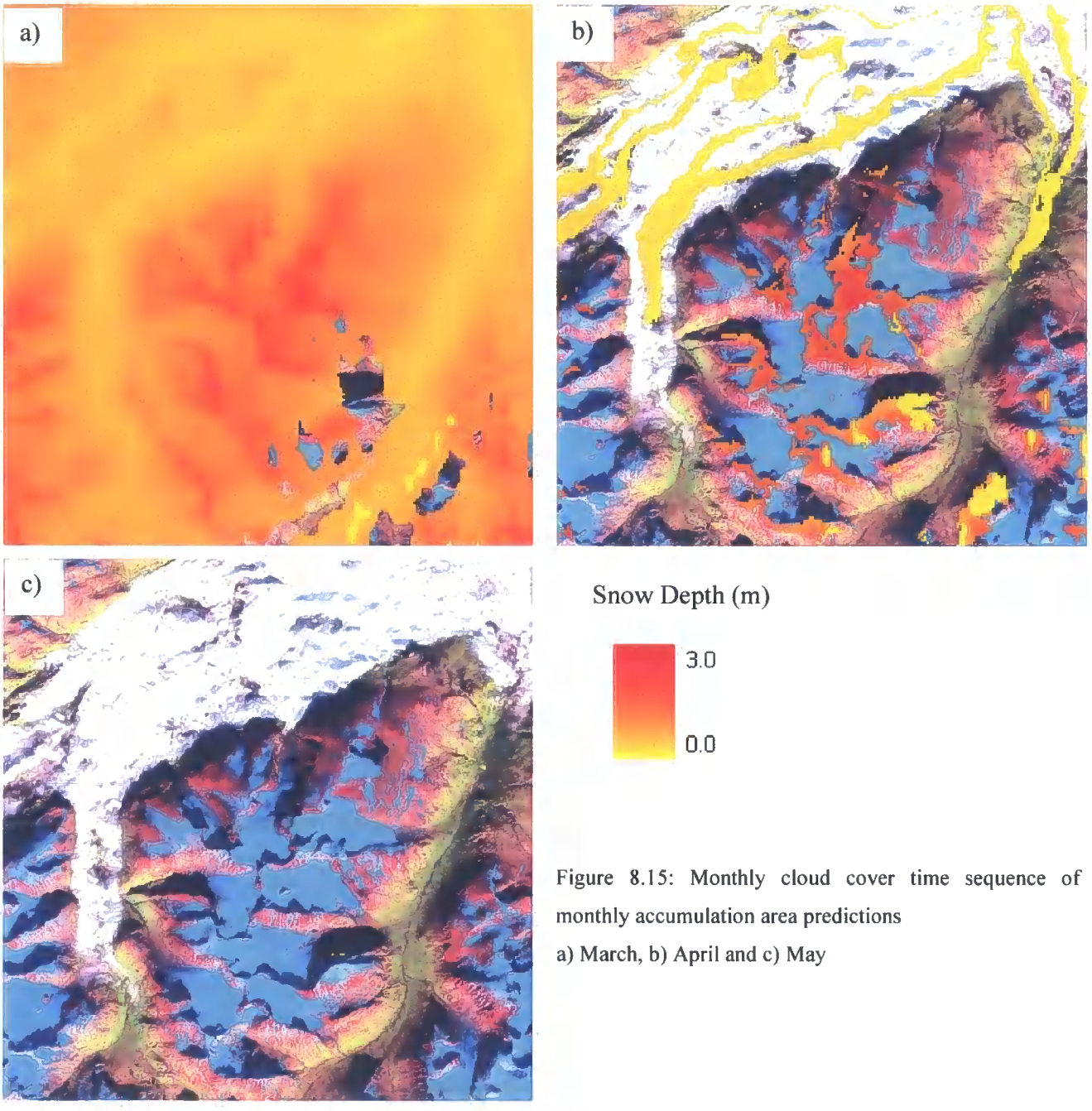

Figure 8.15: Monthly cloud cover time sequence of monthly accumulation area predictions
a) March, b) April and c) May

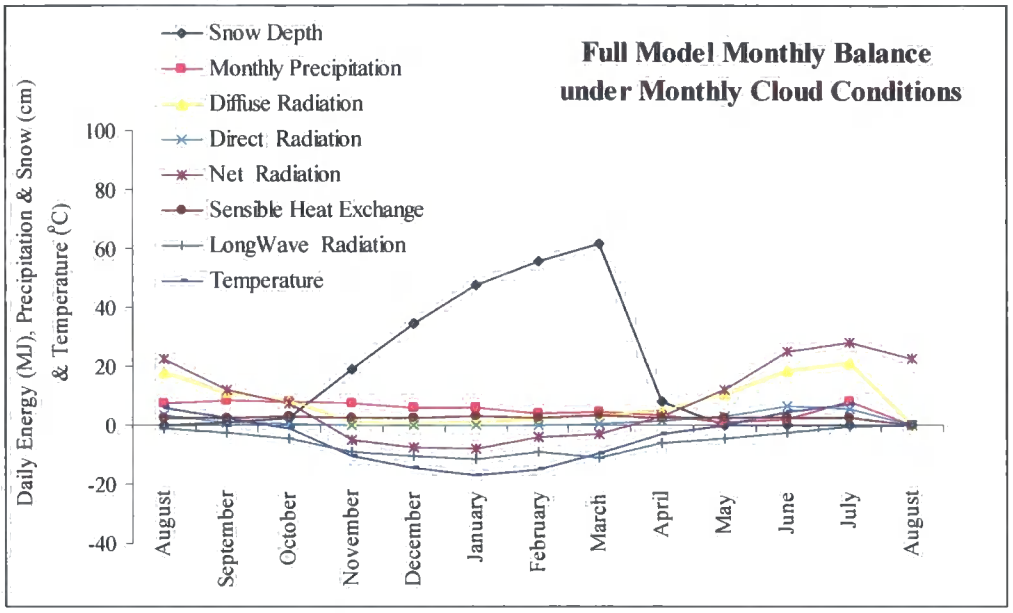

Figure 8.16: Full model monthly balance for monthly cloud cover model

8.5.7. **Variable Cloud Cover**

Pronounced sensitivity to average monthly cloud cover necessitated an alternative representation: it was believed that average conditions did not provide representative values for monthly conditions, where extremes provide a more dominant control on accumulation and melt. The distribution of monthly conditions were used to drive the accumulation model where overcast and clear sky conditions exert dominant changes to monthly net radiation values.

Conditions: Temperature: Seasonal Adjusted Lapse Rates
Precipitation: Adjusted Log Surface (Section 6.6.3.3)
Cloud Cover: Variable Cloud Cover – constant for 5 days
Albedo: 0.8 new snow, - 0.05 per month with no new snow
Energy Balance: Full

Accumulation occurred between December and March where the maximum was recorded (Figure 8.17). The snow cover gained during the shorter accumulation period (limited by positive net radiation balance until November) is rapidly ablated in April as a result of the positive net radiation balance and a shallower accumulated snow pack. Spatial patterns of melt indicate little discrimination where all upland areas are ablated, diffuse radiation drives this homogenous melt with sheltered lowland areas maintaining some snow cover (Figure 8.17 b). Remaining high altitude sheltered sites are ablated in May.

Energy balance maximum occurs in June, when overcast skies lead diffuse radiation to provide the dominant melt component (Figure 8.18). Results indicate high sensitivity to extreme values.

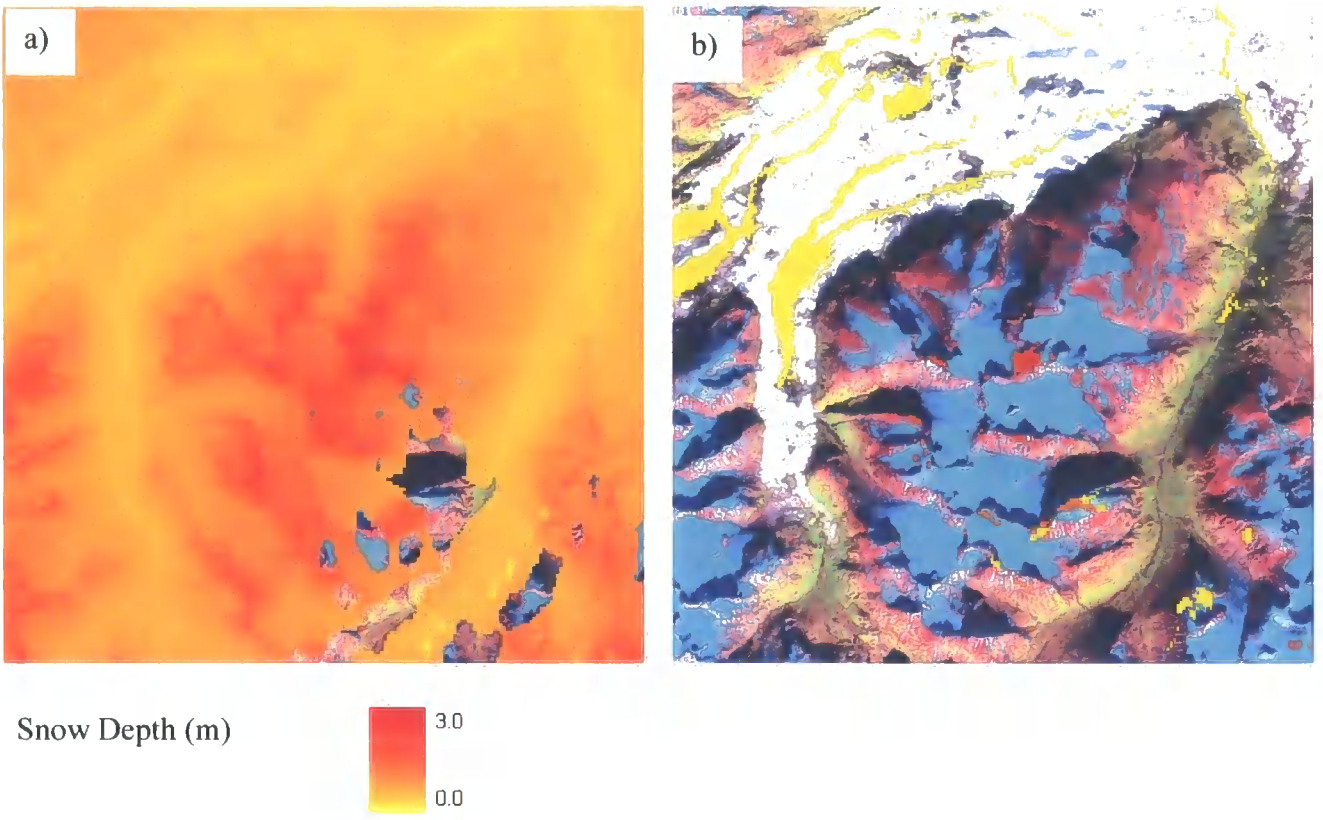

Figure 8.17: Variable cloud cover time sequence of monthly accumulation area predictions for a) March; and b) April.

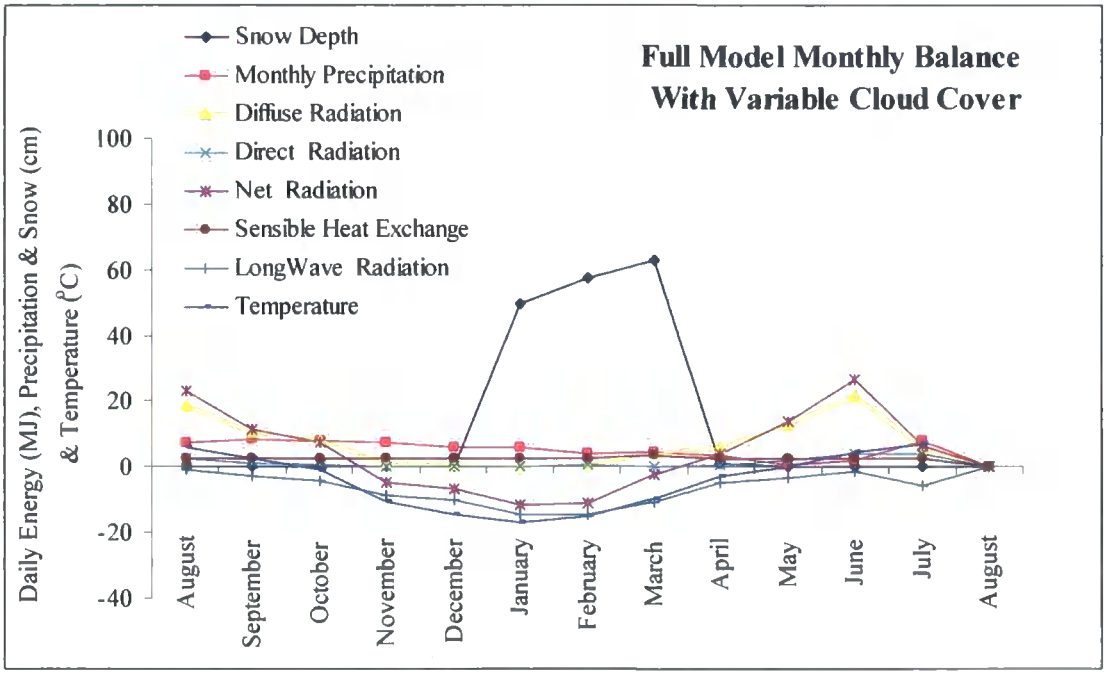

Figure 8.18: Full model monthly balance for variable cloud cover model

8.5.8. Diffuse Fraction Parameterisation

Variable cloud cover provided a more realistic representation of sky conditions but over estimated melt. Simple parameterisation of the magnitude of diffuse radiation under cloudy conditions employed within previous model simulations (Sections 8.4.1 – 8.4.7) failed to simulate observed accumulation areas where net balance and diffuse components were over predicted. Partitioning short wave radiation normal to the surface into direct and diffuse components as a function of cloud cover was employed in an attempt to improve surface energy balance predictions.

Conditions: Temperature: Seasonal Adjusted Lapse Rates
Precipitation: Adjusted Log Surface (Section 6.6.3.3)
Cloud Cover: Variable Cloud Cover – constant for 5 days
Albedo: 0.8 new snow, - 0.05 per month with no new snow
Energy Balance: Full with diffuse fraction

Accumulation occurred between December and March when it reached its maximum (Figure 8.20). The greatest rate of melt occurred in April when the net radiation balance was positive and cloud cover determined the fraction of incident radiation that is distributed as diffuse and direct components.

Melt at low altitudes is extensive in April but cooler and sheltered locations maintain snowcover (Figure 8.19 b). Extensive melt occurs in May when only localised high altitude accumulations remain. All snow has melted by June when the maximum net balance is received (Figure 8.20).

Partitioning incoming short wave radiation into diffuse and direct components extended the duration of snow cover but still over predicted melt. Simple parameterisations of the complex role that cloud cover has on surface energy balance and melt highlight the sensitivity of model predictions to these components and the subsequent attention that they require.

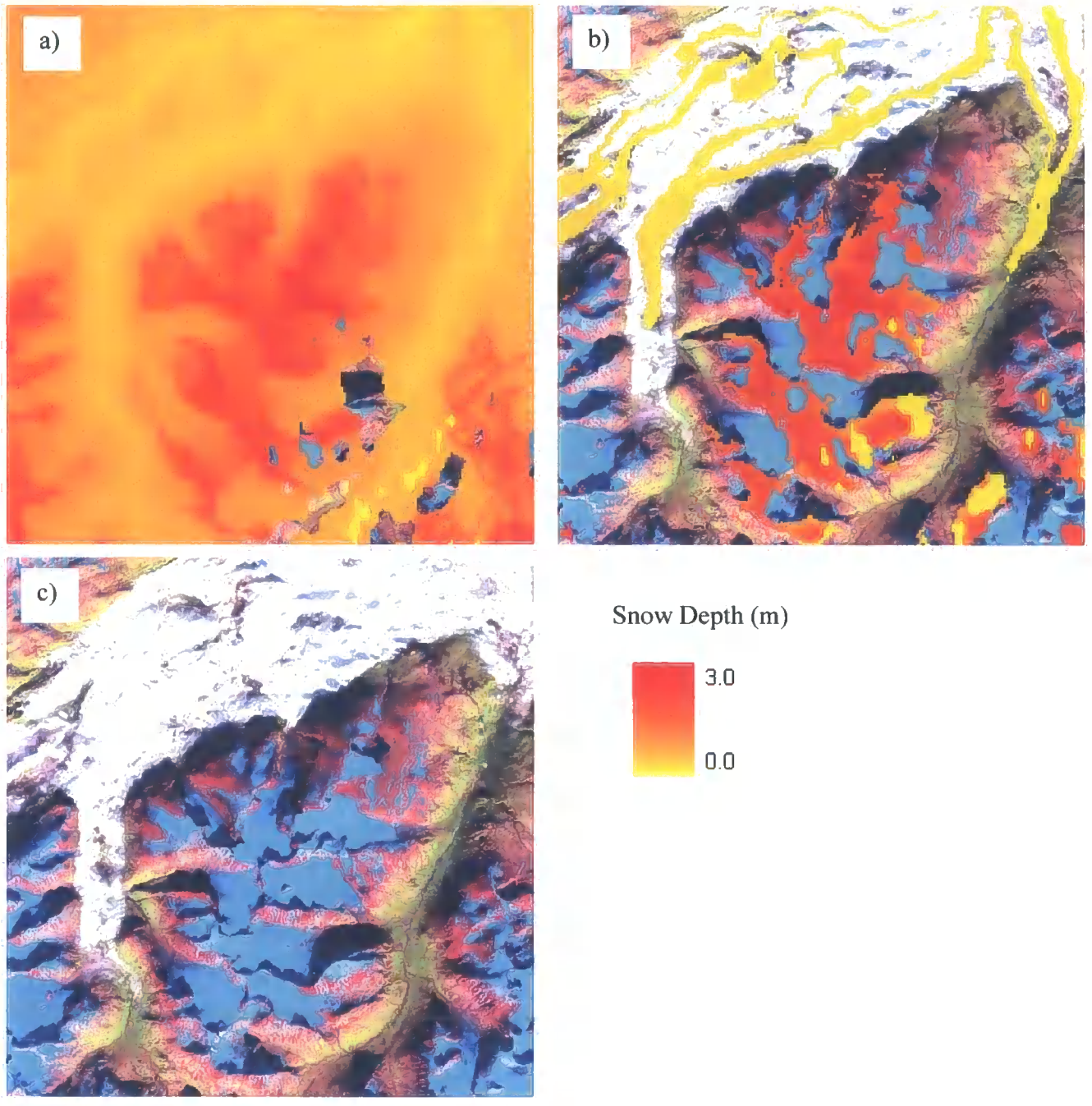

Figure 8.19: Diffuse fraction time sequence of monthly accumulation area predictions
a) March, b) April and c) May

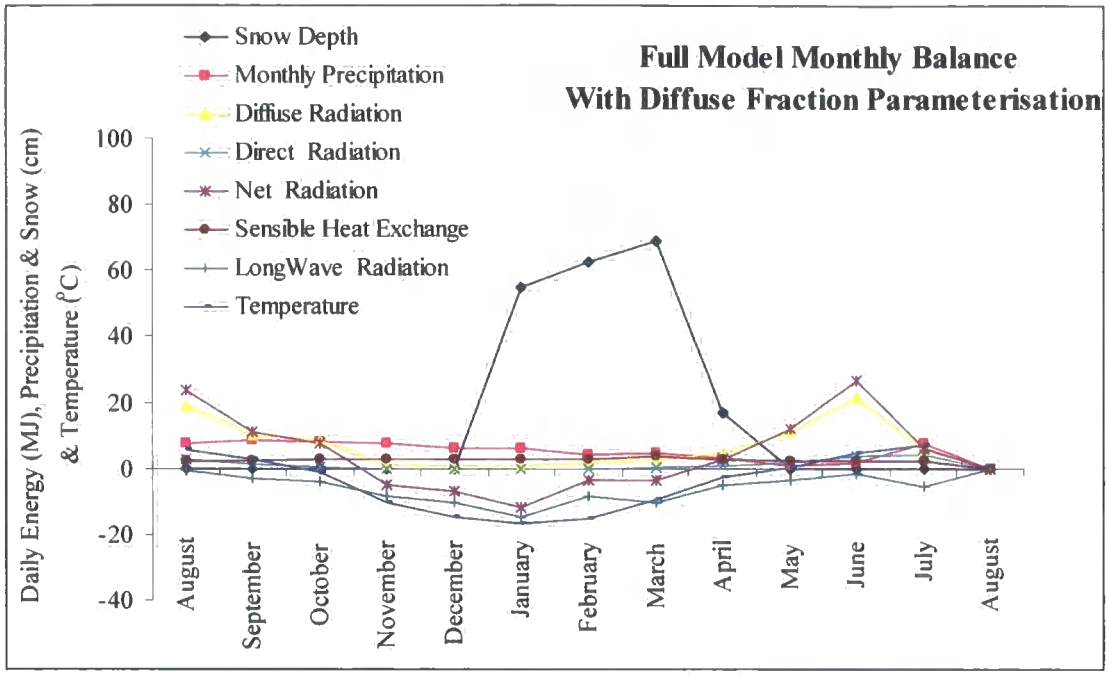

Figure 8.20: Full model monthly balance for diffuse fraction model

8.5.9. **Cloud Parameterisation 1**

Parameterisation of the direct and diffuse components of incoming short wave radiation did adjust trends within the annual radiation balance, but still over estimated melt. Simply using cloud cover to determine the characteristics of incoming short wave radiation cannot alone be used to determine surface energy balance where the reduction of incoming solar radiation by cloud cover reflectance and absorption imposes a strong control. Reduction of incoming radiation using monthly variable cloud cover was used to investigate the role of cloud cover on annual snow accumulation.

Conditions: Temperature: Seasonal Adjusted Lapse Rates
Precipitation: Adjusted Log Surface (Section 6.6.3.3)
Cloud Cover: Variable Cloud Cover – constant for 5 days
Albedo: 0.9 new snow, 0.85 old snow
Energy Balance: Full with diffuse fraction and reduction of normal to surface by percentage cloud cover

Maximum snow accumulation occurred in April but snow cover remained throughout the year (Figure 8.22). Maximum melt occurred in June when air temperatures rose above 0 °C. Maximum energy balance occurred in July when direct beam radiation provided the largest component of energy for melt.

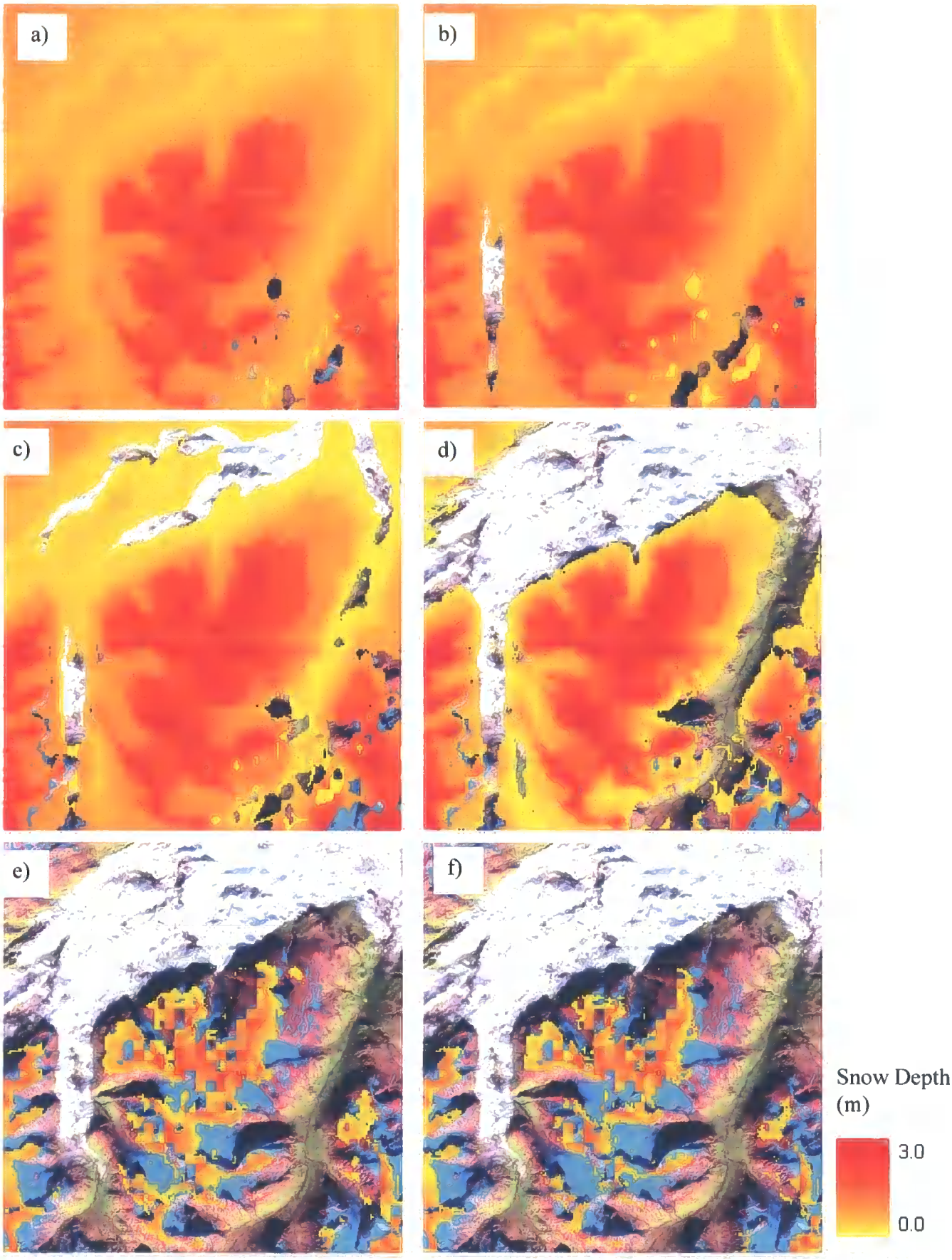

Figure 8.21: Cloud parameterisation 1 time sequence of monthly accumulation area predictions

a) March, b) April, c) May, d) June, e) July and f) August.

Seasonally derived lapse rates and improved albedo parameterisation provided more topographically constrained predictions with melt largely contained to valley floor locations until July. Simulated July snow cover predicted the accumulation areas for some glaciers but over predicts the extent of others. August melt reduces the extent of predictions but still classifies ablation areas of some glaciers as accumulation zones (Figure 8.21f).

Both topographically constrained and altitudinal glaciers are predicted and accumulation areas are well simulated. Some data resolutions issues are identified where topographically derived variables are propagated into the simulated snow accumulation surfaces, identifying the dominant role of sensible heat in summer ablation (Figure 8.22 and Figure 8.21f).

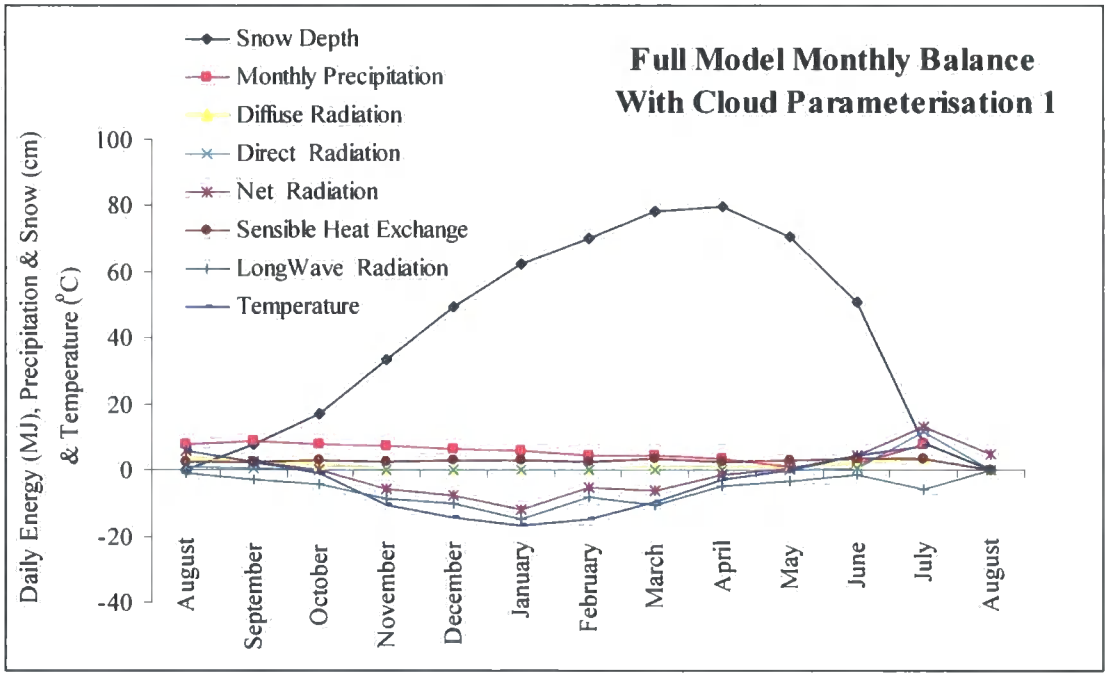

Figure 8.22: Full model monthly balance for cloud parameterisation 1 model

8.5.10. **Cloud Parameterisation 2**

Discrete glacier accumulation areas were accurately predicted using cloud parameterisation 1, however melt was under predicted with some glacier ablation areas identified as accumulation zones. Quantification of the role of cloud cover in reducing incident radiation is complex and uncertain (Geiger, 1965), cloud cover is believed to refract radiation at cloud edges and a direct correlation between cloud cover and incident radiation is not found. Increasing the fraction of radiation reaching the surface under cloudy conditions by 10 % per okta was investigated as an improved energy balance parameterisation.

Conditions: Temperature: Seasonal Adjusted Lapse Rates
Precipitation: Adjusted Log Surface (Section 6.6.3.3)
Cloud Cover: Variable Cloud Cover – constant for 5 days
Albedo: 0.9 new snow, 0.85 old snow
Energy Balance: Full with diffuse fraction and reduction of normal to surface by (percentage cloud cover – 10%)

Maximum accumulation occurred in April and melt occurred gradually through spring and summer, largely driven by direct beam radiation (Figure 8.24). Limited differences occur in the pattern of melt from those outlined for cloud parameterisation 1 where again, melt is topographically constrained, but higher net radiation receipts lead to more extensive melt and thinning of the accumulation areas predicted in Section 8.4.9; resulting in more accurate accumulation area predictions.

The role of cloud cover in reducing the short wave radiation reaching the surface and the relative proportions of direct and diffuse radiation have been found to impose dominant controls on surface energy balance and accumulation.

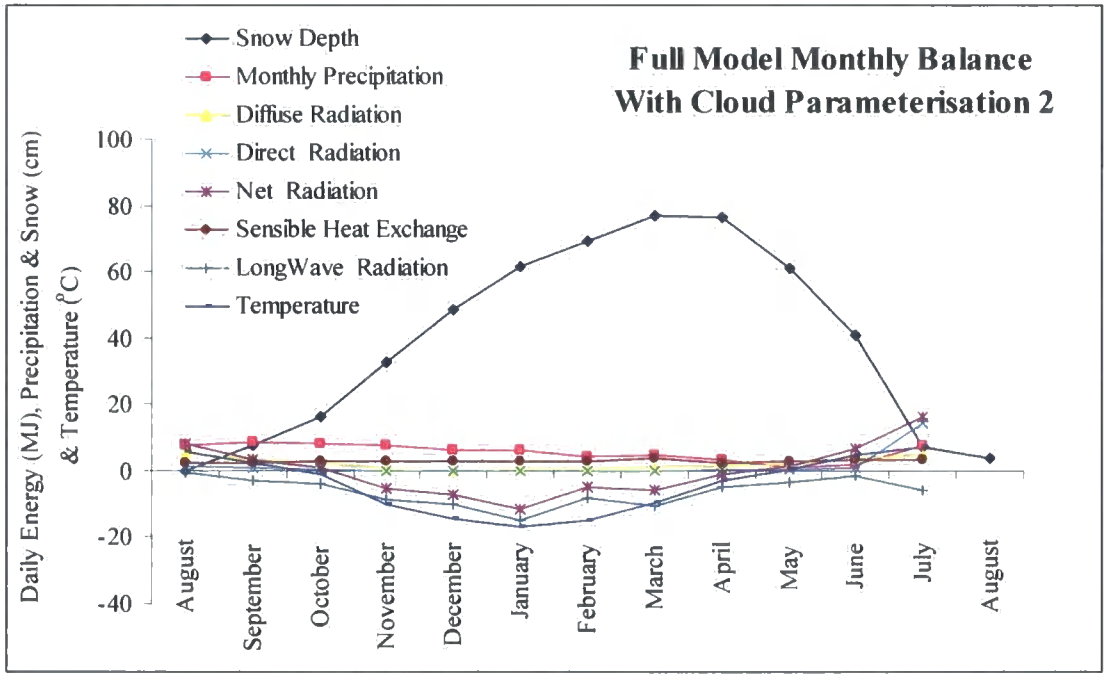

Figure 8.24: Full model monthly balance for cloud parameterisation 2 model

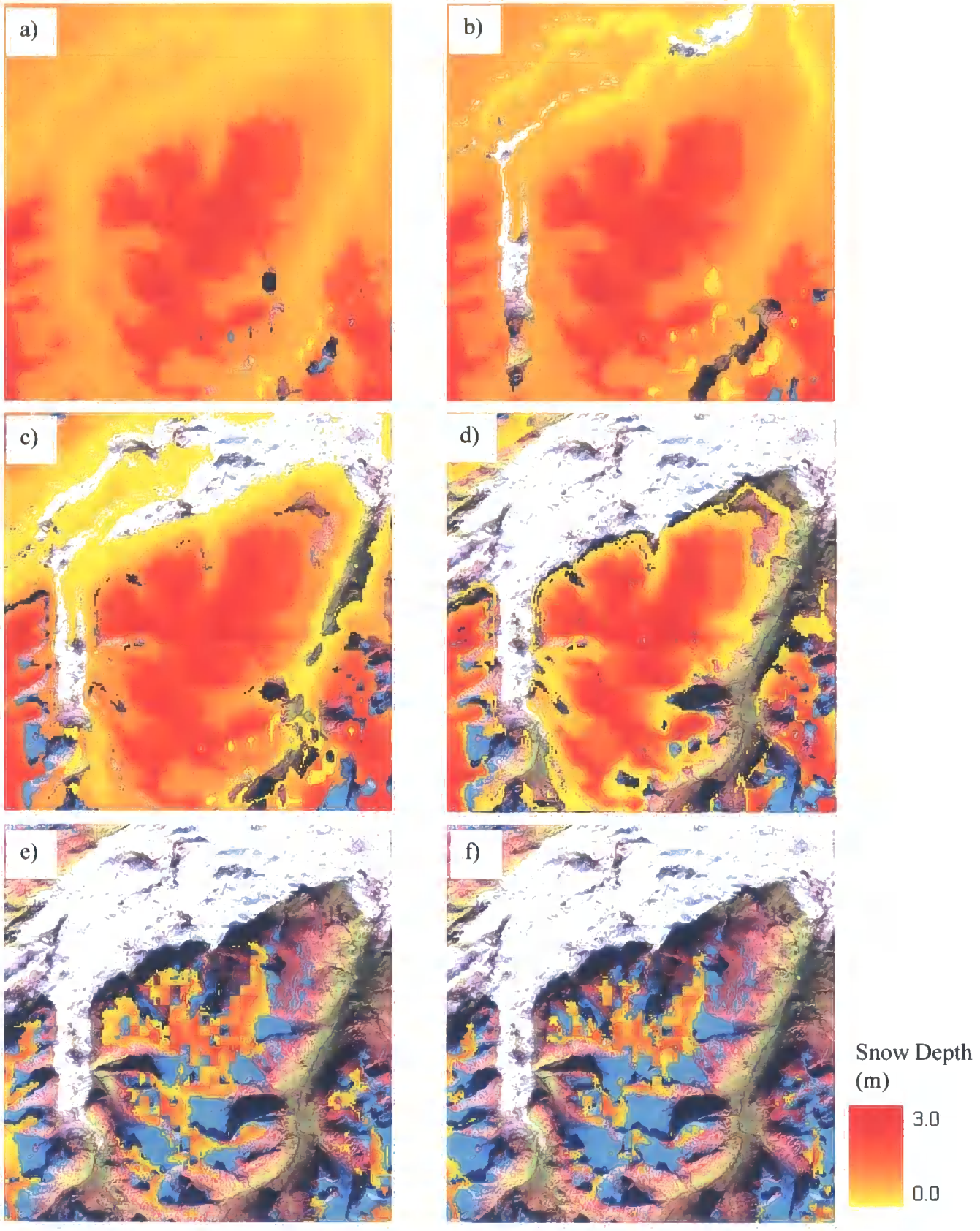

Figure 8.23: Cloud parameterisation 2 time sequence of monthly accumulation area predictions a) March, b) April, c) May, d) June, e) July and f) August.

b)

8.5.11. **No Diffuse Radiation**

Diffuse shortwave radiation has been identified as an important driver of melt: its effects were further investigated by removing it as an energy balance component.

Conditions: Temperature: Seasonal Adjusted Lapse Rates
Precipitation: Adjusted Log Surface (Section 6.6.3.3)
Cloud Cover: Variable Cloud Cover – constant for 5 days
Albedo: 0.9 new snow, 0.85 old snow
Energy Balance: No diffuse Radiation, using diffuse fraction and reduction of normal to surface by percentage cloud cover

Maximum winter accumulation occurred in April with snowcover remaining all year; gradual melt occurred from April with a maximum net balance occurring in July (Figure 8.26).

Removal of diffuse radiation highlights the significant contribution it provides to spatially distributed melt. Northerly aspects maintain extensive snow cover throughout the mass balance year, where southerly aspects and low altitude warmer areas loose snow through ablation from direct beam and sensible heat exchanges, this is in agreement with Nunez (1980) and Olyphant (1986) who identify diffuse radiation as an important contribution to the radiation flux due to its isotropic nature, minimising spatial heterogeneity in receipt. Intermediate altitudes on less exposed slopes do experience active melt, but are only thinned during the ablation season. Thinning also occurs on northerly slopes through melt by sensible heat exchanges, which contributes to melt during May, June and July (Figure 8.25 c, d and e).

The minimum snow cover occurs in August although high altitude sheltered locations do still accumulate snow during this period. August experiences active thinning on snow accumulation margins and in higher valleys although glacier accumulation areas are over predicted and discrete glaciers are not identified (Figure 8.25 f): the result is excessively altitude-dependent.

Diffuse radiation plays a fundamental role in predicting spatially distributed glacier accumulation areas where melt occurs on a range of aspects and is not restricted to southerly and warm sites alone.

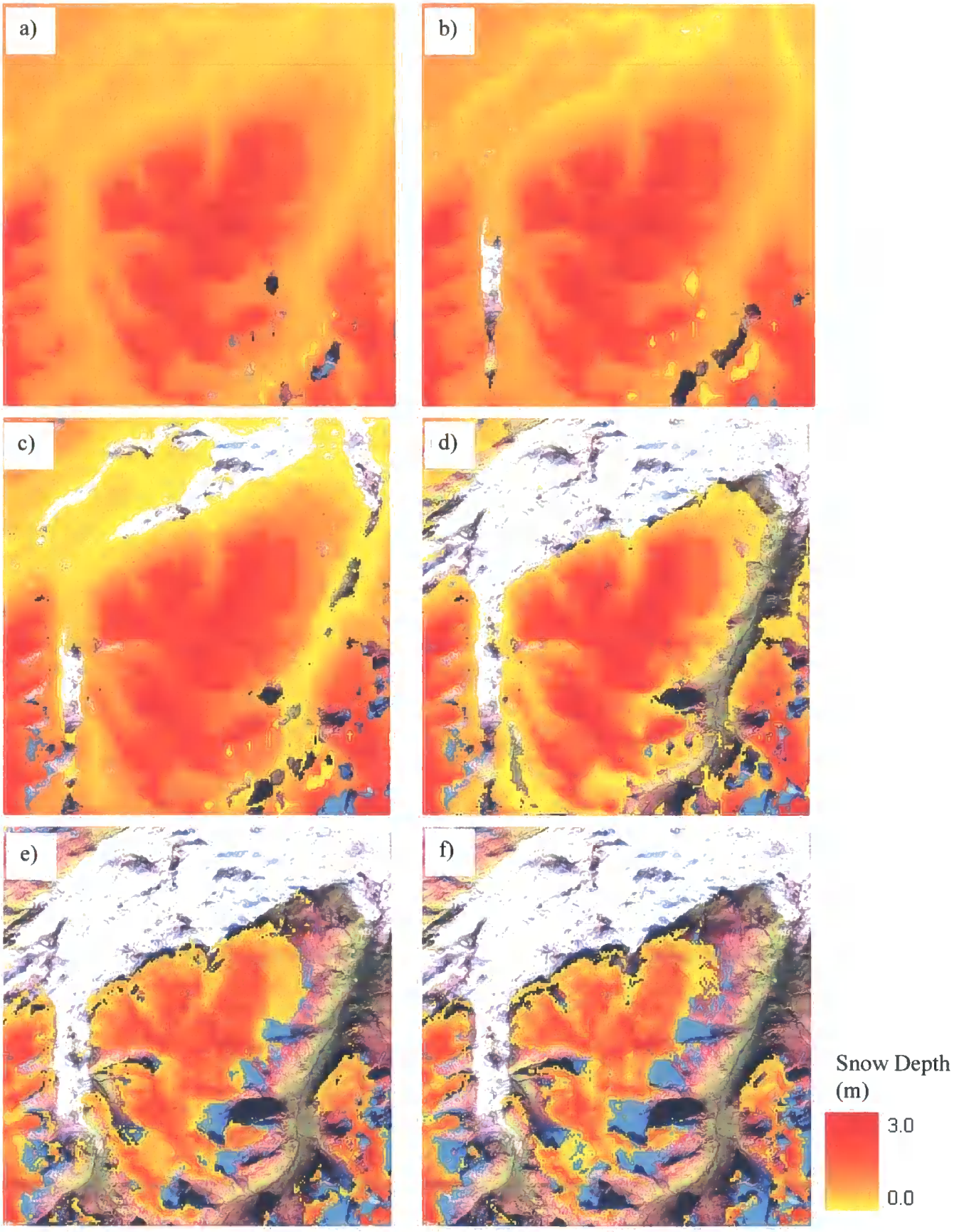

Figure 8.25: No diffuse radiation model time sequence of monthly accumulation area predictions a) March, b) April, c) May, d) June, e) July and f) August.

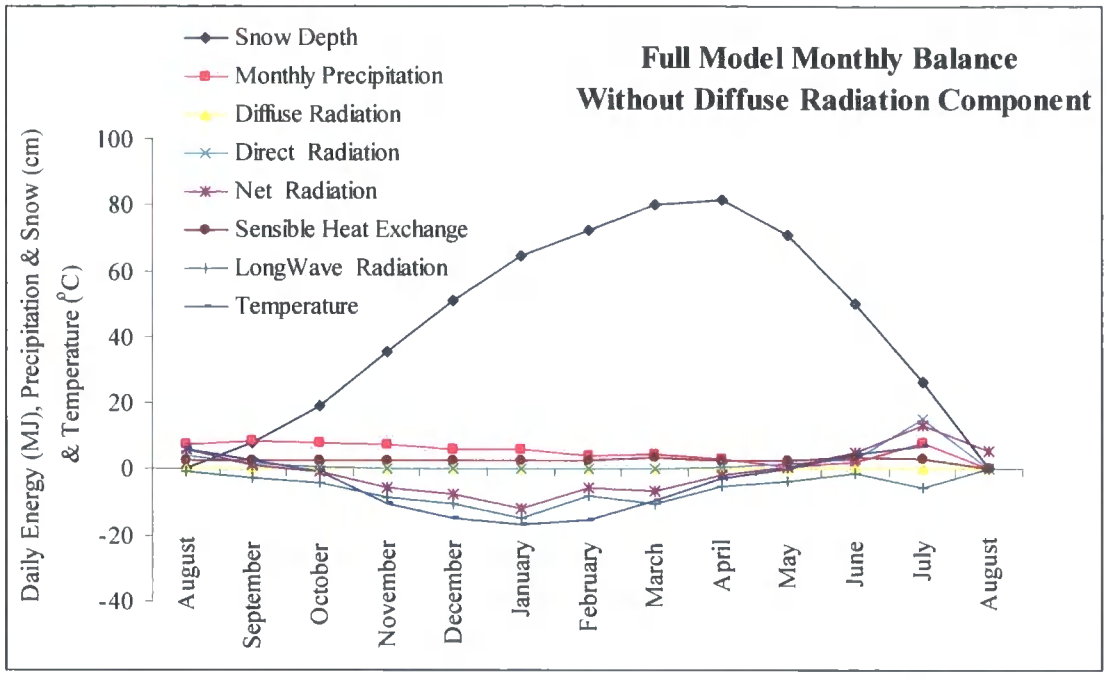

Figure 8.26: Full model monthly balance for no diffuse radiation model

8.5.12. **No Sensible Heat Exchange**

The role of individual energy components have already been identified as critical components to representing spatially distributed melt, however the considerable data requirements for accurate simulations of sensible heat exchange necessitate a justification of its inclusion.

Conditions: Temperature: Seasonal Adjusted Lapse Rates
Precipitation: Adjusted Log Surface (Section 6.6.3.3)
Cloud Cover: Variable Cloud Cover – constant for 5 days
Albedo: 0.9 new snow, 0.85 old snow
Energy Balance: No sensible heat exchange, using diffuse fraction and reduction of normal to surface by percentage cloud cover

Maximum accumulation occurs in April with very little melt in May (Figure 8.28). Slower melt through summer (when sensible heat would provide a larger contribution to melt, with larger positive fluxes occur towards the surface) is observed, direct beam radiation provides the dominant source of melt during this period.

Little melt occurs until June, when exposed and cooler valley floors experience active melt. July and August record extensive melt, with shrinking of snow cover up and along valley floors.

Thinning is less extensive than found under previous model scenarios and glacier accumulation areas are over predicted.

Sensible heat is found to play a more significant role in melt than diffuse radiation resulting in extensive melt in summer months. Resultant distributions exhibit a dominant altitudinal component, where topographically derived wind fields play a significant role in predicting distributed melt patterns.

As found in Section 8.4.11, discrete distributions are not predicted without a sensible heat component.

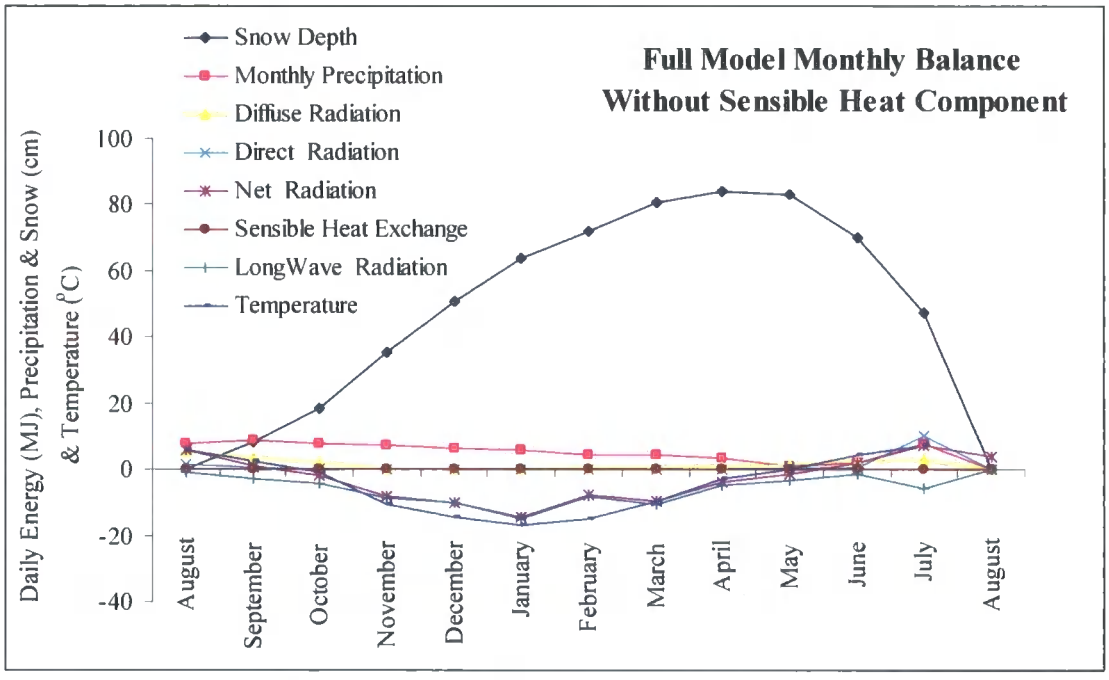

Figure 8.28: Full model monthly balance for no sensible heat exchange model

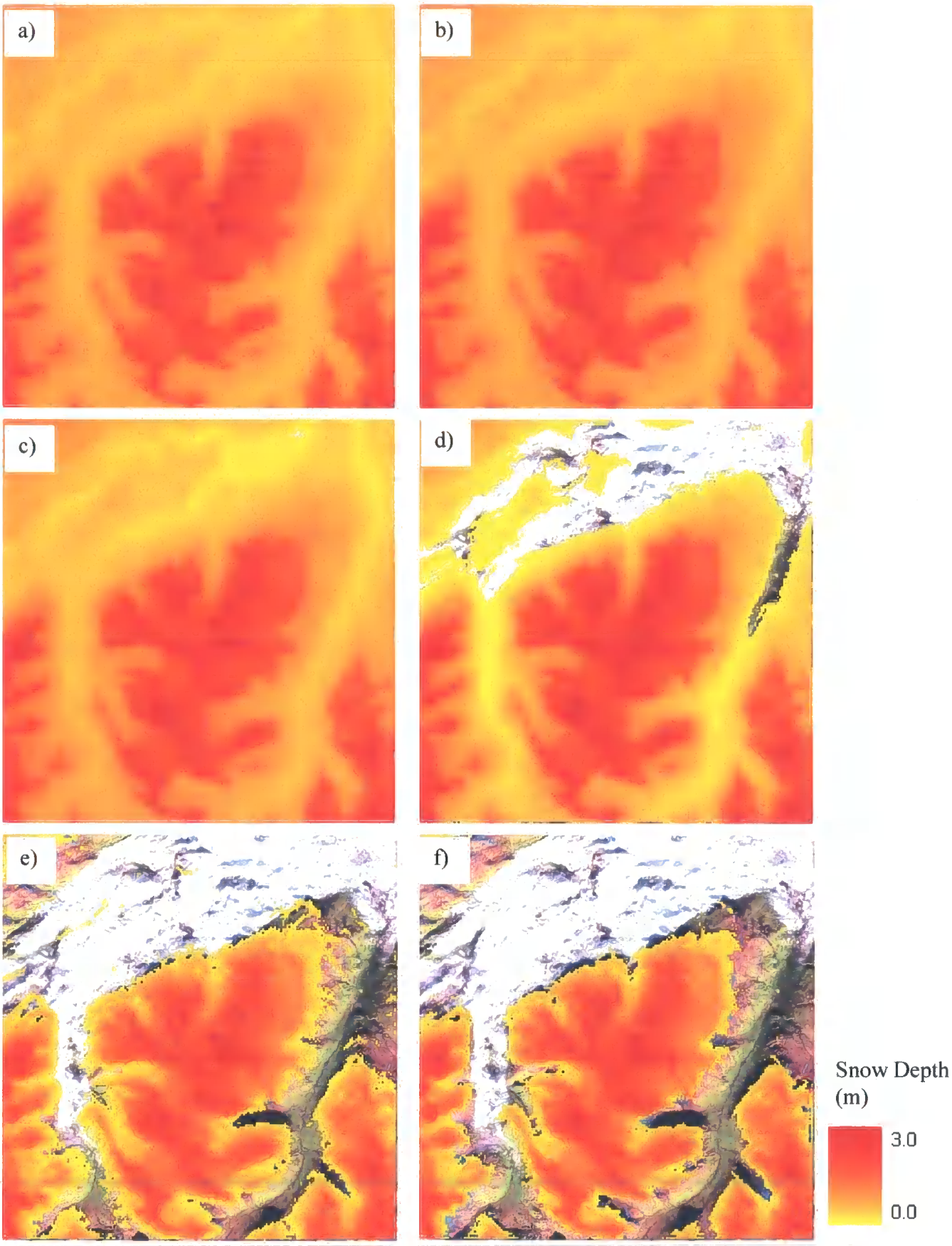

Figure 8.27: No sensible heat exchange model time sequence of monthly accumulation area predictions a) March, b) April, c) May, d) June, e) July and f) August.

8.5.13. **No topographic Shade**

Topography has already been identified as a dominant control on predicted glacier accumulation areas (Sections 8.4.1 – 8.4.12), but topographic shading is often not included in spatially distributed melt models. Inclusion of topographic shade does increase the computational intensity of model predictions and its contribution to the accuracy of predictions was assessed.

Conditions: Temperature: Seasonal Adjusted Lapse Rates
Precipitation: Adjusted Log Surface (Section 6.6.3.3)
Cloud Cover: Variable Cloud Cover – constant for 5 days
Albedo: 0.9 new snow, 0.85 old snow
Energy Balance: No topographic shade, using diffuse fraction and reduction of normal to surface by percentage cloud cover

Maximum accumulation occurred in March within limited melt in April and May (Figure 8.30). Extensive low altitude melt occurred in June and July when temperatures and net radiation balance rose. Maximum net balance occurred in July and August with a minimum in January (Figure 8.30). Comparison with cloud parameterisation 1 model reveals localised melt on glacier surfaces in June which lie within topographically shaded areas, suggesting delayed melt at these locations under the topographic shading model (Figure 8.21d and Figure 8.29 d).

More extensive melt occurs in June along valley sides which are partly shaded during June. Less distinct differences occur in July and August when the solar altitude is higher and topographic shading is less extensive. August reveals most distinct differences where snow cover is less extensive and restricted to higher altitudes. Lower sheltered sites are not predicted exhibiting a stronger altitudinal component to accumulations and strong topographic shading controls.

Topographic shade imposes local controls on glacier accumulation, where melt is over predicted under no shading conditions.

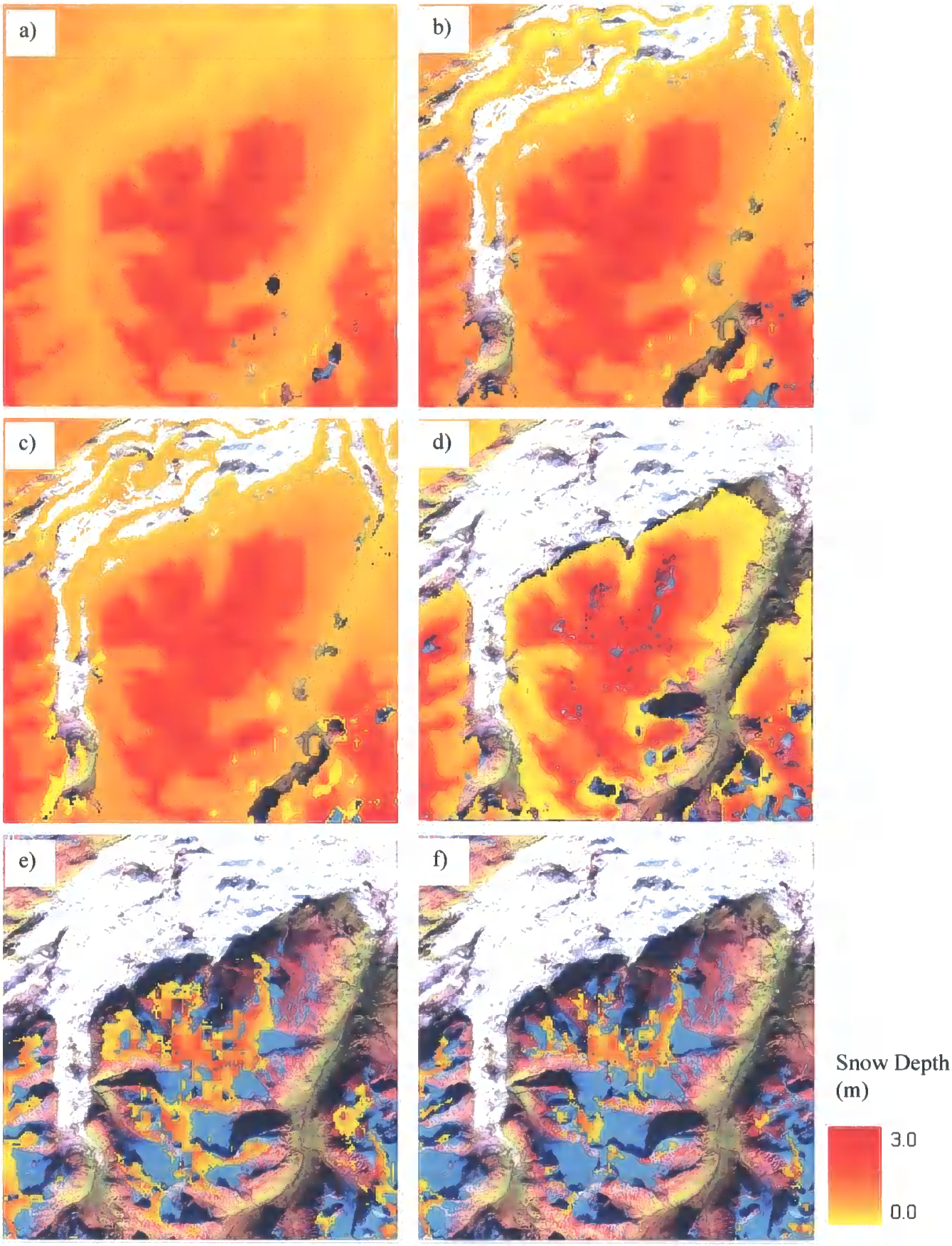

Figure 8.29: No topographic shade model time sequence of monthly accumulation area predictions a) March, b) April, c) May, d) June, e) July and f) August.

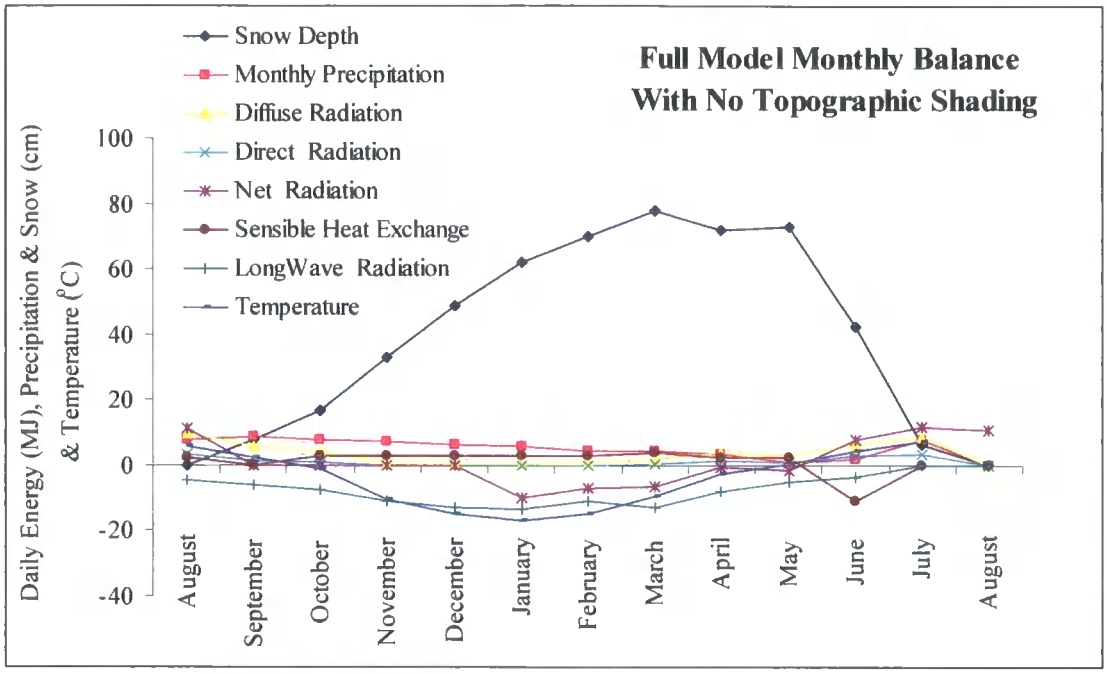

Figure 8.30: Full model monthly balance for no topographic shading model

8.5.14. **No cloud cover**

The role of cloud cover has received attention in sections 8.4.6 – 8.4.10, however an assessment of the dominant role it has on snow accumulation is most effective by removing it as an energy balance component.

Conditions: Temperature: Seasonal Adjusted Lapse Rates
Precipitation: Adjusted Log Surface (Section 6.6.3.3)
Cloud Cover: None
Albedo: 0.9 new snow, 0.85 old snow
Energy Balance: Full

Maximum accumulation occurred in March with very localised snow cover remaining in June. Increased incident radiation with no reduction from cloud cover leads to high summer net radiation balances where diffuse radiation as incorporated by the model provides the largest contribution to melt (where diffuse fractions were not included). Maximum net balance occurred in July and the minimum occurred in January. Greatest melt occurs in April when net balance is positive and radiation is available to heat and melt the snow cover.

Localised melt occurs in March on exposed low altitude sites but extensive melt occurs on shallow and exposed sites in April where surface slope provides the dominant control (Figure

8.31 b). Accumulation areas are still present in May with some seasonal snowcover but little snow remains in May where widespread high altitude melt occurs. Localised snow cover remains in July and August but accumulation areas are not predicted and melt is overestimated.

The most striking result from these predictions is the dominant role that increased albedo has on winter accumulation and spring ablation. In contrast to 8.4.7 and 8.4.8 accumulation occurred from September where although no cloud cover increases incident radiation (under modelled diffuse parameters), this produces the greatest contribution: this is an unrealistic prediction where all shortwave radiation would come from direct beam and is only an artefact of inbuilt cloudy absorption assumptions.

Increased snow albedos from 0.8 to 0.9 and a constant albedo of 0.85 (following Arnold *et al.*, 1996) have a major impact on accumulation, but still result in extensive ablation.

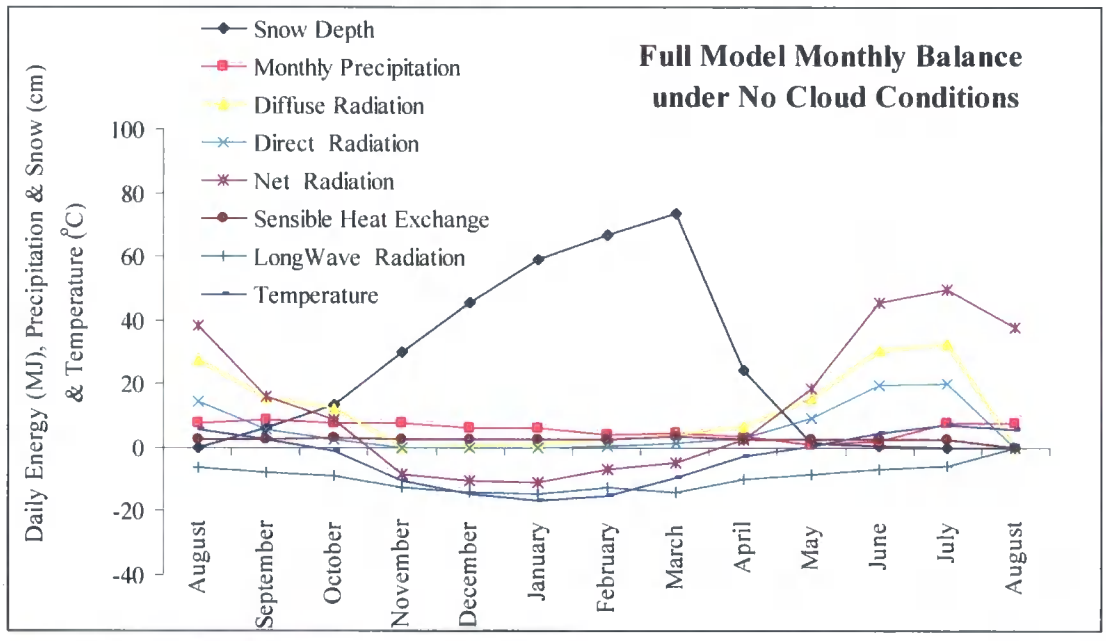

Figure 8.32: Full model monthly balance for no cloud cover model

Analysis and interpretation of model predictions for different climatic and radiative conditions highlights both as important controls on the rate and extent of melt. Discussion of these sensitivities follows, initially identifying sensitivities of energy balance components to different model scenarios, moving then to discussion of mean and maximum snow accumulation sensitivity to the models outlined above and concluding with a discussion of any topographic controls on resultant glacier distributions.

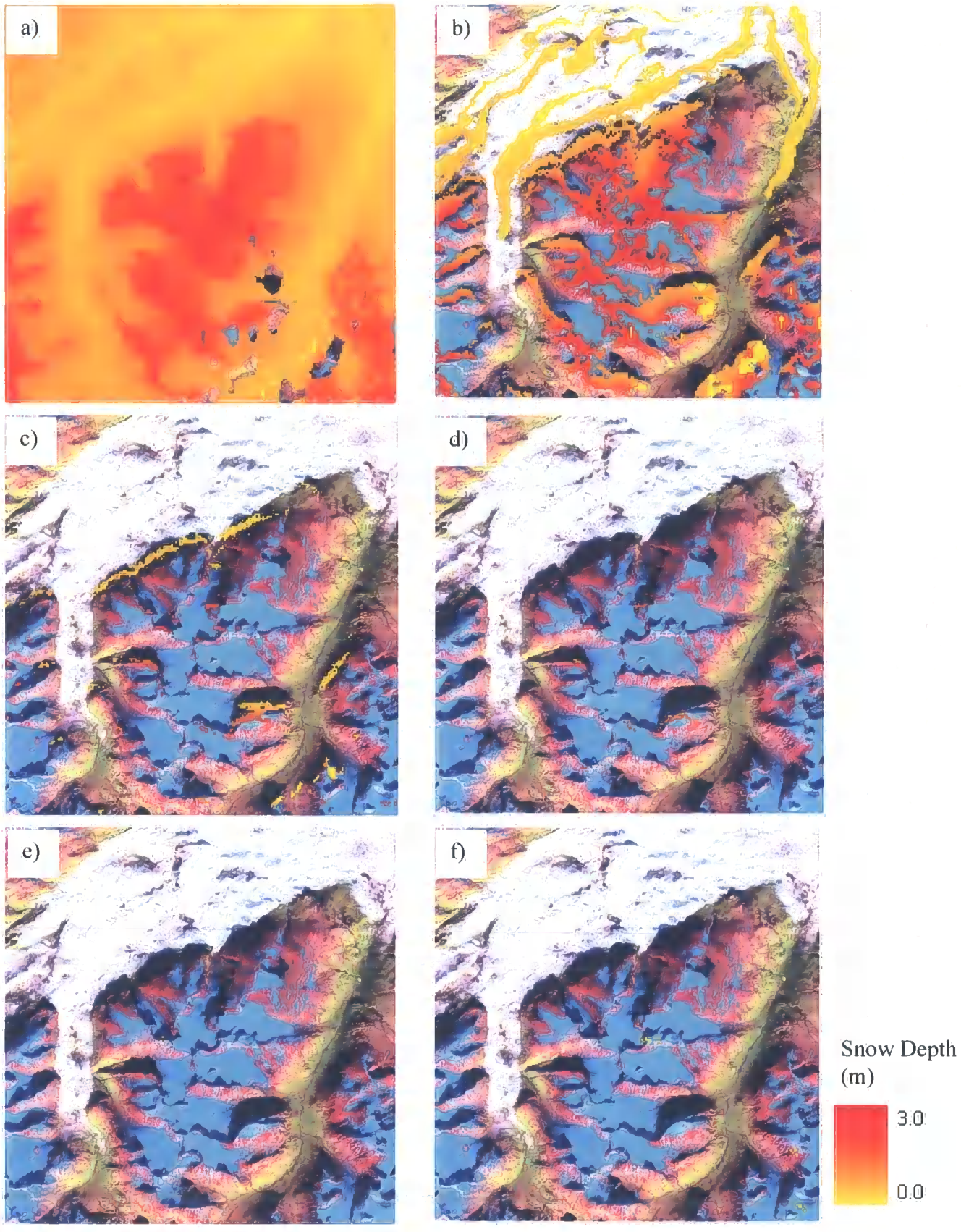

Figure 8.31: No cloud cover model time sequence of monthly accumulation area predictions a) March, b) April, c) May, d) June, e) July and f) August.

8.6. Controls on Energy Balance Components

Feedbacks included within the model, specifically albedo and surface temperature in conjunction with cloud cover, lead to variations in monthly radiation receipt. Sensitivities to both climatic and radiative components are present within the predictions, with the magnitude of sensitivity to these different components varying between sensible heat exchange, diffuse, longwave and direct beam radiation.

Sensitivity is not defined as recorded difference from a known or observed value but as the difference between predicted estimates.

Each of the following graphs uses the legend below:

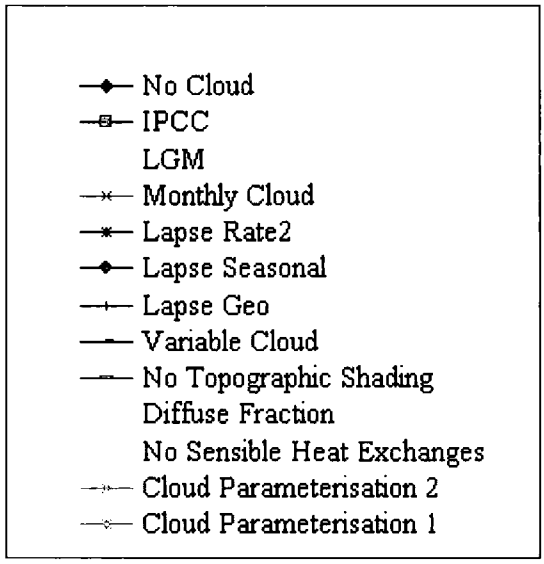

8.6.1. Sensible Heat Exchanges

Predicted sensible heat exchanges exhibit sensitivity to climatic parameters: where greatest fluxes occur when warmer air temperatures are combined with extensive snow cover, this is congruent with expectations (Male and Granger, 1981). These conditions are most pronounced with the geomorphic lapse rates (Figure 8.33). Simulations with limited snow cover have low sensible heat exchanges, where air and surface temperatures are equivalent. All average monthly sensible heat exchanges are positive, although daily cycles driven by predicted diurnal temperature changes exhibit negative evening components. Cloud parameterisation 1, 2 and geomorphic lapse rate models all record a rise in sensible heat exchanges in June over snow cover when air temperatures rise (Figure 8.33).

Sensible heat exchanges only seem to provide a significant contribution to melt during summer months when positive temperature gradients exist between the 2m air temperature and the surface. The magnitude of this contribution to melt is dependent upon temperature lapse rates and simulated wind speeds. The detailed climatic study (Chapter 6) and predictions completed within this research support the findings of Male and Granger (1981) who stress the need for detailed climatic datasets in predicting sensible heat exchanges.

Simulating early spring melt would not require inclusion of sensible heat exchanges where maximum energy for melt originates from short wave radiation, however extensive summer melt does require the inclusion of sensible heat (Sections 8.7 and 8.4.12).

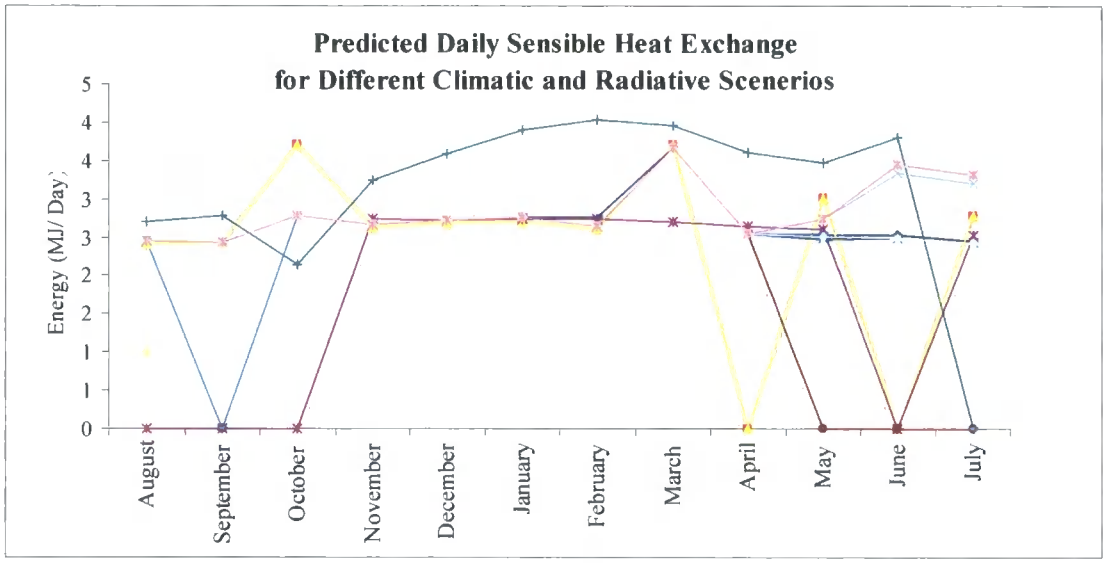

Figure 8.33: Sensitivity of predicted sensible heat exchanges

8.6.2. **Longwave Radiation**

Confirming the research presented by Male and Granger (1981) longwave radiation exhibited most pronounced sensitivity to temperature lapse rates and cloud cover. Modelled fluxes in this research predict warmer, cloudier conditions to give greater fluxes to the surface (i.e. reduced losses, Figure 8.34). These predictions are in line with those reported by Male and Granger (1981). Longwave fluxes provide the least critical component to melt, where small net fluxes occur during summer months under cloudy warm conditions. Except under IPCC warming, fluxes are always negative and therefore slow the rate of melting. The reported fluxes are small during summer and negative fluxes are still expected (Oke, 1987), but under changing climatic conditions assumptions of constant outward longwave flux may no longer be viable.

Longwave fluxes are not computationally intensive and currently limit spring and summer melting. Removing longwave fluxes from the model would advance and quicken the rate of melt, current model predictions do not require such an adjustment and long wave radiation is found to provide an important role in delaying the onset of melt in spring when fluxes of between –8 and -10 MJ Day^{-1} are recorded.

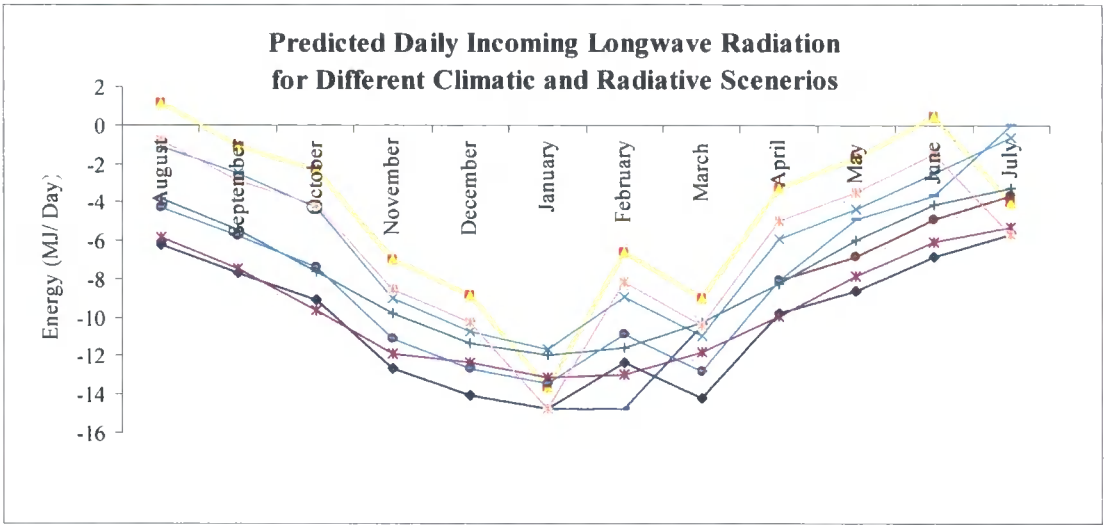

Figure 8.34: Sensitivity of predicted long wave radiation

8.6.3. **Diffuse Shortwave radiation**

Predicted diffuse radiation exhibits pronounced sensitivity to cloud cover during the summer ablation period. Highest receipts are recorded under clear sky conditions when a simple parameterisation of the magnitude of diffuse radiation is employed. This reflects the ability of the model to predict diffuse radiation. As identified in 8.4.14 the clear sky results do not predict a realistic diffuse contribution. Diffuse radiation appears to be over predicted in all but the cloud parameterisation models 1 and 2, this over prediction under different cloud cover predictions has also been reported by Fierz *et al.* (2003) when global radiation has not been correctly predicted. Much published research attempts to derive empirical relationships between global radiation and cloud cover (Geiger, 1965). Following the optimal parameterisation by outlined by Geiger (1965), represented here as cloud parameterisation 2, global radiation and its diffuse and direct components are more robustly predicted. Predictions are less sensitive to temperature lapse rate variations where all predictions are ± 5 MJ day^{-1}. Cloud parameterisation 1 and 2 predict the lowest mean diffuse radiation receipts, but exhibit an annual trend comparable to observed receipts (Oke, 1987).

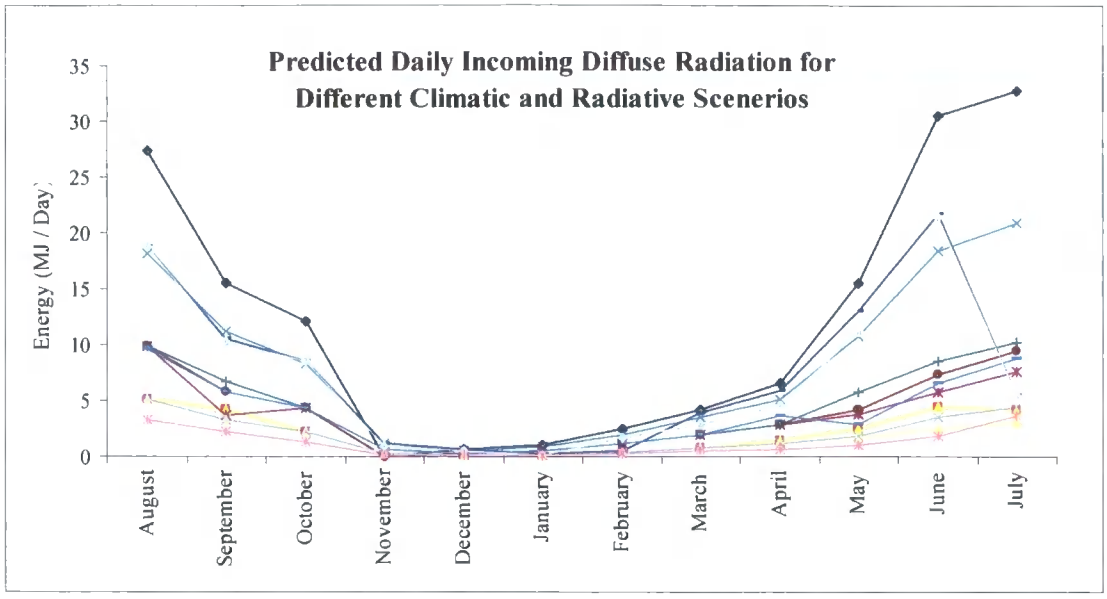

Figure 8.35: Sensitivity of predicted diffuse radiation

8.6.4. **Direct beam shortwave radiation**

Incoming direct beam shortwave radiation exhibits greatest sensitivity to cloud cover, especially during the summer ablation period, although this is less pronounced than seen in diffuse radiation where cloud cover is implicit within magnitude calculations. This supports the research presented by McKenney *et al.* (1999) who found greatest sensitivities in predicted radiation from cloud cover. Predictions using variable and parameterised cloud cover exhibit the greater sensitivity and smallest receipts, but are believed to provide more accurate representations of incident radiation. Predictions are not markedly sensitive to climatic parameters where different lapse rates lead to a mean difference of ± 2 MJ day^{-1}. Cloud parameterisation 1 and 2 provide the lowest direct beam radiation contributions, where daily cloud cover reduces incoming solar radiation. Significantly higher receipts are found in July, when lower cloud cover, high contributions to direct beam radiation and maximum solar radiation at the top of the atmosphere combine to provide a high mean monthly receipt.

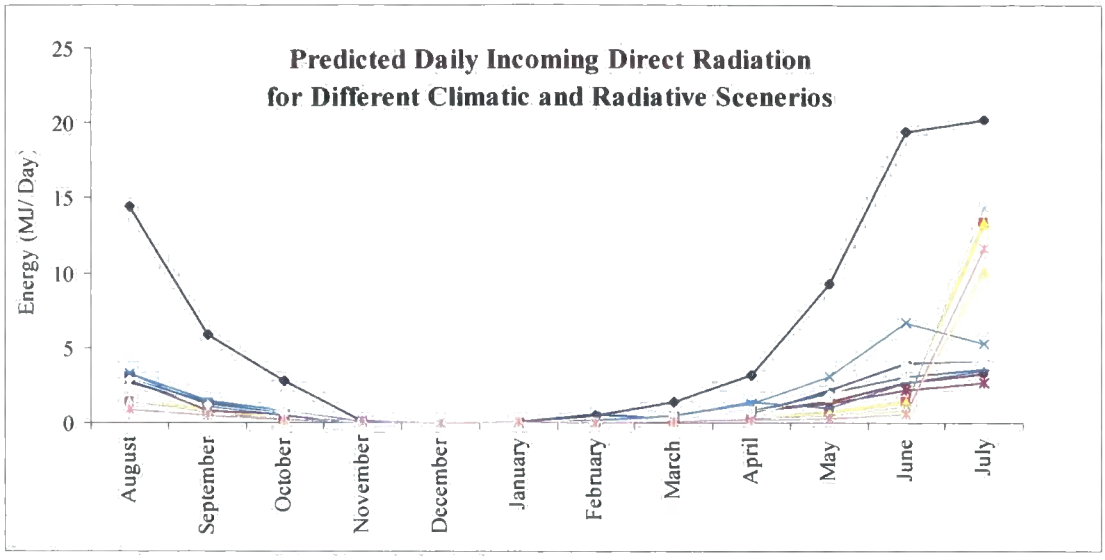

Figure 8.36: Sensitivity of predicted direct beam radiation

8.6.5. Net Radiation

Monthly net radiation highlights a composite signal of dependencies, most pronounced in summer when net radiation balance is most critical. Assuming clear sky conditions predicts 400 % greater net radiation in June than under cloud parameterisation 2 and was found to over estimate melt, necessitating the inclusion of cloud cover in glacier accumulation area models. Monthly mean cloud cover variables reduced the over estimation of net radiation but still failed to account for reduced radiation normal to the surface and consequently over estimated melt throughout the study area.

Net balances for cloud adjusted predictions are lower than those expected, with a negative balance from November to March driven by sensible heat when snow surfaces warmed from incoming short wave radiation heat the air above the snow surface; this combined with small shortwave fluxes, cloudy skies, high albedos and short daylight hours significantly reduces the radiation absorbed by the ground. Summer estimates are in line with results presented within the literature including McKenney *et al.* (1999) and Oke (1978). Predictions excluding sensible heat exchanges provide the lowest summer net balance, which was found to overestimate snowcover and consequently cannot be used to simulate discrete accumulation areas. Monthly mean net balance predictions for different lapse rate models provide estimates of ± 5 MJ day^{-1}: although this appears a minor difference in monthly mean net radiation plots, it was found to produce a more dominant influence on the spatial distribution of snow accumulation.

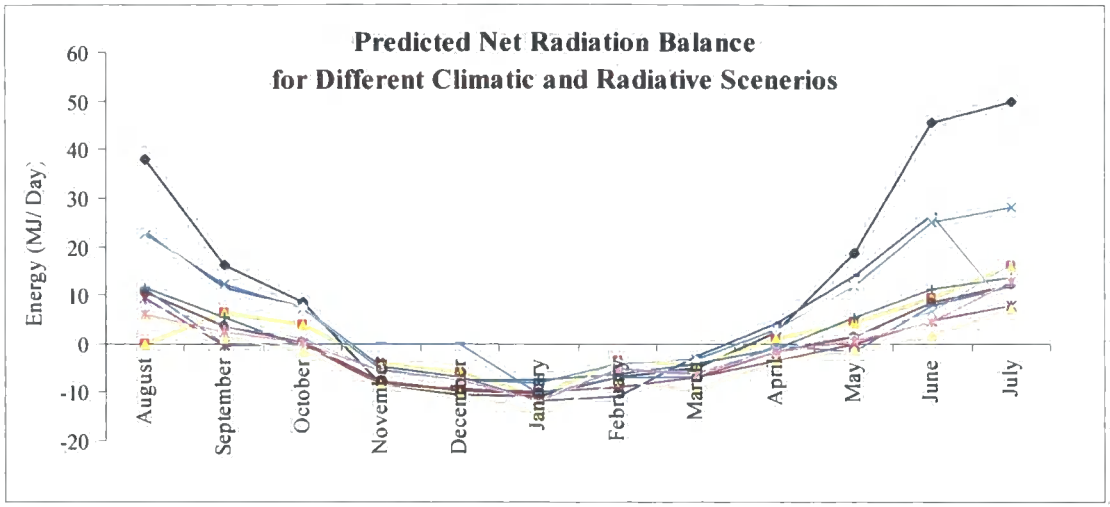

Figure 8.37: Sensitivity of predicted net radiation

Direct, diffuse, longwave and net radiation exhibit sensitivities to cloud cover which are most pronounced during the summer ablation period when cloud cover is lower and daylight hours are longer. This is congruent with expectations, for example McKenney *et al.* (1999). Longwave and sensible heat exchanges exhibit sensitivity to air temperature but feedbacks between cloud cover, net radiation and albedo are also evident.

Consideration of feedbacks between radiative and other climatic parameters revealed the dominant control of cloud cover and the seasonal role of sensible heat in summer. Interpretation and discussion of the predictive capabilities of the model also necessitates analysis of the sensitivity of predicted snow accumulation to climatic and radiative model variables. Mean and maximum monthly snow accumulation were compared for each model and are summarised in Figures 8.38, 8.39, 8.40 and 8.41 and discussed in the subsequent sections.

8.7. Climatic sensitivity of predicted snow accumulation

Lapse rate 2 with cold summer temperatures predicted the greatest mean accumulation during winter through summer, although LGM predictions with coldest temperatures and reduced precipitation predicted the greatest accumulation in July as increased monthly precipitation and minimal melt throughout the year resulted in deeper snow accumulation at the end of the ablation season when insufficient energy was available to heat and melt the snow (Figure 8.38).

IPCC warming scenario predicted the shortest and thinnest snow accumulation with the fastest and earliest melt (Figure 8.38). Warm spring temperatures initiated melt identifying sensible heat as dominant melt driver under future warming conditions.

Seasonal lapse rates with cooler autumns and summers predicted slower melt, which was not initiated until April, and predicted the second highest mean accumulation in July (Figure 8.38). Geomorphic lapse rates with cooler winter temperatures predicted a greater rate of melt in summer when temperatures were warmer than those simulated in the seasonal model. Both seasonal and geomorphic lapse rates created using topographic variables better simulated melt than initial altitudinal and mathematical modelling lapse rates (where all snow ablated by April) or lapse rate 2 (initial lapse rates with a steeper altitudinal component) which could not account for the spatial distribution of melt and temperature. The reported sensitivity of accumulation and melt to temperature supports the findings of Martin *et al.* (1997), Kayastha *et al.* (1999) and Richard and Gratton (2001) who stress the need for representative climatic datasets that predict extreme as well as average climatic events. Modelling approaches that use a constant lapse rate of 0.006 $^{o}C\ m^{-1}$ or 0.0055 $^{o}C\ m^{-1}$ (for example Kayastha *et al.* (1999), Hock *et al.* (2002) and Lie *et al.* (2003a,b)) limit the resolution of predictions, where significant efforts and detailed parameterisations of energy balance are restricted by over simplification of climatic parameters. This research suggests that high-resolution climate datasets must be used in conjunction with robust energy balance modelling to create accurate and distributed melt and accumulation estimates.

The topographically modified wind speed outlined in section 6.3.1. underpredicted sensible heat exchanges and the three dimensional wind flow model (section 7.3.2) provided better results and was therefore used in all predictions.

Conclusions from analysis of mean snow depth accumulations are three fold: summer temperatures provide the critical drive for melt, which is not dependent upon winter temperatures or reduced precipitation. Simulations of warming and cooling predict distinct variations in snow cover from present day conditions and predictions suggest that current climate is most effectively simulated using seasonal lapse rates to model the seasonality in the processes controlling temperature.

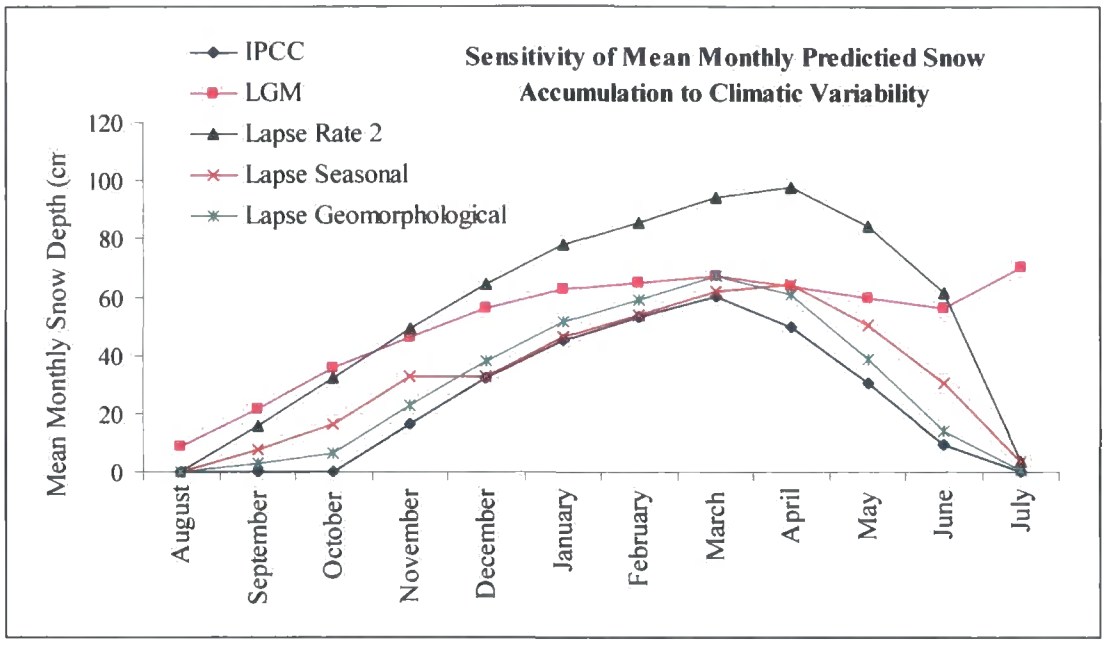

Figure 8.38: Sensitivity of mean monthly snow cover to climatic variables

Interpretation of maximum monthly snow accumulation revealed similar trends although three subtle differences are apparent;

I. Melt at high altitudes is lagged two months after melt at low altitudes for IPCC and seasonal lapse rates and one month later for lapse rate 2 and seasonal lapse rates, suggesting that accurate representation of the altitudinal variation in precipitation and temperature is critical in simulating the onset and duration of melt (Figure 8.39).

II. LGM reconstructions predicted maximum snow accumulation until March and July when colder temperatures minimised melt resulting in greater accumulation. Lapse rate 2 and the geomorphic lapse rates with greater precipitation and cool winter temperatures accumulated greater snow until the onset of melt at high altitude in June and May respectively. With cool temperatures at high altitude, lapse rate 2 and LGM scenarios predict little melt in summer, maintaining deep snow cover (greater than 2m) at high altitudes (Figure 8.39).

III. Delayed onset of melt for seasonal lapse rate predictions results in deeper snow in June and July, creating a more representative accumulation distribution; suggesting that the timing of the onset of melt at high altitudes is critical in accurately simulating accumulation area distributions. Early melting permits loss of too much snow by the end of the accumulation season and a delayed onset of melt results in a higher proportion of snow remaining at the end of the accumulation season (Figure 8.39).

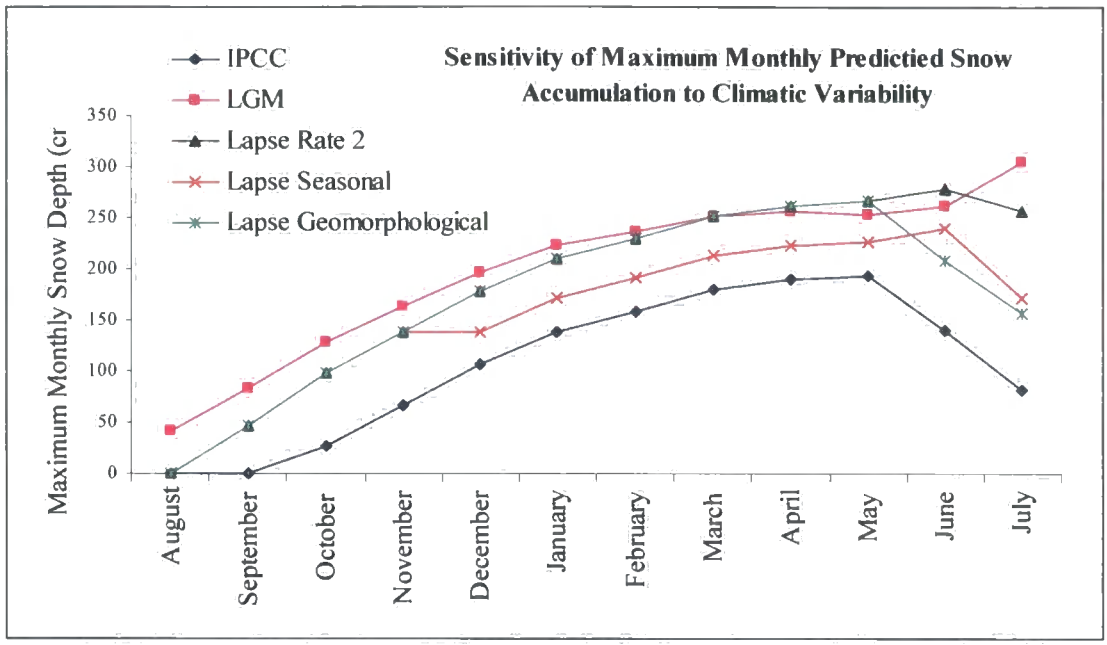

Figure 8.39: Sensitivity of maximum monthly snow cover to climatic variables

Climatic variables are critical in determining the onset and duration of melt and accumulation where topographically derived lapse rates provide better simulations of spatially distributed melt. Climatic parameters alone cannot drive and control melt and radiative parameters are evaluated to determine how they control and drive melt under different model scenarios.

8.8. Energy Balance Sensitivity of predicted snow accumulation

Mean monthly accumulation for all radiative models predicts similar rate and depth of accumulation until March where greatest and lowest predictions are within ± 25 cm (Figure 8.40). Excluding simplified cloud cover parameterisations, differences in mean accumulation are less than 10 cm, suggesting that it may not be necessary to model mean accumulation through the accumulation period where negligible melt occurs leading to minimal differences in net accumulation if over simplifications of cloud cover effects are not used.

Diffuse fraction, monthly mean cloud cover, variable cloud and no cloud cover all predict melt from March with maximum melt in April when positive net radiation balances result in wide spread melt (Figure 8.40). Limited accumulation periods and extensive early melt form unrealistic predictions and indicate that it is not possible to oversimplify cloud cover parameterisations in a glacier accumulation model as melt is over predicted and accumulation periods are shortened. Brock and Arnold (2000) successfully used the diffuse fraction parameterisation to predict local net balance, however this was used in conjunction with local

recorded global radiation and this research suggests that it is a successful mechanism of proportioning incident radiation into its direct and diffuse components but is most appropriately used after accounting for cloud cover reduction of radiation normal to the surface. This research also suggests that clear sky solar radiation models such as Dozier (1980) can only be successfully employed to predict spatially distributed melt if used in conjunction with cloud cover data, or including equivalent parameterisations from measured global radiation.

Although accumulation rates are consistent between models, their rate and onset of melt differ. Greatest accumulation occurred when sensible heat exchanges were excluded, delaying the onset of and slowing the rate of melt during summer. The results indicate that sensible heat exchanges account for nearly 20 cm of melt in June and July when summer temperatures initiate positive sensible heat exchanges over the remaining snowcover (Figure 8.40). The importance of sensible heat exchanges reported here are supported by the work presented by Sverdrup (1936), Male and Grainger (1981) and Marsh *et al.* (1997) who state that sensible heat is required to initiate large scale melt.

Topographic shade is most critical in April and May when solar altitudes are lower (Figure 7.3) and when potential melt is occurring at lower altitudes (Figure 8.29). Although only imposing a local control, topographic shade affects local energy balance: the sensitivities identified here were also reported by Wendler and Ishikawa (1974), Isard (1983), Kayastha *et al.* (1999), Heggem *et al.* (2001), Hock *et al.* (2002) and Fierz *et al.* (2003) who stress the need to incorporate topographic shading. Topographic shading was modelled using solar altitude and azimuth, however other published models use a simplified approach from a predicted sky view factor following Dozier (1980). Heggem *et al.* (2001) found this approach to introduce errors, where the greatest impact was recorded on sloping surfaces with maximum net radiation differences of up to 5 MJ day^{-1}. This research proposes that an efficient shading algorithm (Section 4.8) incorporated within the direct beam radiation calculations does not increase computational complexity and provides valuable local energy balance estimates.

Cloud parameterisations 1 and 2 produce similar rates and patterns of melt, where more radiation reaches the surface under paramerisation 2 conditions, resulting in higher rates of melt. Greatest monthly accumulation is predicted for conditions without sensible or diffuse components where accumulation is over predicted. Diffuse radiation appears to be most critical in July where it accounts for over 20 cm of melt.

Mean accumulation is under-predicted when simplified cloud parameterisations are employed and over-estimated if sensible or diffuse components are excluded from the energy balance model. Sensible heat plays a dominant role in melt throughout summer from May to August, and diffuse radiation drives melt later in summer, both are critical in predicting the onset and extent of melt.

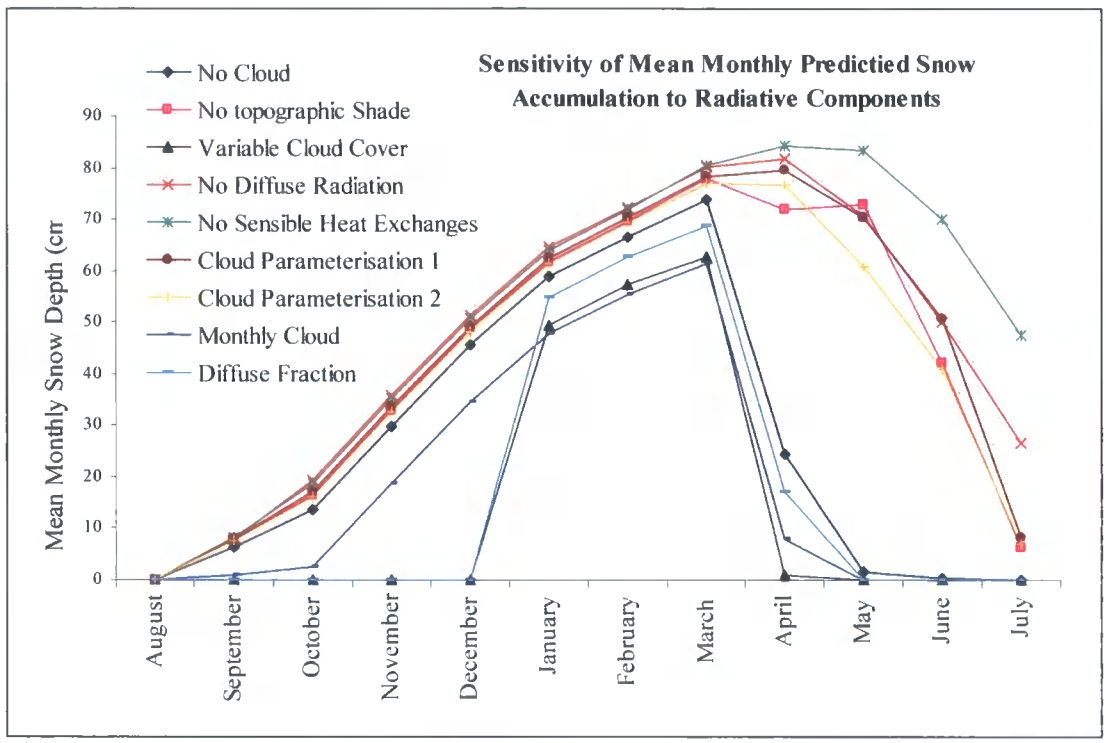

Figure 8.40: Sensitivity of mean monthly snow cover to radiative variables

Examination of monthly maximum snow accumulation reveals similar patterns (Figure 8.41), exclusion of radiative parameters under predicts melt and over simplification of cloud cover over predicts melt.

Although exclusion of sensible heat generates highest monthly mean snow cover, exclusion of diffuse radiation predicts monthly maximum snow accumulation throughout the year until July. Exclusion of sensible heat is the only model to predict a steady increase in the maximum accumulation through the year with only minimal melt occurring in July.

Onset of high altitude melt occurs in June for all but the oversimplified cloud models, with all models predicting consistent melt rates. Maximum snow depths appears less sensitive to radiative parameters where high altitude sheltered locations maintain deep snow cover all year. Predicted accumulation of snow until June for cloud parameterisation 1 and 2 suggests robust results, where summer snowfall events were reported, by Brock *et al.* (2000), as critical to

accurate simulation of glacier distributions. Monthly average snow depth provides a more useful dataset.

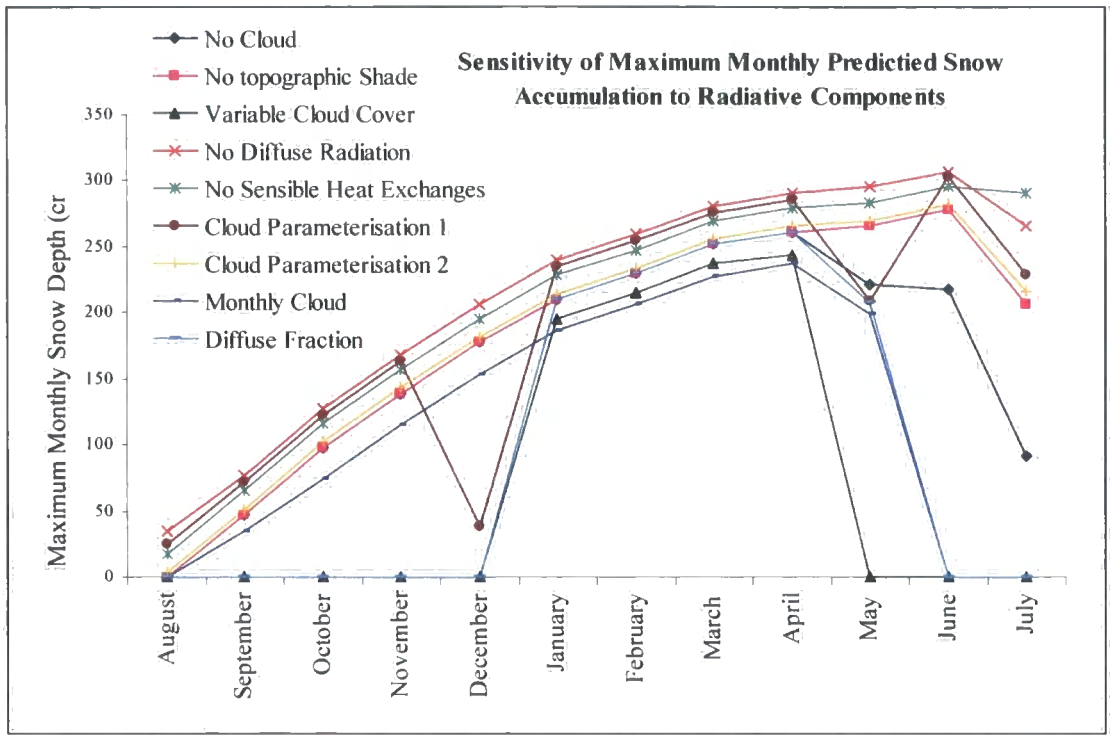

Figure 8.41: Sensitivity of maximum monthly snow cover to radiative variables

Predicted radiation surfaces have a pronounced topographic distribution (Figure 7.21). Examination of the resultant topographic dependency highlights marked altitudinal and aspect component.

8.9. Topographic Controls on predicted snow accumulation

Topography modelled through net radiation balance components has a dominant control on surface accumulation where south facing slopes accumulate less snow (Figures 8.42,8.43 and 8.44). Patterns of annual accumulation mirror those of all aspects with pronounced differences in summer months when direct beam radiation appears to be a dominant driver of melt.

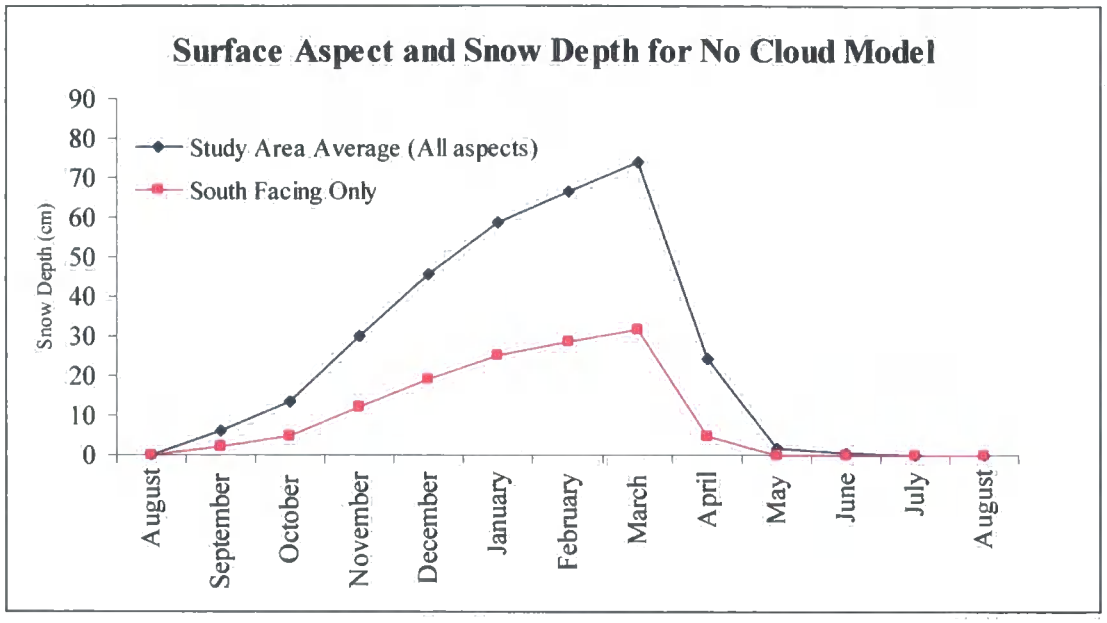

Figure 8.42: Aspect and predicted snow depth for no cloud model

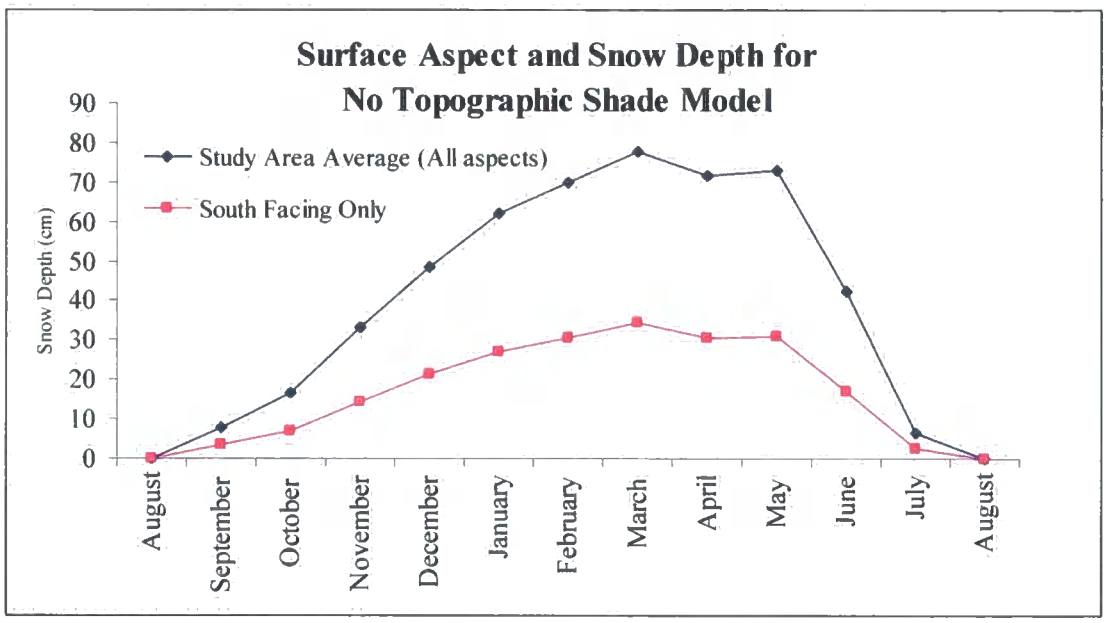

Figure 8.43: Aspect and predicted snow depth for no topographic shade model

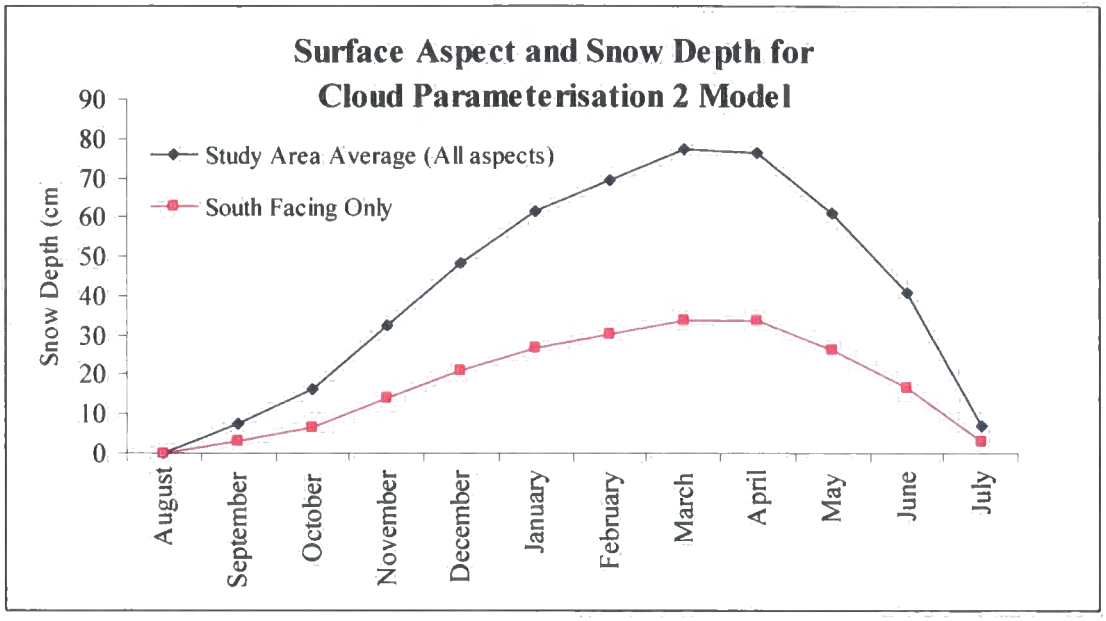

Figure 8.44: Aspect and predicted snow depth for cloud parameterisation 2 model

Parameterisation of geomorphic position and detailed climate modelling was completed in an attempt to simulate the complex patterns of snow accumulation with altitude and aspect. Examination of the resultant July snow cover for cloud parameterisation 2 (Figure 8.45) reveals that parameters other than altitude provide dominant controls on snow cover and it is possible to consider this as an indication that the model advances upon existing approaches which are largely driven by observed energy balance records or altitudinal lapse rates. Resultant distributions are influenced by elevation, solar radiation and topographic position, as in the research of Williams *et al.* (1972) and Isard (1983). The variables included in this research, and the topographic variability modelled, also support the findings of Wendler and Ishikawa (1974), Luce *et al.* (1998), Ferguson (1999) and Fierz *et al.* (2003). They stressed the need to model small-scale topographic influences at the snow surface, where variability in topographically distributed radiation balance also has a temporal component (Dubayah and Katwijk, 1992) and cannot simply be parameterised based on slope and aspect.

Topographic variability and control on glacier accumulation is not modelled as effectively using altitudinal lapse rates or degree day models as applied by Hock (2003), Rasmussen and Conway (2003) or Lie *et al.* (2003a, b). Those studies predict ELAs and glacier distributions, where regional ELAs are successfully identified, but localised or topographically constrained glaciers are not well predicted, being dependent upon variables other than temperature and precipitation. This research suggests that all components of the energy balance model are important in controlling the spatial distribution of melt, which suggests that parameterised models such as Hock (1999) which extends the classic degree day model to include potential clear sky direct solar radiation, cannot accurately simulate snow accumulation without accounting for the

important role of sensible heat in summer melt (Sverdrup, 1936; Male and Grainger, 1981 and Marsh *et al.*, 1997).

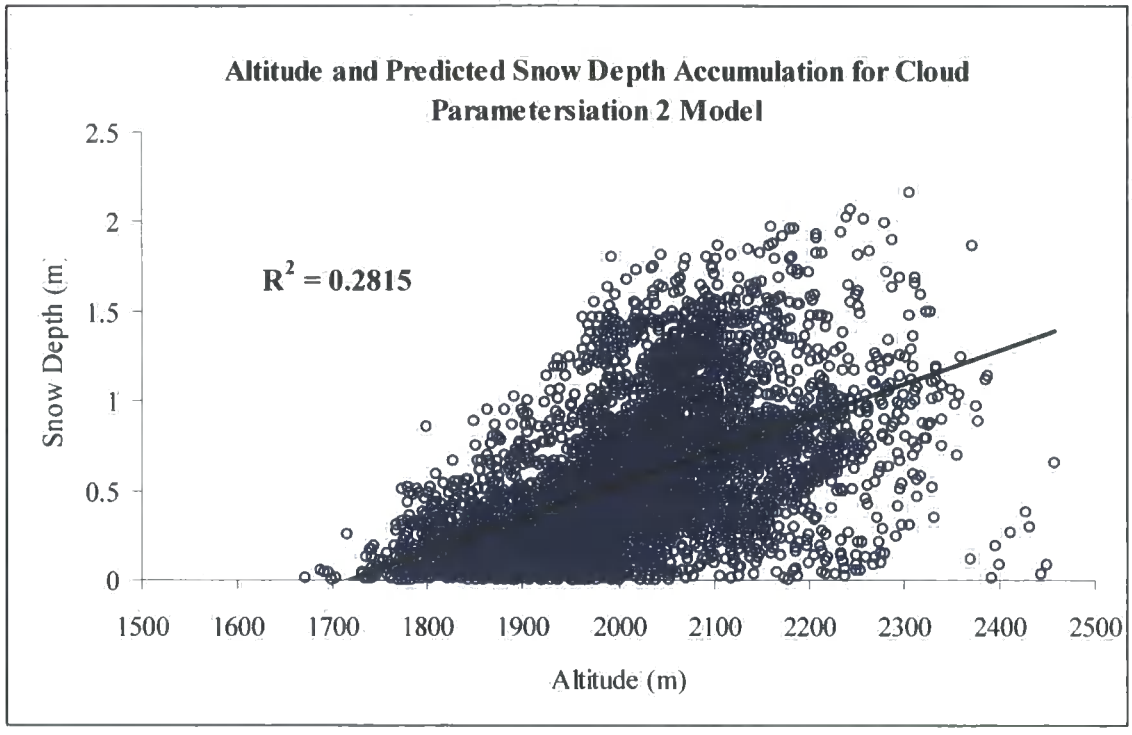

Figure 8.45: Correlation between snow accumulation and altitude

8.10. Evaluation of snow accumulation distributions

Prediction of discrete glacier accumulation areas suggests that topographically derived climatic lapse rates and spatially distributed melt play a significant role in accurate prediction of accumulation areas. The results reported by Tappeiner *et al.* (2001) in their largely correlation and regression based model achieved an R^2 value of 0.72, but accumulation areas not predicted within their model still exhibited spatial organisation. Accumulation areas not predicted within the research presented here are consistent and suggest that conditions required for accumulation in all glaciers within the study area differ and local processes including redistribution, extreme microclimate modifications or extreme cold or wet past climatic events may have initiated their accumulation. This explanation is also supported by the work of Elder *et al.* (1991) and Chang and Li (2000) who found that elevation and radiation receipt could only in part account for observed spatial distributions of snowcover. Catchment scale snow accumulation patterns are most effectively simulated using distributed melt models, rather than using altitudinal temperature and precipitation relationships (for example Tangborn, 1999) that cannot simulate topographically organised melt.

Cloud parameterisation 2 predicted the most accurate accumulation area distributions where more refined radiation estimates, topographically organised climatic and accumulation predictions simulated observed accumulation area distributions (Figure 6.47).

Failure to predict snow accumulation under cloud parameterisation 2 model, can be attributed to the following factors:

- DEM elevations were assumed representative of the underlying topography, inclusion of this subsurface elevation data would steepen slopes and increase topographic shade on the back wall of the cirques where accumulation would initiate. These topographic parameters would decrease the net radiation balance within the cirque, reducing the energy for melt and increasing the opportunity for accumulation.
- Initial model conditions of no snow cover adjust the local energy balance conditions, specifically surface temperature and albedo. Inclusion of a cold snow pack would favour greater and earlier accumulation in the cirque glaciers currently not predicted within the model. Adjustments to the pattern of accumulated snow have known implications on extent of melt (Anderton *et al.*, 2002) and would increase the opportunity for accumulation.
- Luce *et al.* (1998), Tappeiner *et al.* (2001) and Mittaz *et al.* (2002) discussed the role that redistribution can play in adjusting local energy balances. This could account for failure to predict some accumulation areas, including those in Figure 8.46, Box A. However Luce *et al.* (1998) stress that detailed snow drifting information is required to predict spatially and temporally distributed estimates of adjusted accumulation.
- Strong local climatic gradients not simulated within this research may significantly reduce local temperature or increase precipitation enabling snow accumulation. This too could account for failure to predict some accumulation areas, including those in Figure 8.46, Box B.
- Diffuse sky view factor was not included which decreases the diffuse radiation component at sheltered sites. Extension of accumulation areas into the ablation zone would be reduced in sheltered areas. This could account for the over prediction some accumulation areas, including those in Figure 8.46, Box D.
- Not all shallow perennial snowpatches were predicted by the model Figure 8.46, Box C. Localised energy balance conditions, where topographic form with a spatial resolution not captured by the DEM or accounted for in local deposition of avalanched or wind blown snow, were not resolved with the model output. It is also likely that these are not all permanent features and do not persist from year to year.

- Average air temperature and precipitation could under predict cold wet periods, which can be critical to accumulation. This phenomenon was also reported by Semádeni-Davies (1997).

Over prediction of snow accumulation in boxes D, F, G and H under cloud parameterisation 2 model, can be attributed to the following factors:

- Failure to model snow redistribution by drifting was found by Luce *et al.* (1998) to under predict late season melt. This could account for the over prediction some accumulation areas, including those in Figure 8.46, Box F.
- Strong local climatic gradients not simulated within this research may lead to locally warmer or drier conditions that enable greater snow ablation. This could account for the over prediction some accumulation areas, including those in Figure 8.46, Box D and E.
- Long wave emittance from surrounding bedrock would ablate localised snow patches and thin predicted accumulation areas which could account for the over prediction highlighted in Figure 8.46, Box G.
- Thermally induced wind speeds were not modelled, failing to predict increased wind speeds under katabatic wind conditions. This resulted in under predicted sensible heat exchanges reducing the energy available for melt. Increased melt rates would be expected in the ablation zone, reducing predicted snow cover. This could account for the over prediction of some accumulation areas, including those in Figure 8.46, Box H and D.
- Average air temperature and precipitation could under predict hot periods, which can be critical to accumulation. This was also reported by Semádeni-Davies (1997).

Using a regional 30 year normal climate data does limit the study climatic predictions to average or 'normal' conditions that may fail to simulate extreme events that contribute to significant accumulation or ablation events. However, the approach adopted here is supported by the work of Hannah *et al.* (2000). They concluded that short temporal scale datasets cannot be used to model accumulation and melt and propose more representative longer term datasets as the most appropriate scale dataset, where a wider range of melt conditions can be modelled, essential when a range of scales of climatic variables are important.

The model accurately predicted snow cover where accumulation was topographically and altitudinally constrained, where aspect and geomorphic position played important roles in determining glacier extent and localised net balance gradients controlled accumulation.

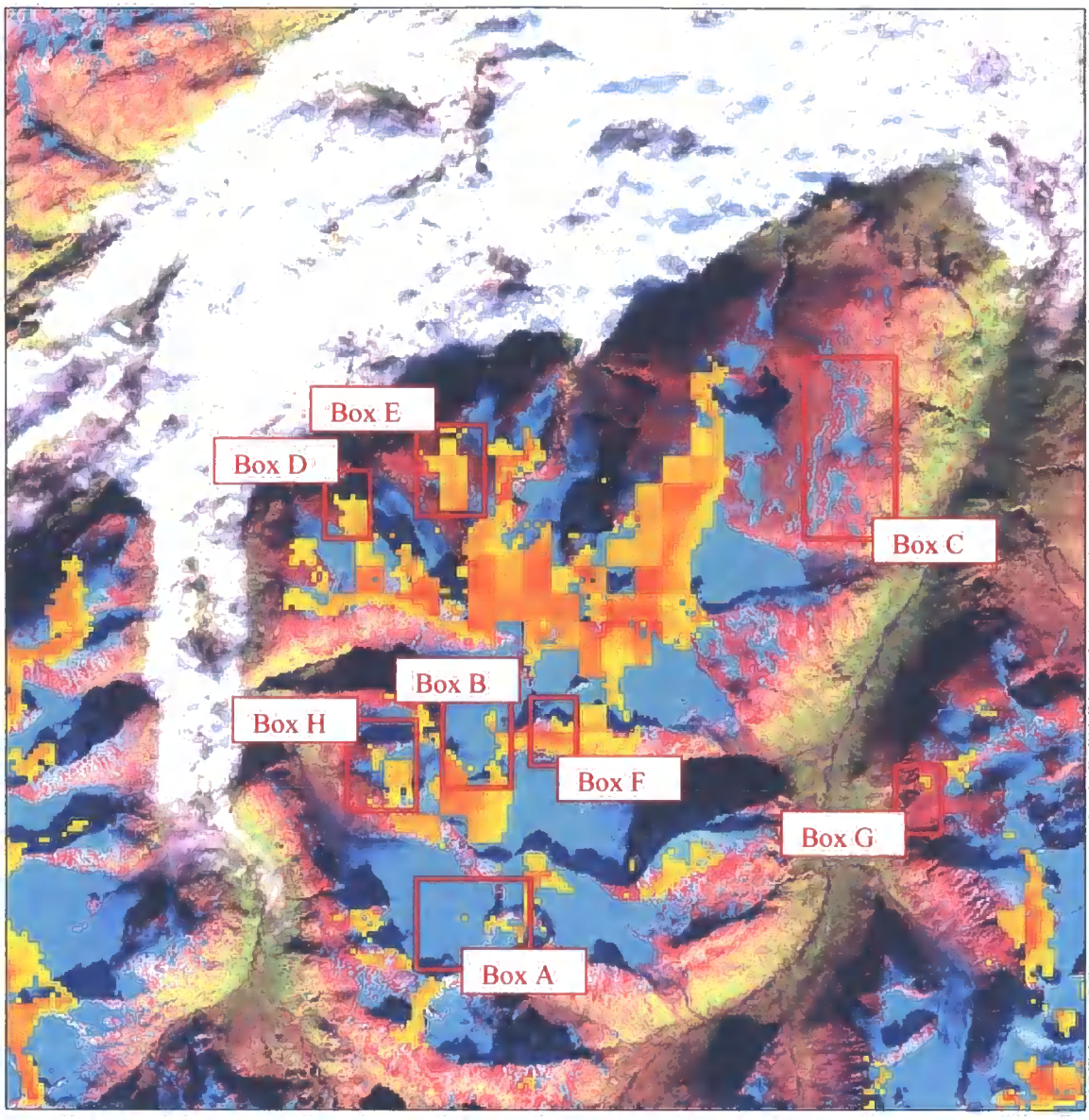

Figure 8.46 Analysis of over and under prediction of glacier accumulation areas

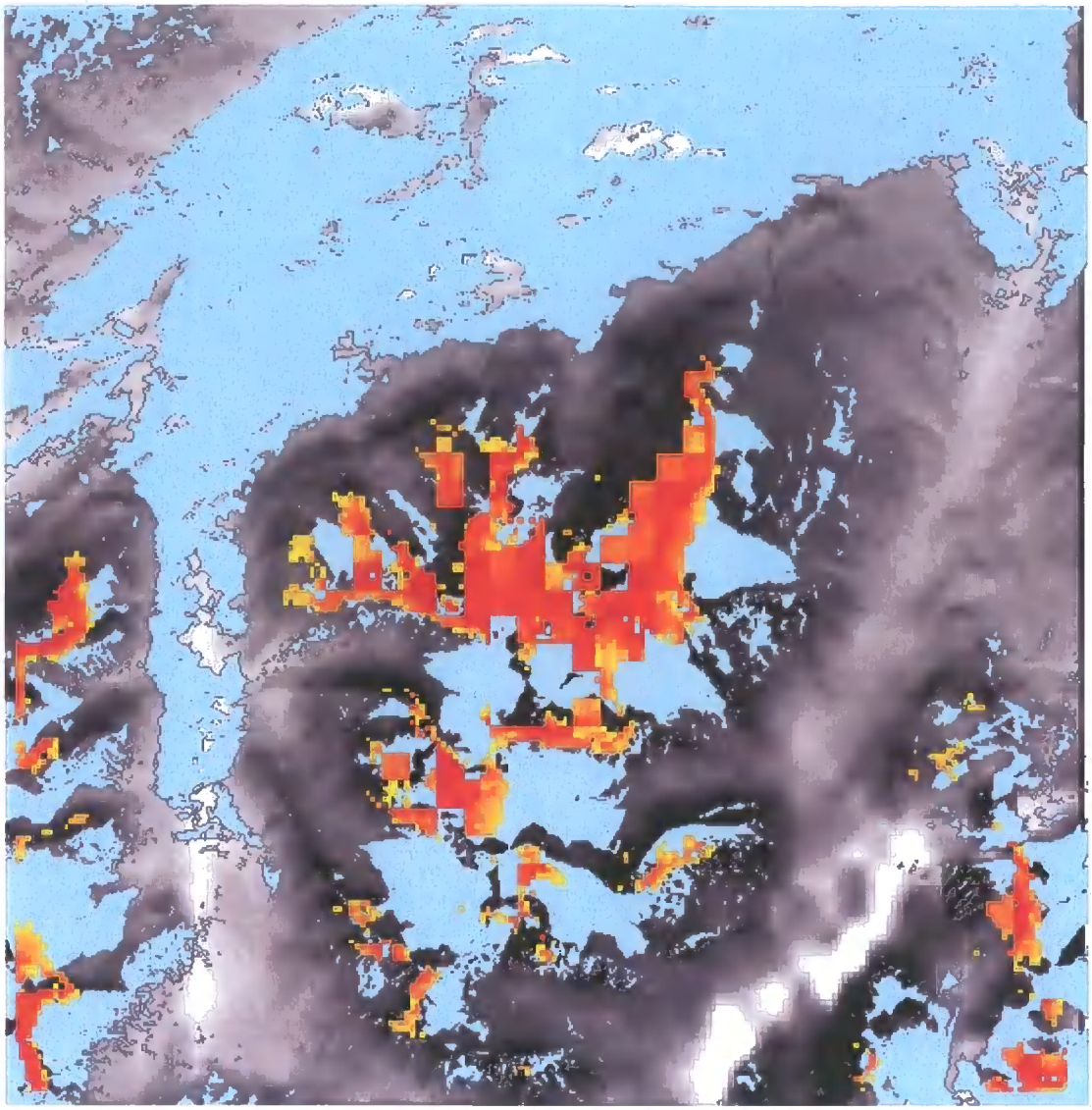

Figure 8.47: August cloud parameterisation 2 predictions draped on the Landsat image classification and net radiation surface

Flexible and repeatable algorithms and an adaptable model structure maximise the value and optimise a model over less robust alternatives (Brock and Arnold, 2000). The model presented here with minimal data input requirements and no radiative local parameterisations is a valuable and progressive tool that can be used to predict present day snow accumulation and predict or reconstruct accumulation distributions for future or past environmental conditions. Equivalent highly parameterised and locally calibrated models were seen by Fierz *et al.* (2003) as a method of masking model inadequacies as tuned coefficients. These calibrated models cannot easily be applied to new areas and form less robust alternatives (for example Hock *et al.*, 2002; Verbunt *et al.*, 2003). Equally models heavily dependent on locally recorded data (Brock and Arnold, 2000; Fierz *et al.*,1997; Mittaz *et al.*, 2002; Semádeni-Davies, 1997; Cline *et al.*, 1998;

Kayastha *et al.*, 1999; Hock *et al.*, 2002; Oerlemans and Klok, 2002) are restricted in their application and are not as robust.

8.11. Discussion of assumptions and potential errors

The physical basis of the model and the lack of parameter fitting within the model increases its flexibility, facilitating applications in different study areas (Cline *et al.*, 1998). However, simplifications of reality and assumptions of homogeneity are essential within any modelling application.

The following simplifications were made in the model presented:

- DEM surface is assumed to be a true representation of sub glacier surface
- Homogeneity is assumed within each 100 m pixel
- Snow free surfaces at start of mass balance year are assumed
- Daily incident radiation is assumed constant for 5 days
- Constant average land cover albedo of 0.4
- Simplistic atmospheric absorption and attenuation
- Outgoing long wave radiation is assumed constant
- Snow cover emissivity is assumed spatially and temporally constant
- Diffuse radiation is assumed from an isotropic sky
- Sky view factor is not included
- Rain on snow events are not included
- Advection between and within pixels is ignored
- Snow surface albedo is assumed to be spatially constant throughout equal age snow cover, decreasing only as a function of time
- Snow surface temperature is predicted using air temperature and solar heating
- All melted snow or rain runs off the snow pack
- Multiple reflections between snow and cloud surfaces were not modelled
- Advection is not modelled: although identified by Granger *et al.* (2002) as an important consideration, inclusion of advection would extend and infill accumulation areas, but it would not address the main areas of under prediction, where all snow cover is ablated.

All of these assumptions affect the magnitude of predicted net balance and snow accumulation. However, a high degree of matching between predicted and observed distributions confirms that errors propagated through the model by employing these assumptions are limited. The validity of these assumptions is under current review by the author and within the wider research

community. Comparison of model output with other published models suggests that the balance of modelled and parameterised phenomena is satisfactory and does not limit the usefulness or accuracy of the model.

A five day energy balance time step within the model is supported by the work of Fierz *et al.* (2003) who proposed that the complexity of daily time steps cannot be effectively modelled, and by Ferguson (1999) who stressed that more complex snow melt models do not ensure more accurate results.

Limitations to model predictions by spatial resolution are not only an inevitable consequence of data availability, but provide a realistic dataset for climate data interpolation accuracy and net radiation variance. Dubayah *et al.* (1990) investigated the role of spatial scale on energy balance models and identify reduced variance in spatially distributed estimates as the main limitation of coarse resolution models. This needs to be evaluated with respect to predicted and observed variance in snowcover (a function of terrain variability). The model results presented here accurately simulate observed variance suggesting that a 100 m model resolution satisfies model requirements.

Albedo parameterisation was investigated within the model, but greater sensitivities were found with cloud cover.

Errors are incorporated at every step of the model, rendering an accurate propagated error estimate challenging: one is not provided here. Dubayah and Rich (1995) and Brock *et al.* (2000) identified DEM error as the most serious error component of topographic solar radiation models, where high variation in local slope and aspect (which were identified as more sensitive to altitudinal error earlier) can lead to large variations in net radiation balance: southerly aspects, steep slopes and topographic shading create steep local gradients in net balance estimates. Error removal cannot be performed after net balance predictions as high local gradients in energy balance exist in the landscape and cannot be differentiated from error artefacts. This research project has confirmed this sensitivity and identified digital elevation data error as a critical limitation on snow accumulation estimates. It developed an efficient and effective error removal mechanism to improve prediction accuracy and limit error propagation. Propagation of errors through the model without error removal are visible in Figure 8.48 a and b where diagonal snow accumulations are predicted.

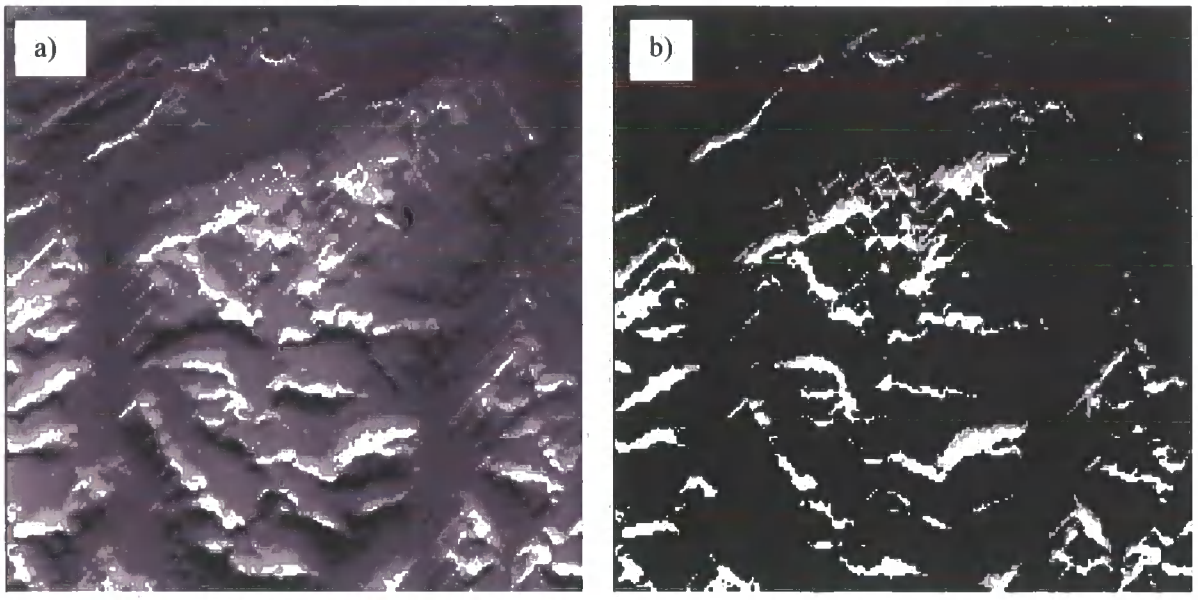

Figure 8.48: a) December and b) April accumulation predictions before accounting for DEM error

8.12. **Conclusions**

Driven by spatially distributed temperature, precipitation and radiation all models predicted spatially distributed melt with areas of thinner snow cover melting first: melt patterns indicated spatially organised accumulation. This research addressed current limitations to existing melt models, where Cline *et al.* (1998) identified the lack of spatial distributed climatic data as a major obstacle in snow melt modelling. Glacier accumulation area distributions were improved by seasonal and geomorphic lapse rates and more complex parameterisation of cloud. Sensitivities result from both climatic and radiative variables, but were most pronounced to changes in snow cover albedo, cloud cover and DEM error.

All energy balance components were found to contribute to predicted accumulation areas with diffuse radiation and sensible heat exchanges most dominant in controlling the timing and rate of summer melt.

The most robust predictions were made using the cloud parameterisation model 2. Seasonal temperature lapse rates created using geomorphic parameters and the three dimensional wind flow modelling produced the most robust climatic predictions. Cloud parameterisations of reduced global radiation and partitioning of diffuse and direct components created the most realistic radiative components with diffuse radiation over predicted in all other models.

Prediction under warming and cooling scenarios result in markedly different distributions where warmer summers and drier winters have the most dominant effect.

CHAPTER NINE

CONCLUSIONS AND FUTURE STUDY

9.1. Introduction

In Chapter one, the overall aim of the thesis was defined: " *to predict small glacier accumulation areas using accessible data, providing a repeatable and flexible model that could be applied to other geographical areas in the future.* ".

To address the above aim, this thesis has addressed the following research aims:

1. *To create a suite of topographic variables from digital elevation data to improve earth surface process modelling*
2. *To create a local climate dataset of temperature and precipitation, wind and cloud cover using regional climate and topographic data.*
3. *To predict spatially distributed glacier accumulation areas using regional climate and topographic data.*

This chapter concludes this thesis by reviewing the main findings of the work in the context of the original aim stated above. It also reflects on the strengths and weaknesses of the work and makes recommendations for future research in spatially distributed mass balance modelling.

9.2. Main Findings of the PhD Research

1. *To create a suite of topographic variables from digital elevation data to improve earth surface process modelling*

Digital elevation data in the form of a 100 m DEM were used to create a suite of topographic variables that characterised surface form, context and position. Attempts to extend existing topographic descriptors were presented, termed composite or contextual terrain parameters. Methodologies for extraction of relative height, slope position, valley context, valley

orientation, maritimity, surface roughness and topographic exposure were presented that characterised local conditions using information on the surrounding area and their scale based variability.

Attempts to characterise topographic position to better inform process modelling used information on the proximity and nature of surrounding topographic features in an attempt to relate surface form to surface process. Effectiveness of characterisations varied, where measures using information on relative attributes or focal characteristics provided robust topographic indicators and measures that attempted to relate topographic form to distinct landform attributes were less effective and sensitive to extraction algorithms and spatial scale. Methodologies for addressing these limitations were presented.

The research confirmed the need to account for error within digital elevation data where spectrally and spatially organised error present in the DEM was found to propagate through the model. An effective removal procedure, using Fourier transforms was employed and largely removed the observed error without over smoothing the data, minimising any associated error propagation. This presented a new application of Fourier transforms and information on interpretation of Fourier frequency outputs for digital elevation data was presented.

Measures of surface roughness were used to inform a viewshed algorithm, where surface roughness was found to correlate with algorithm efficiency. Search algorithms extending from the study pixel were found to be more effectively analysed using a tracking in algorithm and rougher surfaces were found to be more effectively analysed using a tracking out algorithm. This sensitivity of algorithm performance to surface roughness can be applied to other surface calculations, where local and focal estimates of surface characteristics are seen to inform computational efficiency.

2. *To create a local climate dataset of temperature and precipitation, wind and cloud cover using regional climate and topographic data.*

30 year monthly normal climate data were investigated to identify spatial and temporal variability that could be simulated using time series and terrain information. Topographic parameters were found to improve temperature and precipitation predictions from those using standard lapse rates alone.

The most effective variables for improving the accuracy of temperature predictions accounted for valley locations where strong temperature gradients exist. Accounting for these topographic

locations better allowed the model to simulate observed trends in temperature. Monthly variability was most effectively simulated using seasonal lapse rates that accounted for seasonality in process. Precipitation was most effectively predicted using maritimity and altitude with a power law function that accounted for the non-linear distribution of precipitation receipt. Restricted altitudinal range of climate datasets limited the variability within the resultant climate predictions where it was necessary to steepen precipitation lapse rates to account for observed winter accumulation.

Cloud cover was found to be the most difficult parameter to predict, where sparse data and weak topographic controls provided little information to inform predictions. Simulation of observed trends of daily variability in cloud cover were used where greater uncertainties would be introduced if correlations present within the data were used to drive predictions.

A method of predicting wind vectors was presented using estimates of terrain modification to wind speeds by flow separation and surface roughness, these created realistic spatial distributions of wind speeds but under predicted flow magnitude.

Methodologies presented in climate data prediction, although applied to the Jotunheimen can be applied to any geographical area, where controls on temperature, precipitation and wind speed show little variation based on location when driven by regional climate and topographic data.

3. *To predict spatially distributed glacier accumulation areas using regional climate and topographic data.*

The research presented in this thesis has made a valuable contribution to mass balance modelling, developing a spatially and temporally distributed model with low data requirements. The model predicts monthly snow accumulation, driven by regional climate and topographic data without the need for parameter fitting or coefficient tuning.

The research drew upon terrain analysis, climatic and energy balance modelling to create a model optimised for predicting cirque and localised glaciers. The research adopted a distinct spatial analysis approach to prediction where topographic controls on climate and accumulation were identified as critical for predicting observed spatial variability in snow accumulation.

Predicted snow accumulations exhibited marked sensitivity to climate data, where the timing and rate of melt was critical to end of mass balance year accumulation patterns. Summer temperatures were found to impose the greatest control on resultant accumulation patterns.

Sensible heat was found to provide a valuable contribution to melt in summer months when greater positive fluxes to the surface exist.

All of the modelled energy balance components were found to provide a positive contribution to melt predictions, where shortwave radiation accounted for the greatest contribution to melt. Sensitivity to climatic and radiative components of the mass balance model were investigated where summer conditions were found to be the most critical. Radiative parameters were most sensitive to cloud cover measurements, where parameterisations of global radiation and diffuse and direct components provided the most robust estimates. Snow albedo was also found to impose controls on predicted snow accumulation patterns.

9.3 Strengths and Weaknesses of the Research

The main strengths of the research described in this thesis include the following:

- A holistic approach to predicting glacier accumulation areas was developed, that drew upon topographic, climatic and energy balance components that were identified in chapter 1 as dominant controls on glacier accumulation. Published approaches to simulating snow melt do not attempt to account for each of these components and cannot simulate observed variability. The model presented here accounts for spatial variability in observed accumulation areas, where local topographic, climatic and energy balance gradients are predicted.
- Low data requirements and no local parameterisation or tuning coefficients maximise the potential applications of this research. Alternative models are largely limited by study area and data requirements identifying this research as an accessible and robust mechanism of predicting accumulation in unmonitored or inaccessible areas.
- Local scale energy balance and climate predictions were accurately simulated using information contained within a DEM. Exploration of the information contained within digital elevation data and how this can inform process studies forms an invaluable future research direction. New methods of identifying and removing DEM error and improving algorithm efficiency using surface characteristics form valuable research contributions.
- Analysis of sensitivities to changing climatic and radiative components provided an insight into system responses to changing environmental conditions. The model presented here provides a robust tool for examining these responses where observed changes were congruent with expectations.

The following weaknesses in the PhD research study are also identified:

- Error present within the study area DEM propagated error through the topographic and climate modelling to the mass balance model. Although spatially organised error is not present within the model snow accumulation predictions, evidence of error is clear within some predicted energy balance components.
- A lack of information on sub glacier topography limited analysis to predictions on glacier surfaces, where shallower gradients, reduced curvature and topographic shade alter local energy balance conditions reducing the ability of the model to predict realistic distributions.
- Poor altitudinal range in climate station data limited the effectiveness of predictive approaches based upon correlations present within the dataset. Precipitation predictions required a steepening of the altitudinal lapse rate to simulate high altitude precipitation receipts
- Simplistic cloud cover predictions, a result of minimal observed data restricted the spatial variability in accumulation simulated within the model.
- Limited quantitative validation of predictions limits the analysis of areas where the model poorly simulates observed accumulation areas. Limited by noisy remotely sensed classifications and topographic maps, efficient and accurate validation mechanisms could not be developed within the scope of this research.

9.4 Recommendations for Future Work

This final section makes suggestions for the possible direction of future work, both in the mass balance modelling and also in the context of wider geomorphological and terrain analysis applications.

An initial extension of this PhD will attempt to develop a more robust validation methodology. Initial steps would involve the manipulation of the vector representation of classified snow cover, by applying a size threshold, removing small snow covered areas and cloud cover. Delineation of estimated accumulation area extent down the glacier and subsequent Boolean overlays using raster representations of these refined observed accumulation area extents would facilitate analysis of areas of over and under prediction. An alternative approach would be to digitize vector polygon coverages of the glaciers delineated in the topographic map, using contours to identify accumulation area extent.

The ability of the model to improve the spatial variability in snow accumulation in comparison to alternatives will be assessed by running a comparative study with other models. The low data requirements of the model presented here facilitate such an exercise where other models would require extensive recalibration. This would provide quantitative estimates of improvements and variability in model output, creating a rich resource.

Application of the model to additional study areas and assessing any variability in model performance will provide information on the sensitivity of the model to local conditions (this will primarily be driven by the spatial distribution of regional climate data). Further extension of the model to reconstruct past conditions could be applied to further our understanding of system responses to changing environmental conditions. One application would be to investigate the use of the model to reconstruct past climatic conditions using known paleo-glacier extent.

The model presented in this research is shown to over and under predict snow accumulation in some areas. Using topographic and wind vector data derived in chapters 4 and 6 areas of snow entrainment, deposition, and avalanching will be predicted to assess the role of snow redistribution in controlling accumulation. Movements of snow through the DEM after a precipitation event, before melt, will improve our understanding of the dynamics of a glacial environment and our knowledge of the spatial organisation of these processes.

Extension of the terrain analysis components of this research also create exciting new future directions, where further development of the application of Fourier transforms in removing DEM error and the use of terrain surface characteristics to inform efficient terrain based algorithms are both innovative research projects. Perhaps the most notable future project addresses the characterisation and extraction of valleys from digital elevation data. A methodology was proposed within this research, which will be implemented to assess the ability with which it can predict valley floor, walls and extent. If successful, a methodology for extracting and characterising valleys will provide an invaluable contribution to geomorphology and climatology for better informing earth surface systems process modelling.

LIST OF SYMBOLS AND ABBREVIATIONS

Symbol	Definition
A_d	Slope aspect (Ryan, 1977 and Purves *et al.*, 1992)
A_{sd}	Standard deviation of the sine of aspect in degrees
ANN	Artificial neural networks
α_{SD}	Albedo for deep snow cover
°C	Degrees Centigrade (or Celsius)
c_p	Specific heat of dry air at constant pressure
c_0	Rainfall at sea level
c_1	Rate of increase in precipitation with altitude
DALR	Dry adiabatic lapse rate
DEM	Digital Elevation Model
D_{tr}	Diurnal temperature range.
E	Elevation (m)
E'	Varies as a function of the maximum elevation in the data (ranges from 0 to 1, from Ryan, 1977)
ELR	Environmental lapse rate
exp	Exponential
ε_{cs}	Effective emissivity of the sky
FFT	Fast fourier transform
F_d	Wind diverting factor (Ryan, 1977)
F_u	Ryan's (1997) sheltering effect
GIS	Geographical information system
GPS	Global position system

G_p	Slope gradient (%) (Purves *et al.*, 1992)
I_b	terrestrial radiation (Kreith and Kreider, 1978)
I_o	the solar flux entering the atmosphere (Kreith and Kreider, 1978)
I	The wind sheltering created by and obstacle (Lapen and Martz, 1993)
K	Degrees Kelvin
KDE	Kernel density estimate
K^*	Net short-wave radiation
$K\downarrow$	Incoming short-wave radiation
$K\uparrow$	Reflected short-wave radiation
L^*	Net long-wave radiation
$L\downarrow$	Incoming long-wave radiation from the atmosphere
$L\uparrow$	Outgoing long-wave radiation from the surface
ln	Log to the base n
m	Metres
ms^{-1}	Metres per second
m asl	Metres above sea level
mb	Millibar (pressure)
m	air mass ratio
P	Precipitation
P_t	Proportion of clear sky transmissivity.
p	Pressure (mb)
Q_e	Latent heat flux from snow-air interface
Q_{en}	Net emitted radiation from surrounding terrain
Q_g	Heat flux from the snow-ground interface
Q_h	Sensible heat flux from the air
Q_p	Heat flux from precipitation
Q_{ln}	Net long-wave radiation
Q_m	Energy flux available for melt
Q_{sn}	Net short-wave radiation
Q_{rt}	Net reflected radiation from surrounding terrain
Q^*	Net all-wave radiation flux
$Q\downarrow$	Total incoming short- and long-wave radiation
$Q\uparrow$	Total outgoing short- and long-wave radiation
R	Gas constant for dry air
R	Roughness

R_r	Rate of change of roughness
R_s	Scaled roughness values
R_{rs}	Rate of change of scaled roughness value
R_{12}	Surface roughness in a 12 pixel width kernel
R_3	Surface roughness in a 3 pixel width kernel
Ri	Richardson number
S_r	Surface roughness
SALR	Saturated adiabatic lapse rate
Sx	Maximum upwind slope parameter (Winstral and Marks, 2002a, 2002b)
T	Temperature
T_A	Air temperature
T_D	Dew point temperature
T_m	Terrain modification effect to wind flow
τ_b	Atmospheric transmittance (Kreith and Kreider, 1978)
U_m	Predicted meso scale winds
U_s	Measured wind speed
V	Wind velocity
V_i	
V_p	Predicted wind velocity after application of altitudinal flow factor
V_{sd}	Wind speed after terrain modification
V_u	
V_{ue}	
V_{ur}	Roughness parameter
W_d	Wind direction (Purves *et al.*, 1992)
Y_d	Slope percent downwind
Z	Altitude
Z_b	Cumulus cloud cover base height (from Barry, 1992)
Z_f	Altitudinal wind flow factor
Z_{sd}	Standard deviation of altitude
Θ_b	Wind direction
θ	Potential temperature

REFERENCES

Aizen, V.B., Aizen, E.M. and Malack, J.M. (1997) Snow distribution and melt in central Tien Shan, Susamir Valley. *Arctic and Alpine Research.* **29**(4), 403-413.

Ahlmann, H.W. (1922) Glaciers in Jotunheimen and their physiography. *Geografiska Annaler.* **4**, 1-57.

Aizen, V.B., Aizen, E.M., Malack, J.M., Nakamura, T. and Kobayashi, S. (2002) Estimation of the energy used to melt snow in the Tien Shan Mountains and Japanese Islands. *Global and Planetary Change.* **32**, 349-359.

Allen, T.R. (1998) Topographic context of glaciers and perennial snowfields, Glacier National Park, Montana. *Geomorphology.* **21**, 207-216.

Anderton, S.P., White, S.M. and Alvera, B. (2002) Micro-scale spatial variability and the timing of snow melt runoff in a high mountain catchment. *Journal of Hydrology.* **268**, 158-176.

Andreassen, L.M. (1999) Comparing traditional mass balance measurements with long-term volume change extracted from topographical maps: a case study of Storbreen Glacier in Jotunheimen, Norway, for the period 1940-1997. *Geografiska Annaler.* **81A**(4), 467-476.

Andreassen, L.M., Elvehoy, H. and Kjøllmoen, B. (2002) Using aerial photography to study glacier changes in Norway. *Annals of Glaciology.* **34**, 343-348.

Angstrom, A. (1924) Solar and Terrestrial Radiation *Quarterly Journal of the Royal Meteorological Society,* **50**, 210, 121-125.

Arck, M. and Scherer, D. (2002) Problems in the determination of sensible heat flux over snow. *Geografiska Annaler.* **84A**, 157-169.

Arendt, A. (1999) Approaches to modelling the surface albedo of a high arctic glacier. *Geografiska Annaler.* **81A**(4), 477-487.

Arnold, N.S., Willis, I.C., Sharp, M.J., Richards, K.S. and Lawson. W.J. (1996) A distributed surface energy-balance model for a small valley glacier. I. Development and Testing for Haut Glacier d'Arolla, Valais, Switzerland. *Journal of Glaciology.* **42**, 77-89.

Arrell, K. (2000) *Fuzzy Classification of Natural Landforms.* Unpublished M.Sc. Dissertation, University of Leicester.

Arrell, K.E., Fisher, P.F. and Tate, N. (2001) A fuzzy K-means classification of elevation derivatives to extract the natural landforms in Snowdonia, Wales. *Proceedings of the 9th National Conference on GIS Research UK (GISRUK 2001).*

Arrell, K.E. and Evans, I.S. (2003) 'Using a GIS to predict glacier accumulation areas', *Proceedings of the 60th Annual Eastern Snow Conference*, University of Sherbrooke, Quebec, Canada

Ashwell, I and Hannell, F. (1960) Wind and temperature variations at the edge of an icecap. *Meteorological Magazine.* **89**, 17-24.

Atkinson, B. (1981) *Mesoscale Atmospheric Circulations.* Academic Press, New York.

Atkinson, B.W. and Smithson, P.A. (1976) Precipitation. In: Chandler, T.J. and Gregory, S. (eds.) *The Climate of the British Isles.* London, Longman. 129-182.

Aulitsky, H. (1967) Lage und Ausmass der 'warmen Hangzone' in einen Quertal der Innenalp. *Ann. Met.* **3**, 159-165.

Avissar, R. and Verstraete, J. (1990) The representation of continental surface processes in atmospheric models. *Review of Geophysics.* **28**, 35-52.

Balk, B. and Elder, K. (2000) Combining binary decision tree and geostatistical methods to estimate snow distribution in a mountain watershed. *Water Resources Research.* **36**(1), 13-26.

Barry, R.G. (1973) A climatological transect on the east slope of the Front Range, Colorado. *Arctic and Alpine Research.* **5**, 89-110.

Barry, R.G. (1992) *Mountain Weather and Climate.* 2nd Edition, Routledge, London.

Barry, R.G. (2003) Mountain cryospheric studies and the WCRP climate and cryosphere (CliC) project. *Journal of Hydrology.* **282**, 177-181.

Barry, R.G. and Chorley, R. (1982) *Atmosphere, Weather and Climate.* 4th edition. Methuen. London.

Bartelt, P. and Lehning, M. (2002) A physical SNOWPACK model for the Swiss avalanche warning part I: numerical model. *Cold Regions Science and Technology.* **35**, 123-145.

Bartsch, A., Gude, M., Jonasson, C. and Scherer, D. (2002) Identification of geomorphic process units in Kärkevagge, Northern Sweden, by remote sensing and digital terrain analysis. *Geografiska Annaler.* **84A**(3-4), 171-178

Basist, A., Bell, G. and Meentemeyer, V. (1994) Statistical relationships between topography and precipitation patterns. *Journal of Climate.* **7**, 1305-1315.

Bates, R.H.T. and McDonnell, M.J. (1986) *Image Restoration and Reconstruction.* Clarendon Press, Oxford.

Benn, D.I. and Evans, D.J. (1998) *Glaciers and Glaciation.* Arnold, London.

Bent, R.B. and Hutchinson, W.C.A. (1965) Electric space charges over melting snow on the ground. *Journal of Atmospheric and Terrestrial Physics.* **27**, 91-99.

Berstad, I.M., Sejrup, H.P., Klitgaard-Kristensen, D. and Haflidason, H. (2003) Variability in temperature and geometry of the Norwegian Current over the past 600 yr; stable isotope and grain size evidence from the Norwegian margin. *Journal of Quaternary Science.* **18**(7), 591-602.

Bintanja, R. (1998) The interaction between drifting snow and atmospheric turbulence. *Annals of Glaciology.* **26**,

Bitner, D., Carroll, T., Cline, D and Romanov, P. (2002) An assessment of the differences between three satellite snow cover mapping techniques. *Hydrological Processes.* **16**, 3723-3733.

Black, R.F. (1954) Precipitation at Barrow, Alaska, greater than recorded. *American Geophysical Union Transactions.* **35**(2), 203-206,

Bloschl, G., Gutknecht, D. and Kirnbauer, R. (1991) Distributed snowmelt simulations in an alpine catchment. 2. Parameter study and model prediction. *Water Resources Research.* **27**, 3181-3188.

Blöschl, G. and Kirnbauer, R. (1992) An analysis of snow cover patterns in a small alpine catchment. *Hydrological Processes.* **6**, 99-109.

Blumer, F. and Lang, H. (1995) Precipitation conditions in the Eastern Swiss Alps. *In* Climate Dynamics and the Global Change Perspective Online Conference Proceedings, Cracow, Poland. http://www.cyf-kr.edu.pl/~ziniedzw/conf.html.

Boike, J., Roth, K. and Ippisch, O. (2003) Seasonal snow cover on frozen ground: Energy balance calculations of a permafrost site near Ny-Alesund, Spitsbergen. *Journal of Geophysical Research-Atmospheres.* **108**, 435-449.

Bonacina, L.C.W. (1945) Orographic rainfall and its place in the hydrology of the globe. *Quarterly Journal of the Royal Meteorological Society.* **71**, 41-55.

Boresjö-Bronge, L. and Bronge, C. (1999) Ice and snow-type classification in the Vestfold Hills, East Antarctica, using Landsat-TM data and ground radiometer measurements. *International Journal of Remote Sensing.* **20**(2), 225-240.

Bowman, A.W. and Azzalini, A. (1997) *Applied Smoothing Techniques for Data Analysis: the Kernel Approach with S-Plus Applications.* Oxford University Press, Oxford.

Braithwaite, R.J. (2002) Glacier mass balance: the first 50 years of international monitoring. *Progress in Physical Geography.* **26**(1), 76-95.

Braithwaite, R.J. and Olesen, O.B. (1989) Calculation of glacier ablation from air temperature, West Greenland. In: Oerlemans, J. (ed.) *Glacier Fluctuations and Climate Change, Glaciology and Quaternary Geology.* Dordrecht. 219-233.

Braithwaite, R.J. and Olesen, O.B. (1990) Response of the energy balance on the margin of the Greenland ice sheet to temperature changes. *Journal of Glaciology.* **36**(123), 217-221.

Braithwaite, R.J. and Zhang, Y. (1999) Relationships between interannual variability of glacier mass balance and climate. *Journal of Glaciology.* **45**, 456-462.

Bristow, K. and Campbell, G. (1984) On the relationship between incoming solar radiation and daily maximum and minimum temperature. *Agricultural and Forest Meteorology.* **31**, 159-166.

Brock, B.W. (2004) An analysis of short-term albedo variations at Haut Glacier d'Arolla, Switzerland. *Geografiska Annaler.* **86A**(1), 53-65.

Brock, B.W. (1997) Seasonal and spatial variations in the surface energy-balance of valley glaciers. *Unpublished PhD thesis*, University of Cambridge.

Brock, B.W. and Arnold, N.S. (2000) A spreadsheet-based (Microsoft Excel) point surface energy balance model for glacier and snow melt studies. *Earth Surface Processes and Landforms.* **25**, 649-658.

Brock, B.W., Willis, I.C. and Sharp, M.J. (2000a) Measurement and parameterization of albedo variations at Haut Glacier d'Arolla, Switzerland. *Journal of Glaciology.* **46**, 675-688.

Brock, B.W., Willis, I.C, Sharp, M.J. and Arnold, N.S. (2000b) Modelling seasonal and spatial variations in the surface energy balance of Haut Glacier d'Arolla, Switzerland. *Annals of Glaciology.* **31**, 53-62.

Brooks, C. (1918) Continentality and temperature – second paper: The effect of latitude on the influence of continentality on temperature. *Quarterly Journal of the Royal Meteorological Society.* **44**, 253-270.

Brown, D.G. and Bara, T.J. (1994) Recognition and reduction of systematic error in elevation and derivative surfaces from 7.5 minute DEMs. *Photogrammetric Engineering and Remote Sensing.* **60**, 189-194.

Brown, D.G., Lusch, D.P. and Duda, K.A. (1998) Supervised classification of types of glaciated landscapes using digital elevation data. *Geomorphology.* **21**, 233-250.

Brun, E., Martin, E. and Spiridonov, V. (1997) Coupling a multi-layered snow model with a GCM. *Annals of Glaciology.* **25**, 66-72.

Brunsdon, C., McClatchey, J. and Unwin, D. (2001) Spatial variations in the average rainfall-altitude relationship in Great Britain: an approach using geographically weighted regression. *International Journal of Climatology.* **21**, 455-466.

Burrough, P.A. and McDonnell, R.A. (1998) *Principles of Geographical Information Systems.* Oxford University Press, Oxford.

Carroll, J.J. and Fitch, B.W. (1981) Effects of solar elevation and cloudiness on snow albedo at the South Pole. *Journal of Geophysical Research.* **86,** 5271-5276.

Cartwright, T.J. (1993) *Modelling the World in a Spreadsheet: Environmental simulation on a Microcomputer.* Johns Hopkins University Press. Baltimore.

Catchpole, A. (1969) The solar control of diurnal temperature variation at Winnipeg. *Canadian Geographer.* **8**, 255-268.

Catchpole, A. (1972) Time and temperature: A model of temporal interrelationships. *Canadian Geographer.* **16**, 365-373.

Cawkwell, F.G.L. and Bamber, J.L. (2002) The impact of cloud cover on the net radiation budget of the Greenland ice sheet. *Annals of Glaciology.* **34**, 141-149.

Cazorzi, F. and Fontana, G.D. (1996) Snowmelt modelling by combining air temperature and a distributed radiation index. *Journal of Hydrology.* **181**, 169-187.

Champeney, D.C. (1973). *Fourier transforms and their physical applications.* Academic Press, New York.

Chang, K-T. and Li, Z. (2000) Modelling snow accumulation with a geographic information system. *International Journal of Geographical Information Science.* **14**(7), 693-707.

Chaun, G. and Lockwood, J. (1974) An assessment of topographical controls on the distribution of rainfall in the central Pennines. *Meteorological Magazine.* **103**, 275-287.

Chen, D. (1999) A monthly circulation climatology for Sweden and its application to a winter temperature case study, Earth Sciences centre, University of Gothenburg, Report C16, 34-59.

Chorley, R.J. (1979) The application of statistical methods to geomorphology. *Essays in Geomorphology.* 275-387.

Chorlton, J.C. and Lister, H. (1971) Geographical control of glacier budget gradients in Norway. *Norsk Geografiska Tidsskrift.* **25**(3-4), 159-164.

Chorowicz, J., Kim, J., Manoussis, S. and Rudant, J-P. (1989) A new technique for recognition of geological and geomorphological patterns in digital terrain models. *Remote Sensing of Environment.* **29**(3), 229-239.

Chua, S., and Bras, R.L. 1982. Optimal Estimators of Mean Areal Precipitation in Regions of Orographic Influence. *Journal of Hydrology.* **57**, 23-48.

Cline, D., Bales, R., and Dozier, J. (1998) Estimating the spatial distribution of snow in moutain basins using remote sensing and energy balance modelling. *Water Resources Research.* **34**(5), 1275-1285.

Cogley, J.G. (1999) Effective sample size for glacier mass balance. *Geografiska Annaler.* **81A**(4), 497-507.

Cogley, J.G., Ecclestone, M.A. and Andersen, D.T. (2001) Melting on glaciers: environmental controls examined with orbiting radar. *Hydrological Processes.* **15**, 3541-3558.

Conway, H., Hall, B., Denton, G., Gades, A. and Waddington, E. (1999) Past and Future Grounding-Line Retreat of the West Antarctic Ice Sheet. *Science.* **286**, 280-283.

Corault, D. and Monestiez, P. (1999) Spatial interpolation of air temperature according to atmospheric circulation patterns in southeast France. *International Journal of Climatology.* **19**, 365-378.

Corripio, J.G. (2002) *Snow surface albedo estimation using terrestrial photography.* Unpublished Paper, University of Edinburgh.

Cotton, W.R. and Pielke, R.A. (1976) Weather modification and three-dimensional models. *Bulletin of the American Meteorological Society.* **57**, 788-796.

Coughlan, J.C. and Running, S.W. (1997) Regional ecosystem simulation: a general model for simulating snow accumulation and melt in mountainous terrain. *Landscape Ecology.* **12**(3), 119-136.

Cox, N. (1992) Precipitation statistics for geomorphologists: variations on a theme by Frank Ahnert. *Catena Supplement.* **23**, 189-212.

Cox, N. (2002) Speaking Stata: how to face lists with fortitude. *The Stata Journal.* **2**(2), 202-222.

Cramer, O. (1971) Potential temperature analysis for mountainous terrain. *Journal of Applied Meteorology.* **11**, 44-50.

Cutler, P.M. and Munro, D.S. (1996) Visible and near-infrared reflectivity during the ablation period on Peyto Glacier, Alberta, Canada. *Journal of Glaciology.* **42**, 333-340.

Dahl, S, O., and Nesje, A. (1992) Paleoclimatic implications based on equilibrium-line altitude depression of reconstructed Younger Dryas and Holocene cirque glaciers in inner Nordfjord, western Norway. *Palaeogeography, Palaeoclimatology, Palaeoecology.* **94**, 87-97.

Daly, C., Neilson, R. and Phillips, D. (1994) A statistical – topographic model for mapping climatological precipitation over mountainous terrain. *Journal of Applied Meteorology.* **33**, 140-158.

Daly, S.F., Davis, R., Ochs, E. and Pangburn, T. (2000) An approach to spatially distributed snow modelling of the Sacramento and San Joaquin basins, California. *Hydrological Processes.* **14**, 3257-3271.

Davies, J.A. (1967) A note on the relationship between net radiation and solar radiation. *Quarterly Journal of the Royal Meteorological Society.* **93**(395), 109-115.

Davies, J.A. and Buttimor, P.H. (1969) Reflection coefficients, heating coefficients and net radiation at Simcoe, Southern Ontario. *Agricultural Meteorology.* **6**, 373-386.

Davies, J.A., Schertzer, W. and Nunez, M. (1975) Estimating global solar radiation. *Boundary-Layer Meteorology.* **9**, 33-52.

Davis, W.M. (1899) The geographical cycle. *Geographical Journal.* **14**, 481-504.

Deems, J.S., Birkeland, K.W. and Hansen, K.J. (1977) Topographic influence on the spatial patterns of snow temperature gradients in a mountain snowpack.

Demuth, M. and Pietroniro, A. (1999) Inferring glacier mass balance using Radarsat: results from Peyto Glacier, Canada. *Geografiska Annaler.* **81A**(4), 521-529.

Denby, B. and Greuell, W. (2000) The use of bulk and profile methods for determining surface heat fluxes in the presence of glacier winds. *Journal of Glaciology.* **46**(154), 445-452.

Depraetere, C. (1987) Classification automatique interrégionale à partir de MNT issus de la BDZ. *Institut Géographique National.* Paris, EO/DELI/SCME Rapport 4.

De Ruyter de Wildt, M.S., Oerlemans, M, S., and Bjõrnsson, H (2003) A method for monitoring glacier mass balance using satellite albedo measurements: application to Vatnajõkull, Iceland. *Journal of Glaciology.* **48**(161), 267-278.

Dingman, S.L., Seely-Reynolds, D.M. and Reynolds R.C.III. (1988) Application of kriging to estimating mean annual precipitation in a region of orographic influence. *Water Resources Bulletin.* **24,** 329-339.

Dobromez, J.F. (1976) Climatologie. In: *Le Nepal. Ecologie et Biogeographie.* C.N.R.S. Paris. 31-91.

Doran, J., Barnes, F., Coulter, R., Crawford, T., Baldocchi, D., Balick, L., Cook, D., Cooper, D., Dobosy, R., Dugas, W., Fritschen, L., Hart, R., Hipps, L., Hubbe, J., Gao, W., Hicks, R., Kirkham, R., Kunkel, K., Martin, T., Meyers, T., Porch, W., Shannon, J., Shaw, W., Swiatek, E. and Whiteman, C. (1992) The Boardman regional flux experiment. *Bulletin of the American Meteorological Society.* **73**, 785-795.

Douguédroit, A. and Saintignon, F.F. de (1970) Method de l'etude de la decroissance des temperatures en montagne de latitude moyenne: exemple des Alpes francaises du sud. *Rev. Geog. Alp.* **58**, 453-472.

Douglas, D.H. (1986) Experiments to locate ridges and channels to create a new type of digital elevation model. *Cartographica.* **23**(4), 29-61.

Dozier, J. (1980) A clear-sky spectral solar radiation model for snow-covered mountainous terrain. *Water Resources Research.* **16**(4), 709-718.

Dozier, J. (1989) Spectral signature of alpine snow cover from Landsat Thematic Mapper. *Remote Sensing of Environment.* **28**, 9-22.

Dozier, J. and Frew, J. (1990) Rapid calculation of terrain parameters for radiation modelling from digital elevation data. *Transactions on Geoscience and Remote Sensing.* **28**(5), 963-969.

Driedger, H.L. and Catchpole, A.J.W. (1970) Estimation of solar radiation receipt from sunshine duration at Winnipeg. *Meteorological Magazine.* **99**, 285-291.

Dubayah R. (1992) Estimating net solar radiation using Landsat Thematic Mapper and digital elevation data. *Water Resources Research.* **28**(9), 2469-2484.

Dubayah, R., Dozier, J. and Davis, F.W. (1990) Topographic distribution of clear-sky radiation over the Konza Prairie, Kansas. *Water Resources Research.* **26**(4), 679-690.

Dubayah, R. and van Katwijk, V. (1992) The topographic distribution of the annual incoming solar radiation in the Rio Grande River Basin. *Geophysical Research Letters.* **19**(22), 2231-2234.

Dubayah, R. and Rich, P.M. (1995) GIS-based solar radiation modelling. In: Authors (eds.) *GIS and Environmental Modelling.* Publisher. 129-134.

Dubayah, R. and Rich, P.M. (1995) Topographic solar radiation models for GIS. *International Journal of Geographical Information Systems.* **9**(4), 405-419.

Duguay, C.R. (1993) Radiation modelling in mountainous terrain review and status. *Journal of Climatology.* **14**, 339-357.

Duguay, C.R. (1992) Estimating surface reflectance and albedo from Landsat-5 Thematic Mapper over rugged terrain. *Photogrammetric Engineering and Remote Sensing.* **58**(5), 551-558.

Duguay, C.R. and LeDrew, F. (1992) Estimating surface reflectance and albedo from Landsat-5 Thematic Mapper over rugged terrain. *Photogrammetric Engineering and Remote Sensing.* **58**(5), 551-558.

Duffie, J., and Beckman. P, (1991) *Solar Engineering of Thermal Processes.* John Wiley and Sons.

Dunn, S.M. and Colohan, R.J.E. (1999) Developing the snow component of a distributed hydrological model: a step-wise approach based on multi-objective analysis. *Journal of Hydrology.* **223**, 1-16.

Dymond, J.R., DeRise, J. and Trotter, D. (1992) DTMs for terrain evaluation. *Geocarto International.* **7**, 53-58.

Dymond, J.R., Derose, F. and Harmsworth, A. (1995) Automated mapping of land compenents from digital elevation data. *Geocarto International.* **9**, 123- 138.

Dyurgerov, M. and Meier, M.F. (1999) Analysis of winter and summer glacier mass balances. *Geografiska Annaler.* **81A**(4), 541-554.

Dyurgerov, M. (2003) Mountain and subpolar glaciers show an increase in sensitivity to climate warming and intensification of the water cycle. *Journal of Hydrology.* **282**, 164-176.

Ekström, M. (2002) Estimating monthly surface winds for Scania, Southern Sweden, using geostrophic wind (1899 – 1997) *Geografiska Annaler.* **84 A**, 113-126.

Elder, K., Dozier, J. and Michaelsen, J. (1991) Snow accumulation and distribution in an Alpine watershed. *Water Resources Research.* **27**(7), 1541-1552.

Erxleben, J., Elder, K. and Davis, R. (2002) Comparison of spatial interpolation methods for estimating snow distribution in the Colorado Rocky Mountains. *Hydrological Processes.* **16**, 3627-3649.

Essery, R. (1997a) Modelling fluxes of momentum, sensible heat and latent heat over heterogeneous snow cover. *Quarterly Journal of the Royal Meteorological Society.* **123**, 1867-1883.

Essery, R. (1997b) Seasonal snow cover and climate change in the Hadley Centre GCM. *Annals of Glaciology.* **25**, 362-366.

Essery, R. (2000) Spatial statistics of windflow and blowing-snow fluxes over complex topography. *Boundary Layer Meteorology.* **100**, 131-147.

Essery, R., Li, L. and Pomeroy, J. (1999) A distributed model of blowing snow over complex terrain. *Hydrological Processes.* **13**, 2423-2438.

Etzelmüller, B., Ødegard, R.S., Berthling, I. and Sollid, J.L. (2001) Terrain parameters and remote sensing data in the analysis of permafrost distribution and periglacial process: principles and examples from Southern Norway. *Permafrost and Periglacial Processes.* **12**, 79-92.

Evans, I.S. (1970) General geomorphometry, derivatives of altitude and descriptive statistics. Paper presented at the British Geomorphological Research Group Symposium on Spatial Analysis in Geomorphology, Cambridge, 31st October 1970.

Evans, I.S. (1972) General geomorphometry, derivatives of altitude and descriptive statistics. In Chorley, R. (ed.) *Spatial analysis in geomorphology.* Methuen, London. 17-90.

Evans, I.S. (1977) World-wide variations in the direction and concentration of cirque and glacier aspects. *Geographiska Annaler.* **59A**, 151-175.

Evans, I.S. (1979) An integrated system of terrain analysis and slope mapping. The final report of grant DA-ERO-591-73-G0040 for 'Statistical characterization of altitude matrices by computer'. University of Durham.

Evans, I.S. (1980) An integrated system of terrain analysis and slope mapping. *Zeitschrift für Geomorphologie Suppl.* **36**, 274-295

Evans, I.S. (1987) The morphometry of specific landforms. In Gardiner, V. (Ed.) *International Geomorphology.* 1986 Part II, 105-124, J. Wiley, Chichester

Evans, I.S. (2003) Scale-specific landforms and aspects of the land surface. *Concepts and modelling in Geomorphology: International Perspectives.* Tokyo Terrapub. 61-84.

Evans, I.S. (in prep) Global variations of local asymmetry in glacier altitude: separation of north-south and east-west components.

Evans, I.S. and Cox, N.J. (1995) The form of glacial cirques in the English Lake District. *Zeitschrift fur Geomorphologie. N. F.* **39**(2), 175-202.

Evans, I.S. and Cox, N.J. (1999) Relations between land surface properties: altitude, slope and curvature. In: Hergarten, S. and Neugebauer, H.J. (eds.) *Process Modelling and Landform Evolution. Lecture Notes in Earth Sciences Volume 78.* Springer-Verlag, Berlin. 13-46.

Felleman, J. and Griffin, C. (1990) The Role of Error in GIS-based Viewshed Determination: A Problem Analysis. IEPP Report No EIPP-90-2, Syracuse, New York. In: Fisher, P.F. (ed.) First Experiments in Viewshed Uncertainty: Simulating Fuzzy Viewsheds. *Photogrammetric Engineering and Remote Sensing.* **58**, 345-352.

Fenneman. N., (1946) Physical Divisions of the United States. United States Department of the Interior, Geological Survey.

Ferguson, R.I. (1999) Snowmelt runoff models. *Progress in Physical Geography.* **23**(2), 205-227.

Ficker, H. von (1926) Vertikale Temperaturgrdienten im Gebirge. *Veroff. Preuss. Meteorlogie Institut.* **335**, 45-62.

Fierz, C., Plüss, C. and Martin, E. (1997) Modelling the snowcover in a complex Alpine topography. *Annals of Glaciology.* **25**, 312-316.

Fierz, C., Riber, P., Adams, E.E., Curran, A.R., Föhn, P.M.B., Lehning, M. and Plüss, C. (2003) Evaluation of snow-surface energy balance models in alpine terrain. *Journal of Hydrology.* **282**, 76-94.

Fisher, P,F. (1991) First experiments in viewshed uncertainty: the accuracy of the viewshed area. *Photogrammetric Engineering and Remote Sensing.* **57**, 1321-1327.

Fisher, P.F. (1992) First experiments in viewshed uncertainty: simulating fuzzy viewsheds. *Photogrammetric Engineering and Remote Sensing.* **58**, 345-352.

Fisher, P.F. (1993) Algorithm and implementation uncertainty in viewshed analysis. *International Journal of Geographical Information Systems.* 7(4), 331-347.

Fisher, P.F. (1995) An exploration of probable viewsheds in landscape planning. *Environment and Planning B: Planning and Design.* **22**, 527-546.

Fisher, P.F., Wood, J., and Cheng, T. (2004) Where is Helvellyn? Fuzziness of multi-scale landscape morphometry. *Transactions of the Institute of British Geographers.* **29**. 106-128

Fleming, P.M., Austin, M.P. and Nicholls, A.O. (1995) Notes on a radiation index for use in studies of aspect effects on radiation climate. *CSIRO Technical Bulletin (In Press).* Division of Water Resources, Canberra.

Flemming, M. and Hoffer, R. (1979) Machine processing of Landsat MSS data and DMW topographic data for forest cover type mapping LAERS technical report 062879, *Laboratory for Application of Remote Sensing*, Purdue University, West Lafayette, Indiana.

Floriani, L. de., Marzano, P. and Puppo, E. (1994) Line-of-sight communication on terrain models. *International Journal of Geographical Information Systems.* **8**, 329-342.

Florinsky, I.V. (1998) Accuracy of local topographic variables derived from digital eleation models. *International Journal of Geographical Information Science.* **12**(1), 47-61.

Flowers, G., and Clarke, G. (2000) An integrated modelling approach to understanding subglacial hydraulic release events. *Annals of Glaciology.* **31**, 222-228.

Folland, C. K. (1988) Numerical models of the raingauge exposure problem, field experiments and an improved collector design. *Quarterly Journal of the Royal Meteorolgy Society.* **114**, 1485-1516.

Fontaine, T.A., Cruikshank, T.S., Arnold, J.G. and Hotchkiss, R.H. (2002) Development of a snowfall-snowmelt routine for mountainous terrain for the soil water assessment tool (SWAT). *Journal of Hydrology.* **262**(1-4), 209-223.

Forbes, G. (1922) *cited in* Ahlmann, H.W. (1922) Glaciers in Jotunheimen and their physiography. *Geografiska Annaler.* **4**, 1-57.

Frei, A., Miller, J.A. and Robinson, D.A. (2003) Improved simulations of snow extent in the second phase of the Atmospheric Model Intercomparison Project (AMIP-2). *Journal of Geophysical Research.* **108**(D12), 4369, 10-17.

Fu, P. and Rich, P.M.A. (1999) Design and implementation of the Solar Analyst: an ArcView extension for modeling solar radiation at landscape scales. *Proceedings of the 19th Annual ESRI User Conference, San Diego, USA.* <http://www.hemisoft.com/doc/esri99>

Fuh, B. (1962) The Influence of slope orientation on the microclimate. *Acta Meteorologica Sinica.* **32**, 71-86.

Fujita, K. and Ageta, Y. (2000) Effect of summer accumulation on glacier mass balance on the Tibetan Plateau revealed by mass balance models. *Journal of Glaciology.* **46**(153), 244-252.

Furman, R.W. (1978) Wildfire zones on a mountain ridge. *Annals of the Association of American Geographers.* **68**, 89-94.

Gallée, H. (1998) Simulation of blowing snow over the Antarctic ice sheet. *Annals of Glaciology.* **26**, 203-206.

Gao, J. (1997) Resolution and accuracy of terrain representation by grid DEMs at a micro-scale. *International Journal of Geographical Information Science.* **11**(2), 199-212.

Gao, J. and Liu, Y. (2001) Applications of remote sensing, GIS and GPS in glaciology: a review. *Progress in Physical Geography.* **25**(4), 520-540.

García-Ruiz, J., Gómez-Villar, A., Ortigosa, L. and Martí-Bono, C. (2000) Morphometry of glacial cirques in the central Spanish Pyrnenes. *Geografiska Annaler.* **82A**(4), 433-442.

Garen, D. C., Johnson, G. L. and Hanson, C. L. (1994) Mean areal precipitation for daily hydrologic modelling in mountainous regions. *Water Resources Bulletin* **30**, 481-491.

Garnier, B.J. and Ohmura, A. (1968) A method of calculating shortwave radiation income on slopes. *Journal of Applied Meteorology.* **7**, 796-800.

Garnier, B.J. and Ohmura, A. (1970) Evaluation of surface variations in solar radiation income. *Solar Energy.* **13**, 21-34.

Gates, D.M. (1980) *Biophysical Ecology.* Springer-Verlag, New York.

Gauer, P. (1998) Blowing and drifting snow in Alpine terrain: numerical simulation and related field measurements. *Annals of Glaciology.* **26**, 174-178.

Geiger, R. (1965) *Climate Near the Ground.* Harvard University Press, Cambridge, Massachusetts.

Gerland, S., Winther, J.G., Orbaek, J.B., Liston, G.E., Oritsland, N.A., Blanco, A. and Ivanov, B. (1999) Physical and optical properties of snow covering Arctic tundra on Svalbard. *Hydrological Processes.* **13**, 2331-2343.

Ghinoi, A. and Chung, C-J.F. (2002) STARTER: a topography based prediction model for localising potential snow avalanche release areas. The case study of Sölden (Tyrol, Austria). *Relationships Between Man and the Mountain environment in Terms of Geomorphological Hazards and Human Impact in Europe.* IAG Symposium Proceedings, Dornbirn (Austria), 14 July 2002. 69-70.

Gill, J.S. (1982) *Simulation of Cirque Glacier Distribution.* Unpublished PhD Thesis, University of Durham.

Gjessing, J. (1967) Norway's Paleic Surface. *Norsk Geografisk Tidsskrift.* **21**, 69-123.

Glassy, J. and Running, S. (1994) Validating diurnal climatological logic of the MT-CLIM model across a climatic gradient in Oregon. *Ecological Applications.* **4**, 248-257.

Glen, J.W. (1963) *International Association of Scientific Hydrologists Bulletin.* **8**(2), 68 (contribution to discussion).

Goetz, A.F.H. (1987) Spectral remote sensing in geology. In: Asrar, G. (ed.) *Theory and Applications of Optical Remote Sensing.* 491-507.

Goswami, D.Y., Kreith, F. and Kreider, J.F. (2000) *Principles of Solar Engineering.* 2nd Edition. Taylor and Francis, Philadelphia, Pennsylvania.

Granger, R.J., Pomeroy, J.W. and Parviainen, J. (2002) Boundary-layer integration approach to advection of sensible heat to a patchy snow cover. *Hydrological Processes.* **16**, 3559-3569.

Grainger, M.E. and Lister, H. (1966) Wind speed, stability and eddy viscosity over melting ice surfaces. *Journal of Glaciology.* **6**, 101-127.

Gratton, D.J., Howarth, P.J. and Marceau, D.J. (1993) Using Landsat-5 Thematic Mapper and digital elevation data to determine the net radiation field of a mountain glacier. *Remote Sensing of Environment.* **43**, 315-331.

Gray, D.M. and Male, D.H. (eds.) (1981) *Handbook of Snow: Principles, Processes, Management and Use.* Pergammon Press, Oxford.

Greenland, D.E. (1973) Application of climatonomy to an alpine valley. *New Zealand Journal of Science.* **16**, 811-823.

Gregory, S. (1968) The orographic component in rainfall distribution patterns. In: Sporck, J.A. (ed) *Melenges de Geographie. I. Geographie Physique et Geographie Humaine.* J. Duculot, Gembloux, Belgium. 234-252.

Greuell, W. and Genthon, C. (2004) Modelling land-ice surface mass balance. In: Bamber, J.L. and Payne, A.J. *Mass Balance of the Cryosphere: Observations and Modelling of Contemporary and Future Changes.* Cambridge University Press, Cambridge. 117-168.

Greuell, W. and Smeets, P. (2001) Variations with elevation in the surface energy balance on the Pasterze. *Journal of Geophysical Research-Atmospheres.* **106**, 31717-37127.

Greuell, W., Knap, W, H and Smeets, P.C. (1997) Elevational changes in meteorological variables along a midlatitude glacier during summer. *Journal of Geophysical Research.* **102**(25), 941-954.

Groisman, P.Ya., Knight, R,W. and Karl, T.R. (2000) Heavy precipitation and high streamflow in the United States: Trends in the 20th century. Bulletin of the American Meteorological Society, 82, 219-246.

Grunow, J. (1952) Nebelniederschlag: Bedeutung und Erfassung einer Zusatzkomponente des Niederschlags. Berichte des Deutschen Wetterdienst in der US-Zone, **42,** 30-34.

Gudmunsson, G., and Bauder, A., (1999) Towards an Indirect Determination of the Mass-balance Distribution of Glaciers using the Kinematic Boundary Condition *Geografiska Annaler: Series A, Physical Geography.* **81**, 575-583

Guglielmin, M., Aldighieri, B. and Testa, B. (2003) PERMACLIM: a model for the distribution of mountain permafrost, based on climatic observations. *Geomorphology.* **51**, 245-257.

Guth, P.L. (1999) Contour line ghosts in USGS level 2 DEMs. *Photogrammetric Engneering and Remote Sensing.* **65**(3), 289-297.

Hagen, J.O., Melvold, K., Eiken, T., Isaksson, E. and Lefauconnier, B. (1999) Mass balance methods on Kongsvegen, Svalbard. *Geografiska Annaler.* **81A**(4), 593-601.

Halberstam, I. and Schieldge, J.P. (1981) Anomolous behaviour of the atmospheric surface layer over a melting snowpack. *Journal of Applied Meteorology.* **20**, 255-265.

Hall, D.K. and Chang, A.T.C. (1988) Reflectances of glaciers as calculated using Landsat-5 Thematic Mapper data. *Remote Sensing of Environment.* **25**, 311-321.

Hall, D.K., Chang, A.T.C., Foster, J.L., Benson, C.S. and Kovalick, W.M. (1989) Comparison of *in situ* and Landsat derived reflectance of Alaskan glaciers. *Remote Sensing of Environment.* **28**, 23-31.

Haltiner, G.J., and Williams, R.T. (1980) *Numerical Prediction and Dynamic Meteorology* (second edition), John Wiley and Sons, New York.

Hammond. E. (1964) Analysis of Properties in Land Form Geography: An Application to Broad-scale Land Form Mapping. *Annals of the Association of American Geographers.* **54**, 11-19.

Hannah, D.M., Gurnell, A.M. and McGregor, G.R. (2000) Spatio-temporal variation in microclimate, the surface energy balance and ablation over a cirque glacier. *International Journal of Climatology.* **20**, 733-758.

Harris, C. and Cook, J.D. (1986) The detection of high altitude permafrost in Jotunheimen, Norway using seismic refraction techniques: an assessment. *Arctic and Alpine Research.* **18**(1), 19-26.

Hartman, M.D., Baron, J.S., Lammers, R.B., Cline, D.W., Band, L.E., Liston, G.E. and Tague, C. (1999) Simulations of snow distribution and hydrology in a mountain basin. *Water Resources Research.* **35**(5), 1587-1603.

Hay, J.E. and Fitzharris, B.B. (1988) A comparison of the energy-balance and bulk-aerodynamic approaches for estimating glacier melt. *Journal of Glaciology.* **34**(117), 145-153.

Hay, L.E. and Clark, M.P. (2003) Use of statistically and dynamically downscaled atmospheric model output for hydrolic simulations in three mountainous basins in the western United states. *Journal of Hydrology.* **282**, 56-75.

Hay, T. (1948) Rainfall in East Scotland in relation to the synoptic situation. *Professional Notes Meteorological Office.* **6**, 12-18.

Hayhoe, H. and Lapen, D. (1999) Spatially modeling temperature normals in the Rocky Mountains with Kriging and cokriging estimators using ANN produced secondary information. Presented at *2nd Conference on Artificial Intelligence*, AMS Annual meeting, Long Beach, California.

Heggmen, E., Etzelmuller, B. and Berthling, I. (2001) Topographic radiation balance models: sensitivity and application in periglacial geomorphology. *Norsk Geografisk Tidsskrift.* **55**(4), 203-211.

Helmke, J.P., Bauch, H.A. and Erlenkeuser, H. (2003) Devewlopment of glacial and interglacial conditions in the Nordic seas between 1.5 and 0.35 Ma. *Quaternary Science Reviews.* **22**, 1717-1728.

Helvey, R. A. (1983) Radiosonde Errors and Spurious Surface-Based Ducts, *IEEE Proceedings (Communications, Radar and Signal Processing)*, **130**, 643–648.

Henderson-Sellers, A. (1978) Surface type and its effect upon cloud cover: a climatological investigation. *Journal of Geophysical Research.* **83**(C10), 5057-5062.

Henderson-Sellers, A. (1979) Clouds and the long-term stability of the Earths atmosphere and climate. *Nature.* **279**(5716), 786-788.

Hess, M., Niedzwiedz, T. and Obrebska-Starkel, B. (1975) The methods of constructing climatic maps of various scales for mountainous and upland territories, exemplified by the maps prepared for southern Poland. *Geog. Polonica.* **31**, 167-187.

Heuvelink, G.B.M., Burrough, P.A. and Stein, A. (1989) Propagation of errors in spatial modelling with GIS. *International Journal of Geographical Information Systems.* **3**(4), 303-322.

Heuvelink, G.B.M. and Burrough, P.A. (1993) Error propogation in cartographic modelling using Boolean logic and continuous classification. *International Journal of Geographical Information Systems.* **7**(3), 231-246.

Heuvelink, G.B.M. and Burrough, P.A. (2002) Developments in statistical approaches to spatial uncertainty and its propagation. *International Journal of Geographical Information Science.* **16**(2), 111-113.

Hevesi, J. A., Istok, J. D. and Flint, A. L. (1992a) Precipitation estimation in mountainous terrain using multivariate geostatistics. Part I: Structural analysis. *Journal of Applied Meteorology* **31**, 661-676.

Hevesi, J.A., Flint,A.L. and Istok, J.D. (1992b) Precipitation estimation in mountainous terrain using multivariate geostatistics. Part II: Isohyetal maps, *Journal of Applied Meteorology*, **31**, 677-688.

Hiemstra, C.A., Liston, G.E. and Reiners, W.A. (2002) Snow redistribution by wind and interactions with vegetation at upper treeline in the Medicine Bow Mountains, Wyoming, U.S.A. *Arctic, Antarctic, and Alpine Research.* **34**(3), 262-273.

Hill, F., Browning, K. and Bader, M. (1982) Orographic rainfall over low hills and associated corrections to radar measurements. *Quarterly Journal of the Royal Meteorological Society.* **107**, 642-670.

Hock, R. (1999) A distributed temperature-index ice- and snowmelt model including potential direct solar radiation. *Journal of Glaciology.* **45**, 101-112.

Hock, R. (2003) Temperature index melt modelling in mountain areas. *Journal of Hydrology.* **282**, 104-115.

Hock, R. and Holgrem, B. (1996) Some aspects of energy balance and ablation of Storglacieren, Northen Sweden. *Geografiska Annaler.* **78A**(2-3), 121-131.

Hock, R. and Jensen, H. (1999) Application of kriging interpolation for glacier mass balance computations. *Geografiska Annaler.* **81A**(4), 611-619.

Hock, R., Johansson, M., Jansson, P. and Bärring, L. (2002) Modeling climate conditions required for glacier formation in cirques of the Rassepautasjtjakka Massif, Northern Sweden. *Artic, Antarctic and Alpine Research.* **34**, 3-11.

Hodgkins, R. (2001) Seasonal evolution of meltwater generation, storage and discharge at a non-temperate glacier in Svalbard. *Hydrological Processes* **15**, 441–460.

Hodgson, M.E. (1995) What cell size does the computed slope/aspect angle represent? *Photogrammetric Engineering and Remote Sensing.* **61**(5), 513-517.

Hoe, G. (2002) Modelling precipitation over ice sheets: an assessment using Greenland. *Journal of Glaciology.* **48**, 70-80.

Hofierka, J., Parajka, J., Mitasova, H. and Mitas, L. (2002) Multivariate interpolation of precipitation using regularized spline with tension. *Transaction in GIS.* **6**(2), 135-150.

Horn, B. (1981) Hill shading and the reflectance map. *Proceedings IEEE.* **69**, 14-47.

Hottel, H.C. (1976) A simple model for estimating the transmittance of direct solar radiation through clear atmospheres. *Solar Energy.* **18**, 129-134.

Houmark-Nielsen, M. and Kjær, K.H. (2003) Southwest Scandinavia, 40-15 kyr BP: palaeogeography and environmental change. *Journal of Quaternary Science.* **18**(8), 769-786.

Hudson, G. and Wackernagel, H. (1994) Mapping temperature using kriging with external drift – Theory and an example form Scotland, *International Journal of Climatolgy*, **14**(1), 77-91.

Huff, F.A. and Neill, J.C. (1957) Areal representativeness of precipitation rainfall . *Transactions of the American Geophysical Union.* **38** (3), 341-342.

Humlum, O. (1997) Younger Dryas glaciation in Söderåsen, south Sweden: an analysis of meteorologic and topographic controls. *Geografiska Annaler.* **79A**(1-2), 1-15.

Huss, R.E. and Pumar, M.A. (1997) Effects of database errors on intervisibility estimation. *Photogrammetric Engineering and Remote Sensing.* **63**, 415-424.

Hutchinson, M.F. (1993) Development of a Continent-Wide DEM with Applications to Terrain and Climate Analysis. In: Goodchild, M.F., Parks, B.O. and Steyaert, L.T. (eds.) *Environmental modeling with GIS.* Oxford University Press, Oxford. 392-399.

Hutchinson, M.F. (1989) A new procedure for gridding elevation and streamline data with automatic removal of spurious pits. Jo*urnal of Hydrology.* **106**, 211-232.

Hutchinson, M.F. and Gallant, J.C. (2000) Digital elevation models and representation of terrain shape. In: Wilson,J.P. and Gallant,J.C. (eds), *Terrain Analysis*, Wiley, New York, Chapter 2, 29-50.

Huth, R. (2001) Disaggregating climatic trends by classification of circulation patterns, *International Journal of Climatology.* **21**, 135-153.

Intergovernmental Panel on Climate Change (IPCC) (2001) *Summary for Policy Makers: a Reportof Working Group I of the Intergovernmental Panel on Climate Change.* Geneva, WMO, UNEP, IPCC.

Irvin, B., Ventura. S. and Slater. B. (1997) Fuzzy and Isodata Classification of Landform Elements From Digital Terrain Data in Pleasant Valley, Wisconsin. *Geoderma.* **77**, 137-154.

Isard, S.A. (1983) Estimating potential direct insolation to alpine terrain. *Arctic and Alpine Research.* **15**(1), 77-89.

Iziomon, M.G. and Mayer, H. (2001) Performance of solar radiation models – a case study. *Agricultural and Forest Meteorology.* **110**, 1-11.

Jackson, M. L. (1969) *Soil Chemical Analysis*. Jackson, Madison, WI.

Jackson, P. and Hunt, J. (1975) Turbulent wind flow over a hill. *Quarterly Journal of the Royal Meteorological Society.* **101**, 929-955.

Jaedicke, C. (2002) Snow drift losses from an Arctic catchment on Spitsbergen: an additional process in the water balance. *Cold Regions Science and Technology.* **34**, 1-10.

Jansson, P. (1999) Effect of uncertainties in measured variables on the calculated mass balance of Storglaciären. *Geografiska Annaler.* **81A**(4), 633-642.

Jansson, P., Richardson, C. and Jonsson, S. (1999) Assessment of requirements for cirque formation in northern Sweden. *Annals of Glaciology.* **28**, 16-22.

Jansson, P., Hock, R. and Schneider, T. (2003) The concept of glacier storage: a review. *Journal of Hydrology.* **282**, 116-129.

Jarvis, R. and Clifford, D. (1990) In: Goudie, A. (ed.) *Gemorphological Techniques*. Routledge, London. 63-71.

Jenson, S., and Dominique, J., (1988) Extracting topographic structure from digital elevation data for geographic information system analysis. *Photogrammetric Engineering and Remote Sensing*, **54**, 1593-1600.

John, B. (1984) *Scandinavia A new Geography*. Longman, Harlow.

Johnsson, O. (1937) The distribution of precipitation in Norway *Geografiska Annaler.* **19**, 104-117.

Jones, K. (1997) In: Burrough, R. and McDonnell (eds.) Principles of Geographical Information Systems. Oxford University Press, Oxford.

Jonsson, S. (1995) Synoptic forcing of wind and temperature in a large cirque 300 km from the coast of East Antarctica. *Antarctic Science.* 7(4), 409-420.

Kane, D. L., Gieck, R. E. and Hinzman. L. D. (1997) Snowmelt Modeling at a Small Alaskan Arctic Watershed. *ASCE Journal of Hydrologic Engineering*, **2,** 204-210.

Kasten, F. (1983) Parametrisierung der Globalstrahlung durch Bedeckungsgrad und Trubungsfaktor. *Annals of Meteorology.* **20**, 49-50.

Kayastha, R.B., Ohata, T. and Ageta, Y. (1999) Application of mass-balance to a Himalayan glacier. *Journal of Glaciology.* **45**, 559-567.

Kjøllmoen, B. (2000) *Glaciological Investigations in Norway 1999.* NVE.

Klok, E.J. and Oerlemans, J. (2002) Model study of the spatial distribution of the energy and mass balance of Morteratshcgletscher, Switzerland. *Journal of Glaciology.* **48**, 505-518.

Klok, E.J., Greuell, W. and Oerlemans, J. (2003) Temporal and spatial variation of the surface albedo of Morteratschgletscher, Switzerland, as derived from 12 Landsat images. *Journal of Glaciology.* **49**(167), 491-502.

Knap, W.H., Brock, B.W., Oerlemans, J. and Willis, I.C. (1999) Comparison of Landsat TM-derived and ground-based albedos of Haut Glacier d'Arolla, Switzerland. *International Journal of Remote Sensing.* **20**(17), 3293-3310.

Knight, P. (1999) *Glaciers.* Stanley Thornes Ltd, Cheltenham.

Koch, H.G. (1961) Die warme Hangzone. Neue anschauungen zur nachlichten Kaltluftschichtung in Talern und an Hangen. *Zeitschrift fur Meteorologie.* **15**, 151-171.

Konzelmann, T., Vandewal, R.S.W. and Greuell, W. (1994) Paramaterisation of global and longwave incoming radiation for the Greenland ice sheet. *Global Planetary Change.* **9**(1-2), 143-164.

Kreith, F. and Kreider, J.F. (1978) *Principles of Solar Engineering.* McGraw and Hill, New York.

Kuhn, M. (2003) Redistribution of snow and glacier mass balance from a hydrometeorological model. *Journal of Hydrology.* **282**, 95-103.

Kumar, L., Skidmore, A.K. and Knowles, E. (1997) Modelling topographic variation in solar radiation in a GIS environment. *International Journal of Geographical Information Science.* **11**(5), 475-497.

Kustas, W.P., Jackson, R.D. and Asrar, G. (1984) Estimating surface energy-balance components from remotely sensed data. In: Asrar, G. (ed.) *Theory and Applications of Optical Remote Sensing.* 604-627.

Kustas, W.P, Rango, A. and Uijlenhoet, R. (1994) A simple energy budget algorithm for bthe snowmelt runoff model. *Water Resources Research.* **30**(5), 1515-1527.

Laffan, S.W. (2002) Using process models to improve spatial analysis. *International Journal of Geographical Information Science.* **16**(3), 245-257.

Lagacherie.P., Cazemier.D., Van Gaans.p. and Burrough. P., (1997) Fuzzy k-means clustering of fields in an elementary catchment and extrapolation to a larger area. *Geoderma*, **77**, 197-216.

Lane, D.E., Goris, K. and Somerville, R.C.J. (2002) Radiative transfer through broken clouds: observations and model validation. *Journal of Climate.* **16**(20), 2921-2933.

Lane, P.W. (2002) Generalised linear models in soil science. *European Journal of Soil Science.* **53**, 241-251.

Lane, S.N. and Chandler, J.H. (2003) "Editorial: The generation of high quality topographic data for hydrology and geomorphology: new data sources, new applications and new problems". *Earth Surface Processes and Landforms.* **28**, 229-230.

Lane-Veron, D.E. and Somerville, R.C.J. (2004) Stochastic theory of radiative tranfer through generalized cloud fields. *Journal of Geophysical Research-Atmostpheres.* **109**, 374-386.

Lang, H. (1986) Forecasting meltwater runoff from snow-covered areas and from glacier basins. In: Kraijenhoff, D.A. and Moll, J.R. (eds.) *River Flow Modelling and Forecasting.* D. Reidel Publishing Company. 99-127.

Lapen, D.R. and Martz, L.W. (1993) The measurement of two simple topographic indices of wind sheltering-exposure from raster digital elevation models. *Computers and Geosciences.* **19**(6), 769-779.

Lapen, D. and Martz, L. (1996) An investigation of the spatial association between snow depth and topography in a Prairie agricultural landscape using digital terrain analysis. *Journal of Hydrology.* **184**, 277-298.

Lapen, D. and Hayhoe, H. (1998) A comparison of geostatistical techniques for interpolating seasonal temperature and precipitation data for Southern Ontario, Canada. In: *Proceedings of the 14th Conference on Probability and Statistics in Atmospheric Sciences.* Phoenix, Arizona. 123-125.

Larson, E. and Peck, E.L. (1974) Accuracy of Precipitation Measurements for Hydrologic Modeling. *Water Resources Research*, 857-862.

Larsen, E., Frødis, E., Longva, O. and Mangerud, J. (1984) Allerød-Younger Dryas climatic inferences from cirque glaciers and vegetational development in the Nordfjord Area, western Norway. *Arctic and Alpine Research.* **16**(2), 137-160.

Laumann, T. and Reeh, N. (1993) Sensitivity to climate change of the mass balance of glaciers in southern Norway. *Journal of Glaciology.* **39**(133), 656-665.

Lauscher, F. (1976) Welweit Typen der hohenabhangigkeit des niederschlags. *Wetter u. Leben.* **28**, 80-90.

Lautensach, H. and Bogel, R. (1956) Der Jahrsgang des mittleren geographischen Hohengradienten der luftemperatur in den verscheiden Klimagbieten der Erde. *Erdkunde.* **10**, 270-282.

Lee, J. (1991) Analyses of visibility sites on topographic surfaces. *International Journal of Geographical Information Systems.* **5**, 413-429.

Lee, J. (1994) Digital anaylsis of viewshed inclusion and topographic features on digital elevation models. *Photogrammetric Engineering and Remote Sensing.* **60**, 451-456.

Lehning, M., Bartelt, P., Brown, B., Fierz, C. and Satyawali, P. (2002) A physical SNOWPACK model for the Swiss avalanche warning part II: Snow microstructure. *Cold Regions Science and Technology.* **35**, 147-167.

Lehning, M., Bartelt, P., Brown, B. and Fierz, C. (2002) A physical SNOWPACK model for the Swiss avalanche warning part III: meteorological forcing, thin layer formation and evaluation.. *Cold Regions Science and Technology.* **35**, 169-184.

Lennon, J.L. and Turner, J.R. (1995) Predicting the spatial distribution of climate: temperature in Great Britain. *Journal of Animal Ecology.* **64**, 370–392.

Leonard, K.C. and Fountain, A.G. (2003) Map-based methods for estimating glacier equilibrium-line altitudes. *Journal of Glaciology.* **49**(166), 329-336.

Li, X., Cheng, G., Wu, Q. and Ding, Y. (2003) Modelling Chinese cryospheric change by using GIS technology. *Cold Region Science and Technology.* **36**, 1-9.

Li, Z. (1991) Effects of check points on the reliablity of DTM accuracy estimates obtained from experimental tests. *Photogrammetric Engineering and Remote Sensing.* **57**(10), 1333-1340.

Li, Z. (1994) A comparative study of the accuracy of digitial terrain models (DTMs) based on various data models. *ISPRS Journal of Photogrammetry and Remote Sensing.* **49**(1), 2-11.

Lie, Ø., Dahl, S.O. and Nesje, A. (2003a) A theoretical approach to glacier equilibrium-line altitudes using meteorological data and glacier mass-balance records from southern Norway. *The Holocene.* **13**(3), 365-372.

Lie, Ø., Dahl, S.O. and Nesje, A. (2003b) Theoretical equilibrium-line altitudes and glacier buildup sensitivity in southern Norway based on meteorological data in a geographical information system. *The Holocene.* **13**(3), 373-380.

Lindersson, M. (2001) Objective classification of atmospheric circulation over Southern Scandinavia. *International Journal of Climatology.* **21**, 155-169.

Liu, B.Y. and Jordan, R.C. (1960) The interrelationship and characteristic distribution of direct, diffuse and total solar radiation. *Solar Energy.* **4**, 1-19.

Liu, H. and Jezek, K.C. (1999) Investigating DEM error patterns by directional variograms and fourier analysis. In: (ed.) *Geographical Analysis.*

Longley, P.A., Goodchild, M.F., Maguire, D.J. and Rhind, D.W. (eds.) (1999a) *Geographic Information Systems. Volume 1.* John Wiley & Sons. Chichester.

Longley, P.A., Goodchild, M.F., Maguire, D.J. and Rhind, D.W. (eds.) (1999b) *Geographic Information Systems. Volume 2.* John Wiley & Sons. Chichester.

Lossen, K.S. (1967) The role of avalanches in mass budget of glaciers. In: Oura, H. (ed.) *Physics of Snow and Ice.* 385-379.

Lowe, J. and Walker, M. (1997) *Reconstructing Quaternary Environments.* Second Edition. Prentice Hall.

Lubin, D. and Morrow, E. (1998) Evaluation of an AVHRR cloud detection and classification method over the central Arctic Ocean. *Journal of Applied Meteorology.* **37**(2), 166-183.

Luce, C.H., Tarboton, D.G. and Cooley, K.R. (1998) The influence of the spatial distribution of snow on basin-averaged snowmelt. *Hydrological Processes.* **12**, 1671-1683.

Luckman, B.H. (1977) The geomorphic activity of snow avalanches. *Geografiska Annaler.* **59A**(1-2), 31-48.

MacMillan, R.A., Pettapiece, W.W., Nolan, S.C. and Goddard, T.W. (2000) A generic procedure for automatically segmenting landforms into landform elemanets using DEMs, heuristic rules and fuzzy logic. *Fuzzy Sets and Systems.* **113**, 81-109.

Male, D.H. and Granger, R.J. (1981) Snow surface energy exchange. *Water Resources Research.* **17**(3), 609-627.

Manley, G. (1938) On the Occurance of snow cover in Great Britain.

Marchand, W-D. and Killingtveit, Å. (2001) Analyses of the relation between spatial snow distribution and terrain characteristics. *Proceedings of the 58th Eastern Snow Conference, Ottowa, Ontario, Canada.*

Mark, D.M. (1975) Geomorphometric parameters: a review and evaluation. *Geografiska Annaler.* **57A**(3-4), 165-177.

Mark, D.M. (1975) Computer analysis of topography: a comparison of terrain storage methods. *Geografiska Annaler.* **57A**(3-4), 179-188.

Marks, D., Domingo, J., Susong, D., Link, T. and Garen, D. (1999) A spatially distributed energy balance smowmelt model for application in mountain basins. *Hydrological Processes.* **13**, 1935-1959.

Marks, D., Winstral, A. and Syefried, M. (2002) Simulation of terrain and forest shelter effects on patterns of snow deposition, snowmelt and runoff over a semi-arid mountain catchment. *Hydrological Processes.***16**, 3605-3626.

Marsh, R., Pomeroy, J.W. and Neumann, N. (1997) Sensible heat flux and local advection over a heterogeneous landscape at an Arctic tundra site during snowmelt. *Annals of Glaciology.* **25**, 132-136.

Martin, E., Brun, E. and Durand, Y. (1997) Snow-cover simulations in mountainous regions based on general circulation model outputs. *Annals of Glaciology.* **25**, 42-45.

Martin, E. and Lejeune, Y. (1998) Turbulent fluxes above the snow surface. *Annals of Glaciology.* **26**, 179-183.

Martins, F.R., Souza, M.P. and Pereira, E.B. (2003) Comparative study of satellite and ground techniques for cloud cover determination. *Calibration, Characterization of Satellite Sensors, Physical Parameters Derived from Satellite Data..* **32**(11), 2275-2280

Martz, L.W. and de Jong, E. (1988) Catch: a fortran program for measuring catchment area from digital elevation models. *Computers and Geosciences.* **14**(5), 627-640.

Matheussen, B.V. and Thorolfsson, S.T. (2003) Estimation of snow covered area for an urban catchment using image processing and neural networks. *Water Science and Technology.* **48**(9), 155-164.

Mases, M., Font, D. and Vilaplana, J.M. (1998) Relationship between snowdrift development and drifted snow during a wind episode. *Annals of Glaciology.* **26**, 144-148.

Mases, M., Buisson, L., Frey, W. and Marti, G. (1998) Empirical model for snowdrift distribution in avalanche-starting zones. *Annals of Glaciology.* **26**, 237-242.

Mather, P.M. (1999) *Computer Processing of Remotely-Sensed Images: An Introduction. 2nd Edition.* John Wiley and Sons, Chichester.

McClean, C.J. and Evans, I.S. (2000). Apparent fractal dimensions from continental scale digital elevation models using variogram methods. *Transactions in GIS.* **4,** 361-378.

McClung, D.M. (2001) Extreme avalanche runout: a comparison of empirical models. *Canadian Geotechnical Journal.* **38**, 1254-1265.

McClung, D.M. and Schaerer, P. (1993) *The Avalanche Handbook.* The Mountaineers, Seattle, Washington.

McCutchan, M. and Fox, D. (1986) Effect of elevation and aspect on wind, temperature and humidity. *Journal of Climate and Applied Meteorology.* **25**, 1996-2013.

McGregor, G.R. and Gellatly, A.F. (1996) The energy balance of a melting snowpack in the French Pyrennes during warm anti-cyclonic conditions. *International Journal of Climate.* **16**, 479-486.

McIlveen, J.F.R. (1992) *Fundamentals of Weather and Climate.* Chapman and Hall. London.

McKay, G.A. and Gray, D.M. (1981) The distribution of snowcover. In: Gray, D.M. and Male, D.H. (eds.) *Handbook of Snow: Principles, Processes, Management and Use.* Pergammon Press, Oxford. 153-190.

McKendry, I. (1983) Spatial and temporal aspects of the surface wind regime on the Canterbury plains, New Zealand. *Journal of Climatology*, **3**, 155 – 166.

McKenny, D.W., Mackey, B.G. and Zavitz, B.L. (1999) Calibration and sensitivity analysis of a spatially-distributed solar radiation model. *International Journal of Geographical Information Science.* **13**(1), 49-65.

Melloh, R.A., Hardy, J.P., Bailey, R.N. and Hall, T.J. (2002) An efficient snow albedo model for the open and sub-canopy. *Hydrological Processes.* **16**, 3571-3584.

Mennis, J.L. and Fountain, A.G. (2001) A spatio-temporal GIS database for monitoring Alpine glacier change. *Photogrammetric Engineering and Remote Sensing.* **67**(8), 967-975.

Mittaz, C., Imhof, M., Hoelzle, M. and Haeberli, W. (2002) Smowmelt evolution mapping using an energy balance approach over an alpine terrain. *Arctic, Antarctic and Alpine Research.* **34**(3), 274-281.

Mitsudera, M. and Numata, M. (1967) Meteorology of Eastern Nepal. *Journal of the College of Arts and Sciences Chiba University.* **5**, 75-83

Molg, T. and Hardy, D.R. (2004) Ablation and associated energy balance of a horizontal glacier surface on Kilimanjaro. *Journal of Geophysical Research-Atmospheres.* **109**(D16).

Monckton, C.G. (1994) An investigation into the spatial structure of error in digital elevation data. In: Worboys, M.F. (ed.) *Innovations in GIS 1.* Taylor and Francis, London. 201-211.

Montieth, J. and Unsworth, M. (1990) *Principles of Environmental Physics.* Routledge, New York.

Moore, I.D., Grayson, R.B. and Ladson, A.R. (1991) Digital terrain modelling: a review of hydrological, geomorphological and biological applications. *Hydrological Processes.* **5,** 3-30.

Moore, I.D., Lewis, A. and Gallant, J.C. (1993) Terrain attributes: estimation methods and scale effects. In: Jakeman, A.J., Beck, M.B. and McAleer M.J. (eds.) *Modelling change in Environmental Systems.*

Moore, R.D. and Owens, I.F. (1984) Controls on advective snowmelt in a maritime alpine basin. *Journal of Climate and Applied Meteorology.* **23**, 135-142.

Munro, D.S. and Davies, J.A. (1977) An experimental study of the glacier boundary over melting ice. *Journal of Glaciology.* **18**(80), 425-436.

Naaim, M., Naaim-Bouvet, F. and Martinez, H. (1998) Numerical simulation of drifting snow: erosion and deposition models. *Annals of Glaciology.* **26,**

Neff, E.L. (1977) How much rain does a rain gauge gage? *Journal of Hydrology* **35,** 213–220.

Nishimura, K., Sugiura, K., Nemoto, M. and Maeno, N. (1998) Measurements and numerical simulations of snow-particle simulation. *Annals of Glaciology.* **26**, 184-190.

Nordli, P.Ø., Lie, Ø., Nesje, A. and Dahl, S.O. (2003) Sprong-summer temperature reconstruction in western Norway 1734-2003: a data-synthesis approach. *International Journal of Climatology.* **23**, 1821-1841.

Nolin, A.W. and Stroeve, J. (1997) The changing albedo of the Greenland ice sheet: implications for climate modelling. *Annals of Glaciology.* **25**, 51-57.

Nunez, M. (1980) The calculation of solar and net radiation in mountainous terrain. *Journal of Biogeography.* **7**, 173-186.

Obled, C. and Harder, H. (1979) A review of snowmelt in the mountain environment. In: Colbeck, S.C. and Ray, M. (eds.) *Proceedings of a Meeting on Modelling of Snow Cover Runoff, 26-28 September 1978, Hanover, New Hampshire.* U.S. Army Cold Regions Research and Engineering Laboratory. 179-204.

Obrebska-Starkel, B. (1970) Uber die thermische Temperaturschichtung in Bergtälern. *Acta Climatologica.* **9**, 33-47.

Oerlemans, J., Van de Wal, R.S. and Conrads, L.A. (1991/1992) A model for the surface balance of ice masses: part II. Application to the Greenland ice sheet. *Z. Gletscherkd. Glazialgeol.* **27/28,** 85-96.

Oerlemans, J., Björnsson, H., Kuhn, M., Obleitner, F., Palsson, F., Smeets, C.J.P.P., Vugts, H.F. and De Wolde, J. (1999) Glacio-meteorological investigations on Vatnajökull, Iceland, summer 1996: an overview. *Boundary-Layer Meteorology.* **92**, 3-26.

Oerlemans, J. and Grisogono, B. (2002) Glacier winds and parameterisation of the related surface heat fluxes. *Tellus Series A – Dynamic Meteorology and Oceanography.* **54**, 440-452.

Oerlemans, J. and Klok, E. (2002) Energy balance of a glacier surface: Analysis of automatic weather station data from the Morteratschgletscher, Switzerland. *Artic, Antarctic and Alpine Research.* **34**, 477-485.

Ohata, T. (1989a) Katabatic wind on melting snow and ice surfaces (I) Stationary glacier wind on large maritime glacier. *Journal of the Meteorological Society of Japan.* **67**, 104-113.

Ohata, T. (1989b) Katabatic wind on melting snow and ice surfaces (II) Application of a theoretical model. *Journal of the Meteorological Society of Japan.* **67**, 113-122.

Ohmura, A, Kasser, P. and Funk, M. (1992) Climate at the equilibrium line of glaciers. *Journal of Glaciology.* **38**(140), 397-411.

Oke, T.R. (1978) *Boundary Layer Climates.* 2nd edition. Methuen, London.

Olyphant, G.A. (1986a) Longwave radiation in mountainous areas and its influence on the energy balance of alpine snowfields. *Water Resources Research.* **22**(1), 62-66.

Olyphant, G.A. (1986b) The components of incoming radiation within a mid0latitude alpine watershed during the snowmelt season. *Arctic and Alpine Research.* **18**(2), 163-169.

Østrem, G., Liestøl, O. and Wold, B. (1988) Glaciological investigations at Nigardsbreen, Norway. *Norsk Geografiska Tiddskrift.* **30**, 187-209.

Østrem, G. and Haakensen, N. (1999) Map comparison or traditional mass-balance measurements: which is better ? *Geografiska Annaler.* **81A**(4), 703-711.

Owens, I.F. and Fitzharris, B.B. (1985) Assessing avalanche hazard on the Milford Track. *Proceedings of the 13th New Zealand Geography Conference 1985.* 122-124.

Park, J., Jung, H. and Oh, J. (2000) Changes of precipitation trend and distribution in South Korea. Presented at Climatic Change and Variability and their impacts, IGC Conference Paper.

Peppler, W. (1931) The vertical extent of cloud layers. *Monthly Weather Review* **49**, 6, 347–348.

Paterson, W.S.B. (1981) *The Physics of Glaciers.* 2nd Edition. Pergammon Press, Oxford.

Paterson, W.S.B. (1984) *The Physics of Glaciers.* 3rd Edition. Pergammon Press, Oxford.

Perle, R.A. and Martinelli, Jr. (1976) *Avalanche Handbook.* US Department of Agriculture.

Petrie, G. and Price, R.J. (1966) Photogrammetric measurements of the ice wastage and morphological changes near the Casement Glacier, Alaska. *Canadian Joutnal of Earth Sciences.* **3**, 827-840.

Phillips, J.D. (1998)The role of spatial scale in geomorphic systems. *Geographical Analysis.* **20**(4), 308-317.

Pielke, R. (1984) *Mesoscale Meteorological Modeling.* Academic Press, New York.

Pielke, R., Baron, J., Chase, J., Copeland, Tkittel, T., Lee, T., Walso, R. and Zeng, X. (1996) Use of mesoscale models for simulation of seasonal weather and climate change for the Rocky Mountain States. In: *GIS and Environmental Modeling.*

Pielke, R. and Mehring, P. (1977) Use of mesoscale climatology in mountainous terrain to improve the spatial representation of mean monthly temperatures. *Monthly Weather Review.* **105**, 108-112.

Pielke, R. and Segal, M. (1986) Mesoscale circulations forced by differential terrain heating. In: Ray, R. (ed.) *Mesoscale Meteorology and Forecasting.* 516-548.

Pietroniro, A. and Leconte, R. (2000) A review of Canadian remote sensing applications in hydrology, 1995-1999. *Hydrological Processes.* **14**, 1641-1666.

Pike, R. (1988) The geometric signature: quantifying landslide-terrain types from digital elevation models. *Mathematical Geology*, **20**, 5 491-510.

Pike, R. (1995) Geomorphometry- progress, practice and prospect. *Zeitschrift Fur Geomophologie, Supplementband.* **101**, 221-238.

Pinchak, A.C. (1968) Avalanche activity on the Vaughan Lewis Icefall, Alaska. *Journal of Glaciology.* **7**(51), 441-448.

Plummer, M.A. and Phillips, F.M. (2003) A 2-D numerical model of snow/ice energy balance and ice flow for palaeoclimatic interpretation of glacial geomorphic features. *Quaternary Science Reviews.* **22**, 1389-1406.

Plüss, C. (1997) *The energy balance over an alpine snowcover: point measurements and areal distribution.* Zurcher Geographische Schriften. 65 Verlag Geographisches Institut ETH, Zurich.

Pomeroy, J.W., Gray, D.M. and Landine, P.G. (1993) The prairie blowing snow model: characteristics, validation, operation. *Journal of Hydrology.* **144**(1-4), 165-192.

Pomeroy, J.W., Marsh, P. and Gray, D.M. (1997) Application of a distributed blowing snow model to the Arctic. *Hydrological Processes.* **11**, 1451-1464.

Pomeroy, J.W., Gray, D.M., Shook, K.R., Toth, B., Essery, R.L.H., Pietroniro, A. and Hedstrom, N.R. (1998) An evaluation of snow accumulation and ablation processes for land surface modelling. *Hydrological Processes.* **12**, 2339-2367.

Pomeroy, J.W., Gray, D.M., Hedstrom, N.R. and Janowicz, J.R. (2002) Prediction of seasonal snow accumulation in cold climate forests. *Hydrological Processes.* **16**, 3543-3558.

Price, A.G. (1986) Modelling of snowmelt rates in a deciduous forest. In: Jones, H.G. and Orville-Thomas, W.J. (eds.) *Seasonal Snowcovers: Physics, Chemistry, Hydrology Symposium, Les Arcs, France, 13-25 July 1986.* NATO ASI Series C, Mathematical and Physical Sciences, Volume 211. 1521-165.

Price, A.G. and Dunne, T. (1976) Energy balance computations of snow melt in a subarctic area. *Water Resources Research.* **12**, 686-694.

Price, J.C. (1983) Estimating surface temperatures from satellite thermal infrared data – a simple formulation for the atmospheric effect. *Remote Sensing of Environment.* **13**, 353-361.

Prihodko, L and Goward, S.N. (1997) Estimation of air temperature from remotely sensed surface observations. *Remote Sensing of Environment.* **60**, 335-346.

Prowse, A.G. and Owens, I.F. (1982) Energy balance over melting snow, Craigieburn Range, New Zealand. *Journal of Hydrology (N.Z.).* **21**, 133-147.

Purves, R., Barton, J., Mackaness, W. and Sugden, D. (1998) The development of a rule-based spatial model of wind transport and deposition of snow. *Annals of Glaciology.* **26**, 197-202.

Purves, R.S., Mackaness, W.A. and Sugden, D.E. (1999) An approach to modelling the impact of snow drift on glaciation in the Cairngorm Mountains, Scotland. *Journal of Quaternary Science.* **14**(4), 313-321.

Rana, S. and Morley, J. (2002) Optimising visibility analyses using topographic features on the terrain. *Centre for Advanced Spatial Analysis. Working Paper Series. CASA* Paper 44. University College London. London.

Rasmussen, L.A. and Conway, H.B. (2003) Using upper-air conditions to estimate South Cascade Glacier (Washington, USA) summer balance. *Journal of Glaciology.* **49**, 456-462.

Raunholm, S., Sejrup, H.P. and Larsen, E. (2003) Lateglacial landform associations at Jæren (SW Norway) and their glaci-dynamic implications. *Boreas.* **32**, 462-475.

Raupach, M. and Finnigan, J. (1997) The influence of topography on meteorological variables and surface-atmosphere interactions. *Journal of Hydrology.* **190**, 182-213.

Rayner, J.N. (1971) *An Introduction to Spectral Analysis.* Pion Limited, London.

Reiter, E.R. (1963) *Jet Stream Meteorology.* University of Chicago Press, Chicago.

Rentsch, H., Welsch, W., Heipke, C. and Miller, M.M. (1990) Digital terrain models as a tool for glacier studies. *Journal of Glaciology.* **36**(124), 273-279.

Rhea, J.O. and Grant, L.O. (1974) Topographic influences on snowfall patterns in mountainous terrain. In: *Advanced Concepts and Techniques in the Study of Snow and Ice Resources.* National Academy of Science, Washington D.C. 182-192.

Richard, C. and Gratton, D. (2001) The importance of the air temperature variable for the snowmelt runoff modeling using the SRM model. *Hydrological Processes.* **15**, 3357-3370.

Richards, K.S. (1981) Introduction to morphometry, *in* Goudie, A.S. (ed.), *Geomorphological Techniques,* 25-30.

Ritter, P. (1987) A vector-based slope and aspect generation algorithm. *Photogrammetric Engineering and Remote Sensing.* **53**, 1109-1011.

Robinson, D.A. (1997) Hemispheric snow cover and surface albedo for model validation. *Annals of Glaciology.* **25**, 241-245.

Robinson, D.A. and Kukla, G. (1985) Maximum surface albedo of seasonally snow-covered lands in the northern hemisphere. *Journal of Climate and Applied Meteorology.* **24**, 402-411.

Roe, G.H. (2002) Modeling orographic precipitation over ice sheets: an assessment over Greenland. *Journal of .Glaciology.* **48**, 70-80.

Röthlisburger, H and Lang, H. (1987) Glacial hydrology. In: Gurnell, A.M and Clark, M.J. (eds.) *Glacio-Fluvial Sediment Transfer: an Alpine Perspective.* Wiley, New York. 207-284.

Running, S., Nemani, R. and Hungerford, R. (1987) Extrapolation of synoptic meteorological data in mountainous terrain and its use for simulating forest evaporatranspiration and photosynthesis, *Canadian Journal of Forestry Research.* **17**, 472-483.

Ryan, B. (1977) A mathematical model for diagnosis and prediction of surface winds in mountainous terrain. *Journal of Applied Meteorology.* **16**, 571-584.

Saintigon, M.F. de, (1976) Decroissance de temperatures et montagne de latitude moyenne: exemple des Alpes francaises du Nord. *Rev. Geog. Alp.* **64**, 483-494.

Sakai, A., Nakawa, M. and Fujita, K. (2002) Distribution characteristics and energy balance of ice cliffs on debris-covered glaciers, Nepal Himalaya. *Arctic, Antarctic and Alpine Research.* **34**(1), 12-19.

Sauberer, F. and Dirmhirn, I. (1951) *The influence of the radiation factor on the growing and shrinking of glaciers*. Translated by Van Tienhoven, J.C. Tanslation No. 51-1, US Army Corps of Engineers.

Schaerer, P. (1981) Avalanches. In: Gray, D.M. and Male, D.H. (eds.) *Handbook of Snow: Principles, Processes, Management and Use.* Pergammon Press, Oxford. 475-518.

Scheidegger, A. (1970) *Theoretical Geomorphology.* Springer-Verlag, Berlin, Heidelberg, New York, Second, Revised Edition.

Scherer, D., Gude, M., Gempeler, M. and Parlow, E. (1998) Atmospheric and hydrological boundary conditions for slushflow initiation due to snowmelt. *Annals of Glaciology.* **26**, 377-380.

Schmidt, D.S., Dent, J.D. and Schmidt, R.A. (1998) Charge-to-mass ratio of individual blowing-snow particles. *Annals of Glaciology.* **26**, 207-211.

Schmidt, J., Evans, I.S. and Brinkmann, J. (2003) Comparison of polynomial models for land surface curvature calculation. *International Journal of Geographical Information Science*, **17**(8), 797-814.

Schneeberger, C, Blatter, H., Abe-Ouchi, A. and Wild, M. (2001) Modelling changes in the mass balance of glaciers of the northern hemisphere for a transient 2 x CO_2 scenario. *Journal of Hydrology.* **282**(1-4), 145-163.

Schumm. S. and Lichty. R. (1965) Time, Space, and Causality in Geomorphology. *American Journal of Science*, **263**, 110-119.

Schwartz, K.P., Sideris, M.G. and Forsberg, R. (1990) The use of FFT techniques in physical geodesy. *Geophysical Journal International.* **100**, 485-514.

Schweiger, A.J. (2004) Changes in seasonal cloud cover over the Arctic seas from satellite ans surface observations. *Geophysical Research Letters.* **31**(12).

Segal, M. and Arritt, R. (1992) Nonclassical mesoscale circulations caused by surface heat-flux gradients. *Bulletin of the American Meteorological Society.* **73**, 593-604.

Semádani-Davies, A. (1997) Monthly snowmelt modelling for large-scale climatic change studies using the degree day approach. *Ecological Modelling.* **101**, 303-323.

Sevruk, B. (1983) Correction of measured precipitation in the Alps using the water equivalent of new snow. *Nordic Hydrology.* **14**, 49-58.

Sevruk, B. (1986) Correction of precipitation measurements. In: Sevruk, B. (ed.) *Proceedings of the international Workshop on the Correction of Precipitation Measurements. Instruments and observing methods.* Report No. 24 (WMO/TD no. 104). WMO, Geneva. 13-23.

Sharon, D. (1980) The distribution of hydrologically effective rainfall incident on sloping ground. *Journal of Hydrology* **46**(1/2), 165-188.

Sharon, D., Arazi, A., Khain, A., Huss, A., and Mahrer, Y. (1995) The Effect of Topography on the Local Distribution of Rainfall and Its Modeling by Means of CSU/RAMS, in Albert, P. and Lomas, J. (eds.), *Jehuda Neumann Symposium on Meso-Scale Models*, Jerusalem, January 4–6, 1995, Israel Meteorological Society, Bed Dagan, Israel, 125–128.

Silverman, B.W. (1986) *Density estimation for statistics and data analysis*. Chapman and Hall, London.

Simonoff, J.S. (1996) *Smoothing methods in statistics*. Springer, New York.

Sjoberg, R.W. and Horn, B.K.P. (1983) Atmospheric effects in satellite imaging of mountainous terrain. *Applied Optics*. **22**, 1702-1716.

Skidmore, A. (1989) A comparison of techniques for calculating gradient and aspect from a gridded DEM. *International Journal of Geographical Information Systems*. **3**(4), 323-334.

Smeets, C.J.P.P., Duynkerke, P.G. and Vugts, H.F. (1999) Observed wind profiles and turbulence fluxes over an ice surface with changing surface roughness. *Boundary-Layer Meteorology.* **92**, 101-123.

Smith, R.B. (2003) A linear upslope-time-delay model for orographic precipitation. *Journal of Hydrology.* **282**, 2-9.

Solbjørg, E. Heggem, F., Etzelmüller, B. and Berthling, I. (2001) Topographic radiation balance models: sensitivity and application in periglacial geomorphology. *Norsk Geografisk Tidsskrift.* **55**, 203-211.

Sorensen, P.A. and Lanter, D.P. (19930 Two algorithms for determining partial visibility and reducing data structure induced error in viewshed analysis. *Photogrammetric Engineering and Remote Sensing.* **59**, 1149-1160.

Spackman, E. (1993) Spatial variations in the average rainfall-altitude relationship in Great Britain: an approach using geographically weighted regression. *International Journal of Climatology.* **21**, 455-466.

Speight, J. (1974) A parametric approach to landform regions. *Special Publication of the Institute of British Geographers* **7**, 213-230.

Spreen, W.C. (1947) Determination of the effect of topography on precipitation. *Transactions of the American Geophysical Union.* **28**, 285-290.

Srasser, U., Corripio, J., Pellicciotti, F., Burlando, P., Brock, B. and Funk, M. (2004) Spatial and temporal variability of meteorological variables at Haut Glacier d'Arolla (Switzerland) during the ablation season 2001: Measurements and simulations. *Journal of Geophysical Research – Atmospheres.* **109**, 234-245.

Sridhar, V., Elliott, R.L. and Chen, F. (2003) Scaling effects on modelled surface energy-balance components usings the NOAH-OSU land surface model. *Journal of Hydrology.* **280**, 105-123.

Srinivasan, R. Cannon, M. and White, J. (1988) Landsat data destriping using power spectral filtering. *Optical Engineering.* **27**, 939-943.

Steinhauser, F. (1967) Methods of evaluation and rawing of climatic maps in mountainous countries. *Arch. Met. Geophys. Biokl.* **B 15**, 329-358.

Stenning, A., Banfield, C. and Young, G. (1981) Synoptic controls over katabatic layer characteristics above a melting glacier. *Journal of Climatology.* **1**, 309-324.

Stephens, G.L. (1984) Then parameterization of radiation for numerical weather prediction and climate models. *Monthly Weather Review.* 826-867.

Stoddart, D.R. (1997) (ed.) *Process and Form in Geomorphology.* Routledge, London.

Streten, N.A. and Wendler, G. (1968) The midsummer heat balance of an Alaskan maritime glacier. *Journal of Glaciology.* **7**(51), 431-440.

Sturman, A. (1987) Thermal influences on airflow in mountainous terrain. *Progress in Physical Geography.* **11**, 183-206.

Suckling, P.W. and Hay, J.E. (1976) Modelling direct, diffuse, and total solar radiation for cloudless days. *Atmosphere.* **14**, 298-308.

Sugita, M. and Brutsaert, W. (1993) Cloud effect in the estimation of instantaneous downward longwave radiation. *Water Resources Research.* **29**(3), 599-605.

Sumner, G. (1988) *Precipitation Process and Analysis*. Wiley, Chichester.

Susong, D., Marks, D. and Garen, D. (1999) Methods for developing time-series climate surfaces to drive topographically distributed energy-and water-balance models *Hydrological Processes*. **13**, 2003-2021.

Sutherland, D. (1984) In: *Quaternary Science Reviews.* **3**, 291-309.

Swift, L.W. Jr. (1976) Algorithm for solar radiation on mountain slopes. *Water Resources Research.* **12**(1), 108-112.

Tabony, R.C. (1985) Relations between minimum temperature and topography in Great Britain. *Journal of Climatology.* **5**, 503-520.

Takeuchi, Y., Naruse, R., Satow, K. and Ishikawa, N. (1999) Comparison of heat balance characteristics at five glaciers in the Southern Hemisphere. *Global and Planetary Change.* **22**, 201-208.

Tangborn, W. (1999) A mass balance model that uses low-altitude meteorological observations and the area-altitude distribution of a glacier. *Geografiska Annaler.* **81A**, 753-765.

Tappeiner, U., Tappeiner, G., Aschenwald, J., Tasser, E. and Ostendorf, B. (2001) GIS-based modelling of spatial pattern of snow cover duration in an alpine area. *Ecological Modelling.* **138**, 265-275.

Tarboton D.G., Bras, R.L. and Rodriguez-Iturbe, I. (1991). On the Extraction of Channel Networks from Digital Elevation Data. *Hydrological Processes.* **5**, 81-100.

Theakstone, W.H., Jacobsen, F.M. and Knudsen, N.T. (1999) Changes of snow cover thickness measured by conventional mass balance methods and by global positioning system surveying. *Geografiska Annaler.* **81A**(4), 767-776

Theobald D.M. (1989) Accuracy and bias issues in surface representation. In: Goodchild M.F. and Gopal (eds.) *Accuracy of spatial databases*, Taylor and Francis, London. 99-106.

Thorton, P., Running, S. and White, M. (1997) Generating surfaces of daily meteorological variables over large regions of complex terrain, *Journal of Hydrology.* **190**, 214-251.

Tian, Y., Weeks, E., Ide, K., Urbach, J., Baroud, C., Ghil, M. and Swinney, H. (2001) Experimental and numerical studies of an eastward jet over topography, *Journal of Fluid Mechanics*. 438, 129-157.

Tobler, W. (1969) Geographical Filters and their Inverses. *Geographical Analysis,* I, **3**, 234-253.

Tomlin, C.D. (1980) *Geographical Information Systems and Cartographical Modelling.* Englewood Cliffs, New York.

Tompkins, A. (2003) Impact of temperature and humidity variability on cloud cover assessed using aircraft data. *Quarterly Journal of the Royal Meteorological Society.* **29**, 2151-2170.

Travis, M.R., Elsner, G.H., Iverson, W.D., and Johnson, C.G. (1975) VIEWIT: computation of seen areas, slope, and aspect for land-use planning. *USDA F.S. Gen. Tech. Rep.* PSW-11/1975, 70p. Berkeley, California, U.S.A.

Turnipseed, A.A., Anderson, D.E., Blanken, P.D., Baugh, W.M. and Monson, R.K. (2003) Airflows and turbulent flux measurements in mountainous terrain part 1. canpy and local effects. *Agricultural and Forest Meteorology.* **119**, 1-21.

Tveito, O. (2003) Spatial distribution of winter temperatures in Norway related to topography and large scale atmospheric circulation. On line article.

Tveito, O.E. and Førland, E.J. (1999) Mapping temperatures in Norway applying terrain information, geostatistics and GIS. *Norsk geogr.tidsskrift.* **53**, 202-212.

Tveito, O., Førland, E.J., Heino, R., Hanssen-Bauer, I., Alexandersson, H., Dahlstrøm, I., Drebs, A., Kern-Hansen, C., Jónsson, T., Vaarby Laursen, E., and Westman, Y. (2000) Nordic Temperature Map. Klima Report no. 09/00 DNMI.

Unwin, D. (1973) The distribution and orientation of corries in northern Snowdonia, Wales. *Transactions of the Institute of British Geographers.* **58**, 85-97.

Unwin, D. (1975) *An Introduction to Trend Surface Analysis.* Concepts and Techniques in Modern Geography No. 5. Geo Abstracts, Norwich.

USGS (2004) USGS MIPS Filter Documentation
http://terraweb.wr.usgs.gov/software/mips/link/filter.html

Valentine, V., Echelmeyer, K. and Harrison, W. (2001) The use of GIS methods for determining changes in mountain glaciers. Abstract in *Proceedings of the Arctic GIS Workshop 22-24 Janaury 2001, Seattle Washington.*

Van der Avoird, E. and Duynkerke, P.G. (1999) Turbulence in katabatic flow: does it resemble turbulence in stable boundary layers over flat surfaces?. *Boundary-Layer Meteorology.* **92**, 39-66.

Verbunt, M., Gurtz, J., Jasper, K. Lang, H. Warmerdam, P. and Zappa, M. (2003) The hydrological role of snow and glaciers in alpine riverbasins and their distribution modeling. *Journal of Hydrology.* **282**, 36-55.

Verge, R. and Williams, G. (1981) Drift Control. In: Gray, S. and Male, D. (eds.) *Handbook of Snow*, Pergamom Press, Toronto. 630 – 647.

Von Buch, P. (1922) *cited in* Ahlmann, H.W. (1922) Glaciers in Jotunheimen and their physiography. *Geografiska Annaler.* **4**, 1-57.

Vosper, S. (2002) *A three- dimensional linearised numerical model for turbulent flow over hills. 3dvom2.6.5- Model description and documentation.* Meteorology Office Paper.

Vosper, S. (2003) Development and testing of a high resolution mountain-wave forecasting system. *Meteorological Application.* **10,** 75-86.

Waldinger, R. (1999) The spatial distribution of alpine glaciers and snowlines: influencing factors and controls. http://www.utexas.edu/depts/grg/hudson/grg394k/studentprojects/waldinger/waldinger.bak1

Walker, H. and Leone, J.M. Jr. (2001) The effect of elevation data representation on nocturnal drainage wind simulations. In: (ed.) *GIS and Environmental Modelling.* 105-110.

Walmsley, J., Slamon, J. and Taylor, P. (1982) On the application of a model of boundary-layer flow over low hills to real terrain. *Boundary Layer Meteorology.* **23**, 17-46.

Wand, M.P. and Jones, M.C. (1995) *Kernel smoothing.* Chapman and Hall, London.

Wang, J., Robinson, G.J. and White, K. (1996) A fast solution to local viewshed computation using grid-based digital models. *Photogrammetric Engineering and Remote Sensing.* **62**, 1157-1164.

Wang, J., White, K. and Robinson, G.J. (2000) Estimating surface net solar radiation by use of Landsat-5 TM and digital elevation models. *International Journal of Remote Sensing.* **21**(1), 31-43.

Warren, C.R. (1991) Terminal environment, topographic control and fluctuations of West Greenland glaciers, *Boreas.* **20**, 1–15.

Warren, S. (1982) Optical properties of snow. *Review of Geophysical Space Physics.* **20**(1), 67-89.

Weibel, R. and BrŠndli, M. (1995) Adaptive methods for the refinement of digital terrain models for geomorphic applications. *Z.Geomorph.N.F. Suppl.Bd.* **101**, 13-30.

Weibel, R. and Heller, M. (1991) Digital Terrain Modelling. In: Maguire, D.J., Goodchild, M.F. and Rhind, D.W. (eds.) *Geographical Information Systems*, Volume 1. Longman, Harlow. 269-297.

Wendler, G. and Ishikawa, N. (1974) The effect of slope, exposure and mountain screening on the solar radiation of McCall Glacier, Alaska: A contribution to the international hydrological decade. *Journal of Glaciology.* **13**, 213-226.

Wendler, G. and Weller, G. (1974) A heat-balance study on McCall Glacier, Brooks Range, Alaska: a contribution to the international hydrological decade. *Journal of Glaciology.* **13**, 13-26.

Weston, K. and Roy, M. (1994) The directional – dependence of the enhancement of rainfall over complex topography. *Meteorological Applications.* **1**, 267-275.

Whiteman, C.D. (2000) *Mountain Meteorology: Fundamentals and applications*. University Press Oxford, Oxford.

Wieringa, J. (1986) Roughness-dependent geographical interpolation of surface wind speed averages. *Quarterly Journal of the Royal Meteorological Society*. **112**, 867-889.

Wilcock, P.R. and Iverson, R.M. (eds.) (2003) *Prediction in Geomorphology. Geophysical Monograph; 135.* American Geophysical Union. Washington.

Wilks, D.S. (1995) Theoretical probability distributions. In: Dmowska, R. and Holm, J.R. (eds.) *Statistical Methods in the Atmospheric Sciences: An Introduction.* Volume 59 of the International Geophysics Series. Academic Press. 76-111.

Williams, L.D., Barry, R.G. and Andrews, J.T. (1972) Application of computed global radiation for areas of high relief. *Journal of Applied Meteorology.* **11**, 526-533.

Willis, I.C., Arnold, N.S. and Brock, B.W. (2002) Effect of snowpack removal on energy balance, melt and runoff in a small supraglacial catchment. *Hydrological Processes.* **16**, 2721-2749.

Wilson, B. and Gallant, . (1997) Terrain based approaches to environmental resource evaluation In: Lane, S.N., Richards, K.S. and Chandler, J.H. (eds.) *Landform Monitoring, Modelling and Analysis.* Wiley, Chichester.

Winstral, A. and Marks, D. (2002a) Simulating wind fields and snow redistribution using terrain-based parameters to model snow accumulation and melt over a semi-arid mountain catchment. *Proceedings of the 59th Eastern Snow Conference.* Stowe, Vermont, USA. 161-180.

Winstral, A. and Marks, D. (2002b) Simulating wind fields and snow redistribution using terrain-based parameters to model snow accumulation and melt over a semi-arid mountain catchment. *Hydrological Processes*. **16**, 3185-3603.

Wiscombe, W. and Warren, S. (1980) A model for the spectral albedo of snow. 1: pure snow. *Journal of Atmospheric Science.* **37**, 2712-2733.

Wise, S.M. (1998) The effect of GIS interpolation errors on the use of DEMs in geomorphology" In S.N.Lane, K.S.Richards and J.H.Chandler (eds) *Landform Monitoring, Modelling and Analysis*. Wiley, Chichester, 139-164.

Wise, S.M. (2004) Error assessment for Digital Terrain Models
http://www.shef.ac.uk/geography/staff/wise_stephen/dtm/dtm.htm

WMO (1986) *Intercomparison of models for snowmelt runoff.* Operation Hydrology Report 23 (WMO No. 646).

Wood, J.D. (1986) *The Geomorphological Characterisation of Digital Elevation Models*, Unpublished PhD. Thesis, University of Leicester, UK.

Wood, J.D. (1996) Scale-based characterization of digital elevation models. In: (ed.) *Frontiers of Complexity.* 163-175

Wood, J.D. and Fisher, P.F. (1993) Assessing interpolation accuracy in elevation models. *IEEE Comp. Graphics and Applications.* **13**(2), 48-56.

Xin, L., Koike, T. and Guodong, C. (2002) Retrieval of snow reflectance from Landsat data in rugged terrain. *Annals of Glaciology.* **34**, 31-37.

Yamada, T., Suizu, S., Nishimura, H. and Wakahama, G. (1979) Relationships between snow distribution and climate in mountain areas. In: (ed.) *Sea Level, Ice, and Climatic Change.* IAHS Publication No. 131. 109-118.

Yoshino, M.M. (1975) *Climate in a Small Area.* University of Tokyo Press, Tokyo.

Young, K., and Woo, M. (1997) Modelling Net Radiation in a High Arctic Environment using Summer Field Camp Data. *International Journal of Climatology.* **17**, 1211 – 1229.

Zevenberg, L.W. and Thorne, C.R. (1987) Quantitative analysis of land surface topography. *Earth Surface Processes and Landforms.* **12**, 47-56.

Zhang, T., Barry, R.G. and Haeberli, W. (2001) Numerical simulations of the influence of the seasonal snow cover on the occurrence of permafrost at high latitudes. *Norsk Geografisk Tidsskrift.* **55**, 261-266.

Zheng, X. and Basher, R. (1996) Spatial modeling of New Zealand temperature normals. *International Journal of Climatology.* **16**, 307-319.

APPENDIX I

GUIDE TO RUNNING THE MODEL FOR A NEW GEOGRAPHICAL AREA

To run the glacier prediction model for a selected geographical region the following data and modelling steps are required.

Data requirements

Terrain data: A UTM WGS 1984 georeferenced gridded DEM of the area: resolution is not restricted although coarse resolutions will produce coarser scale results.

Climate data: Monthly precipitation, temperature, cloud and wind speed surfaces of the area at the same spatial resolution as the terrain data. If available data is restricted to point climate stations, regression and predictive approaches outlined in Chapter six can be employed to generate continuous surfaces for the study area. The accuracy of glacier accumulation area predictions will be highly dependent upon the quality of these surfaces (Chapter eight).

Validation data: An optional data requirement forms a validation dataset, this can be used to assess the accuracy of the delineated accumulation areas. This could consist of a topographic map, a remotely sensed image or a field survey.

Modelling Steps

Prediction of glacier accumulation areas follows four main steps.

I. Prediction of surface albedo.
II. Prediction of surface temperature
III. Prediction of surface energy balance
IV. Prediction of surface melting.

Each of these steps needs to be performed for each month, as outlined below and the Java programs outlined in the ReadMe file (seen below)(downloadable from the author's website). Each month's outputs are used as the following month's inputs.

The Java programs required to run the prediction model are downloadable from the author's website and read in and out ArcInfo ascii rasters. Programs can be edited to alter local read and write locations.

****
JAVA Program files for snow accumulation prediction model
Author: Katherine Arrell
Contact: K.Arrell@leeds.ac.uk
****

This is read-me file for the Java program. This folder contains the following files:

Each process Java program has a run (main method) file - RunFileName.java
Each Java program has a class file - this is a compiled program - FileName.class

Comments are included in the program prefixed with //
Open the .java file that is not prefixed with Run to view the process code within a text or Java editor E.G Notepad or NetBeans
You will need Java Runtime environment to run the programs

FourierRaster.java RunFourierRaster.java	This program creates artificial rasters for FFT transform
UpSlope.java RunUpslope.java	This program identifies and records upslope obstacles
GetDownWindSlope.java RunGetDownWindSlope.java	This program identifies and records downwind slope
Deflection.java RunDeflection.java	This program measures wind deflection by terrain
GetSurfaceTemp.java RunGetSurfaceTemp.java	This program calculates surface temperature
NetRad.java RunNetRad.java	This program predicts net radiation receipt within a DEM
GetAlbedo.java RunGetAlbedo.java	This program predicts surface albedo
MeltingMonth.java RunMeltingMonth.java	This program predicts monthly snow melt
Count.java RunCount.java	This program counts values within a raster

Additional files required to run the programs are included in the folder named: RequiredFiles
These files contain classes from Jo Wood's Landserf v2.0 package

STRUCTURE OF ACCUMULATION PREDICTIONS